

ACS SYMPOSIUM SERIES **353**

# Supercomputer Research in Chemistry and Chemical Engineering

**Klavs F. Jensen**, EDITOR

*University of Minnesota*

**Donald G. Truhlar**, EDITOR

*University of Minnesota*

Developed from a symposium sponsored  
by the Division of Industrial and Engineering Chemistry  
of the American Chemical Society, the Minnesota Supercomputer  
Institute, Cray Research, Inc., and ETA Systems, Inc.,  
at the Industrial and Engineering Chemistry Winter Symposium,  
Minneapolis, Minnesota  
March 16-17, 1987



American Chemical Society, Washington, DC 1987



## Library of Congress Cataloging-in-Publication Data

Supercomputer research in chemistry and chemical engineering.

(ACS symposium series, ISSN 0097-6156; 353)

“Developed from a symposium sponsored by the Division of Industrial and Engineering Chemistry of the American Chemical Society, the Minnesota Supercomputer Institute, Cray Research, Inc., and ETA Systems, Inc., at the Industrial and Engineering Chemistry Winter Symposium, Minneapolis, Minnesota, March 16-17, 1987.”

Bibliography: p.  
Includes index.

1. Chemistry—Data processing—Congresses.
2. Supercomputers—Congresses.

I. Jensen, Klavs F., 1952– . II. Truhlar, Donald G., 1944– . III. American Chemical Society. Division of Industrial and Engineering Chemistry. IV. American Chemical Society. Division of Industrial and Engineering Chemistry. Winter Symposium (1987: Minneapolis, Minn.) V. Series.

QD39.3.E46S927 1987 542'.8 87-24127  
ISBN 0-8412-1430-1

Copyright © 1987

American Chemical Society

All Rights Reserved. The appearance of the code at the bottom of the first page of each chapter in this volume indicates the copyright owner's consent that reprographic copies of the chapter may be made for personal or internal use or for the personal or internal use of specific clients. This consent is given on the condition, however, that the copier pay the stated per copy fee through the Copyright Clearance Center, Inc., 27 Congress Street, Salem, MA 01970, for copying beyond that permitted by Sections 107 or 108 of the U.S. Copyright Law. This consent does not extend to copying or transmission by any means—graphic or electronic—for any other purpose, such as for general distribution, for advertising or promotional purposes, for creating a new collective work, for resale, or for information storage and retrieval systems. The copying fee for each chapter is indicated in the code at the bottom of the first page of the chapter.

The citation of trade names and/or names of manufacturers in this publication is not to be construed as an endorsement or as approval by ACS of the commercial products or services referenced herein; nor should the mere reference herein to any drawing, specification, chemical process, or other data be regarded as a license or as a conveyance of any right or permission, to the holder, reader, or any other person or corporation, to manufacture, reproduce, use, or sell any patented invention or copyrighted work that may in any way be related thereto. Registered names, trademarks, etc., used in this publication, even without specific indication thereof, are not to be considered unprotected by law.

PRINTED IN THE UNITED STATES OF AMERICA

**American Chemical Society**  
**Library**  
**1155 16th St., N.W.**  
**Washington, D.C. 20036**

# ACS Symposium Series

**M. Joan Comstock, *Series Editor***

## *1987 Advisory Board*

**Harvey W. Blanch**  
University of California—Berkeley

**Alan Elzerman**  
Clemson University

**John W. Finley**  
Nabisco Brands, Inc.

**Marye Anne Fox**  
The University of Texas—Austin

**Martin L. Gorbaty**  
Exxon Research and Engineering Co.

**Roland F. Hirsch**  
U.S. Department of Energy

**G. Wayne Ivie**  
USDA, Agricultural Research Service

**Rudolph J. Marcus**  
Consultant, Computers &  
Chemistry Research

**Vincent D. McGinniss**  
Battelle Columbus Laboratories

**W. H. Norton**  
J. T. Baker Chemical Company

**James C. Randall**  
Exxon Chemical Company

**E. Reichmanis**  
AT&T Bell Laboratories

**C. M. Roland**  
U.S. Naval Research Laboratory

**W. D. Shults**  
Oak Ridge National Laboratory

**Geoffrey K. Smith**  
Rohm & Haas Co.

**Douglas B. Walters**  
National Institute of  
Environmental Health

# Foreword

The ACS SYMPOSIUM SERIES was founded in 1974 to provide a medium for publishing symposia quickly in book form. The format of the Series parallels that of the continuing ADVANCES IN CHEMISTRY SERIES except that, in order to save time, the papers are not typeset but are reproduced as they are submitted by the authors in camera-ready form. Papers are reviewed under the supervision of the Editors with the assistance of the Series Advisory Board and are selected to maintain the integrity of the symposia; however, verbatim reproductions of previously published papers are not accepted. Both reviews and reports of research are acceptable, because symposia may embrace both types of presentation.

# Preface

**T**HE 1987 WINTER SYMPOSIUM of the Division of Industrial and Engineering Chemistry, hosted by the Minnesota Supercomputer Institute, was supported by grants from the American Chemical Society, the Minnesota Supercomputer Institute, Cray Research, Inc., and ETA Systems, Inc. The symposium consisted of four half-day sessions with four lectures per session and a two-part poster session with 15 poster papers. This book includes chapters by the lecturers plus five papers contributed by the session chairs. All contributions were refereed anonymously according to usual procedures of the ACS Symposium Series.

This volume appears with a short time lag because of the cooperation of the participants. Fifteen of the lecturers and both out-of-town session chairs brought their manuscripts to the symposium. We thank Robin Giroux of the ACS Books Department for her coordination of the publisher's tasks.

**KLAVS F. JENSEN**  
Minnesota Supercomputer Institute  
and Department of Chemical  
Engineering and Materials Science  
University of Minnesota  
Minneapolis, MN 55455

**DONALD G. TRUHLAR**  
Minnesota Supercomputer Institute  
and Department of Chemistry  
University of Minnesota  
Minneapolis, MN 55455

April 1, 1987

## Chapter 1

# Supercomputer Research in Chemistry and Chemical Engineering

### An Introduction

Klavs F. Jensen<sup>1</sup> and Donald G. Truhlar<sup>2</sup>

<sup>1</sup>Minnesota Supercomputer Institute and Department of Chemical Engineering and  
Materials Science, University of Minnesota, Minneapolis, MN 55455

<sup>2</sup>Minnesota Supercomputer Institute and Department of Chemistry,  
University of Minnesota, Minneapolis, MN 55455

This chapter gives a selected overview of the current status of supercomputing research in chemistry and chemical engineering and places the research areas discussed in the rest of the book in the context of current work.

The first ACS Symposium volume on supercomputing was published in 1981 (1). That symposium already included mature applications of the Cray-1 machine, usually thought of as the first supercomputer. A more recent supercomputer symposium, the Second International Conference on Vector Processors in Computational Science, held at Oxford in August, 1984, is published as Volume 37 in Computer Physics Communications. In their introduction the editors of the latter proceedings commented that the most notable change in the field over the past few years had not been new hardware but rather the sophistication of the hardware and the maturity of the user community. To a large extent that observation holds for the 1984-87 period as well, especially regarding the use of supercomputer resources in chemistry and chemical engineering.

Multiple processors have been widely discussed as a tool for achieving high compute speeds, but most of the progress on achieving higher computation speeds for applications has been achieved by better utilization of the vectorization strategies that were already possible even in 1981. The hardware available at the time of this writing is about a factor of two-to-four faster, on a per processor basis, than that available on the original Cray-1, and the fastest supercomputers have at most four processors. Since most calculations are still run in the single-processor mode though, we have achieved far less than an order of magnitude in effective top speed in five years. Nevertheless many application fields have advanced to systems much more than five times as demanding, not only because of the increases in user and software sophistication mentioned above, but also because of algorithmic advances and the availability of a greater number of supercomputers, allowing more processing hours to be devoted

0097-6156/87/0353-0001\$06.00/0  
© 1987 American Chemical Society

to specific applications and allowing utilization of this kind of resource at a greater number of sites. It is unfortunately true though that this kind of research is still severely underfunded, and this accounts for the fact that its potential is still largely untapped.

Although the increase in speed of supercomputers has not been dramatic in the last five years, there has been a very notable hardware advance in the size of computer memories. Whereas the 1-Megaword memory of the Cray-1 was once considered generous, the opportunities created by the Control Data Corporation Cyber 205, with 8 Megawords of real memory and a huge virtual address space, and the Cray-2, with 256 Megawords of real memory, are much greater and these opportunities are only very recently being appreciated and exploited. Another advance that is rapidly becoming more important is networking. As users get accustomed to taking advantage of the best available hardware, software, and databases in terms of what can be reached easily by network, even if it is across the continent or the ocean, supercomputer capabilities may be expected to have very significant effects on larger and larger areas of chemistry and engineering.

In keeping with the above remarks on the relative importance over the last few years of hardware advances versus utilization and application-mode advances, the present volume centers on the latter. The chapters are arranged in terms of four underlying scientific subfields. First comes the study of electronic structure as based on the Schrödinger equation. Next comes the study of equilibrium systems, based on thermodynamics and equilibrium statistical mechanics, including also some aspects of quantum mechanics, especially with regard to quantized degrees of freedom and spectra. The third application area consists of the study of kinetics and dynamics, either classical or quantum, but at the microscopic level where complications like flow do not come in. Quasiequilibrium theories of rate processes, such as transition state theory, technically belong to dynamics, but may also be considered with equilibrium properties, since the techniques are similar. The fourth and final set of chapters deals with complexities of flow and transport. In general the applications in the later sections must include at least some of those involved in the earlier ones; thus in some sense the organizational principle is one of increasing complexity. For example, the study of dynamics always presupposes some knowledge of interaction energies such as intermolecular forces and binding energies, and such knowledge may usually be traced back to quantum mechanics, spectra, or properties of equilibrium systems. Similarly many problems involving transport also involve chemical reactions and at a detailed level all transport is intimately related to the microscopic atomic and molecular dynamics. This kind of connection is discussed at greater length by Clementi and Liu (Chapter 14), and it comes more and more into play in the large-scale simulations that are made possible by supercomputers. This creates some clear problems in assigning a few of the chapters to one of the four sections of the book. Nevertheless we have

made choices, and in general a chapter is assigned to the farthest down of the sections to which it is directly relevant.

As large-scale computations make their presence felt in more and more areas of chemistry and chemical engineering, and as the context of these applications develops a significant history, it becomes impossible to include a comprehensive discussion in any one volume. Thus the present set of chapters is more illustrative than complete. And although many of the chapters contain reasonably complete introductory remarks, the book cannot serve to put whole subfields into focus. This is all symptomatic of a proceedings in a rapidly developing field. In the rest of this introduction we try to complement the proceedings papers by discussing some of the work in the book and a small subset of other interesting and especially recent work in the field, with the goal of slightly broadening the context in which the proceedings and the current status of supercomputer research in these fields is viewed. The topics will be discussed in terms of roughly the same ordering scheme as used for arranging the topics in the book.

### Electronic Structure

In many respects materials science is the branch of chemistry that has the most obvious opportunities to gain from the supercomputer revolution. Experimental, empirical knowledge of materials is difficult to organize without theoretical understanding. For many material properties such understanding is in principle afforded by the analysis of accurate electronic wavefunctions and energies and in favorable cases unknown material properties can even be predicted. But the calculations require enormous computations even when they are feasible, hence supercomputers are required. An example in the present book is afforded by calculations on metal-containing compounds (Chapter 2). Recent advances in methodology have improved the reliability of *ab initio* calculations on such systems. New calculations give insight into the nature of the bonding and define the two- and three-body parameters used for modelling larger clusters. Comparison of *ab initio* and model results for Al clusters and  $\text{Cu}_{18}\text{Be}$  suggests that composite materials can also be modelled based on parameterization from the *ab initio* calculations. The theoretical calculations are especially useful for obtaining model interaction parameters for interactions of unlike atoms. These are much harder than like-atom interactions to obtain from experimental information on bulk properties, in particular because they don't even occur in single-component metals. The theoretical studies indicate that large clusters are required before the bulk structure becomes the most stable. The study of adsorbates on  $\text{Be}_{13}$  shows that the chemistry of clusters can be very different from the bulk as a result of the cluster's increased freedom to expand and distort. This leads to interesting insight into the differences between bulk metallic systems and small metallic clusters, which may be very active in catalysis but which are hard to characterize experimentally. The need for powerful supercomputer resources becomes very evident when we consider the



eventual necessity to extend the theoretical studies of multicomponent systems and clusters to include vibrational effects and nonzero temperatures.

Another example from the field of materials science is provided by the chapter (Chapter 5) on conducting polymers and materials with nonlinear optical properties. The potential understanding to be derived from the availability of supercomputers for this research is immense. The materials under study are expected to play a critical role in the future development of molecular electronic and optical devices for information storage and communication. Large-scale *ab initio* simulations lead to detailed understanding of properties which are hard to extract from experimental data or from more approximate and less demanding calculations. The methods of quantum chemistry have reached a point where they constitute tools of semi-quantitative accuracy and have significant predictive value. Further developments for quantitative accuracy are still needed for many purposes though and will require the application of reliable methods for describing electron correlation in large systems. The need for supercomputer power will be very acute for such correlated calculations.

Another area where electronic structure calculations can have an enormous impact on industrial chemistry is the design of efficient catalysts. Very few catalytic systems have been studied so far because of the large computer time requirement, which is where supercomputers come in. The most complete protostudy currently available in this area is the modelling of the full catalytic cycle of olefin hydrogenation by Wilkinson catalyst as calculated by Morokuma, Danle, and Koga with the *ab initio* molecular orbital method. Even though these authors committed about 200 hours of supercomputer time to the project they still had to make several simplifications, such as replacing some phenyl groups by hydrogen, neglecting solvent effects, and ignoring side reactions. Clearly even more resources are required to make the modelling more realistic, but already these authors were able to determine the rate determining step, to predict a possible intermediate, and to illustrate where and why there is a special sensitivity to choice of ligand. This kind of calculation is clearly very stimulating.

One important aspect of the supercomputer revolution that must be emphasized is the hope that not only will it allow bigger calculations by existing methods, but also that it will actually stimulate the development of new approaches. A recent example of work along these lines involves the solution of the Hartree-Fock equations by numerical integration in momentum space rather than by expansion in a basis set in coordinate space (2). Such calculations require too many floating point operations and too much memory to be performed in a reasonable way on minicomputers, but once they are begun on supercomputers they open up several new lines of thinking.

Finally, we mention the very encouraging successes combining atomic natural orbitals and full CI calculations for small molecules (Almlöf, Bauschlicher, and Taylor). With this method the singlet-triplet splittings

of  $\text{CH}_2$  and  $\text{SiH}_2$  have been computed to an accuracy of about 0.1 kcal/mol, and the dissociation energies of CH and OH are within 0.03 eV of experiment. The extension of these techniques to transition metals will be very interesting.

### Equilibrium Properties and Spectra

The rapid advances in electronic structure applications are causing the field to be discussed under many new names, such as computer-aided molecular design or computer-aided materials design (both abbreviated CAMD as a rather obvious variation on CAD/CAM). One especially promising subfield concerns the design of bioactive molecular agents (computer-aided macromolecular design).

The interaction energies important for biological systems are often the weak nonbonding forces that govern such phenomena as conformational changes, tertiary structure of proteins, and the hydrophobic interaction. Because of the weakness of these interactions, the electronic energy cannot be considered apart from such additional factors as the thermal energy and entropy of the substrate and the solvent. Biochemical systems, being complex, clearly require large calculations. Once the possibility of these calculations is opened up, however, interesting approaches become available that illustrate some extremely important advantages of the computational mode of science over the experimental, observational mode. For example, many researchers are very excited about an approach to calculating free energy differences in which one of the compared systems is incrementally "mutated" into the other; this kind of process is clearly impossible in the laboratory, but of course we can nevertheless learn a lot from it theoretically. This technique, whose recent developments are due to Jorgensen and McCammon and their coworkers, is being applied to the binding constants of drugs to macromolecular receptors, the effects of site-specific mutation on enzyme catalysis, and solvent effects (3). This technique is discussed further in the chapter by Berendsen (Chapter 7), who has applied it to the binding of enzyme inhibitors to enzymes.

Another biochemical example (Chapter 8) involves the conformational exploration of an octapeptide with the aim thereby to develop a breast cancer vaccine. Other work by the same author, in this case on the 41-mer of a tetrapeptide, leads to constructive suggestions for a malarial vaccine. It is of course very encouraging to see these humanitarian applications of supercomputers. Rational drug design and protein engineering are clearly fields in which molecular mechanics and conformational analysis combined with interactive computer graphics and molecular dynamics have exciting opportunities to lead to progress. Even though the fields are young, the status of computer-aided drug (and vaccine) design is very greatly advanced compared to its status when an ACS Symposium Series volume (4) appeared on this subject in 1979; that volume may be consulted for a snapshot of this very active field just before the availability of supercomputers.

Most common approaches to simulations, whether biochemical or otherwise, rely on some variant of the Monte Carlo method. In general a Monte Carlo method is a way to compute a quantity by interpreting it as the average of a random sample, usually a computer-generated one. The method was pioneered for the study of small systems and is still very useful for such systems. For example, one of the poster papers at the Symposium concerned vectorization strategies for binary collisions of Ar with CO and He with  $\text{CH}_3\text{CN}$  (5). The Monte Carlo method becomes more important, however, for large, complex systems with many degrees of freedom, for which it may be the only practical simulation technique. Since these systems are often treated classically, a variant of the Monte Carlo method in which the classical equations of motion are used to generate the ensemble, is often used; this is called molecular dynamics. Monte Carlo calculations may require enormous amounts of computer time, taxing any conceivable computer system. The Monte Carlo method yields imprecise estimators with a variance that may be reduced by increasing the size of the sample set. Because the samples may be uncorrelated, Monte Carlo methods are well suited to the next generation of highly parallel computers. A challenge to theorists will be to include quantum effects where required so as not to rely on large classical simulations just because they can finally be carried out. Several groups are now working on large-scale quantum simulations. For example, in one study (6), an excess electron in a sample of 300 water molecules at room temperature was simulated by path integral techniques involving up to 1000-point discretizations of the electron path. The highly quantum nature of this system is obvious from the small mass of the electron, which has a thermal free-particle deBroglie wavelength of about 17 Å.

A repeated theme in discussions of supercomputer simulations is that they allow us to ask and answer questions that cannot be asked experimentally, especially questions about details and about the "why" of various processes. (This same note was struck in the discussion above of electronic properties of materials.) One striking example of this kind of extra detail was provided by a recent classical dynamical simulation of DNA counterion motions in aqueous salt solutions (7). This simulation required calculating the sequence of counterion positions on a very fine time grid, while the total time involved in determining the simulated experimental observable, which was an NMR signal, is very long. Each step requires the calculation of roughly 10,000 interactions among the charged atoms of the polymer and the small ions. The calculation required about 40 hours of computer time on the Minnesota Supercomputer Center Cray-2 computer. Without supercomputers the simulation would have been completely infeasible. Clementi and Lie (Chapter 14) have also considered the counterion structure near DNA, and have considered the time scale question of how long do water molecules near DNA retain their liquid structure as compared to the time scale for those far away; this is clearly another question that would be hard to answer by experiment.

Levy (Chapter 6) has also explored the use of supercomputers to study detailed properties of biological macromolecules that are only indirectly accessible to experiment, with particular emphasis on solvent effects and on the interplay between computer simulations and experimental techniques such as NMR, X-ray structures, and vibrational spectra. The chapter by Jorgensen (Chapter 12) summarizes recent work on the kinetics of simple reactions in solutions. This kind of calculation provides examples of how simulations can address questions that are hard to address experimentally. For example Jorgensen's simulations predicted the existence of an intermediate for the reaction of chloride ion with methyl chloride in DMF which had not been anticipated experimentally, and they indicate that the weaker solvation of the transition state as compared to reactants for this reaction in aqueous solution is not due to a decrease in the number of hydrogen bonds, but rather due to a weakening of the hydrogen bonds.

Supercomputers become more and more useful, and the insights they can generate become more and more unique, as the complexity of the system modelled is increased. Thus interfacial phenomena are a very natural field for supercomputation. In addition to the examples in this volume it may be useful to mention the work of Linse on liquid-liquid benzene-water interfaces, which he studied with 504 H<sub>2</sub>O molecules, 144 C<sub>6</sub>H<sub>6</sub> molecules, and 3700 interaction sites. He generated over 50 million configurations in 56 hours on a Cray-1A, and he was able to quantitatively assess the sharpness of the interfacial density gradient, which is very hard to probe experimentally. Similarly Spohr and Heinzinger have studied orientational polarization of H<sub>2</sub>O molecules at a metallic interface, which is also hard to probe experimentally.

### Microscopic Dynamics

The present volume contains only one chapter (Chapter 11) on small-molecule gas-phase dynamics. In this field the role of the supercomputer is diverse, but perhaps the most critical area is allowing essentially exact quantal dynamics to be carried out for previously intractable systems. A recent example is the essentially exact calculation of the reaction threshold for D atoms reacting with vibrationally excited H<sub>2</sub> ( $\underline{g}$ ). The same research group has completed the first numerically converged solutions of the Schrödinger for reaction probabilities in a system with an atom heavier than an isotope of H, in particular O + H<sub>2</sub> → OH + H. Both calculations were carried out with a new basis-set approach that specifically takes advantage of the large memory and high vector speed of the Cray-2. Another new computational approach to small-molecule dynamics that is stimulated in part by the availability of fast vector machines is based on the computation of quantal propagators with very large basis sets by recursive transformation of a large sparse Hamiltonian matrix into a much smaller tridiagonal one; a recent application is to time-dependent energy deposition in a molecule by a laser ( $\underline{g}$ ). Abraham (10) has provided an

excellent review of recent simulations on two-dimensional condensation and melting at surfaces and in thin films. His review also provides some relevant background reading for the chapter in the present volume by Gilmer and Grabow (Chapter 13). This review also contains an exciting chapter section entitled "super problems for super computers" (*sic*), in which the author discusses some of the very large computational problems that still defy attack.

We have already mentioned the application of supercomputers to biochemical simulations. Internal dynamics may play an important role in such simulations. An example would be enzyme binding-site fluctuations that modulate reactivity or the dynamics of antigen-antibody association (11). In the specific case of diffusion-controlled processes, molecular recognition may occur because of long-range steric effects which are hard to assess without very expensive simulations (12).

In addition to the already mentioned insights into materials properties obtained through electronic structure calculations, materials science has much to gain from supercomputer simulations of microscopic and macroscopic elements of materials processing. Microelectronic components, optical devices (solid state lasers and detectors), optical fibers and high performance ceramics are artificially microstructured materials made by carefully controlled nucleation, solidification, deposition, and etching procedures. Since the performance of the materials strongly depends on the degree of crystalline perfection and the nature of the interface, a microscopic understanding of the atomic scale growth and etching processes is essential. Direct molecular dynamic simulations of crystal growth from the vapor are discussed by Gilmer and Grabow (Chapter 13). The difficulty in this procedure is the large amount of computation required to obtain the atomic trajectories and the large number of atoms required because of the very slow growth rates. Present computation power may not be sufficient for a direct simulation of molecular beam epitaxy of an elemental semiconductor (e.g. Si) and it limits studies of the many fundamental problems of interface formation and growth found in molecular beam epitaxy of compound semiconductor structures (e.g. AlGaAs/GaAs). Because of the small correlation between samples in molecular dynamic simulations of crystal growth, this application seems well suited for new, special purpose, highly parallel computers.

Metal-hydrogen systems and superionic conductors are examples of other solid systems of great technological importance on which progress has been hampered by the inability to make realistic enough simulations. The reader is directed to recent work by Gillan and Catlow and their coworkers for recent progress in studying these kinds of systems.

Supercomputers can be directed to the study of techniques as well as materials and processes. For example, one can simulate neutron scattering experiments with the goal of elucidating the effects of approximations usually made in "standard" treatments of the experimental data.

The understanding of fluid flow is one of the areas where supercomputing has already had a significant impact. General fluid mechanics falls

outside the scope of this volume, but applications of fluid mechanics to chemical problems are characteristic of the chapters grouped under the transport heading. As an interesting transition between the microscopic dynamics and macroscopic transport chapters, Clementi and Lie (Chapter 14) describe the simulation of a macroscopic fluid flow example in terms of constituent molecular motions. Another example of molecular simulation of fluids concerns transport and fluid properties in microporous media as discussed by Davis *et al.* (Chapter 15). Because of the molecular or nanometer dimensions involved in these systems, experimental characterization is difficult. Moreover, fluids can be strongly inhomogeneous in the confined pore space so that the usual macroscopic theories of fluid structure and transport may not be applicable. Thus, supercomputer simulations become an important tool for understanding fluid structure and transport in microporous media as well as for developing appropriate theories suitable for analyzing related macroscopic phenomena, such as processes involving porous catalysts (e.g. hydrodesulfurization), lubrication and wetting, drying of paper products and clay dispersions, and enhanced oil recovery. The study of these practical problems are also natural areas for supercomputer research which will be discussed in the subsequent section.

### Transport Processes

Macroscopic analysis of complex chemical processes, including materials processing, requires numerical solution of the equations for local conservation of momentum, energy, mass, and chemical species on irregular domains and often with free boundaries. In their general form, the equations are nonlinear partial differential equations in space and time, where the nonlinearities are introduced by the constitutive equations for fluxes (e.g. multicomponent diffusion, non-Newtonian flow), reaction rates, convective coupling between flow and mass/energy transport, and the dependence of boundary shapes on field variables. These nonlinear interactions severely complicate the numerical solution of the conservation equations by causing transitions in the solution structure, including multiple solutions, spatially and temporally periodic solutions, and even chaotic phenomena. Other complications are caused by multiple length and time scales. Length scales different than those characteristic of the domain arise from the nature of the problem; for example, in the case of a catalytic reactor the active material may be 5 nm metal crystals imbedded in a 5 mm porous particle stacked among thousands of particles in a 0.50 m diameter tube. In addition, different length scales arise as a result of boundary and internal layers caused by rapid changes in the field variables near solid boundaries, interfaces, and reaction fronts. For example, the flame front in a combustion system may be a few mm wide while the characteristic dimension of the system is in order of meters. Multiple time scales originate from the mixing of transport processes and reaction kinetics, which have order-of-magnitude differences in their time scales, and they lead to stiff integration problems that can tax or even exceed the

capabilities of current supercomputer hardware. Ortega and Volgt (13) review numerical methods for partial differential equations on supercomputers along with a brief description of applications to fluid dynamics, reservoir simulation, and weather prediction. They specifically discuss the influence of parallel and vector computing on algorithm design and selection.

The nonlinear nature of detailed models of complex chemical processes is a central issue in their solution and one that contributes heavily to computational demands. If the nonlinearities are strong enough it may be essentially impossible to find a solution for a particular set of parameters from a simple initial guess. In such cases the solution must be found by connecting it by homotopy to a known solution of the same set of equations but with a different set of parameters or perhaps a solution to a simpler, but analogous problem. The procedure involves following the solution family for varying parameters and it is commonly referred to as continuation. Thus, even though a single calculation perhaps could be carried out on a VAX8600 in a few hours, the large number of calculations involved in reaching the desired solution by continuation necessitates supercomputing. Furthermore, because the nonlinearities lead to non-uniqueness of the steady state and a multitude of periodic phenomena, it is necessary to understand the structure of solution space, which again means tracking solution families for varying parameters by using specialized continuation techniques (13-16). If the stability of the solution is also of interest, the eigenvalues of the linearized problem must be determined. For large-scale systems this requires extensive supercomputer calculations and many problems still defy attack.

The nonlinear behavior of physicochemical systems is brought up in several of the application examples in this volume. Brown *et al.* (Chapter 17) consider the evolution of cellular microstructures during directional solidification, which is a nonlinear free-surface problem. Jensen *et al.* (Chapter 19) describe nonlinear flow transitions adversely affecting the growth of compound semiconductor superlattices by organometallic chemical vapor deposition, while Smooke addresses a flame extinction problem (Chapter 20). Both sets of investigators use an arclength continuation technique due to Keller (14). Kevrekidis (Chapter 18) specifically addresses computational issues in the analysis of complex dynamics that cannot be understood through local stability considerations. Because of the nature of the instabilities underlying the dynamic phenomena, it is extremely difficult, if not impossible, to extract an understanding of the transitions between the various periodic behaviors through simple simulations of the physical experiments. Two illustrative examples based on flame front and thermal convection descriptions are presented.

In the remaining parts of this introductory chapter we return to discussion of specific applications of supercomputing -- starting with materials growth and proceeding through increasingly complex physicochemical systems. One of the application areas where large-scale simulations have already had an impact on understanding is the process of crystal growth

from the melt including morphological solidification phenomena. The latter is a classical problem and is addressed by Brown *et al.* (Chapter 17), who use large scale numerical finite element solutions of two-dimensional models to study pattern selection of the solidification front. Central issues in this fundamental problem include the cell shape, the apparent wavelength for the crystallization front, and the evolution to dendritic growth with side branches. The simulations provide significant new insight into the morphological stability phenomena. However, to address the central question of whether the observed dynamics are deterministic or a "snapshot" of a stochastic behavior would require the next generation of supercomputers.

The growth of the thin films from the gas phase by chemical vapor deposition (CVD) involves a complex mixture of homogeneous reactions, surface reactions, fluid flow, heat transfer, and mass transfer that is difficult to understand without a comprehensive model of the process. The work of Kee, Coltrin, and coworkers (17, Chapter 18) represents a significant effort to include detailed kinetic models in CVD reactor simulations analogous to what has been done in combustion modelling. By using sensitivity analysis they derived a mechanism of 20 reactions from a detailed pyrolysis mechanism for  $\text{SiH}_4$  involving 120 elementary reactions. Their simulations demonstrated the importance of including detailed descriptions of homogeneous and heterogeneous reactions in CVD reactor models and they compared well to species measurements by laser spectroscopy (18). This type work can only be realized by the use of supercomputers. In addition to treating Si deposition, the authors' contribution to the present volume (Chapter 18) also addresses the implementation of large-scale models of physicochemical processes, e.g. the computation and organization of thermodynamic quantities, transport coefficients, and rate constants. This is an issue that transcends CVD analysis to simulation of other complex chemically reacting systems.

Jensen *et al.* (Chapter 19) focus on two- and three-dimensional transport phenomena as well as transient behavior in the growth of thin films and superlattices of compound semiconductors (e.g. GaAs/AlGaAs). Previous CVD models have been based on simplified transport descriptions unable to provide a complete enough picture of spatial and temporal variations in the deposition rate. However, accurate control of the deposition rate is essential to the further development of advanced optoelectronic and microelectronic devices. Because of the complex gas flows in irregular domains, supercomputing is necessary to simulate the process models. Further analysis will have to consider transient, three-dimensional reacting flow phenomena which will severely tax, and in some cases exceed, the capabilities of current supercomputer hardware. There are many other opportunities for supercomputer applications in materials processing in addition to the crystal growth studies in this volume. For example plasma and laser processing (19,20) could gain considerably from studies of detailed process models. The goal of modelling materials processing should be the theoretical understanding and, eventually, quantitative



prediction of the relationship between macroscopic processing conditions and the microstructure of the materials, which governs the mechanical, optical, and electrical properties.

Combustion of gaseous and solid fuels is another application area that has much to gain from large-scale simulations of detailed process models. The issues are similar to those in CVD, but complicated by large energy releases and multiphase flows. The questions related to the organization of the database of rate constants, transport coefficients, and thermodynamic quantities are essentially the same as in CVD modelling. In fact, the aforementioned work by Kee *et al.* (Chapter 18) benefits from their extensive experience in combustion modelling. Large-scale computational analysis of combustion involves several critical elements including the chemistry code, the fluid flow treatment, and the resolution of sharp flame fronts. The latter issue, which is part of the general problem of differing length scales in detailed process models, poses significant challenges to numerical procedures. The size of large-scale physicochemical problems combined with the need to accurately resolve local structures (e.g. a flame front) necessitates the use of dynamic, self-adaptive, local grid modifications. Uniform gridding on the basis of the length scale of the local phenomenon would lead to finite element/finite difference discretizations with a huge number of equations whose solution would be prohibitively expensive on even the largest supercomputers. Therefore, adaptive gridding is a rapidly evolving area in numerical analysis for large-scale models. Two examples from gaseous and solid fuel combustion modelling are included in the present volume (Chapters 20 and 21). A recent survey by Babuska *et al.* (21) shows the principal directions of work adaptive gridding techniques.

Atmospheric chemistry modelling to predict the effect of pollutants (intentionally or unintentionally released) on the environment is a natural application for supercomputing. The problem involves a large number of reactions among hydrocarbons, fluorocarbons, nitrogen compounds, and sulfur compounds in sunlight (22,23). In addition, these reactions have rate constants that differ by as much as 14 orders of magnitude. Simulations of the transport processes in the atmosphere require three-dimensional fluid flow simulations with very large grids and many transporting constituents. Furthermore, aerosol particle nucleation and growth play important roles in the overall behavior. Supercomputer simulations of atmospheric chemistry not only increase the scientific understanding of such complex systems but also provide a tool for regulatory agencies to study effects of existing and proposed pollutant emission standards.

There are several other applications where significant gains could be made through the use of supercomputer simulations of detailed physical models. Reservoir simulations was one of the first areas where the value of supercomputing was recognized by industrial companies. It is only possible to measure a few properties of interest to enhanced oil recovery. Furthermore, field tests are extremely expensive, and the monetary

decisions involved in the choice of methods for driving the oil out of a particular reservoir can equal or perhaps even exceed the cost of supercomputer hardware. Thus, supercomputer simulations become a more cost effective method than field experiments (25). Chemical plant design is another area that could benefit from the use of supercomputers. A large chemical plant involves many different units including separation, reactors and heat exchangers, which are interconnected. Some of the units may require the same detailed modelling as the above mentioned applications. Therefore the plant model will involve large numbers of interconnected equations offering considerable challenges to supercomputing (26). The large-scale plant simulations could serve design, optimization, and control purposes.

### Conclusions

Many significant applications of supercomputing in chemistry and chemical engineering are emerging as facilities for large-scale computations become more and more accessible. The present volume intends to illustrate recent advances and applications, but already the field is so broad that no single volume can put all the subfields into perspective. The purpose of combining chemistry and chemical engineering applications in a single symposium was to emphasize their strong relationships, and we hope that these relationships will be further strengthened by continuing interactions between these fields.

### Literature Cited

1. Lykos, P.; Shavitt, I. *Supercomputers in Chemistry*; American Chemical Society: Washington, 1981.
2. Alexander, S. J.; Monkhorst, H. J.; to be published.
3. Selbel, G. *Chemical Design Automation News* 1987, **2**, 1.
4. Olson, E. C.; Christoffersen, R. E. *Computer-Assisted Drug Design*; American Chemical Society: Washington, 1979.
5. Cochrane, D.; Truhlar, D. G. *Parallel Computing*, in press, and additional work to be published elsewhere.
6. Schnltker, J.; Rossky, P. J. *J. Chem. Phys.* 1987, **86**, 3471.
7. Reddy, M. R.; Rossky, P. J.; Murthy, C. S. *J. Phys. Chem.*, to be published.
8. Haug, K.; Schwenke, D. W.; Shima, Y.; Truhlar, D. G.; Zhang, J.; Kouri, D. J. *J. Phys. Chem.* 1986, **90**, 6757.
9. Friesner, R. A.; Brunet, J.-P.; Wyatt, R. E.; Leforestler, C. *Int. J. Supercomputer Applications*, in press.
10. Abraham, F. F. *Advances in Physics* 1986, **35**, 1.
11. McCammon, J. A. *Rep. Prog. Phys.* 1984, **47**, 1.
12. McCammon, J. A.; Northrup, S. H.; Allison, J. A. *J. Phys. Chem.* 1986, **90**, 3901.

13. Ortega, J. M.; Volght, R. G. *SIAM Review* 1985, **27**, 149.
14. Keller, H. B. *SIAM J. Scient. and Stat. Comp.* 1983, **4**, 573.
15. Kubicek, M.; Marek, I. *Computational Methods in Bifurcation Theory and Dissipative Structures*; Springer Verlag: New York, 1983.
16. Rheinboldt, W. C. *Numerical Analysis of Parameterized Nonlinear Equations*; Wiley Interscience: New York, 1986.
17. Coltrin, M. E.; Kee, R. J.; Miller, J. A. *J. Electrochem. Soc.* 1984, **131**, 425; 1986, **133**, 1206.
18. Brelland, W. G.; Coltrin, M. E.; Ho, P. *J. Appl. Phys.* 1986, **59**, 3276; **60**, 1505.
19. Graves, D. B.; Jensen, K. F. *IEEE Trans. Plasma Sci.* 1986, **14**, 78.
20. Skouby, D. C.; Jensen, K. F. *SPIE Proceedings* 1987, **797**; *J. Appl. Phys.* to be published.
21. Babuska, I.; Zienkiewicz, O. C.; Gago, J.; Oliviera, E. R. *Accuracy Estimates and Adaptive Refinements in Finite Element Computations*; John Wiley and Sons: New York, 1986.
22. McRae, G. J.; Goodin, W. R.; Seinfeld, J. H. *J. Computational Phys.* 1982, **45**, 1.
23. Rood, R. B.; Kaye, J. A.; Nielsen, J. E.; Schoerberl, M. R.; Geller, M. A. *Phys. Scr.* 1987, **35**, in press.
24. Ewing, R. E.; In ref. 21, pp. 299.
25. Levesque, J. M. *Soc. Pet. Eng. J.* 1985, **25**, 275.
26. Stadthere, M. A.; Vegeals, J. A. *Chem. Eng. Proc.* 1985, **81**, 21.

RECEIVED July 6, 1987

## Chapter 2

# Theoretical Approaches to Metal Chemistry

Charles W. Bauschlicher, Jr.<sup>1</sup>, Stephen R. Langhoff<sup>1</sup>, Harry Partridge<sup>1</sup>,  
Timur Halicioglu<sup>2</sup>, and Peter R. Taylor<sup>3</sup>

<sup>1</sup>Ames Research Center, National Aeronautics and Space Administration,  
Moffett Field, CA 94035

<sup>2</sup>Department of Materials Science and Engineering, Stanford University,  
Stanford, CA 94305

<sup>3</sup>ELORET Institute, Sunnyvale, CA 94087

Recent advances in methodology have made possible accurate ab initio calculations on transition metal diatomic systems as well as small (3-6 atom) simple metal clusters. These accurate calculations can in turn be used to define two- and three-body potentials for use in modelling much larger clusters. Calculations on clusters containing Be, Al and Cu atoms illustrate the accuracy of current work and the diversity of metal bonding. The structure and reactivity of small clusters vary dramatically with size, and very large clusters are required before the cluster structure approaches that of the bulk. For example, even though the bulk structure of Be is hcp, the fcc structure is still considerably more stable than hcp for a 55 atom Be cluster. Comparison of ab initio and model calculations for small Al clusters demonstrates that it is necessary to include three-body terms in the model for quantitative results. The impact of adsorbates on metal-metal bonding is studied for  $\text{Be}_{13}\text{X}_n$  and  $\text{Al}_{13}\text{X}_n$  clusters. The optimal sites for adsorption are often different for small clusters than the bulk, owing to the enhanced ability of small clusters to distort.

Computational chemistry is being applied at NASA Ames to numerous problems in chemistry, physics and materials science. One important application is to problems in re-entry physics that are intractable to experiment, such as the extreme conditions occurring in the bow shock wave of the aeroassisted orbital transfer vehicle (AOTV) (1). Nonequilibrium radiation is a significant component of the heating, owing to the large blunt heat shield of the AOTV and its trajectory through the thin upper atmosphere. Accurate knowledge of the chemistry of hot mixtures of nitrogen and oxygen are required for input into computational fluid dynamics (CFD) codes involved in the heat shield design. Also, the chemistry of hydrogen and air mixtures is being studied to aid design of supersonic combustion ramjet engines.

0097-6156/87/0353-0016\$06.00/0  
© 1987 American Chemical Society

In addition to the gas-phase work, we are computing (2) the vibrational spectra and rotational barriers of polymer fragments to help interpret experiments. By achieving a better understanding of polymers and their chemistry, we hope to design longer lifetime and more corrosion resistant polymers.

Another major computational effort is in the area of metals and their chemistry, which comprises the subject of this manuscript. The studies are directed towards both catalysis and the development of improved materials, such as stronger matrix composites. The materials and gas phase work have some overlap. For example, surface recombination affects the heating on the AOTV heat shield and on the walls of the scramjet. In addition, desorption of these molecules from the walls of the scramjet could impact the chemistry in the flow.

The study of molecular systems containing metal atoms, particularly transition metal atoms, is more challenging than first-row chemistry from both an experimental and theoretical point of view. Therefore, we have systematically studied (3-5) the computational requirements for obtaining accurate spectroscopic constants for diatomic and triatomic systems containing the first- and second-row transition metals. Our goal has been to understand the diversity of mechanisms by which transition metals bond and to aid in the interpretation of experimental observations.

While accurate calculations on transition metal compounds are restricted to three or fewer transition metal atoms, it is possible to consider much larger clusters of Al and Be atoms. We have considered (6-9) Al clusters of up to six atoms using correlated wave functions, and Al<sub>13</sub>, Be<sub>13</sub> and Be<sub>55</sub> at the SCF level. These calculations give insight into how the bonding changes with cluster size. Since even for these simple metals the ab initio calculations are time consuming, we have interfaced (9) our ab initio methods with a parameterized model approach where the potential is expanded in two- and three-body interaction terms. For single component systems, these potentials can be determined from either bulk data or calculations. With the parameterized model we can consider larger clusters and identify interesting clusters for further ab initio study. The parameterized model can also be used for multi-component materials, although in this case the two- and three-body parameters are not easily deduced from bulk data. The model approach appears well-suited for the study of alloys and matrix composite materials, especially large multi-component systems not directly amenable to ab initio study, but it must rely on ab initio calculations to define the two- and three-body interaction potentials.

The study of small metal clusters and their chemistry is an active area of experimental research (10). Gas phase experiments have shown (11) a very large variation in reactivity with cluster size, but have been unable to determine the geometry of the cluster, or the adsorption site if the clusters have been reacted with other molecules. Experiments on supported clusters have determined (12) the average metal-metal bond lengths, but only for a distribution of clusters, and the effect of the support is unknown. The reactivity and metal-metal bond lengths are often considerably different from the well-studied perfect crystal faces. Theoretical calculations on metal clusters are therefore important for determining optimal geometries, and to explain the large changes in reactivity with cluster size.

The cluster model is also useful for studying the chemistry of perfect crystal faces. With current super computers, it has become possible to model Ni<sub>25</sub>X and Ni<sub>25</sub>X<sub>5</sub> clusters (where X=O, F, S, Cl), and thereby study changes in bonding with coverage. These calculations (13) explain the experimental observation that oxygen shows a large shift in vibrational frequency with coverage, while sulfur does not. The theoretical study of perfect crystals, as well as coverage dependence where experimental data is available for comparison, also helps to delineate the accuracy of the small metal cluster work.

Section II describes recent improvements in methodology that have significantly improved the accuracy of calculations on small metal clusters. Section III describes the calculation of some accurate dimer and trimer potentials, and the insight they give into the nature of metal chemistry. Section IV reviews the work on small metal clusters and discusses how the ab initio and parameterized model approaches are interfaced. Section V contains our conclusions.

### Methodological Advances

In this section we give a brief overview of recent methodological advances that have significantly improved our capabilities for accurate calculations on molecules containing transition metals as well as on small clusters. Accurate results for transition metals require both large one-particle basis sets including high angular momentum functions and a careful treatment of the correlation (or n-particle) problem. Recently we have carried out (14-20) full configuration-interaction (FCI) calculations on molecules to assess the accuracy of correlation methods that truncate the n-particle expansion. The most important result from the FCI benchmark calculations is that a carefully designed complete-active-space self-consistent field (CASSCF) calculation to optimize the orbitals, followed by a multi-reference singles plus doubles configuration-interaction (MRCI) calculation from the important configurations in the CASSCF wave function, gives consistently the best agreement with the FCI. Hence this is the method of choice when the resulting configuration expansion is of manageable size (i.e. less than about 1 million configurations).

One important implication of the FCI studies is that if the n-particle problem is treated at the CASSCF/MRCI level, the limiting factor in the accuracy of the wave function becomes the one-particle basis. However, a recent development by Almlöf and Taylor (21) has greatly increased the size of the gaussian primitive valence and polarization basis sets that can be used in CI calculations. This is accomplished by using general contractions with coefficients determined from the natural orbitals of CI calculations on the atoms. Atomic natural orbitals (ANOs) define a method of truncating the basis set to equal accuracy in each shell. The following prescription has led to extremely accurate results for excitation energies and dissociation energies of diatomic molecules (15,16). In a double-zeta plus polarization ANO basis set we find a CASSCF/MRCI treatment that reproduces the FCI result for the n-particle problem, and this CASSCF/MRCI treatment is then taken to near the one-particle limit. As shown later, this approach (17) gives a definitive prediction for the ground state of  $Al_2$ , even though the lowest two triplet states are separated by less than  $200\text{ cm}^{-1}$ . At present, we are optimizing (22) ANO contractions for the first-row transition metals that are based on the average of the  $3d^n 4s^2$  and  $3d^{n+1} 4s^1$  occupations to satisfy the extensive basis set requirements for an accurate description of transition metal diatomics.

Although a properly designed CASSCF/MRCI treatment in a large ANO basis set is expected to give quantitative results for molecular systems including transition metals, it can be computationally very intensive. Indeed, this approach quickly becomes intractable for larger clusters, especially when a large number of electrons are correlated. We have, therefore, devoted considerable effort to calibrating single reference-based correlation methods against CASSCF/MRCI and FCI calculations. When the molecular system is reasonably well described by a single reference configuration, we have found that the coupled pair functional (CPF) approach (23), a size-consistent reformulation of

SDCI, gives an accurate representation of the molecular state. This is in contrast to single-reference singles-plus-doubles CI (SDCI), which is often not very satisfactory for transition-metal diatomics, especially when the molecular state arises from a mixture of atomic states with different *d* occupations.

The CPF approach gives quantitative agreement with the experimental spectroscopic constants (24-25) for the ground state of  $\text{Cu}_2$  when large one-particle basis sets are used, provided that relativistic effects are included and the 3*d* electrons are correlated. In addition, CPF calculations have given (26) a potential surface for  $\text{Cu}_3$  that confirms the Jahn-Teller stabilization energy and pseudorotational barrier deduced (27-28) from the  $\text{Cu}_3$  fluorescence spectra (29). The CPF method has been used (9) to study clusters of up to six aluminum atoms.

The choice of both the one-particle and the molecular orbital basis is much more critical for transition-metal diatomics than for first-row molecular systems. Extensive basis sets and correlation treatments are required for quantitative accuracy in the transition metal atom excitation energies, in contrast to first-row atoms where very accurate results are obtained even when a common molecular orbital basis is used for all states. The Hartree-Fock (HF) description is often not satisfactory for molecular states of transition-metal diatomics when the wave function contains a significant mixture of two atomic states with different 3*d* occupations. This is a common occurrence for transition metals such as Ni where the  $3d^94s^1$  and  $3d^84s^2$  atomic states are nearly degenerate (30). For example, the  $^2\Delta$  ground state of NiH requires a high level of correlation treatment for an accurate description (31,32). At the HF level, the state is almost of pure  $3d^94s^1$  character and is too ionic, as manifested by a calculated dipole moment that is significantly too large. At both the CASSCF and CPF level too much  $3d^84s^2$  character is mixed into the wave function, resulting in a dipole moment that is smaller than experiment. The tendency of the CPF method to overestimate the  $3d^84s^2$  character in the wave function in NiH is greatly reduced by a modified form (33) of CPF (denoted MCPF). The MCPF method gives more quantitative results for transition metal systems that are not well described by a single reference configuration, especially when this arises from configurational mixing of two atomic states. For NiH the MCPF method gives a dipole moment in good agreement with large CASSCF/MRCI treatments and with experiment (32,34).

For transition metal diatomic systems such as the first- and second-row hydrides, carbides, nitrides, oxides and sulfides (3,32,35-40), we use either a CASSCF/MRCI or CPF (MCPF) approach with the goal of determining accurate spectroscopic constants and a detailed understanding of the bonding. For triatomic systems and larger clusters where the CASSCF/MRCI procedure is not feasible, we generally use the CPF method. For very large clusters, particularly when adsorbates are present, correlation effects are generally not included and the resulting insight is of a more qualitative nature, e.g. trends in geometries and vibrational frequencies. For very large clusters and composite materials we have adopted a modelling approach that describes the total interaction potential (cohesive energy) of the system in the form of a many-body expansion. As a first approximation only two- and three-body interactions were taken into consideration, and they were further approximated by a Lennard-Jones and an Axilrod-Teller function (41), respectively. These functions have very simple analytical forms, and were chosen in this study to acquire insight into the utility of model-potential methods. The parameters in these functions are defined from either bulk data or from our accurate calculations on diatomic and triatomic systems. More details of this approach are given later when we present our modelling results for aluminum clusters.

### Accurate Calculations on Small Molecules

Theoretical studies on the first- and second-row transition-metal hydrides, carbides, nitrides, oxides, sulfides and dimers have given considerable insight into transition-metal compounds. On the left side of the row where the valence  $(n+1)s$  and  $nd$  orbitals are more comparable in spatial extent, the bonding often involves a considerable degree of  $s$ - $d$  hybridization on the metal. As one proceeds to the middle of the row where the low-lying atomic states are high-spin coupled, there is a tendency to form multiple bonds. However, the bonding is weak since the  $d$  orbitals have smaller overlap than do  $s$  and  $p$  orbitals and there is a considerable loss in  $d$ - $d$  exchange energy. Extensive correlation treatments are required to obtain accurate bond energies. Low levels of correlation treatment give bonds that are both too long and too weak. Correlation of the  $d$  electrons is essential for quantitative results, especially on the right side of the row. Also  $s$ - $d$  correlation effects can have an important differential effect, even when the  $s$ - $d$  correlation energy is a small fraction of the  $d$ - $d$  correlation energy.

Many of these points are well illustrated by  $\text{Cu}_2$ , which has become a benchmark for theoretical calculations owing to its relative simplicity and the availability of accurate experimental data. The theoretical spectroscopic constants are quite poor unless the  $3d$  electrons are correlated, even though both  $\text{Cu}$  atoms nominally have a  $3d^{10}4s^1$  occupation. In fact, quantitative agreement with experiment is achieved only if both the  $3d$  and  $4s$  electrons are correlated, both higher excitations and relativistic effects are included, and large one-particle basis sets, including several sets of polarization functions, are used (24,25). This level of treatment is difficult to apply even to  $\text{Cu}_3$ , let alone larger  $\text{Cu}$  clusters.

Although our long-range goal is accurate studies of transition metal clusters, the computational complexity precludes accurate studies of these clusters at present. We have therefore focused our cluster work on simple metal ( $\text{Be}$  and  $\text{Al}$ ) clusters as well as mixed  $\text{Cu}$  simple-metal clusters. For these metals accurate calculations of diatomic and triatomic potentials are feasible. Hence it is possible to define accurate two- and three-body interactions for use in modelling large clusters, and possible to compare the *ab initio* and model results for clusters of moderate size (4-6 atoms). In this section, devoted to accurate calculations on small molecules, we describe our theoretical work on  $\text{Al}_2$ , while in the next section we describe our theoretical studies of  $\text{Al}$  clusters. The  $\text{Al}_2$  diatomic is of considerable interest in its own right, because of the controversy (43,44) concerning the identity of the ground state.

The spectroscopic constants at the FCI and MRCI level for the  $X^3\Pi_u$  and  $A^3\Sigma_g^-$  states of  $\text{Al}_2$  are summarized in Table I using different ANO basis sets. The MRCI and FCI spectroscopic constants agree exceptionally well using both the  $(4s3p1d)$  and  $(4s3p2d)$  ANO basis sets. The results using the single-reference based SDCI and CPF methods are not as good, especially for  $T_e$ . Since the FCI calibration calculations show that the MRCI treatment accounts for nearly all of the valence correlation effect on  $T_e$ , the MRCI  $T_e$  should converge to the valence limit as the one-particle basis becomes complete. Extension to a large ANO basis places the  $^3\Pi_u$  state just  $165\text{ cm}^{-1}$  below the  $^3\Sigma_g^-$  state, and this result is expected to be very close to the FCI result in this basis. The inclusion of relativistic effects using first-order perturbation theory (45) increases the MRCI  $T_e$  value by only  $9\text{ cm}^{-1}$  in the  $(6s5p3d2f)$  ANO basis. Also, including the  $2s$  and  $2p$  electrons in the correlation treatment increases  $T_e$  by only  $26\text{ cm}^{-1}$  at the CPF level. Hence, neither relativistic effects nor  $2s$  and  $2p$  correlation are likely to change our prediction of a  $^3\Pi_u$  ground state. Our best value for



Table I. Theoretical spectroscopic constants for the  ${}^3\Pi_u$  and  ${}^3\Sigma_g^-$  states of  $Al_2$ 

	${}^3\Pi_u$		
	$r_e$ ( $a_o$ )	$\omega_e$ ( $cm^{-1}$ )	$D_e$ (eV)
MRCI <sup>a</sup> (4s3p1d)	5.241	265	1.206
FCI (4s3p1d)	5.240	265	1.206
MRCI (4s3p2d)	...	...	1.231
FCI (4s3p2d)	...	...	1.233
MRCI (6s5p3d2f)	5.153	277	1.401
MRCI+Rel <sup>b</sup> (6s5p3d2f)	5.154	277	1.386
EXPT <sup>c</sup>			1.55±0.15
	${}^3\Sigma_g^-$		
	$r_e$ ( $a_o$ )	$\omega_e$ ( $cm^{-1}$ )	$T_e$ ( $cm^{-1}$ )
MRCI (4s3p1d)	4.790	325	252
FCI (4s3p1d)	4.790	325	289
MRCI (4s3p2d)	...	...	128
FCI (4s3p2d)	...	...	158
MRCI (6s5p3d2f)	4.710	344	165
MRCI+Rel <sup>b</sup> (6s5p3d2f)	4.710	343	174
EXPT <sup>c</sup>	4.660	350	

<sup>a</sup>The MRCI calculation is a second-order CI from all configurations in the CASSCF wave function resulting from all arrangements of the 3s and 3p electrons in the 3s and 3p orbitals.

<sup>b</sup>The Darwin and mass velocity contributions were included using first-order perturbation theory.

<sup>c</sup>Huber and Herzberg, Ref. 42.

$D_0$  of 1.40 eV for  $\text{Al}_2$  is within the error bounds of the experimental value of  $1.55 \pm 0.15$  eV determined by Stearns and Kohl (46) using a Knudsen cell mass spectrometric method and assuming a  ${}^3\Sigma_g^-$  ground state.

Since accurate modelling of larger clusters requires the inclusion of a three-body interaction function, we have devoted considerable effort to the understanding of triatomic systems containing Cu, Al and Be. This work is also directed at understanding the nature of bonding in alloys and composites. Although it is not possible to compute the potential energy surface of these triatomics to the same accuracy as for the diatomics, a good estimate of the errors in the triatomic calculations can be obtained by performing the same level of calculations on the diatomics.

Like the  $\text{Al}_2$  molecule, the  $\text{Cu}_3$  molecule is interesting in its own right, and has been the subject of many experimental and theoretical papers (see for example 26-28 and references therein). Our ab initio study of  $\text{Cu}_3$  gives a  ${}^2B_2$  ground state corresponding to a  $C_{2v}$  Jahn-Teller distortion away from a  ${}^2E'$  equilateral triangle geometry. The  ${}^2B_2$  state was found to lie  $59 \text{ cm}^{-1}$  below the  ${}^2A_1$  state and  $280 \text{ cm}^{-1}$  below the  $D_{3h}$  equilateral geometry, thus confirming the pseudorotation barrier and Jahn-Teller stabilization energy deduced by Truhlar and Thompson (27) from an analysis of the fluorescence spectrum of Rohlfing and Valentini (29). Based on our experience (25) with  $\text{Cu}_2$  where both higher excitations and relativistic effects are important, our ab initio study of  $\text{Cu}_3$  included relativistic effects via first-order perturbation theory and correlation effects using the CPF formalism. However, this level of correlation treatment required some reduction in the one-particle basis set and yielded errors of  $0.056 a_0$  in  $r_e$ ,  $0.08 \text{ eV}$  in  $D_e$  and  $8 \text{ cm}^{-1}$  in  $\omega_e$  for  $\text{Cu}_2$  compared with the accurate experimental values. This provides a good estimate of the errors in the bond lengths and binding energy of the  $\text{Cu}_3$  cluster. This level of treatment for  $\text{Cu}_3$  is expected to yield an accurate three-body interaction term for use in modelling Cu clusters.

The existence of two nearly degenerate triplet states with substantially different  $r_e$  values in  $\text{Al}_2$  manifests itself in the  $\text{Al}_3$  (9) and  $\text{CuAl}_2$  (47) triatomics in terms of low-lying states with considerably different geometries. For example,  $\text{Al}_3$  has three nearly degenerate states; the  ${}^4A_2$  and  ${}^4B_1$  states, which are two Jahn-Teller components of a  ${}^4E'$  state, and the  ${}^2A'_1$  state. Experiments yield conflicting data as to the ground state. Matrix isolation ESR (48) shows a quartet state with equivalent Al atoms (either an equilateral or pseudorotating triangle), while magnetic deflection experiments have been interpreted (49) as showing a doublet ground state. Like the  ${}^3\Pi_u$  and  ${}^3\Sigma_g^-$  states of  $\text{Al}_2$ , the three states of  $\text{Al}_3$  have different geometries, with a  $0.39 a_0$  variation in bond length and  $15^\circ$  variation in bond angle. Since one expects the bonding in small clusters to arise from a mixture of these low-lying states in  $\text{Al}_2$  and  $\text{Al}_3$ , we have averaged the results for the low-lying states for evaluation of the two- and three-body parameters. In the next section we describe our ab initio and parameterized model results for larger Al clusters.

Our theoretical results (47) for the  $\text{Cu}_x\text{Be}_y$  systems are summarized in Table II. For  $\text{CuBe}_2$  we find two linear structures, Cu-Be-Be where the bonding is very directional owing to the formation of s-p hybrids, and Be-Cu-Be where the bonding is much more delocalized.  $\text{Cu}_2\text{Be}$  also has two low-lying linear structures, one of which contains delocalized metal bonding. In both isomers of the  $\text{Cu}_2\text{Be}$  and  $\text{CuBe}_2$  linear structures, the very directional bonding implies a repulsive three-body contribution. As we show later, this large three-body force explains the apparently strange behavior of Be on a Cu(111) surface (50). As in the case of  $\text{Cu}_2$  and  $\text{Cu}_3$ , the ab initio calculations give more than input into

Table II. Spectroscopic constants for selected  $\text{Cu}_x\text{Be}_y$  systems

	SDCI	CPF
	CuBe $^2\Sigma^+$ (8s6p4d/4s3p) basis	
$r_e(a_0)$	4.098	4.090
$D_e(\text{eV})$	0.55	0.68
	(9s7p4d3f1g/6s3p3d1f) basis	
$r_e(a_0)$	4.022	3.999
$D_e(\text{eV})$	0.77	0.92
	Cu <sub>2</sub> Be linear symmetric $^1\Sigma_g^+$	
$r_e(a_0)$	4.089	4.017
atomization (eV)		2.87
$D_e(\text{CuBe-Cu})(\text{eV})$		2.18
	linear asymmetric $^1\Sigma^+$	
$r_e(\text{Cu-Cu})(a_0)^a$	4.462	4.415
$r_e(\text{Cu-Be})(a_0)$	4.402	4.206
$T_e(\text{eV})$	...	0.62
	Be <sub>2</sub> Cu linear asymmetric $^2\Sigma^+$	
$r_e(\text{Be-Be})(a_0)$	4.119	4.169
$r_e(\text{Cu-Be})(a_0)$	4.055	4.011
atomization energy (eV)		1.23
$D_e(\text{Be-BeCu})(\text{eV})$		0.56
	linear symmetric $^2\Sigma_g^+$	
$r_e(a_0)$	4.353	4.312
$T_e(\text{eV})$	...	0.15

<sup>a</sup>In this basis set the spectroscopic parameters for Cu<sub>2</sub> are:  $r_e=4.148 a_0$  and  $D_e=1.77\text{eV}$ .

the modeling approach, they yield insight into the chemistry. This is especially important when the complexity of the systems precludes performing calculations on all small systems of interest.

### Be Clusters

Computationally the study of small Be clusters is straightforward, since structures are qualitatively correct using small basis sets and neglecting the effects of electron correlation. For example, at the SCF level using only a DZ basis, the Be-Be bond length in Be<sub>4</sub> (of 3.97  $a_0$ ) is just 0.05  $a_0$  longer than at the SDCl level using a much larger triple-zeta basis with two sets of polarization functions (TZ2P) (6.51). However, the atomization energy per atom ( $D_e$ /atom) is significantly larger (0.70 eV) at the TZ2P-SDCl level than at the DZ-SCF level (0.39 eV). Therefore, questions of structure can be answered at the SCF level, while correlation must be included to accurately compute the cohesive energy of the cluster.

An important question in materials science is how large a cluster must be before its structure and chemistry is the same as that of the bulk. The smallest strongly bound Be cluster is Be<sub>4</sub>, which has tetrahedral geometry. A tetrahedron can be considered the building block for both the fcc and hcp structures, the latter being the structure of Be metal (52). A central atom in either the hcp or fcc structure is surrounded by 12 nearest neighbors, with trigonal symmetry for hcp and octahedral symmetry for fcc. SCF calculations on Be<sub>13</sub> clusters, with the constraint that all Be-Be bond lengths are equal, yield a  $D_e$ /atom that is more than twice as large as Be<sub>4</sub>; 0.87 eV (hcp) and 0.91 eV (fcc) (6). However, the fcc structure is more stable than the hcp structure for the 13 atom Be cluster, whereas the bulk structure is hcp. While all of the bond lengths are equal in the bulk fcc structure, there is always some distortion in the bulk hcp structure. If the constraint of equivalent bond lengths is eliminated (except that the clusters are still required to have trigonal symmetry— $D_{3h}$  or  $D_{3d}$ ), both clusters show modest distortions (up to 0.27  $a_0$ ). The fcc structure is stabilized by an additional 0.24 eV due to distortion. Therefore, not only is the lowest energy Be<sub>13</sub> structure different from the bulk, the 13 atom fcc structure differs from the fcc bulk structure by undergoing significant distortion.

The addition of nearest neighbors to the twelve surface Be atoms of Be<sub>13</sub> results in a 55 atom cluster. At the SCF level, using a slightly smaller basis set than used in our best treatment of Be<sub>13</sub>, the fcc structure of Be<sub>55</sub> is also observed to be more stable than the hcp structure (7). However, the relative stability between the two structures decreases to 0.03 eV per atom (favoring fcc) in Be<sub>55</sub> compared to 0.10 eV for Be<sub>13</sub>. The  $D_e$ /atom for Be<sub>55</sub> is significantly larger than that for Be<sub>13</sub> (1.33 vs. 0.86 eV/atom), which is in turn about twice that found for Be<sub>4</sub>, but it is still significantly less than the bulk value of 3.38 eV/atom. Although part of this difference arises from neglect of electron correlation and basis set limitations, scaling the Be<sub>55</sub> binding energy by 1.80 (the increase in  $D_e$  between the equivalent and best Be<sub>4</sub> calculations) does not fully account for differences with the bulk. Note, however, that the  $D_e$ /bond increases only slightly (0.07 eV) between Be<sub>4</sub> and Be<sub>13</sub>, and by even less (0.03 eV) between Be<sub>13</sub> and Be<sub>55</sub>. If the factor of 1.8 for basis set and correlation errors is applied to the 0.34 eV/bond for Be<sub>55</sub>, the resulting value of 0.59 eV is in good agreement with the 0.56 eV/bond deduced from bulk data. Thus, the  $D_e$  per bond is converging quite quickly with cluster size. The structure, however, is probably more influenced by the number of bonds per atom, which is 3.93 for Be<sub>55</sub>, compared to 6 for the bulk. Hence the structure of clusters can be quite different

from the bulk, and rather large clusters, probably between 100 and 300 atoms, are required before the bulk structure is optimal.

### Al Clusters

Although Al is less important than transition metals as a catalyst, it is a simple metal for which some experimental data is available for comparison with theory (48,49,53). Unlike Be clusters, Al clusters are not adequately described at the SCF level in a small one-particle basis set. Theoretical bond lengths (6,8,9) given in Table III for the Al<sub>4</sub> and Al<sub>13</sub> clusters indicate that the Al-Al distance decreases with both extensions of the one-particle basis and with the inclusion of electron correlation. In the larger basis sets the Al-Al bond lengths show an increase with increasing cluster size in analogy with Be clusters. The bond lengths in both cases approach that of the bulk from below. The inclusion of correlation shortens the Al<sub>4</sub> bond length by more than in Be<sub>4</sub>, but by less than the change with basis set improvement. Since electron correlation increases the binding energy by a factor of 1.5, it must be included for a quantitative determination of the cohesive energy.

We have considered the larger Al<sub>4</sub>-Al<sub>6</sub> clusters using both ab initio calculations and the parameterized model (9). The results for Al<sub>4</sub> and Al<sub>5</sub>, summarized in Table IV, show that the parameterized model and ab initio calculations agree well on the relative energetics if both the two- and three-body interactions are included. For Al<sub>6</sub> it is difficult to treat all the structures at the TZ2P-CPF level, but for the structures considered, there is reasonable agreement between the ab initio and model results.

When the parameters deduced from the calculations on Al<sub>2</sub> and Al<sub>3</sub> are applied to bulk Al, the cohesive energy is too small and the bond length is too large. The small cohesive energy is expected because our computed Al<sub>2</sub> D<sub>e</sub> at the TZ2P-CPF level is only 71% of the experimental value (42,46). The bulk values are in much better agreement with experiment if the model is parameterized using the experimental D<sub>e</sub> and r<sub>e</sub> values for the <sup>3</sup>Σ<sub>g</sub><sup>-</sup> state. Hence, the

Table III. Bond lengths for metal clusters of Al and Be

Cluster/method	r <sub>e</sub> (a <sub>0</sub> )
Be <sub>4</sub> DZ SCF	3.97
Be <sub>4</sub> large basis set CI	3.92
Be <sub>13</sub> (fcc) DZ SCF	4.06
Be <sub>13</sub> (hcp) DZ SCF	4.11
Bulk <sup>a</sup> (hcp)	4.26
Al <sub>4</sub> DZ-SCF rhombus	5.30
Al <sub>4</sub> large basis SCF	5.10
Al <sub>4</sub> large basis CI	5.02
Al <sub>13</sub> (hcp) DZ SCF	5.44
Al <sub>13</sub> (fcc) DZ SCF	5.44
Al <sub>13</sub> (hcp) large basis set SCF	5.26
Al <sub>13</sub> (fcc) large basis set SCF	5.26
bulk <sup>a</sup> (fcc)	5.41

<sup>a</sup>Ref. 52 —for Be the average of the two values in the bulk, 4.32 and 4.21 is given.

Table IV. Comparison of stability and structure of  $Al_n$  clusters between ab initio and parameterized interaction results with two- and three-body terms (2+3-b) as well as using only the two-body (2-b) interaction. Binding energies ( $D_e$  in eV) per atom, and bond distances ( $r_e$  in  $a_0$ ) are given

Structure	$D_e$ /atom			$r_e$		
	Ab initio	2+3-b	2-b	Ab initio	2+3-b	2-b
$Al_4$ Rhombus	1.08	1.13	1.48	5.04	5.10	4.97
$Al_5$ $C_{2v}$	1.32	1.27	1.67	4.96	5.14	4.97
$C_{4v}$	1.27	1.24	1.96	5.18	5.25	4.96
$C_s$	1.18	1.23	1.93	5.19	5.26	4.97
$D_{2h}$	1.15	1.20	1.44	5.02/4.94	5.13/5.07	4.98/4.95
$D_{3h}$	1.05	1.24	2.11	4.74	5.32	4.98
bulk	3.43 <sup>a</sup>	2.75 3.70 <sup>b</sup>	9.97 13.4 <sup>b</sup>	5.41 <sup>a</sup>	5.75 5.41 <sup>b</sup>	4.84 4.25 <sup>b</sup>

<sup>a</sup>Experimental value (52).

<sup>b</sup>For better comparison, these values have been calculated using the two-body potential calibrated with the experimental  $Al_2$  data (42,46) ( $D_e$  1.55 eV and  $r_e$  4.66  $a_0$  for the  $^3\Sigma_g^-$  state).

parameters needed to reproduce the bulk properties appear to be closer to those for the  $^3\Sigma_g^-$  excited state, although this could be a consequence of the form of the potential, which is discussed in more detail below. It is interesting to note that if the experimental  $Al_2$  data is used, this method has errors in the lattice constant and cohesive energy that are of the same magnitude as those found in density functional methods developed to study solids (54).

Since the calculated lowest energy structure of  $Be_{13}$  is fcc, whereas the bulk structure is hcp, we have carried out SCF calculations on  $Al_{13}$  using a large basis set to see if its structure is also different from that of the bulk. This is in fact the case since the nearly degenerate icosahedral and hcp structures are both about 1 eV more stable than fcc, which is the bulk structure. In addition, neither the hcp structure nor the fcc structure is significantly distorted from all bonds equal. This is also opposite to the situation in the bulk where the hcp structure undergoes distortion. Application of the parameterized model (with parameters based upon  $Al_2$  and  $Al_3$ ) leads to a planar  $Al_{13}$  being about 1 eV more stable than hcp, fcc or icosahedral, whereas this structure is 2.6 eV above the most stable structure at the ab initio level.

At present, our modelling approach uses a Lennard-Jones potential for the two-body term

$$u(\mathbf{r}_i, \mathbf{r}_j) = \epsilon \left( \left( \frac{r_0}{r_{ij}} \right)^{12} - 2 \left( \frac{r_0}{r_{ij}} \right)^6 \right) \quad (1)$$

where  $r_0$  is the equilibrium bond distance of the dimer,  $r_{ij}$  is the distance between atoms  $i$  and  $j$  and  $\epsilon$  is the energy at  $r_{ij}=r_0$ . For the three-body interaction we considered the Axilrod-Teller form:

$$u(\mathbf{r}_i, \mathbf{r}_j, \mathbf{r}_k) = \frac{Z(1 + 3\cos\alpha_1\cos\alpha_2\cos\alpha_3)}{(r_{ij}r_{jk}r_{ki})^3} \quad (2)$$

where  $r_{ij}$ ,  $r_{jk}$ ,  $r_{ki}$  and  $\alpha_1$ ,  $\alpha_2$ ,  $\alpha_3$  represent the sides and angles, respectively, of the triangle formed by the three particles  $i$ ,  $j$  and  $k$ . The intensity of the three-body interaction is given by the parameter  $Z$ , which is specific to each combination of different species in the tri-atom interaction. The poor results for  $\text{Al}_{13}$  using this model may be either due to our choice of potential functions with simple analytical forms or to the neglect of four-body and higher-order interactions. It might be possible to avoid these higher-order terms by having effective two- and three-body parameters that vary smoothly with cluster size. However, much of the problem may be that the Lennard-Jones potential rises more steeply than the ab initio potential, so that the two-body term underestimates the two-body contributions of second nearest neighbors. The three-body function is probably incapable of accounting for both the limitations of the two-body term and three-body effects. Alternate forms for the potential are presently under investigation.

In addition, we have developed a modified model potential, where the three-body interaction has been reduced slightly to give the ab initio ordering of structures for  $\text{Al}_{13}$ , i.e. the  $Z$  value in Equation 2 is fitted to the 13-atom ab initio results. This model potential was then used to study (55) the midsized clusters  $\text{Al}_7$ - $\text{Al}_{15}$ . The optimal structures are summarized in Table V and shown graphically in Figure 1. The binding energy per atom increases monotonically with increasing cluster size, but the energy required to remove the an atom varies with a pattern reminiscent of that observed (56) in mass spectroscopic experiments for the ionization potential and abundance. Figure 1 demonstrates that changes in cluster geometry with increasing cluster size can be quite dramatic. For example, the  $\text{Al}_9$  and  $\text{Al}_{11}$  clusters are three-dimensional while  $\text{Al}_{10}$  is planar. These studies must be considered qualitative because of unresolved questions about the potential, but such geometrical variations could explain the large changes in cluster properties with size.

### Mixed Clusters of Be and Cu

Since the relative simplicity of Cu-simple metal systems make them ideal for studying mixed component systems, SCF and model calculations have been carried out (50) for selected  $\text{Cu}_{18}\text{-Be}_x$  systems. The two- and three-body functions in the model are taken from ab initio calculations (26) on  $\text{Cu}_2$  and  $\text{Cu}_3$ , and the

Table V. The binding energy for  $\text{Al}_7$  to  $\text{Al}_{15}$  based on the modified three-body potential

cluster	$D_e/\text{atom}^a$	$\Delta D_e^b$
$\text{Al}_7$ planar	1.38	2.05
$\text{Al}_8$ planar	1.44	1.82
$\text{Al}_9$ 3-dimensional	1.49	1.94
$\text{Al}_{10}$ planar	1.56	2.17
$\text{Al}_{11}$ 3-dimensional	1.60	2.03
$\text{Al}_{12}$ planar	1.65	2.20
$\text{Al}_{13}$ 3-dimensional	1.69	2.14
$\text{Al}_{14}$ 3-dimensional	1.72	2.15
$\text{Al}_{15}$ 3-dimensional	1.76	2.26

<sup>a</sup> The  $D_e$  has been normalized to that of  $\text{Al}_2$ .

<sup>b</sup> The energy required to remove one Al atom.

cross terms are determined from calculations (47) on  $\text{CuBe}$  and  $\text{Cu}_2\text{Be}$ . We have not used  $\text{Be}_2$  and  $\text{Be}_3$  to define the Be-Be interaction terms, since these systems are weakly bound and not indicative of larger Be clusters. Therefore we have used the parameterized model only for  $\text{Cu}_{18}\text{Be}$ . The Cu cluster was previously designed (57,58) to model chemisorption at a three-fold hollow site on the (111) surface. For this reason the three Cu atoms at the adsorption site are treated using an all-electron treatment, while all of their nearest neighbors in the first layer and the six atoms in the second layer are modelled using an effective core potential (ECP) that explicitly treats only the 4s electrons. The geometry of the bare Cu cluster was taken from bulk data (52), which along with the details of the Cu basis set are described in earlier studies of O and  $\text{NH}_3$  chemisorption (57,58). The Be atom was described using a  $(9s4p)/(4s2p)$  gaussian basis set (59). The chemisorption of one Be atom into the three-fold hollow is found to be repulsive at the SCF level. The inclusion of correlation could lead to a bound system, but it is unlikely that Be will be strongly bound in the three-fold hollow of  $\text{Cu}_{18}$ . Analysis of the parameterized model results shows that the repulsive three-body interaction overcomes the attractive two-body interaction at these geometries. The same three-body forces lead to the directional bonding noted for  $\text{Cu}_2\text{Be}$  and  $\text{CuBe}_2$ . However, the parameterized model does predict that Be is bound for the on-top site.

The interaction of  $\text{Be}_4$  with the  $\text{Cu}_{18}$  cluster was also considered at the SCF level. The  $\text{Be}_4$  was constrained to have  $T_d$  symmetry and one face of the tetrahedron was aligned parallel to the  $\text{Cu}_{18}$  (111) surface. The  $\text{Be}_4$  was chemisorbed above the three-fold hollow, with the three chemisorbing Be atoms at bridging sites. Unlike the single Be atom,  $\text{Be}_4$  is bound by 0.92 eV with the closest Be atoms  $3.75 a_0$  above the plane of the surface. The fact that  $\text{Be}_4$  is more strongly bound to  $\text{Cu}_{18}$  is due both to the improved orientation, i.e. a reduction in the repulsive three-body interaction, and the fact that the Be atoms are already hybridized in  $\text{Be}_4$ . The optimal Be-Be distance (with the constraint of equal bond lengths) for the chemisorbed  $\text{Be}_4$  is  $0.04 a_0$  shorter than for the isolated  $\text{Be}_4$  molecule. Thus chemisorption decreases the bond length in  $\text{Be}_4$ , as observed upon chemisorption of H, Cl or F atoms (60). This is opposite to the trend of increasing Be-Be bond lengths with the size of  $\text{Be}_x$  clusters.

Presently it is not possible to relax the Cu lattice at the SCF level, since from a computational point of view it is composed of two different kinds of Cu atoms (those with and without the ECP). Also questions of wetting, i.e. whether the chemisorbed  $\text{Be}_4$  would prefer to remain as a tetrahedron (or distorted tetrahedron) or to spread out to a single layer are still not amenable to ab initio study. These questions have not yet been investigated using the parameterized model approach, because of the problems associated with modeling  $\text{Be}_2$  and  $\text{Be}_3$  as accurately as larger Be clusters. Nonetheless, these preliminary results show that the parameterized and ab initio calculations can be used to complement each other in a multicomponent system, just as for single component systems.

### Clusters with Adsorbates

Gas phase experiments show that the reactivity of small clusters varies greatly with cluster size (11), and experimental work with small clusters on supports has shown (12) that adsorbed molecules or atoms affect the metal-metal bond length. In both experiments the adsorption site is not known. Also the reactions proceed to completion so that only the high coverage case has been measured. We have considered the chemisorption of several atoms on  $\text{Be}_{13}$  and  $\text{Al}_{13}$  clusters. For both clusters trigonal symmetry is maintained, and only the metal-metal



and metal-adsorbate distances are optimized. We have considered (60-62) the chemisorption of two atoms into three-fold hollows and the chemisorption of six atoms into the three-fold hollows or the four-fold hollows. The results are summarized in Table VI and illustrated in Fig. 2. For  $\text{Be}_{13}$  at low coverages, addition of H, F and Cl atoms all result in a small contraction of the cluster, while addition of O and S atoms expand the metal cluster to about that of the bulk. If the coverage is increased, all of the adsorbates considered expand the metal lattice. For chemisorption in the four-fold hollows, the expansions are all relatively small, with only O expanding the cluster to its bulk dimensions. In fact, six O atoms in the four-fold hollows expands the cluster by the same amount as two O atoms in the three-fold hollows. Chemisorption of six O atoms into the three-fold hollows causes a large expansion of the Be-Be distance, making the cluster bond length significantly longer than the bulk. Six H or F atoms in the three-fold hollows expands the cluster, with H yielding a Be-Be bond distance about equal to the bulk. Since the energetic difference between having six atoms in the three- or four-fold hollows is small, the chemisorption site cannot be definitely determined. However, experiments (12) on transition metals show that high H coverage expands the clusters to about that of the bulk, while high O coverage causes a much larger expansion. The chemisorption into the three-fold hollow is consistent with these experiments. Hence, H and O atoms probably chemisorb into the three-fold hollows on the small clusters, in contrast to the bulk where atoms that become negatively charged always chemisorb into the biggest hollow, four-fold in this case. The difference in adsorption site can be explained in terms of the greater ease with which metal clusters can expand. Our calculations show that low coverages can have the opposite effect on the metal-metal bond lengths of the cluster than high coverages. At present no experimental data is available for chemisorption of F, Cl and S atoms on metal clusters. The theoretical trends in the cluster expansion should provide insight into the changes expected when these adsorbates react with small clusters on supports.

Al clusters are computationally more difficult than Be clusters, but are more amenable to parameterized model and experimental studies. Therefore we have studied (61,62) chemisorption on an  $\text{Al}_{13}$  cluster at the SCF level—see Table VI. Although the bare  $\text{Al}_{13}$  cluster bond lengths are longer than the bulk, the relative changes in geometry with chemisorption are expected to be correct. Hydrogen causes a sizable expansion even at low coverage, because it enters the cluster with little or no barrier. The very large cluster expansion with only two O atoms chemisorbed suggests that Al clusters could be destroyed by exposure to high O coverage. This is in marked contrast to our results for Be, and experiments on transition metals. The availability of experimental studies of Al clusters on supports would provide an excellent test of our cluster models.

## Conclusions

We have discussed our theoretical calculations on metals ranging from very accurate *ab initio* studies of diatomic and triatomic systems to model studies of larger clusters. Recent improvements in the accuracy to which we can represent both the one-particle and *n*-particle spaces has significantly improved the reliability of theoretical calculations on small molecules. For example, we are able to predict definitively that  $\text{Al}_2$  has a  $^3\Pi_u$  ground state even though the  $^3\Sigma_g^-$  state lies within  $200\text{ cm}^{-1}$ . Calculations on clusters indicate that their geometry varies dramatically with cluster size, and that rather large clusters are required before the bulk structure becomes optimal. Since clusters are more

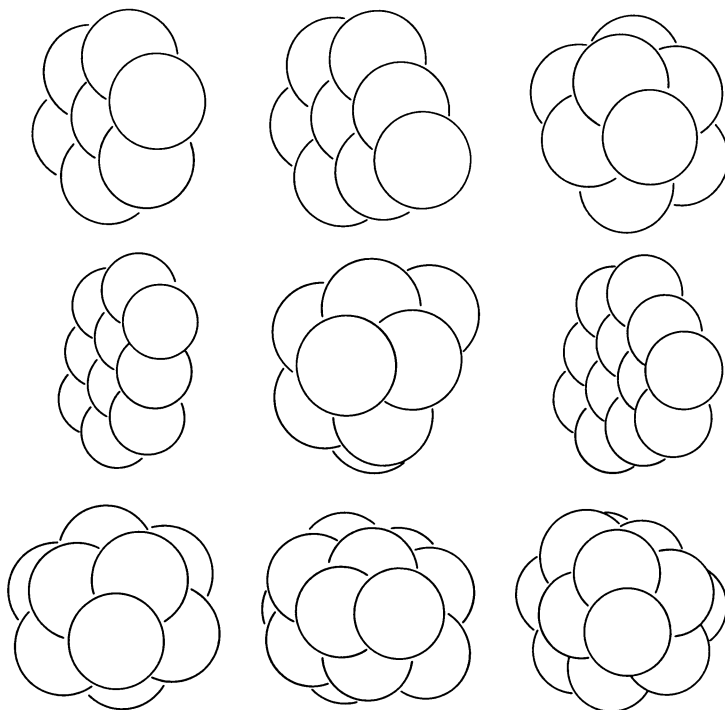


Figure 1. The most stable  $Al_n$  clusters, for  $n=7, 15$ , determined using the three-body parameter deduced from the ab initio  $Al_{13}$  results.

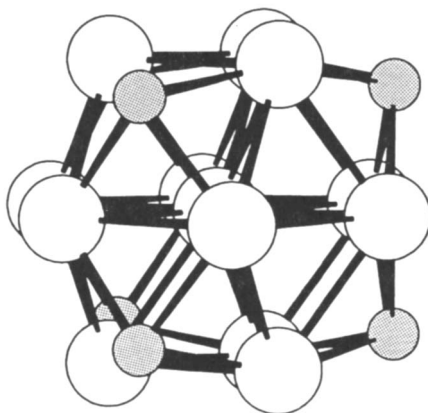


Figure 2. The  $Be_{13}X_6$   $D_{3h}$  cluster used to model chemisorption into the four-fold hollows. The  $Be_{13}X_6$  cluster used to model chemisorption into the three-fold hollows is generated by a  $60^\circ$  rotation of the six adsorbate atoms about the vertical axis. The  $D_{3d}$  metal cluster is formed by rotating the bottom three metal atoms by  $180^\circ$  about the vertical axis.

Table VI. The M-M and M-adsorbate bond lengths ( $a_0$ ) for Be and Al clusters with adsorbates,  $M_{13}X_2$ , and  $M_{13}X_6$ . Also shown is the expansion relative to the bare  $M_{13}$  cluster

X	M-M	$Be_{13}X_2$ three-fold hollows expansion <sup>a</sup>	M-X
H	4.03	-0.08	2.97
O	4.24	+0.13	2.89
S	4.22	+0.11	3.80
F	4.09	-0.02	3.24
Cl	4.07	-0.04	4.08
$Be_{13}X_6$ three-fold hollows			
H	4.33	+0.22	3.09
O	4.73	+0.62	3.10
F	4.19	+0.08	3.44
$Be_{13}X_6$ four-fold hollows			
H	4.14	+0.03	3.41
O	4.25	+0.14	3.21
F	4.14	+0.03	4.03
$Al_{13}X_2$ three-fold hollows			
H	5.61	0.17	inside
O	5.85	0.42	3.54
$Al_{13}X_6$ three-fold hollows			
H	6.01	0.57	inside

<sup>a</sup>The  $Be_{13}$  value is taken from reference (6). Note that the expansion entries in this table supercede those in Ref. 60 where an incorrect value was used for the bare cluster.

<sup>b</sup>Ref. 52, the average of the two values in the bulk, 4.32 and 4.21.

easily distorted than the bulk, the optimal adsorption sites are also often different from perfect crystal faces. Studies of Al clusters with a parameterized model indicate that three-body terms are essential for quantitative agreement with *ab initio* calculations. The use of parameterized models to study alloys and composite materials with the two- and three-body potentials defined from *ab initio* calculations shows much promise, but further studies to determine the optimal functional forms are required.

### Literature Cited

1. Cooper, D. M.; Jaffe, R. L.; Arnold, J. O. J. Spacecraft and Rockets 1985, **22**, 60.
2. Laskowski, B. C.; Jaffe, R. L.; Komornicki, A. Int. J. Quantum Chem. 1986, **29**, 563.
3. Bauschlicher, C. W.; Walch S. P.; Langhoff S. R. In Quantum Chemistry: the Challenge of Transition Metals and Coordination Chemistry; Veillard, A., Ed.; Reidel Publishing Company: Dordrecht Holland, 1986; p 15.
4. Walch S. P.; Bauschlicher, C. W. In Quantum Chemistry: the Challenge of Transition Metals and Coordination Chemistry; Veillard, A., Ed.; Reidel Publishing Company: Dordrecht Holland, 1986; p 119.
5. Walch S. P.; Bauschlicher C. W. In Comparison of *ab initio* Quantum Chemistry with Experiment; Bartlett, R., Ed.; D. Reidel Publishing Company: Boston, 1985; p 17.
6. Bauschlicher, C. W.; Pettersson, L. G. M. J. Chem. Phys. 1986, **84**, 2226.
7. Pettersson, L. G. M.; Bauschlicher, C. W. Chem. Phys. Lett. 1986, **130**, 111.
8. Bauschlicher, C. W.; Pettersson, L. G. M. J. Chem. Phys. (submitted).
9. Pettersson, L. G. M.; Bauschlicher, C. W.; Halicioglu, T. J. Chem. Phys. (submitted).
10. See Vol. 156 of Surface Science, which contains the proceedings of the Third International Meeting on Small Particles and Inorganic Clusters, Berlin, West Germany, July 9-13, 1984.
11. Richsmeier, S. C.; Parks, E. K.; Liu, K.; Pobo, L. G.; Riley, S. J. J. Chem. Phys. 1985, **82**, 3659; Parks, E. K.; Liu, K.; Richsmeier, S. C.; Pobo, L. G.; Riley, S. J. J. Chem. Phys. 1985, **82**, 5470.
12. Poppa, H. Vacuum 1985, **34**, 1081; Ultramicroscopy 1983, **11**, 105.
13. Bauschlicher, C. W. J. Chem. Phys. 1986, **84**, 250.
14. Bauschlicher, C. W.; Langhoff, S. R.; Partridge, H.; Taylor, P. R. J. Chem. Phys. 1986, **85**, 3407.
15. Bauschlicher, C. W.; Langhoff, S. R. Chem. Phys. Lett. (in press).
16. Bauschlicher, C. W.; Langhoff, S. R. J. Chem. Phys. (in press) and Langhoff, S. R.; Bauschlicher, C. W.; Taylor, P. R. Chem. Phys. Lett. (in press).
17. Bauschlicher, C. W.; Partridge, H.; Langhoff, S. R.; Taylor, P. R.; Walch, S. P.; J. Chem. Phys. (in press).
18. Bauschlicher, C. W.; Taylor, P. R. J. Chem. Phys. 1986, **85**, 2779.
19. Bauschlicher, C. W.; Taylor, P. R. J. Chem. Phys. 1987, **86**, 858.
20. Bauschlicher, C. W.; Taylor, P. R. J. Chem. Phys. 1986, **85**, 6510. and Bauschlicher, C. W.; Langhoff, S. R.; Taylor, P. R. J. Chem. Phys. (submitted).
21. Almlöf, J.; Taylor, P. R. J. Chem. Phys. in press.
22. Partridge, H.; Taylor, P. R.; and Bauschlicher, C. W.; unpublished.

23. Ahlrichs, R.; Scharf, P.; Ehrhardt, C. *J. Chem. Phys.* 1985, 82, 890.
24. Scharf, P.; Brode S.; Ahlrichs, R. *Chem. Phys. Lett.* 1985, 113, 447.
25. Langhoff, S. R.; Bauschlicher, C. W. *J. Chem. Phys.* 1986, 84, 4485.
26. Langhoff, S. R.; Bauschlicher, C. W.; Walch, S. P.; Laskowski, B. C. *J. Chem. Phys.* 1986, 85, 7211.
27. Truhlar, D. G.; Thompson, T. C.; Mead, C. A. *Chem. Phys. Lett.* 1986, 127, 287.
28. Zwanzier, J. W.; Whettien, R. L.; and Grant, E. R. *J. Phys. Chem.* 1986, 90, 3298.
29. Rohlfiing E. A.; Valentini, J. J. *Chem. Phys. Lett.* 1986, 126, 113.
30. Moore, C. E. Atomic energy levels; Natl. Bur. Stand. (US) circ.; 1949, p 467.
31. Walch, S. P.; Bauschlicher, C. W.; Langhoff, S. R. *J. Chem. Phys.* 1985, 83, 5351.
32. Chong, D. P.; Langhoff, S. R.; Bauschlicher, C. W.; Walch, S. P.; Partridge, H. *J. Chem. Phys.* 1986, 85, 2850.
33. Chong D. P.; Langhoff, S. R. *J. Chem. Phys.* 1986, 84, 5606.
34. Gray, J. A.; Rice S. F.; Field, R. W. *J. Chem. Phys.* 1985, 82, 4717.
35. Langhoff, S. R.; Pettersson, L. G. M.; Bauschlicher, C. W.; Partridge, H. *J. Chem. Phys.* 1987, 86, 268.
36. Bauschlicher, C. W.; Nelin C. J.; Bagus, P. S. *J. Chem. Phys.* 1985, 82, 3265.
37. Langhoff, S. R.; Bauschlicher, C. W.; Chong, D. P. unpublished.
38. Langhoff S. R.; Bauschlicher, C. W. *Chem. Phys. Lett.* 1986, 124, 241.
39. Bauschlicher, C. W.; and Langhoff, S. R. *Chem. Phys. Lett.* 1986, 126, 163.
40. Bauschlicher, C. W.; and Langhoff, S. R. *J. Chem. Phys.* 1986, 85, 5936.
41. Axilrod B. M.; Teller, E. *J. Chem. Phys.* 1943, 11, 299.
42. Huber K. P.; Herzberg, G. Molecular Spectra and Molecular Structure; Van Nostrand Reinhold: New York, 1979).
43. Douglas, M. A.; Hauge, R. H.; Margrave, J. L. *J. Phys. Chem.* 1983, 87, 2945.
44. Basch, H.; Stevens, W. J.; Krauss, M. *Chem. Phys. Lett.* 1984, 109, 212.
45. Cowan R. D.; Griffin, D. G. *J. Opt. Soc. Am.* 1976, 66, 1010; Martin, R. L. *J. Chem. Phys.* 1983, 78, 5840.
46. Stearns C. A.; Kohl, F. J. *High Temp. Science* 1973, 5, 113.
47. Bauschlicher, C. W.; Langhoff, S. R.; Partridge, H.; Walch, S. P.; *J. Chem. Phys.* (in press).
48. Howard, J. A.; Sutcliffe, R.; Tse, J. S.; Dahmane, H.; Mile, B. *J. Phys. Chem.* 1985, 89, 3595.
49. Cox, D. M.; Trevor, D. J.; Whetten, R. L.; Rohlfiing, E. A.; Kaldor, A. *J. Chem. Phys.* 1986, 84, 4651.
50. Bauschlicher, C. W.; Halicioglu, T. unpublished.
51. Bauschlicher, C. W.; Bagus P. S.; Cox, B. N. *J. Chem. Phys.* 1982, 77, 4032.
52. Wyckoff, R. B. Crystal Structures, Second edition; Interscience: New York, 1964.
53. Hanley L.; Anderson, S. L. *Chem. Phys. Lett.* 1986, 129, 429.
54. Moruzzi, V. L.; Janak J. F.; Williams, A. R. Calculated Electronic Properties of Metals, Pergamon Press: New York, 1978.
55. Halicioglu, T. unpublished.
56. Powers, D. E.; Hansen, S. G.; Geusic, M. E.; Michalopoulos, D. L.; Smalley, R. E. *J. Chem. Phys.* 1983, 78, 2866.

57. Bauschlicher, C. W. J. Chem. Phys. 1985, 83, 2619.
58. Bauschlicher, C. W. Chem. Phys. Lett. 1985, 118, 544.
59. This is same Be basis set as used in reference 6.
60. Bauschlicher, C. W. Chem. Phys. Lett. 1985, 117, 33.
61. Partridge, H.; Bauschlicher, C. W. J. Chem. Phys. 1986, 84, 6507.
62. Taylor, P. R.; Partridge, H.; Bauschlicher, C. W. unpublished.

RECEIVED June 15, 1987

## Chapter 3

# Theoretical Methods and Results for Electronic Structure Calculations on Very Large Systems Carbon Clusters

Jan Almlöf and Hans Peter Lüthi

Department of Chemistry and Minnesota Supercomputer Institute,  
University of Minnesota, Minneapolis, MN 55455

Large clusters of carbon atoms have been studied with ab initio calculations using basis sets of double- $\zeta$  quality. Planar, single-sheet graphite fragments with 6 - 54 atoms were investigated, as well as the spherical "Buckminsterfullerene"  $C_{60}$  molecule. Partly hydrogenated clusters have also been considered, both graphite- and diamond-like. The largest of these,  $C_{150}H_{30}$ , was treated with 1560 basis functions, and constitutes the largest ab initio Hartree-Fock calculation performed so far. Saturation of the peripheral bonds with hydrogen is found to provide a smooth and uniform convergence of the properties with increasing cluster size. For the graphite-like clusters the convergence of properties to bulk values is much slower than for the three-dimensional complexes.

Due to their scientific and technical importance, carbon clusters have long been subject to a variety of experimental(1-24) and theoretical(25-51) investigations. The areas of interest are of great diversity, including heterogeneous catalysis, the composition of graphite vapor, soot formation during combustion(15) and early stages of synthetic natural gas production from coal. Several small clusters have been identified spectroscopically in the atmospheres of red giant stars and in comet tails(6-9).

The experimental work reported for carbon clusters ranges from the early investigations of Honig and Drowart on small clusters(1-3) to the recent studies in the groups of Smalley and Kaldor(10-16) on larger clusters with up to 200 atoms.

A striking observation that lacks a satisfactory explanation is the existence of 'magic numbers', i.e. the fact that in a distribution of clusters some species with a certain number of carbon atoms are much more abundant than others. The exact clustering mechanisms are not completely understood, and, as noted by Rohlfing et al.(10), the origin of the observed distribution of clusters may depend upon instrumental factors. Accounting for this fact, however, there still seems to be a preference for clusters with certain numbers of atoms which cannot be explained solely as due to the experimental conditions.

There are several methods in use for producing these clusters. Particle bombardment or laser vaporization of a graphite surface leads to direct formation of ions that can be detected by mass spectrometry. These are normally of relatively small size ( $n < 30$ ). By laser vaporization of graphite into a molecular beam neutral

0097-6156/87/0353-0035\$06.00/0  
© 1987 American Chemical Society

clusters can also be formed. For the purpose of mass-spectrometric analysis the neutral clusters are subsequently laser photoionized. Ions formed using this technique show a bimodal distribution, with a second broad distribution band in the range  $30 < n < 150$ .

In the lower-mass distribution, cluster ions are observed with an interval of  $\Delta n = 1$ , while the high-mass distribution is characterized by  $\Delta n = 2$ , with only even  $n$  values being observed. The low mass distribution is essentially the same in each method, and observation of high-mass clusters has not been reported with direct formation methods.

Great interest has recently been generated by the observation that certain 'magic numbers' appearing in the high-mass lobe of carbon cluster mass spectra could be strongly enhanced by changes in cluster growth and/or photoionization conditions. In a remarkable series of experiments Smalley and coworkers have identified long-lived carbon clusters in the product of laser vaporization of graphite. Many clusters with  $n = 40-80$  possess some stability, but under certain conditions the most stable species seems to be the 60 atom cluster, for which an icosahedral structure "Buckminsterfullerene" (BF) has been suggested. The proposal that the large relative abundance of  $C_{60}$  reflects the unusual stability of a specific geometrical configuration has provoked a growing number of experimental and theoretical studies.

Evidently, several aspects of this exciting area are difficult to study with experimental techniques. The different species are short-lived, reactive, and exist only under rather extreme conditions. These are conditions under which theoretical studies can contribute a lot to our understanding. Theoretical work has indeed been reported on smaller clusters with  $n = 2-10$  (42-50) as well as on some of the larger ones (25-41). The present work reports *ab initio* calculations for a number of large carbon clusters of relevance to the chemical problems addressed above.

### **Computational Methods**

Even though recent progress in hardware and software development has made it possible to study quite large molecules, systems of the size considered here do not lend themselves to studies with any *ab initio* technique. The Hartree-Fock method has the advantage of being size consistent, which is a necessity for this type of study when results for molecules of vastly different size are to be compared. In addition, the method is technically and economically feasible for these large systems.

The Restricted Hartree-Fock (RHF) method was used in all calculations reported here. The 'Direct SCF' scheme as implemented in the program DISCO(52) was used in most of the cases. That approach avoids the I/O and disk storage bottleneck encountered in traditional schemes by recalculating the two-electron integrals whenever needed, rather than retrieving them from external storage. In a scientific supercomputing environment the total elimination of I/O in very large calculations is especially attractive since these jobs can run as low-priority background processes without significantly interfering with the main load on the system.

A 7s3p basis(54) for carbon was contracted to double zeta (7s3p/4s2p), leaving 10 contracted basis functions per carbon atom. For the hydrogen-containing clusters a hydrogen 3s basis with exponents scaled to an effective nuclear charge of 1.2 was contracted to two functions.

All calculations were performed on the Cray-2 computers at the Minnesota Supercomputer Center. In some cases the two-electron integrals could be kept in the 256 megaword central memory of the Cray-2, and in these cases an "in-core" integral and SCF code(53) was used. The largest in-core calculations possible in



that environment were the calculations on Buckminsterfullerene using 600 contracted basis functions. In comparison, the largest Direct SCF calculation reported here, i.e. the one on  $C_{150}H_{30}$ , used 1,560 contracted basis functions.

### Graphite Fragments

For all but the few smallest clusters, the number of possible structures is virtually unlimited. In order to be able to treat the larger systems, quite restrictive assumptions about their geometry has to be made. For those clusters where well-defined equilibrium structures do exist, these are likely to possess a non-trivial point-group symmetry (in many cases the highest possible symmetry). It therefore seemed justified to focus the study on high-symmetric systems. Symmetry can also be used to simplify the calculation of electronic structure, and reduces the number of geometrical degrees of freedom to be optimized.

For graphite-like systems the six-fold ring is the natural building block. In an initial series of calculations, the systems  $C_6$ ,  $C_{24}$  and  $C_{54}$  ( $D_{6h}$  symmetry, 1, 2 and 3 in Figure 1) were computed in a high spin form with all unpaired electrons having parallel spins ( $S=3,6$ , and 9). All carbon-carbon bond distances were kept equal at 1.42 Å. The total energies computed, -226.5321 au for  $C_6$ , -907.0085 au for  $C_{24}$  and -2041.5720 au for  $C_{54}$ , can be interpreted in terms of cohesive energies of 71.0, 97.1 and 106.5 kcal/mol per carbon atom, respectively.

Apparently, the cohesive energy of these clusters shows a very slow convergence with the size of the molecule. This should not be surprising, since the number of unsaturated valences "dangling bonds" per carbon atom is one in 1, 1/2 in 2 and 1/3 in 3.

Assuming an approximately constant cohesive energy per C-C bond, that trend is understandable. With clusters on the above general type, the number of carbon atoms is  $6N^2$ , the number of dangling bonds is  $6N$ , and the number of C-C bonds is  $9N^2-3N$ . The energy per bond shows a smoother trend, the numbers being 71.0, 77.6 and 79.9 kcal/mol, respectively. Alternatively, the energies can be fitted to a two-parameter expression of the form

$$E_{\text{tot}} = 6N^2E_c + 6NE_{\text{db}} \quad (1)$$

where  $E_c$  (energy per carbon atom) and  $E_{\text{db}}$  (energy per dangling bond) are parameters to be determined. The optimum coefficients are  $E_c = -37.8366$  au and  $E_{\text{db}} = +0.0891$  au. For large values of  $N$  the total energy per carbon atom will converge towards  $E_c$ , so that the cohesive energy per carbon atom in graphite can be expressed as the difference between  $E_c$  and the atomic energy of carbon (-37.6371 au), leading to a value of 0.1995 au or 125 kcal/mol. (i.e. 83.3 kcal/mol per C-C bond, since in graphite there are 3/2 bonds per carbon atom). The parameter  $E_{\text{db}}$ , for which a value of +0.0891 au is derived, can be interpreted as the energy loss for introducing a dangling bond in a graphite-like sheet of carbon atoms. Its value corresponds to a loss of bond energy of 111.8 kcal/mol, actually somewhat higher than the value derived from the cohesive energy. One might have expected the electrons that become unpaired by the bond-breaking to redistribute into other bonding orbitals, or, in valence-bond language, that the broken peripheral bonds would rehybridize to contribute to a stabilization of the framework. The opposite turns out to be true, though; breaking some bonds weakens others due to an interrupted electron delocalization, a phenomenon illustrated by the fact that the C-C bond in cyclic  $C_6$  is considerably weaker than in graphite.

For the larger clusters  $C_{24}$  and  $C_{54}$  the carbon atoms are not symmetry equivalent, and fluctuations in the local properties from atom to atom may occur. It is of some interest to study the details of that fluctuation. For instance, it is important to know how large the molecule needs to be before its interior is reasonably close to that of a single-sheet graphite. The population analysis for  $C_{24}$  shown in Figure 2 demonstrates that the charge originating from the unpaired electrons is located to a large extent in the peripheral carbon sigma-bonding orbitals.

So far, only high-spin systems have been discussed. However, when the dangling bonds interact, spin-pairing may lead to a lower energy. In the case of  $C_{24}$  all adjacent dangling bond electrons can be paired up, which would result in a singlet state of the molecule. A partial structure optimization on this state leads to very short peripheral carbon-carbon bonds (1.20 Å) with essentially triple bond character. All other bond lengths change very little despite the strain introduced by shortening one bond of the six-membered ring by more than 0.2 Å. For  $C_{54}$  a similar structure may be obtained. Pairing up electrons from adjacent carbon atoms of the same six-membered ring, and leaving all the other (lonestanding) dangling bond electrons with parallel spins, a low spin state ( $S=3$ ) is obtained. The total populations for the low- and high-spin forms of  $C_{54}$  are shown in Figures 3 and 4.

Figure 5 shows the spin density distribution of the low-spin form of  $C_{54}$ . It is interesting to note that also here the spin density is almost entirely localized on the carbon atom that would carry the dangling bond in a simple valence orbital picture.

The energy calculations show that the low spin state of  $C_{54}$  is indeed about 1.3 eV lower in energy than the high spin state, at least for the molecular geometries used here, whereas for  $C_{24}$  nearly identical energies for the two states are found. Inclusion of electron correlation would favor the low spin form further, possibly by as much as 6 eV (1 eV per new bond formed) in both  $C_{24}$  and  $C_{54}$ . The cohesive energy per carbon atom of  $C_{54}$ , however, would not be affected significantly.

The ionization potentials (Koopmans' values) for the high spin and the low spin form of  $C_{54}$  are 6.8 and 7.3 eV respectively, which would fit into the bracket of IP's reported for carbon clusters with 40 to 100 atoms ( $6.42 \text{ eV} \leq \text{IP} \leq 7.87 \text{ eV}$ , Ref. 11). The corresponding values for  $C_{24}$  are higher, 8.0 and 8.3 eV respectively.

### Clusters with Saturated Peripheral Bonds

The above studies show that properties in the interior of the graphite-like clusters do not converge readily to bulk values. Even for the  $C_{54}$  cluster, the populations in the center show a significant deviation from neutrality. Despite the possibility of exploiting the high point-group symmetry of these systems, the complicated open-shell structure places severe limits on the maximum size of the clusters that can be studied. Therefore, the calculation of a graphite cluster large enough to ensure convergence of the properties to bulk values would be computationally unfeasible.

If the focus of interest is on the carbon clusters themselves, then of course no substitute system can be used. However, for studying the convergence of properties towards bulk values one can minimize the termination effects by saturating the dangling bonds in the simplest possible way, i.e. with hydrogen. By that approach one can both avoid the problem of handling an excessive number of open shells, and obtain a series of molecules that converge towards bulk properties more smoothly than the bare carbon clusters.

The series of benzenoid aromatic hydrocarbons shown in Figure 6 have been studied in the present work, and should allow for an extrapolation towards an

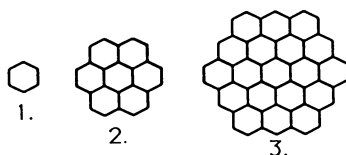


**Figure 1.** Graphite fragments of  $D_{6h}$  symmetry.  $C_6$ (1),  $C_{24}$ (2) and  $C_{54}$ (3).

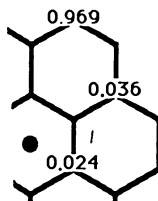


**Figure 2.** Spin-density populations for the high-spin form ( $S=6$ ) of  $C_{24}$ .

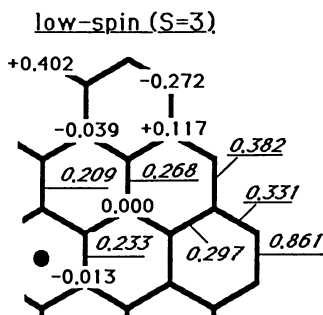


**Figure 3.** Net atomic and overlap populations for the low-spin form of  $C_{54}$ .

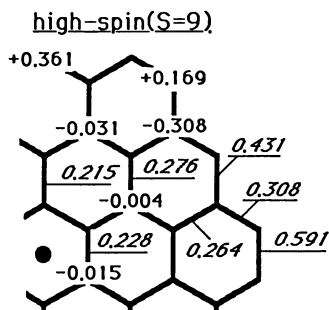


**Figure 4.** Net atomic and overlap populations for the high-spin form of  $C_{54}$ .

infinite single layer of graphite. The total energies of these systems with the general formula  $C_{6N}2H_{6N}$  are presented in Table 1. For all molecules except 8 an overall C-C bond distance was optimized. This seems to converge smoothly towards 1.406 Å, a value somewhat shorter than that experimental distance of 1.421 Å found in bulk graphite(55). The Hartree-Fock approximation is the main source of this discrepancy. It should be noted, however, that the bond distance in a graphite monolayer is expected to be somewhat shorter than the bulk value(56).

**Table 1:** Total energies and C-C bond distances computed for  $C_{6N}2H_{6N}$  and energies estimated using expression (2) with the parameters  $E_C = -37.8363$ ,  $E_H = -0.5685$  au. The C-H distances were kept fixed at 1.10Å

n	system	$-E_{tot,calc}$	$-E_{tot,pred}$	$\Delta$	$R_{CC}$ (Å)
1	$C_6H_6$	230.4320	230.4288	0.0032	1.384
2	$C_{24}H_{12}$	914.8938	914.8932	0.0006	1.401
3	$C_{54}H_{18}$	2053.3942	2053.3932	0.0010	1.404
4	$C_{94}H_{24}$	3645.9003	3645.9288	-0.0285	1.406
5	$C_{150}H_{30}$	5692.4981	5692.5000	-0.0019	1.406 <sup>a</sup>

<sup>a</sup>assumed without geometry optimization.

The total energy can be accurately fitted with a two-parameter expression similar to that given in Equation 1:

$$E_{tot,est} = 6N^2E_C + 6NE_H \quad (2)$$

Table 1 shows that the total energies of the systems studied here are reproduced by Equation 2 with an error smaller than 0.2 kcal/mol per carbon atom.

The optimum coefficients in Equation 2 are  $E_C = -37.8363$  and  $E_H = -0.5685$  au.  $E_C$  is very close to the value -37.8366 found for the pure graphite clusters. The value of  $E_H$  corresponds to a contribution of 47.1 kcal/mol to the total energy of  $C_{6N}2H_{6N}$  for each bonded H-atom (the hydrogen atom has an energy of -0.4935 au in the basis set used). Alternatively, the parameter values can be interpreted as 83.3 kcal/mol per C-C bond, 88.7 kcal/mol per C-H bond.

The value 125 kcal/mol represents an upper bound to the cohesive energy per carbon atom in graphite, since the interaction between layers in the bulk has not been accounted for. Given the relatively large distance and the physical properties of graphite, the interlayer interaction energy is estimated to be < 5 kcal/mol.

This leaves us with a computed result in less than satisfactory agreement with the experimental value of about 170 kcal/mol(57). The neglect of electron correlation and the limited basis set used are the most important sources of the discrepancy. In a previous study on monolayer graphite(56), basis set effects were found to lead to a significant underestimation of the cohesive energy.

The orbital energies show a surprisingly slow convergence as the size of the molecule increases. Even for the largest system studied, the HOMO-LUMO gap is about 4 eV. From the values shown in Figure 7 one may expect semiconducting

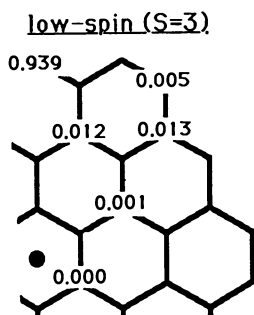


**Figure 5.** Spin density distribution in the low-spin form of  $C_{54}$ .

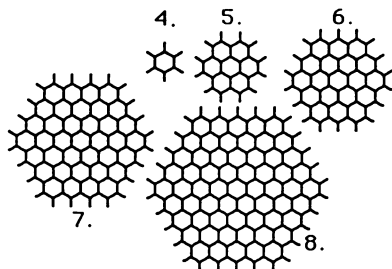


**Figure 6.** The condensed aromates  $C_6H_6$  (4),  $C_{24}H_{12}$  (5),  $C_{54}H_{18}$  (6),  $C_{96}H_{24}$  (7), and  $C_{150}H_{30}$  (8)

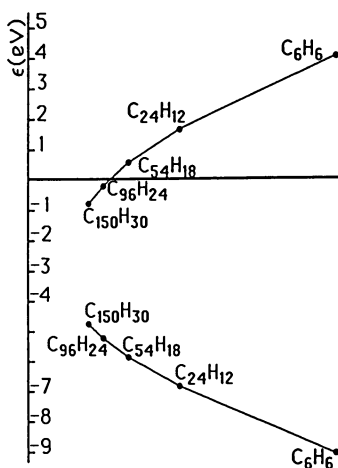


**Figure 7.** HOMO and LUMO orbital energies for  $C_{6N}2H_{6N}$ , plotted vs  $1/N$ .

behavior to occur at  $N=8-10$ , i.e. for clusters with 400-600 atoms. At that point a conventional Hartree-Fock approach would of course break down.

The HOMO and LUMO orbital energies seem to converge towards a value of about -4 eV, which would be an estimate of the work function for single-sheet graphite. This is in reasonable agreement with the work function of 4.9 eV experimentally found for bulk graphite(58).

### Diamond-like Clusters

From the two-dimensional, graphite-like clusters, the extension to three-dimensional structures is obvious. Symmetric structures developed in a similar fashion to the planar systems would grow in three dimensions with increasing  $N$ , and the number of atoms would increase faster. In this work clusters of  $T_d$  symmetry were studied, resembling a small fragment of a diamond structure. Only systems with saturated external bonds were considered. The number of carbon and hydrogen atoms in such a structure is given by

$$\begin{aligned} N_C &= N(4N^2-1)/3 \\ N_H &= 4N^2 \end{aligned}$$

Here we present some results from studies on systems with  $N=2,3$ , and 4. ( $N=1$  would correspond to the methane molecule). The molecules are shown in Figure 8.

For all three molecules, an overall C-C distance was optimized. The values obtained for the three systems are 1.542Å, 1.540Å and 1.539Å, smoothly converging to a value slightly shorter than the equilibrium distance in diamond. (Table 2).

Fitting the energies to an expression similar to Eq 2 gives  $E_C = -37.8360$ ,  $E_H = -0.5732$  for the tertiary hydrogens, and  $E_H = -0.5742$  for methylene carbons. The extrapolated cohesive energy is 125 kcal/mol, the same as for graphite. A breakdown of the bond energies per bond gives a C-C bond energy of 62 kcal/mol. The C-H bond energies are 82 and 81 kcal/mol for the methylene and the tertiary hydrogens, respectively.

**Table 2:** Total computed energies and distances for the diamond-like clusters. The C-H distances were kept fixed at 1.09Å

n	system	$-E_{tot}(\text{a.u.})$	$R_{CC}$ (Å)
2	$C_{10}H_{16}$	387.54332	1.542
3	$C_{35}H_{36}$	1344.90665	1.540
4	$C_{84}H_{64}$	3214.91903	1.539

The convergence pattern for the orbital energies is dramatically different from that found in the graphite-like clusters as shown in Figure 9. The extrapolated band gap is somewhat uncertain but seems to lie around 10 eV, and is definitely larger than the experimental value of about 4.6 eV. This difference is

mainly due to neglect of electron correlation in our calculations. A similar discrepancy was observed in a recent study on polyacetylene(59).

### Structures Containing Carbon Chains

Another, simple form of elemental carbon would be chains formed from carbon atoms. As a prototype model a single-stranded chain is most suitable. If branching were to be considered, all intermediate forms up to and including the diamond- and graphite-like clusters would be included. For non-branched chains, the two variants to choose from are a system of alternating singly and triply bonded carbon atoms (poly-yne), and a system with all double bonds (cumulenes). Cumulene structures are assumed to be the preferred ones for odd-membered chains, whereas the even ones may have some poly-yne character. Recent studies on linear  $C_6$  show that a cumulene-like structure is preferred, both at the SCF level and when correlation is accounted for(50).

As an alternative to linear chains, a simple ring-shaped molecule should also be considered. Regardless of whether poly-yne or cumulenes are considered, the gain in bond energy due to the new bond formed should be relatively independent of the size of the chain. In contrast, the strain involved in forming a ring is inversely proportional to the number of atoms, assuming a harmonic C-C-C bending potential. Clearly, ring structures should be thermodynamically preferred for chains above a certain size (even though their formation might be kinetically or statistically unfavorable). In fact, already for as small a system as  $C_6$  the ground state structure is found to be cyclic, although the omission of electron correlation would predict a linear, cumulene-like geometry to be marginally lower in energy(50).

Studies on  $C_6$  show that cyclic cumulenes are not well described by a one-determinant wavefunction. In a valence-CASSCF calculation on cyclic  $C_6$ , for example, the Hartree-Fock determinant has a weight of only 0.40. The problem is assumed to be aggravated for larger systems, as the HOMO-LUMO gap diminishes.

We have chosen the  $C_{20}$  poly-yne ring as a reasonable representative for a large chain molecule. The bond lengths optimized at the Hartree-Fock level are 1.37 Å and 1.20 Å, respectively. The same values are found for the experimental bond lengths in 1,3-buta-di-yne  $CH_3-C=C-C-H$ , indicating that there is very little  $\pi$  conjugation in the system.

The cohesive energy per carbon atom in a poly-yne ring is only 99.1 kcal/mol, clearly lower than the value in  $C_{54}$ . Anticipating a long and complicated route of formation when starting from graphite, it does not seem likely that any of the larger clusters observed experimentally would have a linear or cyclic chain structure.

### Non-planar Clusters Containing Five-membered Rings

The existence of a stable  $C_{60}$  molecule, Buckminsterfullerene(BF) was recently proposed(14). In the suggested structure, twelve regular pentagons and twenty hexagons are connected to form an almost perfectly spherical pattern of icosahedral symmetry as in Figure 10.

Previous theoretical work seems to support the existence of this amazing molecule. Several calculations(25-41) on BF at various degree of approximation find a resonance stabilization larger than in benzene, and only slightly smaller than in graphite. From these calculations it has been concluded that the molecule is likely to exist. A recent MNDO study(41) concludes that large polyhedral complexes (> 40 atoms) are more stable than the corresponding graphite-like ones. However, the predictive power of these approximate methods is limited, in

particular for problems where planar and non-planar systems are compared. The interpretation of the original experiment postulating the existence of BF has recently been challenged(11), and *ab initio* calculations of the relative energies involved would resolve the controversy.

The optimized geometry has twelve regular five-membered rings with an edge of 1.453Å. Each of the thirty hexagons shares three sides with pentagons, whereas the three others, shared with adjacent hexagons, are substantially shorter (1.369Å). The structure is very similar to that obtained in recent STO-3G calculations(25). Our calculated HOMO-LUMO splittings are around 8 eV, both at the minimal-basis and double-zeta level. The results of our calculations on BF were reported fully in Ref 39, and are summarized in Table 3.

**Table 3:** Computed properties for BF

**Bond lengths:**

R1 1.453 Å

R2 1.369 Å

**Ionization potential:**

$\Delta$ SCF 7.92 eV

HOMO energy 8.24 eV

**Electron affinity:**

$\Delta$ SCF 0.80 eV

LUMO energy 0.60 eV

**Cohesive energy/carbon atom 114 kcal/mol**

The ionization potential (7.9 eV) falls right outside the bracket of experimental IP's reported for carbon clusters with 40 to 100 atoms ( $6.42 \text{ eV} \leq \text{IP} \leq 7.87 \text{ eV}$ , Ref. 11). Inclusion of correlation effects will lower the calculated  $\Delta$ SCF IP by 0.25 to 0.50 eV, so that the corrected IP will be at the upper end of the experimental IP-bracket. Due to the diffuseness of the  $\pi$  orbital from which an electron is removed, the correlation error in the  $\Delta$ SCF value will be smaller than in cases where an electron is removed from a well localized bond. In these cases a correction of 1 eV is usually applied.

The cohesive energy per carbon atom in BF, 114 kcal/mol, is 11 kcal/mol lower than the value extrapolated for graphite, but 7 kcal/mol higher than the value computed for the  $\text{C}_{54}$  graphite-like sheet or 14.5 kcal/mol higher than for the  $\text{C}_{20}$  poly-acetylene ring. Accordingly, the heat of formation for BF is 650 kcal/mol, suggesting a high degree of instability with respect to graphite.

At the Hartree-Fock level, comparisons between systems with very different molecular and electronic structures have to be made with some care. Strained geometries of the type found in  $\text{C}_{60}$  are usually difficult to describe without polarization functions. The basis set used is therefore expected to slightly favor the planar systems. Repeating the calculations with d-functions added would be unnecessarily time-consuming, and another approach has instead been used. The bowl-shaped corannulene molecule ( $\text{C}_{20}\text{H}_{10}$ , Fig 11) has a geometry resembling a fragment of a  $\text{C}_{60}$  ball, and the strain in the C-framework ought to be similar as well.

To investigate the basis set effect in connection with geometric strain in BF, we have performed calculations with and without d-type functions on corannulene. The d-functions improve the binding with about 10 kcal/mol per C-atom in  $\text{C}_{20}\text{H}_{10}$ ; the corresponding improvement in coronene ( $\text{C}_{24}\text{H}_{12}$ ) is 8 kcal/mol.



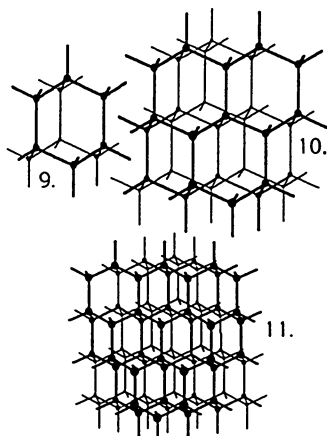


Figure 8. The diamond-like systems  $C_{10}H_{16}$ (9),  $C_{35}H_{36}$ (10) and  $C_{84}H_{64}$ (11).

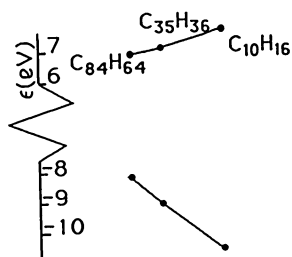


Figure 9. HOMO and LUMO energies for the diamond-like clusters, plotted vs  $1/N$ .

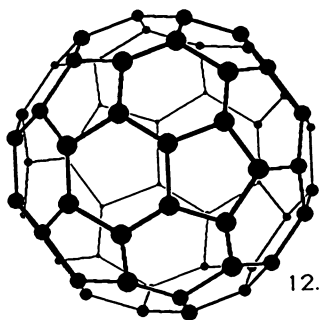


Figure 10 (left). The Buckminsterfullerene molecule.

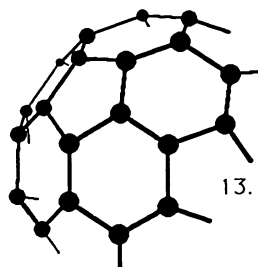


Figure 11 (right). The Corannulene molecule  $C_{20}H_{10}$ .

Within reasonable limits, these numbers are not crucially dependent on the  $d$ -exponents used (0.4-0.6). One can therefore estimate that the inclusion of  $d$ -orbitals in BF would decrease the heat of formation by about 120 kcal/mol.

Even though the predicted relative instability of BF would be somewhat diminished by such an extension of the basis, the main conclusion remains; the  $C_{60}$  molecule is still about 530 kcal/mol higher in energy than a corresponding fragment of bulk graphite.

In conclusion, these calculations suggest that the Buckminsterfullerene molecule is thermodynamically unstable with respect to graphite by about 23 eV. In general, thermodynamically unstable molecules can often be readily synthesized, and frequently exist with virtually infinite lifetimes. The unusually large instability observed in this case might seem almost prohibitive, however no other good candidate for the pronounced peak seen at  $n=60$  in the reported mass spectra has been found. Apparently, the bond strain in BF is still more favorable than a situation with 20 unpaired electrons. Multiple-sheet models have not been considered in this work, since the number of dangling bonds in these would be even larger.

### **Discussion**

We have demonstrated that large-scale quantum-chemical calculations using supercomputers are capable of providing new and unique information about large molecular systems, which would have been very difficult to obtain with other means.

Even though our calculations on condensed aromates show a fairly slow convergence of properties, they allow for an extrapolation on the cohesive energy per carbon atom in bulk graphite. The data obtained from the Mulliken population analysis further show that the inner parts of the larger molecules studied have a domain with little total charge or spin density, which therefore may mimic a graphite surface rather well. Since the problem of dealing with a large number of open shells can be circumvented by these calculations, the approach offers an attractive way of modeling a graphite surface as well as a way to study graphite intercalation compounds.

The fact that pairing up dangling bond electrons may lead to more stable graphite fragments is somewhat surprising. This suggests that the edge of a graphite fragment may look different from what is commonly assumed. This may have far-reaching consequences for the understanding of the chemistry and reactivity of large carbon clusters.

Energetically, the lively debated soccerball-form of  $C_{60}$  compares rather favorably with a graphite-like sheet of carbon atoms. This, of course, does not prove that BF really is (fully or partly) responsible for the  $C_{60}$  peak observed. Due to the large number of degrees of freedom, a study of all plausible isomers would be a prohibitively cumbersome task. Even if such a complete coverage were possible the existence of different molecular species at these conditions is not likely to be governed only by thermodynamic stabilities.

### **Acknowledgments**

The present work was supported by the National Science Foundation, grant #CHE-8610809. We are indebted to Dr Peter Taylor for a copy of his in-core SCF code for the Cray-2.

**Literature Cited:**

1. R.E. Honig, J. Chem. Phys. 1954, **22**, 126.
2. J. Drowart, R.P. Burns, G. DeMaria and M.G. Inghram, J. Chem. Phys. 1959, **31**, 1131.
3. J. Berkowitz and W.A. Chupka, J. Chem. Phys. 1964, **40**, 2735.
4. N. Fürstenau, F. Hillenkamp and R. Nitsche, Int. J. Mass Spectr. Ion Phys. 1979, **31**, 85.
5. N. Fürstenau and F. Hillenkamp, Int. J. Mass Spectr. Ion Phys. 1981, **37**, 135.
6. A. McKellar, Astrophys. J. 1948, **108**, 453.
7. P.Swings, Rev. Mod. Phys. 1942, **14**, 190.
8. P.Swings and A. McKellar, Astrophys. J. 1948, **108**, 458.
9. W.R.M. Graham, K.I. Dismuke and W. Weltner, Jr. Astrophys. J., 1976, **204**, 301.
10. E.A. Rohlfing, D.M. Cox and A. Caldor, J. Chem. Phys. 1984, **81**, 3322.
11. D.M. Cox, D.J. Trevor, K.C. Reichmann and A. Kaldor, J. Amer. Chem. Soc. 1986, **108**, 2457.
12. Y. Liu, S.C. O'Brien, Q.L. Zhang, J.R. Heath, F.K. Tittel, R.F.Curl, H.W. Kroto and R.E. Smalley, Chem Phys Lett. 1986, **126**, 215.
13. J.R. Heath, Q.L. Zhang, S.C. O'Brien, R.F.Curl, H.W. Kroto, and R.E. Smalley, J. Am. Chem. Soc. 1987, **109** 359.
14. H.W. Kroto, J.R. Heath, S.C. O'Brien, R.F.Curl and R.E. Smalley, Nature 1985, **318**, 162.
15. Q.L. Zhang, S.C. O'Brien, J.R. Heath, Y. Liu, R.F.Curl, H.W. Kroto and R.E. Smalley, J. Phys. Chem. 1986, **90**, 525.
16. J.R. Heath, S.C. O'Brien, Q.L. Zhang, Y. Liu, R.F.Curl, H.W. Kroto, F.K. Tittel and R.E. Smalley, J. Am Chem Soc. 1985, **107**, 7779.
17. L.A. Bloomfield, M. Geusic, R.R. Freeman and W.L.Brown, Chem.Phys. Letters 1985, **121**, 33.
18. M.E. Geusic, T.J. McIlrath, M.F. Jarrold, L.A. Bloomfield, R.R. Freeman and W.L.Brown, J. Chem. Phys. 1986, **84**, 2421.
19. R.D. Knight, R.A. Walsh, S.C. Foster, T.A. Miller, S.L. Mullen and A.G. Marshall, Chem. Phys. Letters 1986, **129**, 331.
20. S.W. McElvany, W.R. Creasy and A. O'Keefe, J. Chem. Phys. 1986, **85**, 632.
21. A. O'Keefe, M.M. Ross and A.P. Baronavski, Chem Phys Letters 1986, **130**, 17.
22. M.Y. Hahn, E.C. Honea, A.J. Paguia, K.E. Schriver, A.M. Camarena and R.L. Whetten, Chem. Phys. Letters 1986, **130**, 12.
23. S.C. O'Brien, J.R. Heath, H.W. Kroto, R.F.Curl, and R.E. Smalley, Chem Phys Letters 1986, **132**, 99.
24. J.Bernholz and J.C. Phillips, Phys. Rev B 1986, **33**, 7395.
25. R.L. Disch and J.M. Schulman, Chem. Phys. Letters 1986, **125**, 465.
26. A.J. Stone and D.J. Wales, Chem. Phys. Letters 1986, **128**, 50.
27. D.S. Marynick and S. Estreicher, Chem. Phys. Letters 1986, **132**, 383.
29. D.J. Klein, T.G. Schmalz, G.E. Hite and W.A. Seitz, J. Amer. Chem. Soc. 1986, **108**, 1301.
30. T.G. Schmalz, W.A. Seitz, D.J. Klein and G.E. Hite, Chem. Phys Letters 1986, **130**, 203.
31. P.D. Hale, J. Amer. Chem. Soc. 1986, **108**, 6087.
32. P.W. Fowler and J. Woolrich, Chem. Phys. Letters 1986, **127**, 78.
33. P.W. Fowler, Chem. Phys. Letters 1986, **131**, 444.

**American Chemical Society  
Library**

1155 16th St. N.W.  
Washington, D.C. 20036

34. M. Ozaki and A. Takahashi, Chem Phys. Letters 1986, **127**, 242.
35. A.D.J. Haymet, Chem. Phys. Letters 1985, **122**, 421.
36. A.D.J. Haymet, J. Amer. Chem. Soc. 1986, **108**, 319.
37. R.C. Haddon, L.E. Brus and K. Raghavachari, Chem. Phys. Letters, 1986, **125**, 459.
38. R.C. Haddon, L.E. Brus and K. Raghavachari, Chem. Phys. Letters, 1986, **131**, 165.
39. H.P. Lüthi and J. Almlöf, Chem. Phys Letters in press.
40. S. Satpathy, Chem Phys Lett. 1986, **130**, 545.
41. M.D. Newton and R.E. Stanton, J. Amer. Chem. Soc. 1986, **108**, 2469..
42. J.P. Ritchie, H.F. King and W.S. Young, J. Chem. Phys. 1986, **85**, 5175
43. R.A. Whiteside, R. Krishnan, D.DeFrees, J.A. Pople and P.v.R. Schleyer, Chem. Phys. Lett. 1981, **78**, 538.
44. R.A. Whiteside, R. Krishnan, M.J. Frish, J.A. Pople and P.v.R. Schleyer, Chem. Phys. Lett. 1981, **80**, 547.
45. K. Raghavachari and J.S. Binkley, J. Chem. Phys., in press.
46. P. Joyes and M. Leleyter, J. Phys. 1984, **45**, 1681..
47. K.S. Pitzer and E. Clementi, J. Amer. Chem. Soc. 1959, **81**, 4477
48. R. Hoffmann, Tetrahedron, 1966, **22**, 521.
49. D.W. Ewing and G.V. Pfeiffer, Chem. Phys. Lett. 1982, **86**, 365.
50. K. Raghavachari, R.A. Whiteside and J.A. Pople, J. Chem. Phys. 1986, **85**, 6623
51. J.R. Dias, J. Mol. Structure Theochem, 1986, **137**, 9.
52. J. Almlöf, K. Faegri, Jr, and K. Korsell, J. Comput Chem. 1983, **3**, 3003
53. P.R. Taylor, private comm.
54. F.B. Van Duijneveldt, IBM Res. Report RJ 945 1971.
55. J.D. Donohue, *The Structure of the Elements* Wiley; New York, 1974.
56. W. Weinert, E. Wimmer and A.J. Freeman, Phys. Rev B, 1982, **26**, 4571.
57. P.D. Zavitsanos and G.A. Cariso, J. Chem. Phys. 1973, **39**, 2966.
58. R.F. Willis, B. Fuebacher and B. Fritton, Phys. Rev. B 1971, **4**, 2441.
59. M. Dupuis, H.O. Villar and E. Clementi, this volume.

RECEIVED June 15, 1987

## Chapter 4

# Local Density Functional Theory of Surfaces and Molecules

## Unified Electronic Structural Approach

E. Wimmer<sup>1</sup>, A. J. Freeman<sup>2</sup>, C.-L. Fu<sup>2</sup>, P.-L. Cao<sup>2</sup>, S.-H. Chou<sup>2</sup>, and B. Delley<sup>3</sup>

<sup>1</sup>Cray Research, Inc., 1333 Northland Drive, Mendota Heights, MN 55120

<sup>2</sup>Department of Physics and Astronomy, Northwestern University, Evanston, IL 60201

<sup>3</sup>RCA Laboratories, Badenerstrasse 569, CH-8048 Zurich, Switzerland

In this contribution it is shown that local density functional (LDF) theory accurately predicts structural and electronic properties of metallic systems (such as W and its (001) surface) and covalently bonded systems (such as graphite and the ethylene and fluorine molecules). Furthermore, electron density related quantities such as the spin density compare excellently with experiment as illustrated for the di-phenyl-picryl-hydrazyl (DPPH) radical. Finally, the capabilities of this approach are demonstrated for the bonding of Cu and Ag on a Si(111) surface as related to their catalytic activities. Thus, LDF theory provides a unified approach to the electronic structures of metals, covalently bonded molecules, as well as semiconductor surfaces. Consistently, the agreement with experiment is about 1% for geometric parameters and 5-10% for force constants. On the other hand, binding energies are found to be usually too large by 1-2eV per atom. The computational efforts in the LDF approach scale with the third power in the number of orbitals. Consequently, the speed and memory capabilities of supercomputers will allow the study of systems with a hundred atoms and more.

It is well established that quantum chemical approaches based on Hartree-Fock (HF) theory provide a successful and thoroughly tested framework to calculate the electronic structure and energetics of inorganic and organic molecular systems (1). A number of well tested and documented computer programs are available such as GAUSSIAN, GRADSCF, GAMESS, and HONDO to perform SCF calculations, geometry optimizations, calculations of vibrational frequencies, normal mode analysis, and to include correlation effects on different levels such as perturbation theory and CI expansions. There are, however, two major limitations to the HF approach: (i) the HF model breaks down in the limit of the ideal metal (2); (ii) if the one-particle wave functions are expanded variationally in a basis set, usually

0097-6156/87/0353-0049\$06.00/0

© 1987 American Chemical Society

Gaussian-type orbitals, the computational requirements grow, in the limit, with the fourth power in the number of basis functions on the SCF level and with even a higher power for methods including correlation. Both the conceptual and the computational aspects prevent the computational study of important problems such as the chemistry of transition metal surfaces, interfaces, bulk compounds, and large molecular systems.

These limitations, most urgently felt in solid state theory, have stimulated the search for alternative approaches to the many-body problem of an interacting electron system as found in solids, surfaces, interfaces, and molecular systems. Today, local density functional (LDF) theory (3-4) and its generalization to spin polarized systems (5-6) are known to provide accurate descriptions of the electronic and magnetic structures as well as other ground state properties such as bond distances and force constants in bulk solids and surfaces.

The aim of the present paper is to illustrate that the LDF approach, although originally designed for metallic systems, can be successfully applied also to isolated organic and inorganic molecules yielding the same level of accuracy in bond lengths, bond angles, forces, charge densities, and spin densities as in condensed systems. Thus, the LDF approach provides a unified theoretical framework for the study of extended surfaces as well as localized systems such as organic molecules. As a consequence, this approach opens up the systematic theoretical/ computational study of surface and interface chemistry.

As the computational effort in the LDF approach grows, in the limit, only with the third power in the number of orbitals, it can be expected that fairly large systems with a hundred atoms, including transition metals, rare earth, and actinide elements, will become tractable.

### Local Density Functional (LDF) Theory

In the Hartree-Fock approach, the many-body wave function in form of a Slater determinant plays the key role in the theory. For instance, the Hartree-Fock equations are derived by minimization of the total energy expressed in terms of this determinantal wave function. In density functional theory (3,4), the fundamental role is taken over by an observable quantity, the electron density. An important theorem of density functional theory states that the correct ground state density,  $n(\mathbf{r})$ , determines rigorously all electronic properties of the system, in particular its total energy. The total energy of a system can be expressed as a functional of the density  $n'(\mathbf{r})$  and this functional,  $E[n'(\mathbf{r})]$ , is minimized by the ground state density.

The total energy as a functional of the density can be written in the form

$$E[n] = T[n] + U[n] + E_{xc}[n] \quad (1)$$

where  $T[n]$  is the kinetic energy of a system of non-interacting particles of density  $n$ ;  $U[n]$  is the classical electrostatic energy due to the Coulomb interactions, and

$E_{xc}[n]$  includes all many-body contributions to the total energy, in particular the exchange and correlation energies.

The next step is the decomposition of the total density into single particle densities which are related to single particle wave functions by

$$n(\mathbf{r}) = \sum_i |\psi_i(\mathbf{r})|^2 \quad (2)$$

where the sum goes over all occupied states. Using this decomposition, the conditions to minimize  $E[n]$  lead to effective one-particle Schrödinger equations of the form

$$[-1/2\Delta + V_{\text{eff}}(\mathbf{r})]\psi_i = \epsilon_i \psi_i \quad (3)$$

The effective potential is written as a sum of the Coulomb potential and the exchange-correlation potential:

$$V_{\text{eff}}(\mathbf{r}) = V_C(\mathbf{r}) + V_{xc}(\mathbf{r}) \quad (4)$$

The Coulomb potential is related to the charge density via Poisson's equation

$$-\Delta V_C(\mathbf{r}) = 4\pi e^2 n(\mathbf{r}) \quad (5)$$

and the exchange-correlation potential is given by

$$V_{xc}(\mathbf{r}) = \delta E_{xc}[n(\mathbf{r})]/\delta n(\mathbf{r}) \quad (6)$$

So far, the expressions given are formally rigorous. Clearly, the last term in eq.(1) requires approximation. A simple and, as it turns out, surprisingly good approximation is the so-called local-density approximation (LDA). Using the known many-body energy,  $\epsilon[n]$ , of an electron in a homogeneous, interacting electron gas of density  $n$  (7-9), this first-principles result is used to approximate the inhomogeneous case by setting

$$E_{xc}[n] \equiv \int n(\mathbf{r}) \epsilon[n(\mathbf{r})] d\mathbf{r} \quad (7)$$

With this approximation, the effective potential in the LDF equations (3) can be evaluated explicitly via eqs.(4)-(6), provided the charge density is known. In turn, the charge density is defined by the solutions of the LDF equations (3) via eq. (2). This leads to a familiar self-consistent procedure: an initial charge density is constructed by, e.g. overlapping atomic charge densities. From this ("input") charge density the effective one-particle potential is calculated by solving Poisson's equation (5) and by evaluating the exchange-correlation potential (6) which is given by an analytic function of the density,  $n$ .

In the next step, which is numerically the most demanding, the differential equations (3) are solved. Two possible strategies using a variational expansion of the single particle wave functions,  $\psi_i$ , are described below. After the eigenvalues and eigenfunctions have been found, a new ("output") charge density can be

constructed using Fermi-Dirac statistics (Aufbau principle) in equation (2). This closes one iterative step. The output charge density can be fed back into the evaluation of the effective-potential energy operator and the procedure is repeated until the output charge density equals the input charge density to within a given tolerance. Usually, sufficient self-consistency (stable total energies to within better than 0.1 kcal/mole) are achieved when the difference between the input and output charge densities averaged over all space is less than 0.1 electrons/(a.u.)<sup>3</sup>. To construct the input density for a given iteration, the input and output charge densities from previous iterations are combined to ensure damping and an efficient extrapolation. Depending on the system, between 10 and 50 iterations are necessary (magnetic systems such as Ni are more difficult to converge than systems with a low density of states at the Fermi level).

Once the self-consistent charge density is evaluated for a given choice of nuclear coordinates, the corresponding total energy can be found using eqs. (1)-(7).

### Computational Approaches

**Single slab.** A number of recent calculations of surface electronic structures have shown that the essential electronic and structural features of the bulk material are recovered only a few atomic layers beneath a metal surface. Thus, it is possible to model a surface by a single slab consisting of 5-15 atomic layers with two-dimensional translational symmetry parallel to the surface and vacuum above and below the slab. Using the two-dimensional periodicity of the slab (or thin film), a band-structure approach with two-dimensional periodic boundary conditions can be applied to the surface electronic structure.

One of the most accurate approaches to solve the LDF equations for the single slab geometry is the full-potential linearized augmented plane wave (FLAPW) method (10). Here, we highlight only the essential characteristics of this approach; for further details the reader is referred to a recent review article (11).

The basic idea in this variational method is the construction of each basis function in the following way: the real space of the slab is divided into three different regions, spheres around the nuclei, the vacuum region above (and below) the slab, and the remaining interstitial region. In each region, the "natural" form of the wave function is used, i.e. radial functions multiplied by spherical harmonics inside the spheres, plane waves in the interstitial region, and a product of z-dependent functions and two-dimensional plane waves for the vacuum region (z is the direction perpendicular to the slab). Across the various boundaries, each basis function is continuous in value and first derivative. The radial functions inside the spheres and the z-dependent functions in the vacuum are generated numerically in each iterative step, thus reflecting changes in the potential in these regions. Inside the spheres, angular momentum components up to  $l=8$  are included. Between 50 and 100 basis functions per atom ensure high variational freedom. The charge density and the potential are treated without any shape approximation ("full-potential"). Poisson's equation for this full potential is solved using a method described by Weinert (12). The exchange-correlation part of the effective



potential is obtained numerically by using a least-squares fitting technique. It should be noted that the actual values of the sphere radii and the position of the vacuum boundaries do not influence the results; these values are chosen simply to ensure the best convergence of various expansions. All electrons of the system are included in the self-consistency procedure: the core electrons fully relativistically within a central field approximation and the valence electrons semi-relativistically, i.e. spin-orbit coupling is neglected (13), within the full potential. Total energies are calculated using a scheme introduced and described by Weinert et al. (14). It should be noted that the FLAPW method, of course, also exists for bulk systems with three-dimensional periodicity (15).

**Molecules and Clusters.** The local nature of the effective Hamiltonian in the LDF equations makes it possible to solve the LDF equations for molecular systems by a numerical LCAO approach (16,17). In this approach (17), the atomic basis functions are constructed numerically for free atoms and ions and tabulated on a numerical grid. By construction, the molecular basis becomes exact as the system dissociates into its atoms. The effective potential is given on the same numerical grid as the basis functions. The matrix elements of the effective LDF Hamiltonian in the atomic basis are given by

$$\int \phi_i [-1/2\Delta + V_{\text{eff}}(\mathbf{r})] \phi_j \, d\mathbf{r} \quad (8)$$

The result of the kinetic energy operator on the basis function  $\phi_j$  is known from the atomic calculations. The remaining integrals, the overlap integrals

$$\int \phi_i \phi_j \, d\mathbf{r} \quad (9)$$

and the potential integrals

$$\int \phi_i V_{\text{eff}}(\mathbf{r}) \phi_j \, d\mathbf{r} \quad (10)$$

can be evaluated by a numerical integration as all functions in the integrands are tabulated on a real space grid.

After the determination of eigenvalues and eigenvectors in a given iteration, the charge density is first obtained numerically on each grid point. In order to solve Poisson's equation, this density is fitted by a least-squares fitting technique to a multicenter- multipolar expansion (17) which then allows the analytic solution of eq. (5). The exchange-correlation potential is evaluated numerically on each grid point leading to the effective potential needed to set up the effective Hamiltonian for the next iteration. Among the integrals, only the potential integrals need to be updated during the iterative process whereas the other parts of the matrix elements can be stored.

It is important to note that the only physical approximation here is the LDA. All other approximations are of a numerical nature and their convergence can be monitored and improved in a systematic way. Thus, this method allows a probe of the LDA limit for molecules and clusters without any further approximations such

as muffin-tin potentials which have been used in the past but, conceptually, are not at all related to the LDA.

### Illustrative Results

**The W(001) Surface.** One of the most fundamental questions in surface chemistry is the actual structure of the surface. For example, knowledge of the position of the atoms on a surface is crucial for understanding surface diffusion, chemisorption, and catalysis (18). The W(001) surface is one of the best studied transition metal surfaces and thus can serve as an excellent testing ground for theoretical/computational approaches. This system presents a number of theoretical challenges: (i) tungsten is in the middle of the 5d transition metal series and thus correlation effects play an important role in the binding as can be seen from the isoelectronic transition metal dimers  $\text{Mo}_2$  and  $\text{Cr}_2$  (19,20), (ii) tungsten with  $Z=74$  requires a relativistic treatment, (iii) the tungsten surface is well known for its richness in electronic surface states and surface resonance states (21), (iv) this surface is known to undergo a thermally induced phase transition from a high-temperature (1x1) phase (which, possibly, is disordered) to an ordered c(2x2) phase (22). It is now generally believed that relaxation and reconstruction effects on surfaces are the rule rather than the exception.

LDF theory is well suited to handle metallic tungsten. FLAPW calculations for the bulk material show (15) that LDF theory gives a theoretical value for the bcc-lattice constant of 3.148 Å which is 0.4% smaller than the experimental value. However, the theoretical binding energy of 9.76 eV/atom is markedly larger than the experimental value of 8.90 eV/atom. This over-estimate of binding energies in the LDF approach is systematic and will be discussed below. Furthermore, the bulk calculations demonstrate that the bcc structure, which is the experimentally observed phase, is 0.46 eV/atom more stable than the fcc structure. This computational result shows that, as expected, relative energy differences are well described despite the overestimation of the binding energies.

Upon cooling the W(001) surface below room temperature, the observed low-energy electron diffraction (LEED) pattern changes from a (1x1) into a c(2x2) structure. Originally, an alternating displacement perpendicular to the surface was suggested (22) to account for the c(2x2) LEED pattern. Currently, the most widely accepted model, suggested by Debe and King (23) to explain the observed reconstruction, namely alternating lateral displacements of W atoms along the <110> directions, has met with conflicting experimental results: Melmed et al. (24) concluded that W(001) is reconstructed with alternating vertical displacements of the surface atoms in the temperature range from 15 to 580 K. On the other hand, results of ion-scattering experiments by Stensgaard et al. (25) supported neither a lateral nor vertical displacive model for the reconstructed surface, but instead provided evidence for an order-disorder transition on this surface.

Self-consistent LDF total energy calculations (26) using the single slab FLAPW method revealed that alternating vertical displacements of the surface atoms do not lead to a lowering in the total energy. In contrast, alternating lateral displacements yield a minimum in the total energy (cf. Fig.1). The theoretical

result of  $0.18 \text{ \AA}$  for the displacement is in excellent agreement with the value deduced from experiment (23).

The driving force for this surface reconstruction can be related to the high density of surface states and surface resonance states near  $E_F$ , the Fermi level (cf. Fig.2). These states of mostly d-character are involved in the in-plane as well as inter-plane bonding as can be seen from the single particle density of a typical occupied state near  $E_F$  (cf. Fig.3). The calculations show that an alternating vertical displacement does not affect the high density of surface states at  $E_F$  whereas a lateral displacement breaks the symmetry such that the single peak at  $E_F$  is split into a bonding and antibonding partner where the antibonding partner becomes unoccupied. Thus, a Jahn-Teller like mechanism is the driving force of the reconstruction of the W(001) surface.

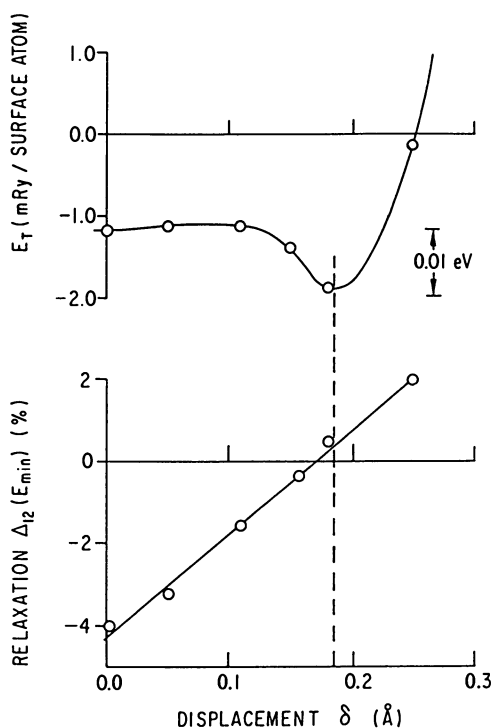


Fig.1. Total energy (1mRy=0.314 kcal/mole) per unit cell for a five-layer W(001) slab as a function of lateral displacement,  $\delta$ , and spacing between the surface and sub-surface layers,  $\Delta$ ; the latter is given relative to the bulk spacing of  $1.581 \text{ \AA}$  (after Ref. 26).

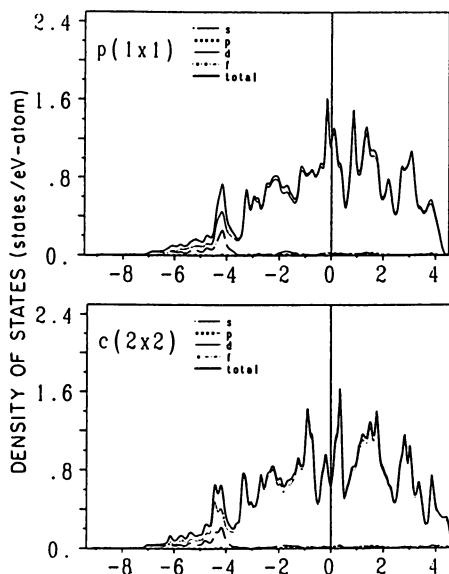


Fig.2. Density of states in a five-layer W(001) slab, projected on the surface atomic layer. The upper panel shows the results for the unreconstructed and the lower panel for the reconstructed (lateral displacements) surface (after Ref. 26).

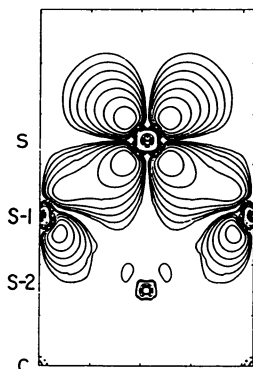


Fig.3. Single particle density of a characteristic surface resonance state on the W(001) surface shown in the (110) plane perpendicular to the surface (after Ref. 21).

The accuracy of LDF calculations in the prediction of surface geometries not only holds for clean metal surfaces such as the W(001) surface discussed above, but is also found for adsorbates such as H (27), O (28), and S (29) on Ni(001) surfaces. Rather than going into detail on clean and adsorbate covered surfaces, we will now focus on the description of the C-C bond by LDF theory. To this end, we first discuss a layer of condensed benzene rings, i.e. a graphite monolayer, and then focus our attention on the ethylene molecule.

**Graphite monolayer.** Using the single slab FLAPW method, the electronic structure and binding curve of a monolayer of graphite has been calculated near the equilibrium geometry (14). The calculated C-C bond length at equilibrium is 1.416 Å which is 0.35% smaller than the value found experimentally for bulk graphite. Due to the dominant in-plane interactions in graphite compared with the weak inter-planar bonding, the C-C bond length in the monolayer should be very close to that in bulk graphite. Hence, these results indicate that LDF theory describes the C-C bond length to within a few tenths of a percent.

On the other hand, as in the case of W, the binding energy is overestimated: the calculated binding energy in a graphite monolayer is found (14) to be 8.69 eV per atom compared with the experimental value of 7.39 eV/atom for graphite. As discussed in Ref. (14), this over-estimate appears to be related to the fact the LDF makes a larger error for the free atom than it does for the condensed phase. Therefore, the total energy of the free atom is too high and the binding energy of the solid or molecule comes out too large. It can be hoped that future systematic studies on a number of systems and compounds will show that this is indeed the case. Provided the error can be attributed to the free atoms, it would be easy to correct it in an ad-hoc way or density functional methods can be developed to improve the results for the free atom.

In the following examples we will focus on isolated molecules. In these cases, the LDF equations are solved by the molecular method described above using the DMOL/86 program (17).

**Rotational Barrier in Ethylene.** It is well known that the rotational barrier of the ethylene molecule cannot be adequately described by a single reference Hartree-Fock calculation: SCF calculations on this level resulted in values of 126 kcal/mole (30) and 129 kcal/mole (31) whereas the experimental value is 65 kcal/mole (32). Open-shell ab initio calculations of double zeta+polarization quality give the more acceptable value of 48 kcal/mole (33). Inclusion of correlation such as in CEPA calculations yield theoretical results within the experimental error bar (34), albeit at a considerable computational cost.

Using local spin density functional (LSDF) theory, we obtain 70 kcal/mole for the rotational barrier of the ethylene molecule (35). In these calculations, we use the equivalent of a double-zeta+polarization basis set, i.e. for C two 2s functions,

six 2p functions and five 3d functions, and two 1s functions and three 2p functions for the H atoms. No symmetry restrictions are used in this spin-polarized calculation. A total number of 5380 integration points are used. The multi-polar expansion of the density includes angular momentum components up to  $l=2$  on the C atoms and up to  $l=1$  on the H atoms. A series of total energy calculations for different geometries are performed to optimize the C-C and C-H bond lengths and the HCH bond angle. The results of this geometry optimization are summarized in Table I.

As can be seen from Table I, the C-C bond distance as described by LDF is closer to experiment than the corresponding HF value obtained with a 6-31G\* basis. Including correlation via second and third order Moller-Plesset perturbation theory and via CI leads to very close agreement with experiment. The C-H bond length is significantly overestimated in the LDF calculations by almost 2%. The HCH bond angle is reasonably well described and lies close to all the HF and post-HF calculations. Still, all the theoretical values are too small by more than one degree compared with experiment; the deviation from experiment is particularly pronounced for the semi-empirical MNDO calculation.

As expected, the C-C bond length widens significantly for the rotational transition state. Here, the agreement between the semi-empirical MNDO results and the first-principles LDF results is remarkable. The discrepancy in the C-H bond length remains, but the trend of a small bond shortening from the ground state to the rotational transition state can be found for both the MNDO and the LDF calculation.

**Fluorine molecule.** The  $F_2$  molecule (cf. Table II) is notoriously difficult to describe in the HF approach. In this method, the molecule is unbound and the equilibrium distance is too short by almost 6% using a 6-311G\*\* basis (1). The vibrational frequency is found to be  $1254\text{ cm}^{-1}$  (36) compared with the significantly lower experimental value of  $923\text{ cm}^{-1}$  (37). Using a correlated many-body perturbation theory approach, SDTQ-MBPT(4), Laidig et al. (36) obtained a F-F equilibrium bond length of  $1.434\text{ \AA}$  and a vibration frequency of  $850\text{ cm}^{-1}$ . Using a multi-reference linearized coupled-cluster method, MR-LCCM-10, the same authors obtained values of  $1.435\text{ \AA}$  for the bond length and  $842\text{ cm}^{-1}$  for the frequency.

Using the computationally much less demanding LDF approach with the equivalent of a double-zeta-polarization basis, we obtain (38)  $1.420\text{ \AA}$  for the bond length which is astonishingly close to the experimental value of  $1.412\text{ \AA}$ . The vibrational frequency from the LDF calculations is found to be  $994\text{ cm}^{-1}$ , i.e. about 8% higher than the experimental value. LDF theory substantially overestimates the binding energy of the fluorine molecule. Instead of the experimental value of  $1.66\text{ eV}$  (37), LDF theory gives  $3.25\text{ eV}$ . Again, we see the trend of overestimating the binding energy. In the case of  $F_2$ , this effect is more pronounced than with carbon.

Table I. Bond lengths (in Å) and bond angles (in degrees) for the ethylene molecule

	R(C-C)	R(C-H)	$\alpha$ (HCH)
<b>ground state</b>			
MNDO (a)	1.334	1.089	113.6
HF (b)	1.317	1.076	116.4
MP2 (b)	1.336	1.085	116.6
MP3 (b)	1.334	1.086	116.4
CID (b)	1.328	1.084	116.3
LDF (c)	1.332	1.105	116.1
expt.	1.339	1.085	117.8
<b>rotational transition state</b>			
MNDO (a)	1.434	1.084	117.2
LDF (c)	1.432	1.103	114.6

(a) this work using MOPAC version 3.11, J.J.P.Stewart (1987)

(b) Ref. (1), p.156

(c) this work

Table II. Bond lengths (in Å) and vibrational frequencies (in  $\text{cm}^{-1}$ ) for the fluorine molecule

	R(F-F)	$\omega$
HF/6-31G* (a)	1.345	1245
HF/6-311G** (a)	1.331	
MP2/6-31G*		1008
CID/6-31G* (a)	1.399	
SDTQ-MBPT(4) (b)	1.434	850
MR-LCCM-10 (b)	1.435	842
LDF (c)	1.420	994
exp. (a)	1.412	923

(a) Ref. (1), p.151 and p.232

(b) Ref. (36)

(c) this work

**$\alpha,\alpha'$ -diphenyl- $\beta$ -picryl-hydrazyl (DPPH) radical.** So far, we have discussed fairly small molecules that are computationally accessible by ab initio methods including correlation effects. As pointed out earlier, one of the advantages of the LDF approach is the fact that the computational implementation can be achieved by an  $N^3$  algorithm. This enables one to treat relatively large systems on the same level of numerical accuracy and basis set quality as those used for the small molecules discussed above.

As an example of a larger molecule, we now discuss the electronic structure of the DPPH radical (cf. Figs.4 and 5). This stable free radical is well known from paramagnetic-resonance studies (39,40) which devoted considerable effort to estimate the spin density and delocalization of the unpaired electron (40). Using spin-polarized neutron diffraction, the spin density of the DPPH radical was mapped out using a multipole expansion on the different atoms (41,42). These experiments show that there is a nearly equal spin density on the two N-atoms of the hydrazyl group and that there is a fair amount of delocalization over the entire molecule. Furthermore, these measurements reveal oscillations of the spin density between positive and negative values in the aromatic rings.

We have carried out (43) a self-consistent spin-polarized LDF calculation on the DPPH radical using the experimental structure of the molecule. A projection of the resulting spin density containing the two N-atoms of the hydrazyl group is displayed in Fig.4. The spacial distributions of the charge density and spin density are illustrated in color in Fig.5. The theoretical results show, in agreement with experiment, that the spin density on these two N-atoms is nearly equal. Furthermore, there is clear evidence of an oscillation of the spin density in one of the phenyl rings. It is interesting to note that this oscillation is pronounced in only one of the two phenyl rings (denoted "A" in Fig.4) in excellent agreement with the experimental data. This effect is related to the particular orientation of the two phenyl rings which favors the spin oscillation only in the ring which is nearly coplanar with the hydrazyl N-atoms. The spin density on these N-atoms is caused by the occupation of  $p_z$  orbitals (the z axis being perpendicular to the plane drawn in Fig.4). The calculations reveal a fair degree of delocalization of the spin density also over the picryl ring with a significant positive spin density on the O atoms (particularly one marked with an arrow in Fig.4).

**Cu and Ag on Si(111) surfaces.** In the last example, we come back to surfaces. It is well known (44-46) that Cu catalyzes the formation of dimethyl-dichlorosilane from methylchloride and solid silicon, which is a crucial technological step in the synthesis of silicone polymers. Even today, the details of the catalytic mechanism are unclear. Cu appears to have unique properties; for example, the congener Ag shows no catalytic activity. Thus, the investigation of the differences between Cu and Ag on Si surfaces can help in understanding the catalytic process. Furthermore, the bonding of noble metal atoms to Si surfaces is of great importance in the physics and chemistry of electronic devices.

We have carried out a local density functional study of the interactions



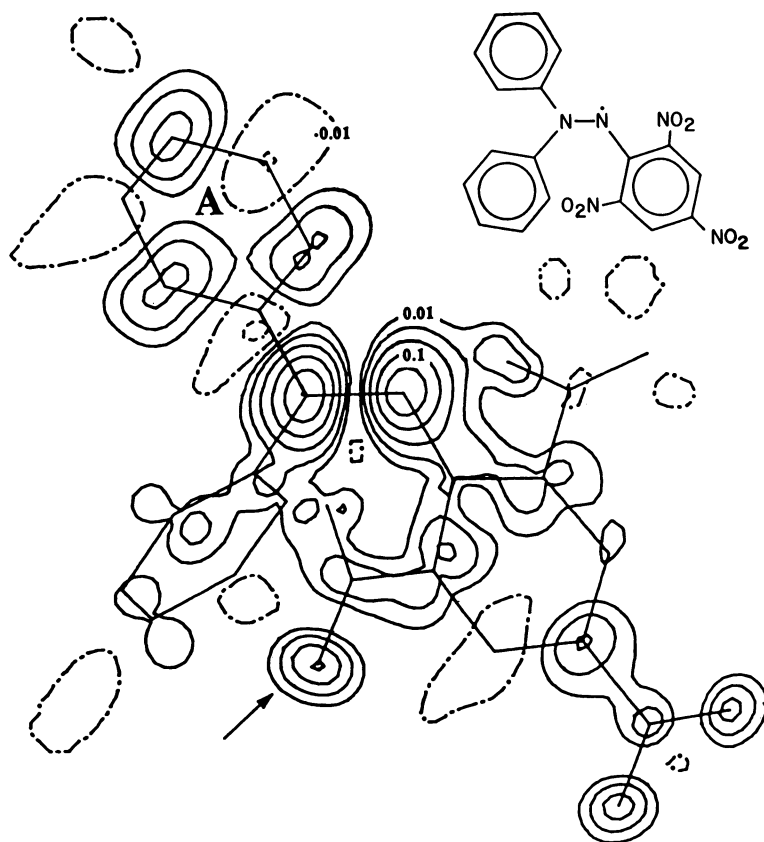
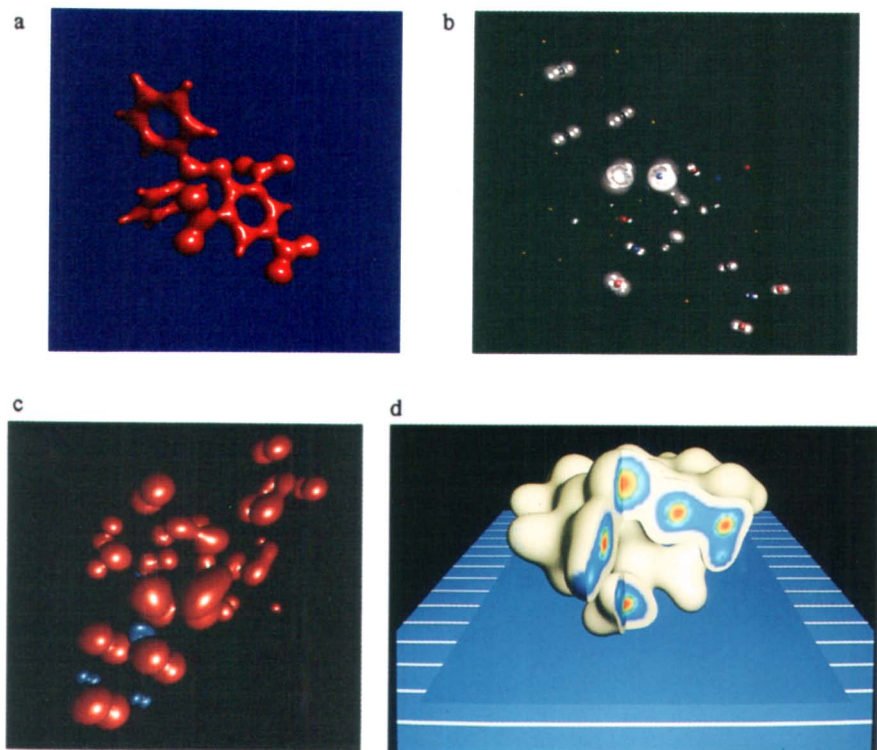


Fig.4 Spin density in the DPPH molecule projected onto a plane containing the two N-atoms of the hydrazyl group. Densities are given in units of  $e/\text{\AA}^2$ ; negative spin densities are indicated by broken lines.



**Fig.5** (a) Charge density in the DPPH molecule: the three-dimensional contour surface connects points with a charge density of  $0.2 \text{ e}/(\text{a.u.})^3$ . (b) and (c) Spin density in DPPH: the three-dimensional contours connect points with a spin density value of (b)  $0.005$  and (c)  $0.01 \text{ e}/(\text{a.u.})^3$ ; negative spin densities are given in blue. (d) Charge density in the Cu/Si cluster: the outer surface corresponds to a charge density value of  $0.02 \text{ e}/(\text{a.u.})^3$ ; in the cutting planes, the range of colors from blue to red represents increasing electron density.

between Cu and Ag atoms on a Si(111) surface (47). In these calculations, the Si surface was represented by a cluster of 20 Si atoms (cf. Fig.6). The bonds to the bulk Si were saturated with H atoms. Using the equivalent of a double-zeta+ polarization basis for all atoms, self consistent, spin-polarized calculations were carried out for hollow, top, and bridge sites for the adsorbate. As can be seen from the binding energy curves (Fig.6), both Cu and Ag are found to be adsorbed in the three-fold hollow sites in their ground states with adsorption heights of 0.74 and 1.48 Å and binding energies of 92 and 72 kcal/mole, respectively.

The calculations reveal one striking difference between Cu and Ag: it is found that it requires only 4 kcal/mole for the Cu atoms to move into the plane of the surface Si atoms whereas for Ag this geometry is 53 kcal/mole higher than the ground state - even when the nearest Si atoms are allowed to move away from the noble metal atom. Thus, Cu is seen to penetrate fairly easily into the Si lattice whereas Ag stays above the surface. These theoretical findings are substantiated by thermal desorption and Auger spectroscopy measurements (48) showing that at elevated temperatures Ag desorbs into the gas phase whereas Cu remains in the solid phase.

In addition, the calculations also provide evidence for differences in the electronic structures: Cu weakens the Si-Si bond between adjacent surface and sub-surface atoms to a larger extent than does Ag. Thus, Cu promotes the Si-Si bond-breaking without blocking access to the surface whereas Ag has a smaller electronic effect and blocks the Si surface from a direct interaction with methylchloride molecules.

Finally, these calculations may shed new light on a controversy concerning the adsorption geometry of Ag atoms on a Si(111) surface: recent scanning tunneling microscopy studies for the system Ag/Si carried out by two research groups (49,50) lead to conflicting conclusions. Whereas van Loenen et al. (50) derive evidence for Ag trimers being embedded underneath the surface Si atoms, Wilson and Chiang (49) cannot unambiguously resolve the position of the Ag atoms, yet favour the assumption that Ag atoms are the topmost layer. In fact, recent impact scattering spectroscopy studies (51) place the Ag atoms on top of the surface Si atoms. This model is consistent with our theoretical studies which reveal a very high barrier for the penetration of Ag atoms into the surface. It should be added, however, that our calculations do not include long-range surface reconstruction effects and refer to a static situation. At elevated temperature, the dynamics on the surface may allow the diffusion of Ag atoms into the Si crystal. Future combined electronic structure and molecular dynamics studies would be able to provide answers to these questions.

## Discussion and Conclusion

We have shown that local density functional (LDF) theory provides a methodology that allows a unified theoretical/computational study of such diverse systems as bulk W and its surface, graphite, the ethylene, fluorine, and DPPH

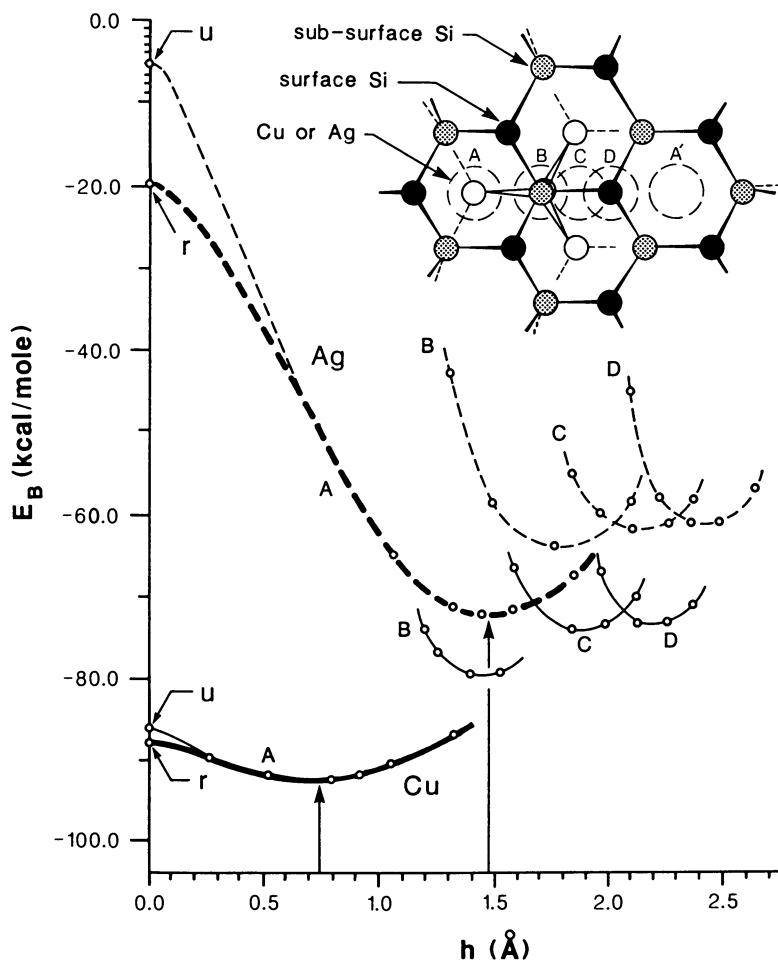


Fig.6 Binding energies of Cu (full lines) and Ag (broken lines) on a Si(111) surface. The perpendicular distance between the adsorbate atoms and the plane of the surface silicon atoms is denoted by  $h$ . Hollow, top, and bridge positions of the adsorbate atoms are indicated by the labels A, B, etc. as shown in the insert. "u" corresponds to an unrelaxed and "r" to a relaxed geometry of the neighboring surface Si atoms (after Ref.47)

molecules, as well as noble metals (Cu and Ag) on a Si(111) surface. The present results show that the theory is capable of providing information on bond lengths and bond angles within the one-percent range compared with experiment for both metallic systems and covalently bound molecules. Furthermore, the value for the rotational barrier of the ethylene molecule is fairly close to experiment, in contrast to restricted and unrestricted HF calculations. Starting from the HF description, inclusion of correlation is needed to exceed the accuracy of the LDF calculation for the rotational barrier. The C-C bond distances are very well described by the LDF calculations both in graphite as well as in the ethylene molecule (to within 0.4% of experiment). On the other hand, the C-H bond length in LDF is too large by about 2%. For bulk W, the graphite monolayer, and the fluorine dimer, the LDF binding energies are too large by more than 1eV/atom. A possible explanation for this fact could be that the local density approximation (LDA) is more appropriate in the molecular or solid state system (extended system) than in the isolated atom. Further investigations on a wide class of compounds will be necessary to substantiate this point.

It is remarkable that LDF theory also describes the bond length and vibrational frequency of the fluorine molecule with the same error bar as the other systems discussed here. This finding is significant as it shows that the error made in the LDF approach appears to be consistent in a wide class of different systems. In fact, recent calculations on ferrocene (52) show that also this type of metallo-organic compound does not present an exception - the Fe/ring distance agrees within 0.002 Å with experiment.

The calculation of the spin density in the DPPH radical demonstrates that quantities related to the charge distribution of electrons are very well described by this approach. The spin-density is a particularly sensitive test as it is the difference of two large quantities, namely the electron densities of each spin system.

Finally, the investigation of noble metal bonding on semiconductor surfaces provides evidence that at moderate temperatures Cu diffuses easily into the Si surface whereas the penetration barrier for Ag is almost as large as its binding energy. The theoretical results help in the understanding of an important catalytic process in the synthesis of silicone polymers and shed light on the Cu/Si and Ag/Si interface formation.

It is remarkable that LDF theory, which was originally designed to describe the electronic structure of metallic solid state systems, works consistently well also for isolated inorganic and organic molecules in predicting ground state properties such as equilibrium geometries and interatomic forces and force constants. Currently, one shortcoming of LDF theory as compared with the many-body theories based on the HF approach is that there is no simple and systematic way to go beyond the local density approximation. Consequently, there is active research in this field and several interesting possibilities have been suggested (9,53-55). It can be hoped that the combination of the wealth of experience obtained by high-precision HF-CI and multi-reference methods and the use of rigorous density functional methods will advance our knowledge and capabilities to treat the great variety of systems which we encounter in computational chemistry. The present examples, it is hoped, provide encouraging evidence that

density functional theory offers a unified framework to treat metallic systems such as transition metal surfaces as well as inorganic and organic molecules and semiconductor surfaces. Thus, this approach - with its computational efficiency - allows the theoretical chemist to expand his scope to the fascinating and technologically important chemical phenomena in materials science, surface chemistry, and catalysis.

**Acknowledgments.** Work at Northwestern University was supported by the National Science Foundation (DMR 85-18607) and the Office of Naval Research (grant 00014-81-K-0438). Stimulating discussions with the author of MOPAC, James J. P. Stewart, are gratefully acknowledged. The three-dimensional computer-generated images in this article were computed on a CRAY X-MP/48 using the OASIS image synthesis package. OASIS was written, and the images were rendered, by Gray Lorig of Cray Research's application department.

## References

1. Hehre, W. J; Radom, L.; Schleyer, P. v. R.; Pople, J. A. ; *Ab initio molecular orbital theory*, John Wiley & Sons, New York, 1986 and references therein
2. Pines, D.; *Solid State Physics* 1, 367 (1955)
3. Hohenberg, P.; Kohn, W.; *Phys. Rev.* 136, B 864 (1964)
4. Kohn, W.; Sham, L. J.; *Phys. Rev.* 140, A1133 (1965)
5. von Barth, U.; Hedin, L., *J. Phys. C*5, 1629 (1972)
6. Gunnarsson, O.; Lundqvist, B. I.; Lundqvist, S.; *Solid State Commun.* 11, 149 (1972)
7. Hedin, L.; Lundqvist, B. I.; *J.Phys.C: Solid State Phys.* 4, 2064 (1971)
8. Ceperley, D. M.; Alder, B. J.; *Phys. Rev. Lett.* 45, 566 (1980)
9. Lundqvist, S.; March, N.; Editors: *Theory of the Inhomogeneous Electron Gas*, New York, N.Y. 1983
10. Wimmer, E.; Krakauer, H.; Weinert, M.; Freeman, A.J.; *Phys. Rev.* B24, 864 (1981) and references therein

11. Wimmer, E.; Krakauer, H.; Freeman, A. J.; *Advances in Electronics and Electron Physics*, Hawkes, P. W.; Editor, vol.65, 357, Academic Press, New York, 1985
12. Weinert, M.; *J. Math. Phys.* 22, 2433 (1981)
13. Koelling, D. D.; Harmon, B. N.; *J. Phys. C10*, 3107 (1977)
14. Weinert, M.; Wimmer, E.; Freeman, A. J.; *Phys. Rev. B26*, 4571 (1982)
15. Jansen, H. J. F.; Freeman, A. J.; *Phys. Rev. B30*, 561( 1984)
16. Rosen, A.; Ellis, D. E.; Adachi, H.; Averill, F. W.; *J. Chem. Phys.* 65, 3629 (1976)
17. Delley, B.; Ellis, D. E.; *J. Chem. Phys.* 76, 1949 (1982)
18. Marks, L. D.; Heine, V.; *J. Catalysis* 94, 570 (1985)
19. Goodgame, M. M.; Goddard III, W. A.; *Phys. Rev. Lett.*48, 135 (1982)
20. Delley, B.; Freeman, A. J.; Ellis, D. E.; *Phys. Rev. Lett.*50, 488 (1983)
21. Ohnishi, S.; Freeman, A. J.; Wimmer, E.; *Phys. Rev. B29*, 5267 (1984) and references therein
22. Felter, T. E., Baker, R. A., Estrup, P. J.; *Phys. Rev. Lett.* 38, 1138 (1977)
23. Debe, M. K.; King, D. A.; *Phys. Rev. Lett.* 39, 708 (1977)
24. Melmed, A. J.; Tung, R. T.; Graham, W. R.; Smith, G. D. W.; *Phys. Rev. Lett.* 43, 1521 (1979)
25. Stensgaard, I.; Feldman, L. C.; Silverman, P. J.; *Phys. Rev. Lett.* 42, 247 (1979)
26. Fu, C.-L.; Freeman, A. J.; Wimmer, E.; Weinert, M.; *Phys. Rev. Lett.* 54, 2216 (1985)
27. Weinert, M.; Davenport, J. W.; *Phys. Rev. Lett.* 54, 1547 (1985)
28. Chubb, S. R.; Wimmer, E.; Freeman, A. J.; *Bull. Am. Phys. Soc.* 30, 599 (1985) and to be published
29. Fu, C.-L.; Freeman, A. J.; to be published
30. Buenker, R. J.; *J. Chem. Phys.* 48, 1368 (1968)
31. Kaldor, U.; Shavitt, I.; *J. Chem. Phys.* 48, 191 (1968)
32. Douglas, J. E.; Rabinovitch, B. S.; Looney, F. S.; *J. Chem. Phys.* 23, 315 (1955)
33. Staemmler, V.; *Theor. Chim. Acta* 45, 89 (1977)
34. Staemmler, V.; Jaquet, R.; *Energy Storage Redistrib. Mol.* 261-72, Edited by Hinze, J.; Plenum, New York (1983)

35. Chou, S.-H.; Freeman, A. J.; Delley, B.; Wimmer E.; unpublished
36. Laidig, W. D.; Saxe, P.; Bartlett, R. J.; J. Chem. Phys. 86, 887 (1987)
37. Huber, K. P.; Herzberg, G.; *Molecular Spectra and Molecular Structure. IV. Constants of Diatomic Molecules*, Van Nostrand Reinhold, New York, 1979
38. Cao, P.-L.; Freeman, A. J.; Delley, B.; Wimmer E.; unpublished
39. Holmberg, R. W.; Livingston, R.; Smith, W. T.; J. Chem. Phys. 33, 541 (1960)
40. Dalal, N. S.; Kennedy, D. E.; McDowell, C. A.; J. Chem. Phys. 59, 3403 (1973) and references therein
41. Boucherle, J. X.; Gillon, B.; Maruani, J.; Schweizer, J.; J. Phys., Colloq., (C-7) 227 (1982)
42. Gillon, B.; Thesis, University Pierre and Marie Curie, Paris 6, France (1983)
43. Delley B.; Wimmer, E.; unpublished
44. Rochow, E. G.; J. Amer. Chem. Soc. 67, 963 (1945)
45. Voorhoeve, R. J. H.; *Organosilanes; Precursors to Silanes*, Elsevier Publishing Co.; New York, 1967
46. Ward, W. J.; Ritzer, A.; Carroll, K. M.; Flock, J. W.; J. Catalysis 100, 240 (1986)
47. Chou, S.-H.; Freeman, A. J.; Grigoras, S.; Gentle, T. M.; Delley B.; Wimmer, E.; J. Amer. Chem. Soc. 109, 1880 (1987)
48. Gentle, T. M.; Owen, M. J.; to be published
49. Wilson, R. J.; Chiang, S.; Phys. Rev. Lett. 58, 369 (1987)
50. van Loenen, E. J.; Demuth, J. E.; Tromp, R. M.; Hamers, R. J.; Phys. Rev. Lett. 58, 373 (1987)
51. Aono, M.; Souda, R.; Oshima, C.; Ishizawa, Y.; Surf. Sci. 168, 713 (1986)
52. Cao, P.-L.; Chou, S.-H.; Freeman, A. J.; Delley, B.; Wimmer, E.; unpublished
53. Langreth, D. C.; Mehl, M. J.; Phys. Rev. B28, 1809 (1983)
54. Perdew, J. P.; Zunger, A.; Phys. Rev. B23, 5048 (1982)
55. Becke, A. D.; J. Chem. Phys. 84, 4524 (1986)

RECEIVED June 15, 1987



## Chapter 5

# Ab Initio Self-Consistent Field-Molecular Orbital Calculations Including Long-Range Coulomb Effects Alpha-Quartz and Defects

F. Sim<sup>1</sup>, C. R. A. Catlow<sup>2</sup>, M. Dupuis, J. D. Watts, and E. Clementi

Scientific and Engineering Computations, Department 48B-MS428,  
IBM Corporation, Kingston, NY 12401

A series of calculations on defect centers induced by radiation damage in alpha-quartz is reported. *Ab initio* SCF-MO calculations were carried out on a 21 atom cluster,  $\text{Si}_5\text{O}_{16}^{12-}$ , surrounded by 956 point-ions, designed to simulate alpha-quartz. This 'two-region' approach made it possible to represent the long-range electrostatic effects, present in the crystal, in the SCF-MO cluster. First, a group of SCF-MO treated atoms which gave a physically realistic representation of quartz was determined. Following this, calculations were performed using a 3-21G basis set on a variety of defects containing  $\text{Al}^{3+}$  substitutionals and electron holes in quartz.

Advances in both computer architecture and software in the last thirty years have made it possible to calculate routinely the properties of small molecules using the *ab initio* self-consistent field-molecular orbitals (SCF-MO) formalism. However, extended systems, such as liquids and solids, contain important long-range contributions to their overall behavior, which it is difficult to simulate in this type of calculation without making it prohibitively expensive. For this reason, SCF-MO calculations on the solid-state have been restricted in general to small model molecules (a review of this approach for silicates is given by Gibbs<sup>(1)</sup>), and to semi-empirical calculations on large clusters of up to 80 atoms<sup>(2)</sup>. Unfortunately, neither of these approaches can introduce the long-range electrostatic effects, nor is able to solve the problem of how to 'truncate' the SCF-MO representation in a physically realistic way.

In the calculations presented here, the long-range effects present in a crystal were introduced explicitly for the SCF-MO treated cluster, by surrounding it with point-ions situated at the X-ray determined atomic positions of alpha-quartz<sup>(3)</sup>. This method has been used for the more ionic systems of alpha-NaOH, and MgO with some success<sup>(4,2)</sup>, and the calculations described in this paper show that it is equally applicable for semi-covalent materials.

<sup>1</sup>Current address: Department of Chemistry, University College of London, 20 Gordon Street, London, United Kingdom, WC1H 0AJ

<sup>2</sup>Current address: Department of Chemistry, University of Keele, Staffordshire, United Kingdom, ST5 5BG

0097-6156/87/0353-0069\$06.00/0  
© 1987 American Chemical Society

Although in this paper we will concentrate on describing the methodology used in these calculations; first, we summarize the chemical problem which was investigated.

Alpha-quartz has many useful properties which lead to its wide use in industry as a glass, ceramic and molecular sieve. However, undoubtedly its most technically important use occurs by virtue of its piezo-electric properties, which allow it to be used as a frequency regulating device in satellites, computers, and the ubiquitous 'quartz-watch'. Unfortunately, it has been found that quartz crystals are susceptible to damage by radiation, and that this is associated with the presence of defects in the crystal lattice. These defects, particularly aluminum and hydrogen, are grown into the crystal and so far have proved impossible to remove. This problem has been the cause of intensive research, which has led to some information on the possible types of defects involved, but has failed to produce details of their geometries, and the way in which they interact.

To study these defects in detail, it is necessary to treat the immediate region surrounding the defect by a high level quantum mechanical method. However, owing to the polar nature of the silica lattice, long-range effects should be included. This problem was well suited to test the models previously developed for ionic systems. Furthermore, a detailed study of this problem has been carried out using the isolated model-molecule method<sup>(7,8)</sup>, and it was therefore possible to evaluate the effect of including the point-ions on the results obtained.

## METHODS

THE REPRESENTATION OF LONG-COULOMB INTERACTIONS BY A FINITE POINT-ION CLUSTER. In a crystal, the two most important contributions to the interaction energy of the ions are the long-range Coulomb interactions, and the short-range repulsive interactions. The Coulomb interactions vary as the first power of the inter-ionic distance, and because the interactions fall off so slowly, this is only a conditionally convergent series for the infinite crystal. This mathematical problem, which may be overcome by an Ewald-type summation<sup>(9)</sup>, reflects the physical fact that the interactions are of such long-range, that the energy of any group of ions may depend crucially on the configuration of another group of ions some distance away. Therefore, it would seem intuitively obvious, that these long-range Coulomb interactions must be included in any calculations on the solid-state.

In the approach described here, the interactions between the atoms in the SCF-MO treated cluster were calculated explicitly, including the 'local' Coulomb interactions. The long-range Coulombic effects were included by surrounding the explicitly treated cluster by a finite, point-ion cluster in which the ions were placed at the crystal lattice sites. There were several important factors which had to be considered when choosing a set of point-ions which would accurately represent the crystal structure. The first of these arose from the need to use existing program suites, (HONDO<sup>(9)</sup> and GAMESS<sup>(11,12)</sup>). These could not accommodate

the inclusion of an infinite set of point-ions without substantial alteration of the code to allow an Ewald summation to be performed. Therefore, a method has to be developed, in which a finite cluster would mimic an infinite crystal, by reproducing the electrostatic energies and forces calculated for the equivalent infinite crystal.

**GENERATION OF THE POINT-ION CLUSTER.** The cluster was built from  $\text{SiO}_4^{4-}$  units which have  $C_{2v}$  symmetry. This departure from  $T_d$  symmetry leads to the presence of multipole moments which will have a contribution to the energy of each lattice site. Furthermore, the directionality of these moments may lead to the electric field being substantially different to those calculated for the infinite crystal. To test this, a correction was made for the largest of these moments, the dipole moment, by adjusting the charges of the surface oxygens. It was found that the dipole correction became increasingly insignificant as the size of the point-ion cluster was increased. Indeed for the 977 point-ion cluster used in this work, the dipole correction was less than  $0.01 \text{ eV/\AA}$  for the SCF-MO treated sites. However, it should be mentioned that when an attempt was made to construct an oxygen centered cluster, using an  $\text{Si}_2\text{O}_7^{6-}$  basic building block, the large dipole moment of this unit led to large errors of hundreds of eV's, in the electric forces at the cluster sites. Thus, care must be taken to ensure that the correct point-ion 'unit' is chosen to minimize the multipole-moment errors.

Using the program PLUTO<sup>(3)</sup>, electrostatic energies and forces were calculated by an Ewald summation for an infinite series of point-ions at the lattice sites of quartz. It should be noted that the energies and forces calculated, depend on the charges chosen for the silicon and oxygen point-ions. In the case of a semi-covalent crystal, like alpha-quartz, it is often difficult to assign charges to individual ions unambiguously, and in this sense, the energies are arbitrary, as they scale with the values chosen for the charges.

From the results shown in Table I, it can be seen that the 977 point-ion cluster does not reproduce the absolute electrostatic energies, or Madelung energies, of the infinite crystal. However, if the ratio of the differences of the electrostatic energies are calculated, in both cases shown, it is found to be almost exactly -2.0. For example, in the 'fully-ionic' case ( $\text{Si}^{4+}$ ,  $\text{O}^{2-}$ ):  $E(\text{Ewald})-E(\text{pt. ion})$  for  $\text{Si}^{4+}$  is given by  $-193.633 + 160.620 = -33.013$ ;  $E(\text{Ewald})-E(\text{pt. ion})$  for  $\text{O}^{2-}$  is given by  $-61.706 + 18.230 = -43.476$ ; the ratio of  $-33.013 / -43.476$  is -1.997. This shows that the variation in the electrostatic potential within the cluster, accurately follows that for the infinite lattice, where this ratio is also -2.0; the absolute value of the potential however differs by approximately 8 volts. By introducing extra charge on the ions on the surface of the finite cluster, it was possible to alter the electrostatic energies of the ions near the center of this cluster, to a value close to the infinite, Madelung energies. However, the agreement between the two clusters quickly became worse as the distance of the ion from the center increased. Furthermore, the electrostatic forces, which had previously show very good agreement, were made badly in error by the introduction of the correction, it was therefore removed. As mentioned before, the Madelung energies calculated depend on the point charges chosen. The electric forces

depend on energy gradients, and the results showed that these were maintained in both the fully-ionic and half-ionic finite cluster. The behavior of an ion will depend on the forces acting on it, and therefore, it seemed more important to reproduce the gradients accurately, rather than the absolute energies.

**Table I.** The electrostatic energies of the central silicon site and one nearest-neighbor oxygen site for a 977 point-ion cluster, and the Madelung energies for silicon and oxygen in alpha-quartz

Point-ion and Its Charge(e)	Calculated Electrostatic Energy of the Site(eV)	
	Ewald Summation	977 Pt. Ion Cluster
Si <sup>4+</sup>	-193.633	-160.620
O <sup>2-</sup>	-61.706	-78.230
Si <sup>2+</sup>	-48.706	-40.155
O <sup>-</sup>	-15.426	-19.558

**CHOICE OF THE SCF-MO TREATED CLUSTER.** One of the main criteria governing the choice of the cluster to be treated using the SCF-MO formalism, must always be the amount of computer memory and time available. A balance has to be struck between the size of the cluster needed to produce a credible representation of the crystal, and the size of calculation which can be reasonably performed several hundred times. Using the parallel version of the highly efficient program HONDO, on the LCAP systems at IBM-Kingston<sup>(19)</sup>, it was possible to perform calculations on a large fragment of alpha-quartz, namely Si<sub>5</sub>O<sub>16</sub><sup>12-</sup> (see Figure 1). one of the main advantages of this cluster was that the central SiO<sub>4</sub> unit, which would contain the defects of interest, was well shielded from the point-ions. Thus any problems associated with the cluster-point-ion boundary should be minimal. As the behavior of the defects under investigation is thought to arise from geometrical differences of the central four oxygen atoms<sup>(19)</sup>, these atoms were given as close to the same 'SCF' environment as possible. In some previous studies<sup>(2)</sup>, asymmetric clusters have been used, and this may lead to spurious results arising from the asymmetry of the basis functions.

The representation of an essentially infinite framework by a finite SCF treated cluster of atoms, (with or without point-ions), inevitably leads to the problem of how to truncate the 'model-molecule'. Previous attempts at this have included using hydrogen atoms<sup>(1,7,8)</sup>, and 'ghost atoms'<sup>(2)</sup>. Other possibilities include leaving the electron from the broken bond in an open shell, or closing this shell to form an ionic cluster. A series of calculations were performed to test which was the most physically realistic, and computationally viable, solution to this problem for this system.

Following the most commonly used approach, that of truncating the cluster with hydrogen atoms, calculations were performed on an Si<sub>5</sub>O<sub>16</sub>H<sub>12</sub> molecule, using a 3-21G basis set. Four variants of this system were tested, and the

results obtained from the Mulliken population analyses are given in Table II. In the 956 point-ion cluster calculations, the hydrogen atoms were positioned 0.97Å along the nearest-neighbor Si-O bond. In the 944 point-ion cluster calculations, that nearest-neighbor silicon atom was removed from the cluster. Inspection of the results will show that although the four inner oxygen atoms have similar Mulliken populations, the silicon atoms differ in character quite markedly. In quartz, all atoms of the same type are chemically equivalent. Therefore, a model of the system which clearly produces three types of silicon atoms is not acceptable. Furthermore, when the initial Hellmann-Feynman forces of this cluster were calculated, they were so large that geometry optimization of this cluster seemed to be an impossible task.

**Table II.** Differences in Mulliken population analyses for an  $\text{Si}_5\text{O}_{16}\text{H}_{12}$  molecule and four combinations of point-ion cluster, using a 3-21G basis set

Number of Point-ions Present	Charge on Ions(e)		Differences in Mulliken Populations (e)				
	Si	O	Silicon		Oxygen	Oxygen	
			(outer-inner)	(outer-inner)	(outer-inner)	(outer-inner)	
956	4+	2-	+0.05	-0.14	0.19	0.28	0.01
944	4+	2-	-0.85	-0.70	0.15	0.52	0.03
956	2+	1-	-0.38	-0.20	0.18	0.47	0.02
944	2+	1-	-0.54	-0.74	0.20	0.57	0.02

Next, the inner region was treated as an  $\text{Si}_5\text{O}_{16}$  unit with 12 open shells, using the UHF formalism. The remaining 956 point-ion sites of the 977 site cluster, were given a 4+ charge, to represent a silicon ion, and a 2- charge, to represent an oxygen ion. It proved extremely difficult to obtain convergence of the energy of this system. Even for a smaller system treated in this manner ( $\text{SiO}_4$ ), several hundred cycles of the SCF part of the calculation were required before the energy would converge within acceptable limits. Thus, this approach was deemed impractical.

Closing the 12 open shells produced an  $\text{Si}_5\text{O}_{16}^{12-}$  unit. The point-ions were given 4+ and 2- charges, as in the open shell case. This converged easily, even when a defect was introduced to the basic cluster, and the UHF method was used to treat the system. It also gave acceptably consistent Mulliken populations for the atoms of the  $\text{Si}_5\text{O}_{16}^{12-}$  group. There was no calculated difference between the populations of the inner four oxygens, and between the outer and central silicon atoms, the difference was about 0.08e. The outer layer of oxygen atoms had approximately 0.44 e more than the inner, but this was thought to reflect the close proximity of the first layer of point-ions to the outer oxygen atoms, and to be, to a certain extent, unavoidable. In this case, the initial Hellman-Feynman force indicated that the inner  $\text{Si}_5\text{O}_4$  unit of the cluster could be geometry optimized straightforwardly. However, the larger forces on the outer 12 oxygens showed that if geometry optimized they would tend to drift out onto the point-ions. Following these results, it was decided that the  $\text{Si}_5\text{O}_{16}^{12-}$  SCF-MO treated cluster gave the best representation of a quartz crystal. We decided that the oxygen layer might be best viewed as sufficing to absorb the extra charge produced by closing the 12 open shells, and therefore, in subsequent geometry

optimizations, these atoms were held fixed at their X-ray determined lattice positions. The main advantage of this cluster over clusters used previously, is that the inner region, which was of particular interest, was well shielded from the cluster edge; and its homogeneity, as shown by the Mulliken populations of the atoms, was similar to what would be expected of a crystal, that is all chemically equivalent atoms were equal.

**CHOICE OF BASIS SET.** In all *ab initio* SCF-MO calculations, the choice of basis set can critically affect the results obtained. The effect of the basis set on molecular calculations has been widely studied, with the result that a series of reliable, good quality basis sets now exist for most atoms, up to and including, the transition metals<sup>(16-18)</sup>. However, as pointed out by Colburn and Kendrick<sup>(19)</sup>, the suitability of these essentially atomic basis sets for use on the solid-state, has not been thoroughly investigated. They suggest, for example, that negative ions such as O<sup>2-</sup>, are inadequately represented, and that significantly lowering of the energies calculated occurs if diffuse p-functions are added. It is also suggested that the addition of more diffuse functions to anions has little effect on the energy.

Earlier work on the hydroxyl group in quartz (Sim, F., Leslie, M., Catlow, C. R. A., to be published.) bore out the conclusions drawn in the above mentioned paper. However it has been found that in calculations on solids, using the periodic boundary method developed by Pisani et al.<sup>(20,21)</sup> that minimal basis sets give good results (Saunders, V. R.; private communication.). Furthermore, in the method outlined here, the exceedingly diffuse nature of the oxygen ions may be due to the surrounding highly charged point-ions. Thus, more consideration of the behavior of the crystal wavefunction is needed before a reliable method of producing suitable basis sets can be developed. In view of these problems, the choice of basis set to be used in this work, was limited to standard molecular basis sets.

Calculations were performed on the basis cluster and a trial series of defects using an STO-3G basis<sup>(22)</sup> and a 3-21G basis<sup>(23)</sup>. It was found that both basis sets gave a good crystal like description of quartz - from the Mulliken population analyses. However, defect binding energies calculated using the minimal basis were higher than those calculated using the 3-21G basis. Therefore, the 3-21G basis was chosen for use in the remaining calculations.

**BASIS SET SUPERPOSITION ERROR (BSSE)<sup>(24)</sup>.** To test for this possible source of error, calculations were performed on the basic Si<sub>5</sub>O<sub>16</sub><sup>12-</sup> cluster, using the 3-21G basis. The total energy of the cluster was calculated with and without the presence of hydrogen atom functions. From the results presented in Table III., it can be seen that the effect of including the hydrogen functions leads to BSSE of approximately 0.2 eV. The effect of including the functions for Si<sub>5</sub>O<sub>16</sub><sup>12-</sup> cluster in a calculation on a hydrogen atom can be seen to be about 0.1 eV. However, the inclusion of the point-ion field causes a change in the total energy of approximately 10 eV. In this situation BSSE seems relatively unimportant.

**THE EFFECT OF VARYING THE VALUES OF THE POINT CHARGES.** From the beginning of this investigation, calculations were carried out in two different point-ion environments. One was the fully-ionic cluster, (Si<sup>4+</sup>, O<sup>2-</sup>) - analogous to the classical simulation of quartz possible with the CASCADE program<sup>(25,26)</sup>. The other was the half-ionic cluster, chosen for two reasons. First, although there is still some debate over this<sup>(27,28)</sup>, alpha-quartz is thought to be approximately 50% ionic. Secondly, an iterative procedure, starting with the fully-ionic cluster, was carried out in which the charges calculated from the Mulliken populations of the internal, SCF-MO treated cluster, were returned to the point-ions. When repeated until the calculated populations were consistent with the charges on the point-ions, this yielded values of 2+ for the silicons and 1- for the oxygens.

Table III. Results of the calculations to test BSSE

Cluster	Basis Set	Point-ions Included	Final Total Energy (Hartrees)
Si <sub>5</sub> O <sub>16</sub> <sup>12-</sup>	3-21G	no	-2621.37939
Si <sub>5</sub> O <sub>16</sub> <sup>12-</sup>	3-21G	yes	-3021.97588
Si <sub>5</sub> O <sub>16</sub> <sup>12-</sup>	3-21G plus H functions	yes	-3021.98369
H atom	3-21G	no	-0.49620
H atom	3-21G	yes	-388.92690
H atom	3-21G plus Si <sub>5</sub> O <sub>16</sub> functions	yes	-388.93034

Later calculations showed that the defect binding energies were invariant to the values chosen for the point charges. As those calculated for the fully-ionic system may be directly compared to those obtained using classical simulation, geometry optimizations were carried out using the fully-ionic point-ions.

#### APPLICATION OF THE METHOD

**RADIATION INDUCED DEFECTS IN ALPHA-QUARTZ.** *Starting geometry:* The atoms and the point-ions were initially placed at the lattice sites corresponding to the geometry of the right-handed alpha-quartz (space group P3 21). Each silicon was surrounded by four chemically equivalent oxygen atoms, forming a slightly distorted tetrahedron. These oxygens were at two pairs of distances from the silicon, 1.616Å and 1.598Å; each oxygen has a bond of each bond-length to a silicon atom. However, when an aluminum impurity is introduced at the silicon site, the equivalence is broken, the aluminum has two distinct types of oxygen around it. Following Mombourquette et al.<sup>9</sup> we shall use the symbol O(<) and O(>), to indicate oxygen atoms located initially 1.598Å and 1.616Å from the central silicon site, respectively. In these calculations, O(<) corresponds to O(2) and O(4), and O(>) corresponds to O(1) and O(3) on Figure 1.

*Geometry optimized basic alpha-quartz structure Si<sub>5</sub>O<sub>16</sub><sup>12-</sup>:* The central atoms of Si<sub>5</sub>O<sub>16</sub><sup>12-</sup> cluster moved very little from their X-ray determined positions - Si(1) moved 0.016Å; both O(<) moved 0.018Å and both O(>) moved 0.005Å. However, the relative length of the two pairs of oxygen bonds changed. The longer one became 1.621Å, and the shorter one became 1.616Å. If the accuracy of the bond length calculated by this method is taken to be approximately 0.01Å, then all Si-O bonds within the inner Si<sub>5</sub>O<sub>4</sub> cluster can be taken to be 1.62Å. This was exactly the situation calculated by Mombourquette et al.<sup>9</sup>, however, they calculated larger displacements from the X-ray determined structure and much longer bond lengths. This was probably caused by their use of a minimal basis set.

*Geometry optimized basic cluster minus one electron : Si<sub>5</sub>O<sub>16</sub><sup>11-</sup>:* This defect contains an electron 'hole,' which was created by removing an electron from the calculation. This was then treated with the UHF formalism to see where it localized. It was found that the bond lengths from O(1) to its nearest silicon atoms increased significantly, to 1.825Å and 1.772Å, (see Figure 2.). This is about a 13% increase in bond length. The same calculations performed by classical simulation, using the program CASCADE, produced a 21% increase in bond length (Sim, F.; Ph.D Thesis, University of London, to be published.). Some

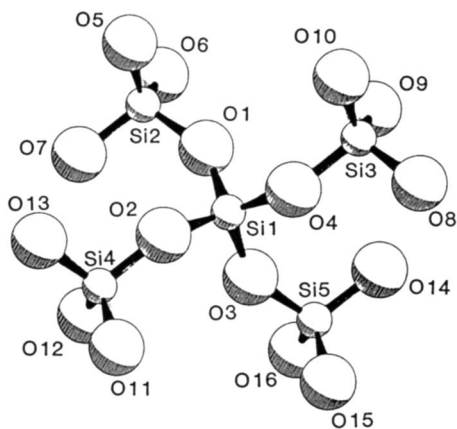


**Figure 1.** Geometry of the basic  $\text{Si}_5\text{O}_{16}^{12-}$  cluster.

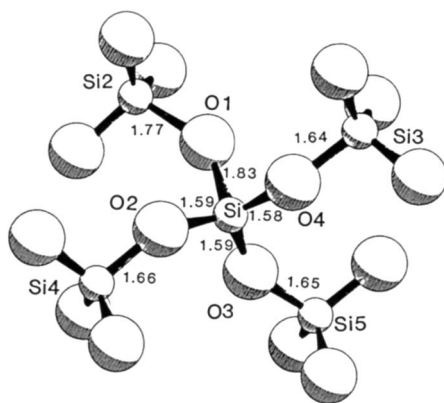


**Figure 2.** Geometry optimized basic cluster with an electron hole :  $\text{Si}_5\text{O}_{16}^{11-}$



rearrangement of the orientation of the inner four oxygen atoms also took place, with the angles between them either increasing or decreasing by about 7°.

*Geometry optimized basic cluster with an aluminum substitutional: Si<sub>4</sub>AlO<sub>16</sub><sup>13-</sup>:* This center contains an Al<sup>3+</sup> ion substituting for an isoelectronic Si<sup>4+</sup>; this account for the formal charge of 13- given to the cluster. The introduction of the Al<sup>3+</sup> ion caused the bond pair order to return to its original state. However, again the difference in calculated bond length was very small, 0.08Å. A small lengthening of the bonds from the central site, to the nearest four oxygen atoms was observed, about 3%. This was accompanied by a very little alteration in the bond angles around the site - less than 4°. This is consistent with the fact that this substitution occurs so readily in quartz.

*Geometry optimized Al substitutional minus one electron : Si<sub>4</sub>AlO<sub>16</sub><sup>12-</sup>:* This center consists of an electron hole, located on an adjacent oxygen atom, charge compensating for the Al<sup>3+</sup> ion. This hole is localized on one of the O(>) sites in the ground state, or, in a thermally accessible excited state, on one of the O(<) sites<sup>(15,29)</sup>. In this calculation, the electron hole has localized on O(4), originally a short bond oxygen. The bonds to Al and Si from this atom have increased to 1.864Å and 1.719Å respectively (see Figure 3.). This represents a 10% increase in the Al-O bond length, which is 15% shorter than that calculated using a classical simulation (Sim, F.; Ph.D Thesis, University of London, to be published.). In the optimized geometry there seem to be no discernible pairs of bonds (see Figure 3.). The Al-O distances are now: O(1) 1.662Å, O(2) 1.654Å, O(3) 1.638Å, O(4) 1.864Å. This change has been accompanied by a large amount of rearrangement around O(4).

**DISCUSSION OF RESULTS.** From the final total energies of the optimized configurations of these four defects, it is possible to calculate a defect binding energy, for the hole to the Al, of 5.36 eV. This is done in the following way:

$$\begin{aligned} \text{Defect binding energy} = & \left[ E(\text{Si}_4 \text{AlO}_{16}^{12-}) - E(\text{Si}_4 \text{AlO}_{16}^{13-}) \right] \\ & - \left[ E(\text{Si}_5\text{O}_{16}^{11-}) - E(\text{Si}_5\text{O}_{16}^{12-}) \right] \end{aligned}$$

This binding energy is higher than would be expected for a defect of this type. The value calculated using the classical simulation was 1.86 eV, which is much more realistic (Sim, F.; Ph.D Thesis, University of London, to be published.). Furthermore, geometry optimization only produced a lowering of the defect binding energy of 1.0 eV. This is slightly puzzling since this method gives excellent agreement with EPR results which predict 10% and 12% relaxation<sup>(15,30)</sup> around the Al substitutional, on the formation of an electron hole. Stapelbroek et al.<sup>(31)</sup> concluded from calculations based on classical dipole-dipole interactions alone, that the relaxation would be about 40%. The calculations performed using CASCADE included polarization, which the former method did not, and this may explain why a lower estimate of the relaxation, 25%, resulted. However, even though polarization was included, the use of the fully-ionic model, in the classical simulation, might have led to an exaggeration of this effect, which caused by essentially electrostatic interactions. Mombourquette et al. calculated relaxation of 17% around the Al, this over-estimate may have been caused by the small size of the cluster that they used, or their use of an STO-3G basis set. Or indeed it may have been caused by their failure to include long-range electrostatic effects, which would have had a restraining effect on the atoms which have relaxed.

Our estimate of 10% relaxation of the Al-O bonds, caused by the electron hole is exactly in agreement with the 10% relaxation predicted by Adrian et al.<sup>(30)</sup>,

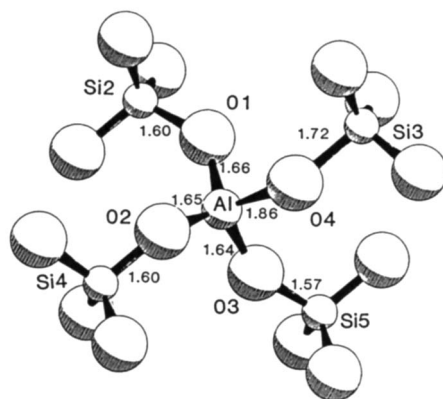


**Figure 3.** Geometry optimized aluminum substituted cluster with an electron hole  $:\text{Si}_4\text{AlO}_{16}^{12-}$ .

from EPR data. This confirms that the previously predicted relaxation of around 40% was much too large. Thus to obtain results in quantitative agreement with experiment, it is necessary to use large SCF-MO clusters, a good basis set and to include long-range interactions present in a crystal.

**FURTHER APPLICATIONS.** This method represent a simple and inexpensive way of including long-range effects in quantum mechanical calculations on the solid-state, or any extended system. Indeed, because it is relatively inexpensive, it is possible to use this method to develop potentials, for use in classical calculations on crystals. Previous attempts at using Hartree-Fock methods to evaluate potentials, have been restricted to evaluating potentials for individual pairs of atoms - usually with no inclusion of long-range Coulomb interactions. However, this method can be used to calculate the total energy for different configurations of the entire SCF-MO treated cluster, and these resultant energies parametrized to give two- and three-body potentials for use in classical calculations. Work is currently underway to produce Si-Si, O-O and Si-O potentials for use in the program CASCADE, from over 150 different configurations of the  $\text{Si}_5\text{O}_{16}^{12-}$  cluster mentioned in this paper. The advantage of this approach is that many-body effects are included explicitly. The limiting factor in the potential's accuracy then becomes the method of parametrizing the energies for the classical model, and this may depend on the classical method itself. Several parameters sets may be obtained from the one set of data, for example, ones for use in both static and dynamic simulations. In this way, the SCF-MO method may be extended to use on materials, which would previously have been considered completely out with the limitations of present day computers.

#### ACKNOWLEDGMENTS

F.S. would like to thank the Department of Chemistry, UCL and IBM Corporation for financial support, and Dr. V. R. Saunders for many helpful suggestions.

#### LITERATURE CITED

1. Gibbs, G. V., Am. Mineral., 1982, **67**, 421.
2. Hagon, J. P.; Stoneham, A. M.; Jaros, M., UKAEA Report, 1986, AERE-TP.1175.
3. Jorgensen, J. D., J. Appl. Phys. 1978, **49**, 5473.
4. Saul, P.; Catlow, C. R. A.; Kendrick, J. PHIL. MAG. 1985, **B 51**, 107.
5. Vail, J. M.; Harker, A. H.; Harding, J. H.; Saul, P. J. Phys. C Solid State Phys., 1984, **17**, 3401.
6. Weil, J. A. Radiation Effects, 1975, **26**, 261; 1984, **62**, 21.
7. Mombourquette, J. M.; Weil, J. A. Can. J. Phys. 1985, **63**, 1282.
8. Ewald, P. Ann. Phys. (Leipzig) 1921, **64**, 253.
9. Dupuis, M.; Rys, J.; King, H. F. J. Chem. Phys. 1976, **65**, 111.
10. Dupuis, M.; Spangler, D.; Wendoloski, J. J. NRCC Software Catalogue, 1980, Vol. I, Prog. No. QC01 (Manchester National Regional Computing Center).
11. Guest, M. F.; Kendrick, J. GAMESS user manual, 1985, Daresbury Technical Memorandum.
12. Norgett, M. J. UKAEA Report, 1974, AERE-R. 7650.
13. Clementi, E.; Chin, S.; Logan, D. in Supercomputer Simulations in Chemistry, 1986, Vol. 44 of Lecture Notes in Chemistry, Dupuis, M., Ed., Springer-Verlag (Berlin).
14. Nuttall, R. H. D.; Weil, J. A. Can. J. Phys. 1981, **59**, 1696.
15. Dunning, Jr., T. H. J. Chem. Phys. 1970, **53**, 2823.

16. Dunning, Jr., T. H.; Hay, P. J. in Methods of Electronic Structure Theory, Schaefer, III, H. F., Ed., Plenum (New York) 1977.
17. Veillard, A. Theor. Chim. Acta 1968, **12**, 405.
18. Wachters, A. J. H. J. Chem. Phys. 1970, **52**, 1033.
19. Colburn, E. A.; Kendrick, J. in Computer Simulations of Solids, 1982, Vol. 166 of Lecture Notes in Physics, Catlow, C. R. A.; MacKrodt, W. C., Eds., Springer-Verlag (Berlin).
20. Pisani, C.; Dovesi, R. Int. J. Quantum Chem. 1980, **17**, 501.
21. Dovesi, R.; Pisani, C.; Roetti, C.; Saunders, V. R. Phys. Rev. 1983, **B 28**, 5781.
22. Hehre, W. J.; Stewart, R. F.; Pople, J. A. J. Chem. Phys. 1969, **51**, 2657.
23. Binkley, J. S.; Pople, J. A.; Hehre, W. J. J. Am. Chem. Soc. 1980, **102**, 939.
24. Davidson, E. R.; Feller, D. Chem. Rev. 1986, **86**, 681.
25. Smith, W. Daresbury Laboratory Report, DL/SCI/TM25T.
26. Leslie, M. Daresbury Laboratory Report, DL/SCI/TM31T.
27. Pauling, L. Am. Mineral 1980, **65**, 321.
28. Stewart, R. F.; Whitehead, M. A. Am. Mineral. 1980, **65**, 324.
29. Schnadt, R.; Schneider, J. Phys. Kondens. Mater. 1970, **11**, 19.
30. Adrian, F. J.; Jette, A. N.; Spaeth, J. M. Phys. Rev. 1985, **B 31**, 3923.
31. Stapelbroek, M.; Bartram, R. H.; Gilliam, O. R.; Madacsi, D. P. Phys. Rev. 1976, **B 13**, 1960.

RECEIVED June 15, 1987

## Chapter 6

# Using Computer Simulations To Probe the Structure and Dynamics of Biopolymers

Ronald M. Levy, Fumio Hirata, Kwang Kim, and Peisen Zhang

Department of Chemistry, Rutgers University, New Brunswick, NJ 08903

The use of computer simulations to study internal motions and thermodynamic properties is receiving increased attention. One important use of the method is to provide a more fundamental understanding of the molecular information contained in various kinds of experiments on these complex systems. In the first part of this paper we review recent work in our laboratory concerned with the use of computer simulations for the interpretation of experimental probes of molecular structure and dynamics of proteins and nucleic acids. The interplay between computer simulations and three experimental techniques is emphasized: (1) nuclear magnetic resonance relaxation spectroscopy, (2) refinement of macromolecular x-ray structures, and (3) vibrational spectroscopy. The treatment of solvent effects in biopolymer simulations is a difficult problem. It is not possible to study systematically the effect of solvent conditions, e.g. added salt concentration, on biopolymer properties by means of simulations alone. In the last part of the paper we review a more analytical approach we have developed to study polyelectrolyte properties of solvated biopolymers. The results are compared with computer simulations.

The use of computer simulations to study the internal motions and thermodynamic properties of biological macromolecules is receiving increased attention as it becomes possible to simulate biologically important processes, e.g. the binding of a ligand to an enzyme.<sup>1,2</sup> In the molecular dynamics computer simulation method, an empirical potential energy function is used to represent the energy of the system as a function of atomic coordinates, and the classical equations of motion for the macromolecule are solved on this potential surface. This approach has its roots in computational studies of the liquid state where molecular dynamics simulations have proven to be a very powerful tool for studying liquid properties. Many factors, however, distinguish molecular dynamics simulations of biopolymers (e.g. proteins and nucleic acids) from liquid state simulations so that it is difficult to use experience gained from molecular dynamics simulations of liquids to estimate the precision inherent in macromolecular simulations. While both liquid state and macromolecular simulations employ empirical po-

0097-6156/87/0353-0082\$07.00/0  
© 1987 American Chemical Society

tential functions, the molecular mechanics potentials used to describe proteins and nucleic acids have far more adjustable parameters in the potential than is the case for liquids. Furthermore, for liquid simulations the basic system contains at least 100 identical molecules so that it is possible to take advantage of considerable statistical averaging in the calculation of quantities for comparison with experiment. For protein molecular dynamics simulations in contrast, the computational effort required to evaluate the large number of interatomic interactions within a single protein molecule limits the simulated system to one or at most a very small number of macromolecules. The highly anisotropic nature of the protein interior and intrinsic interest in extracting site-specific information further complicates the computational problem.

Additional features of macromolecular simulations that make them different from and more difficult than simulations of liquids and solids include the difficulty in obtaining exact results for comparison with trajectory averages, the slow convergence of the macromolecular simulations, the difficulty of incorporating the crystal or liquid environment in a realistic way, and the problem of treating quantum effects for large systems. A central feature of our research during the past few years has been the development of procedures for comparing the results of simulations with a wide variety of experiments. Such studies are necessary if the methodology is to be reliably used to study properties that are only indirectly accessible to experiment. Equally important, these studies lead to deeper insights into the relationship between experimental measurements and underlying molecular processes. In this paper we briefly review our past work concerning the use of molecular dynamics simulations to construct and interpret NMR relaxation and x-ray refinement models for macromolecules. We then discuss the development of new methods for simulating vibrational spectra using detailed molecular simulations. Methods we are working on to incorporate quantum effects in molecular simulations are also reviewed.

The treatment of solvent effects in biopolymer simulations is a difficult problem. While a few simulations have explicitly included the solvent surroundings<sup>3-7</sup>, most have been carried out *in vacuo*. With the increasing access to supercomputers it is becoming possible to include solvent explicitly in the simulation. It is still not possible to study systematically the effect of solvent conditions e.g. salt concentration, on biopolymer properties by means of brute force simulations because of the enormous amounts of computer time required. In this regard the development of more analytical methods for studying the interactions of biopolymers with the solvent surroundings not only makes it possible to study a range of environmental parameters not accessible to simulations but can provide limiting results useful for comparing with computer simulations and for focusing the computationally demanding simulations on the most interesting set of environmental variables. We have developed an approach suitable for treating the interactions of a polymeric solute molecule with the solvent surroundings, based on an integral equation method.<sup>8</sup> The theory can be used to study polyelectrolyte properties in solution. In the final part of this paper we review the theory and the application to simple models in which atoms are arranged along a linear chain and on a helix. We use the new theory to consider the effect of added salt on the relative free energy stabilizing different forms of DNA.

### **Nuclear Magnetic Resonance Relaxation**

Since NMR relaxation in proteins is determined by dynamics on the picosecond to nanosecond time scale, experimental NMR relaxation parameters can provide important information concerning picosecond motions. Time correlation func-

tions required for determining NMR parameters may be calculated directly from molecular dynamics trajectories. Protein trajectories have been used to study motional models used in the analysis of NMR  $T_1$ ,  $T_2$ , and Nuclear Overhauser Enhancements and as an aid in the interpretation of experiments.<sup>9-13</sup> A direct comparison between the results of a 96 ps molecular dynamics simulation<sup>14</sup> of pancreatic trypsin inhibitor (PTI) and an experimental  $^{13}\text{C}$  NMR relaxation study<sup>15</sup> of this protein has been reported.<sup>11</sup> This represented the first detailed comparison of the results of molecular dynamics simulations of a protein with experimental probes of motion on a similar time scale. Order parameters, which are measures of the extent of angular motion of the bonds were calculated from a 96-ps trajectory and compared with values extracted from the relaxation data. Although the relative flexibility of the residues studied was reasonably well described by the simulation, the theoretical order parameters were systematically larger than the experimental ones, indicating that there is less motional averaging in the 96 ps simulation than detected in experiment. It was suggested that this behavior occurred because the length of the trajectory was too short to statistically sample all accessible orientations. Recently, we have used a 300 ps molecular dynamics simulation of myoglobin to reexamine this question.<sup>16</sup> For  $^{13}\text{C}$  NMR of protonated carbons with fixed bond lengths, the contribution of internal protein motions to NMR relaxation is determined by the angular correlation function,  $C(t)$ :

$$C(t) = \sum_{\alpha=-2}^{+2} \langle Y_{\alpha}^{2*}[\theta(t)\phi(t)] \cdot Y_{\alpha}^2[\theta(o)\phi(o)] \rangle \quad (II.1)$$

where  $Y_{\alpha}^2$  are spherical harmonics and  $(\theta, \phi)$  specifies the orientation of a  $^{13}\text{C}$ -H bond in a macromolecule fixed frame. Because of the restricted nature of the motion in the protein interior, the internal correlation function (Eq.II.1) usually does not decay to zero. Instead a plateau value is reached for which the internal correlation function is equal to the equilibrium orientation distribution obtained from the entire run:<sup>9-11,17</sup>

$$S^2 = \frac{4\pi}{5} \sum_{\alpha} | \langle Y_{\alpha}^2(\Omega) \rangle |^2 \quad (II.2)$$

The quantity  $S$  defined by Eq.II-2 is the order parameter describing the restricted motion of the  $^{13}\text{C}$ -H vector; for a rigid system  $S^2 = 1$ , while for a completely flexible system  $S^2 = 0$ .

To illustrate the convergence characteristics of NMR order parameters, in Fig. 1 selected order parameters for leucine residues calculated using the complete 300-ps myoglobin simulation are compared with the values calculated using the first 100-ps portion of the trajectory. The results shown in the figure are representative of the effects observed for all the residues studied. As expected order parameters for bond vectors ( $C^{\alpha} - C^{\beta}$ ) closer to the backbone are in general larger than those ( $C^{\gamma} - C^{\delta 1}$ ) further out along the side chain. For the  $C^{\alpha} - C^{\beta}$  bonds, the order parameters calculated from the different portions of the trajectory agree well; for the leucine methyl axis order parameters however, there are large discrepancies between the values calculated over the first 100-ps

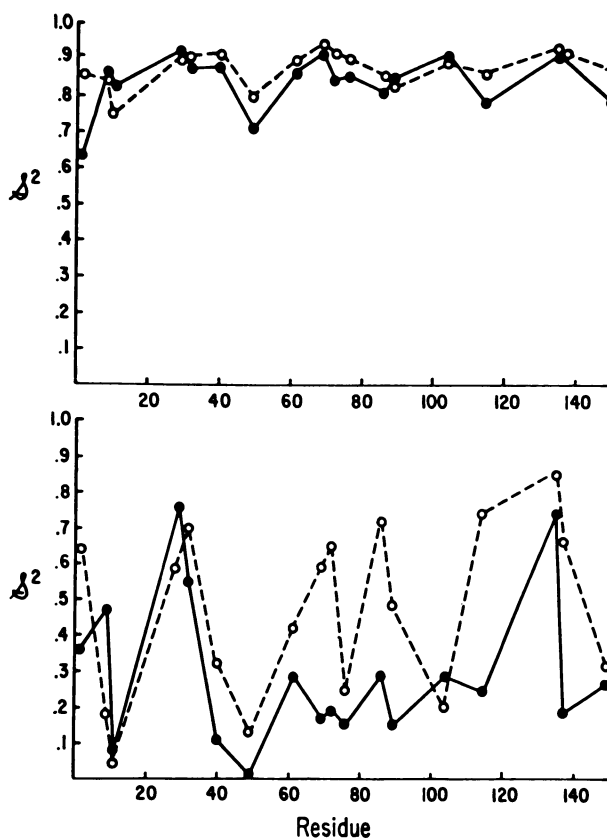


Figure 1. (Top) Order parameters for each of the Leucine  $C^\alpha-C^\beta$  bond vectors. - - -, order parameters calculated using the 0–100 picosecond portion of the trajectory; —, order parameters calculated using the entire 300 picosecond simulation. (Bottom) Same as top figure except that the calculations are for the leucine  $C^\gamma-C^\beta$  bond vectors. (Reproduced with permission from Ref. 16. Copyright 1985 Rockefeller University Press.)



of the trajectory as compared with the complete simulation. For fourteen of the eighteen leucines studied, the order parameters are smaller when the entire trajectory is used to evaluate the correlation functions as compared with the first 100-ps; for seven of the eighteen residues the order parameters decrease by more than 50% when the entire 300-ps distribution of bond vector orientations is used to evaluate the order parameters. It is clear from these results that the order parameter calculations have not converged for this 300-ps trajectory. The order parameter depends on the longtime behavior of the NMR correlation function which is determined by both the higher frequency local motions and more extensive conformational changes. We have examined the extent to which the decay of the NMR angular correlation function at short times varies for different portions of the simulation. We obtained results consistent with a model of protein motion in which groups of atoms (e.g. leucine side chains) oscillate about a mean conformation for tens of picoseconds and then move rapidly to a new conformation.<sup>16</sup> The conformational change has a large effect on the order parameter. In addition, the effective potential in which the atoms move are somewhat different in the different conformations. From our study of NMR order parameters as well as atomic fluctuations in myoglobin a qualitative picture emerged which suggests that the longer time motions of proteins involves multiple minima. For myoglobin, temperature dependent kinetic experiments on oxygen rebinding<sup>18</sup> and studies of x-ray temperature factors<sup>19</sup> have provided experimental evidence for the existence of multiple conformational states of this protein. In the following section we review our use of computer simulations of biopolymers to analyze molecular information concerning macromolecular flexibility contained in crystallographic Debye-Waller temperature factors.

### Restrained X-Ray Refinement of Biopolymers

Molecular dynamics simulations of proteins and nucleic acids provide a very powerful method for testing crystallographic refinement models. The simulations constitute the most detailed theoretical approach available for studying the internal motions of these macromolecules. From the time evolution of the atomic positions, time averaged X-ray intensities can be calculated and treated as data for crystallographic refinement. The final structure and temperature factors obtained from the refinement can then be compared with the "exact results" obtained directly from the trajectory. In this review, we discuss the results of an analysis<sup>20</sup> of the temperature dependent molecular dynamics and X-ray refinement of a Z-DNA hexamer 5BrdC-dG-5BrdC-dG-5BrdC-dG for which the experimental X-ray data are available and whose crystal structure has been refined to high resolution.<sup>21</sup> This hexamer crystallizes in the left-handed Z-conformation with the cytosine bases in the anti conformation and C(2')-endo sugar puckers, and the guanine bases in the syn orientation with C(3')-endo sugar puckers, except at the 3'-terminal guanine bases. The phosphodiester conformations are (gauche-plus, gauche-plus) at the CpG phosphates and (gauche-minus, trans) at the GpC phosphates. The refinement program used was NUCLSQ, which is the restrained least squares refinement program of Hendrickson and Konnert adapted to nucleic acids.<sup>21,22</sup> The section is divided in two parts. First, the molecular dynamics calculations are described. The simulations were carried out at a series of temperatures between 100 K and 300 K. Second, the restrained refinements of the time averaged structure factors obtained from the molecular dynamics simulations at the various temperatures are discussed and the results compared with "exact" values calculated directly from the simulations and with experimental X-ray results. During the course of the work, it was found that low temperature molecular dynamics simulations

may be used advantageously in the refinement process against experimental data.<sup>20</sup>

### Methods for simulating restrained x-ray refinement data from molecular dynamics trajectories.

Molecular dynamics simulations were carried out on the 248 atom Z-DNA hexamer, using the AMBER nucleic acid force field with a distance dependent dielectric and excluding counterions.<sup>23</sup> Although the model treats electrostatic effects only in a qualitative way, recent molecular dynamics simulations for both peptides<sup>24</sup> and nucleic acids<sup>25</sup> have demonstrated that for localized conformations sampled during short molecular dynamics simulations, average properties are not very sensitive to the electrostatic model; it is the packing and hydrogen bonding terms which together with the vibrational potential (bond, bond angle and torsional stretching) which dominate the calculated equilibrium and dynamical properties. The crystal structure of the Z-DNA hexamer was first energy minimized with 200 conjugate gradient steps to relieve any initial strain in the structure before the molecular dynamics simulations were begun. The rms displacement between the crystal and energy minimized coordinates are less than 0.1 Å. Simulations were performed at a series of temperatures defined by the mean kinetic energy of the system between 100 K and 300 K. For each temperature, 10 trajectories, each 2 ps in length, were calculated by solving simultaneously the classical equations of motion for the atoms of the helix. The use of multiple short trajectories instead of a single long trajectory has been found to be a more efficient method for sampling conformations for macromolecular systems containing many harmonic degrees of freedom.<sup>26</sup>

Crystallographic refinement is a procedure which iteratively improves the agreement between structure factors derived from X-ray intensities and those derived from a model structure. For macromolecular refinement, the limited diffraction data have to be complemented by additional information in order to improve the parameter-to-observation ratio. This additional information consists of restraints on bond lengths, bond angles, aromatic planes, chiralities, and temperature factors.

In the restrained refinement procedure a function of the form:

$$\Phi = \sum_{\mathbf{Q}} W_{\mathbf{Q}} \|F_o(\mathbf{Q}) - F_c(\mathbf{Q})\|^2 + \sum_i W_i \Delta_i^2 \quad (III.1)$$

is minimized.  $W_{\mathbf{Q}}$  is the weight assigned to the structure factors and it varies linearly with  $Q$  with coefficients adjusted so that low resolution structures are weighted more strongly than high resolution ones.  $F_o(\mathbf{Q})$  and  $F_c(\mathbf{Q})$  are respectively the observed and calculated structure factors. The second term in equation 1 contains the stereochemical restraint information,  $\Delta$  is the deviation of a restrained parameter (bond lengths, bond angles, volumes, non bonded contacts, and temperature factors) from its ideal value and  $W_i$  is the weight assigned to the restraint. The form of equation 1 is such that the weights  $W_i$  correspond to the inverse of the variance  $\Delta^2$  for each set of observations.

The structure factor  $F(\mathbf{Q})$  in X-ray crystallography is the fourier transform of the electron density for the molecule:

$$F(\mathbf{Q}) = \int d\mathbf{r} \rho(\mathbf{r}) e^{i\mathbf{Q} \cdot \mathbf{r}} \quad (III.2)$$

where  $\rho(\mathbf{r})$  is the electron density at  $\mathbf{r}$ . In a crystallography experiment the electron density varies with time due to thermal motion and the observed structure factor amplitude is the time average of equation III.2:

$$F_o(\mathbf{Q}) = \langle F(\mathbf{Q}) \rangle = \int d\mathbf{r} \langle \rho(\mathbf{r}) \rangle e^{i\mathbf{Q} \cdot \mathbf{r}} \quad (\text{III.3})$$

In order to generate a set of calculated structure factors  $F_c(\mathbf{Q})$  from a set of coordinates, it is necessary to introduce a model for the time variation of the electron density. The usual assumptions in macromolecular crystallography include harmonic isotropic motion of the atoms and in addition, the molecular scattering factor is expressed as a superposition of atomic scattering factors. With these assumptions the calculated structure factor (equation III.2) is given by:<sup>27</sup>

$$F_c(\mathbf{Q}) = \sum_{j=1}^N e^{i(\mathbf{Q}) \cdot \mathbf{r}_j} \cdot e^{W_j(\mathbf{Q})} \cdot F_j(\mathbf{Q}) \quad (\text{III.4})$$

where  $F_j(\mathbf{Q})$  is the atomic scattering factor for atom  $j$  and  $\mathbf{r}_j$  is the position of atom  $j$  in the model structure. The thermal averaging of atomic motion is contained in the atomic Debye-Waller factor  $\exp(W_j(\mathbf{Q}))$ .  $W_j$  is given by:

$W_j(\mathbf{Q}) = -B_j|\mathbf{Q}|^2$  where  $B_j$  is the atomic temperature factor. The mean square atomic fluctuation  $(\Delta r_j)^2$  for atom  $j$  is obtained from the refined temperature factors through the relation:<sup>42</sup>

$$\langle (\Delta r_j)^2 \rangle = \frac{3}{8\pi^2} B_j \quad (\text{III.5})$$

There are therefore four adjustable parameters per atom in the refinement ( $x_j$ ,  $y_j$ ,  $z_j$ ,  $B_j$ ). In the computer experiments we have carried out to test the assumptions of the nucleic acid refinement model we have generated sets of "observed" structure factors  $F_o(\mathbf{Q})$ , from the Z-DNA molecular dynamics trajectories. The thermal averaging implicit in Equation III.3 is accomplished by averaging the atomic structure factors obtained from coordinate sets sampled along the molecular dynamics trajectories at each temperature:

$$F_o(\mathbf{Q}) = \langle F(\mathbf{Q}) \rangle = \frac{1}{M} \sum_{k=1}^M \sum_{j=1}^N F_j(\mathbf{Q}) e^{i\mathbf{q} \cdot \mathbf{r}_j^k} \quad (\text{III.6})$$

where  $\mathbf{r}_j^k$  is the position of the  $j$ th atom in the  $k$ th coordinate set along the trajectory and  $M$  is the number of coordinate sets sampled. In the present study

structure factors corresponding to 3,195 reflections between  $10\text{\AA}$  and  $1.7\text{\AA}$  were calculated for each of 50 coordinate sets at each temperature. Only the 246 heavy atoms of the hexamer were included in the structure factor calculations; hydrogen atoms were not included in the refinement.

### Restrained X-Ray Refinement of the Z-DNA Molecular Dynamics Trajectories.

Refinement of molecular dynamics average structures against simulated X-ray diffraction intensities was carried out at four temperatures between 165 K and 300 K. The R factors, average temperature factors, rms deviations of the temperature factors and the number of "bad" distances obtained for the refinement of the molecular dynamics average structures against the simulated X-ray intensities at 165 K and 300 K are listed in Table I. At 165 K the initial R factor and number of bad distances before refinement are both very small (1.6% and 1 respectively) and are not changed significantly after refinement. At 300 K the initial R factor and number of bad distances are 22% and 50 respectively. With tight restraints on temperature factors the R factor decreased to 7% after three refinement cycles and the number of bad distances increased to 76. With no restraints on B the R factor decreased to 6.3% after three refinement cycles with 50 bad distances.

At the low temperature (165 K) the effect of refinement with strong temperature factor restraints is to increase the average temperature factor from  $0.5\text{\AA}^2$  (exact result) to  $0.7\text{\AA}^2$  and to decrease the variances in the temperature factors for the different classes of stereochemical constraints. With strong restraints on B, the refinement resulted in sharp differences between the cytosines and the guanines both for the sugars and bases which were not present in the temperature factors calculated directly from the 165 K trajectories. For example, the ratio of the temperature factors for guanine bases to cytosine bases which is 1.1 calculated directly from the molecular dynamics simulation, increases to 2.6 after refinement with strong B restraints. In contrast, when refinement is done without temperature factor restraints at 165 K the average temperature factors and the variances in the temperature factors are very close to the exact molecular dynamics values.

At 300 K the effect of the refinement both with and without strong restraints on temperature factors is to decrease the average thermal factor compared to the exact values. The temperature factor averaged over all atoms calculated directly from the room temperature trajectories is  $5.9\text{\AA}^2$  and is reduced by 15% to  $5.1\text{\AA}^2$  after refinement with strong B restraints. The average temperature factor ( $5.5\text{\AA}^2$ ) obtained from the 300 K refinement without temperature factor restraints is closer to the exact value. The error in the temperature factors introduced by the refinement at 300 K is largest for the atoms with the largest thermal fluctuations, the phosphates. This result is clearly demonstrated in Figure 2 which compares the phosphate temperature factors calculated directly from 300 K trajectories with the results of the two refinements, with and without temperature factor restraints. For example, the two atoms with the largest thermal fluctuations are the C5 and C11 phosphates. The exact B values for these atoms are  $15.1\text{\AA}^2$  and  $17.0\text{\AA}^2$ , respectively; after the refinement without temperature factor restraints the B values are reduced to  $10.8\text{\AA}^2$  and  $10.9\text{\AA}^2$  and they are reduced even further to  $8.8\text{\AA}^2$  and  $8.3\text{\AA}^2$  respectively after the refinement with temperature factor restraints. The errors introduced by the refinement are also apparent in the effect on the temperature factor variances. At room temperature the actual variances in temperature factors computed for each stereochemical class are considerably greater than  $1\text{\AA}^2$  (they range from  $2.4\text{\AA}^2$  for atoms connected by bonds not involving a phospho-

TABLE I

Parameters for refinement of simulation X-ray intensities of Z-DNA hexamer. First line before starting refinement; second line after refinement with strong B restraints; third line after refinement without B restraints

Parameter	165 K	300 K
Number of bad distances(+)	1	50
	0	76
	0	56
R-factor	1.6	22.0
	1.6	7.0
	0.9	6.2
Average temperature factor ( $A^2$ )	0.5	5.9
	0.7	5.1
	0.5	5.5
RMS of delta B's (*)	0.3,0.3,0.4,0.3	2.4,3.5,8.2,5.6
	.06,.08,.10,.13	0.6,0.7,0.2,0.6
	0.3,0.3,0.3,0.3	3.0,3.5,3.8,4.1

(+) Distances which deviate from ideality by more than two stand deviations.

(\*) The four values correspond to the difference in temperature factors for atoms connected by a bond length, for atoms connected by a bond angle, for P-O bond lengths, and for phosphate atoms connected by a bond angle or for atoms involved in hydrogen bonding.

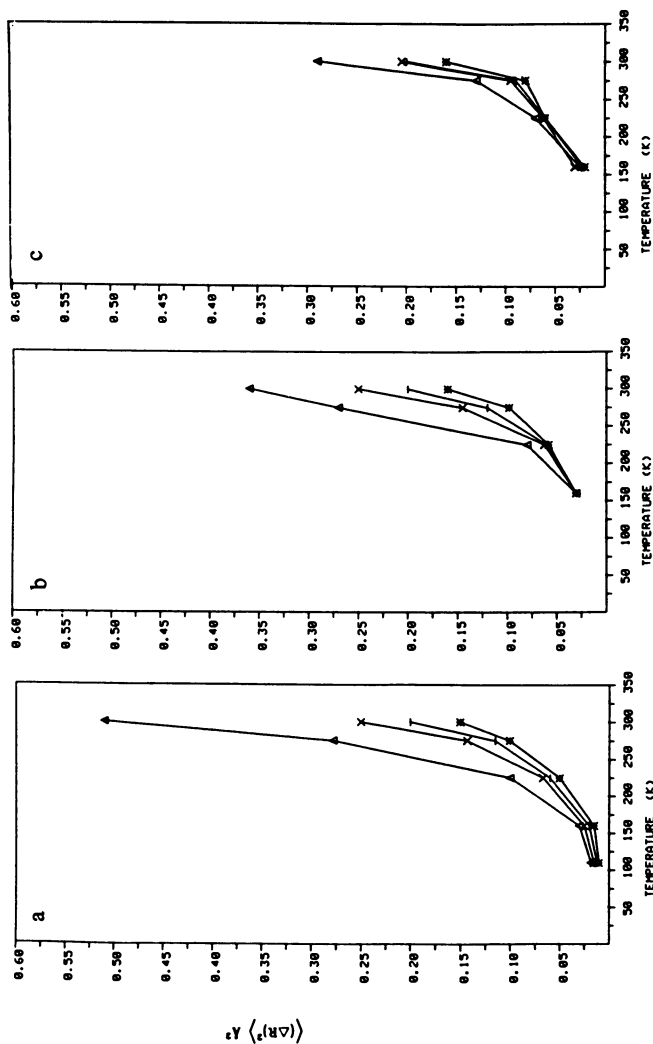


Figure 2. Temperature dependence of mean square atomic fluctuations of the Z-DNA hexamer. (a) Mean square atomic fluctuations were calculated directly from the molecular dynamics trajectories. (b, c) Mean square atomic fluctuations were calculated using  $\langle \Delta r^2 \rangle = (3/8\pi^2)B$  with the Debye-Waller temperature factors B obtained from the X-ray refinement of the molecular dynamics trajectories with no restraints (b) and with tight restraints (c). Symbols: \*, bases; —, sugars; x CpG, phosphates;  $\Delta$  GpC, phosphates. (Reproduced with permission from Ref. 20. Copyright 1986 Academic Press.)

rous to  $8.2\text{\AA}^2$  for P and O atoms connected by a P-O bond). The refinement of the simulated X-ray intensities at 300 K with temperature factor restraints greatly reduces the variances in the B values for each of the stereochemical classes so that the final variances are all less than  $1\text{\AA}^2$  (Table I). These results are in accord with a recent analysis of the use of restraints in temperature factor refinements for proteins<sup>28</sup> for which it was shown that the weights used to restrain neighboring atom temperature factors are much more restrictive than the variation in neighboring temperature factor values obtained from protein molecular dynamics simulations. Restraints on the differences in temperature factors between bonded atom pairs have been shown to be uncorrelated with variances in the corresponding bond length distributions. From the present results concerning errors in predicted temperature factor restraints we conclude that the commonly used value of  $1\text{\AA}^2$  or less between temperature factors on adjacent atoms is too restrictive.

Although, as discussed above there are quantitative errors in temperature factors introduced by the refinement procedure, the temperature dependence of the atomic mobilities as estimated by the refined temperature factors provides a reasonably accurate description of the true temperature dependence of the system. In fig. 2b and 2c the mean square atomic fluctuations extracted from the refinement simulations at each temperature and averaged by group are plotted as a function of temperature for comparison with the exact results shown in fig. 2a. As to the refinement without temperature factor restraints (fig. 2b), except for the phosphates at the highest temperature, the extent of anharmonicity (curvature) is in good agreement with the exact result despite the fact the refinement model assumes isotropic, harmonic motion. The ordering of the atomic fluctuations by groups (bases < deoxyriboses < CpG phosphates < GpC phosphates) at the two higher temperatures (275 K and 300 K) agrees with the exact results although the agreement is not as good at 165 K and 225 K even though the harmonic model would be expected to be more accurate at low temperature. It is clear from fig. 2c that when strong temperature factor restraints are introduced in the refinement, differences in the temperature dependence of the atomic fluctuations among the groups are suppressed, although the shapes of the curves agree qualitatively with the results calculated directly from the simulations (fig. 2a). The present results provide a theoretical foundation for the use of Debye-Waller factors obtained from refinements at several temperatures to extract information concerning the anharmonicity of the atomic displacements and underlying potential surface.<sup>18,19</sup>

### Vibrational Spectroscopy

Vibrational spectroscopy has played a very important role in the development of potential functions for molecular mechanics studies of proteins. Force constants which appear in the energy expressions are heavily parameterized from infrared and Raman studies of small model compounds. One approach to the interpretation of vibrational spectra for biopolymers has been a harmonic analysis whereby spectra are fit by geometry and/or force constant changes. There are a number of reasons for developing other approaches. The consistent force field (CFF) type potentials used in computer simulations are meant to model the motions of the atoms over a large range of conformations and, implicitly temperatures, without reparameterization.<sup>29</sup> It is also desirable to develop a formalism for interpreting vibrational spectra which takes into account the variation in the conformations of the chromophore and surroundings which occur due to thermal motions.

We have introduced a new method for calculating vibrational spectra from

classical molecular dynamics or Monte Carlo simulations.<sup>30</sup> The method involves a quasiharmonic oscillator approximation in which a temperature dependent quadratic Hamiltonian is parameterized from the results of a simulation on the complete (anharmonic) potential. The parameterization is accomplished by fitting the first and second moments of the coordinate and momentum distributions obtained from a simulation on the exact surface to a harmonic model. The model provides a method for partially incorporating anharmonicity in the evaluation of spectroscopic and thermodynamic properties and estimating quantum corrections to the classical simulations.

As an illustration of the method, we recently reported the results of a vibrational analysis of a small molecule (butane) with six internal degrees of freedom using the quasiharmonic oscillator model.<sup>30</sup> The empirical potential contained all the terms present in the potential for macromolecules, namely, bond stretching, bending, and torsional terms as well as nonbonded interactions. A novel aspect of the simulation procedure was the use of normal-mode eigenvectors as the independent coordinates for Monte Carlo sampling, which was demonstrated to substantially increase the convergence rate of the simulation. From a conventional normal mode analysis we extracted the frequencies of the model which ranged from 119 cm<sup>-1</sup> for a pure torsional vibration to 1044 cm<sup>-1</sup> for a mixed bond stretch-angle bend vibration. Classical simulations were performed on the complete surface at a series of temperatures between 5 K and 300 K. We demonstrated how anharmonic effects at higher temperatures can rotate the normal coordinates and shift the frequencies with respect to the harmonic values. For the lowest frequency mode (a torsion) increasing the temperature lowered the effective frequency and this was rationalized in terms of the shape of the quasiharmonic torsional potential. The quasiharmonic frequencies calculated from Monte Carlo trajectories on the anharmonic potential surface for *trans* and *gauche* butane are listed in table 2. The effective frequency of the torsional mode is lowered by 25 cm<sup>-1</sup> to 91 cm<sup>-1</sup> at 300K. The anharmonicity of the exact potential results in the decreasing curvature of the quasiharmonic potential and the lowering of the effective torsional frequency with temperature. Fig. 3 shows a schematic illustration of the exact potential, the harmonic approximation, and quasiharmonic approximations at 100K and 300K for the torsional coordinate of *trans* butane.

The approach to the evaluation of vibrational spectra described above is based on classical simulations for which quantum corrections are possible. The incorporation of quantum effects directly in simulations of large molecular systems is one of the most challenging areas in theoretical chemistry today. The development of quantum simulation methods<sup>31</sup> is particularly important in the area of molecular spectroscopy for which quantum effects can be important and where the goal is to use simulations to help understand the structural and dynamical origins of changes in spectral lineshapes with environmental variables such as the temperature. The direct evaluation of quantum time-correlation functions for anharmonic systems is extremely difficult. Our initial approach to the evaluation of finite temperature anharmonic effects on vibrational lineshapes is derived from the fact that the moments of the vibrational lineshape spectrum can be expressed as functions of expectation values of positional and momentum operators. These expectation values can be evaluated using extremely efficient quantum Monte-Carlo techniques. The main points are summarized below.

The starting point is the quantum partition function  $Z$  in the coordinate representation:

$$Z = \int dx_1 \langle x_1 | e^{-\beta H} | x_1 \rangle \quad (IV.1)$$



TABLE II  
 Quasi-Harmonic Frequencies<sup>a</sup> Calculated from Monte Carlo Trajectories on the Exact Potential Surface for Trans and Gauche Butane

	<u>trans</u>		<u>gauche</u>
100 K	200 K	300 K	300 K
113 (5)	102 (17)	91 (25)	99 (33)
407	406	407	419
435	437	436	602
899	911	892	857
1008	1014	1002	966
1045	1055	1043	1034

a. Frequency in  $\text{cm}^{-1}$ .

b. Monte Carlo trajectories constructed with  $Q_k$  (mass-weighted Cartesian) as independent coordinates.

c. Numbers in parentheses indicate percent deviation from harmonic normal-mode eigenvalues; only deviations greater than 1% indicated.

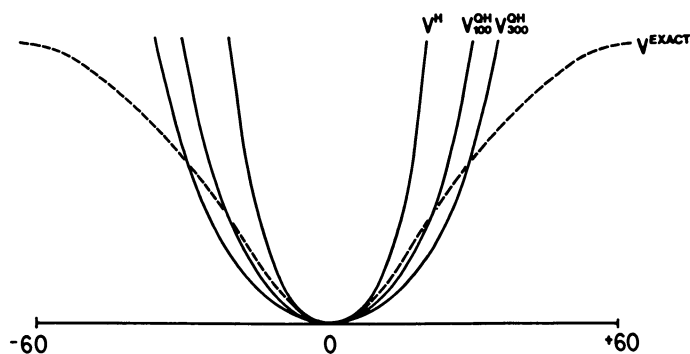


Figure 3. Schematic illustration of the exact potential  $V^{\text{exact}}$ , the harmonic approximation  $V^H$ , and quasi-harmonic approximations at 100K,  $V^{QH}$ , and 300K,  $V^{QH}$ , for the torsional coordinate  $Q$  of trans butane. The anharmonicity of the exact potential results in the decreasing curvature of the quasi-harmonic potentials with increasing temperature. (Reproduced from Ref. 30. Copyright 1984 American Chemical Society.)

The  $p$  point discretized path integral for  $Z$  is obtained by inserting complete sets of states  $p$  times:

$$Z = \int dx_1 \cdots dx_p \langle x_1 | e^{-\beta H/P} | x_2 \rangle \langle x_2 | e^{-\beta H/P} | x_3 \rangle \cdots \langle x_p | e^{-\beta H/P} | x_1 \rangle \quad (IV.2)$$

It is not possible in general to evaluate the matrix elements in the path integral for arbitrary  $H$ . We define the exact Hamiltonian  $H$  and a reference Hamiltonian  $H_0$  by:

$$H = \frac{p^2}{2m} + V \quad (IV.2a)$$

$$H_0 = \frac{p^2}{2m} + V_0 \quad (IV.2b)$$

where  $V$  is the exact anharmonic potential and  $V_0$  is a quadratic "reference" potential discussed below. Clearly:

$$H = H_0 + (V - V_0) = H_0 + V' \quad (IV.3)$$

We wish to separate the matrix elements involving  $H$  in equation 10 into matrix elements of  $H_0$  and  $V$ . For  $p$  "large enough" we have:

$$\langle x_i | e^{-\beta \frac{H_0 + V'}{P}} | x_{i+1} \rangle \approx e^{-\beta V'(x_i)/2P} \langle x_i | e^{-\beta H_0/P} | x_{i+1} \rangle e^{-\beta V'(x_{i+1})/2P} \quad (IV.4)$$

A lot has been accomplished in the separation, eq. IV.4 because for quadratic Hamiltonians the matrix elements can be evaluated analytically. As  $P \rightarrow \infty$  eq. IV.4 becomes exact. In a  $p$  point discretized path integral Monte Carlo simulation each quantal degree of freedom is simulated by  $p$  "classical" degrees of freedom. If we wish to apply discretized path integral methods to simulate polyatomic systems, it is essential that eq. 6 hold for small values of  $p$ . The approximation of the path integral by  $p$  discretized points for small  $p$  depends on the construction of an appropriate reference Hamiltonian. Quadratic reference systems provide a promising avenue for study because the quantum density matrix elements have an analytical form. In a previous paper, we proposed the use of a temperature dependent harmonic (quasiharmonic) reference system for path integral Monte-Carlo simulations.<sup>32</sup> We demonstrated that the use of this reference system resulted in a substantial computational advantage as compared to the use of the conventional free particle propagator. However, the use of a single fixed reference system over the entire range of the potential is clearly not optimal. We have recently developed a series of approximations to the propagator and diagonal density matrix which employ a different quadratic form (Variable Quadratic Reference System, VQRS) at each point on the potential.<sup>33</sup> The VQRS Hamiltonian is given by:

$$H_0(x_i, x_{i+1})(x) = \frac{P^2}{2m} + \omega_{(x_i, x_{i+1})}^2 (x - x_0)^2 + b \quad (IV.5)$$

The notation is meant to suggest that the frequency is variable and depends on the propagator matrix elements. The following criteria have proved valuable in choosing the variable coefficients of eq. IV.5: (1) at low temperature, the VQRS reference should weight the region around the potential minimum most heavily, and (2) at high temperature, our approximation should approach the classical limit:

$$\lim_{\beta \rightarrow 0} G(x, x', \beta) = \exp \left[ \frac{(x - x')^2}{2\beta} + \frac{\beta}{2} (V(x) + V(x')) \right] \quad (IV.6)$$

For a potential with a single minimum, a straightforward interpolation scheme suggests itself. We choose  $x_0$  to be the true minimum,  $b$  to be  $V(x_0)$ . The frequency is determined by requiring that eq. IV.6 be satisfied. This condition is found to be:

$$\omega^2(x_i, x_{i+1}) = \left[ \frac{V(x_i) + V(x_{i+1})}{(x_i - x_0)^2 + (x_{i+1} - x_0)^2} \right] \quad (IV.7)$$

For a potential with multiple minima, a simple generalization of the above is available; this will be discussed elsewhere.

We briefly review results we have obtained on model potentials with the VQRS reference system. The results obtained with the diagonal approximation to the propagator are superior to any previous such approximations that we are aware of. In table 3 classical and quantum results are presented for various moments of the quartic oscillator:

$$H = \frac{P^2}{2m} + ax^2 + bx^4 \quad (IV.8)$$

Results for a range of temperatures and anharmonicities are listed. The diagonal approximation to the propagator is very good. For example, at a reduced temperature corresponding to  $\beta\hbar\omega = 10$  (i.e. a 2,000 cm<sup>-1</sup> vibration at room temperature) and anharmonicity  $b=0.05$ , the classical second moment  $\langle X^2 \rangle = 0.084$  whereas the exact quantum result (calculated by basis set methods) is 0.445. Not surprisingly, quantum effects are very important at this reduced temperature. The  $p=1$  quantum Monte-Carlo result for the second moment is within 10% of the exact value. This means that the computational effort required to calculate quantum expectation values for this model system is only slightly greater than that required to evaluate classical ensemble averages.

Given equilibrium quantum expectation values, we can calculate moments of the infra-red vibrational lineshape using a procedure originally outlined by Gordon.<sup>34</sup> The infrared vibrational lineshape is given as the Fourier transform of the dipole moment correlation function:

$$I(\omega) = \frac{1}{2\pi} \int_{-\infty}^{\infty} \langle u(o)u(t) \rangle e^{i\omega t} dt \quad (IV.9)$$

TABLE IIIa Evaluation of  $\langle X^2 \rangle$ 

Reference System	Exact Quantum Result	Discretized Path Integral		
		Quadrature Points		
A. $\beta\hbar\omega = 10$ Anharmonicity $b=0.05$				
basis set	0.445 (Classical = 0.094)	1	4	8
free particle		0.093	0.262	0.358
quasiharmonic		0.320	0.397	0.431
Variable harmonic		0.446		
B. $\beta\hbar\omega = 2$ Anharmonicity $b=5$				
basis set	0.161 (Classical - 0.093)			
free particle		0.094	0.143	0.159
quasiharmonic		0.140	0.155	0.159
Variable harmonic		0.165		
Evaluation of $\langle X^4 \rangle$				
A. $\beta\hbar\omega = 10$ Anharmonicity $b=5$				
basis set	0.071			
free particle		0.003	0.017	0.029
quasiharmonic		0.010	0.023	0.034
Variable harmonic		0.068		

TABLE IIIb Evaluation of Higher Moments

Property	Exact Quantum	Variable Quadratic
$\langle X^8 \rangle$	1.45	1.15 (p=1)
		1.52 (p=2)
$\langle P^2 \rangle$	0.680	0.597 (p=1)
		0.645 (p=2)
$\langle P^2 X^2 \rangle$	-0.198	-0.175 (p=1)
		-0.192 (p=2)

By inverse Fourier transformation of eq. 1 and expansion of both sides in a Taylor series we obtain:

$$\sum_{n=0}^{\infty} \frac{t^n}{n!} \left| \frac{d^n}{dt^n} \langle u(o)u(t) \rangle_{t=0} \right| = \sum_{n=0}^{\infty} \frac{(it)^n}{n!} \int w^n I(w) dw \quad (IV.10)$$

Equating coefficients of powers of t:

$$\frac{d^n}{dt^n} \langle u(o)u(t) \rangle_{t=0} = (i)^n \int w^n I(w) dw \quad (IV.11)$$

Thus the nth vibrational spectral moment is equal to an equilibrium correlation function, the nth derivative of the dipole moment autocorrelation function evaluated at t=0.<sup>34</sup> By using the repeated application of the Heisenberg equation of motion:

$$\frac{du}{dt} = \frac{i}{\hbar} [H, u] \quad (IV.12)$$

and substitution into equation IV.11, we can express the nth vibrational spectral moment as an expectation value of nested commutators of H with the dipole moment operator:

$$\int w^n I(w) dw = \hbar^n \langle u(o) \cdot [H, [H, \dots [H, u(o)]]] \rangle \quad (IV.13)$$

The expectation values on the right hand side of this equation depend only on the ensemble averages of position and momentum operators, which can be evaluated using the VQRS Monte-Carlo sampling scheme outlined above.

In table IV we present the first and second moments of the vibrational spectrum of the quartic oscillator calculated by the moments method. The quantum results were obtained from path integral Monte Carlo simulations using the variable quadratic reference. For comparison, the average frequency and linewidth obtained from classical Monte-Carlo evaluation of the moments is also listed. Spectral features for two values of the temperature ( $\beta\hbar\omega = 5$  and 1.0) and two anharmonicities ( $b=0.05$  and  $b=1.0$ ) are listed. As the anharmonicity or the temperature is increased the oscillator frequency and linewidth increase for both the classical and quantum simulations. The important point is that the classical spectrum is shifted less and broadened more as the temperature and anharmonicity increase. For example, choosing  $\beta\hbar\omega = 1$  and  $b = 0.05$  the classical spectrum is almost twice as broad as the quantum spectrum. The results presented in table IV demonstrate that for realistic values of the temperature and anharmonicity, quantum effects on the vibrational spectrum are important. However, the strong coupling of the lineshape broadening with the frequency shifting is a limitation of one dimensional models for which the only broadening mechanism is anharmonicity in the vibrational degree of

TABLE IV

## Vibrational Spectrum of Quartic Oscillator by Moments Method

	Spectral Moment <sup>a)</sup>	Quantum	Classical
A. $\beta\hbar\omega = 5$	$\langle \omega \rangle$	1.12	1.05
<b>b = 0.05</b>	$\langle \omega^2 \rangle^{1/2}$	0.03	0.06
B. $\beta\hbar\omega = 5$	$\langle \omega \rangle$	1.96	1.4
<b>b = 1.0</b>	$\langle \omega^2 \rangle^{1/2}$	0.3	0.4
C. $\beta\hbar\omega = 1$	$\langle \omega \rangle$	1.19	1.12
<b>b = 0.05</b>	$\langle \omega^2 \rangle^{1/2}$	0.12	0.20

a)  $\omega_o = 1, \hbar = 1, m = 1$

freedom. Significant population of vibrationally excited states is required for thermal broadening. In contrast, it is the coupling of the vibrational degree of freedom to other modes, protein and or liquid which is of primary interest with respect to an understanding of the structural information content of chromophore lineshapes. The coupling of a chromophore vibration to a bath results in the time and spatial modulation of the energy spacing of the first few vibrationally excited states. This broadening mechanism can give rise to line broadening without significant frequency shifting. Path integral computer simulations of models for chromophoric molecules coupled anharmonically to additional solvent and biopolymer modes are presently underway.

We have described in this section methods for calculating vibrational lineshapes for anharmonic systems which incorporate quantum properties in a fundamental way. The methods have been demonstrated to be very powerful when applied to a variety of one dimensional problems. However, for one dimensional models alternative methods for calculating spectra are more direct. We are pursuing path integral approaches to the problem of calculating lineshapes because we believe the numerical methods can be generalized to polyatomic systems and that they will be much more stable and accurate than alternative approaches. One particularly attractive aspect of our approach is the ability to combine quantum and classical Monte-Carlo algorithms in a single simulation. For example the simulation of the vibrational spectrum of a chromophore with 10-20 degrees of freedom imbedded in a protein could be accomplished by combining quantum Monte-Carlo methods for the chromophore coordinates with classical Monte-Carlo trajectories for the protein atoms.

### Modeling Solvation Effects on Biopolymers

A complete theoretical treatment of the structural, thermodynamic, and dynamical properties of biological macromolecules requires an analysis of solvation effects. Proteins and nucleic acids contain both polar and charged groups whose interactions are strongly influenced by solvent. To date, most simulations of biopolymers have not explicitly incorporated solvent. Instead, a primitive model is used in which a dielectric constant is employed to account for solvent screening implicitly. Various empirical forms have been suggested for the dielectric constant.<sup>23,24,35,36</sup> It is very difficult to judge the accuracy of such ad hoc treatments of electrostatic interactions in biopolymers. While short time dynamical simulations of biopolymers starting from the x-ray structure reflect primarily packing effects, and thus are not very sensitive to solvent screening of long range interactions, accurate modeling of larger conformational changes will require a much more accurate treatment of solvent. Furthermore, to evaluate quantities such as the free energy of binding of ligands to proteins or electrolyte effects on nucleic acid conformation, brute force computer simulations are both very time consuming and subject to large sampling errors so that it is very difficult to obtain a complete set of results over a wide enough range of structural parameters. Alternative methods which can guide the development of appropriate computer simulations and provide limiting results for comparison with simulations are greatly needed. In this section we describe an approach we are pursuing in this area.

Considerable progress has been made in the last decade in the development of more analytical methods for studying the structural and thermodynamic properties of liquids. One particularly successful theoretical approach is based on an Ornstein-Zernike type integral equation for determining the solvent structure of polar liquids as well as the solvation of solutes.<sup>37</sup> Although the theory provides a powerful tool for elucidating the structure of liquids in

which the component solute and solvent molecules are small, its application to biopolymers requires extension of the theory to a large number of interaction sites. This is in general a formidable task due to the size and complication of the intramolecular correlation matrix which appears in the integral equation. One approach involves the application of a superposition approximation.<sup>38</sup> Alternatively, we have formulated a new integral equation applicable to solvated biopolymers which possess periodicity (e.g. DNA).<sup>8,39</sup> An outline of the theory, preliminary results, and comparison with computer simulations are presented below.

The general form of the (RISM) integral equation appropriate for treating solute-solvent interactions which has been derived in the literature is given by:<sup>40</sup>

$$\rho \mathbf{h} \rho = \omega * \mathbf{c} * \omega + \omega * \mathbf{c} * \rho \mathbf{h} \rho \quad (V.1)$$

where  $\mathbf{h}$  is the matrix of intermolecular pair correlation functions,  $\mathbf{c}$  is the matrix of direct correlation functions,  $\rho$  is a diagonal matrix of site densities, and  $\omega$  is an intramolecular correlation function matrix. The solution of the RISM equations is obtained by supplementing them with a closure relation and then iterating. Because this set of coupled integral equations grows as the square of the number of sites on the solute molecule, its application has been limited to solutes containing no more than three or four atomic centers. However, when the solute molecule consists of a periodic array of atoms; for example the sites on a rod-like polyelectrolyte such as DNA, the size of the RISM matrix equations is reduced to those corresponding to a repeating unit of the polymer. We have carried out such a reduction and solved the RISM equations for several model systems of increasing complexity.<sup>8</sup> Here, we summarize results we have recently obtained for a linear chain of ions immersed in water and for helical charge distributions corresponding to B and Z DNA.<sup>8,39</sup>

In the first example the model considered is a linear chain of positive ions solvated by water. The TIPS water model is employed for this study. The cations have unit charge, are placed along the  $z$  axis with a linear spacing of 2.07 Å and have Lennard-Jones parameters  $\sigma = 1.897$  Å and  $\epsilon = 1.116 \times 10^{-13}$ . As an initial test of the polymer RISM theory, two sets of molecular dynamics simulations have also been carried out with parameters corresponding to this model. The results of simulations of a single ion in water and an ion-chain in water are compared with the polymer RISM results. The simulations of a single ion included 215 water molecules and one ion at the center of a cubic box with edge length 18.62 Å. The linear chain simulation included 9 ions equally spaced ( $l = 2.07$  Å) along the  $z$ -axis. Ion-water site pair correlation functions were calculated from 10 ps. and 5 ps. trajectories for the single ion and the ion chain respectively.

The cation-oxygen correlation functions obtained from the molecular dynamics simulations are compared with the polymer RISM theory in fig. 4. In the results from the simulations two striking features are observed: a significant increase in the height of the first peak of the water distribution around the ion-chain as compared with the single ion, and the appearance of a well defined second peak in the distribution around the chain at about 3.73 Å. The new RISM theory reproduces the first peak very well. This increase is not intuitively obvious, because the existence of neighboring chain ions reduces the number of solvent molecules in the first coordination shell due to volume exclusion. The appearance of a second peak corresponds to configurations in which a water molecule is bound by an adjacent ion along the chain. The polymer RISM result also produces a second peak close to the position found in the molecular dynamics simulations, although it is less well developed. A full analysis of the



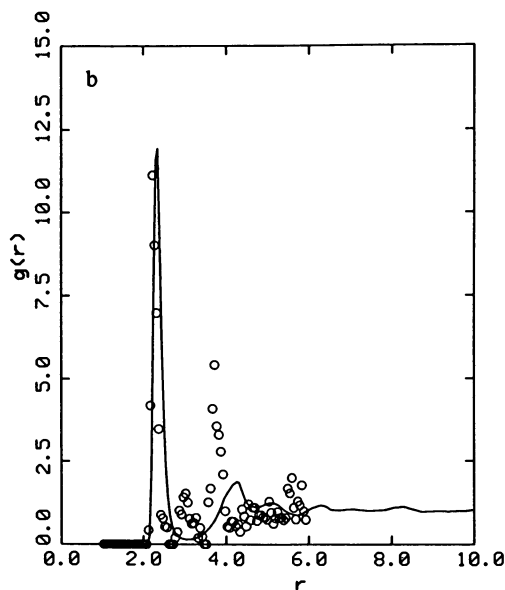
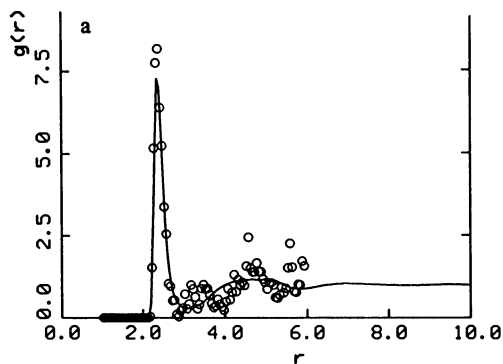


Figure 4. The solute-oxygen distribution function for a linear chain of cations in water ( $1 \text{ g/cm}^3$ ) at 298 K, (a) single ion; (b) chain of ions. Circles: simulation; solid lines: polymer RISM. (Reproduced with permission from Ref. 8. Copyright 1987 North Holland Press.)

molecular dynamics simulation and comparison with the polymer RISM result will be presented elsewhere.<sup>42</sup>

One important area in which the polymer RISM theory will have applications is in the study of salt effects on DNA conformation. It is well known that the B to Z DNA transition is induced by high ionic strength. Qualitatively, this can be understood in terms of increased electrolyte shielding required to stabilize the higher negative (phosphate) charge density on the Z DNA helix. Using the polymer RISM theory we are in a position to evaluate how the solute-solvent free energy changes with helical parameters, as well as electrolyte valency and ionic strength. We note that alternative theories for treating this problem such as counter ion condensation<sup>43</sup> or Poisson-Boltzmann<sup>44</sup> drastically simplify the geometry of the phosphate charge configuration and do not appear to describe the electrostatics of the B to Z transition well.<sup>45</sup> Alternatively, a study of ionic effects on DNA structural transitions based on an integral equation analysis of solvent screened phosphate interactions has appeared. While the phosphates were located correctly on the DNA helix in this study, the screened polyion potential was derived from a superposition approximation which amounts to ignoring the effect of helix excluded volume and charge on the local solvent structure<sup>46</sup>. These drastic approximations are avoided in the polymer RISM theory<sup>8,39</sup>.

The solute solvent contribution to the free energy stabilizing the DNA polyion can be calculated within the polymer RISM theory by a charging up process:<sup>47</sup>

$$\Delta F = 4\pi\rho \int_0^1 d\lambda \int r^2 dr u_{uv}(r) g_{uv}(r; \lambda) \quad (\text{V.2})$$

where  $g_{uv}$  is the polyion (u) - electrolyte (v) radial distribution function  $u_{uv}$  is the polyion - electrolyte interaction potential (for which we have used a primitive model) and  $\lambda$  is the charging parameter. That is, the polymer RISM equation is solved numerically for several intermediate values of the phosphate charge between zero and one and then equation V.2 is integrated numerically. The polymer RISM model predicts that the Z DNA geometry is differentially stabilized over B DNA as the salt (NaCl) concentration increases above 2.5M. This is the salt concentration range within which the B to Z conformational change is observed to occur.<sup>48</sup> These preliminary results are very encouraging. We have begun detailed Monte-Carlo simulations of the distribution of electrolyte around B and Z DNA forms for comparison with the polymer RISM model.

#### Acknowledgment

This work has been supported in part by grants from the NIH (GM-30580), the Petroleum Research Fund of the American Chemical Society, and the National Science Foundation Office of Advanced Scientific Computing. RML is the recipient of a NIH Research Career Development Award.

#### REFERENCES

1. J. A. McCammon and B. L. Tembe, *Comput. Chem.* **8**, 281 (1984).
2. P. A. Bash, U. Chandra Singh, F. K. Brown, R. Langridge, and P. A. Kollman, *Science* **235**, 574 (1987).
3. W. F. van Gunsteren and M. Karplus, *Biochemistry* **21**, 2259 (1982).

4. W. F. van Gunsteren, H. J. C. Berendsen, J. Hermans, W. G. J. Hol, and J. P. M. Postma, *Proc. Natl. Acad. Sci. USA* **80**, 4315 (1983).
5. G. L. Seibel, U. C. Singh, and P. A. Kollman, *Proc. Natl. Acad. Sci. USA* **82**, 6537 (1985).
6. E. Clementi, *J. Phys. Chem.* **89**, 4426 (1985).
7. K. S. Kim and E. Clementi, *J. Am. Chem. Soc.* **107**, 227 (1985).
8. F. Hirata and R. M. Levy, "A New RISM Integral Equation for Solvated Polymers," *Chem. Phys. Lett.*, in press.
9. Levy, R. M., M. Karplus, and J. A. McCammon, *J. Am. Chem. Soc.* **103**, 994 (1981).
10. Levy, R. M., C. M. Dobson, and M. Karplus, *Biophys. J.* **39**, 107 (1982).
11. Lipari, G., A. Szabo, and R. M. Levy, *Nature (Lond.)* **300**, 197 (1982).
12. Hoch, J. C., C. M. Dobson, and M. Karplus, *Biochemistry* **21**, 1118 (1982).
13. Olejniczak, E. T., C. M. Dobson, M. Karplus, and R. M. Levy, *J. Am. Chem. Soc.* **106**, 1913 (1984).
14. M. Karplus and J. A. McCammon, *Nature (London)* **277**, 578 (1979).
15. R. Richarz, K. Nagayama, and K. Wuthrich, *Biochemistry* **19**, 5189 (1980).
16. R. M. Levy, R. P. Sheridan, J. W. Keepers, G. S. Dubey, S. Swaminathan and M. Karplus, *Biophys. J.* **48**, 509 (1985).
17. G. Lipari and A. Szabo, *J. Am. Chem. Soc.* **104**, 4546 (1982).
18. H. Frauenfelder and E. Gratton, *Methods Enzymol.* **127**, 207 (1986).
19. G. A. Petsko and D. Ringe, *Ann. Rev. Biophys. Bioeng.* **13**, 331 (1984).
20. Westhof, E., B. Chevrier, S. Gallion, P. Weiner and R. M. Levy, *J. Mol. Biol.* **91**, 699 (1986).
21. Westhof, E., T. Prange, B. Chevrier and D. Moras, *Biochimie* **67**, 811 (1985).
22. Konnert, J. H. and W. A. Hendrickson, *Acta Cryst.* **A36**, 344 (1982).
23. Weiner, S., P. Kollman, D. Case, U. Singh, G. Ghio, G. Alagon, S. Profeta and P. Weiner, *J. Am. Chem. Soc.* **106**, 765 (1984).
24. Pettit, J. and M. Karplus, *J. Am. Chem. Soc.* **107**, 1166 (1985).
25. Levitt, M. *Cold Spring Harbor Symp. Quant. Biol.* **47**, 251 (1982).
26. Levy, R. M., D. Perahia, and M. Karplus, *Proc. Natl. Acad. Sci. USA* **79**, 1346 (1982).
27. Willis, B. T. and W. Pryor, "Thermal Vibrations in Crystallography. University Press, London.
28. Kuriyan, J., G. A. Petsko, R. M. Levy and M. Karplus, *J. Mol. Biol.* **90**, 227 (1986).
29. Warshel, A. *J. Chem. Phys.* **55**, 3327 (1971).
30. Levy, R. M., O. Rojas, and R. A. Friesner, *J. Phys. Chem.* **88**, 4233 (1984).
31. D. Chandler and P. G. Wolynes, *J. Chem. Phys.* **74**, 4078 (1981).
32. R. A. Friesner and R. M. Levy, *J. Chem. Phys.* **80**, 4488 (1984).
33. R. M. Levy, P. Zhang and R. A. Friesner, "Variable Quadratic Reference System for Evaluating Discretized Path Integrals." *Chem. Phys. Lett.*, submitted.
34. R. G. Gordon, *J. Chem. Phys.* **43**, 1307 (1965).
35. B. Brooks, R. Brucoleri, B. D. Olafson, D. J. States, S. Swaminathan and M. Karplus, *J. Comp. Chem.* **4**, 187 (1983).
36. M. Gilson, A. Rashin, R. Fine and B. Honig, *J. Mol. Biol.* **183**, 503 (1985).
37. H. L. Friedman, "A Course in Statistical Mechanics," Prentice-Hall, (1985).
38. B. M. Pettit and M. Karplus, *J. Chem. Phys.* **83**, 781 (1985).
39. F. Hirata and R. M. Levy, to be submitted.
40. P. J. Rossky, *Ann. Rev. Phys. Chem.* **36**, 321 (1985).
41. D. Chandler, *Ann. Rev. Phys. Chem.* **29**, 441 (1978).
42. P. Redfern, F. Hirata, and R. M. Levy, manuscript in preparation.

43. G. Manning, *Quart. Rev. Biophys.* **11**, 2 (1978).
44. C. F. Anderson and M. T. Record, *Ann. Rev. Phys. Chem.* **33**, 191 (1982).
45. M. Behe and G. Felsenfeld, *Proc. Natl. Acad. Sci. USA* **78**, 1619 (1981).
46. D. M. Soumpasis, *Proc. Natl. Acad. Sci. USA* **81**, 5116 (1984).
47. D. Zichi and P. J. Rossky, *J. Chem. Phys.*, **84**, 1712 (1986).
48. F. M. Pohl, *Cold Spring Harbor Symp. Quant. Biol.* **47**, 113 (1984).

RECEIVED June 15, 1987

## Chapter 7

# Dynamic Simulation of Complex Molecular Systems

H. J. C. Berendsen, W. F. van Gunsteren, E. Egberts, and J. de Vlieg

Laboratory of Physical Chemistry, University of Groningen, Nijenborgh 16,  
9747 AG Groningen, Netherlands

A review is given of the application of Molecular Dynamics (MD) computer simulation to complex molecular systems. Three topics are treated in particular: the computation of free energy from simulations, applied to the prediction of the binding constant of an inhibitor to the enzyme dihydrofolate reductase; the use of MD simulations in structural refinements based on two-dimensional high-resolution nuclear magnetic resonance data, applied to the lac repressor headpiece; the simulation of a hydrated lipid bilayer in atomic detail. The latter shows a rather diffuse structure of the hydrophilic head group layer with considerable local compensation of charge density.

Theoretical descriptions in Chemistry involve the physics of complex molecular systems. The relative complexity of (bio)chemical systems limits the ability of physical theory to treat them properly, and this makes chemistry especially difficult. But in a way molecular systems are also simple; for most practical purposes they are built up from just two types of particles: nuclei, with negligible size and irrelevant internal structure, and electrons. And for most practical purposes the Born-Oppenheimer approximation is applicable, separating electronic and nuclear motion. Thus a complex molecular system can be described as a system of point masses moving in an effective potential field. It further simplifies things that in the majority of applications this effective potential field is also conservative, i.e., dependent on coordinates only. Finally, for applications at normal temperatures and not involving details of the behaviour of hydrogen atoms, the laws of classical mechanics apply with a sufficient degree of accuracy. Of all the approximations mentioned, the latter is the least safe and there are many exceptions to classical behaviour. For example, high frequency motions in covalently bonded molecules do not behave classically. However, a quantum correction to a classical treatment is generally sufficiently accurate.

0097-6156/87/0353-0106\$06.00/0  
© 1987 American Chemical Society

The applicability of the Born-Oppenheimer approximation for complex molecular systems is basic to all classical simulation methods. It enables the formulation of an effective potential field for nuclei on the basis of the Schrödinger equation. In practice this is not simple, since the number of electrons is usually large and the extent of configuration space is too vast to allow accurate ab initio determination of the effective fields. One has to resort to simplifications and semi-empirical or empirical adjustments of potential fields, thus introducing interdependence of parameters that tend to obscure the pure significance of each term. This applies in particular to descriptions of potential fields in terms of pair-additive site-site potentials.

No realistic potential can be described correctly by pair potentials, particularly in systems of polar molecules. In practice pair-additive potentials are effective potentials in the sense that they include the average effects of the many-particle interactions. Thus effective pair potentials are an approximation of the full potentials, valid only for certain ranges of density, composition and temperature. A notorious example is the set of site-site potentials used to simulate liquid water (1-3). Several of such potentials have been devised and are fairly successful in reproducing liquid properties; they all have in common that the molecular dipole moment is 20 to 30 % larger than the experimental dipole moment of the water molecule in the gas phase, and that the second virial coefficient for the model is almost twice the experimental value. These deviations from reality are quite significant; they are necessary to take the average effect of electronic polarizability into account. Of course, introduction of polarizability in the potential field description is a better solution to this weakness, which will also solve an ambiguity concerning the internal energy in effective pair potentials (4), but it comes at the expense of adding complexity to the model.

Let us assume that a sufficiently reliable description of the potential field is available. We are interested to derive macroscopic properties of a complex system on the basis of these interaction functions. Such macroscopic properties either concern equilibrium properties of a static nature, including all thermodynamic quantities, or they concern dynamic properties as various transport coefficients, measurable in non-equilibrium systems. To derive such properties is the task of statistical mechanics. This is a mature science with a precise machinery providing a reliable basis for the computation of macroscopic quantities. Unfortunately, complex molecular systems are almost never amenable to analytic treatment in statistical mechanics, with the rather dull exceptions of dilute gases, very simple liquids and almost perfect crystals. So we have to resort to simulation of macroscopic behaviour by constructing a representative statistical ensemble of a size large enough to provide us with sufficient statistical accuracy. If we are interested in static equilibrium properties only, it is sufficient to generate an ensemble of equilibrium states, irrespective of their correct temporal correlation, as is done by Monte Carlo (MC) methods. For dynamic and non-equilibrium properties this does not suffice and one (or many) trajectories in phase space have to be generated. This is done by the method of Molecular Dynamics (MD). Since MD is a richer method than MC, without much extra computer effort, we shall concentrate entirely on MD.

The method of MD (5-6) simply solves Newton's equations of motion for each atom in the system during a certain length of time. The algorithms have been well worked out (7), although for highly polar systems the proper inclusion of long range electrostatic terms still is problematic (8). Given appropriate potential functions, there are two main concerns:

- a. the size of the simulated system should be kept as small as possible while avoiding adverse boundary effects,
- b. the time span of the simulation should be as short as possible while retaining sufficient statistical accuracy and without running into ergodicity problems. The latter consideration is serious: many systems of interest have the awkward habit of residing for fairly long periods of time in a certain region of configuration space before traversing to another region. In order to cover a representative part of configuration space, very long simulations are necessary or special tricks must be applied.

We will now turn to applications of brute force MD simulations, reserving to the last section special tricks to avoid problems of large size and long time.

#### Computational aspects of MD

Applying MD to systems of biochemical interest, such as proteins or DNA in solution, one has to deal with several thousands of atoms. Models for systems with long spatial correlations, such as liquid crystals, micelles, or any system near a phase transition or critical point, also must involve a large number of atoms. Some of these systems, including synthetic polymers, obey certain scaling laws that allow the estimation of the behaviour of a large system by extrapolation. Unfortunately, proteins are very precise structures that evade such simplifications. So let us take 10,000 atoms as a reasonable size for a realistic complex system.

Turning to time: local events will generally be equilibrated in 100 ps and reasonable statistics can be obtained in such times. However, when conformational changes involving more than a local region occur, times up to seconds may be involved. Such events (including the folding process of a protein) can clearly not be treated by brute force MD. But in many cases one would like to extend simulations into the nanosecond region.

The time step used for integrating the equations of motion is 1 to 2 femtoseconds. Each atom interacts with roughly 100 neighbours, so that  $10^8$  pair interactions must be calculated per step,  $10^9$  per ps and  $10^{11}$  per "experiment". The simulation time on a supercomputer (CRAY 1 or Cyber 205) varies between 2 and 10  $\mu$ s per pair interaction (9,10): this means that the simulation of 10,000 particles for 100 ps takes of the order of 100 hours supercomputer time. Although this seems a substantial amount, it is not too discouraging, since the price-performance ratio of supercomputers has improved by a factor 10 every 6 years over the last 30 years (11). This trend seems to strengthen with the realisation of massively parallel designs: it is likely that within a decade special purpose parallel computers will provide one or two orders of magnitude more computational power than present-day supercomputers in a desk-top machine for the price of a minicomputer. This means that MD runs which would now take 1000 hours

of supercomputer time will become cheap routine jobs in ten years time. Whether the development of reliable potential fields will keep abreast of the development of computational power is not so sure; here a concentrated scientific effort may become necessary in the near future.

#### Derivation of relevant properties from MD

Given the ability to simulate and store long dynamic trajectories of a complex system, how can macroscopic properties be derived? We must realise that the precise details of any trajectory are totally irrelevant: not only are all interesting properties related to statistical averages, but the precise course of a trajectory is even unpredictable. Any error, however slight, will cause at some later time a significant deviation of the exact trajectory. But that need not bother us since also in real physical systems the predictability of trajectories in phase space is destroyed e.g. by gravitational noise from distant galaxies. This leaves aside the fundamental notion that we can never have precise knowledge of initial conditions, either in a classical or in a quantum mechanical sense. So we can (and must) concentrate on statistical averages. From a computational point of view this is a happy circumstance since it relaxes the requirements for precision.

Consider first equilibrium properties. Assuming that a reliable equilibrium trajectory is available, ensemble averages of any directly measurable quantity can be obtained by simple averaging. The only concern is the accuracy of the average; the statistical treatment is not quite straightforward because the obtained series of data is strongly correlated (12). Quantities which can be obtained by averaging include the kinetic and potential energy, pressure, and all structural properties such as radial distribution functions, structure factors, etc. Other properties such as specific heat, compressibility and other derivatives of directly measurable quantities can be obtained from fluctuations. From auto- and cross-correlation functions of time dependent quantities transport properties can be found: diffusion coefficients, viscosity, mobilities, conductance, and relaxation properties measurable by nuclear magnetic resonance and optical techniques. Reliable techniques have been developed to constrain global parameters such as temperature and pressure or gradients of such quantities (13-15). The equations of motion can also be modified to couple the system of interest to a bath of constant temperature or pressure (16). These techniques allow the simulation of non-equilibrium systems, producing transport properties in a natural way. A difficulty in deriving transport properties from response functions in non-equilibrium systems is that one generally simulates a periodic system in order to avoid boundary effects. This limits the disturbance or driving force to Fourier components with  $k$ -vectors fitting the periodicity of the system, setting an upper limit to the wavelength and a lower limit to the frequency range of the response function. This poses no problems if extrapolation is allowed, but serious problems arise when the long time scale behaviour (the "tail" of correlation functions) is essential for the problem studied (17).

Thus far we have considered "directly measurable quantities", i.e., quantities that can be defined for each frame or snapshot in



the simulation. Unfortunately a large class of very relevant thermodynamic quantities are not directly measurable since they depend on an integral over phase space, rather than an ensemble average. These quantities are the entropy  $S$ , the Helmholtz free energy  $A$ , the Gibbs free energy  $G$ , the thermodynamic potential  $\mu$ , and all quantities derived from these, such as equilibrium constants of reactions, binding constants, association and dissociation constants, solubilities, distribution coefficients, adsorption coefficients, activity coefficients, fugacities, electrochemical potentials and the descriptions of phase boundaries. It can safely be said that these quantities are of more fundamental and practical interest than the directly measurable quantities. Wide application of simulation techniques in chemistry can be expected only if practical methods are available to determine free energy. Fortunately such methods exist and they work in practice, be it at the expense of considerable computational effort. We describe them in the next section.

### Free energy determination

Methods to determine free energy (18,19) can be divided into three classes: (i) Direct determination of distribution functions, (ii) Probe methods, (iii) Perturbation and integration methods.

In order to discuss the various techniques we must distinguish between diffusive and non-diffusive systems (18). Diffusive systems, such as liquids, are characterized by the eventual diffusion of particles over all of the available space; non-diffusive systems such as solids, glasses and macromolecules with a definite average structure are characterized by time independent average positions around which the atoms fluctuate.

The Helmholtz free energy  $A$  is given by

$$A = -kT \ln Z \quad (1)$$

where  $Z$  is the canonical partition function, determined by the hamiltonian  $H(p,q)$  that describes the total energy in terms of momenta  $p$  and coordinates  $q$ :

$$Z = (h^{3N} N!)^{-1} \int dp \int dq \exp[-H(p,q)/kT] \quad (2)$$

The problem is that for diffusive systems the multidimensional configuration space is so vast that it can never be integrated by simulation techniques. This is immediately clear from the occurrence of  $N!$  in  $Z$ . The number of integrand evaluations should vastly exceed  $N!$ , which for  $N = 1000$  and one evaluation per picosecond on the futuristic ultrasupercomputer requires vastly longer than the age of the universe.

For non-diffusive systems the configuration space is limited and determinations of free energy and entropy are possible. Using knowledge of the covariance matrix  $\langle \Delta x_i \cdot \Delta x_j \rangle$  of atomic fluctuations, accumulated during a simulation, a good estimate can be made of entropy and free energy (20-22). The method has been applied to an  $\alpha$ -helix (20), a dipeptide (23,24) and a dodecapeptide hormone (25). It turns out that good statistics is required since insufficient statistics yields systematic errors in the entropy function (22). Knowledge of the covariance matrix can also be used to describe a

large molecule as a quasiharmonic system, allowing the derivation of quasi-normal modes (26-28). These are much more relevant for room temperature behaviour than real normal modes derived at some (local) minimum in the multidimensional configuration space. They can be used to derive slow cooperative motions in macromolecules. However, quasiharmonic modes are an approximation of a very non-linear system; both anharmonicity and damping by the solvent broaden the modes, possibly to the point where they lose their significance. Also the influence of the solvent on the entropy cannot be estimated from a study of the macromolecular distribution functions alone; it is not at all clear how the solvent can be included in this type of treatment. It seems that for solvated complex molecules the determination of entropy by evaluation of positional fluctuations will have little future.

Probe methods like particle insertion and test particle methods (29-32) are quite useful for computing chemical potentials of constituent particles in systems with low densities. Test particles are randomly inserted; the average Boltzmann factor of the insertion energy yields the free energy. For dense systems these methods work poorly because of the poor statistics obtained.

The methods of choice for complex dense systems are the perturbation and integration methods, in which changes in free energy are calculated relative to a known reference state (18, 19, 33-40). In general the path from known to unknown state is traversed by a coupling parameter  $\lambda$ , running from 0 to 1. The free energy determinations rest on the following two equations:

$$\frac{\partial A}{\partial \lambda} = \left\langle \frac{\partial H}{\partial \lambda} \right\rangle_{\lambda} \quad (3)$$

and

$$\Delta A = -kT \ln \langle \exp(-\Delta H/kT) \rangle_{\lambda} \quad (4)$$

where  $\Delta A = A(\lambda + \Delta\lambda) - A(\lambda)$ , and similarly for  $\Delta H$ ; the ensemble averages are taken over an equilibrium ensemble for the hamiltonian  $H(\lambda)$ . Eq (4) is useful for perturbations; a complete path can be reconstructed by performing a number of separate equilibrium simulations at different values of the coupling parameter  $\lambda$ , and fitting them by overlapping perturbations. This approach has been successfully applied to compute the free energy of cavity formation in water (2,35) as a first step in the process of hydrophobic hydration. It turns out that the cavity free energy of simple Scaled-Particle Theory (40) is surprisingly close to the simulation results. The second step in hydrophobic hydration is the introduction of a solute into an appropriate cavity. It is hoped that this step is small enough to carry out as a single perturbation according to Eq 4. As it turns out, for a neon atom this is just barely the case; for other solutes a single perturbation step does not suffice (36).

Eq (3) provides a means to construct a free energy path by integration:

$$A(1) - A(0) = \int_0^1 \left\langle \frac{\partial H}{\partial \lambda} \right\rangle_{\lambda} d\lambda \quad (5)$$

In practice this integration can be carried out during a slow continuous simulation (2, 36) in which the hamiltonian changes from  $H(0)$  to  $H(1)$ . If the "growth" process is slow enough, the system will be in equilibrium at all intermediate stages: we simulate a reversible process and we compute the reversible work done in the process. The growth process may be a change from one type of atom into another, creation or annihilation of a particle, a change in a potential field parameter, etc. Many of these processes are more alchemy than chemistry and they yield meaningless thermodynamic results; however, realistic processes can often be constructed from two such unrealistic processes.

The potential usefulness of free energy computations by "slow growth" is quite considerable. It will be possible to predict binding constants of inhibitors to enzymes or hormones to receptor sites, aiding the process of drug design. Also the prediction of the behaviour of modified enzymes in terms of stability, binding of substrates, and possibly thermodynamic parameters of transition states, should become possible in the future, aiding the process of protein engineering. Applications in chemical technology will include the prediction of the thermodynamic behaviour of mixtures, phase separations, adsorption and possibly catalysis.

An illustrative example of a biologically relevant study is the prediction of the binding properties of an inhibitor of the enzyme DHFR (dihydrofolate reductase) by Zwinderman (41). DHFR is an essential enzyme in the process of cell growth; inhibitors to bacterial DHFR are antibiotics, those to the human enzyme are cytostatic agents. A well-known inhibitor is TMP (trimethoprim); in an analogous compound, TEP, three methoxy groups bound to a benzene ring are replaced by ethyl groups. It was attempted to predict the binding constant of TEP to DHFR relative to that of TMP by slowly transforming TMP into TEP and vice versa while it remains bound to the enzyme. By subtracting the same transformation in aqueous solution the difference in binding free energy of the two compounds was found. The enzyme MD runs were carried out on a Cray-1 and the water runs on a Cyber 205 computer, each at a speed of about 2 ps per CPU hour. The final result was in accordance with the experimental data; however it was not yet possible to obtain sufficient accuracy. Two difficulties emerged from this study. First the enzyme and water run both gave a large free energy difference between TMP and TEP (of 55 and 60 kJ/mol), but it is the difference of these values that is the relevant quantity. Secondly it appears that there are two or more possible local structures of the enzyme-inhibitor complex, which are similar enough to be thermodynamically possible but which do not rapidly interconvert. Furthermore the accuracy of the potential functions is not yet quite sufficient. But these bottlenecks can and will be solved to open up an important field of practical application.

#### Molecular Dynamics for interpretation of 2D NMR data

A field of application of MD that is beginning to bear fruit is the refinement of data from nuclear magnetic resonance (NMR) and from diffraction experiments. High-resolution NMR at frequencies around 500 MHz is able to resolve individual proton resonances of biological macromolecules in solution with molecular weights exceeding 10,000

dalton. A very rich two-dimensional Nuclear Overhauser Effect (NOE) spectrum can be obtained that contains data on the distances of several hundred proton pairs. The problem is how to derive reliable three-dimensional structures from distance data. Geometrical methods (42,43) have been developed and can indeed deliver a number of structures fulfilling the constraints (44,45). But the definition of a structure with 250 essential degrees of freedom (the dihedral angles) yielding  $10^{20}$  conformations (assuming 3 minima per angle) from 169 interproton distances which are only measured as lower and upper bound, is an underdetermined problem, requiring additional constraints. The numbers cited above apply to the case of the head piece of lac repressor, a DNA-binding protein of 51 amino acids, studied experimentally in Groningen and Zürich (46-49). The method of restrained dynamics, i.e., MD with inclusion of restraining potentials based on experimental NOE distances, was applied in Groningen to refine the structure (50-52). Others (53-55) have applied similar techniques to other proteins and oligonucleotides. The strategy is as follows:

1. First obtain a number of 2D NMR spectra (NOE, as well as J-coupling)
2. Find peak assignments by exploring through-bond and through-space connectivity maps. Deduce a set of assigned atom-atom distance constraints or restraints from NOE cross peaks. It may be necessary to resolve direct and indirect NOE couplings from 2D spectra with different mixing times.
3. Define a crude initial structure by either distance geometry algorithms or by model building. The latter starts by defining elements of secondary structure (helices,  $\beta$ -sheets) from the NMR data. Even starting from an extended structure is feasible (53).
4. Perform MD with inclusion of potential energy terms related to the experimental restraints. The latter may also include so-called non-NOE contacts, the absence of NOE cross peaks between assigned protons indicates a minimum distance between them. In lac repressor there are 9529 non-NOE's. We use two simple forms, a repulsive one for the lower limit distances and an attractive one for the higher limit-distance. Both consist of a quadratic potential with a linear extension (51,52). It is not necessary to use an all-atom potential field, since a hydrogen atom can be constructed as a "virtual atom" which is reconstructed from the coordinates of the group to which it is attached. In cases where assignments are not possible or ambiguous, a "pseudo atom" is constructed at an average position, for example for the protons of a methyl group.

Before MD was applied, a structure was generated by crude model building and subsequently relaxed by a few hundred steps of a conjugate gradient energy minimisation, followed by MD. After 20 ps of MD the violations of the NOE restraints did not further improve, with a maximum deviation of 2.5 Å occurring. Investigation by graphics inspection showed that a particular loop had to be reoriented (see fig. 1) in order to satisfy several of the constraints. This reorientation could not be accomplished by MD because of the high energy barrier involved. Once forced by hand, the subsequent MD run of another 43 ps converged to a structure in which virtually all NOE's are satisfied (largest deviation 0.5 Å). This

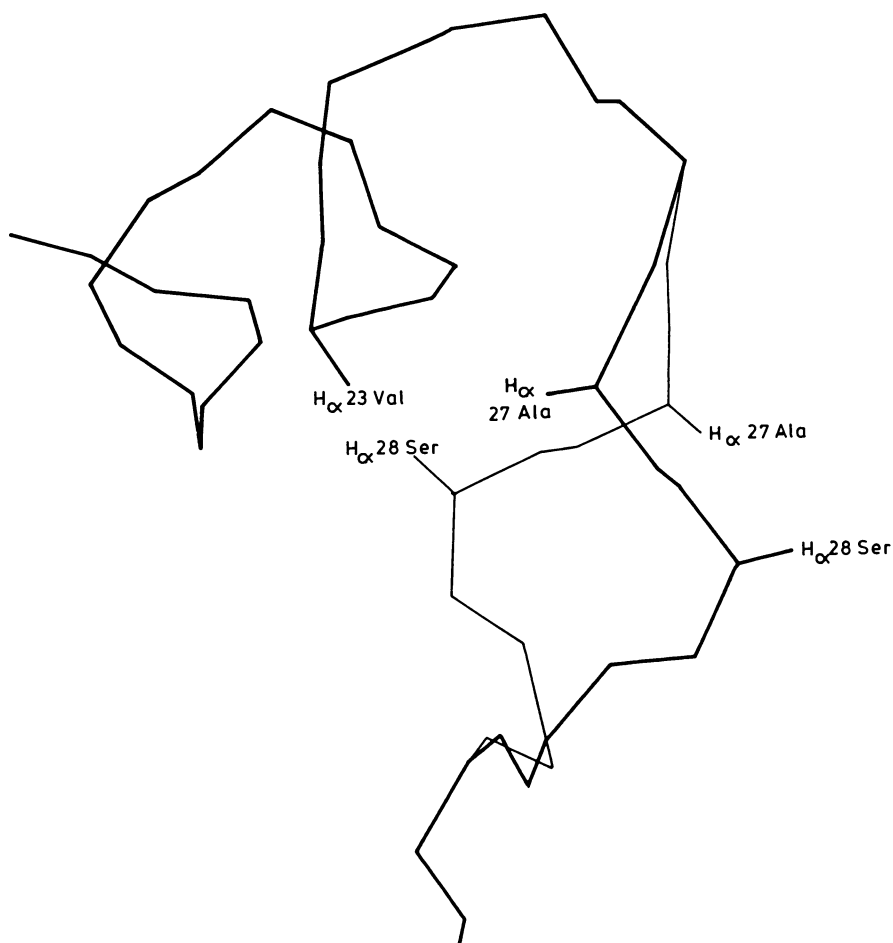


Figure 1. Manual reorientation of a backbone loop in lac-repressor was necessary to satisfy NOE constraints. Thin line: original structure; thick line: modified structure.

structure (fig. 2) has a r.m.s. deviation of 2.3 Å for the backbone C- $\alpha$  atoms from the original model, which is a substantial change.

It can be concluded that MD is a very powerful tool to refine structures of proteins and polypeptides in solution, based on 2D NMR data. This combination of techniques emerges as an important means to determine the 3 D structure of macromolecules up to a molecular weight of 20,000 in solution or in micelles or membrane fragments.

#### Simulations of bilayer membranes

A final example of the simulation of a complex system is a series of MD simulations of bilayer membranes. Membranes are crucial constituents of living organisms; they are the scene for many important biological processes. Experimental data are known for model systems; for example for the system sodium decanoate, decanol and water that forms smectic liquid crystalline structures at room temperature, with the lipids organized in bilayers.

In previous studies (56,57) a bilayer was modeled with atomic detail of the hydrocarbon chain, including the proper dihedral angle functions and using flexible bond angles, but the aqueous layer was not represented.

In order to mimic the energetic interaction with the aqueous phase, the head groups were restrained by a harmonic force to their average position in each bilayer. The harmonic force constant was chosen such that the head groups could move about one carbon-carbon bond length in or out of the plane determined by the average position of the head groups. The thickness of the layer adjusted itself, under the influence of an external pressure of 1 bar applied to the system.

The experimental order parameters were well reproduced by the simulation. There appears to be a cooperative tilt of the molecules with respect to the bilayer normal. This simplified model accounted well for the behaviour of the hydrocarbon chain; it could not account for the detailed behaviour of the head groups and could give no insight into the charge and electric field distributions and penetration of water into the bilayer. One particular result of the simplified simulation was disturbing: the diffusion constant of the lipid molecules was found to be an order of magnitude larger than the experimental value. This discrepancy was ascribed to the lack (in the model) of viscous damping by hydrodynamic interaction with the aqueous layer (57).

Subsequently a simulation of a bilayer including all atomic details of the head groups and aqueous phase was carried out (58). The system consists of 52 Na<sup>+</sup>, 52 decanoate ions, 76 decanol and 526 H<sub>2</sub>O, forming one bilayer in a rectangular three-dimensionally periodic box. A weak coupling to a bath of constant temperature (300 K) and pressure (1 bar) was applied. The aqueous phase was modeled in atomic detail, with full charges on the ions, using a dielectric constant of one, and incorporating the Simple Point Charge (SPC) model of water (3). Electrostatic interactions in this anisotropic system were calculated with inclusion of long-range interactions. A long equilibration run of 100 ps was performed, during which time a slow drift of the periodic box dimensions occurred. After equilibration the surface area stabilised at 0.236 nm<sup>2</sup> per chain and the z-repeat became 3.63 nm. These values agree within experimental error with density and X-ray data. Also the order parameters of the chain

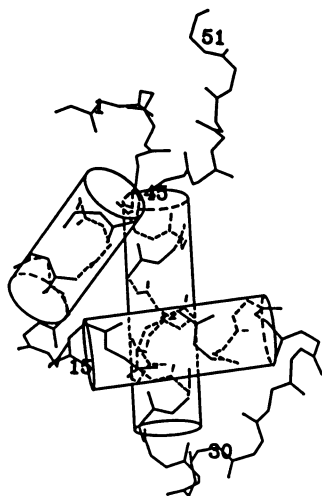


Figure 2. Final structure of lac-repressor in solution derived from 2D NMR combined with MD.

are in reasonable agreement with experiment. Fig. 3 shows a snapshot of the equilibrated structure.

The density distributions of water,  $\text{Na}^+$  and the  $\text{COO}^-$  and  $\text{COH}$  head groups are given in fig. 4. It is apparent that the sodium and water distributions are very similar and that the charged head groups lie well within the water layer but the alcoholic groups are situated more on the lipid side of the interface. The interface is very diffuse indeed, extending over almost 1 nm. The overlap of the sodium ion and carboxylic acid distributions suggests a charge compensation rather than a double layer as pictured in most textbooks.

Lateral diffusion coefficients were determined by monitoring mean-square displacements in the xy-plane, which are proportional to  $4Dt$ , where  $D$  is the diffusion coefficient and  $t$  the time. The following values were found:

Na	$2.7 \times 10^{-6} \text{ cm}^2/\text{s}$
decanoate	2.7
decanol	5.2
$\text{H}_2\text{O}$	$1.2 \times 10^{-5}$

The values for the lipid molecules compare well (although they are still somewhat larger) with the experimental value of  $1.5 \times 10^{-6} \text{ cm}^2/\text{s}$  as measured with the use of a nitroxide spin label. We note that the discrepancy of one order of magnitude, as found in the previous simulation with simplified head groups, is no longer observed. Hence we may safely conclude that the diffusion coefficient of the lipid molecules is determined by hydrodynamic interactions of the head groups with the aqueous layer rather than by the interactions within the lipid layer. The diffusion coefficient of water is about three times smaller than the value of the pure model water; thus the water in the bilayer diffuses about three times slower than in the bulk.

### Beyond limitations

The examples given above have been illustrative both for successful applications and for the limits of applicability of present-day brute force MD to complex chemical and biochemical systems. The limitations are those of (i) accuracy of force fields, (ii) simulation time and (iii) size of the system.

We will not discuss the more obvious but very tedious and cumbersome task to improve force fields. Electrostatic interactions are the weakest parts of the force fields: polarisability has to be introduced and dependable ways have to be found to include long range effects.

The limited time span and system size that can be treated will improve in two ways: first by a very substantial improvement in computer performance, and second by the use of stochastic techniques. In stochastic dynamics only the most relevant degrees of freedom are treated individually; less relevant degrees of freedom are averaged out and their influence on the relevant degrees of freedom are incorporated through appropriate potentials of mean force and stochastic forces. The methods have been well established but are not yet applied on a significant scale to (bio)macromolecules. A great deal of inventiveness can still be applied to define the relevant degrees of freedom in an appropriate way and compute the concomitant



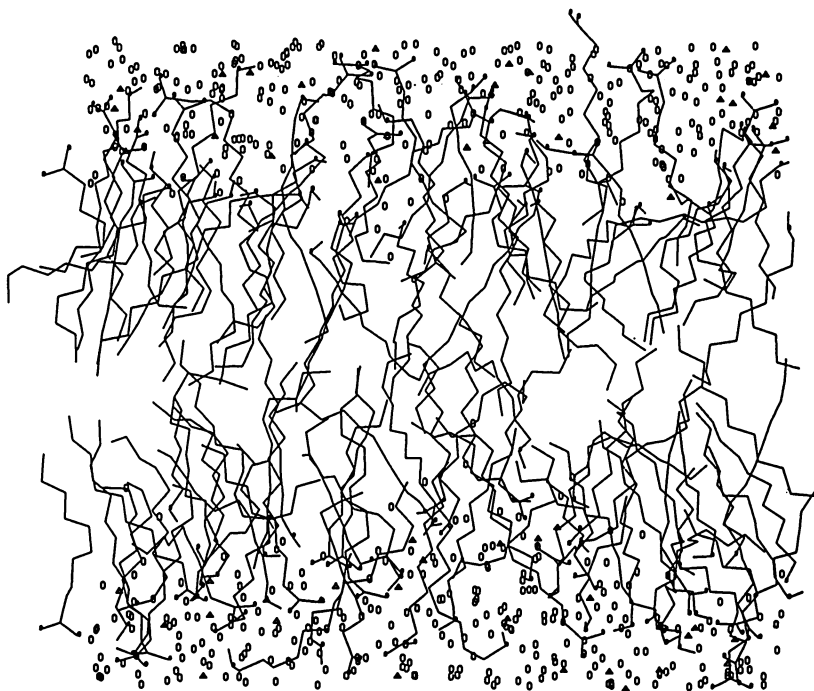


Figure 3. Snapshot from an equilibrated simulation of a smectic bilayer system: sodium ions ( $\Delta$ ), decanoate ions (chain with forked end) and decanol molecules (linear chain). The projection of all atoms is given.

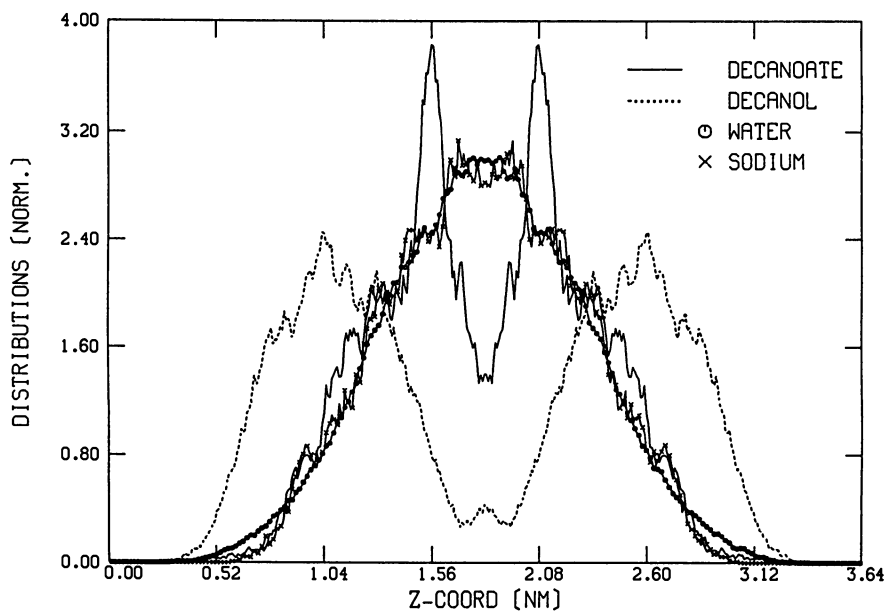


Figure 4. Density distribution in the direction normal to the bilayer plane for indicated groups.  $z = 0$  corresponds to the middle of the lipid layer;  $z = 1.8$  corresponds to the center of the aqueous layer.

potentials of mean force. Simplifications by clustering of atoms in groups and concentrating on slow cooperative motions still have to be implemented.

When processes are slow because they involve an activation barrier, the time scale problems can be circumvented by applying (corrected) transition state theory. This is certainly useful for reactive systems (59), requiring a quantummechanical approach to define the reaction path in a reduced system of coordinates. The development in these fields is only beginning and a very promising future lies ahead.

### Literature Cited

1. Finney, J.L.; Quinn, J.E.; Baum, J.O. In: Water Science Reviews, Franks, F., Ed.; Plenum: New York, 1985; Vol. 1, p 93.
2. Postma, J.P.M., Thesis, University of Groningen, 1985.
3. Berendsen, H.J.C.; Postma, J.P.M.; van Gunsteren, W.F.; Hermans, J. In Intramolecular Forces; Pullmann, B., Ed; Reidel: Dordrecht, 1981; p 331.
4. Berendsen, H.J.C.; Grigera, J.R.; Straatsma, T.P. J. Phys. Chem. in print (Rahman issue, 1987)
5. Hockney, R.W.; Eastwood, J.W. Computer Simulation using Particles; McGraw Hill: New York, 1981.
6. Berendsen, H.J.C.; van Gunsteren, W.F. In Molecular Liquids-Dynamics and Interactions; Barnes, A.J. et al, Eds.; NATO ASI Series C 135, 475; Reidel: Dordrecht, 1984.
7. Berendsen, H.J.C.; van Gunsteren, W.F. In: Molecular Dynamics Simulation of Statistical-Mechanical Systems; Soc. Italiana di Fisica, Bologna; North-Holland, Amsterdam, 1986; p 43.
8. Berendsen, H.J.C. Europhysics News 1986, 17, 8.
9. van Gunsteren, W.F.; Berendsen, H.J.C.; Colonna, F.; Perahia, D.; Hollenberg, J.P.; Lellouch, D. J. Comput. Chem. 1984, 5, 272.
10. Teleman, O.; Jönsson, B.J. J. Comput. Chem. 1986, 7, 58.
11. Berendsen, H.J.C. In Molecular Liquids-Dynamics and Interactions; Barnes, A.J. et al, Eds.; NATO ASI Series C 135, 561; Reidel: Dordrecht 1984.
12. Straatsma, T.P.; Berendsen, H.J.C.; Stam, A.J. Mol. Phys. 1986, 57, 89.
13. Nosé, S. Mol. Phys. 1984, 52, 255.
14. Nosé, S. J.Chem. Phys. 1984, 81, 511.
15. Evans, D.J. In Molecular Dynamics Simulation of Statistical-Mechanical Systems; Soc. Italiana di Fisica: Bologna; North-Holland; Amsterdam, 1986; p 221.
16. Berendsen, H.J.C.; Postma, J.P.M.; van Gunsteren, W.F; DiNola, A. Haak, J.R. J. Chem. Phys. 1984, 81, 3684.
17. Alder, B.J. In Molecular Dynamics Simulation of Statistical-Mechanical Systems; Soc. Italiana di Fisica: Bologna; North-Holland; Amsterdam, 1986; p 66.
18. Berendsen, H.J.C.; Postma, J.P.M.; van Gunsteren, W.F. In Molecular Dynamics and Protein Structure; Hermans, J., Ed.; Polycrystal Book Service: Western Springs, Ill., 1985; p 43.
19. Frenkel, D. In Molecular Dynamics Simulation of Statistical Mechanical Systems; Soc. Italiana di Fisica: Bologna; North-Holland, Amsterdam, 1986; p 151.
20. Karplus, M.; Kushick, J.N. Macromolecules 1981, 14, 325.

21. Karplus, M.; Brady, J.; Brooks, B.; Kushick, J.N.; Pettitt, M. In Molecular Dynamics and Protein Structure; Hermans, J., Ed.; Polycrystal Book Service, Western Springs, Ill., 1985; p 47.
22. Edholm, D.; Berendsen, H.J.C. Mol. Phys. 1984, 51, 1011.
23. Brady, J.; Karplus, M. J. Am. Chem. Soc. 1985, 107, 6103.
24. Pettitt, M.; Karplus, M. J. Am. Chem. Soc. 1985, 107, 1166.
25. DiNola, A.; Berendsen, H.J.C.; Edholm, O. Macromolecules 1984, 17, 2044.
26. Levy, R.M.; Karplus, M.; Kushick, J.N.; Perahia, D. Macromolecules 1984, 17, 1370.
27. Levy, R.M. In Molecular Dynamics and Protein Structure; Hermans, J., Ed.; Polycrystal Book Service: Western Springs, Ill., 1985, p 50.
28. Levy, R.M.; Rojas, O.; Friesner, R. J. Phys. Chem. 1984, 88, 4233.
29. Widom, B. J. Chem. Phys. 1963, 39, 2808.
30. Powles, J.G.; Evans, W.A.B.; Quirke, N. Mol. Phys. 1982, 46, 1347.
31. Guillot, B.; Guissani, Y. Mol. Phys. 1984, 54, 455.
32. Shing, K.S.; Gubbins, K.E. Mol. Phys. 1981, 43, 717; *ibid.* 1982, 46, 1109.
33. Beveridge, D.L.; Mezei, M. In Molecular Dynamics and Protein Structure; Hermans, J., Ed.; Polycrystal Book Service: Western Springs, Ill., 1985, p 53.
34. Okazaki, S.; Nakanishi, K.; Touhara, H. J. Chem. Phys. 1979, 71, 2421.
35. Postma, J.P.M.; Berendsen, H.J.C.; Haak, J.R. Faraday Symp. Chem. Soc. 1982, 17, 55.
36. Straatsma, T.P.; Berendsen, H.J.C. Postma, J.P.M. J. Chem. Phys. 1986, 85, 6720.
37. Mezei, M.; Swaminathan, S.; Beveridge, D.L. J. Am. Chem. Soc. 1978, 100, 3255.
38. Berens, P.H.; Mackay, D.H.J.; White, G.M.; Wilson, K.R. J. Chem. Phys. 1983, 79, 3375.
39. Jorgensen, W.L.; Ravimohan, C. J. Chem. Phys. 1985, 83, 3050.
40. Reiss, H.; Frisch, H.L.; Lebowith, J.L. J. Chem. Phys. 1959, 31, 369.
41. Zwinderman, H.J.; van Gunsteren, W.F.; Berendsen, H.J.C., in preparation.
42. Crippen, G.M.; Havel, T.F. Acta Cryst. 1978, A 34, 282.
43. Kuntz, I.D.; Crippen, G.M.; Kollman, P.A. Biopolymers 1979, 18, 939.
44. Wüthrich, K.; Wider, G.; Wagner, G.; Braun, W. J. Mol. Biol. 1982, 155, 311.
45. Braun, W.; Wider, G.; Lee, K.H.; Wüthrich, K. J. Mol. Biol. 1983, 169, 921.
46. Kaptein, R.; Zuiderweg, E.R.P.; Scheek, R.M.; Boelens, R.; van Gunsteren, W.F. J. Mol. Biol. 1985, 182, 179.
47. Zuiderweg, E.R.P.; Kaptein, R.; Wüthrich, K. Proc. Natl. Acad. Sci. U.S.A. 1983, 80, 5837.
48. Zuiderweg, E.R.P.; Kaptein, R.; Wüthrich, K. Eur. J. Biochem. 1983, 137, 279.
49. Zuiderweg, E.R.P., Billeter, M., Boelens, R.; Scheek, R.M.; Wüthrich, K.; Kaptein, R. FEBS Letters 1984, 174, 243.

50. van Gunsteren, W.F.; Kaptein, R.; Zuiderweg, E.R.P. In Nucleic Acid Conformation and Dynamics; Report NATO/CECAM Workshop; Olson, W.K., Ed.; CECAM: Orsay, France, 1983, p 79.
51. van Gunsteren, W.F.; Boelens, R.; Kaptein, R.; Scheek, R.M.; Zuiderweg, E.R.P. In Molecular Dynamics and Protein Structure; Hermans, J., Ed.; Polycrystal Book Service: Western Springs Ill., 1985, p 92.
52. de Vlieg, J.; Boelens, R.; Scheek, R.M.; Kaptein, R.; van Gunsteren, W.F. Isr. J. Chem. 1987, in print.
53. Clore, G.M. Gronenborn, A.M. In Structure, Dynamics and Function of Biomolecules; Proc. First EBSA Workshop, Saltsjöbaden; Ehrenberg, A. et al, Eds.; Springer: Berlin, 1987, p 108.
54. Clore, G.M.; Gronenborn, A.M.; Brünger, A.T.; Karplus, M. J. Mol. Biol. 1985, 186, 435.
55. Nilsson, L.; Clore, G.M.; Gronenborn, A.M.; Brünger, A.T.; Karplus, M. J. Mol. Biol. 1986, 188, 455.
56. Van der Ploeg, P.; Berendsen, H.J.C. J. Chem. Phys. 1982, 76, 3271.
57. Van der Ploeg, P.; Berendsen, H.J.C. Mol. Phys. 1983, 49, 133.
58. Berendsen, H.J.C.; Egberts, E. In Structure, Dynamics and Function of Biomolecules; Proc. First EBSA Workshop, Saltsjöbaden; Ehrenberg, A. et al. Eds.; Springer: Berlin, 1987, p 275.
59. Jorgensen, W.L., This Symposium.

RECEIVED June 15, 1987

## Chapter 8

# Applications of Molecular Dynamics for Structural Analysis of Proteins and Peptides

Bernard R. Brooks

Division of Computer Research and Technology, National Institutes of Health,  
Bethesda, MD 20892

A software system, GEMM (Generate, Emulate, and Manipulate Macromolecules), has been developed for the Star Technologies ST-100. This system allows the rapid computation of the energy and forces for use in molecular dynamics, minimization, or interactive modelling. A high degree of efficiency is obtained by the extensive development of microcode designed to run in a pipelined manner, which avoids the conventional problems of vectorization of the pair-interaction problem with a cutoff distance. The result of this implementation is that molecular dynamics simulations on the ST-100 are at least an order of magnitude more cost effective than on any other hardware system currently available. Several applications involving the use of this system are presented. The first application explores the effects of long range cutoffs on protein dynamics. This has been accomplished by carrying out 34 molecular dynamics simulations on carboxy-myoglobin. Each simulation is 150 picoseconds in length. For these calculations, both the distances at which the long range potentials are truncated and the method of truncation have been explored in a systematic manner. The second application demonstrates the utility of molecular dynamics for conformational exploration. This application involves the 3-dimensional structure determination of a glycoprotein N-terminal octapeptide T-cell epitope found on human ductal carcinoma (breast) cells.

Over the last several years, molecular dynamics has been becoming more useful as a practical tool for a wide variety of applications. These include exploring the temporal behavior of macromolecular systems (1,2), exploring energy decay (3), solvent analysis (4), determining 3-dimensional structures using 2-dimensional nuclear overhauser effect (NOE) data from nuclear magnetic resonance (NMR) experiments (5), determining relative free energies of similar

This chapter not subject to U.S. copyright  
Published 1987 American Chemical Society

systems (6-8), conformational sampling for structure determination (Brooks, B. R.; Pastor, R. W.; Carson, F. W. *Proc. Natl. Acad. Sci.* 1987, in press.) (9-11), and for crystallographic R factor refinement (12). For all of these applications areas, extensive access to computers which can rapidly perform molecular simulations is essential. In almost all published work in this field, the length and quality of simulations is balanced by the availability of computer resources. Furthermore, as these simulation methods become more refined and reliable, the total demand for simulation capability will increase many fold in the next few years. One solution to this problem currently being employed is the setting up of large supercomputer facilities from which many different researchers can benefit. Another solution is to build special purpose hardware which is specifically designed to perform the time dominant step (the restricted pair interaction problem) in a molecular dynamics simulation to provide simulation capability in a very fast and cost effective manner as is being done for the FASTRUN project (13). A third solution is to determine the best existing machine architecture for the restricted pair interaction and to implement the simulation on this machine in a highly optimized but general manner. An example of this third solution is presented in this paper which shows how it is possible to achieve supercomputer speeds from a low cost laboratory computer. By placing the task on a local lab computer, it is now also possible to develop reasonable interactive molecular modelling tools which utilize energies and forces in real time.

The GEMM (Generate, Emulate, and Manipulate Macromolecules) system is being used for almost all of the simulation work being performed in the Molecular Graphics Laboratory at the National Institutes of Health (NIH). In this paper, preliminary results of two applications of this system are presented, both of which would have been difficult to carry out on a slower machine. Full results of these projects will be published elsewhere. The first application explores the effects of long range cutoffs on protein dynamics. This has been accomplished by carrying out 34 molecular dynamics simulations on carboxy-myoglobin. Each simulation is 150 picoseconds in length. For these calculations, both the distances at which the long range potentials are truncated and the method of truncation have been explored in a systematic manner. The second application demonstrates the utility of molecular dynamics for conformational exploration. This application involves the structure determination of a glycoprotein N-terminal octapeptide T-cell epitope found on human ductal carcinoma (breast) cells.

#### The Star Technologies ST-100

Innovative computer hardware designs encourage new software algorithms that can perform in a very effective manner. One such example of this is the development of the molecular simulation software GEMM which has been developed for the Star Technologies ST-100. GEMM is a general purpose program that can be applied to any type of molecular system.

At best the ST-100 is capable of 100 million floating point operations per second (MFLOPS); however for reasonably large macro-

molecular systems, the performance of this software runs at about 90% of the speed of an optimized Cray X-MP version of similar software, and even faster than the Cray X-MP for smaller systems where vectorization is difficult. The throughput efficiency of the software on the ST-100 is roughly 50% (i.e. 50 MFLOPS). This high degree of efficiency is obtained by the extensive development of microcode designed to run in a pipelined manner, which avoids the conventional problems of vectorization of the pair-interaction problem with a cutoff distance. The result of this implementation is that molecular dynamics simulations on the ST-100 are at least an order of magnitude more cost effective than on any other hardware system currently available.

The GEMM software on the ST-100 is not a stand-alone package, and it requires a front-end simulation software package that runs on the host to provide data and to send command requests. It was designed and written with CHARMM (Chemistry at Harvard Macromolecular Mechanics) (14) as the primary front-end, but additional software packages, such as AMBER (15), have subsequently been modified to drive GEMM.

The ST-100 is not a typical array processor. Figure 1 shows the data flow through the functional units of the machine for a routine application. There are seven main functional units; (1) The Control Processor runs a FORTRAN-like language which controls all of the functional elements within the ST-100. (2) The input/output (I/O) subsystem handles all data transfer between the host and the ST-100 and is transparent to the user. (3) The main memory is typically 8 megabytes and is byte addressable and has a data transfer rate of 800 megabits/second. (4) The Storage Move Processor (SMP) moves data between the main and cache memories, converts data between host and internal floating point format, and performs integer and Boolean operations (bit packing, etc.). (5) The cache memory consists of three banks of memory each 16384 32-bit words long. Each cache bank can be split into halves and either half can be assigned to the SMP or to the Arithmetic Control Processor (ACP). This allows the double buffering of data transfers between main memory and the cache memory. Data transfers between the computational elements and different cache banks can occur at the same time. (6) The ACP processes the microcode that drives the computational elements. It also performs integer arithmetic, cache bank addressing, and conditional branching. (7) The computational elements are independent and communicate through a data interchange device. The add and multiply elements have three stages so that a new operation may be started on every cycle, but it requires three cycles for a single operation to complete. Since the machine cycle is 40 nanoseconds, each element can perform at 25 MFLOPS. The divide/square-root element is not pipelined and 15 cycles are required for a divide. When an application requires a divide, any other arithmetic operation can proceed concurrently in the other computational elements. By using the data interchange in a variety of ways it is possible to program this machine in the manner of a conventional array processor or as a pipeline processor with up to about 15 concurrent calculations. This is made possible because there are no vector registers as there are on most vector machines, and all memory access can be controlled by the user.



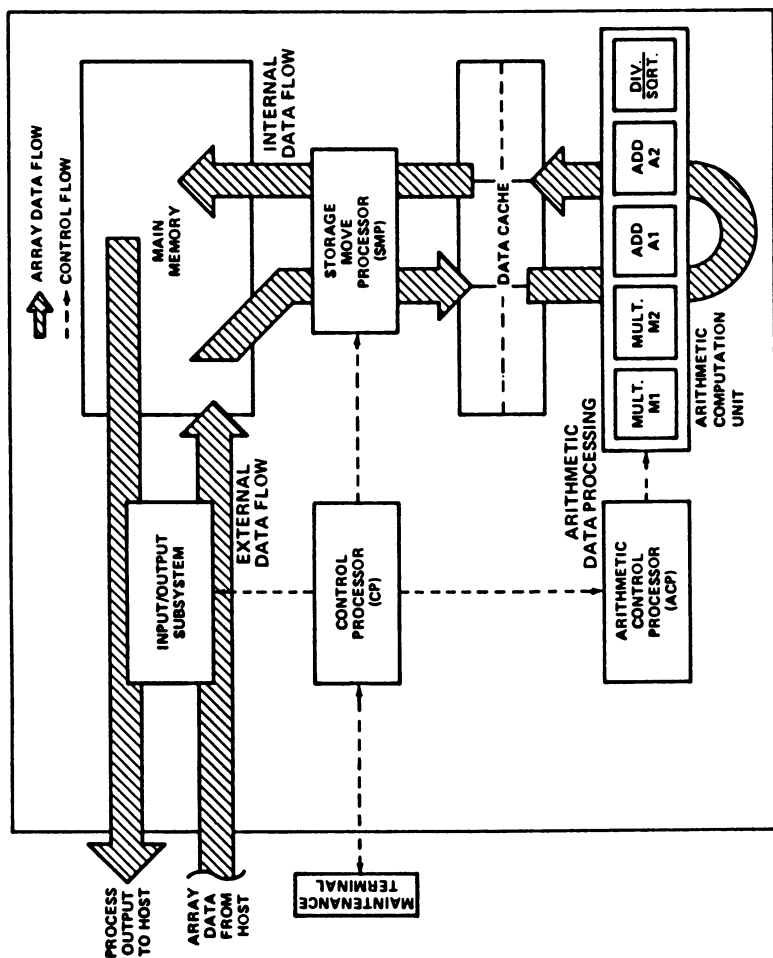


Figure 1. An overview of the ST-100 depicting data flow for a typical application. (Reproduced with permission from Star Technologies, Inc.)

**Goals.** The primary goal in developing GEMM was to provide a very fast general purpose molecular simulation package. This requires the rapid computation of energies and forces for the use of molecular dynamics, energy minimization, and interactive modelling.

It was decided early in development that there would be no sacrifice of the best functional forms that have been used in CHARMM and other molecular simulation programs (14, 15). For example, a great deal of software development effort could have been avoided if simple truncation of long range forces (electrostatic and van der Waals) had been sufficient. In addition, such a restriction would allow the program to run significantly faster (Hagstrom, R., Argonne National Laboratories, personal communication, 1986.). Nevertheless, the presence of large discontinuities in the forces makes minimizations very difficult, and has several deleterious effects on molecular dynamic simulations (Levitt, M., Weizmann Institute, personal communication, 1986.). As the program is currently written, there are many ways in which the long range force terms can be terminated as a function of distance.

One perceived problem with the ST-100 for molecular simulations is that all arithmetic floating point operations are done in single precision (24- or 32-bit mantissa, depending on operation), but some operations require higher precision, particularly those involved with accumulating force components. This problem has been overcome by the creation of six double precision macros (48-bit mantissa) which are employed wherever higher precision is necessary. These macros use several single precision operations to compute a single high precision result. As a result, all individual energy and force components are computed in low precision, but all accumulations are done in higher precision. This gives most of the benefits of high precision, without the extreme difficulties that would entail in the development of a full double precision version.

Another goal of the development of GEMM was to allow very large systems to be studied. This was accomplished by using a compact form of the nonbond list where, on the average, each element requires only one byte. This contrasts to the two bytes employed by CHARMM for a VAX and the eight bytes that are employed on a Cray. Thus for a typical ST-100 installation (with 2 megawords of memory), a system with 8000 atoms and up to 7 million nonbond pairs can be simulated (4000 atoms with high precision). With the 4x-cache memory option, systems with 16000 atoms can be studied in high precision. The limit of 7 million nonbond pairs allows very dense periodic systems to be studied such as a protein in a box of water, or a lipid bilayer.

Another programming consideration is the effective use of the I/O channel between the ST-100 and the host. With a VAX host, the data transfer rates are less than 1 megabit/second. This precludes the possibility of having a fast system where the three-dimensional coordinates are transferred from the host to the ST-100 and the subsequently computed energies and forces retrieved from the ST-100 on every step. The GEMM package has been designed to minimize synchronous data transfers. In an ideal situation, the ST-100 runs without direction from the host, and data that need to be saved are streamed to the host while the ST-100 continues to produce new data.

**Features.** GEMM is written in a host-independent manner and it has been run with an Apollo, a VAX, and a MicroVAX II as a host. GEMM can currently perform the following operations: perform molecular dynamics, perform energy minimizations, compute the energy and forces for a structure, and update the nonbond list (nonbond lists are usually automatic for the other operations). In addition, a wide variety of I/O sequences are possible, such as what is needed for interactive modelling work.

For large systems, the computation of the energy can require 98% or more of the total computational effort, and within the energy computation, the pair interaction energy (van der Waals and electrostatic terms) can represent more than 90% of the total effort. For this reason, the aspects of the program that deal with the generation of the nonbond list and the computation of the non-bond energy are of critical importance.

The nonbond list generation pair searching section finds all pairs of atoms within a given cutoff distance, usually 8 angstroms or more. The inner loop of this code has 5 cycles (0.2 micro-seconds/pair) and performs with 80% efficiency (80 MFLOPS). It allows atoms to be fixed (frozen), and there is also a facility to select by groups, so that all atom pairs between two groups are either included or excluded as a whole. This code works in a double buffered mode (asynchronously) with the list merging operation. The list merging operation removes from the close contact list (from the pair searching step) the nonbond exclusions, which includes bonding (1-2) and angle (1-3) interactions, to generate the final nonbond pair list. The final list is packed in a byte format. The list merging macro has 8 cycles in the inner loop, but only acts on those elements accepted by the pair searching code, so the cost of this operation is completely hidden except in cases where the non-bond cutoff distance is large in relation to the size of the molecular system. This code is extremely messy and it uses unannounced features of the ST-100 to accomplish list processing. There is also special treatment provided for 1-4 interactions so that separate van der Waals parameters can be specified and the electrostatic contributions can be reduced.

The nonbond energy evaluation consists of three macros. Since each individual macro requires several thousand machine cycles to complete, there is no expense in breaking the problem up into several parts because the loading of macros is asynchronous with their execution. The first macro computes the reciprocal of the square of the distance between interacting atoms ( $1/r^{**2}$ ), removes atom pairs beyond the cutoff distance, and processes the minimum image option. Because the cost of processing the minimum image convention is hidden behind the divide, this code is always present and for calculations where there are no periodic boundaries, a very large box size is used. The use of multiple macros simplifies the coding and allows replacement of different sections to allow for different options. For example, there are two versions of the middle macro, one that allows a switching function for long range interaction termination, and one that uses a "shifted" potential. There are also two versions of the last macro. One that accumulates forces in single precision and one that accumulates forces in double precision. Within the middle macros, there is code that computes

the energy with a constant dielectric or with a dielectric that is proportional to the distance. Having many options with no cost in efficiency makes the program useful for a wide class of problems, and for a wider distribution of users.

There are also the internal energy terms, those that account for the connectivity of groups of atoms (bonds, angles, dihedral, and improper dihedrals). Within these terms, all forces can be accumulated in high precision, and there is double buffering both within and between terms. For example, when the last angle energy buffer is being computed, the first dihedral buffer is being loaded into cache memory, thus completely hiding the cost of loading the dihedral data arrays and the gathering of the coordinates. For small systems where these terms can dominate the total computational effort, this can be important, but usually, these terms are not time intensive. Nevertheless, this accounts for much of the code (and coding effort) of GEMM. (See Table I.)

Table I. Timings for Each Section of Code

Code Section	# of macros	# of cycles		time/element ( $\mu$ seconds)
		single-precision	double-precision	
Nonbond list searching	1	5	-	0.2
Nonbond list for images	1	11	-	0.4
Nonbond list merging	1	8	-	0.3
Nonbond energy	3	34	43	1.4
Bond energy	3	41	51	1.6
Angle energy	9	144	159	5.8
Dihedral energy	7	130	150	5.2
Improper torsion energy	9	178	198	7.1
Hydrogen bond energy	26	254	294	10.2
Harmonic constraints	2	18	23	0.7
SHAKE constraints	3	35	40	1.4

**Performance.** The total time for 500 steps of dynamics and 25 nonbond updates for the standard CHARMM benchmark (Brunger, A. T., Harvard University, personal communication, 1985.), a B-DNA elevenmer duplex with 706 atoms and a 11.5 angstrom nonbond cutoff (77000 nonbond pairs) is found in Table II.

Table II. CHARMM Performance on a Variety of Machines

Machine	Time (sec)	Ratio to ST-100
Apollo DSP-160 double precision	22932	299
Apollo DSP-160 single precision	14904	194
VAX 11/780 w/FPA double precision	11650	152
IBM 3090 w/vector double precision	226	2.94
Cray-1S w/vector	186	2.42
Cray-1S w/vector(*)	174	2.27
Cray X-MP/48 no gather/scatter(*)	140	1.82
ST-100 double precision(*)	89.9	1.17
ST-100 single precision(*)	76.8	1.00
Cray X-MP/48 with gather/scatter(*)	70	0.91

(\*) does not include setup time

The timings represent those using the best code for each particular machine. For the system chosen, the vector lengths are longer than usual on average. For small systems that do not vectorize well the ST-100 does even better in relation to the other vector machines because of its pipeline coding and heavy use of double buffering across the different energy terms. For proteins with a polar hydrogen representation and an 8 angstrom cutoff, single precision, and no external water, the timings are given in Table III.

Table III. Timings Per Iteration for Different Proteins

System	Energy only (seconds)	With list updates every 20th step (seconds)
Ductal carcinoma octapeptide	0.014	N/A
BPTI (580 atoms)	0.070	0.072
Lysozyme (1264 atoms)	0.162	0.171
Carboxy-myoglobin (1532 atoms)	0.174	0.189
Hemoglobin (5478 atoms)	0.518	0.674

When one considers that the ST-100 is a \$275k machine and the half speed ST-50 has a list price of \$125k, the real potential for these machines becomes apparent.

Future Directions. The GEMM package is still under development. There are several areas where new capabilities are forthcoming. One feature just completed is the incorporation of periodic boundary conditions so that systems in a water box may be studied. Another feature that has just been completed and is now being tested is the ability to perform Langevin dynamics, so that systems can be coupled to a heat bath (16).

An area of development is the inclusion of code necessary for free energy perturbation calculations for internal, van der Waals and electrostatic energy terms (6). Another area of development is the option to use lookup tables for both nonbond energies and for constraint energy terms such as a solvent boundary energy term (16). Other features and options are routinely added as needed to aid in the execution of current projects underway within the NIH.

Another area of future promise is the interface of GEMM with the FASTRUN device currently being developed at Columbia University under the direction of Professor Cyrus Levinthal (13). The FASTRUN device is a computational unit which is directly interfaced to a ST-100 through a Dataram memory unit and is expected to perform at 700 MFLOPS. It should increase the throughput of GEMM by a factor of 5 to 10 over its current performance. Consideration for interfacing with FASTRUN has been kept in the current design of GEMM, and once FASTRUN is completed, a working version should surface within three months.

Conclusions. GEMM is a program for molecular simulations written for the ST-100 (or ST-50) which performs almost at Cray X-mp speeds for large systems. As such, GEMM running on the ST-100 (or ST-50) is an order of magnitude cost effective in comparison with any other hardware system currently available. GEMM is written in a pipeline manner thereby avoiding the problems of vectorization found on a

conventional machine. Most of the program is written in microcode (~90%) and as such it is fast, but rather inflexible. It is difficult to change the functional forms or to add new ones, and major new features require careful development. Furthermore, the program design is not appropriate for any other machine other than the ST-100 or ST-50. As such, the ST-100 is not the best machine for the development of new methods, but it is better used as a tool in application areas where the methods are proven.

An advantage of the ST-100 is that it is a laboratory machine. The problems associated with running simulations on a remote site do not apply. As a laboratory tool, the ST-100 is ideal for interactive use such as molecular modelling with real time energy determination or energy minimizations. The problems associated with low precision at the hardware level have been overcome, and GEMM has been designed to treat large systems with up to 1600 atoms in high precision and up to 7 million nonbonding atom pairs for a machine with two megawords of main memory.

The current implementation is best with CHARMM as a front-end, though other software packages have been modified to drive GEMM. The only host machines tested have been a VAX, a MicroVAX II, and the Apollo workstations. GEMM is available for distribution.

#### The Effects of Long Range Cutoffs on Protein Dynamics

Throughout the field of molecular simulations there are many ways in which the truncation of long range forces, particularly electrostatic forces, is achieved. There have been several papers detailing the effects of long range truncation for polar and ionic solvents using analytic and statistical methods (17). There have also been examples of cases where problems found in the analysis of simulations have resulted in a better treatment of the long range potential (Levitt, M., to be published), but most of these are imbedded in papers not dealing specifically with long range truncation. There has also been the tendency to diminish some adverse affects, such as discontinuities in the force, by coupling the entire system to a heatbath (18) rather than remove the discontinuity. In all of these cases, there are trade-offs between efficiency, accuracy, ease of programming, vectorizability, and justifiability. Due to the complexity of protein-protein interactions, it is not feasible to accurately predict the effects of long range truncation by methods other than direct simulation.

Methods. To explore the effects of long range truncation on molecular dynamics simulations of proteins, a series of simulations have been performed. The two main questions which have been addressed are:

- 1) What is the best functional form for truncating long range forces?
  - 2) What is the best distance to effect truncation?
- Several additional questions have been addressed such as:
- 3) What is the effect of a short switching function?
  - 4) What is the relationship between a constant dielectric and a distance dependant dielectric for pseudo-vacuum simulations?
  - 5) What is the effect of increasing the dielectric constant?

Four methods for truncation have been explored. These include:

(a) simple atom-atom truncation

$$E_{ij} = F(r) \frac{q_i q_j}{4\pi\epsilon r (2)}, \quad \begin{aligned} F(r) &= 1 & r < r_{\text{cut}} \\ F(r) &= 0 & r \geq r_{\text{cut}} \end{aligned} \quad (1)$$

This functional form is easiest to program and to vectorize. There are discontinuities in the energy and forces which make this inappropriate for minimizations, and causes problems for dynamics particularly if solvent is included.

(b) an atom-atom switching function over a range (14)

$$F(r) = \begin{aligned} &= 1 & r \leq r_{\text{on}} \\ &= (r_{\text{off}}^2 - r^2)^2 (r_{\text{off}}^2 - 2r^2 - 3r_{\text{on}}^2) / (r_{\text{off}}^2 - r_{\text{on}}^2)^3 & r_{\text{on}} < r < r_{\text{off}} \\ &= 0 & r \geq r_{\text{off}} \end{aligned} \quad (2)$$

This functional form has no discontinuities, but there can be large derivatives at long distances if the switching region is short.

(c) a "shifted" potential (14)

$$F(r) = \begin{aligned} &= [1 - 2(\frac{r}{r_{\text{cut}}})^2 + (\frac{r}{r_{\text{cut}}})^4] & r < r_{\text{cut}} \\ &= 0 & r > r_{\text{cut}} \end{aligned} \quad (3)$$

This functional form is continuous and there are no large forces at long range, but there is damage done to the short range potential which should probably be reparameterized to compensate for this.

(d) simple group-group truncation

$$F(r) = \begin{aligned} &= 1 & |\langle \vec{r}_I \rangle - \langle \vec{r}_J \rangle| < r_{\text{cut}} \\ &= 0 & > r_{\text{cut}} \end{aligned} \quad (4)$$

This is similar to the simple atom-atom truncation except that dipolar groups will never be split by the cutoff distance. There is still the problem of discontinuities, but these are less extreme than in the case of atom-atom truncations. In cases where water is explicitly included, this approach exhibits the curious phenomena of hot water and cold protein if the entire system is coupled to a heatbath. This is because the more mobile atoms (the water) are subjected to more discontinuities which makes them hotter than the less mobile atoms (the protein) (Levitt, M., Weizmann Institute, personal communication, 1986.). It should be noted that this is one of the most commonly used methods of truncation for simulations where CHARMM is not used. For the group-group truncation, these calculations are in progress and will be reported elsewhere. For this type of truncation, both methods where the list is updated on

every step and where a fixed list is kept between updates will be reported. All of the functional forms are depicted in Figure 2.

The model system for these calculations is carboxy-myoglobin starting from the X-ray coordinates (19). The polar hydrogen parameter set PARAM19 (20) was used for all calculations. In this representation there are 1532 atoms. It is not expected that the results of this work would change substantially if a different protein or if a different parameter set were used.

Each simulation was carried out using an identical procedure which included:

- 1) 1000 steps of steepest descents minimization to remove large forces,
- 2) 30 picoseconds of heating to 300K using identical random numbers,
- 3) 20 picoseconds of equilibration at 300K, and
- 4) 100 picoseconds of analysis at 300K.

The integration timestep was 0.001 picoseconds for all dynamics. All simulations were performed on the Star Technologies ST-100.

**Results.** For each simulation, several types of analysis were performed, but the values which best reflect the behavior of a simulation are the root-mean-squared (RMS) deviation from the X-ray coordinate values and the RMS atomic fluctuation about the average coordinates. The ideal result is deemed to be the simulation without cutoffs. This is not to say that the simulations without long range cutoffs will always be better than those that employ a cutoff. In fact for a simulation with a constant dielectric, the truncation may be an essential (though perhaps unintentional) part of the screening. However, for most of these calculations, a distance dependant dielectric has been used which incorporates its own screening, so this argument is unlikely. If it were not for the question of efficiency, few researchers would carry out simulations with truncation distances less than 15 angstroms.

The RMS displacement as a function of time for the shifted potential simulations are shown in Figure 3. As expected for this functional form, the longer cutoff distances result in a smaller RMS deviation from X-ray. The results for the 100 picosecond analysis section of all of the simulations are summarized in Table IV. For Table IV, the term "rdie" indicates that a distant dependant dielectric was used, "cdie" indicates that a constant dielectric was used, and "eps2" indicates that the electrostatic forces have been scaled by 0.5.

The results for the most part are expected. In general, short cutoff distances provide structures with large RMS deviations. The one angstrom switch simulations seem to reproduce RMS deviations reasonably well and also reduce the overall fluctuation of the system. It is clear there are balancing effects here. The damage done to the potential by removing atom-atom interactions tends to make the structures deviate more, and the large forces which are imposed at long range tend to restrict motion. For the "shifted" and simple truncation potentials there is nothing to restrict the motion and both deviations and fluctuations are larger. This becomes more evident when the results of the 0.5 and 0.25 angstrom



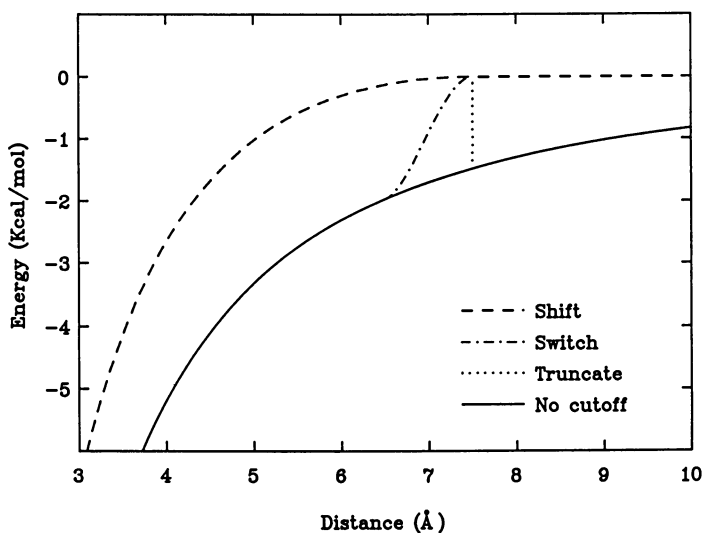


Figure 2. The electrostatic potential energy for atoms with half charges of opposite signs for the different methods of long range truncation.

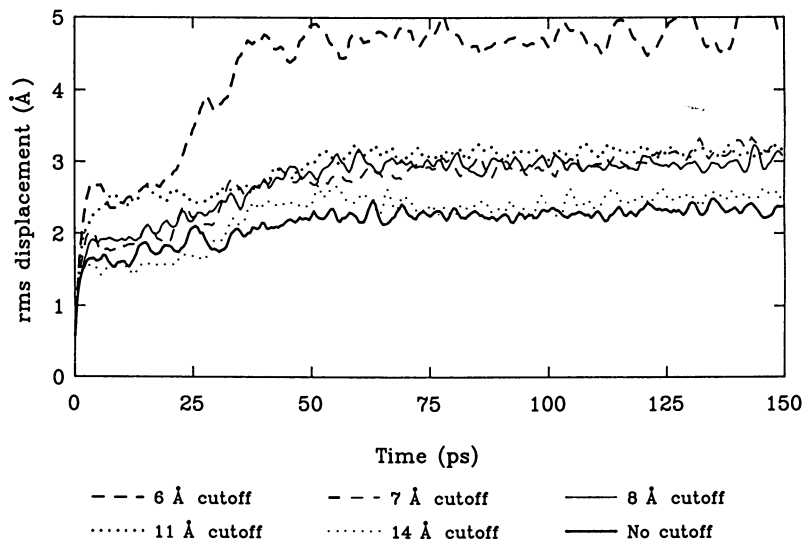


Figure 3. The RMS displacement for all atoms from the X-ray structure as a function of time for the simulations using the "shift" potential.

Table IV. RMS Fluctuations and Displacements for the Last 100 Picoseconds of Each Simulation (in Angstroms)

Truncation Method	Energy Term Cutoff Distance	RMS Fluctuations		RMS Displacement	
		all atoms	main chain	all atoms	main chain
rdie shifted	4.5	2.23	1.96	5.70	5.27
rdie shifted	5.5	1.34	1.10	4.59	3.72
rdie shifted	6.5	0.97	0.81	2.81	2.27
rdie shifted	7.5	0.74	0.59	2.87	2.34
rdie shifted	8.5	0.90	0.77	2.35	1.91
rdie shifted	10.5	0.70	0.59	3.05	2.44
rdie shifted	13.5	0.65	0.53	2.36	1.96
rdie shifted	none	0.63	0.50	2.20	1.68
rdie switched	3.5-4.5	0.58	0.46	2.89	2.54
rdie switched	4.5-5.5	0.53	0.43	2.35	1.82
rdie switched	5.5-6.5	0.63	0.49	1.97	1.63
rdie switched	6.5-7.5	0.58	0.44	1.84	1.43
rdie switched	7.5-8.5	0.60	0.47	2.68	2.26
rdie switched	9.5-10.5	0.62	0.48	1.88	1.39
rdie switched	12.5-13.5	0.51	0.38	2.17	1.69
rdie switched	none	0.63	0.50	2.20	1.68

Continued on next page

Table IV. Continued

Truncation Method	Energy Term Cutoff Distance	RMS Fluctuations		RMS Displacement	
		all atoms	main chain	all atoms	main chain
rdie switched	5.0-9.0	0.77	0.63	2.20	1.75
rdie switched	6.0-8.0	0.73	0.59	2.34	1.86
rdie switched	6.5-7.5	0.58	0.44	1.84	1.43
rdie switched	6.75-7.25	0.50	0.40	1.68	1.27
rdie switched	6.875-7.125	0.42	0.29	1.56	1.16
rdie truncated	4.5	1.40	1.14	5.92	4.74
rdie truncated	5.5	1.44	1.21	4.49	4.04
rdie truncated	6.5	1.07	0.87	2.91	2.49
rdie truncated	7.5	0.81	0.66	2.23	1.78
rdie truncated	8.5	0.79	0.61	2.63	2.16
rdie truncated	10.5	0.77	0.64	2.26	1.70
rdie truncated	13.5	0.77	0.65	2.45	1.96
rdie truncated	none	0.63	0.50	2.20	1.68
cdie shifted	7.5	0.71	0.59	3.23	2.57
cdie shifted	none	0.65	0.53	2.79	2.24
cdie shifted eps2	7.5	0.98	0.77	3.87	3.23
rdie shifted eps2	none	0.78	0.62	2.26	1.81
rdie shifted eps2	7.5	0.99	0.81	2.67	2.25

switching function simulations are considered. In the extreme case both the fluctuations and the deviations are severely restricted.

To further explore the relationship between the various truncation methods, an energy time series for each method was computed for the simulation of each other method for the first 10 picoseconds of the heating phase. In other words, for each step of dynamics, the energy was computed for all of the methods, but only one was chosen to drive the trajectory. The results of these simulations are shown in Figure 4 for the simulations truncating at 7.5 angstroms and for the no truncation simulation. The energies have all been shifted so that the initial energies at the beginning of the simulations are all zero. It is clear from these plots that the switching function is very different from the other methods. The energies of all of the methods look fairly good when compared to the no cutoff surface, but when the switching function energy surface is used to drive the trajectory, the energies of all of the other methods increase by roughly 300 kcal/mol in 10 picoseconds. It is not obvious what causes this, nor is it obvious what effect this will have on other observables. In any case, this effect is greatly reduced if a longer switching region is employed.

Conclusions. For the "shifted" potential, the deviations are too large, but the fluctuations are good at longer cutoff distances. This method should probably be avoided unless the short range potential has been reparameterized or cutoff values of 12 angstroms or more are used. For simple atom-atom truncation, the deviations are reasonably good, but the fluctuations are consistently too large. This should probably improve if neutral groups are employed, but the problems of discontinuities in the potential will still be present. For the switching function, the RMS deviation from X-ray as well as the fluctuations are consistently too small, even if switching off at 14 angstroms. Furthermore, when a short switching function is used, the resultant trajectory is highly disfavored by all other truncation methods. For longer switching function regions (e.g. from 5 to 9 angstroms) both fluctuations and deviations are acceptable. This is because there is no short range damage as is found with the shifted potential and that there are no large forces due to the derivatives of the switching function when switching over a long range. Even a long range atom-atom switching function should probably not be used for a simulation with a constant dielectric. For these calculations, switching based on neutral groups and over a long range is probably best.

A final point to remember is that the simulation with the smallest deviation from the X-ray structure (0.25 angstrom switch) is probably the least realistic of the entire set of simulations that were truncated near 7.5 angstroms, which implies that a simulation should not be judged by this value alone. It is hoped that from these simulations that better methods for handling the truncation of long range potentials can become more universal.

#### Conformational Exploration of Peptides Using Molecular Dynamics

There is great interest in the ability to reliably predict three-dimensional structures for peptides (11,21) or for portions of

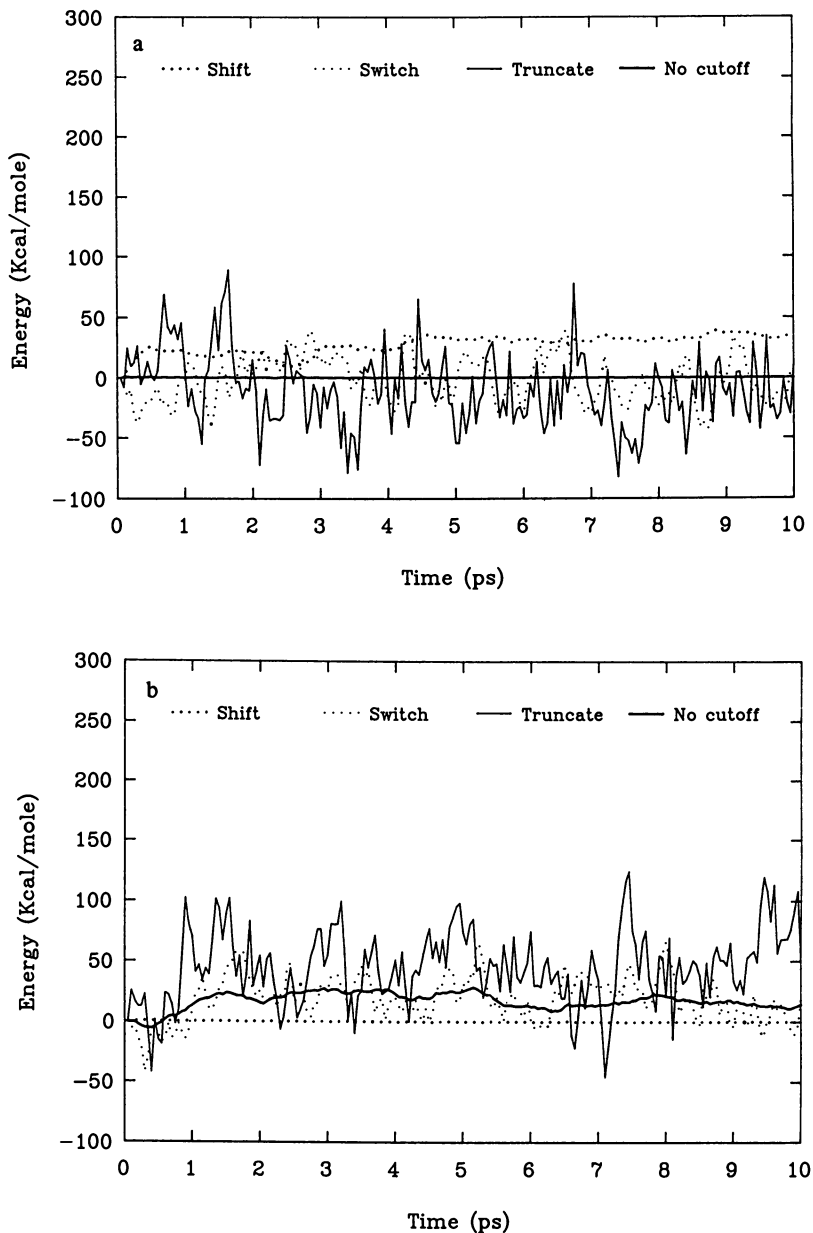


Figure 4. Potential energy of the 7.5 Å cutoff potentials (truncate, shift, switch) and the no cutoff potential on the heating portion of the trajectories of (a) the no cutoff simulation and (b) the 7.5 Å shift simulation. Continued on next page.

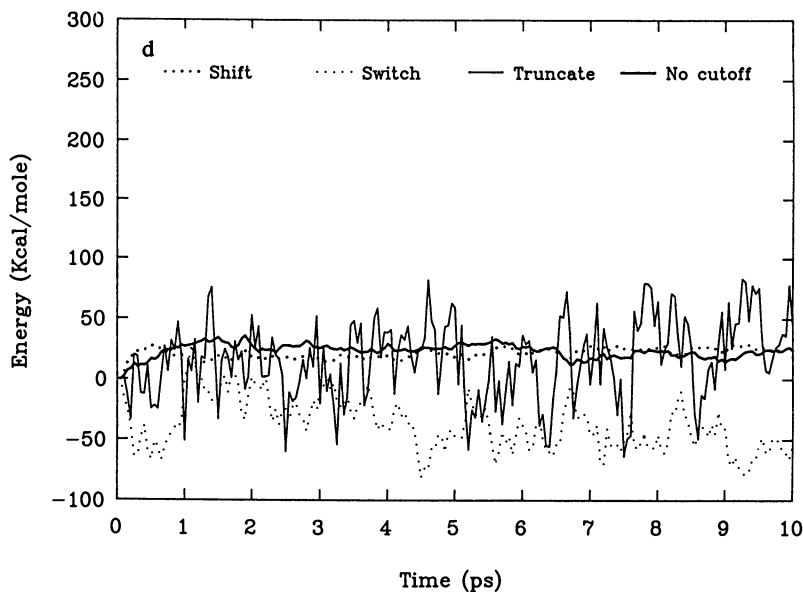
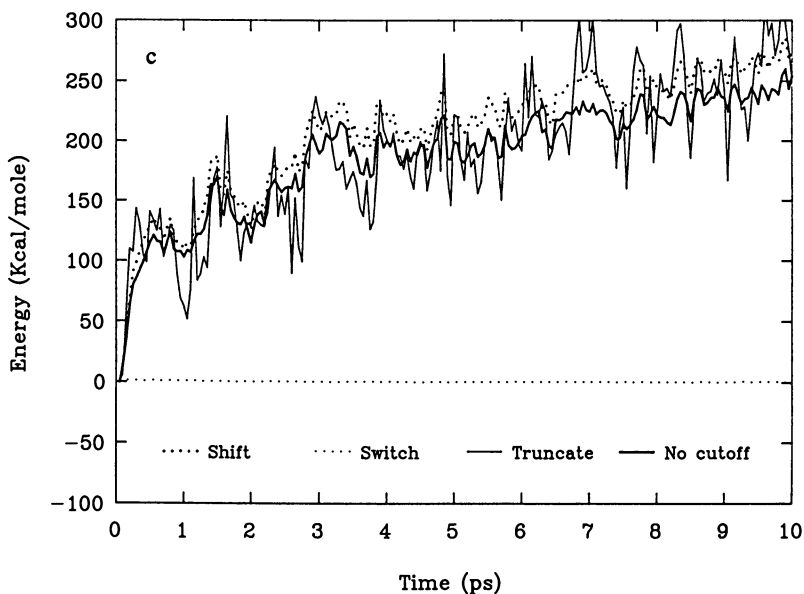


Figure 4.--Continued. Potential energy of the 7.5 Å cutoff potentials (truncate, shift, switch) and the no cutoff potential on the heating portion of the trajectories of (c) the 6.5 to 7.5 Å switching function simulation and (d) the 7.5 Å simple truncation simulation.

proteins (9,22). Though many approaches have been tried with a variety of success, molecular dynamics remains an underutilized tool for these applications primarily because of the cost of performing many millions of iterations of dynamics. With the advent of fast low cost computers, this type of application becomes feasible for a wide variety of systems.

The system chosen for study is a synthetic octapeptide that exhibits the same antigenic behavior as that of a glycoprotein which has been isolated from three established human ductal carcinoma (breast) cell lines (23). The sequence of the octapeptide, GLY-ASN-THR-ILU-VAL-ALA-VAL-GLU, is the same as that of the first eight residues of the glycoprotein. This indicates that the octapeptide contains the antigenic site. A peptide containing only the first seven residues does not elicit a lymphocyte response. This response is potentially important in the efforts to develop a vaccine aimed at the prevention of breast cancer. Obtaining experimental data necessary to determine the structure has been difficult because the peptide is almost insoluble. An understanding of the structure is essential before analogs can be designed. This work specific to this peptide is being carried out in collaboration with Charles A. Hooper and Robert H. Reid of the Walter Reed Army Institute of Research. The results of this work are not presented here and will be published later. The methods presented here will probably be applicable to any peptide or protein section.

Methods. In using molecular dynamics for conformational analysis, there are many possible approaches. Assume that one is able to dedicate a machine for two weeks for this task. For this octapeptide, 70 energy evaluations can be performed each second. This implies that in two weeks, roughly 100 million iterations can be performed. Three distinct approaches could be:

- 1) Generate a few good starting structures and run dynamics on each for many nanoseconds. Analyze the trajectories.
- 2) Generate thousands of trial structures. Minimize, run dynamics, and quench (reminimize) each trial structure. Analyze the final structures.
- 3) Generate millions of structures and minimize each one.

Variations on these include running simulations at a variety of temperatures or running Langevin dynamics with a low friction constant to increase the ability to cross barriers at a given temperature (Pastor, W. R.; Karplus, M., to be published.).

In order to determine the best strategy for conformational analysis using molecular dynamics, a series of simulations were performed. The first set of simulations involved using only two trial structures, an alpha-helix and an extended structure (Nemethy, G., Cornell University, personal communication, 1985) predicted using the ECEPP program (24). The plot of total potential energy as a function of time for simulations carried out at 300K is depicted in Figure 5. The alpha-helical structure, though lower in energy initially, never exhibited a transition to a much lower energy state as did the simulation starting from the ECEPP structure. At 300K the ability to cross barriers is not optimum and the rate at which neighboring wells are explored is not very effective. Figure 6 shows the post transition structure from the simulation from the ECEPP starting structure.

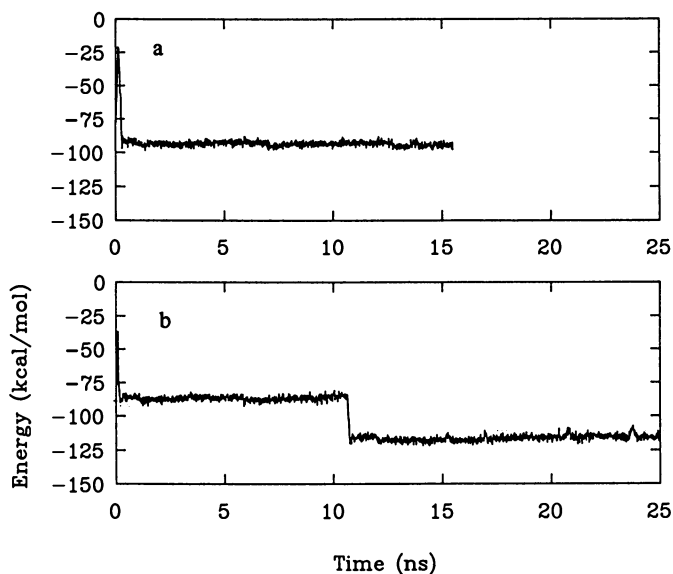


Figure 5. Potential energy as a function of time for the octapeptide simulation at 300K starting from (a) an  $\alpha$ -helix, and (b) from a structure provided by ECEPP.

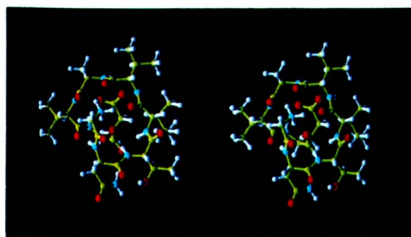


Figure 6. A stereo representation of the "best" minimized structure from the 300K octapeptide simulations.



Figure 7 depicts the time behavior for simulations carried out at 600K except that every saved frame (2.5 picosecond intervals) of the trajectory has been minimized for 2000 steps. The energies have been offset so that the zero energy is the same as the best minimized structure from the previous trajectory. One can see the same transition which took place at 11 nanoseconds at 300K occur at 2.5 nanoseconds at 600K. The structure starting from the alpha-helix had a similar transition at about 1 nanosecond. Since these simulations were carried out at constant temperature, it is possible for the energy to climb considerably in small steps as is seen in the latter portions of the ECEPP run. The distribution of energy states from these simulations are shown in Figure 8.

One drawback of running a single dynamics simulation is that if a large barrier exists between the trial structure and the "true" structure, then it will not be found. The solution to this is to generate many structures and run each for some time. To this end, 1000 random structures were generated by choosing random values for all single bond dihedrals while keeping peptide and other planar groups fixed. These structures were generated without regard to overlapping atoms. All initial random states with high energies had reasonable energies after the initial minimization. From these minimized structures, each was subjected to 5 picoseconds of dynamics at 600K and then quenched with another 2000 steps of minimization. The energy distribution of the 1000 structures are shown in Figure 9. Again the energy values have been offset so

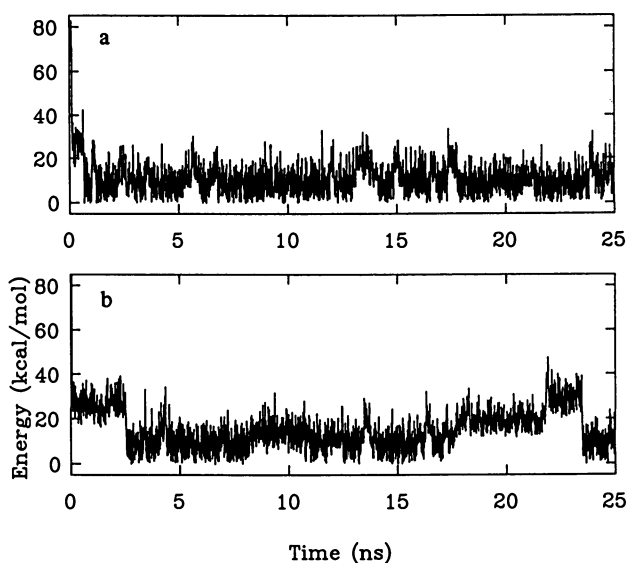


Figure 7. Potential energy of minimized structures as a function of time from the 600K simulations starting from (a) an  $\alpha$ -helix, and (b) the ECEPP structure. Energy values have been offset so that the "best" structure would have a zero value.

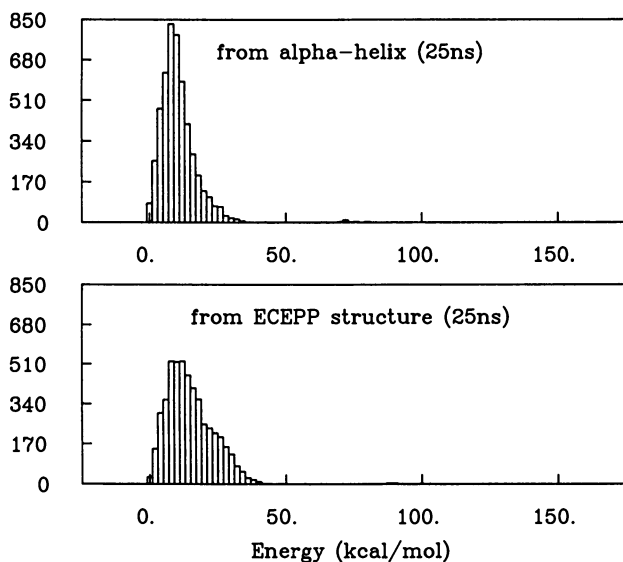


Figure 8. A histogram of the energy distribution of the structures from Figure 7.

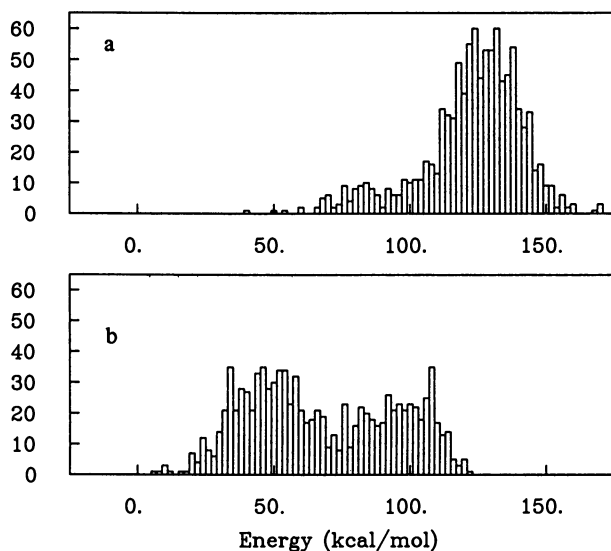


Figure 9. A histogram of the energy distribution of 1000 random structures which have been (a) minimized for 2000 steps, and (b) further subjected to 5 ps of dynamics at 600K and reminimized for 2000 steps.

that the best structure from the first simulation is zero. The results of the minimization from random structures is disappointing. The lowest energy structure found is still 40 kcal/mol above the low energy structures from the previous simulations. After 5 picoseconds, the picture is much better. Several structures are within a few kcal/mol of the "best" structure, but it is clear that only 5 picoseconds is much too short for what is needed here.

Conclusions. Based on the results here, it appears that 600K is sufficient to climb in and out of many wells, but simulations only do a reasonable job of exploration on the nanosecond timescale even for small systems. For large systems such as entire proteins, it will take much longer. Thus the most robust choice appears to be between methods (1) and (2) above such as; Generate 100 trial structures, minimize, run dynamics on each structure for one nanosecond, and analyze the resulting trajectories. Current work is progressing along these lines. This method can be used in conjunction with other methods such as monte-carlo searching algorithms for generating trial structures.

#### Literature Cited

1. Karplus, M.; McCammon, J. A. Scientific Am. 1986, 254, 42.
2. Levitt, M. J. Mol. Biol. 1983, 168, 621.
3. Henry, E. R.; Eaton, W. A.; Hochstrasser, R. M. Proc. Natl. Acad. Sci. 1986, 83, 8982.
4. Jorgensen, W. L.; Gai, J. J. J. Chem. Phys. 1986, 90, 2174.
5. Nilsson, L.; Clore, G. M.; Gronenborn, A. M.; Brunger, A. T.; Karplus, M. J. Mol. Biol. 1986, 188, 455.
6. Bash, P. A.; Singh, U. C.; Brown, F. K.; Langridge, R.; Kollman, P. A. Science 1987, 235, 574.
7. Mezei, M.; Beveridge, D. L. Ann. N. Y. Acad. Sci. 1986, 482, 1.
8. Lybrand, T. P.; Ghosh, I.; McCammon, J. A. J. Am. Chem. Soc. 1985, 107, 7793.
9. Fine, R.; Wang, H.; Schenkin, P. S.; Yarmish, D. L.; Levinthal, C. Proteins 1987, 1.
10. Paine, G. H.; Scheraga, H. A. Biopolymers 1985, 24, 1391.
11. Noguti, T.; Go, N. Biopolymers 1985, 24, 527.
12. Brunger, A. T.; Kuriyan, J.; Karplus, M. Science 1987, 235, 456.
13. Levinthal, C.; Fine, R.; Dimmler, G. In Molecular Dynamics and Protein Structure; Hermans, J., Ed.; Polycrystal Book Service: Western Springs, IL, 1984; p 126.
14. Brooks, B. R.; Bruccoleri, R. E.; Olafson, B. D.; States, D. J.; Swaminathan, S.; Karplus, M. J. Comp. Chem. 1983, 4, 187.
15. Weiner, P.; Kollman, P. J. Comp. Chem. 1981, 2, 287.
16. Brooks, C. L. III; Brunger, A. T.; Karplus, M. Biopolymers 1985, 24, 843.
17. Brooks, C. L. III; Pettitt, B. M.; Karplus, M. J. Chem. Phys. 1985, 18, 2767.
18. Berendsen, H. J. C.; Postma, J. P. M.; Van Gunsteren, W. F.; DiNola, A.; Haak, J. R. J. Chem. Phys. 1984, 81, 3684.
19. Kuriyan, J.; Wilz, S.; Karplus, M.; Petsko, G. J. Mol. Biol. 1986, 192, 133.
20. Reiher, W. E. Ph.D. Thesis, Harvard University, Cambridge, 1985.

21. Purisima, E. O.; Scheraga, H. A. Proc. Natl. Acad. Sci. 1986, 83, 2782.
22. Bruccoleri, R. E.; Karplus, M. Macromolecules 1985, 18, 2767.
23. Reid, R. H.; Hooper, C. A.; Richards, R. L.; Alving, C. R.; Seid, R. C. In PEPTIDES: Structure and Function; Deber, C. M.; Hruby, V. J.; Kopple, K. D., Eds.; Proc. Ninth Am. Peptide Symp.; Pierce Chem. Co., 1985; p 43.
24. Scheraga, H. A. Quantum Chemistry Program Exchange No. 454, 1982.

RECEIVED July 6, 1987

## Chapter 9

# Quantum Mechanical Simulations of Polymers for Molecular Electronics and Photonics

M. Dupuis, H. O. Villar, and E. Clementi

Scientific and Engineering Computations, Department 48B-MS428, IBM Corporation,  
Kingston, NY 12401

*Ab initio* quantum mechanical studies can play an important role in obtaining a detailed understanding of the electronic structure of existing materials, and in predicting the properties of new ones. In this article we give a general outline of our research activity in two areas dealing with new materials, specifically, conducting polymers and polymers with non-linear optical properties. We present the strategy followed for the study of these molecular systems, and an overview of our findings concerning the structure of the prototypical conducting polymer, i.e. pure and doped polyacetylene (PA). We focused our attention on vibrational spectra and infrared and Raman intensities. The results of self-consistent-field (SCF) calculations on charged soliton-like molecules are consistent with experimental observation. In particular we show that the theoretically established accidental mutual exclusion of infrared and Raman bands invalidates the requirement formulated on the basis of the interpretation of experimental data, that defects in PA must have local  $C_{2h}$  symmetry. These conclusions are derived from extensive calculations for which supercomputer performance was imperative and carried out on the parallel supercomputer assembled at IBM-Kingston as a loosely coupled array of processors (LCAP). We briefly describe this computer system which has proven to be ideally suited to the methods of *ab initio* quantum chemistry.

“Advanced materials, specialty polymers, ceramics are the absolute core to advanced technologies of the future”. This one statement taken from a Wall Street Journal article entitled ‘Frontiers of Science’<sup>(1)</sup> indicates clearly that materials research is at the forefront of science. In fact the same feeling emerges when considering several recently published overview articles on developments in the field of new materials. The October 1986 issue of Scientific American<sup>(2)</sup> was fully devoted to this technological area under the heading ‘Materials for Economic Growth.’ A few weeks earlier the feature article in Chemical & Engineering News presented ‘The Organic Solid State’<sup>(3)</sup>, specifically dealing with organic super and semi-conductors. Finally, the National Science Foundation’s report on “Opportunities in Chemistry”<sup>(4)</sup> published in 1985 underlined the key role to be played by chemists in understanding materials and designing new ones. From these articles the reader gets the idea that materials research requires a multidisciplinary effort

0097-6156/87/0353-0146\$06.00/0  
© 1987 American Chemical Society

involving experimental and theoretical chemists, physicists, material scientists, and electrical engineers. In this article we are concerned with the possible role and impact of quantum mechanical simulations on the study of new materials.

As the result of new methodological developments and growing access to supercomputers, theoretical physicists and chemists are in a position to contribute extensively to this research. The present state of methods of theoretical physics is such that it is possible to go beyond idealized models and to examine real materials<sup>(9)</sup>. These studies provide a detailed understanding of structural and electronic properties of solids and may lead to the design of new materials with specific properties. The methods of theoretical chemistry have also evolved tremendously in recent years. Molecular self-consistent-field (SCF) methods are routinely applied to systems with 50 to 100 atoms<sup>(6)</sup>, sometimes more. The information available is no longer restricted to energies. Forces acting on atoms in molecules are readily calculated, leading to optimized molecular structures and vibrational spectra<sup>(7-9)</sup>. The study presented below takes full advantage of these capabilities. The ability to treat very large systems at this level of theory opens new avenues of theoretical research on new materials. We must remark, however, that the key to accurate quantitative prediction resides in new developments aimed at treating the electron-electron correlation effects in large systems. This problem has only started to be addressed and, without any doubt, will require supercomputers. Finally we note that extensions of molecular methods of chemistry to describe 1D- and 3D-periodical systems<sup>(10,11)</sup> have been available for some time, but their computational requirements are such that supercomputer performance is required to extend their domain of application.

We have initiated a research program to study the electronic structure of conducting polymers and materials with non-linear optical properties. As such, these studies of molecular electronics and photonics are only the first step in a global simulation of these materials in the spirit of the approach described by Lie and Clementi (Lie, G. C.; Clementi, E.; this volume.). The two prototype molecular systems often considered in these two areas are polyacetylene (PA) and polydiacetylene (PDA)<sup>(12-14)</sup>. Polyacetylene is the simplest polymer insulator in its pure state and conductor in a doped state. The electronic structure of the defects in the doped state and of the charge carriers is of great importance and the subject of considerable research<sup>(12-14)</sup>. Findings related to this prototype system are critical and should provide a detailed understanding of conductivity in this recently discovered class of polymers. In the following sections we will give an overview of the results obtained so far in our research.

Polydiacetylenes are molecular systems which display the strongest non-linear optical properties<sup>(12)</sup>. These molecules are known to undergo a conformational (rod to coil) transition which is responsible for a change in non-linear response related to the second-order hyperpolarizability  $\gamma$ . Our contribution to this field of research relies on our ability to calculate such electronic properties as polarizability and first and second hyperpolarizabilities which are responsible for the non-linear response of the molecules to incident light. The computational task is much more complex than getting the energy alone, since the first- and second-order response of the electronic wavefunction to the perturbation (here an incident radiation) must be determined<sup>(13)</sup>. A likely technical implication of determining these properties accurately may be that a larger 'basis set' than otherwise used will be needed. The difficulty is also compounded by the size of the molecular systems for which these properties are of interest. It is very noticeable that the systems with non-linear optical characteristics are most often large, even very large by today's computational standards. The calculation of these properties is therefore a challenge in itself for which access to a supercomputer is imperative. Programs for the calculation of these properties are under development in our laboratory.

In section II of this paper we outline the computational strategy that we have used successfully to study the electronic structure of defects in doped PA,

**American Chemical Society  
Library**

1155 16th St., N.W.  
Washington, D.C. 20036

and which has general applicability for the study of electronic structure and reactivity of molecular clusters, in catalysis for example. In section III we describe the physical problem associated with doped PA, mainly the identification of the electronic structure of defects. The combined use of equilibrium structure determination and vibrational spectra calculation, including infrared and Raman absorption intensities, has given a quantitative basis to some experimental observations. We interpreted these results as providing strong evidence for the identification of charged solitons as defects in PA. In section IV we turn our attention briefly to what distinguishes this work from most other research, beyond the content of the scientific problem discussed: the calculations were performed on the experimental parallel supercomputer (LCAP) assembled in our laboratory which has proven very powerful for many scientific and engineering applications.

### COMPUTATIONAL METHODOLOGY

The starting point for all of our research in electronic structure theory is the Hartree-Fock (HF) or self-consistent-field (SCF) method for the solution of the molecular electronic Schrödinger equation<sup>(16)</sup>. The total wavefunction of the molecular system is expressed as an antisymmetrized product (Slater determinant) of molecular orbitals, each orbital being a linear combination of basis functions (also called atomic orbitals) assigned to the atomic centers. The total energy of the molecule is a function of the position of the nuclei  $R$ ,  $E(R)$ . The molecular orbitals are determined by solving the HF equations, which take into account explicitly the electrostatic effects among the electrons, including the electron-electron repulsion. The molecular energy depends on the basis set used to expand the molecular orbitals. The more extended the basis set, the more accurate the description of the molecular system, but the more time consuming the calculation. Note that in this formalism each electron feels the average potential created by the other electrons. Electron correlation is what makes up a more realistic picture of the electron interaction where each electron feels an instantaneous potential created by the other electrons. Electron correlation is a key ingredient for quantitatively accurate molecular calculations. As mentioned earlier methods to treat electron correlation in large molecular systems are seldom used owing to their very high computer time requirements.

In recent years, methods to calculate efficiently, the forces acting on atoms in molecules have been developed: the calculation of energy gradients  $\partial E/\partial R$  and second derivatives  $\partial^2 E/\partial R^2$  are routinely carried out even for large systems<sup>(7)</sup>. Sometimes the second derivative matrix is obtained by finite difference of the energy gradients. The second derivative matrix is just what is needed for a vibrational analysis carried out in the harmonic approximation. From first principles then, without empirical parameters, it is possible to obtain the complete set of vibrational frequencies and normal modes. It is now well established that the vibrational frequencies obtained at the SCF level of theory are 10 to 20% too high compared to the observed frequencies<sup>(8,9)</sup>. With the availability of the normal modes expressed in the cartesian coordinate space or in the internal coordinate space, it is easy to move further toward a more complete representation of the vibrational spectra by calculating the infrared and Raman intensities of the vibrational modes. These quantities are obtained by calculating the derivatives of the molecular dipole moment and polarizability with respect to the cartesian coordinates followed by a transformation to derivatives with respect to the normal modes. An elegant and inexpensive method has been proposed by Komornicki and McIver<sup>(12)</sup> which involves calculating the energy gradients in the presence of a small uniform field. It is based on the simple relationship  $\partial\mu/\partial R = \partial(-\partial E/\partial F)/\partial R = -\partial(\partial E/\partial R)/\partial F$  where  $F$  represents the electric field.

The importance of getting a complete semi-quantitative vibrational spectrum can not be over emphasized. In the study presented below we made use of

all of these computational techniques. The availability of the infrared and Raman intensities was the key to suggesting that charged solitons and not bipolarons are a better description of defects in doped PA.

The SCF method for molecules has been extended into the Crystal Orbital (CO) method for systems with 1D- or 3D- translational periodicity<sup>(10,11)</sup>. The CO method is in fact the band theory method of solid state theory applied in the spirit of molecular orbital methods. It is used to obtain the band structure as a means to explain the conductivity in these materials, and we have done so in our study of polyacetylene. There are however some difficulties associated with the use of the CO method to describe impurities or defects in polymers. The periodicity assumed in the CO formalism implies that impurities have the same periodicity. Thus the unit cell on which the translational periodicity is applied must be chosen carefully in such a way that the repeating impurities do not interact. In general this requirement implies that the unit cell be very large, a feature which results in extremely demanding computations and thus hinders the use of the CO method for the study of impurities.

In the limit of very large clusters of repeating units in one dimension, a molecular system will behave as an infinite chain. The number of units needed to reach this limiting behavior will vary from system to system depending on the short or long range character of the interaction between units. When simulating infinite systems with finite clusters, it is necessary to check the convergence of the properties of interest as a function of the size of the cluster in order to establish some degree of confidence. We have used this approach in our investigation of polyacetylene, where we have compared the band structure calculated for increasingly large clusters with the band structure of an infinite polymer. Other parameters used to gauge the convergence behavior in finite cluster calculations are geometry, atomic charges for example. To study defects or impurities we increase the size of the molecular cluster in which the defect is simulated and again select some criteria to gauge the convergence of the description of the defect. These criteria may be geometrical parameters if we deal with optimized geometries for each cluster size, and/or any properties related to the electron density. In our study of polyacetylene we have used geometrical parameters, atomic charges, and bond indices to characterize charged soliton and bipolaron models by comparison with isolated PA clusters.

#### ELECTRONIC STRUCTURE OF DEFECTS IN PA

Frequent attention has been given to polyacetylene PA for the study of charge carriers in conducting polymers<sup>(14)</sup>. Because of its simplicity PA is amenable to both experimental and theoretical research. It is now well accepted that in its undoped state trans PA displays CC bond length alternation of 0.08 Å (the C-C single bond length is 1.44 Å, the C=C double bond length is 1.36 Å). In a doped state PA conducts electricity. The charge carrier models most often discussed are neutral solitons, positively and negatively charged solitons, polarons and bipolarons. The charged soliton picture led apparently to a successful modeling of the experimental vibrational spectrum of doped PA<sup>(15)</sup>. Recently on the basis of the work of Campbell et al.<sup>(12)</sup> and of Boudreaux et al.<sup>(20)</sup> the idea of bipolarons has gained acceptance<sup>(13)</sup>. One key element in the situation is the experimentally deduced mutual exclusion of the infrared active and Raman active absorption lines. Such a mutual exclusion implies a defect with local symmetry belonging to the  $C_{2h}$  point group, to which bipolaron models belong, thus favoring the bipolaron picture of defects in PA<sup>(21)</sup>.

Previous theoretical studies of isolated and doped PA have mostly dealt with geometrical structures and charge and spin waves<sup>(20)</sup>. A few have dealt with the vibrational spectrum<sup>(21-23)</sup> using force fields derived from fits to experimental infrared and Raman spectra of smaller polyenes or from scaled force constants obtained from semi-empirical SCF calculations on these systems. Very little the-



oretical work has been done on IR and Raman intensities of isolated PA<sup>(22)</sup> and, to our knowledge, no intensity studies on models for doped PA have been published. This work is the first to combine structure and vibrational spectrum determination, including calculation of IR and Raman intensities, for relatively large polyenes at the *ab initio* level of theory. This approach has led to a consistent picture of these molecular systems, and has made it possible to provide a theoretical quantitative basis to the question of mutual exclusion of IR and Raman lines in doped PA. We found that the cations (with  $C_{2v}$  symmetry) used as models for charged solitons show an accidental mutual exclusion of IR and Raman bands. This result would indicate that the requirement that doped PA have local  $C_{2h}$  symmetry in the region of the defect may not be necessary. Further the calculated spectra for the various models show better overall agreement with experiment in the case of cations as models for charged solitons.

We have used the systems  $C_nH_{n+2}$  with  $n=2,4,\dots,22$ ,  $C_nH_{n+2}^+$  with  $n=3,5,\dots,21$ , and  $C_nH_{n+2}^{+2}$  with  $n=4,6,\dots,22$  to represent pure PA, positively charged solitons, and bipolarons respectively. SCF wavefunctions were calculated with a double-zeta quality basis set (denoted 6-31G)<sup>(23)</sup> and optimized geometries for all these systems were determined. In addition for the molecules with  $n$  up to 11 or 12 we calculated the vibrational spectrum, including infrared and Raman intensities.

**ISOLATED PA MODEL.** The calculated structures of the neutral clusters with  $n=22$  display bond alternation. The central unit in  $C_{22}H_{24}$  is characterized by  $R(C-C) = 1.452 \text{ \AA}$ ,  $R(C=C) = 1.337 \text{ \AA}$ , the  $C-C=C$  angle is 124.2 degrees, and the  $H-C=C$  angle 119.2 degrees. The agreement with the experimental bond lengths is very good. The convergence of the  $\pi$  orbital energies with the cluster size can be seen in Figure 1 where the  $\pi$  band edges are shown. The right hand side points are the result of a CO calculation on an infinite polymer using the same basis set and indicate convergence of the electronic properties of the polyenes with increasing chain length. The band gap deduced from the CO calculation is 6.8 eV which is rather far from the accepted experimental value of 1.5 eV. Most of the difference can be attributed to the electron-electron correlation effects which are not accounted for in the SCF formalism. This result underscores the need to go beyond the present level of theory for quantitative prediction. Experimentally three IR active and four Raman active vibrations have been observed in undoped PA. For the neutral clusters up to  $n=12$  we have identified the vibrational modes which best correspond to these bands. The frequencies calculated for  $C_{12}H_{14}$  are presented in Table I.

**Table I.** Experimental frequencies of PA and corresponding calculated frequencies of the  $C_{12}H_{14}$  cluster

Expt. (CH) $_n$	Expt. (CD) $_n$	Calc. ( $C_{12}H_{14}$ )	Calc. ( $C_{12}D_{14}$ )	Activity	Description
3013 (m)	2231	3331	2477	IR	C-H stretch
1474 (s)	1357	1873	1822	Raman	C=C stretch
1292 (vw)	916	1466	991	IR	CH bend
1291 (vww)	1200	1465	1003	Raman	CH bend
1080 (s)	855	1322	1261	Raman	C-C stretch
1016 (w)	745	1081	873	Raman	out of plane bend
1015 (vs)	752	1175	857	IR	out of plane bend

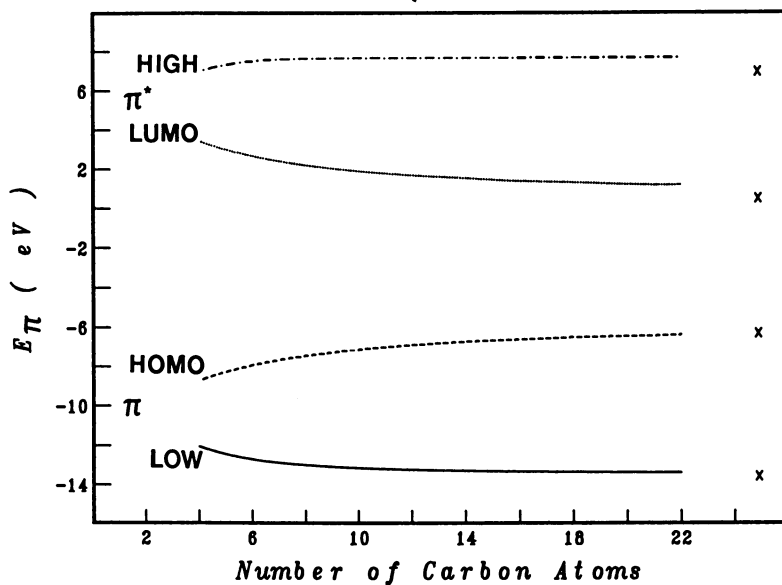


Figure 1.  $\pi$  band edges for neutral  $C_nH_{n+2}$ . The right hand side points correspond to an infinite polymer  $(CH)_n$ .

The frequencies and relative intensities for the clusters  $n=6$  to  $n=12$  are given in Table II. As mentioned earlier, the calculated frequencies are 10 to 20 % too high. The corresponding vibrational modes have the character of PA vibrations in so far as the atoms which vibrate most are in the central region of the cluster.

**Table II.** IR active frequencies and relative intensities

Description	C <sub>6</sub> H <sub>8</sub>	C <sub>8</sub> H <sub>10</sub>	C <sub>10</sub> H <sub>12</sub>	C <sub>12</sub> H <sub>14</sub>
CH <sub>2</sub> asym. stretch	3415 (0.83)	3415 (0.51)	3415 (0.38)	3415 (0.30)
CH stretch	3334 (0.71)	3333 (0.75)	3333 (0.88)	3333 (0.65)
CH stretch	3327 (0.66)	3329 (0.54)	3330 (0.42)	3331 (0.72)
CH out-of-plane	1177 (1.00)	1176 (1.00)	1176 (1.00)	1175 (1.00)
CH <sub>2</sub> out-of-plane	1124 (2.40)	1135 (1.12)	1145 (0.67)	1151 (0.47)
	1087 (0.63)	1097 (0.79)	1105 (0.71)	1113 (0.54)

For each molecular cluster we have chosen the mode with frequency near 1175 cm<sup>-1</sup> (CH out-of-plane bend) as the reference mode for IR intensity analysis. The mode with highest frequency shown in Table II is the antisymmetric stretch of the terminal CH<sub>2</sub> groups. With increasing cluster length its intensity diminishes. The nearly degenerate modes with frequencies close to 3330 cm<sup>-1</sup> do not show a well defined pattern but appear to maintain a significant intensity. The mode with frequency 3333 cm<sup>-1</sup> in C<sub>12</sub>H<sub>14</sub> involves terminal CH stretches, the mode with frequency 3331 cm<sup>-1</sup> involves the bulk CH stretches. This latter mode arises from in phase CH stretches shown in Figure 2 which create a molecular dipole responsible for the absorption. The mode with frequency near 1175 cm<sup>-1</sup>, also displayed in Figure 2 corresponds to in phase out-of-plane CH bends. All the H atoms are displaced out of the molecular plane on the same side. The molecular dipole thus created gives rise to the strongest absorption. The trends in intensity demonstrated by these calculations are in accord with experimental observation. The intensities of the bands have been analyzed by Zannoni and Zerbi<sup>(2)</sup> in terms of charge flux. These authors point out that the CH stretching mode absorbs parallel polarized light as well as perpendicular polarized light, while the CH out-of-plane bend shows a strong preference for perpendicular polarized light. For the mode at 3331 cm<sup>-1</sup> we have obtained:

$$\left[ \frac{\partial \mu}{\partial q} \right]_{//}^{3331} = 1.107 \quad \left[ \frac{\partial \mu}{\partial q} \right]_{\perp}^{3331} = 1.415$$

in units of (D/Å) amu<sup>-1/2</sup>. These results lend quantitative significance to the experimental observation.

**DOPE PA MODELS.** We selected two criteria to characterize the structure of the mono- and di-cations. The wavefunctions of the cations at their respective optimized geometries were used to determine Mayer's bond indices which reflect the strength of the interatomic bonds. The differences in the cations and also the neutral molecule emerge very clearly from Table III.

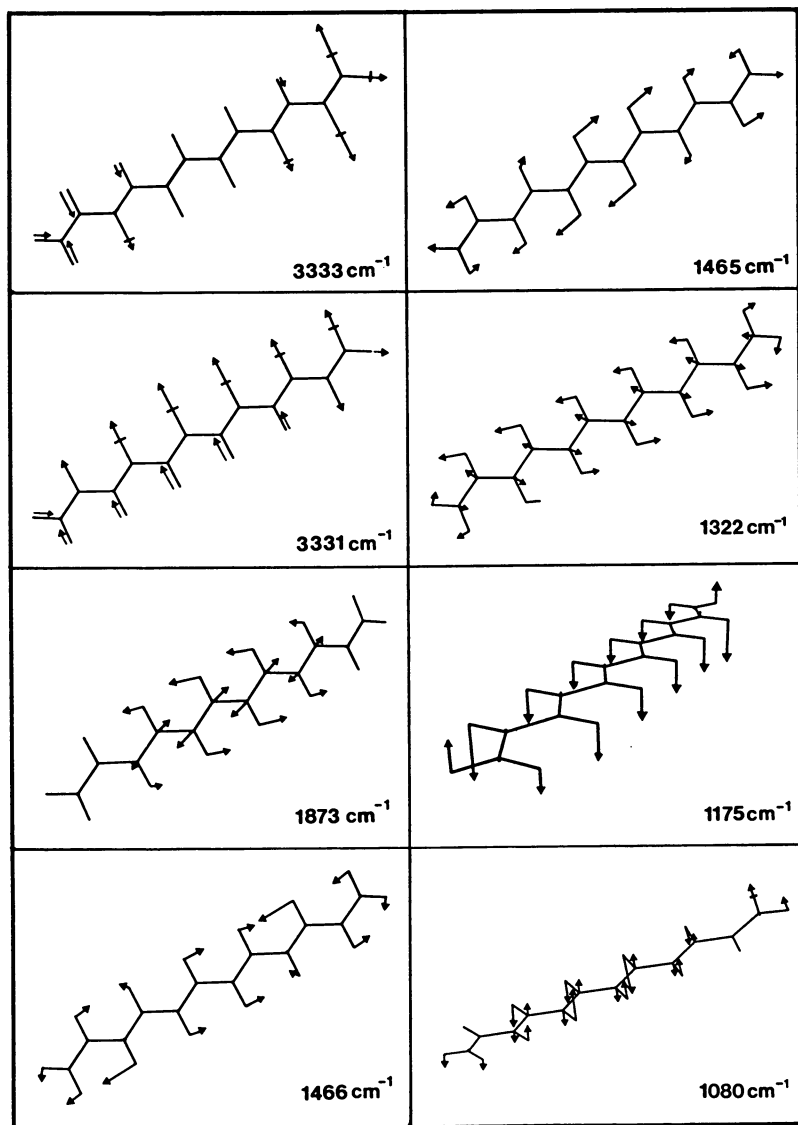


**Figure 2.** Selected infrared and Raman active vibrational modes of C<sub>12</sub>H<sub>14</sub>.

**Table III.** Interatomic CC distances (in angstroms) and Bond Indices for  $C_{22}H_{24}$ ,  $C_{21}H_{23}^+$ ,  $C_{22}H_{24}^{+2}$ . C1 labels the center carbon atom, C11 the terminal carbon atom

		$C_{22}H_{24}$		$C_{21}H_{23}^+$		$C_{22}H_{24}^{+2}$	
		distance	bond index	distance	bond index	distance	bond index
C1	C1'	1.338	1.762	---	---	1.449	1.095
C1	C2	1.450	1.082	1.396	1.332	1.342	1.719
C2	C3	1.338	1.762	1.379	1.442	1.443	1.113
C3	C4	1.450	1.082	1.413	1.238	1.351	1.638
C4	C5	1.338	1.764	1.364	1.552	1.426	1.178
C5	C6	1.451	1.080	1.428	1.166	1.370	1.488
C6	C7	1.337	1.768	1.353	1.646	1.398	1.305
C7	C8	1.453	1.077	1.439	1.117	1.498	1.307
C8	C9	1.337	1.784	1.344	1.726	1.369	1.493
C9	C10	1.458	1.066	1.452	1.078	1.435	1.144
C10	C11	1.329	1.856	1.332	1.832	1.338	1.725

The CC bond lengths follow very closely the variations in the bond indices.  $C_{21}H_{23}^+$ , the charged soliton-like molecule, displays a single defect site at the center of the molecule, and gradually recovers the bond alternation pattern seen in the neutral species.  $C_{22}H_{24}^{+2}$ , the bipolaron-like molecule, has a split defect with bond alternation observed in the middle. These results are in qualitative agreement with the semi-empirical calculations of Boudreaux et al<sup>(20)</sup>. A small difference is obtained in the extend of the defect which extends over 15 carbon atoms in our work, but only 11 carbon atoms in their work. Our results ought to be considered more reliable on the basis of the higher level of theory used here. At the SCF level of theory we found that for  $n > 6$  the band gap of the cation is smaller than for the dication, which in turn is smaller than for the neutral. The calculated band gap for  $C_{21}H_{23}^+$  is 5.8 eV, for  $C_{22}H_{24}^{+2}$  it is 6.4 eV to be compared with 7.2 eV for the neutral system  $C_{22}H_{24}$ . However, we note that the largest dication cluster may be too small to predict accurately the behavior of bipolarons.

The experimental spectrum of doped PA (p-doped and n-doped) shows two IR active modes at 1397 and 888  $cm^{-1}$  which are also active in deuterated doped PA at 1120 and 780  $cm^{-1}$ . The active modes for the mono-cation and dication series are given in Tables IV and V. The active modes of  $C_{11}H_{13}^+$  with frequency of 1656 and 1271  $cm^{-1}$  are shown in Figure 3. They are in plane vibrational modes involving CC stretches mixed with CH bends. For the deuterated cations, one intense mode appears at 1518  $cm^{-1}$ , and a second mode at 990  $cm^{-1}$  seems to gain in intensity as the cluster becomes larger. The spectra of the dications are more complicated. The most intense mode is associated with the stretching of the CC bonds near the two charged sites which comprises the defect. The corresponding deuterated spectra show only one band at 1562  $cm^{-1}$ . The modes of  $C_{12}H_{14}^{+2}$  are shown in Figure 4. There is no indication of the appearance of a second band with low frequency.

The trends in the spectra of the dications are not in as satisfactory an agreement with experiment as the trends observed in the cation spectra. We note, however, that  $C_{11}H_{13}^+$  may be a better representation of charged solitons than

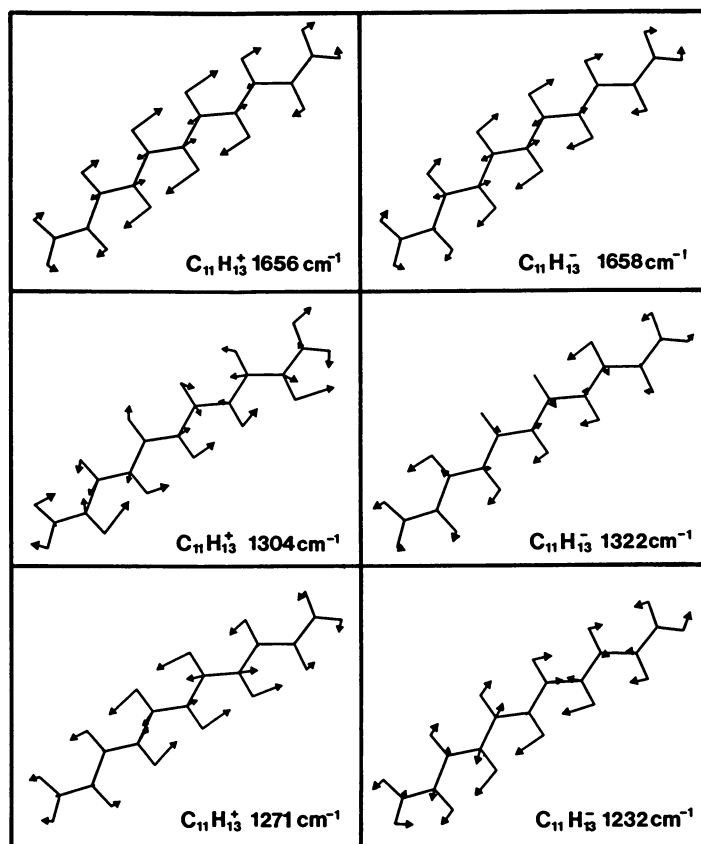


**Figure 3.** Selected infrared and Raman active vibrational modes of  $C_{11}H_{13}^+$  and of  $C_{11}H_{13}^-$ .

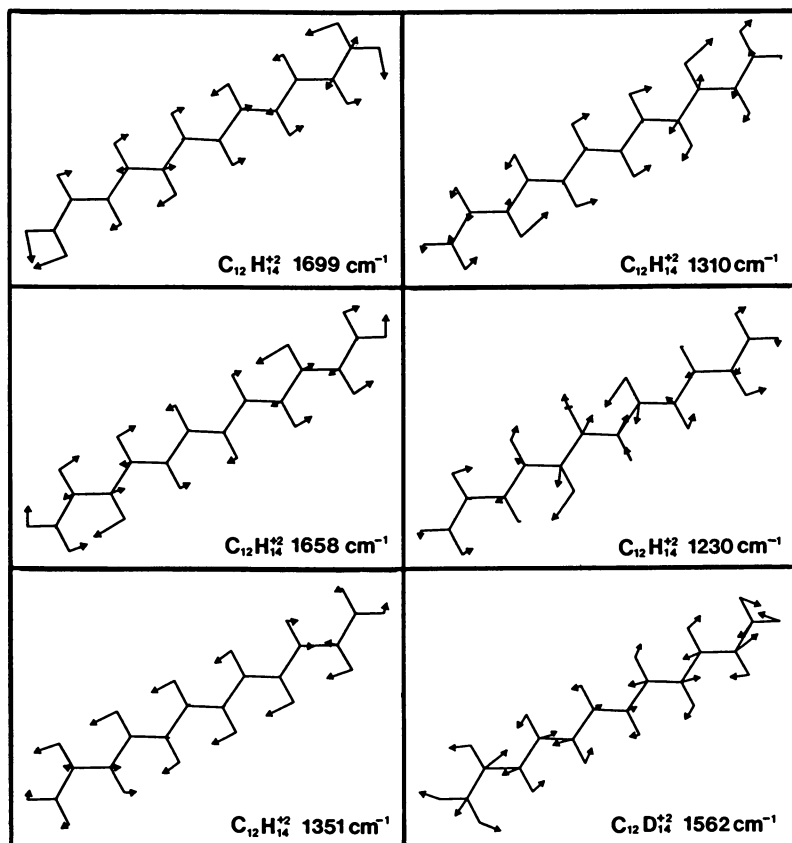


**Figure 4.** Selected infrared and Raman active vibrational modes of  $C_{12}H_{14}^{+2}$ .

$C_{12}H_{14}^{+2}$  of bipolarons from consideration of the cluster size. Further calculations of the spectrum of larger clusters are needed to substantiate the conclusions derived from the present study.

**Table IV.** Calculated vibrational frequencies and IR intensities for the  $C_5H_7^+$  to  $C_{11}H_{13}^+$ . The frequencies are given in  $cm^{-1}$  and the intensities are relative to the most intense mode for each molecule. The types represent the following vibrations : SCI = CH<sub>2</sub> in plane bend , CCS = Carbon carbon stretching, CHB = CH in plane bend

		$C_{11}H_{13}^+$		$C_{11}D_{13}^+$	
MODE	TYPE	FREQ.	INT.	FREQ.	INT.
B <sub>2</sub>	CHB	1271	0.84	990	0.10
B <sub>2</sub>	CCS	1304	0.10	1302	0.01
B <sub>2</sub>	CCS	1656	1.00	1518	1.00
		$C_9H_{11}^+$		$C_9D_{11}^+$	
MODE	TYPE	FREQ.	INT.	FREQ.	INT.
B <sub>2</sub>	CCS	1304	0.19	1295	0.00
B <sub>2</sub>	CHB	1328	0.49	1003	0.08
B <sub>2</sub>	CCS	1690	1.00	1582	1.00
		$C_7H_9^+$		$C_7D_9^+$	
MODE	TYPE	FREQ.	INT.	FREQ.	INT.
B <sub>2</sub>	CHB	1359	0.52	1014	0.06
B <sub>2</sub>	CCS	1713	1.00	1619	1.00
		$C_5H_7^+$		$C_5D_7^+$	
MODE	TYPE	FREQ.	INT.	FREQ.	INT.
B <sub>2</sub>	CHB	1366	0.46	1032	0.05
B <sub>2</sub>	CCS	1435	0.14	1471	0.03
B <sub>2</sub>	SCI	1673	0.36	1200	0.00
B <sub>2</sub>	CCS	1745	1.00	1642	1.00

As indicated earlier, the mutual exclusion of IR and Raman absorption lines deduced from experimental data appears to be an important factor in the acceptance of a bipolaron description of defects in PA. Using the elegant method of Komornicki and McIver, we decided to calculate the Raman intensities for  $C_{11}H_{13}^+$  and for  $C_{12}H_{14}^{+2}$ . Note that the symmetry point group of the dication is  $C_{2h}$ , which implies mutual exclusion of the IR and Raman lines on the basis of symmetry group theoretical arguments. The point group of the monocation is  $C_{2v}$  for which mutual exclusion does not hold.

The data given in Table VI show that the IR active modes of the monocation have weak Raman intensity and vice versa. Thus a de facto mutual exclusion holds for the monocation. This finding constitutes a key factor in the defect characterization as it implies that the requirement of centrosymmetrical defect (i.e. with  $C_{2h}$  symmetry) is not necessary. Rather it establishes clearly that defects with  $C_{2v}$  symmetry are plausible. Further work to substantiate this finding is in progress.



**Table V.** Calculated vibrational frequencies and IR intensities for the  $C_4H_6^{+2}$  to  $C_{12}H_{14}^{+2}$  clusters. The frequencies are given in  $cm^{-1}$  and the intensities are relative to the most intense mode for each molecule. The types represent the following vibrations: CCS = carbon carbon stretching, CHB = CH in plane bend, SCI = CH<sub>2</sub> in plane bend

		$C_{12}H_{14}^{+2}$		$C_{12}D_{14}^{+2}$	
MODE	TYPE	FREQ.	INT.	FREQ.	INT.
$B_u$	CCS	1230	0.25	1268	0.03
$B_u$	CHB	1311	0.89	1020	0.06
$B_u$	CHB	1351	0.40	1017	0.04
$B_u$	CCS	1658	1.00	1505	0.11
$B_u$	CCS	1700	0.96	1562	1.00
		$C_{10}H_{12}^{+2}$		$C_{10}D_{12}^{+2}$	
MODE	TYPE	FREQ.	INT.	FREQ.	INT.
$B_u$	CCS	1275	0.53	1278	0.04
$B_u$	CHB	1365	0.36	1015	0.04
$B_u$	CHB	1404	0.25	1036	0.04
$B_u$	CCS	1650	0.45	1186	0.00
$B_u$	CCS	1700	1.00	1571	1.00
		$C_8H_{10}^{+2}$		$C_8D_{10}^{+2}$	
MODE	TYPE	FREQ.	INT.	FREQ.	INT.
$B_u$	CCS	1243	0.20	1262	0.02
$B_u$	CHB	1372	0.39	1026	0.06
$B_u$	CHB	1391	0.26	1466	0.08
$B_u$	CCS	1680	0.13	1193	0.01
$B_u$	CCS	1693	1.00	1587	1.00
		$C_6H_8^{+2}$		$C_6D_8^{+2}$	
MODE	TYPE	FREQ.	INT.	FREQ.	INT.
$B_u$	CCS	1277	0.76	1343	0.26
$B_u$	CHB	1437	0.11	1058	0.19
$B_u$	CCS	1696	1.00	1608	1.00
		$C_4H_6^{+2}$		$C_4D_6^{+2}$	
MODE	TYPE	FREQ.	INT.	FREQ.	INT.
$B_u$	CCS	1122	1.00	1011	1.00
$A_u$	OOP	1153	0.13	851	0.12
$B_u$	CHB	1514	0.07	1262	0.87
$B_u$	SCI	1625	0.05	1165	0.10
$B_u$	CHS	3281	0.14	2384	0.02
$B_u$	CHS	3409	0.23	2449	0.13

**Table VI.** Frequencies and relative intensities of the IR and Raman most intense active modes for  $C_{11}H_{13}^+$  and  $C_{12}H_{14}^{+2}$ 

$C_{11}H_{13}^+$			$C_{11}D_{13}^+$		
Freq. (cm <sup>-1</sup> ) IR	Raman	IR	Freq. (cm <sup>-1</sup> )	Raman	
1271	0.00	0.84	990	0.00	0.10
1304	0.00	0.10	1032	0.04	0.00
1367	0.34	0.02	1346	0.03	0.00
1656	0.01	1.00	1518	0.00	1.00
1796	0.65	0.00	1747	1.00	0.00
1827	1.00	0.00			

$C_{12}H_{14}^{+2}$			$C_{12}D_{14}^{+2}$		
Freq. (cm <sup>-1</sup> ) IR	Raman	IR	Freq. (cm <sup>-1</sup> )	Raman	
1230	---	0.25	1011	0.04	---
1311	---	0.89	1505	---	0.11
1351	---	0.40	1562	---	1.00
1658	---	1.00	1699	0.11	---
1700	---	0.96	1773	1.00	---
1834	1.00	---			

### THE LCAP SUPERCOMPUTER FOR QUANTUM CHEMISTRY

As indicated earlier, the above research was carried out on a parallel supercomputer (LCAP) assembled in the IBM-Kingston laboratory. In this section we will give a brief description of the LCAP systems. The LCAP systems, LCAP1 and LCAP2, have been described in detail elsewhere<sup>6</sup>. For our present purposes a more concise description will suffice.

The initials, LCAP, stand for "loosely coupled array of attached processors" the adjective "loosely" emphasizing the original conception was of a parallel machine best suited to tasks requiring little or no interprocessor communication. LCAP1 and LCAP2 each comprises an IBM 308X host processor, to which are linked 10 FPS-X64 attached processors (APs). The APs are equipped with extensive mathematical subroutine libraries and two matrix accelerator MAX boards, which further increase the speed of simple matrix and vector operations, and are linked to one another by a large shared memory (512 Mbytes), allowing rapid interprocessor communication, including data exchange and message passing. The shared memory reflects movement away from a loosely coupled system, the original LCAP, wherein all data exchange had to be done via the host, towards a more tightly coupled system, although, somewhat incongruously, the initials LCAP have been retained. Conceptually, the shared memory is best regarded like a high speed disk accessible to all the APs, allowing random access, but with no record structure implied. Data in shared memory are independent of data in any AP's main memory. It need hardly be said that the shared memory greatly

extends the range of applications for which the LCAP systems can be used efficiently<sup>6</sup>.

Programming languages for the LCAP systems comprises traditional FORTRAN and FORTRAN-like directives which are interpreted by a precompiler developed in our laboratory. The directives provide syntactical constructs for interprocessor communication and synchronization. A detailed description of the implementation of our quantum chemistry package HONDO<sup>29</sup> has been given elsewhere. (Dupuis, M.; Watts, J. D.; *Theor. Chim. Acta*, in press.) Our experience indicates that the calculations done in the study described above were executed in parallel at a very high level of efficiency.

### CONCLUSIONS

The work described in this paper is an illustration of the potential to be derived from the availability of supercomputers for research in chemistry. The domain of application is the area of new materials which are expected to play a critical role in the future development of molecular electronic and optical devices for information storage and communication. Theoretical simulations of the type presented here lead to detailed understanding of the electronic structure and properties of these systems, information which at times is hard to extract from experimental data or from more approximate theoretical methods. It is clear that the methods of quantum chemistry have reached a point where they constitute tools of semi-quantitative accuracy and have predictive value. Further developments for quantitative accuracy are needed. They involve the application of methods describing electron correlation effects to large molecular systems. The need for supercomputer power to achieve this goal is even more acute.

### LITERATURE CITED

1. Bulkley, W. *Wall Street Journal*, Nov. 10, 1986.
2. Scientific American, *Materials for Economic Growth*, Oct. 1986. See in particular the articles by Chaudhari, P.; "Electronic And Magnetic Materials," by Rowell, J. M.; "Photonic Materials," and by Mayo, J. S.; "Materials for Information and Communication."
3. Cowan, D. O.; Wiygui, F. M. "The Organic Solid State," *Chemical & Engineering News*, July 21, 1986.
4. *Opportunities in Chemistry*, National Academic Press, Washington, D.C., 1985.
5. Cohen, M. *Science*, 1986, **234**, 549.
6. Clementi, E.; Chin, S.; Logan, D. in *Supercomputer Simulations in Chemistry*, Dupuis, M. Ed., Lecture Notes in Chemistry, Springer-Verlag 1986.
7. Pulay, P.; in *Applications of Electronic Structure Theory*, edited by Schaefer, III, H. F. Plenum, New York, 1977.
8. Fogarasi, G.; Pulay, P. *Ann. Rev. Phys. Chem.* 1985, **35**, 191.
9. Hess, Jr.; B. A., Schaad, L. J. *Chem. Rev.* 1986, **86**, 709.
10. Andre, J. M.; Gouverneur, L.; Leroy, G. *Intern. J. Quant. Chem.* 1967, **1**, 427.
11. Del Re, G.; Ladik, J.; Biczko, G. *Phys. Rev.* 1967, **155**, 997.
12. See for example *Electronic Properties of Polymers and Related Compounds*, Kuzmany, H.; Mehring, M.; Roth, S.; Eds., Springer-Verlag, Berlin, 1985.
13. Bredas, J. L.; Street, G. B. *Acc. Chem. Res.* 1985, **18**, 309.
14. Etemad, S.; Heeger, A. J.; MacDiarmid, A. G. *Ann. Rev. Phys. Chem.* 1982, **33**, 443.
15. Dykstra, C. E.; Jasien, P. G. *Chem. Phys. Lett.* 1984, **109**, 388.
16. Roothaan, C. C. J. *Rev. Mod. Phys.* 1951, **23**, 69.
17. Komornicki, A.; McIver, Jr., J.W. *J. Chem. Phys.* 1979, **70**, 2014.

18. Etemad, S.; Pron, A.; Heeger, A. J.; MacDiarmid, A.G. *Phys. Rev. B*, 1981, 23, 5137.
19. Campbell, D. K.; Bishop, A. R.; Fesser, K. *Phys. Rev. B*, 1982, 26, 6862.
20. Boudreaux, D. S.; Chance, R. R.; Bredas, J. L.; Silbey, R. *Phys. Rev. B*, 1981, 28, 6927.
21. Zannoni, G.; Zerbi, G. *Solid State Comm.* 1983, 47, 213.
22. Rakovic, D.; Bozovic, I.; Stepanian, A. A.; Gribov, L. A. *Phys. Rev. B*, 1983, 28, 1997.
23. Peluso, A.; Seel, M.; Ladik, J. *Solid State Comm.* 1985, 53, 893.
24. Hehre, W. J.; Ditchfield, R.; Pople, J. A. *J. Chem. Phys.* 1972, 56, 2257.
25. Dupuis, M.; Rys, J.; King, H. F. *J. Chem. Phys.* 1975, 76, 111.

RECEIVED June 15, 1987

## Chapter 10

# Simulations of Macromolecular Systems

Peter J. Ludovice, Marc G. Davidson, and Ulrich W. Suter

Department of Chemical Engineering, Massachusetts Institute of Technology,  
Cambridge, MA 02139

Two macromolecular computational problems are considered: (i) the atomistic modeling of bulk condensed polymer phases and their inherent non-vectorizability, and (ii) the determination of the partition coefficient of polymer chains between bulk solution and cylindrical pores. In connection with the atomistic modeling problem, an algorithm is introduced and discussed (Modified Superbox Algorithm) for the efficient determination of significantly interacting atom pairs in systems with spatially periodic boundaries of the shape of a general parallelepiped (triclinic systems).

The simulation of macromolecular systems involves, in principle, the same difficulties as that of compounds of low-molecular mass, but the polymeric nature of the molecules tends to aggravate the computational problems faced by investigators of small molecules. An inordinate number of internal degrees of freedom is the major cause of these amplified complications, and most investigations dealing with macromolecules have, therefore, tended to focus either on a tiny piece of the chain in great detail, or have considered a grossly oversimplified representation of the chain as a whole. Attempts to model a larger part of the system in detail or to refine the chain representation invariably require the computing resources of a supercomputer. In this paper, we discuss two cases of macromolecular simulation, one in which the problem requires high scalar performance and for which a relatively new breed of "super-minis" effectively competes with supercomputers, and one which, due to its "highly vectorizable" nature, is very well suited for a supercomputer. The question of vectorization or, more generally, the one of altering the structure of programs to efficiently use specific features of a computing machine is at the heart of this competition. We want to stress here, that all computations performed by us are written in standard FORTRAN77, and minimal allowance is made for special features of the particular computer. Only in this way, we

0097-6156/87/0353-0162\$06.00/0  
© 1987 American Chemical Society

feel, can we pay sufficient attention to the physical essence of the problems and not have the computer influence the direction of the investigation; an immediate consequence of this is the often relatively inefficient use of high-performance computers.

CASE I - An Inherently Scalar Problem: Detailed Atomistic Modeling of Bulk Amorphous Polymer Systems

The detailed knowledge of the structure of polymeric materials and the fundamental understanding of the mechanisms of their deformation and failure are prerequisites for the design of new polymeric materials. Detailed atomistic modeling for polymeric systems requires the adoption of a rather primitive model for intermolecular and intramolecular interactions; typically, pair-wise additivity of interactions of atoms is assumed. The validity of this obviously incorrect model is usually further strained by the assumption of environment-independent values of the interaction parameters, e.g. effects of polarization are not taken into account. Despite these simplifications, the size of the condensed phase systems that can be modeled remains rather small. Spatially periodic boundaries are commonly introduced and are necessary to alleviate surface effects that would be dominant if the system were enclosed by walls interacting with the contents, but they give rise to an artificial periodicity not found in real systems. Fortunately, the effect of this periodicity on the properties computed from the models is small if the system is chosen to be sufficiently large, and can be estimated from computations with varying system size.

However, periodicity introduces the necessity to solve efficiently two problems, namely the "Minimum Image Problem" and the "Finite Interaction Range Problem." Traditionally, only systems with cube-shaped periodic box have been considered - both problems then become easily solvable (1). As soon as the boxes are deformed and become general parallelepipeds a more refined view is necessary. Several investigations of non-orthogonal periodic systems have been published (for illustrative examples see references 2-4) and more are expected. It is important to realize that any such computation will encounter the problems addressed in the following two sections; in Molecular Dynamics studies it is common practice to circumvent the necessity for frequent solution of these problems by constructing neighbor tables for the rapid evaluation of the significantly interacting atom pairs, but the computation of the neighbor table itself is limited by the two problems.

The Minimum Image Problem. In a periodic d-dimensional system, each box is surrounded by  $(3^d-1)$  nearest neighbors in space, and each atom occurs, therefore, as  $3^d$  images, including the "real" original atom. In evaluating structural characteristics and interatomic interactions within the model system (when considering pair-wise additive energies only) it is necessary to choose, for every pair of atoms 1 and 2, the one image of 2 of the  $3^d$  images which lies nearest in space to 1 (5). Computing all  $3^d$  distances involved and selecting the smallest one is too time-consuming for all but the

simplest projects. For cubic systems, the necessary steps are easy, and can be efficiently programmed (1), but for "triclinic" systems new algorithms are necessary. Two such algorithms have been recently introduced (6), the very efficient "Screening Algorithm" (which compares well in efficiency with those used for cubic systems) which can be used for small deviations from orthogonality only, and the perfectly general "Superbox Algorithm," which is somewhat slower, but still much more efficient than the simple computation of all  $3^d$  distances. A novel implementation of this algorithm is discussed below.

The Finite Range Problem. The minimum image convention requires (1) the use of interaction energy functions that are of finite range, i.e. that are non-zero only for distances below a certain limit,  $R$ . As a consequence, only a fraction of all minimum image pairs actually interact with non-zero energy; this fraction must be less than  $\pi/2d$ , i.e., in two dimensions maximally 0.79, in three dimensions maximally 0.52 (and actually often less than 0.3). It is desirable to efficiently eliminate from consideration all non-interacting atom pairs.

The Modified Superbox Algorithm. The Screening Algorithm mentioned above (6) combines this consideration and the minimum image selection for small deviations of the system from orthogonality. A more general combination of the solution of the Minimum Image Problem and the Finite Range Problem is the following modification of the Superbox Algorithm by a straightforward range-limiting method, illustrated in two dimensions for clarity.

Consider a two-dimensional spatially periodic system defined by a general parallelogram, specified by a vertex and the edge vectors  $\mathbf{a}$  and  $\mathbf{b}$  (see the top part of Figure 1; the structure consists of four such parallelograms). The infinite medium is obtained by repetitive translation of this unit cell by integer multiples of the edge vectors. Any point in the plane can be described by the location of the "parent point" in the unit cell,  $\mathbf{r}$ , and the "continuation coefficients"  $h$  and  $k$ , i.e., by  $\mathbf{r} + h\mathbf{a} + k\mathbf{b}$ . We are now interested in the interaction of atoms 1 and 2 in the unit cell, at positions  $\mathbf{r}_1$  and  $\mathbf{r}_2$ , respectively. To determine which of the 9 images of 2 lies closest to 1, we construct the (hexagonal) minimum image locus corresponding to the unit cell (i.e., the Wigner-Seitz cell) of 1, as well as the parts of all neighboring cells that could be of relevance, by first drawing the four parallelograms that share  $\mathbf{r}_1$  as a vertex, and second, erecting the perpendicular bisectors on all parallelogram sides (6); refer to the top part of Figure 1. The plane is tessellated by these hexagons, and a pair of numbers  $h$  and  $k$  is associated with each that describe the vector  $h\mathbf{a} + k\mathbf{b}$  that must be added to  $\mathbf{r}_2$  to bring it into the minimum image locus hexagon around  $\mathbf{r}_1$  (6). The representation of the range of the interaction energy functions is simply a circle of radius  $R$  around  $\mathbf{r}_1$ , and circles with the same radius around the other 8 unit cell vertices in Figure 1 reflect the effect of spatial periodicity. To insure that only the interaction with the closest image is considered, the circles may never intersect the minimum image tessellation. If  $\mathbf{r}_2$

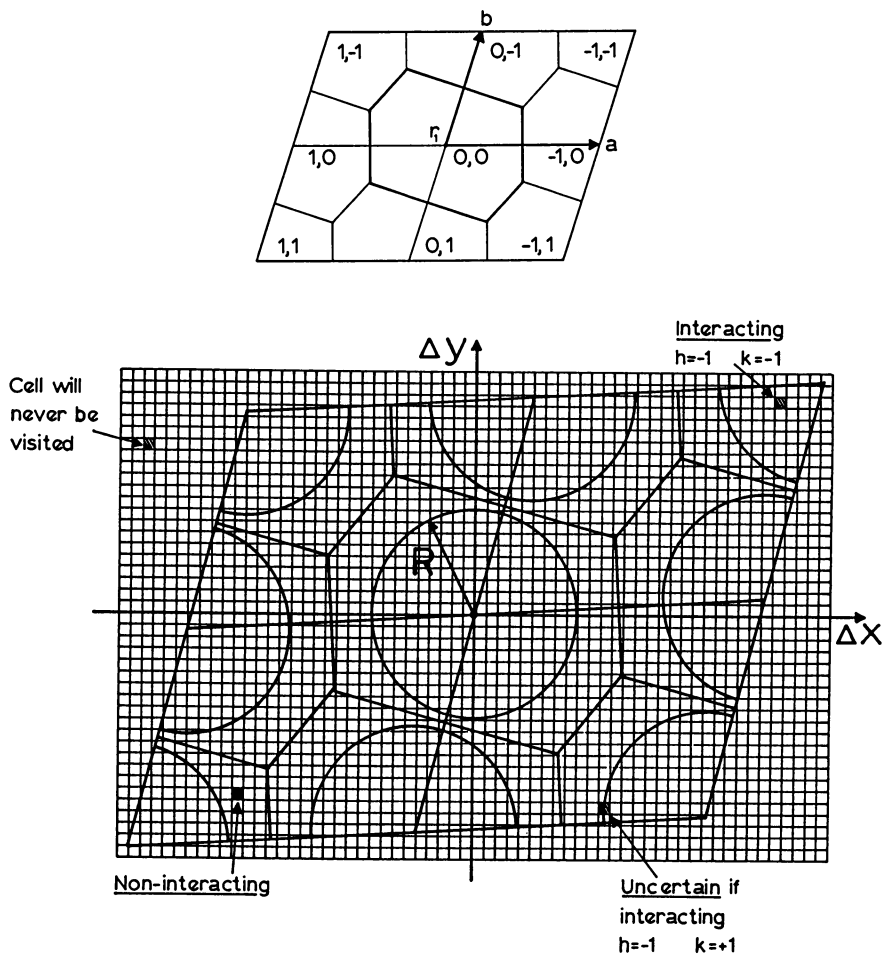


Figure 1. A two-dimensional implementation of the Modified Superbox Algorithm.



lies outside the area of one of these circles, 2 will not interact significantly with 1. If it lies within one of the circles, it will interact with 2 at location  $r_2 + ha + kb$ ,  $h$  and  $k$  being taken from the hexagon which contains the circle.

Thus, the algorithm consists simply of an initialization step, in which the superbox of edges  $2a$ ,  $2b$  and the minimum image tessellation is constructed (top part of Figure 1). This is then superposed on a fine Cartesian grid; every grid cell is assigned a set of continuation coefficients  $h$  and  $k$  as well as an indication if the cell lies inside a circle ("interacting") or outside ("non-interacting"). Cells that are crossed by a circle are specially marked, as well as those that are intersected by the minimum image tessellation (if  $R$  is chosen small enough and the grid fine enough to make it impossible for one grid cell to be crossed by a circle and the tessellation, this last marking is unnecessary). The reader should refer to the bottom part of Figure 1. The simulation procedure is then as follows: (i) For the atom pair (1, 2) the differences  $\Delta x = x_2 - x_1$ ,  $\Delta y = y_2 - y_1$  are calculated; (ii) the grid cell corresponding to  $(\Delta x, \Delta y)$  is determined and (iii) examined for interaction - (iii.a) if non-interacting, the next atom pair is considered; - (iii.b) if interacting the values of  $h$  and  $k$  associated with the grid cell are used to compute the location of the interacting minimum image of 2, i.e.,  $r_2 + ha + kb$ ; - (iii.c) if the cell is specially marked, the minimum image is computed by brute force if necessary (can be avoided by choosing  $R$  smaller), i.e. the distance to all possible images of 2 that lie in the superbox is calculated  $[(h,k) \in \{-1, 0, +1\}^2]$ , and it is determined whether the minimum distance is within the range  $R$ .

This algorithm is readily extendable to three (or more) dimensions. The only computationally costly step is (iii.c), which is very rare if the grid has been chosen fine enough. The Modified Superbox Algorithm is not as efficient as the Screening Algorithm (6), but is very attractive for its generality and simplicity.

It is noteworthy to point out that this procedure, necessary to determine if an atom pair is significantly interacting, prohibits easy and straightforward vectorization of the program, because an index, required for a conditional statement, must be looked up in a  $d$ -dimensional table, where usually  $d=3$ . Performance characteristics are discussed below.

Amorphous Atactic Polyvinylchloride, an Example. Following earlier work with a non-polar polymer, atactic bulk amorphous polypropylene (Z), a polar system, polyvinylchloride, was studied. The "unit cells" under consideration are pictured as small sections of a fully aged (structurally relaxed) bulk amorphous polyvinylchloride, which were initially cubic in shape and in the shape of a general parallelepiped after deformation. The entire bulk of the material, therefore, is thought to be made up of the translated images of a single parent chain, "randomly" coiled and extending beyond the confines of the cube. In the study reported here, this parent chain was of the type  $\text{CH}_3\text{CHCl}(\text{CH}_2\text{CHCl})_{x-1}\text{CH}_3$ . The systems are static embodiments of Cohen and Turnbull's concept of glasses being in a state of frozen-in liquid disorder, with rigid bond lengths and bond

angles. The polymer is regarded as an ensemble of such microscopic structures. The assumption of full aging implies that all parts of the microstructures, i.e., of the cubes, satisfy the requirement of detailed mechanical equilibrium (the sum of all forces and torques, acting through space or through bonds, on each atom must be zero), or, equivalently, that the potential energy of the microstructures is at a minimum with respect to all modeled degrees of freedom (three Euler angles and all torsion angles in the chain). The microstructures are, consequently, the results of potential energy minimizations with respect to the modeled degrees of freedom.

The interaction energy functions are broken down into contributions from static charges or multipole assemblies (Coulombic interactions), short-range repulsive and long-range attractive dispersion interactions (Van der Waals interactions), and special intramolecular interactions (intrinsic torsional energy). We employ a Lennard-Jones 6-12 function for the Van der Waals interactions, suitably splined to zero at a distance somewhat smaller than half the edge-length of the cube. A simple Coulombic function is used for the interaction energy of partially charged centers, splined in the same fashion; here the attenuation of the electrostatic interaction between centers separated by polarizable matter is modeled in a way similar to that followed when a distance dependent dielectric constant is used. In addition, a three-fold intrinsic torsional potential is employed for torsion around each skeletal bond.

The initial cube measures 17.9 Å along one edge, and contains 455 atoms. Accepting the approximation of pair-wise additivity of interactions, we are faced with the requirement for the evaluation of  $455 \times 454 / 2 = 103,285$  pair interactions in order to once estimate the total energy of the system. Fortunately, only roughly 20% of these pairs interact significantly.

To arrive at a minimized microstructure, one must follow an iterative energy minimization procedure that starts with an appropriately chosen initial guess. A Quasi-Newton minimization procedure (g) is used to minimize the highly non-linear objective function (i.e., the total potential energy). Ten microstructures of polyvinylchloride, PVC, (corresponding to a polymer obtained by free radical polymerization in an inert solvent at 40°C, i.e. with 43% meso diads in a Bernoullian distribution) have been produced to date. A space-filling model of the contents of the "unit cell" of one of the microstructures of atactic PVC at room temperature, containing part of the parent chain as well as parts of several translated images of the parent chain, is displayed in Figure 2. The radii of the spheres in this figure are equal to the Van der Waals radii; the high density of the atoms, obvious from this picture, is indicative of the large number of significant interatomic interactions in these systems.

The degree of realism of these model structures can be assessed by comparison of computed properties with experimental ones. The cohesive energy is, by definition, the difference in energy per mole of substance between a parent chain in its bulk environment and the same parent chain in vacuo, i.e., when all intermolecular forces are eliminated. This difference is readily computed from the minimized

microstructures. The corresponding experimentally observable quantity is the Hildebrand solubility parameter  $\delta$ , which is the square root of the cohesive energy density,  $\delta^2 = E_{\text{coh}}/V$ . Values of this quantity have been computed for PVC;  $\delta_{\text{th}} = 16.8 (\pm 2.0) \text{ J}^{1/2} \text{ cm}^{-3/2}$ , while  $\delta_{\text{exp}} = 18.8 - 21.6 \text{ J}^{1/2} \text{ cm}^{-3/2}$ . The agreement is quite satisfactory, if one realizes that no adjustable parameters are involved in the prediction.

Performance of Several Computers for this Problem. The standard FORTRAN77 program that minimizes a model system from an appropriately chosen initial guess to the local minimum of potential energy was compiled and run on the John von Neumann Center's Control Data Corporation Cyber 205, a Cray X-MP, and on several so-called super-minicomputers, in identical form and with identical inputs. Results are collected in Table I. Particularly noteworthy is here the very high performance of all small machines tested, compared to the Class VI vector machines, on this highly scalar problem. It is obvious that this is but one measure of computing efficiency of a machine, and must not necessarily reflect performance on other tasks. To illustrate this point, values from the "Dongarra LINPACK benchmark," a moderately vectorizable program (9), are juxtaposed with our "scalar test" results in the same Table.

Table I. Preliminary Performance Comparison of Several Machines on the "Non-Vectorizable" Minimization Problem, and Data from the Dongarra-LINPACK Test

Machine OS/Compiler	Dense PVC Structure Minimization Full precision FORTRAN77 Funct.Eval./s	(% of CDC)	Dongarra-LINPACK Benchmark <sup>a</sup> Full precision "All Fortran" MFLOPS (% of CDC)
Alliant FX/1 (1CE) Unix/FX-Fortran -gva	0.25	(48%)	1.6 (9%)
Alliant FX/8 (4CE) Unix/FX-Fortran -gvca	0.45	(87%)	4.2 <sup>b</sup> (25%)
CDC Cyber 205 VSOS/FTN-200 impl.vec.& opt.	0.52	(100%)	17 (100%)
Celerity 1260 (one head) Unix/f77 v.3.2 global opt.	0.13	(26%)	0.4 (3%)
Cray X-MP/48 UNICOS/CFT77	3.4	(650%)	24 (141%)
RIDGE 3200 Unix/f77 optimized	0.16	(31%)	-
SUN 3/160M + fpa Unix/f77 optimized	0.14	(27%)	0.4 (3%)

a) Reference 9, July 29, 1986

b) Interpolated

CASE II - An Easily Vectorizable Problem: Equilibrium Partitioning of Freely Jointed Chains: A Monte Carlo Simulation

The distribution of flexible macromolecules in finely porous media plays an important role in processes such as size-exclusion chromatography and enhanced oil recovery. The problem of determining the equilibrium distribution of macromolecules between bulk solution and a porous medium has been treated by analytical methods for idealized hypothetical chain models, including rigid rods, once-broken rods, and random-flight chains with infinitely many bonds of infinitesimal length, as well as linear elastic dumbbell models (see Davidson, M. G.; Suter, U. W.; Deen, W. M. Macromolecules 1987, in press, as well as references cited therein). Stark discrepancies between the results from different models stimulated the Monte Carlo investigation reported here; in particular, it had been suspected that the relationship of bond length to pore radius played an important but unrecognized role. It was decided to investigate a series of so-called "freely-jointed chains," i.e., ideal linear chains consisting of  $n$  mass-points which are connected by  $(n-1)$  rigid bonds of fixed and equal length but without mutual directional correlation.

For purely steric partitioning, i.e., without any interactions between the macromolecule and the pore wall beyond geometric exclusion, the problem of determining the partition coefficient (or equilibrium pore-to-bulk concentration ratio) of a flexible macromolecule between bulk solution and a cylindrical pore reduces to that of determining the probability that the polymer molecule, having many possible conformations, can be placed with its center-of-mass at every position within the pore. For very long pores the problem reduces to a two-dimensional one, and the partition coefficient can be calculated from the probability that the macromolecule can be placed at a particular radial positions,  $r$ , within the pore, denoted  $p(r)$ . Hence, the goal is to determine  $p(r)$  over the range  $0 \leq r \leq R$ , where  $R$  is the pore radius.

The Monte Carlo Procedure. The procedure to determine  $p(r)$  using the Monte Carlo technique was as follows. A chain of  $n$  mass-points was generated by choosing  $(n-1)$  vectors of fixed length and random direction and adding these segment vectors end-to-end until the chain was of the desired length. The direction of each segment vector was found by choosing randomly the orientation angles in a spherical polar coordinate system with its origin at the previous mass point, such that the vector end point would intersect all positions on the sphere with equal probability. When chain generation was completed, the center-of-mass of the chain was determined and placed at a number of radial positions within the pore, and it was tested to determine whether all of its segments fell within the bounding surface of the cylindrical pore at each radial position. If the entire chain fell within the pore a success was recorded. The process was repeated until an ensemble of chains had been tested. The fractional success rate at each radial position defined

$p(r)$ . Appropriate integration of  $p(r)$  over all radial positions then yielded the partition coefficient.

The procedure is obviously a very simple one, but suffers from the fact that the success rate diminishes very rapidly as the pore radius becomes smaller. The root-mean-square radius of gyration of the chain is measured in units of the pore radius,  $\lambda_g = \langle s^2 \rangle_0^{1/2} / R$ , and at  $\lambda_g = 1.4$ , for example, only roughly one out of  $10^5$  trials is successful. As a result, a very high statistical error is associated with the computed probabilities. To keep errors in reasonable limits, test populations of  $10^5$  to  $5 \times 10^6$  were required. A very powerful computer was obviously necessary.

Results. Values computed on the John von Neumann Center's Control Data Corporation Cyber 205 are displayed and compared to literature results for other model-chains in Figure 3. Squares indicate values obtained in our Monte Carlo simulations, while diamonds are results of Priest's (12) analytical approximation for very narrow pores. The dashed line represents values evaluated by Casassa (10) for random-flight chains with infinitely many bonds of infinitesimal length. The dot-dashed line shows results of Giddings et al. (11) for rigid rods.

Explicit Vectorization. The problem in this case is intrinsically suited for vectorization of the program and the Control Data Corporation Cyber 205 proved ideal for this purpose. The Monte Carlo code contains a number of steps that can easily be incorporated in vector operations, e.g., coordinate transformations, array multiplications, and testing an integer vector for the presence of bits. By carefully evaluating the computation time profile of the program it was determined that the vast majority of the computing time was spent in a small loop used in the testing for overlap of chain mass-points with the pore wall. This segment of the program is shown in the left half of Figure 4. In order to explicitly vectorize this time-consuming loop, changes in the executable statements of the program consisted of replacing the five FORTRAN statements contained in the loop beginning with "DO 350 ..." and ending with "350 CONTINUE" by six statements as shown in the right half of Figure 4. No similarly trivial changes could be made to further improve execution speed.

Table II contains a rough comparison of execution times for the generation of one data point:  $6 \times 10^5$  random conformations of chains of 100 mass-points were placed each at 100 equally spaced radial positions of a pore with  $\lambda_g = 0.8$ . It is obvious that the increase in performance, i.e., a reduction in execution time to 20%, is an excellent return on the investment required to change five lines of a FORTRAN program. We fear, however, that this is a relatively rare situation.

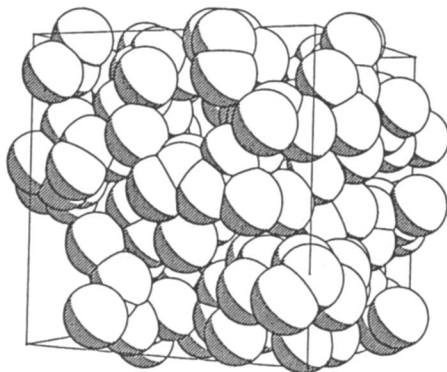


Figure 2. A micro-structure of bulk amorphous Bernoullian atactic polyvinylchloride at ambient temperature.

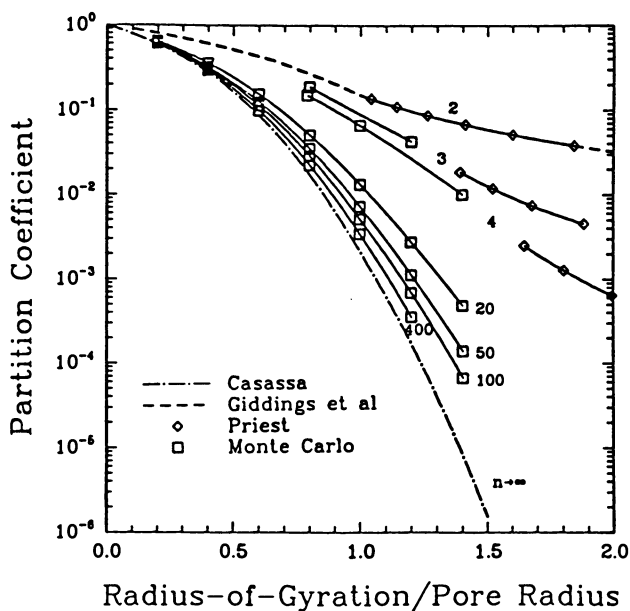


Figure 3. Partition coefficient of freely jointed chains between the bulk solution and a cylindrical pore. The chains have different numbers of mass-points ( $n$ ) and different bond lengths, and are characterized by the root-mean-square radius of gyration measured in units of the pore radius. See text for details.

```

        DO 500 IBETA=1,NBP1
            XBETA=BETA(1BETA)*RP
        C
        C
        C     TEST J--TH SEGMENT FOR SUCCESS -- IF FAILURE OCCURS.
        C     GO TO THE NEXT BETA VALUE. IF ALL STEPS SUCCEED.
        C     RECORD SUCCESS OF MOLECULE.
        C
        DO 350 I=1,NSTEP
            XEXT=X(I)+XBETA
            SEXT=XEXT+XEXT+Y(1)*Y(1)
            IF(SEXT.GT.SQR)GO TO 500
            CONTINUE
            SUCC(1BETA)=SUCC(1BETA)+1.0
        C
        C     IF BETA=0 RECORD THE SUCCESS IN "CSUC" AND STORE
        C     SEGMENT LOCATIONS BY CALLING SUBROUTINE "SEGLOC".
        C
        IF(1BETA.EQ.1)THEN
            CSUC=CSUC+1.0
            CALL SEGLOC(NDIV,NSTEP)
        ENDIF
        500  CONTINUE

        DO 500 IBETA=1,NBP1
            XBETA=BETA(1BETA)*RP
        C
        C
        C     TEST J--TH SEGMENT FOR SUCCESS -- IF FAILURE OCCURS.
        C     GO TO THE NEXT BETA VALUE. IF ALL STEPS SUCCEED.
        C     RECORD SUCCESS OF MOLECULE.
        C
        XEXTV(1;NSTEP) = X(1;NSTEP)+XBETA
        SEXTV(1;NSTEP)=XEXTV(1;NSTEP)*XEXTV(1;NSTEP)
        SEXTV(1;NSTEP)=Y(1;NSTEP)*Y(1;NSTEP)+SEXTV(1;NSTEP)
        BTEST(1;NSTEP)=(SEXTV(1;NSTEP).GT.SQR)
        IBTEST=QBSCNT(BTEST(1;NSTEP))
        IF(1BTEST.GT.0)GO TO 500
        SUCC(1BETA)=SUCC(1BETA)+1.0
        C
        C     IF BETA=0 RECORD THE SUCCESS IN "CSUC" AND STORE
        C     SEGMENT LOCATIONS BY CALLING SUBROUTINE "SEGLOC".
        C
        IF(1BETA.EQ.1)THEN
            CSUC=CSUC+1.0
            CALL SEGLOC(NDIV,NSTEP)
        ENDIF
        500  CONTINUE
    
```

Figure 4. The most CPU time-consuming portion of the scalar version of the Monte Carlo program for the evaluation of chain partitioning between the bulk solution and a cylindrical pore, in the scalar form (left) and the explicitly vectorized form (right).

Table II. Performance Improvement Upon Minimal Explicit Vectorization for the Distribution Problem

Machine	Creation and Testing of $6 \times 10^5$ Conformations 100 mass-points, placed at 100 radial positions $\lambda_G = 0.8$	
	(CPU hours) <sup>-1</sup>	Rel. Performance
Data General MV/4000 + fpa AOS/VS f77 optimized	0.010	0.02
CDC Cyber 205, Scalar Program VSOS/FTN-200 impl.vect.& opt.	0.5	1
CDC Cyber 205, Minimal Explicit Vectorization VSOS/FTN-200 impl.vect.& opt.	2.7	5

### Conclusions

Thus, we have presented two extreme examples of problems in simulating macromolecular systems. For one of them, the atomistic modeling of bulk amorphous polymers, the use of supercomputers, such as the Control Data Corporation Cyber 205 or the Cray X-MP, in generating the solutions offers little advantage over use of a super-minicomputer, due to the inherently scalar nature of the problem. In contrast, the other simulation, that of equilibrium chain partitioning, is performed most efficiently on a supercomputer because the inherently vectorizable nature of the problem can be readily exploited. We feel that most polymer simulations of interest will resemble the first case rather than the second, resisting easy vectorization. Therefore, the performance advantages of supercomputers in simulating most macromolecular systems will be relatively modest, without substantial efforts in programming to accommodate these machines.

### Literature Cited

1. Ceperley, D. M. in Supercomputers in Chemistry, by Lykos, P.; Shavitt, I., Eds., ACS Symposium No. 173, American Chemical Society, 1981, p. 125.
2. Parrinello, M.; Rahman, A. Phys. Rev. Letters 1980, **45**, 1196.
3. Nosé, S.; Klein, M.L. J. Chem. Phys. 1983, **78**, 6928.
4. Theodorou, D. N.; Suter, U. W. Macromolecules 1986, **19**, 139.
5. Wood, W. W.; Parker, F. R. J. Chem. Phys. 1957, **27**, 720.
6. Theodorou, D. N.; Suter, U. W. J. Chem. Phys. 1985, **82**, 955.
7. Theodorou, D. N.; Suter, U. W. Macromolecules 1985, **18**, 1467.
8. Hillstroem, K. Nonlinear Optimization Routines in AMDLIB, Technical Memorandum No. 297, Argonne National Laboratory, Applied Mathematics Division, 1976; Subroutine QQBFGS in AMDLIB, 1976, Argonne, IL.



9. Dongarra, J. Performance of Various Computers Using Standard Linear Equations Software in a Fortran Environment, Technical Memorandum No. 23, Argonne National Laboratory, Mathematics and Computer Science Division, July 29, 1986.
10. Casassa, E. F. J. Polym. Sci., Part B 1967, 5, 773.
11. Giddings, J. C.; Kucera, E.; Russell, C. P.; Myers, M. N. J. Phys. Chem. 1968, 72, 4397.
12. Priest, R. G. J. Appl. Phys. 1981, 52, 5930.

RECEIVED June 15, 1987

## Chapter 11

# Sensitivity of Vibrational and Rotational Energy Transfer to the Potential Energy Surface in the Collision of Two Molecules

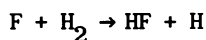
## Large-Scale Quantum Mechanical Calculations

David W. Schwenke and Donald G. Truhlar

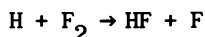
Minnesota Supercomputer Institute and Department of Chemistry,  
University of Minnesota, Minneapolis, MN 55455

We present an overview of our research program on HF-HF collisions, including potential energy surfaces and dynamics calculations, with special emphasis on the sensitivity of the dynamics results to the choice of surface.

The molecules of a gas in a thermally equilibrated state are characterized by a Boltzmann distribution of vibrational and rotational states. Although energy is transferred between modes in individual collisions, there is no net change in the vibrational-rotational distributions. If the equilibrium populations are perturbed in any way, e.g., by heating, cooling, the influx of laser light, or a chemical reaction, then the system will relax to a new equilibrium distribution (1). The change of vibrational state populations with time is usually much slower than the rotational relaxation, but it is critical for understanding many classes of nonequilibrium processes. For example if an exothermic chemical reaction like



or

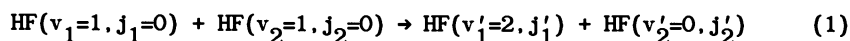


produces vibrationally excited products — HF in the examples — the competition between vibrational-rotational-state redistribution and stimulated emission is critical in determining whether energy can be extracted in the form of infrared laser action. Another example concerns the attempt to force reactions to yield nonspontaneous products by using laser light to pump a selected vibrational mode of a polyatomic molecule, e.g., the stretching vibration of a bond that it is desired to break. If the energy is redistributed rapidly compared to the time scale for the reaction, only the usual products of the reaction that occurs spontaneously upon slow heating will be observed.

0097-6156/87/0353-0176\$07.00/0  
© 1987 American Chemical Society

The simplest models of energy transfer involve an atom and a nonrotating oscillator or an atom and a rigid rotator. But the single oscillator model is insufficient for molecule-molecule collisions or even atomic collisions with a polyatomic molecule because processes involving the transfer of energy between vibrational modes, called vibrational-to-vibrational (V-V) or vibrational-to-vibrational-and-rotational (V-V,R) energy transfer, are usually much more efficient than those involving vibrational-to-translational (V-T) or vibrational-to-translational-and-rotational (V-T,R) energy transfer (2). Furthermore, the coupling of rotational and vibrational degrees of freedom can change the quantitative values of the transition probabilities for vibrational state changes by an order of magnitude or more.

One of the goals of modern scattering theory is the rigorous solution of the quantum mechanical equations governing molecular collisions. Prior to supercomputers, one could solve the equations for the atom-oscillator and atom-rigid-rotator models or for light enough atom-diatom systems at low energy (3). But in order to treat V-V and V-V,R processes accurately, we must do calculations on systems with two or more vibrational degrees of freedom, coupled to rotations, at energies above the second vibrational threshold (the energetic requirement arises because different excited vibrational states are populated before and after the collision for a V-V or V-V,R process). The problem with doing this is one of computational economy. As either the number of degrees of freedom or the energy is increased, the number  $N$  of basis functions required to expand the scattering wave function increases dramatically. For conventional methods of solving the quantum mechanical equations, though, the computer time scales as  $N^3$  and the memory required, which can also be significant, scales as  $N^2$ . Thus one rapidly reaches a point where the calculation becomes impossible on any machine — past, present, or presently envisaged. Nevertheless, with supercomputers one can push the boundaries of feasibility into a new realm, and we have embarked on a study designed to do so. In particular we have made large-scale calculations for the process



where the (unprimed, primed)  $v_i$  ( $i=1,2$ ) are (initial, final) vibrational quantum numbers, and  $j_1, j_2, j'_1, j'_2$  are rotational quantum numbers with the same conventions.

Since HF has a closed-shell electronic structure and no low-lying excited electronic states, HF-HF collisions may be treated quite adequately within the framework of the Born-Oppenheimer electronic adiabatic approximation. In this treatment (4) the electronic and coulombic energies for fixed nuclei provide a potential energy  $V$  for internuclear motion, and the collision dynamics is equivalent to a four-body problem. After removal of the center-of-mass coordinates, the Schroedinger equation becomes nine-dimensional. This nine-dimensional partial differential

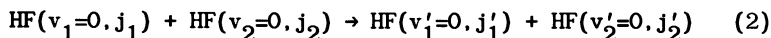
equation is then converted to  $N$  coupled ordinary differential equations by expanding the solution in symmetrized internal-state eigenfunctions (5-7) (which is called the close coupling approximation and is described further below). These coupled differential equations must be solved subject to scattering boundary conditions, and this is accomplished by an invariant-embedding-type (8-10) propagation method (11,12) involving repeated operations on matrices of order  $N$ .

Although our work is primarily directed to the second — dynamical — step, it is necessary for us to start with the potential energy function  $V$ . Unfortunately, as is often the case for systems whose dynamics we wish to study, a completely satisfactory  $V$  function for HF-HF collisions is unavailable. Thus we constructed two new approximate  $V$  functions (13-16) and we considered five potential functions developed by others (17-21) and we performed large-scale ( $N > 250$ ) calculations (13-16,22-24) for several (13-17,19,21) of these. In some calculations we treated the vibrations as rigid and considered only translational-to-rotational (T-R) energy transfer. This reduces the number of degrees of freedom from 9 to 7 and hence reduces computational complexity, but it provides a valuable test of the dynamical significance of the differences in the various  $V$  functions because the final rotational state distributions of the rigid-rotator calculations are primarily sensitive to the anisotropy of  $V$ . We have also performed large-scale calculations including the vibrational coordinates for three of the  $V$  functions. In one case the transition probabilities for process (1) are well converged; unfortunately the potential for that case may be inaccurate. Nevertheless converged quantal dynamics calculations for any given  $V$  provide a benchmark for testing approximate quantal, semiclassical, and classical methods of collision dynamics, and the present results also demonstrate the feasibility — for an expenditure of more computational resources — of obtaining converged quantal dynamics solutions for more realistic  $V$  functions.

The above constitutes a general overview of our quantum mechanical calculations so far (13-16,22-24) on process (1) and rigid-rotator HF-HF collisions. In the sections below we provide further details of selected subtopics in this research program. Section 2 reviews the potential functions we have studied; section 3, the dynamics method; section 4, the results for rigid-rotator collisions; and section 5, the results for process (1). Throughout this overview we place special emphasis on the comparison of the various surfaces and of the dynamical results obtained with one surface to those obtained with another. Another long-range goal of our program, though, is to use converged quantal studies of the dynamics as benchmarks for testing more approximate theories; in this regard, it should be especially interesting to test semiclassical (25-27) and quasiclassical (28-31) theories of V-V, R energy transfer.

### Potential Energy Surfaces

The rigid-rotator collisions may be taken as a model for



We have carried out converged rigid-rotator dynamics calculations for four potentials:

<u>Abbreviation</u>	<u>Reference</u>
AD	Alexander and DePristo (17)
BM	Brobjer and Murrell (19)
RB	Redmon and Binkley (21)
RBST	Reference 16

These surfaces are all based on some combination of *ab initio* electronic structure calculations plus fitting. The AD and BM surfaces are based respectively in whole or in part on extended-basis-set single-configuration self-consistent-field calculations, whereas the RB and RBST calculations are based on calculations including electron correlation by Moller-Plesset fourth-order perturbation theory. For the rigid-rotator calculations  $R_1$  the intramolecular internuclear distances  $R_1$  and  $R_2$  are fixed at  $1.733 a_0$ . The rigid-rotator interaction potential may be expanded as

$$V_{\text{int}} = \sum_{q_1 q_2 \mu} v_{q_1 q_2 \mu}(r) y_{q_1 q_2 \mu}(\hat{r}_1, \hat{r}_2) \quad (3)$$

where

$$y_{q_1 q_2 \mu} = \frac{4\pi}{[2(1+\delta_{\mu 0})]^{1/2}} [Y_{q_1 \mu}(\hat{r}_1) Y_{q_2 -\mu}(\hat{r}_2) + Y_{q_1 -\mu}(\hat{r}_1) Y_{q_2 \mu}(\hat{r}_2)] \quad (4)$$

$Y_{q_1 \mu}$  is a spherical harmonic,  $r$  is the distance between the

molecular centers of mass, and  $\hat{r}_1$  and  $\hat{r}_2$  are unit vectors along the molecular axes in a ("body-fixed") frame of reference in which the  $z$  axis is along the vector connecting the molecular centers of mass. The first several nonzero coefficients are compared for the four surfaces in Figures 1-6. We see qualitatively good agreement for the general shape of the  $r$  dependence in all cases, but apparently significant quantitative differences. To get a better understanding of the effect of these quantitative differences, we consider the transition probabilities calculated with the various surfaces for processes (2) in Section 4.

The AD and BM surfaces are based on *ab initio* calculations carried out only for  $R_1 = R_2 = R_e$ , where  $R_e$  is the value for an isolated diatom. Thus the AD and BM surfaces cannot be used to study V-V and V-V,R (or V-T) energy transfer.

To study processes involving vibration we must add the two diatomic vibrational potentials to  $V_{\text{int}}$  and we must also generalize  $V_{\text{int}}$  to include a dependence on vibrational coordinates. The AD surface was extended to include all geometries by adding two kinds

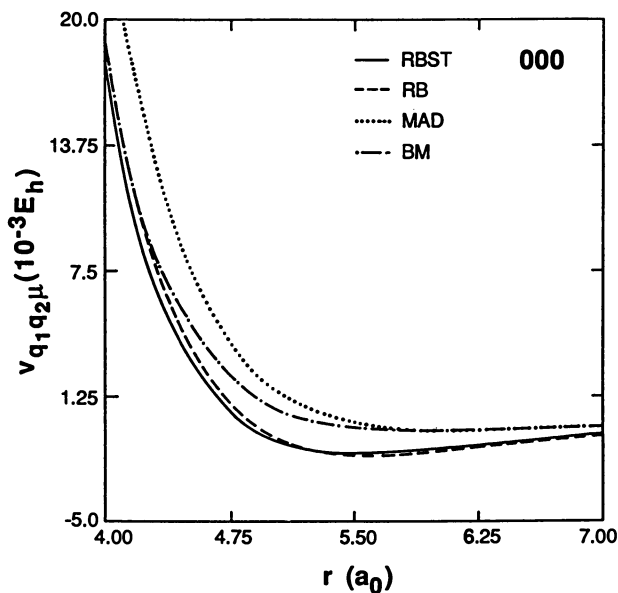


Figure 1. Body-frame expansion coefficients (in hartrees) of eq. (3) for rigid-rotator HF-HF collisions as functions of the collisional separation coordinate  $r$  (in bohrs) for  $q_1 = q_2 = \mu = 0$ .

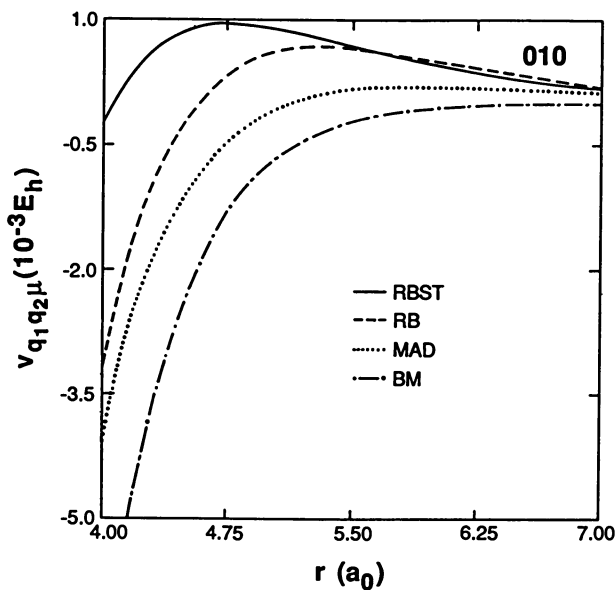


Figure 2. Same as Fig. 1 except  $q_1 = \mu = 0$ ,  $q_2 = 1$ .

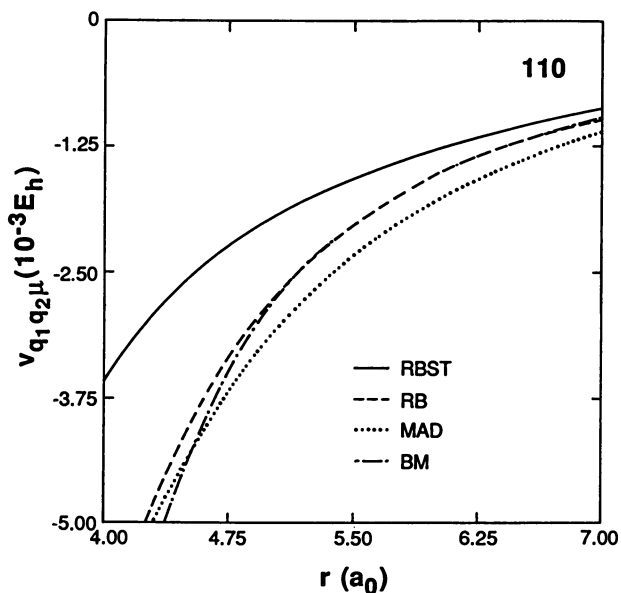


Figure 3. Same as Fig. 1 except  $q_1 = q_2 = 1$ ,  $\mu = 0$ .

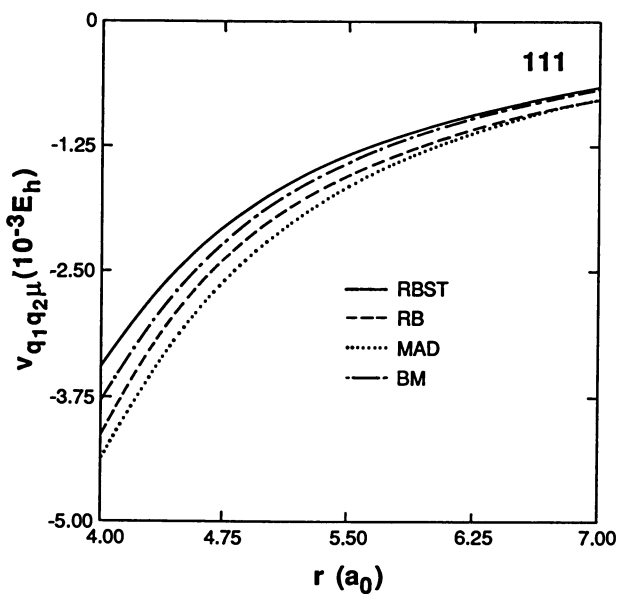


Figure 4. Same as Fig. 1 except  $q_1 = q_2 = \mu = 1$ .

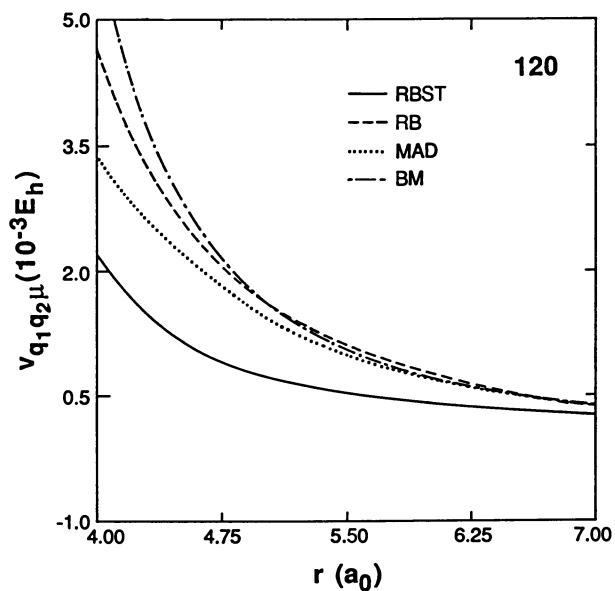


Figure 5. Same as Fig. 1 except  $q_1 = 1$ ,  $q_2 = 2$ ,  $\mu = 0$ .

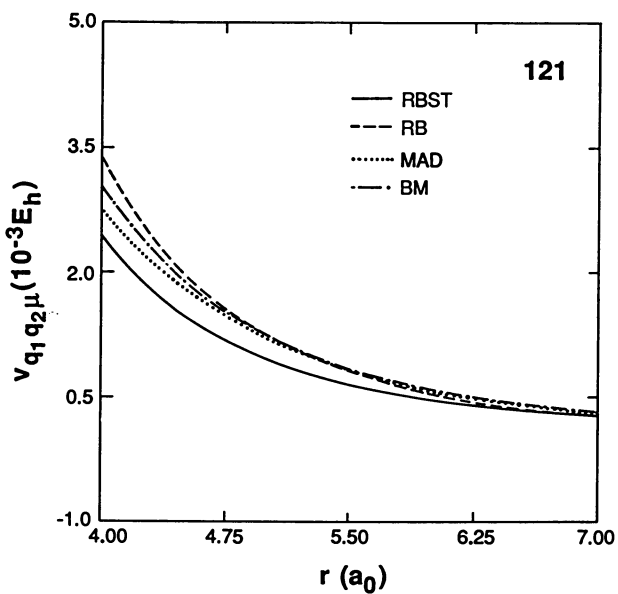


Figure 6. Same as Fig. 1 except  $q_1 = \mu = 1$ ,  $q_2 = 2$ .



of dependence on the intramolecular H-F distances  $R_1$  and  $R_2$ . The long-range (large  $r$ ) dependence on  $R_1$  and  $R_2$  was based on the known dependence (32,33) of the permanent dipole and quadrupole moments on internuclear distance. This may be reasonable since HF-HF interactions are dominated by electrostatic terms at and beyond the van der Waals hydrogen-bonded minimum (34). The dependence of the potential on  $R_1$  and  $R_2$  at short range (small  $r$ ) was included by an approximation based on the idea that when a single interatomic potential dominates the short-range repulsion, the gradient of the whole potential is a function of only the pair distance and so there is a simple geometrical relation between the gradient with respect to changing this distance by changing  $r$  and the gradients with respect to changing this distance by changing  $R_1$  and  $R_2$ .

These simple relations motivate a more formal approximation in which we first re-expand the interaction potential in a space-fixed ("laboratory-frame") coordinate system as

$$V_{\text{int}} = (4\pi)^{3/2} \sum_{\lambda_1 \lambda_2 \lambda} U_{\lambda_1 \lambda_2 \lambda}(r) Y_{\lambda_1 \lambda_2 \lambda}(\hat{r}, \hat{R}_1, \hat{R}_2) \quad (5)$$

where

$$Y_{\lambda_1 \lambda_2 \lambda} = \sum_{m_1 m_2 m} (\lambda_1 m_1 \lambda_2 m_2 | \lambda_1 \lambda_2 \lambda m) Y_{\lambda_1 m_1}(\hat{R}_1) Y_{\lambda_2 m_2}(\hat{R}_2) Y_{\lambda m}^*(\hat{r}) \quad (6)$$

$(\dots | \dots)$  is a Clebsch-Gordan coefficient, and the  $\hat{R}_i$  are unit vectors along the bond axes in the space-fixed system, and then we make the  $U_{\lambda_1 \lambda_2 \lambda}$  depend exponentially on  $R_1$  and  $R_2$  with exponential range parameters based on the  $r$  dependence of the potential (13-15). This kind of parameterization was first applied to a breathing-sphere model of HF-HF by Gianturco *et al.* (35). The resulting potential in the present case is called the MAD potential, which denotes "modified AD".

The Redmon-Binkley potential is a multi-center fit of *ab initio* calculations including separate variations of  $R_1$  and  $R_2$ . The fit was based on minimizing the root-mean-square (rms) value of the difference between the fit values and the originally calculated potential values. The RBST potential differs in three ways: (i) The *ab initio* data set was augmented by over 100 points in which  $R_1$  and  $R_2$  were simultaneously different from  $R_e$ . (ii) The surface was refit by making local fits to the separate vibrational forces,  $-\partial V/\partial R_1$  and  $-\partial V/\partial R_2$ , the cross correlation of the forces,  $\partial^2 V/\partial R_1 \partial R_2$ , and both principal second derivatives,  $\partial^2 V/\partial R_1^2$ , and  $\partial^2 V/\partial R_2^2$ , and then minimizing the relative rms errors in the global fits to the local forces and cross correlation of forces as well as to the potential itself. (iii) For convenience, the new fit was

made directly in terms of the body-frame expansion (3) with a restriction to only 23 terms in the sum. Because of the restriction on the sum, this surface may represent the higher-order angular anisotropy less accurately than the RB potential, especially at high energies, but because of difference (ii) it should be more accurate for the vibrational forces and cross correlation of the forces that would be expected (36) to be very important for V-V and V-V,R energy transfer. Both the RB and RBST surfaces, however, are believed to yield more accurate vibrational forces and vibrational force cross correlations than the MAD surface because they are based on highly correlated *ab initio* calculations at over 1300 geometries (over 1400 for the RBST surface). These *ab initio* calculations (16,21) required over 70 hours of computer time on Cray-1 computers, and they would not have been possible without supercomputer resources. Thus, in summary, we performed large-scale dynamics calculations for three potential energy surfaces for the vibrating rotator case:

<u>Abbreviation</u>	<u>Reference</u>
MAD (modified AD)	References 13-15
RB	Redmon-Binkley (21)
RBST	Reference 16

Figures 7-11 show potential energy contours for two-dimensional cuts through these three surfaces. The contour sets are labelled by  $\theta_1$ ,  $\theta_2$ , and  $\phi$  where the z axis points from molecule 1 to molecule 2,  $\theta_1$  and  $\phi_1$  are the colatitude and longitude of the vector from F to H in molecule 1 ( $\theta_1 = 0$  if this vector points along +z), and  $\phi = \phi_1 - \phi_2$ . Figures 7 and 8 are for the collinear geometries FH...FH and HF...HF, respectively, Figures 9 and 10 are for planar F...FH and FH...F geometries, and Figure 11 is for a nonplanar geometry. In all cases  $R_2$  refers to the molecule on the right. Notice that for all geometries the vibrational force on the repulsive wall is positive for the MAD potential but negative for the RB and RBST potentials. For the collinear geometries the negative force appears more physical since stretching one of the molecules increases the strongest pair repulsion. For the other geometries the determination of the correct force is more problematic.

Much additional work on HF-HF potentials, as discussed elsewhere (37,38), is directed very specifically at that part of the potential energy surface that governs the binding energy, geometry, and internal dynamics of the (HF)<sub>2</sub> dimer near its equilibrium geometry. Since a knowledge of only this limited part of the potential energy surface is insufficient to study the collision dynamics, we do not further review these studies here.

#### Close Coupling Formalism

The close coupling formalism employed for the present calculations

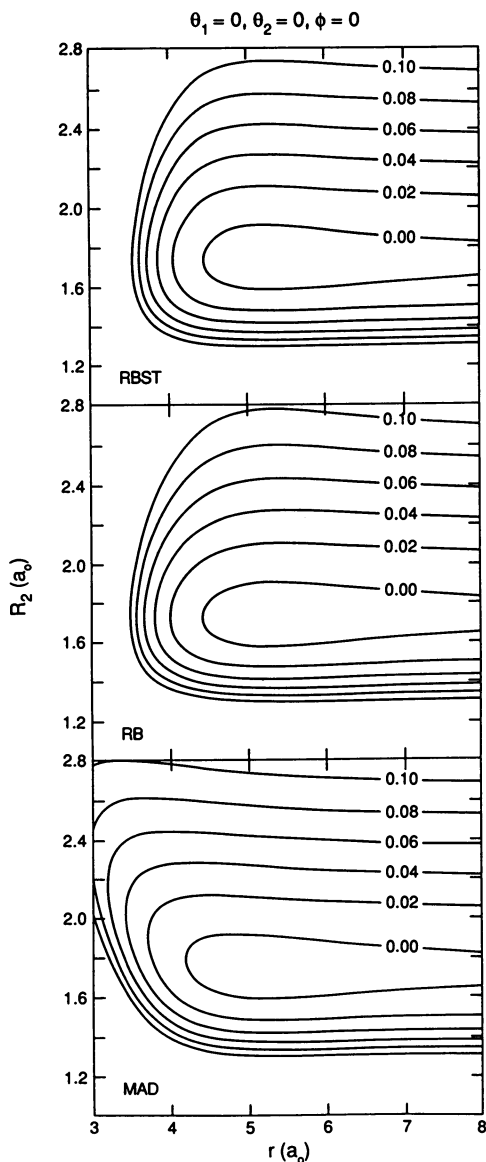


**Figure 7.** Two-dimensional cuts through the potential energy surface for planar HF-HF collisions including vibration. The quantity plotted in the figure is the total potential (in hartrees), which is defined as the sum of the interaction potential and the two diatomic potentials, with the zero of energy corresponding to two infinitely separated HF molecules, each at its classical equilibrium separation. This figure shows cuts through the  $r, R_2$  plane (in bohrs) for  $\theta_1 = \theta_2 = \phi = 0$  and  $R_1 = 1.733 a_0$ .

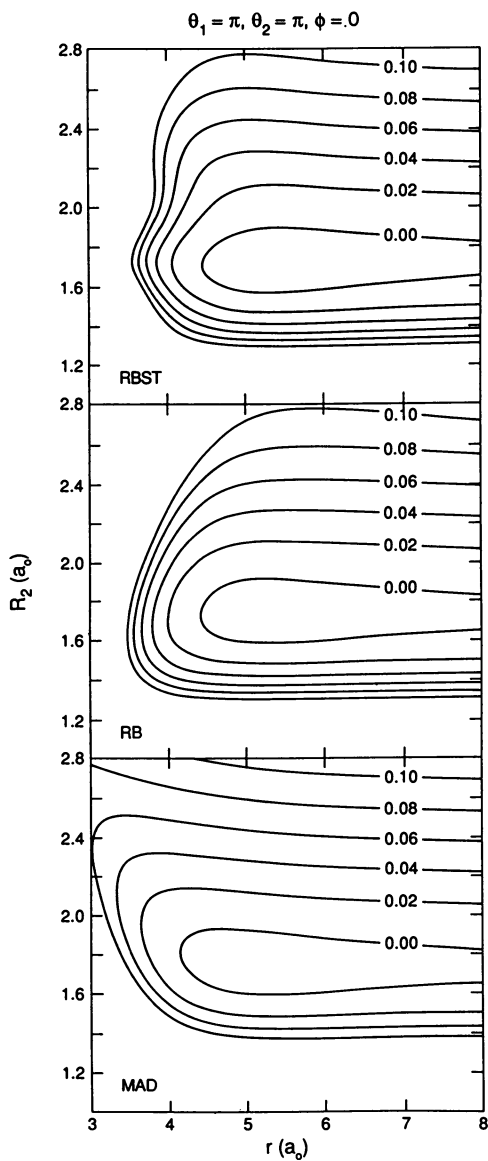


Figure 8. Same as Fig. 7 except for  $\theta_1 = \theta_2 = 180^\circ$ .

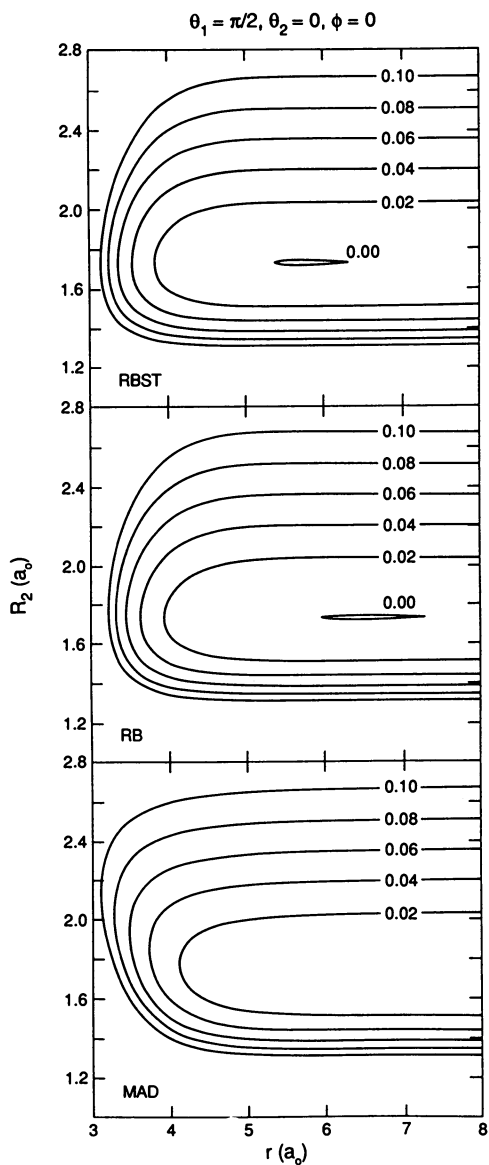


Figure 9. Same as Fig. 7 except for  $\theta_1 = 90^\circ, \theta_2 = 0$ .

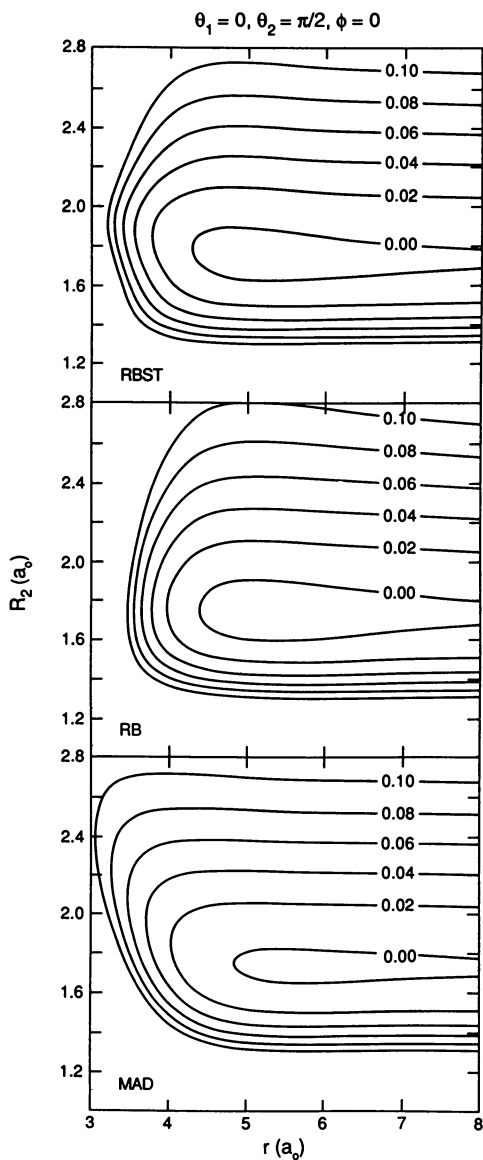


Figure 10. Same as Fig. 7 except for  $\theta_1 = 0, \theta_2 = 90^\circ$ .

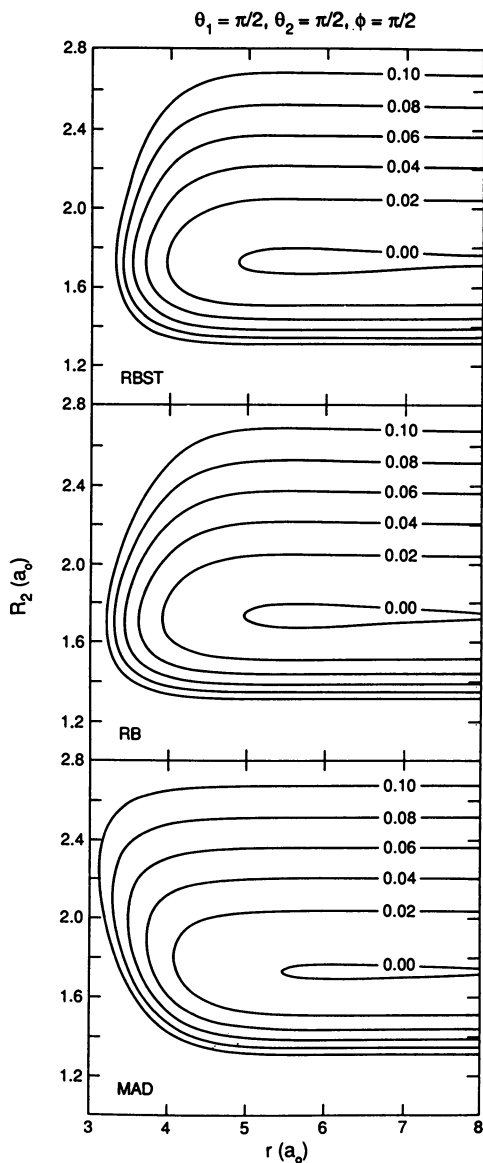


Figure 11. Same as Fig. 7 except for  $\theta_1 = \theta_2 = \phi = 90^\circ$ .

is described in detail elsewhere (6,7,22). In summary it involves expanding the scattering wave function in a set of symmetrized basis functions that are simultaneous eigenfunctions of the sum of the diatomic Hamiltonians (with eigenvalues  $\epsilon_n$ ), of the angular

momentum operators  $J_{12}^2$  (square of the vector sum of the diatomic rotational angular momenta),  $\ell^2$  [square of the orbital angular momentum of relative motion of the two molecules, with eigenvalues  $\ell_n(\ell_n+1)\hbar^2$ ],  $J^2$  (square of the total angular momentum), and  $M_J$  (the component of the total angular momentum along a space-fixed axis), and of the parity and molecular interchange operators. Denoting these symmetrized eigenfunctions by  $X_n$  we write

$$\psi_n^0(\vec{r}, \vec{R}_1, \vec{R}_2, E) = \frac{1}{r} \sum_{n=1}^N f_{nn_0}(r, E) X_n(\vec{R}_1, \vec{R}_2, \hat{r}) \quad (7)$$

where  $r$  and  $\hat{r}$  are the radial and angular parts of the intermolecular vector  $\vec{r}$ ; and  $\vec{R}_1$  and  $\vec{R}_2$  are the molecular internuclear vectors;  $n_0$  denotes the initial channel (set of quantum numbers);  $n$  denotes a general channel;  $f_{nn_0}$  is the radial wave function for relative translational motion; and  $E$  is the total energy. Substituting (1) into the time-independent Schroedinger equation yields

$$\frac{d^2}{dr^2} \underline{f}(r, E) = \underline{D}(r, E) \underline{f}(r, E) \quad (8)$$

where

$$D_{nm}(r, E) = \frac{2\mu}{\hbar^2} V_{nm}(r) + \delta_{nm} \left[ \frac{\ell_n(\ell_n+1)}{r^2} + \frac{2\mu(\epsilon_n - E)}{\hbar^2} \right] \quad (9)$$

and

$$V_{nm}(r) = \int d\vec{R}_1 d\vec{R}_2 d\hat{r} X_n^*(\vec{R}_1, \vec{R}_2, \hat{r}) V_{int}(\vec{R}_1, \vec{R}_2, r) X_m(\vec{R}_1, \vec{R}_2, \hat{r}) \quad (10)$$

The integrals (10) are calculated by evaluating the expansion coefficients of Equation (3) by

$$v_{q_1 q_2 \mu}(r, R_1, R_2) = \frac{1}{4\pi} \int_{-1}^1 \frac{d\cos\phi}{\sin\phi} \int_{-1}^1 d\cos\theta_1 \int_{-1}^1 d\cos\theta_2 y_{q_1 q_2 \mu} V_{int}(\vec{r}, \vec{R}_1, \vec{R}_2) \quad (11)$$

The integrals in (11) are evaluated by Gaussian quadrature for each



value of  $r$  for the rigid rotator calculations and for each combination of  $r$ ,  $R_1$ , and  $R_2$  for the vibrating rotator calculations. The sum in the expansion (3) is truncated at  $M$  terms, and the calculations should be converged with respect to increasing  $M$ . Having obtained this expansion the angular integrals of (10) are performed analytically. For the vibrating rotator calculations this still leaves two integrals over vibrational coordinates and these are performed numerically by an "optimal" quadrature (39), typically with 7 points per degree of freedom.

We solve Equation (8) by an invariant imbedding (8-10) procedure, in particular by the R matrix propagation (11,12) method. In this method we partition the significant range of  $r$  into about 300 sectors, we propagate the solution matrix across each sector in turn, and we match solutions at sector boundaries to construct a global solution. To make the propagation step analytic in each sector, we diagonalize  $\tilde{D}$  at each sector boundary. To avoid repeating the diagonalization step for each  $E$  for which a solution is sought, we propagate the solutions for several (typically 3-7) energies simultaneously. Then we need to calculate  $V$  and diagonalize  $D$  only once for a variable-energy sequence of calculations with a given  $J$  on a given potential energy surface.

Since the calculation of  $V$  scales as  $N^2M$  but the work involved in diagonalizing  $D$  and propagating the solution of (8) scales as  $N^3$ , the  $V$  calculation should become a negligible part of the calculation for large  $N$ . However, even for  $N > 500$ , if the number of terms in the expansion (3) of the potential is large, the  $V$  calculation may involve considerable CPU time, e.g., one to several hours on a supercomputer. The  $N^3$  steps take up to 17 hours of supercomputer time for the largest single run (a 3-energy run with  $N = 948$ ) involved in the present study. All calculations are vectorized, and production runs were carried out on Cray-1 and Cyber 205 computers.

### Rigid Rotator Calculations (14,16,23,24)

In the present overview we concentrate our attention on calculations with  $J=j_1=j_2=j_{12}=\ell=0$ .  $J$  is a conserved quantity and the final values of the other quantum numbers are denoted  $j'_1$ ,  $j'_2$ ,  $j'_{12}$ , and  $\ell'$ . We will also use the notation

$$j'_{\text{sum}} = j'_1 + j'_2 \quad (12)$$

(Do not confuse this simple sum with the magnitude  $j'_{12}$  of the vector sum.) Because the molecules are identical the final energy states are labelled by an un-ordered pair of rotational quantum numbers  $j'_1$  and  $j'_2$  (40). Since the order is not significant we use the convention  $j'_1 \leq j'_2$ . For given values of  $J$ ,  $j'_1$ , and  $j'_2$ , the quantum numbers  $\ell'$  or  $j'_{12}$  may take on all values allowed by the triangle relations. Since  $J = 0$  though,  $j'_{12} = \ell'$ . Summing the

transition probabilities over  $j'_{12}$  (or equivalently over  $\ell'$ ) yields values called  $P_{j'_1 j'_2}^R$ , and summing these over all pairs of  $j'_1 \leq j'_2$  consistent with a given value of  $j'_{\text{sum}}$  yields values called  $P_{j'_{\text{sum}}}^R$ .

The AD and RBST potentials are *defined* in terms of Equation (3) and have finite  $M$  values of 9 and 23, respectively. The BM and RB potentials must be re-expressed as in (3) — by using Equation (11) — and in these cases we converged the dynamics results with respect to increasing  $M$ , yielding the (unexpectedly large) values of 525 and 825, respectively. The calculations must also be converged with respect to increasing the number of channels  $N$ . We did this, and the final calculations involve  $N = 285$  for the AD potential and  $N = 440$  for the other potentials.

Table 1 compares  $P_{j'_{\text{sum}}}^R$  values for all four potentials at a relative translational energy,  $E_{\text{rel}}$ , of 76 meV. We see a great qualitative difference between the results for the AD potential and the others, with smaller differences between the BM, RB, and RBST potentials. Evidently the restriction  $M = 9$  is a serious limitation, greatly decreasing the rotational inelasticity, but the simplifications of the angular anisotropy in the  $M = 23$  potential are less serious.

Table 1. Rigid-rotator transition probabilities for four potentials for  $E_{\text{rel}} = 76$  meV

$j'_{\text{sum}}$	AD	BM	RB	RBST
0	0.934	0.248	0.031	0.211
1	0.004	0.025	0.077	0.055
2	0.047	0.152	0.120	0.074
3		0.105	0.030	0.082
4		0.228	0.228	0.151
5		0.051	0.119	0.141
6		0.191	0.394	0.286

Under some circumstances the rotationally anisotropy may be even further simplified for T-R energy transfer of polar molecules like HF (41). To explore this quantitatively we performed additional rigid-rotator calculations in which we retained only the spherically symmetric and dipole-dipole terms of the AD potential, which yields  $M = 3$  (see Figures 1, 3, and 4). These calculations converge more rapidly with increasing  $N$  and usually yield even less rotationally inelastic scattering. For example Table 2 compares the converged inelastic transition probabilities

Table 2. Inelastic T → R transition probabilities for full (M = 9) and truncated (M = 3) AD potentials as functions of relative translational energy

$E_{\text{rel}}$ (meV)	M = 9	M = 3
76	0.07	0.15
657	0.59	0.28
1550	0.90	0.82

$$P_{\text{inel}}^R = \sum_{j'_{\text{sum}} \neq 0} P_{j'_{\text{sum}}}^R \quad (13)$$

for the two surfaces at three energies. In comparison to the RB potential, for which  $P_{\text{inel}}^R \geq 0.97$  at all three energies, the total inelasticity is low at all energies studied for both surfaces in Table 2. Clearly the dipole-dipole term or even a small subset of low-order anisotropic terms do not account for most of the T-R energy transfer at  $J = 0$ .

The dramatic difference between the AD and the other potentials persists up to higher translational energies. For example,  $P_0^R$  for the AD potential is 0.414 at 657 meV, and the sum of  $P_0^R$ ,  $P_1^R$ , and  $P_2^R$  is 0.713 (14), whereas, for example, for the BM potential these same quantities are 0.005 and 0.035, respectively, and the three largest values of  $P_{j'_{\text{sum}}}^R$  occur for  $j'_{\text{sum}} = 12-14$  (23).

A more detailed comparison of two of the surfaces at a higher energy,  $E_{\text{rel}} = 322$  meV, is given in Table 3. This table compares

$P_{j'_{\text{sum}}}^R$  for all energetically accessible values of  $j'_{\text{sum}}$  at this energy and also twelve selected value of  $P_{j'_1 j'_2}^R$  (the transitions included are those for which  $P_{j'_1 j'_2}^R > 0.035$  for the BM potential).

We see that both  $P_{j'_{\text{sum}}}^R$  distributions peak for  $j'_{\text{sum}} = 6-9$  at this energy with a "shoulder" at  $j'_{\text{sum}} = 4-5$ . Individual transition probabilities typically, but not always, agree within a factor of two and for the most part the same individual final states have large transition probabilities for the two potentials. (Three other final states have larger probabilities for the RB potential — in particular,  $P_{22}^R = 0.055$ ,  $P_{34}^R = 0.061$ , and  $P_{26}^R = 0.073$ .)

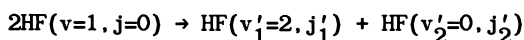
Table 3. Rigid-rotator transition probabilities for two potentials for  $E_{\text{rel}} = 322 \text{ meV}$

$j'_{\text{sum}}$	BM	RB	$j'_1$	$j'_2$	BM	RB
0	0.055	0.021	0	0	0.055	0.021
1	0.001	0.003	1	1	0.036	0.026
2	0.043	0.026	2	3	0.054	0.037
3	0.020	0.033	1	4	0.042	0.021
4	0.048	0.079	2	4	0.044	0.059
5	0.100	0.061	3	3	0.039	0.026
6	0.173	0.135	1	5	0.068	0.046
7	0.222	0.159	2	5	0.122	0.075
8	0.140	0.259	1	6	0.065	0.016
9	0.125	0.165	3	5	0.065	0.140
10	0.047	0.052	4	5	0.069	0.057
11	0.013	0.007	3	6	0.038	0.078
12	0.011	0.001				
13	0.002	0.000				
14	0.001	0.000				

Another perspective on the comparison of the BM and RB surfaces is provided in Figures 12 and 13. This figure shows quantum mechanical values (23,24) of  $P_{j'_{\text{sum}}}^R$  for both potentials and quasiclassical trajectory values (24) of  $P_{j'_{\text{sum}}}^R$  for the RB surface for two relative translational energies. The two sets of quantal results agree with each other much better than either agrees with the classical simulation. Thus, especially when we consider that the approaches used (19,21) to construct the two potentials were very different, we gain some confidence that the dynamically important features of the anisotropy of the potential are probably reasonably accurate for both analytical representations. We thus feel that it is very worthwhile to try to converge the V-V and V-V,R energy transfer probabilities for the RB potential or for the more convenient RBST modification of the RB potential.

#### Vibrating Rotator Calculations (13-16,22)

We consider the V-V,R process (1),



with total angular momentum  $J = 0$ . Therefore we again have  $j_{12} = \ell = 0$ , and we again sum over  $j'_{12}$  or  $\ell'$  for a given  $j'_{\text{sum}}$  defined by

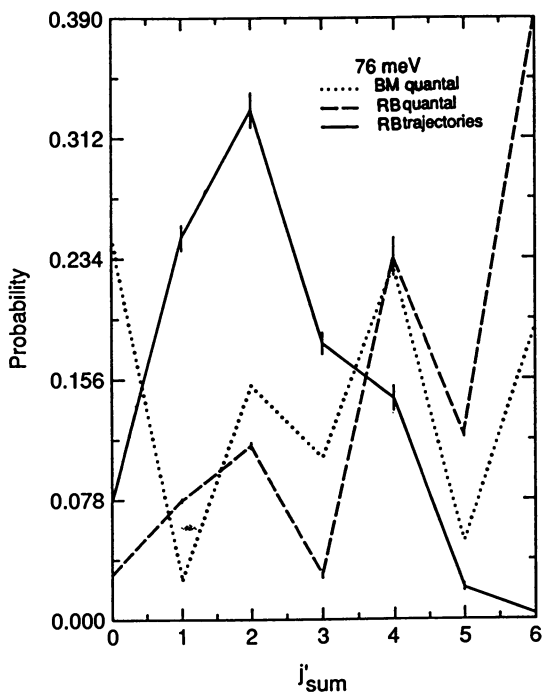


Figure 12. Rotational excitation probability  $P_{j'_{sum}}^R$  as a function of  $j'_{sum}$  for  $E_{rel} = 76$  meV.

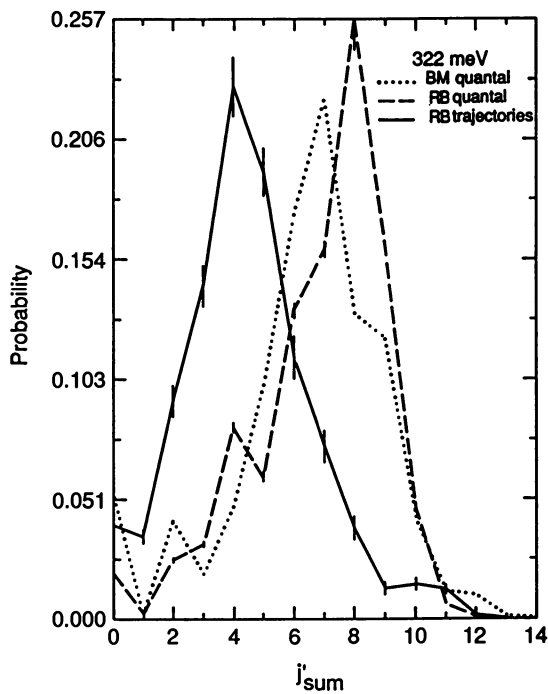


Figure 13. Same as Fig. 12 except for  $E_{\text{rel}} = 322$  meV.

Equation (12); in this case the result is called  $P_{j'_{\text{sum}}}^{\text{VV}}$ . Summing

$P_{j'_{\text{sum}}}^{\text{VV}}$  over  $j'_{\text{sum}}$  yields the total V-V,R transition probability,

which is called  $P^{\text{VV}}$ . Selected results are given in Table 4, where the rows labelled 0-7 are  $P_{j'_{\text{sum}}}^{\text{VV}}$ , and the rows labelled "sum" are

$P^{\text{VV}}$ .

The largest N for which calculations were performed for the MAD potential is 948, and comparison (15) of these calculations to others with N = 694, 824, and 880 shows that the N = 948 calculations are well converged at  $E_{\text{rel}} = 2.455$  meV and

approximately converged at 76 meV. The largest N for which calculations have been performed on the RB potential is N = 694, which is not enough for quantitative convergence, but which is adequate for a discussion of trends. [For these calculations the V matrix was not calculated as accurately as for the calculations with the MAD and RBST potentials, and the sum of Equation (3) was truncated at M = 161, but these approximations should not matter

Table 4. V-V,R energy transfer probabilities

$j'_{\text{sum}}$	N = 694			N = 948	
	MAD	RB	RBST	MAD	RBST
$E_{\text{rel}} = 2.455$ meV					
0	0.85	0.10	0.02	0.90	0.03
1	0.04	0.03	0.17	0.04	0.24
2	0.00	0.19	0.38	0.00	0.35
3 <sup>a</sup>	0.00	0.20	0.42	0.00	0.37
sum	0.89	0.42	0.99	0.94	0.99
$E_{\text{rel}} = 76$ meV					
0	0.81	0.00	0.00	0.73	0.00
1	0.05	0.01	0.05	0.03	0.05
2	0.06	0.01	0.02	0.09	0.02
3	0.01	0.01	0.05	0.01	0.05
4	0.00	0.02	0.06	0.00	0.06
5	0.00	0.02	0.06	0.00	0.06
6	0.00	0.02	0.09	0.00	0.09
7 <sup>a</sup>	0.00	0.02	0.12	0.00	0.12
sum	0.93	0.12	0.45	0.87	0.45

<sup>a</sup>Highest value allowed by conservation of total energy at this  $E_{\text{rel}}$ .

for the present qualitative discussion.] To facilitate comparison of the results for the RB potential to those for the other potentials, the latter are tabulated for both  $N = 694$  and  $N = 948$ . There are two major differences between the results for the RB and the MAD potential. The MAD potential predicts more V-V,R energy transfer, and it also predicts that the V-V,R process involves very little rotational excitation whereas the RB potential predicts a wide  $j'_{\text{sum}}$  distribution peaking for the higher energetically allowed values. We believe that the  $j'_{\text{sum}}$  distribution for the MAD potential is likely to be an artifact of the restricted rotational anisotropy of the AD potential.

Table 4 also shows that the RBST potential, despite the restriction to  $M = 23$ , predicts a broad  $j'_{\text{sum}}$  distribution similar to that obtained for the RB potential, but it predicts a higher value for the total V-V,R transition probability. It is not known at this time which potential is more accurate.

Further work is underway.

### Conclusion

The use of supercomputers has allowed us to test the sensitivity of accurate quantal molecular energy transfer probabilities in diatom-diatom collisions to the choice of potential energy surface, even at total energies great enough to allow both diatoms to be vibrationally excited.

### Acknowledgment

This work was supported in part by the National Science Foundation, the Minnesota Supercomputer Institute, and the Control Data Corporation.

### Literature Cited

1. Kondratiev, V. N.; Nikitin, E. E. Gas Phase Reactions; Springer-Verlag: Berlin, 1981.
2. Yardley, J. T. Introduction to Molecular Energy Transfer; Academic Press: New York, 1980.
3. Secret, D. In Atom-Molecule Collision Theory; Bernstein, R. B., Ed., Plenum: New York, 1979; p. 377.
4. Slater, J. C. Quantum Theory of Molecules and Solids, Vol. 1; McGraw-Hill, New York, 1963, Appendix 2.
5. Arthurs, A. M.; Dalgarno, A. Proc. Roy. Soc. Lond. Ser. A 1960, 256, 540.
6. Davison, W. D. Discussions Faraday Soc. 1962, 33, 71.
7. Green, S. J. Chem. Phys. 1975, 62, 2271.
8. Bellman, R.; Kalaba, R. Proc. Natl. Acad. Sci. 1956, 42, 629.
9. Bellman, R.; Kalaba, R.; Wing, G. M. J. Math. Phys. 1960, 1, 280.
10. Bellman, R.; Kalaba, R.; Wing, G. M. Proc. Natl. Acad. Sci. 1960, 46, 1646.
11. Light, J. C.; Walker, R. B. J. Chem. Phys. 1976, 65, 4272.



## 11. SCHWENKE & TRUHLAR *Vibrational & Rotational Energy Transfer* 199

12. Truhlar, D. G.; Harvey, N. M.; Onda, K.; Brandt, M. A. In: Algorithms and Computer Codes for Atomic and Molecular Quantum Scattering Theory, Vol. 1; Lawrence Berkeley Laboratory: Berkeley, 1979, p. 220.
13. Schwenke, D. W.; Truhlar, D. G. Theor. Chim. Acta 1986, **69**, 175.
14. Schwenke, D. W.; Truhlar, D. G. In: Supercomputer Simulations in Chemistry, Dupuis, M., Ed. Springer-Verlag: Berlin, 1986, p. 165.
15. Schwenke, D. W.; Truhlar, D. G. Theor. Chim. Acta, in press.
16. Schwenke, D. W.; Truhlar, D. G. unpublished.
17. Alexander, M. H.; DePristo, A. E. J. Chem. Phys. 1976, **65**, 5009.
18. Poulsen, L. L.; Billing, G. D.; Steinfeld, J. I. J. Chem. Phys. 1978, **68**, 5121.
19. Brobjer, J. T.; Murrell, J. N. Mol. Phys. 1983, **50**, 885.
20. Cournoyer, M. E.; Jorgensen, W. L. Mol. Phys. 1984, **51**, 119.
21. Redmon, M. J.; Binkley, J. S., J. Chem. Phys., in press.
22. Schwenke, D. W.; Truhlar, D. G. In: Supercomputer Applications, Numrich, R. W., Ed. Plenum: New York, 1985, p. 295.
23. Schwenke, D. W.; Truhlar, D. G. J. Comp. Chem., in press.
24. Schwenke, D. W.; Truhlar, D. G.; Coltrin, M. E. J. Chem. Phys., in press.
25. Poulsen, L. L.; Billing, G. D. Chem. Phys. 1979, **36**, 271.
26. Poulsen, L. L.; Billing, G. D. Chem. Phys. 1980, **46**, 287.
27. Poulsen, L. L.; Billing, G. D. Chem. Phys. 1980, **53**, 389.
28. Coltrin, M. E.; Marcus, R. A. J. Chem. Phys. 1980, **73**, 2179.
29. Coltrin, M. E.; Koszykowski, M. L.; Marcus, R. A. J. Chem. Phys. 1980, **73**, 3643.
30. Coltrin, M. E.; Marcus, R. A. J. Chem. Phys. 1980, **73**, 4390.
31. Coltrin, M. E.; Marcus, R. A. J. Chem. Phys. 1982, **76**, 2379.
32. Sileo, R. N.; Cool, T. A. J. Chem. Phys. 1976, **65**, 117.
33. Maillard, D.; Silvi, B. Mol. Phys. 1980, **40**, 933.
34. Kollman, P. A. In Chemical Applications of Atomic and Molecular Electrostatic Potentials; Truhlar, D. G., Ed. Plenum Press: New York, 1981, p. 243.
35. Gianturco, F. A.; Lamanna, U. T.; Battaglia, F. Int. J. Quantum Chem. 1981, **19**, 217.
36. Truhlar, D. G.; Brown, F. B.; Schwenke, D. W.; Steckler, R.; Garrett, B. C. In Comparison of Ab Initio Quantum Chemistry with Experiment for Small Molecules, Bartlett, R. B., Ed. Reidel: Dordrecht, Holland, 1985, p. 95.
37. Hancock, G. C.; Rejto, P.; Steckler, R.; Brown, F. B.; Schwenke, D. W.; and Truhlar, D. G. J. Chem. Phys. 1985, **85**, 4997.
38. Hancock, G. C.; Truhlar, D. G.; Dykstra, C. E., to be published.
39. Schwenke, D. W.; Truhlar, D. G. Computer Phys. Commun. 1984, **34**, 57.
40. Alexander, M. H.; DePristo, A. E. J. Chem. Phys. 1977, **66**, 2166.
41. Alexander, M. H. J. Chem. Phys. 1980, **73**, 5135.

RECEIVED June 15, 1987

## Chapter 12

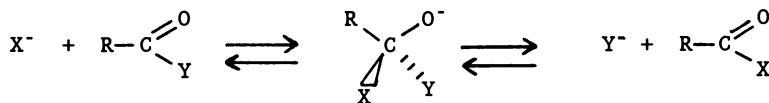
# Computational Investigations of Organic Reaction Mechanisms

William L. Jorgensen, James F. Blake, Jeffry D. Madura<sup>1</sup>, and Scott D. Wierschke

Department of Chemistry, Purdue University, West Lafayette, IN 47907

Ab initio molecular orbital calculations are being used to study the reactions of anionic nucleophiles with carbonyl compounds in the gas phase. A rich variety of energy surfaces is found as shown here for reactions of hydroxide ion with methyl formate and formaldehyde, chloride ion with formyl and acetyl chloride, and fluoride ion with formyl fluoride. Extension of these investigations to determine the influence of solvation on the energy profiles is also underway; the statistical mechanics approach is outlined and illustrated by results from Monte Carlo simulations for the addition of hydroxide ion to formaldehyde in water.

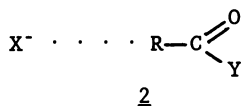
The importance of displacement reactions on carbonyl compounds in chemistry and biochemistry has resulted in numerous mechanistic studies. In solution, there is general acceptance of the following mechanism for addition of anionic nucleophiles which features a tetrahedral intermediate, 1, and is designated B<sub>AC</sub><sup>2</sup> (1). However, recent experimental (2-10) and theoretical (11-17)



studies have found the situation in the gas phase to be intriguingly complex with the possibility of the tetrahedral species as a transition state, the intervention of ion-dipole complexes, 2, as intermediates, and energy profiles featuring one,

<sup>1</sup>Current address: Department of Chemistry, University of Houston, Houston, TX 77004

0097-6156/87/0353-0200\$06.00/0  
© 1987 American Chemical Society

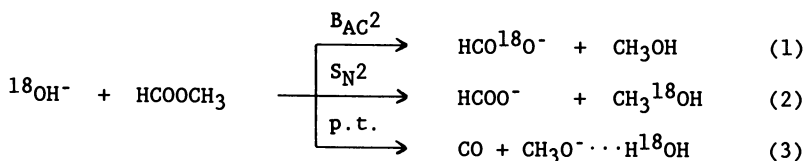


two or three minima. The gas-phase displacement reactions may also be accompanied by competing proton transfer and  $S_N2$  (bimolecular substitution) processes that are not observed in solution. These results have, in turn, led to doubts about the universality of the traditional  $B_{AC}2$  mechanism in condensed phases and have raised many questions concerning the energy surfaces for the reactions in the gas phase, in solution, and in biomolecular environments (12).

The contribution of modern theoretical methods to elucidating organic reaction mechanisms includes the ability of ab initio molecular orbital calculations to provide quantitative characterization of the gas-phase energy surfaces and of the structures of any intermediates and transition states. For the reactions of carbonyl compounds with anions, the size of the systems, their anionic nature, and the need for extensive geometry optimizations make reliable calculations taxing on computer resources. Nevertheless, the availability of supercomputers such as the Cyber 205 at Purdue and superminicomputers such as the Gould 32/8750 in our laboratory now allow significant progress in this area. Some recent results are reviewed here that show the utility of the methodology as well as the variety of energy surfaces and reaction paths that may occur for even relatively simple systems; specifically, the reactions that are considered are for hydroxide ion with methyl formate and formaldehyde, chloride ion with formyl and acetyl chloride, and fluoride ion with formyl fluoride. In addition, the effect of solvation on the gas-phase energy surfaces is beginning to be studied via Monte Carlo statistical mechanics and molecular dynamics calculations for the reacting system surrounded by hundreds of solvent molecules (18). Our initial efforts along these lines on the  $S_N2$  reaction of  $Cl^- + CH_3Cl$  were only made practical by the advent of the Cyber 205 at Purdue in 1983 (19). More recent results (11) on the reaction of  $OH^- + H_2C=O$  in water are also summarized in the following and illustrate the details that are now accessible on the variation of solvation along reaction paths, the origin of solvent-induced activation barriers, and the location of transition states in solution.

### Energy Surfaces from the Ab Initio Calculations

(a)  $OH^- + HCOOCH_3$ . The reactions of hydroxide ion with methyl formate have been studied by several groups in the gas phase and nicely illustrate the variety of available reaction paths (2,9,10). Flowing afterglow experiments found the following  $B_{AC}2$ ,  $S_N2$ , and proton transfer pathways to account for 34%, 5% and 61% of the product distribution, respectively (9). These interesting results leave open numerous questions about the corresponding energy surfaces that we set out to explore with ab initio molecular orbital calculations.



The computations were carried out with the GAUSSIAN/82 program (20) and the split-valence 4-31+G basis set which includes a set of diffuse s and p orbitals on all atoms except hydrogen (21). Diffuse functions are well-known to be important for describing the electronic structure of anions containing first-row elements (21-23). The 4-31+G basis set was also chosen because it has been found to yield excellent proton affinities for organic anions (21). Furthermore, the computed energetics for the three reaction channels are in acceptable accord with experimental data. Specifically, the 4-31+G  $\Delta E$ 's for reactions 1 and 3 are -43.3 and -19.1 kcal/mol, while the experimental enthalpy changes are -44.0 and -27.6 kcal/mol (10,24). For comparison, the  $\Delta E$  for reaction 1 computed with the 4-31G basis set is -62.9 kcal/mol (16). Clearly, the diffuse functions preferentially improve the description of the charge localized hydroxide ion. It may also be noted that the 4-31+G dissociation energy for the methoxide-water complex from the Riveros reaction (3) is 28.4 kcal/mol which compares well with the latest experimental  $\Delta H$  of 23.9 kcal/mol (24). The relatively greater importance of the diffuse atomic orbitals than correlation energy or zero-point effects in this context has been discussed elsewhere (22).

The key structural and energetic results for the three reactions are summarized in Figures 1-3. For the  $\text{B}_{\text{AC}}2$  process, the tetrahedral species, 3, in Figure 1 was found to be an energy minimum with no symmetry constraints. The illustrated conformer with the hydroxyl hydrogen eclipsing the alkoxy oxygen was previously shown to be the lowest energy form at the 4-31G level (16). With the 4-31+G calculations, it is 31.1 kcal/mol lower in energy than the reactants. This species may rearrange to the formate-methanol complex, 6, shown at the bottom of Figure 2 which is 30.1 kcal/mol lower in energy than 3 and 17.8 kcal/mol below the separated products,  $\text{HCOO}^- + \text{CH}_3\text{OH}$ . The hydrogen-bond enthalpy for the formate-methanol complex has also been determined experimentally as 17.6 kcal/mol (24). Though an ion-dipole complex like 2 was sought preceding 3, none was found as an energy minimum with the 4-31+G calculations. However, a transition state was located by gradient methods for the elimination of methanol from 3 on the way to 6; it is labelled TS in Figure 1 and is 10.4 kcal/mol higher in energy than 3. The hydroxyl hydrogen has rotated in this structure to help form the incipient O-H bond of methanol and the C-OCH<sub>3</sub> bond has lengthened from 1.48 to 2.00 Å. Thus, the reaction profile for the  $\text{B}_{\text{AC}}2$  reaction 1 has a double-well form with 3 and 6 as intermediates separated by the transition state for the elimination. The existence of 3 as an energy minimum is consistent with lower-level theoretical results (15,16) and recent observations of proton exchange in such

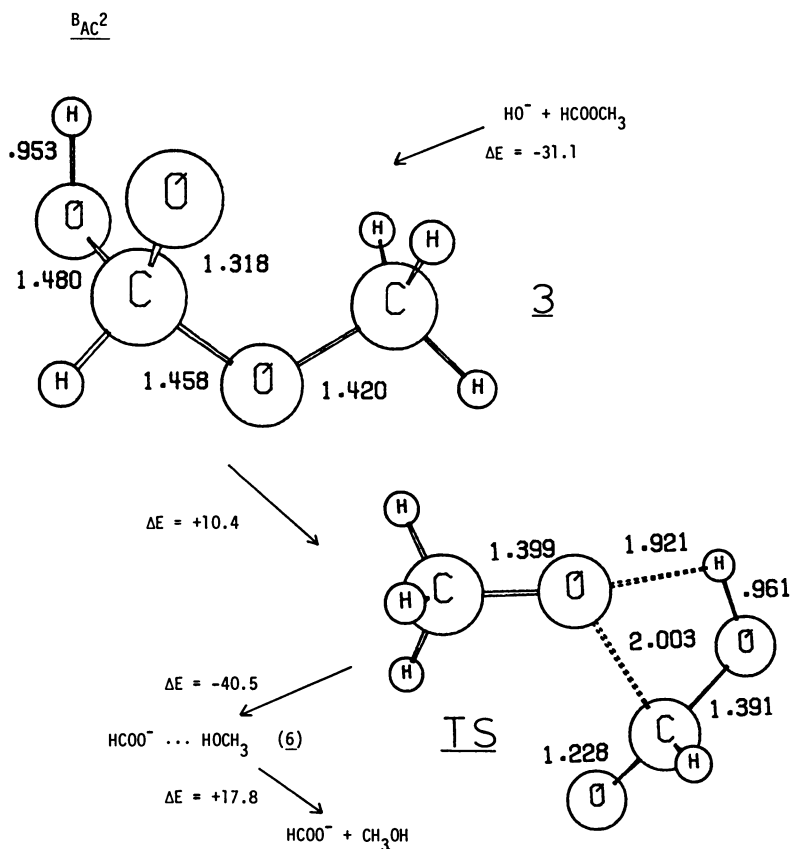


Figure 1. 4-31+G results for reaction 1. Energies in kcal/mol and lengths in angstroms throughout.

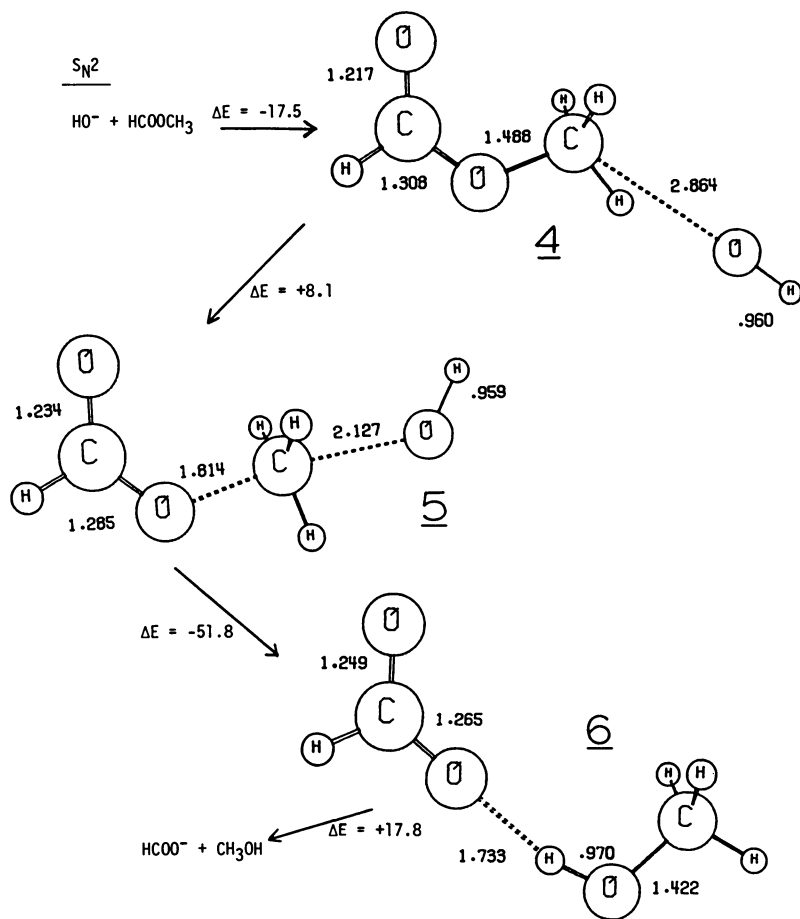


Figure 2. 4-31+G results for reaction 2.

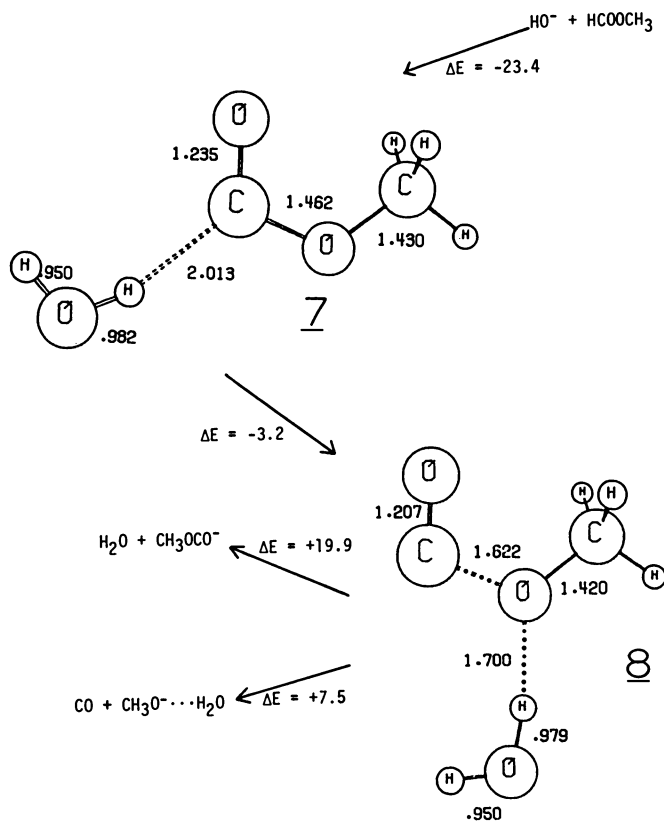
Proton Transfer

Figure 3. 4-31+G results for reaction 3.

intermediates (25), though it contrasts the interpretation of some earlier experimental findings (2c).

The  $S_N2$  reaction was studied in  $C_s$  symmetry and found to have the double-well form typical of gas-phase  $S_N2$  reactions (19,25,27), as summarized in Figure 2. The initial ion-dipole complex 4 is 17.5 kcal/mol below the energy of the reactants. The transition state 5 was located with gradient methods, 8.1 kcal/mol above 4, but still 9.4 kcal/mol below the reactants. Rearrangement of 5 to the exit complex, 6, is then accompanied by release of 51.8 kcal/mol. Separation to the products,  $HCOO^- + CH_3OH$ , requires 17.8 kcal/mol, as discussed above, and yields the overall 4-31+G  $\Delta E$  of -43.3 kcal/mol. These energetic results are all similar to our previous ab initio findings for the  $S_N2$  reaction of  $HO^- + CH_3Cl$  (27); however, the bent arrangement of the nucleophilic, electrophilic and leaving atoms in 4 is unusual.

The proton transfer process was also studied in  $C_s$  symmetry as summarized in Figure 3. The proton transfer occurred spontaneously as the geometry optimization brought the reactants together to yield the water-acyl anion complex, 7. Upon flipping the far hydrogen of water, further optimization yielded 8 which may be called the "Riveros complex" and is 26.6 kcal/mol lower in energy than the reactants. The complex may be viewed as hydrated methoxide ion coordinated with carbon monoxide. Loss of CO to yield  $CH_3O^- \cdots H_2O$  requires only 7.5 kcal/mol, whereas loss of water to give the methyl formyl anion requires 19.9 kcal/mol. Overall, these results suggest that the Riveros reaction (3) has a single-well energy surface with the interesting structure 8 as the only intermediate.

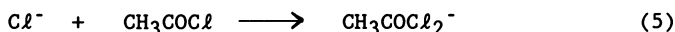
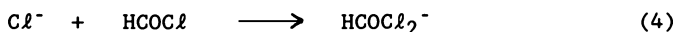
In summary, the 4-31+G calculations find the energy surfaces for the three observed reactions to all contain significantly stabilized intermediates whose structures and relative energies have been characterized. The formate-methanol complex 6 is the global energy minimum, 61 kcal/mol lower in energy than the reactants. It is accessible through both the  $S_N2$  and  $B_{AC}2$  channels. The transition states for these processes have also been located and are significantly lower in energy than the reactants. Thus, none of the reactions has a net positive activation energy which is consistent with their observed facility (2,9,10).

(b)  $Cl^- + HCOCl$  and  $Cl^- + CH_3COCl$ . Asubiojo and Brauman made the provocative proposal that the gas-phase displacement reactions of nucleophiles including halide ions with acyl halides have double-well energy surfaces; the intermediates were suggested to be ion-dipole complexes and the tetrahedral species was likely to be a transition state (4). In order to address this proposal, we expanded our study of substitution reactions to the degenerate exchange reactions of chloride ion with formyl and acetyl chloride, and of fluoride ion with formyl fluoride (12). Key issues are the number of minima on the energy surfaces and the structures of any intermediates and transition states. Han and Brauman also recently extended their ICR investigations of  $Cl^-$  with  $CF_3COCl$  and  $CH_3OCOC$  (5). They were able to show through labeling studies that the two chlorines in the adducts are non-equivalent which supports the double-well picture and the probable



existence of a tetravalent species as a transition state (5). At the same time, Howard and Kollman have carried out a related ab initio study of the reaction of HS<sup>-</sup> and formamide (14). In contrast to their results for HO<sup>-</sup> with formamide (13), an ion-dipole complex rather than the tetrahedral adduct was found as an energy minimum.

The geometry optimizations for reactions 4 and 5 were primarily carried out with the 3-21+G basis set (23). This alternative typically gives results similar to 4-31+G, but it is



notably faster for the gradient calculations which is particularly desirable given the five non-hydrogen atoms in reaction 5. Nevertheless, the effect of basis set extension for the stationary points in reaction 4 was shown to be slight through optimizations with the 6-31+G(d) basis set (12).

The 3-21+G results turned out to be fascinating. The energy surfaces for reactions 4 and 5 indeed have the double-well form. The ion-dipole complex, 9, shown in Figure 4 is the only minimum for reaction 4 and the tetrahedral adduct, 10, is a transition state. Computation of the vibrational frequencies for 9 and 10 unequivocally established these designations. As shown in Figure 5, 9 and 10 are calculated to be 21.7 and 7.1 kcal/mol below the energy of the reactants at the 3-21+G level. More surprisingly, further search for another tetravalent species found the planar adduct 11 with C<sub>2v</sub> symmetry (Figure 6) as a second transition state, again verified by the vibrational analyses. In fact, 11 is 1.6 kcal/mol lower in energy than 10; the two structures sit on a ridge between the reactants and products and were found to be separated by a barrier of only 0.7 kcal/mol (12). The valleys to 10 and 11 both emanate from the ion-dipole complex 9 and are illustrated by the structures in Figures 4 and 6, and by the energy profiles in Figure 5.

However, the structure for 11 is unusual with long C-Cl bond lengths of 2.62 Å as opposed to 2.24 Å for 10. This suggests that the more compact structure 10 might become relatively more favorable when electron correlation is included. Consequently, Møller-Plesset perturbation theory to third-order was used to compute the correlation energies with the 6-31+G(d) basis set on the 3-21+G optimized geometries for the stationary points in reaction 4. In the standard notation (23), these calculations are designated MP3/MP2/6-31+G(d)//3-21+G. The effects on the energetics for the pathway leading to the tetrahedral adduct 10 with C<sub>s</sub> symmetry are not great; 9 and 10 are now 16.7 and 1.4 kcal/mol below the reactants. However, the C<sub>2v</sub> structure 11 is differentially destabilized so that it is 11.6 kcal/mol above 10 and is undoubtedly no longer a transition state. Nevertheless, the barrier to inversion of 10 through 11 is remarkably low.

Though it could be argued that a planar structure analogous to 11 for acetyl chloride would be disfavored by steric crowding between the chlorines and the methyl group, this was not found to

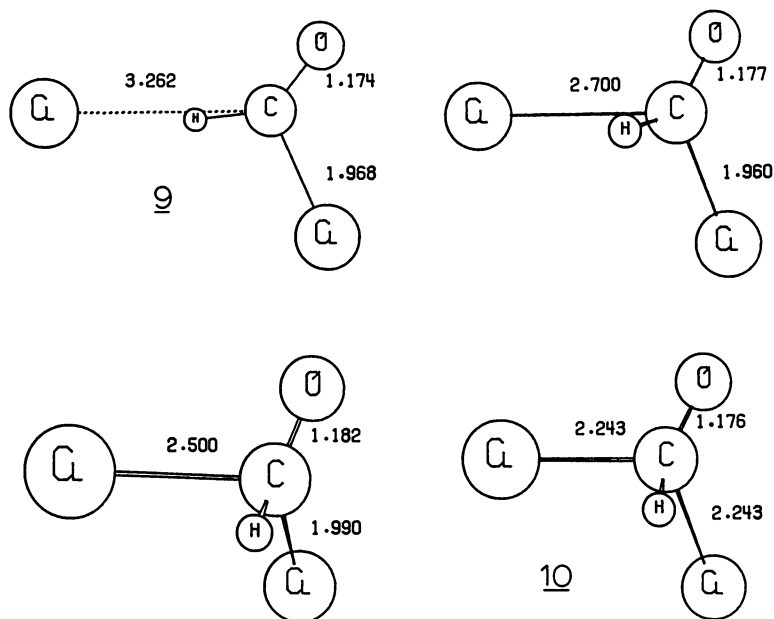


Figure 4. 3-21+G optimized structures along the reaction path to the tetrahedral transition state, 10.

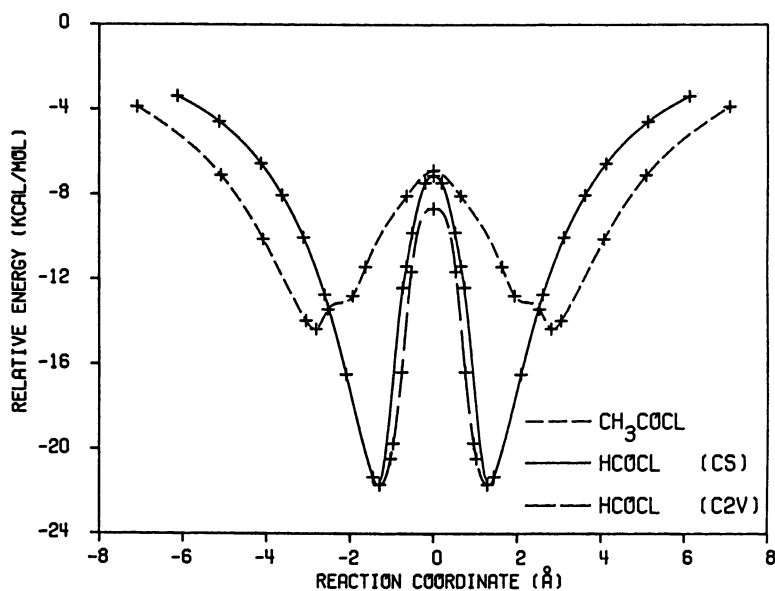


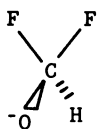
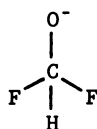
Figure 5. 3-21+G energy profiles for reactions 4 and 5. The reaction coordinate is defined as the difference in the two C-Cl distances.

be a dominant effect with the 3-21+G calculations. Instead adduct 13 in Figure 7 was found to be the only transition state; it is 5.2 kcal/mol lower in energy than a structure analogous to 10 with a CCO angle of 140°. The reason for the increased preference for the C<sub>2v</sub>-like structure can be attributed to the substantial positive charge on the carbonyl carbon that is apparent from population analyses. Thus, the R-C=O fragment in 11 and 13 has significant acyl cation character that is stabilized by the methyl substituent.

The 3-21+G reaction path to 13 is illustrated in Figure 7 and involves the intermediacy of the ion-dipole complex 12. As shown in Figure 5, the well-depth for 12 is reduced to 14.3 kcal/mol since the chloride ion is kept by the methyl group about 1.5 Å farther from the carbonyl carbon than in 9. This interaction energy for Cl<sup>-</sup>...CH<sub>3</sub>COC=O compares favorably with the value of 11 kcal/mol estimated by Asubiojo and Brauman from their ICR experiments (4).

Of course, the long C-Cl bonds in 13 again suggest that electron correlation should significantly affect the results. Assuming the effects are quantitatively similar to those for reaction 4, the tetrahedral transition state would end up about 8 kcal/mol lower in energy than 13 and roughly 4 kcal/mol above the energy of the reactants. Asubiojo and Brauman also addressed this point. Though they could explain the observed efficiency for reaction 5 through RRKM calculations in which the transition state is ca. 7 kcal/mol below the energy of the reactants, a resultant problem is an implied, unreasonably high electron affinity for CH<sub>3</sub>CCl<sub>2</sub>O radical (4). The higher energy for the transition state suggested here would help alleviate the latter dilemma.

(c) F<sup>-</sup> + HCOF. The reaction of fluoride ion with formyl fluoride was also studied with 3-21+G calculations for comparison. Briefly, this system is found to have the triple-well energy profile shown in Figure 8. Two equivalent ion-dipole complexes analogous to 9 now flank the tetrahedral intermediate, 14, which is also an energy minimum. In this case, inversion through the

1415

planar form 15 is highly unfavorable with 15 as a maximum 40 kcal/mol above 14. The required stretching of the C-F bonds is far more costly in energy than for the weaker C-Cl bonds in 11.

Taking all of these results together, some general patterns emerge. Foremost, the tetrahedral adducts 1 are found to be energy minima when the substituents X and Y are both first-row elements. However, when X and Y are both second-row elements, the tetrahedral species is a transition state and the only minima are ion-dipole complexes, 2. Clearly, two key factors in the formation of the tetrahedral adduct 1 are the difference in gas-phase basicities for the two anions (X<sup>-</sup> and 1) and the difference

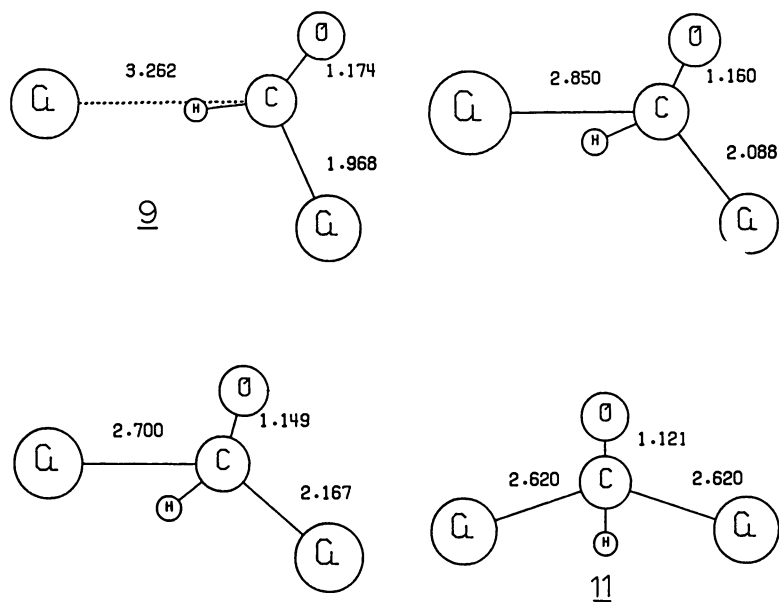


Figure 6. 3-21+G optimized structures along the reaction path leading to the  $C_{2v}$  transition state, 11.

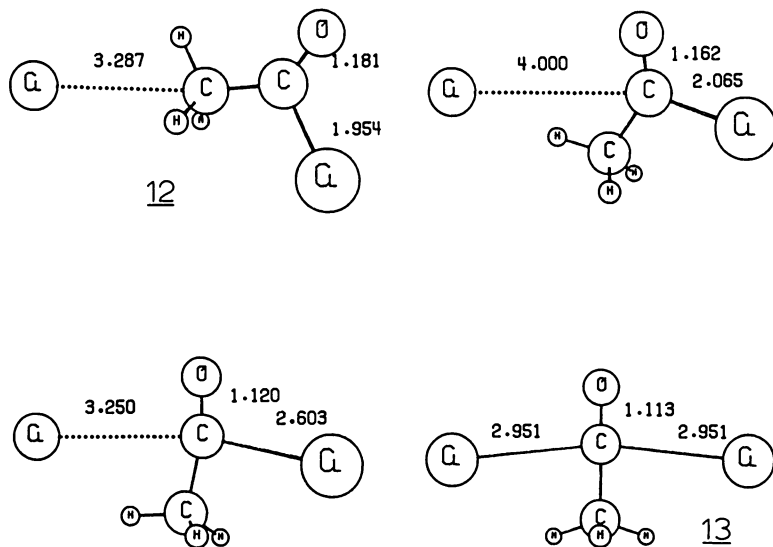


Figure 7. 3-21+G optimized structures along the reaction path for reaction 5.

in bond energies between a C-O  $\pi$ -bond and a C-X single bond. The former is remarkably strong at about 90 kcal/mol (28), while some C-X single bond energies are for X = N (69-75), O (85-91), F (116), S (66), Cl (79), Br (66), and I (52). Furthermore, since thiolate, chloride, bromide, and iodide ions are much weaker bases in the gas phase than alkoxides (29), these nucleophiles should all favor ion-dipole complexation over formation of tetrahedral adducts for most acyl electrophiles including acid halides, amides, and esters. Thus, the tetrahedral adduct will often not be an energy minimum in these cases. In contrast, C-F bonds are unusually strong and fluoride ion is comparable in basicity to alkoxides in the gas phase (29). Therefore, formation of the tetrahedral adduct should be favored by fluoride as the nucleophile and single or triple-well energy surfaces can be expected. Similar analyses propose that less stable alkoxides and OH<sup>-</sup> should yield tetrahedral intermediates with acyl electrophiles, while stabilized alkoxides may prefer ion-dipole complexation. These notions are fully supported by the theoretical and experimental results reviewed here, and provide a rich variety of energy surfaces for nucleophilic reactions with acyl electrophiles in the gas phase.

#### The Effect of Hydration on the Reaction of OH<sup>-</sup> + H<sub>2</sub>C=O

The importance of solvation on reaction surfaces is evident in striking medium dependence of reaction rates, particularly for polar reactions, and in variations of product distributions as for methyl formate discussed above and of relative reactivities (18,26). Thus, in order to obtain a molecular level understanding of the influence of solvation on the energetics and courses of reactions, we have carried out statistical mechanics simulations that have yielded free energy of activation profiles (30) for several organic reactions in solution (11,18,19,31).

The computational procedure typically involves three main steps. First, the minimum energy reaction path is determined for the gas phase using ab initio calculations. The energetic and geometric variations along the reaction path are then fit to continuous functions of the reaction coordinate. Then, intermolecular potential functions are obtained to describe the interactions between the reacting system and a solvent molecule. These usually vary with the reaction coordinate and are represented through Coulomb and Lennard-Jones interactions between sites normally situated on the atoms. For aqueous solutions, the solute-water potential functions are derived from numerous ab initio results for complexes of the reacting system and a water molecule, while the water-water interactions are described by the well-proven TIP4P model (32). Finally, with analytical descriptions of the gas-phase reaction path and of the intermolecular potential functions, Monte Carlo simulations are carried out to calculate the free energy profile for the reaction path in solution. Actually a series of simulations are needed with "importance sampling" to cover the full range of the reaction coordinate (18). The quantity that is ultimately computed is the probability of occurrence,  $g(r_c)$ , of each value of the reaction

coordinate,  $r_c$ . In turn, this is related to the free energy change along the reaction coordinate or "potential of mean force" by  $w(r_c) = -k_B T \ln g(r_c) + \text{const.}$  Besides the thermodynamic results, the simulations also yield a detailed view of the structural and energetic changes in solvation along the reaction path. It should be emphasized that we have only been computing the effects of solvation on the gas-phase reaction paths; changes in mechanism in solution are not provided for so far.

After the initial work on  $S_N2$  reactions, the methodology was applied to the addition of hydroxide ion to formaldehyde. The ab initio calculations for the gas-phase MERP and the potential functions were all carried out with the 6-31+G(d) basis set (11). As illustrated in Figure 9, the approach at large separation is coplanar with the hydroxide ion on the dipole axis of formaldehyde. An apparent ion-dipole minimum occurs at a C-O separation of 2.74 Å with a binding energy of 19 kcal/mol, as shown by the solid curve in the lower part of Figure 10. However, an activation energy of only 1 kcal/mol is needed to reach the transition state with  $r(\text{C-O}) = 2.39$  Å at which point the hydroxyl fragment has lifted out of the plane to assume the more tetrahedral, final approach. The energy change is then rapid as covalent bonding sets in between the transition state and the tetrahedral product at  $r(\text{CO}) = 1.47$  Å. The overall energy change for the reaction is calculated to be -35.2 kcal/mol. The existence of the ion-dipole minimum is clearly tentative and may not survive further increases in the level of theory. Thus, the energy surface could be a single-well, though the approach has two stages dominated respectively by ion-dipole and covalent forces separated near 2.5 Å.

A second trajectory was also studied as indicated by the dashed curves in Figure 10. In this case, the OCO angle was fixed at its value of 127° at the transition state for all separations beyond  $r(\text{CO}) = 2.39$  Å. The more tetrahedral approach corresponds to traditional ideas about approach vectors in addition reactions (33). The ion-dipole minimum no longer occurs for this trajectory, though the energy surface has a relatively flat region between  $r(\text{CO}) = 1.9$  and 2.4 Å.

The Monte Carlo calculations were subsequently executed for the reacting system surrounded by 269 TIP4P water molecules in a rectangular box with periodic boundary conditions at 25°C and 1 atm. The details are reported elsewhere (11), though the key results are in the top part of Figure 10. The free energy curves for the two trajectories in water rise only gradually from the reactants to  $r(\text{CO}) = \text{ca. } 3$  Å. Loss in hydroxide-water interactions is largely offset by increase in the ion-formaldehyde attraction in this region. Then, the charge delocalization sets in, while the gas-phase energy is relatively constant between 2 and 3 Å. Consequently, the weakening solvation is no longer balanced and the free energy of activation curves rise rapidly to the transition state which is predicted to occur at  $r(\text{CO}) = 2.05$  Å. From there, the gas-phase energy descends quickly to the tetrahedral adduct and the potential of mean force follows suit. It is also notable that no evidence is found for any intermediates other than the product in water, and that the activation barrier

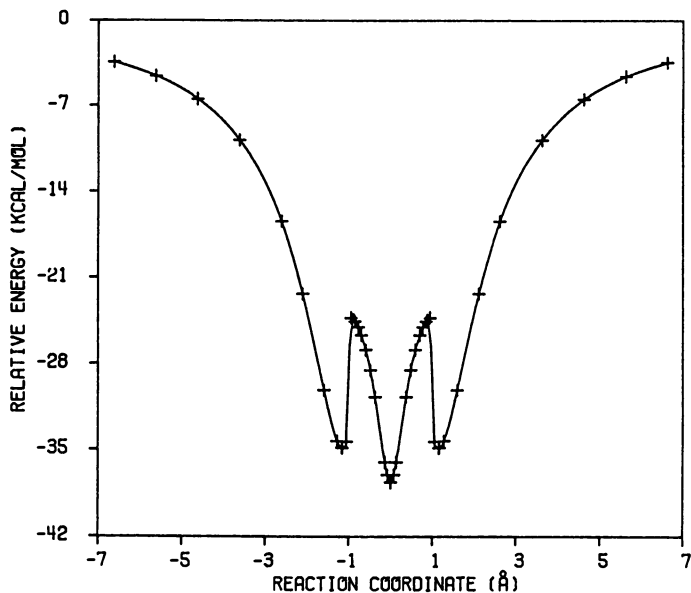


Figure 8. 3-21+G energy profile for the reaction of  $F^- + HCOF$ . The reaction coordinate is the difference in the two C-F distances.

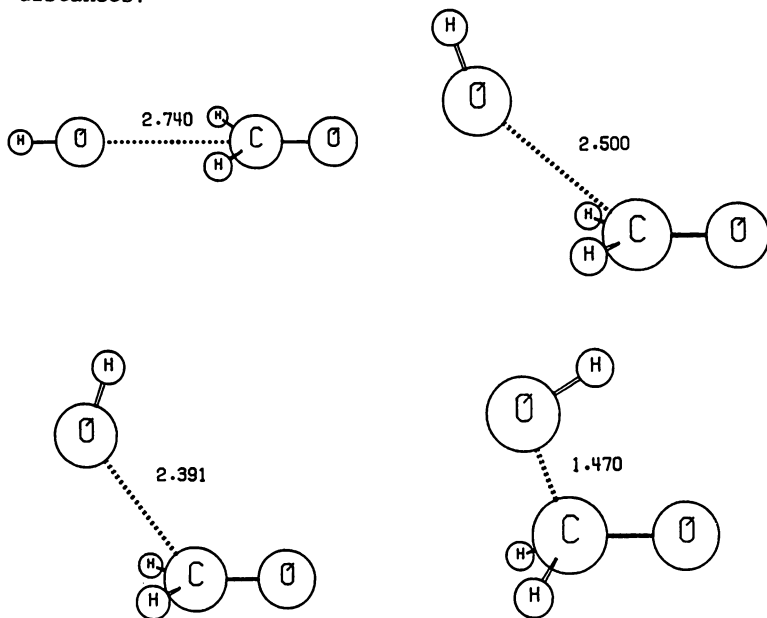


Figure 9. 6-31+G(d) optimized structures along the reaction path for the reaction of  $OH^- + H_2C=O$ .

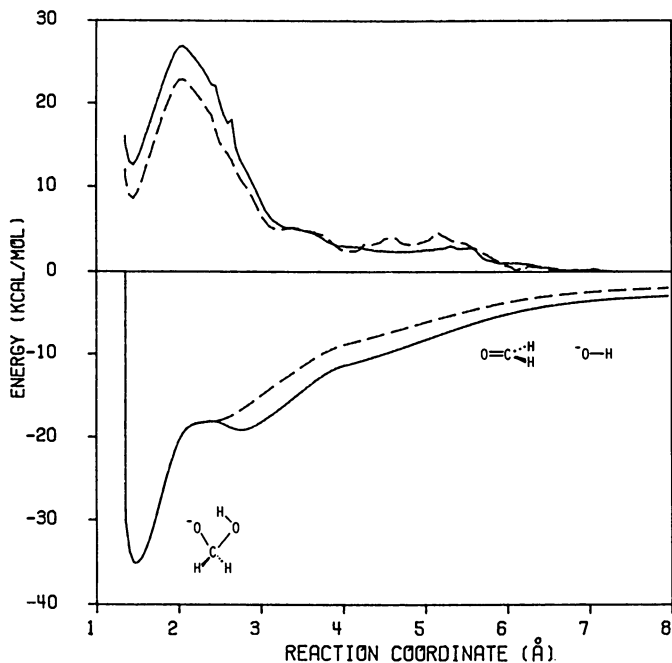


Figure 10. Calculated potential energies in the gas phase (bottom) and potentials of mean force in aqueous solution (top) for the  $A_d_N$  reaction of  $OH^- + H_2C=O$ . Solid lines represent the collinear MERP with  $C_s$  symmetry in the gas phase, while the dashed lines are for a more perpendicular initial approach. The reaction coordinate is the C-O<sub>H</sub> distance.



for the addition reaction is entirely solvent-induced. The solvent effects are clearly profound; the origin of the barrier was carefully studied and is attributable to the weakening of hydrogen bonds to the substrates that accompanies the charge delocalization inside  $r(\text{CO}) = 3 \text{ \AA}$ . The average number of strong hydrogen bonds is constant at 6-7 along the entire reaction path; however, the average water-ion interaction weakens from ca. 20 kcal/mol for the hydroxide ion to 13 kcal/mol for the product (11).

The energetic results are similar to experimental data of Guthrie (34) and the theoretical predictions of Weiner *et al.* (13) for alkaline hydrolyses of amides. For their systems, the activation energy for the addition step is about 22 kcal/mol and the tetrahedral intermediate is 9-18 kcal/mol above the reactants. Ester hydrolyses are typically more facile with activation energies of 15-20 kcal/mol (34). The combined quantum and molecular mechanics approach of Weiner *et al.* also led to a predicted CO distance of about 2.0 Å in the aqueous transition state for the addition of  $\text{OH}^-$  to formamide. Thus, the transition states for these endoergic processes are geometrically very product-like. For formaldehyde, the computed endoergicity overestimates the available experimental data by ca. 15 kcal/mol (34); the computed result is more in line with data for ketones, where formation of hydrates is less favorable. The discrepancy likely comes from overly exothermic hydration of the hydroxide ion which lowers the reactant end of the free energy curves. This results from use of two-body potential functions that do not adequately treat polarization. Nevertheless, the feasibility of performing such calculations in solution has been established and the insights on the variation in solvation along the reaction path are most likely valid, though somewhat amplified. Overall, an exciting period has clearly been entered in which theoretical calculations can provide extreme details on the course of organic reactions both in the gas phase and in solution.

#### Acknowledgments

Gratitude is expressed to the National Science Foundation and National Institutes of Health for support of our research programs.

#### Literature Cited

1. March, J. Advanced Organic Chemistry; Wiley: New York, 1985; Chapters 10 and 16.
2. (a) Faigle, J. F. G.; Isolani, P.C.; Riveros, J. M. J. Am. Chem. Soc. 1976, **98**, 2049. (b) Takashima, K.; Riveros, J. M. ibid. 1978, **100**, 6128. (c) Takashima, K.; Jose, S. M.; do Amaral, A. T.; Riveros, J. M. J. Chem. Soc. Chem Commun. 1983, 1255.
3. Comisarow, M. Can. J. Chem. 1977, **55**, 171.
4. Asubiojo, O. I.; Brauman, J. I. J. Am. Chem. Soc. 1979, **101**, 3715.
5. Han, C.-C.; Brauman, J. I. J. Am. Chem. Soc. 1987, **109**, 589.

6. Fukuda, E. K.; McIver, R. T., Jr. J. Am. Chem. Soc. 1979, 101, 2498.
7. Bartmess, J. E.; Hays, R. L.; Caldwell, G. J. Am. Chem. Soc. 1981, 103, 1338.
8. McDonald, R. N.; Chowdhury, A. K. J. Am. Chem. Soc. 1982, 104, 901.
9. DePuy, C. H.; Della, E. W.; Filley, J.; Grabowski, J. J.; Bierbaum, V. M. J. Am. Chem. Soc. 1983, 105, 2481.
10. Johlman, C. L.; Wilkins, C. L. J. Am. Chem. Soc. 1985, 107, 327.
11. Madura, J. D.; Jorgensen, W. L. J. Am. Chem. Soc. 1986, 108, 2517.
12. Blake, J. F.; Jorgensen, W. L. J. Am. Chem. Soc. 1987, 109, 0000.
13. Weiner, S. J.; Singh, U. C.; Kollman, P. A. J. Am. Chem. Soc. 1985, 107, 2219.
14. Howard, A. E.; Kollman, P. A. J. Am. Chem. Soc. 1987, 109, 0000.
15. Dewar, M. J. S.; Storch, D. M. J. Chem. Soc. Chem. Commun. 1985, 94.
16. Ewig, C. S.; Van Wazer, J. R. J. Am. Chem. Soc. 1986, 108, 4774.
17. Yamabe, S.; Minato, T. J. Org. Chem. 1983, 48, 2972.
18. Jorgensen, W. L. Adv. Chem. Phys. 1987, 00, 0000.
19. (a) Chandrasekhar, J.; Smith, S. F.; Jorgensen, W. L. J. Am. Chem. Soc. 1985, 107, 154. (b) Chandrasekhar, J.; Jorgensen, W. L. ibid. 1985, 107, 2974.
20. Binkley, J. S.; Whiteside, R. A.; Raghavachari, K.; Seeger, R.; DeFrees, D. J.; Schlegel, H. B.; Frisch, M. J.; Pople, J. A.; Kahn, L. R. Gaussian 82 Release H; Carnegie-Mellon University: Pittsburgh, 1982.
21. Chandrasekhar, J.; Andrade, J. G.; Schleyer, P.v.R. J. Am. Chem. Soc. 1981, 103, 5609, 5612.
22. Gao, J.; Garner, D. S.; Jorgensen, W. L. J. Am. Chem. Soc. 1986, 108, 4784.
23. Hehre, W. J.; Radom, L., Schleyer, P.v.R.; Pople, J. A. Ab Initio Molecular Orbital Theory; Wiley: New York, 1986.
24. Meot-Ner, M.; Sieck, L. W. J. Am. Chem. Soc. 1986, 108, 7525.
25. Nibbering, N. M. W., to be published.
26. Olmstead, W. N.; Brauman, J. I. J. Am. Chem. Soc. 1977, 99, 4219.
27. Evanseck, J. D.; Blake, J. F.; Jorgensen, W. L. J. Am. Chem. Soc. 1987, 109, 0000.
28. Reference 1, p. 23
29. Bartmess, J. E.; McIver, R. T., Jr. in Gas Phase Ion Chemistry, Volume 2, Bowers, M. T., Ed.; Academic Press: New York, 1979, p. 87
30. Kreevoy, M. M.; Truhlar, D. G. In Investigation of Rates and Mechanisms of Reactions, 4th edition; Bernasconi, C., Ed.; Wiley: New York, 1986, Part 1, chapter 1.
31. Jorgensen, W. L.; Buckner, J. K.; Huston, S. E.; Rosicky, P. J. J. Am. Chem. Soc. 1987, 109, 1891.

32. Jorgensen, W. L.; Chandrasekhar, J.; Madura, J. D.; Impey, R. W.; Klein, M. L. J. Chem. Phys. 1983, 79, 926. Jorgensen, W. L.; Madura, J. D. Mol. Phys. 1985, 56, 1381.
33. Burgi, H. B.; Dunitz, J. D. Accts. Chem. Res. 1983, 16, 153.
34. Guthrie, J. P. J. Am. Chem. Soc. 1978, 100, 5892; ibid. 1973, 95, 6999; ibid. 1974, 96, 3608.

RECEIVED June 15, 1987

## Chapter 13

# Molecular Dynamics Studies of Crystal Growth and Thin Films

George H. Gilmer and Marcia H. Grabow

AT&T Bell Laboratories, Murray Hill, NJ 07974

We discuss the application of atomic scale computer models to bulk crystal growth and the formation of thin films. The structure of the crystal-fluid interface and the mobility of the material at this interface are discussed in some detail. The influence of strain on thin film perfection and stability is also examined.

An understanding of the atomic scale processes that occur during crystal growth is essential to the development of technologies that utilize highly perfect crystals. The structure of the interface between the crystal and the surrounding liquid or vapor phase is of great importance since the interface serves to order and stabilize the adjacent molecules in the fluid phase, thus facilitating their incorporation into the crystal lattice. In this article some of the basic mechanisms of crystal growth are considered, together with the impact of computer simulations on our perception of these processes. Also included are molecular dynamics (MD) simulations of thin films. These provide information on the stability of strained films against the spontaneous generation of misfit dislocations or a breakup into islands.

The rate of crystal growth can be extremely sensitive to the binding energy of atoms at different sites on the surface. A surface with a dense array of energetic binding sites condenses atoms from the vapor most efficiently. The density of these active sites depends on the surface temperature, crystallographic orientation and impurity content. A surface near a close-packed orientation is illustrated in Fig. 1. Here the active sites are located at the edges of steps, where molecules condensing from the vapor can interact with a large number of neighbors. In the presence of a supersaturated vapor, these steps advance as the edge sites are filled, and eventually the steps annihilate at the edge of the crystal. When all of the existing steps are annihilated in this way, the crystal is bounded by close-packed layers and growth terminates, unless there is a mechanism for the generation of new steps.

0097-6156/87/0353-0218\$06.00/0  
© 1987 American Chemical Society

### Surface Roughening and Crystal Growth

Early attempts to calculate growth rates were based on the nucleation of clusters on the surfaces of a perfect crystal. According to these theories, clusters are generated by a fortuitous series of impingement events that occur on neighboring sites. Very small clusters are likely to disintegrate since few neighbors are present to stabilize the system. But occasionally a large stable cluster may appear, and its periphery then provides the active sites for crystal growth. This cluster could then expand and cover the surface, or merge with neighboring clusters to complete the layer.

A difficulty with this mechanism is the small nucleation rate predicted (1). Surfaces of a crystal with low vapor pressure have very few clusters and two-dimensional nucleation is almost impossible. Indeed, dislocation-free crystals can often remain in a metastable equilibrium with a supersaturated vapor for long periods of time. Nucleation can be induced by resorting to a vapor with a very large supersaturation, but this often has undesirable side effects. Instabilities in the interface shape result in a degradation of the quality and uniformity of crystalline material.

One method to facilitate crystal growth in a crystal-vapor system is to grow at high temperatures. The large equilibrium vapor pressure causes more atoms to adsorb on the surface, and the probability of finding large clusters is increased. In fact, Burton et al. (1) and Jackson (2) predicted that a surface phase transition occurs at high temperatures where the adsorbed atoms occupy about 50% of the available sites, provided that the crystal does not melt at a lower temperature. Although their calculations were mainly derived from a model limited to a single layer of adatoms on the surface of a perfect crystal, later work confirmed the existence of a roughening transition in multilevel surfaces (3,4).

Typical surfaces observed in Ising model simulations are illustrated in Fig. 2. The size and extent of adatom and vacancy clusters increases with the temperature. Above a transition temperature  $T_R$  ( $T_R \approx 0.62$  for the surface illustrated), the clusters percolate. That is, some of the clusters link up to produce a connected network over the entire surface. Above  $T_R$ , crystal growth can proceed without two-dimensional nucleation, since large clusters are an inherent part of the interface structure. Finite growth rates are expected at arbitrarily small values of the supersaturation.

Model calculations of the growth rate  $R$  are shown in Fig. 3. These are plotted as a function of the driving force for crystallization,  $\Delta\mu \approx \ln(p/p_e)$ , where  $p$  and  $p_e$  are the actual and equilibrium vapor pressures, respectively. At very low temperatures, the growth rate is essentially

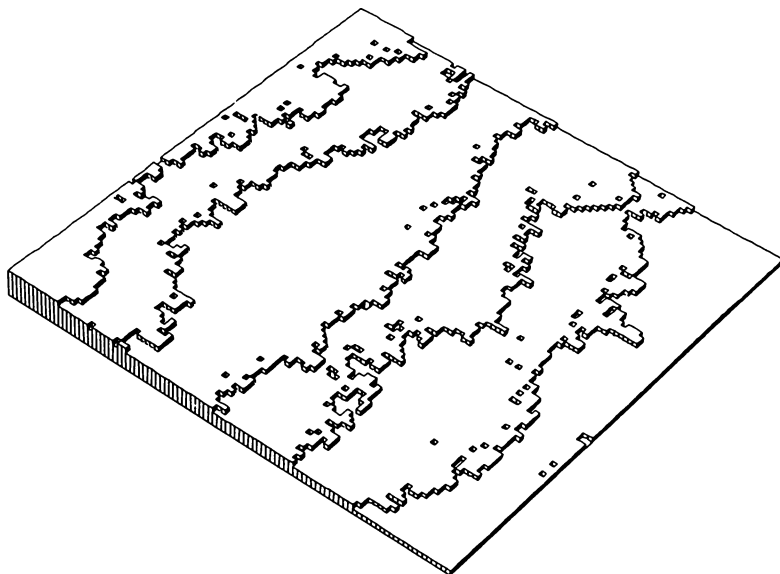


Fig. 1 Schematic representation of a crystal surface inclined at a small angle to a low-index crystallographic orientation.

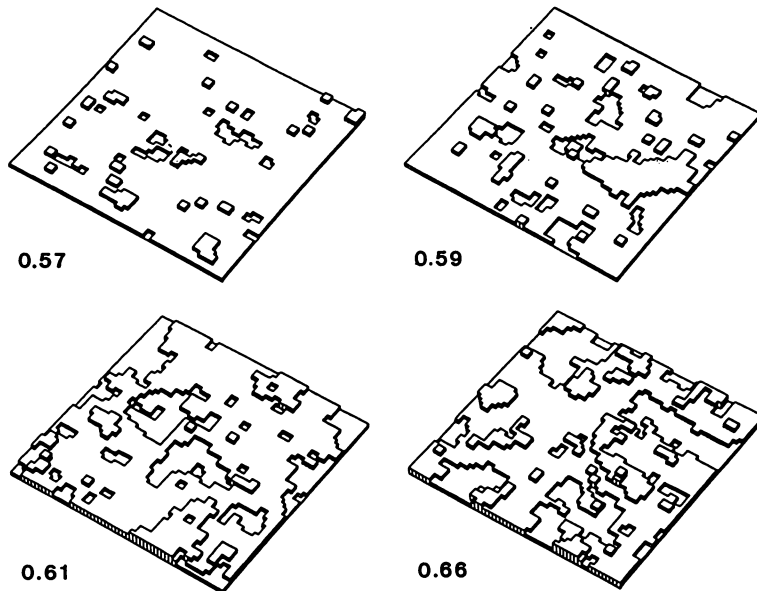


Fig. 2 Typical Ising model surfaces produced by computer simulations. In this system  $T_R=0.62$ , in terms of the dimensionless temperature shown on the figure.

zero for small  $\Delta\mu$ , as predicted by nucleation theory. At higher temperatures measurable growth occurs at smaller values of  $\Delta\mu$ , and above  $T_R$  the metastable region is absent (5).

The morphology of crystals is affected by the temperature. At low temperatures a growing crystal is bounded by the close-packed planes that move most slowly. Fast-moving orientations that may be present on the initial crystal surface move to the crystal edges, disappearing from the growth form. At moderate temperatures the disparity between the kinetics on different faces is reduced; the crystal assumes a more compact shape and rounded edges are present. At high temperatures some of the bounding faces may disappear because of surface roughening, and if all of the faces are rough the crystal assumes a shape that is nearly spherical, according to this model (see below). Using this approach, Jackson (2) has correlated morphology with a normalized interface temperature for crystals grown from the melt.

### Molecular Dynamics Studies of Interfaces

Ising models with elementary lattice structures are not appropriate for calculations of the influence of surface stress, surface reconstruction or other complex surface structures. In most simulations, the surface structure is represented only by the presence or absence of atoms at bulk lattice sites, although more general structures can be included by the use of a fine grid lattice. An important factor in vapor growth systems is the rate of mass transport along the surface to the active growth sites. The migration of atoms along the surface can be included as an additional Monte Carlo event in Ising model simulations. However, the rate constants for this process and their dependence on the local surface configuration must be assigned in a somewhat arbitrary manner. Molecular dynamics calculations permit unambiguous measurements of the surface transport of atoms, although the applicability of the results depends on the validity of the interatomic potential employed.

We now describe a relatively simple MD model of a low-index crystal surface, which was conceived for the purpose of studying the rate of mass transport (8). The effect of temperature on surface transport involves several competing processes. A rough surface structure complicates the trajectories somewhat, and the diffusion of clusters of atoms must be considered. In order to simplify the model as much as possible, but retain the essential dynamics of the mobile atoms, we will consider a model in which the atoms move on a "substrate" represented by an analytic potential energy function that is adjusted to match that of a surface of a (100) face-centered cubic crystal composed of atoms interacting with a Lennard-Jones

(LJ) potential (6). The diffusing atoms also have LJ forces between them. Atoms interact with a ghost atom in the substrate that is subjected to random and dissipative forces that closely match the forces exerted by a neighboring shell of atoms in the crystal. In this way the MD computation is limited to a relatively small number of mobile atoms and their ghost atoms, and the influence of the large number of atoms in the crystal is represented by the forces applied to the ghost atom.

Tully et al (7) have studied the motion of single atoms and small clusters in such a system, and found that the diffusion rates have an Arrhenius temperature dependence. Although it is true that adatoms experience longer jump distances at high temperatures, with an average jump of approximately four atomic diameters at the melting point  $T_m$ , there is no anomaly in the temperature dependence. Clusters of two to six atoms were found to diffuse at a slower rate, as might be expected, but could alter the total mass transport if present in large quantities.

The essential influence of surface roughening is also present in this model. Grand canonical Monte Carlo calculations were used to generate adatom populations at various temperatures up to  $T_m$ . Chemical potentials corresponding to those in the bulk LJ crystal were used, and these produced adatom densities that increased with temperature and roughly approximated the values observed in Ising model simulations below  $T_R$ .

A plot of the adatom density versus  $T^{-1}$  is shown in Fig. 4. An anomalous increase in the density is observed at high temperatures. The dashed line represents the adatom population that would be predicted if there were no lateral interactions. However, the LJ potential between adatoms tends to stabilize them at the higher coverages, and it is this effect that causes the deviation from Arrhenius behavior at high temperatures. A similar temperature dependence is observed in the rate of mass transport on some metal surfaces (8,9), and it is possible that it is caused by the enhanced population of the superlayer at high temperatures.

However, the increased number of adatoms at high temperatures can influence their mobility, since clusters of LJ atoms were observed to have smaller diffusion coefficients than isolated atoms. Figure 5 shows the average diffusion coefficients of adatoms, also as a function of  $T^{-1}$ ; here the deviation from Arrhenius behavior is in the other direction.

The rate of mass transport is the product of these two factors, the density of atoms and the diffusion coefficient per atom, as shown in Fig. 6. Over a large temperature interval up to  $T_m$  the mass transport coefficient is almost perfectly Arrhenius in nature. The enhanced adatom concentrations at high temperatures are offset by the lower mobility of the interacting atoms. Thus, surface roughening does not appear to cause anomalies in the



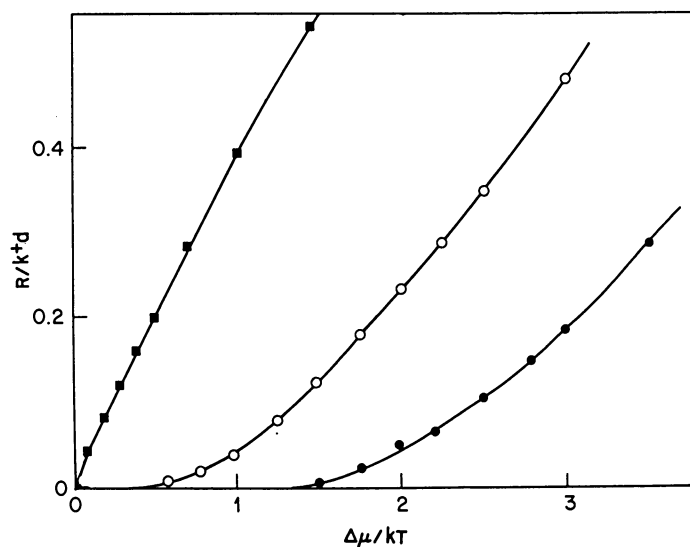


Fig. 3 Ising model calculations of the normalized growth rate  $R$  as a function of the driving force. The surface temperatures are  $0.40T_R$ , closed circles,  $0.54T_R$ , open circles, and  $1.08T_R$ , squares.

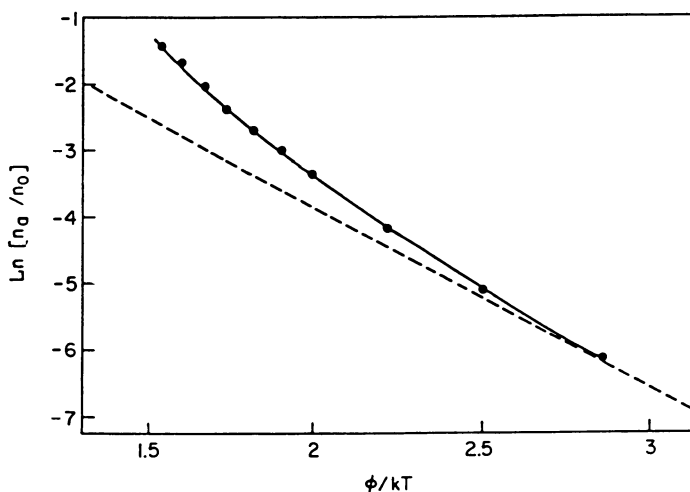


Fig. 4 Number of atoms normalized by the site density plotted as a function of  $T^{-1}$  for the surface model.

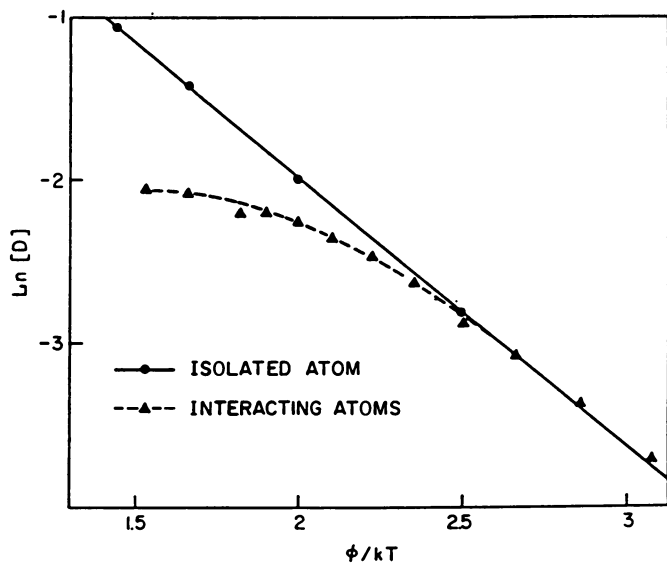


Fig. 5 Diffusion coefficient  $D$  for atoms on surface.

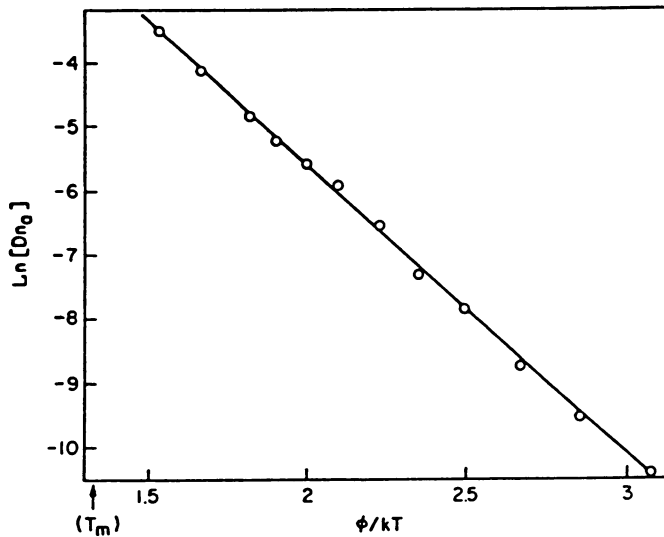


Fig. 6 Mass transport coefficient of surface.

mass transport rate, although it is possible that one of the two effects could dominate if a different interatomic potential were present.

### Crystal Growth

The kinetics of crystal growth have not been obtained by MD techniques for crystal-vapor systems, because of the very slow growth rate and the extensive computation required. The relationship between the growth rate and driving force as shown in Fig. 2 requires growth simulations at small values of the driving force. The difficulty of a direct MD calculation is the large amount of computation required to obtain the atomic trajectories. The complex motion of an atom that impinges from the vapor and is incorporated into the growing crystal is represented in the Ising model by a simple spin flip. The MD simulations of vapor growth that have been attempted to date were performed with an incident flux eight to ten orders of magnitude larger than that of the equilibrium vapor. Under such extreme conditions the evaporation flux is essentially zero, corresponding to a dimensionless growth rate of unity. Surprisingly, LJ systems were found to grow with relatively well ordered layers under these conditions, although the stacking of adjacent layers did not correspond to a regular space lattice (10).

Different results were obtained in the case of the Stillinger-Weber (SW) potential for silicon (10). In this case, material deposited on the (111) orientation was disordered, without distinct layers of atoms. Growth on the (100) face did produce about ten distinct layers at sufficiently high temperatures, although it is not clear whether thicker deposits would retain this order since some degeneration was observed as successive layers were deposited.

Molecular dynamics calculations of solidification at a crystal-melt interface have been performed; the faster growth kinetics of this system make it possible to crystallize a significant amount of material using presently available computer technology. Landman et al (11) have simulated the motion of atoms in a slab of supercooled liquid that was placed in contact with a crystal surface. Ordering of the atoms into layers was observed first, and then the localization of the atoms at lattice sites within the layers. An interface speed of  $\approx 100m/s$  was estimated during the early stages of ordering when parameters appropriate for argon were inserted. The melting and resolidification of a two-component system has also been simulated (12).

Steady-state crystallization rates were measured for a range of temperatures below the melting point by Broughton et al (13). A face-centered cubic (100) crystal-melt interface was equilibrated in a box elongated in the

direction normal to the interface. Periodic boundary conditions were applied in the parallel directions. Particles at the two ends of the box were coupled to a heat bath at a fixed temperature  $T_0$  by means of random and dissipative forces. Crystal growth was observed when  $T_0$  was reduced below  $T_m$ . New liquid particles were supplied at the lower end of the box at a rate that was adjusted to keep the interface roughly at the center of the box. Crystalline material extruding from the top of the box was removed.

The measured growth rates are illustrated by the circles in Fig. 7. The interface velocity is plotted versus the interface temperature  $T$ . The value of  $T$  is always greater than  $T_0$  because of the release of the latent heat at the interface. Dimensionless units for  $T$  and the velocity are used here. The maximum velocity corresponds to  $\approx 80m/s$  for argon. The most surprising aspect is the rapid crystallization at low temperatures. Most materials exhibit sharply reduced rates at low temperatures, as expected for an activated growth process. That is, the kinetics can be represented as the product of an Arrhenius factor  $F(T)$  and a term that accounts for the net production of crystalline material as a result of the atoms ordering and disordering at the interface,

$$R = F(T)[1 - \exp(-\Delta\mu/kT)] \quad (1)$$

The Arrhenius factor is often represented by an expression of the type

$$F(T) = D a f_0 / \Lambda^2 \quad (2)$$

where  $D$  is the diffusion coefficient in the liquid and  $\Lambda$  is the mean free path. It is assumed that atoms in the adjacent liquid of thickness  $a$  impinge on the crystal surface at a rate proportional to  $D/\Lambda^2$ . A site factor  $f_0 < 1$  is included to account for the fact that some of these collisions do not contribute to crystal growth, either because they are not sufficiently close to a lattice site or because the region neighboring the site is relatively disordered. The low entropy of fusion  $\Delta S = 1.62$  (13) insures that the surface temperature is well above the normalized roughening temperature (2), and therefore the growth sites are not limited to the edges of steps supplied by a lateral growth mechanism such as a two-dimensional nucleation or spiral growth. The diffusion coefficient in the liquid has been measured over the range from  $T_m$  down to  $0.4T_m$ , where the high viscosity prevents accurate measurements. An Arrhenius expression fits the data, and can be used to extrapolate to lower temperatures. The driving force  $\Delta\mu$  can be calculated accurately using thermodynamic data for the bulk crystal and the supercooled liquid.

The solid curve in Fig. 7 is a plot of eqs. (1) and (2), with the values of  $\Delta\mu$  and  $D$  obtained as described above. The supercooled LJ liquid becomes

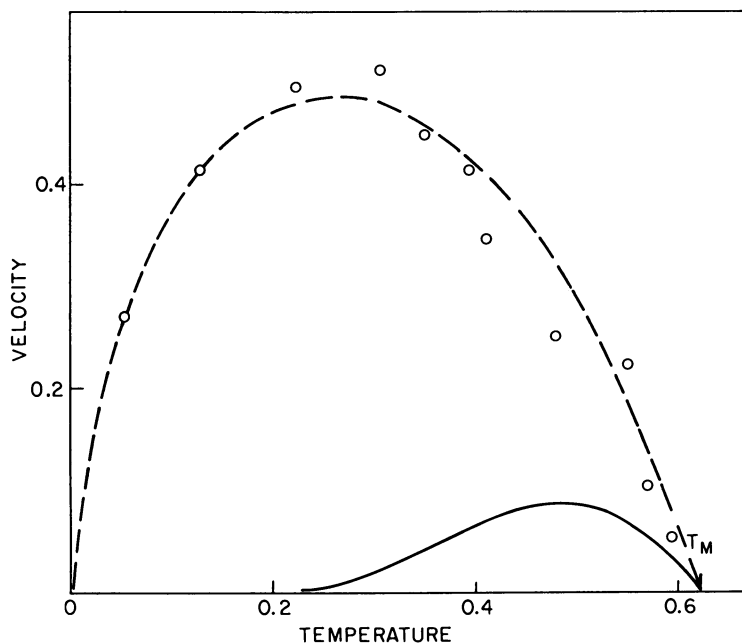


Fig. 7 Molecular dynamics calculations, open circles, for the velocity of the crystal-melt interface versus the temperature of the interface. The solid curve corresponds to eq. (1) and the dashed curve to eq. (3).

highly viscous at low temperatures whereas the measured interface velocities in this region are quite large. Crystallization is apparently not limited by an activated process. Even a small activation barrier would reduce the growth rate significantly at low temperatures. Turnbull and Bagley (14) had argued that crystallization of simple melts should not be limited by the liquid diffusion rates, since the movement across the interface is less impeded by backscattering.

The large mobility in the interface is apparently the result of a density deficit in this region. At the melting point the interfacial densities are intermediate between the two bulk phases. There is no indication of voids, and the mobility of the interfacial atoms is approximately the same as that of the bulk liquid. However, as the temperature is reduced below  $T_m$ , the density of the interface region drops, and at  $T=0.15$  it is 5% lower than that of the liquid phase. Thus, the amount of free volume available for atomic motion increases at low temperatures. This extra free volume could be caused by the large viscosity of the liquid phase. At large growth rates there is little time for the liquid to accommodate to crystalline material, and hence the interface energy is high. Enhanced diffusion of atoms at the interface between two solid phases is commonly observed in experiments on grain boundary diffusion (15).

In the absence of a potential barrier, the rate at which liquid atoms in the interface could move to lattice sites is determined by the average thermal velocity,  $(3kT/m)^{1/2}$ . If they travel a distance  $\lambda$ , the interface velocity is

$$R = (a/\lambda)(3kT/m)^{1/2}f_0[1-\exp(-\Delta\mu/kT)] \quad (3)$$

The dashed curve in Fig. 7 is obtained when  $\lambda=0.4a$ , the average distance from the center of points uniformly distributed in a sphere, and  $f_0=0.27$ . This expression is in good agreement with the data over the full range of  $T$ , and has no activation barrier whatsoever. Apparently the atoms in the liquid can rearrange into a crystal lattice along a path in configuration space that involves a monotonic reduction in energy. This unexpected conclusion applies only to simple atoms and molecules. The crystallization of ordered alloys would involve the diffusion of atoms to the correct sublattice sites, and may involve an activation energy. Similarly, the crystallization of most molecular crystals requires a reorientation of the molecules, and would also be inhibited at low temperatures.

If eq. (1) were applicable to other materials, approximate values of the maximum growth rates could be obtained by scaling with  $(T_m/m)^{1/2}$ . Accordingly, we estimate maximum rates of 400 m/s for nickel and 430 m/s for silicon. Interface velocities of 50 m/s have been measured for Ni

dendrites growing into a supercooled melt at  $0.9T_m$  (16). The velocity data of Fig. 7 imply that the interface temperature is  $\approx 0.96T_m$ . This is a  $70^\circ\text{C}$  undercooling at the interface, a surprisingly large value for such a simple system. The maximum velocity measured for silicon is only 18 m/s, and this indicates that the mobility of interfaces in covalent materials is much smaller than in simple metals and the noble gases.

An increase in the number of lattice defects was noted during the growth of the LJ crystal at low temperatures. The crystallizing material formed at  $T=0.05$  contained 0.5% vacancies, whereas the equilibrium concentration at this temperature is less than  $10^{-30}$ . Twinning was also observed. In every instance this process began as a defect involving a single row of atoms in a partially ordered (100) layer. The atoms were displaced by a distance  $a/2$  in a direction parallel to the row. The next layer to crystallize usually contained two adjacent rows displaced, and so on until the entire layer was in the new position and the crystal was again perfect.

Significant reductions in the growth rate were observed while the defects were in the interface. This contrasts with the usual assumption that defects enhance the growth by providing sources of steps or preferred nucleation sites. In this case the intrinsically rough interface already contains a high density of good growth sites. The strain and reduced bonding in the defective crystal reduce the difference in the free energy between the crystal and the melt, and therefore the effective driving force for crystallization is reduced. Another factor is the presence of new sites at the growth interface where the potential energy is a minimum, but which are not consistent with closely spaced neighboring sites. Competition between the different sites for liquid atoms apparently retards the crystallization process. Recent unpublished data for the (111) interface demonstrates this effect. The close packed layers may stack in the face-centered cubic abcabc... sequence, or as ababab... to form hexagonal close packed material. The energy difference between these two lattices is extremely small, and indeed the crystallized material does not have a regular stacking sequence, although the individual close packed planes are essentially perfect. Near  $T_m$  the growth rate on this face is 50% of that on the (100), and at low temperatures it has the form expected for an activated process. Thus, the (100) and (111) faces have qualitatively different behavior: the (100) growth is limited only by the rate at which liquid atoms can arrive at growth sites, whereas the (111) growth requires that an activation energy barrier be surmounted.

## Thin Films

Epitaxial growth of thin films usually involves the formation of strained material as a result of mismatch between the film and substrate and because of the large surface to volume ratio in the film. Surface stress can be a major factor, even when the lattice constants of film and substrate are perfectly matched. Although it appears to be difficult to eliminate the stress totally, it is important to be able to control it and even use it to produce desired qualities.

We have seen that the deposition of crystals from the vapor is much too slow to model by MD techniques. Most laboratory equipment for producing thin films involves relatively slow crystal growth processes, and is not suitable for direct simulation. Information on the stability and properties of thin films can be obtained by similar modeling techniques, however. We describe below some of our results that provide necessary data to find the equilibrium configuration of thin films at low temperatures.

The motion of particles of the film and substrate were calculated by standard molecular dynamics techniques. In the simulations discussed here, our purpose is to calculate equilibrium or metastable configurations of the system at zero Kelvin. For this purpose, we have applied random and dissipative forces to the particles. Finite random forces provide the thermal motion which allows the system to explore different configurations, and the dissipation serves to stabilize the system at a fixed temperature. The potential energy minima are populated by reducing the random forces to zero, thus permitting the dissipation to absorb the kinetic energy.

All particles of the film and substrate interact with LJ potentials, and for particles  $i$  and  $j$  with separation  $r_{ij}$  this potential is

$$\phi_{ab}(r_{ij}) = 4 \epsilon_{ab} [(\sigma_{ab}/r_{ij})^{12} - (\sigma_{ab}/r_{ij})^6] \quad (4)$$

which is smoothly truncated at  $r_{ij} = 2.5\sigma_{ab}$ , and the subscripts  $a$  and  $b$  indicate the types for particles  $i$  and  $j$ . The energy of the system will be expressed in units of  $\epsilon_{ss}$ , the well depth of the potential between two substrate particles. In addition, we assume that the depth of the film-film potential,  $\epsilon_{ff}$ , is equal to  $\epsilon_{ss}$ , and we will vary the film-substrate value  $\epsilon_{fs}$ . The relative strength of the film-substrate potential is defined as

$$W \equiv \epsilon_{fs}/\epsilon_{ff} \quad (5)$$

Large film-substrate interactions are represented by  $W \gg 1$ . The dimensionless unit of length is taken to be  $\sigma_{ss}$ , a measure of the atomic diameter of the substrate particles. The degree of misfit,  $\eta$ , is the difference between the film and substrate lattice constants, normalized by the substrate lattice constant. In terms of the LJ parameters,



$$\eta = \sigma_{ff} / \sigma_{ss} - 1 \quad (6)$$

and in all cases reported here the film particles are larger than those of the substrate, or  $\eta > 0$ . The film-substrate interaction diameter is assigned the average value  $\sigma_{fs} = (\sigma_{ff} + \sigma_{ss})/2$ . The substrate atoms were arranged to expose a (001) face of the FCC crystal.

In practice, uniform films are obtained for only a limited number of film-substrate material combinations (17). The more common experience is that the deposited material forms 3D clusters. The clusters may form directly on the bare substrate, in the Volmer-Weber growth mode, or on top of a very thin but uniform film of the deposit, the Stranski-Krastanov growth mode. We now discuss a method for determining the equilibrium configuration of the deposited material.

Much of the thermodynamics of the film-substrate system can be obtained from a plot of the system energy,  $E$ , versus the number of atoms in the film,  $N$ . The results for the LJ system are shown in Fig. 8 for  $\eta = 0.04$  and a strong film-substrate interaction,  $W = 2$ . Here  $E - N\mu_B$  is plotted in order to illustrate the approach to bulk thermodynamics;  $\mu_B$  is the chemical potential of the bulk film material (at zero Kelvin this is the average energy per particle). The number of deposited atoms  $N$  is normalized by  $N_0$ , the number in a perfect substrate FCC (100) layer. A single coherent layer is complete at  $N/N_0 = 1$ , where the energy has a local minimum. The sharp drop in  $E - N\mu_B$  as  $N$  increases from 0 to one monolayer is a result of the strong bonding to the substrate, and indicates that this material has a lower potential energy than the bulk film material. As the first few atoms of the next layer are added, the curve rises because the second layer is then populated at a relatively low density which provides only weak interactions within the film.

A second minimum in the energy occurs at  $N = 2N_0$  exactly, when a coherent second layer is completed. Since the bulk lattice constant of the film is 4% greater than that of the substrate, the film is strained. From Fig. 8 it can be seen that  $E - N\mu_B$  for the two-layer film is lower than that of the monolayer. That is, the second layer of atoms also has a lower energy than the equivalent amount of bulk crystal, although in this case the difference is small. This indicates that the interaction energy with the substrate more than offsets the strain energy of the film. Layer three again has a minimum for the coherent film, but in this case  $E - N\mu_B$  increases indicating that it has a *higher* energy than the bulk.

Misfit dislocations are favored for films thicker than five layers. This can be seen from the two data points near the minima shown in Fig. 8 for layers 2–8. In each case the data point at the smaller value of  $N$

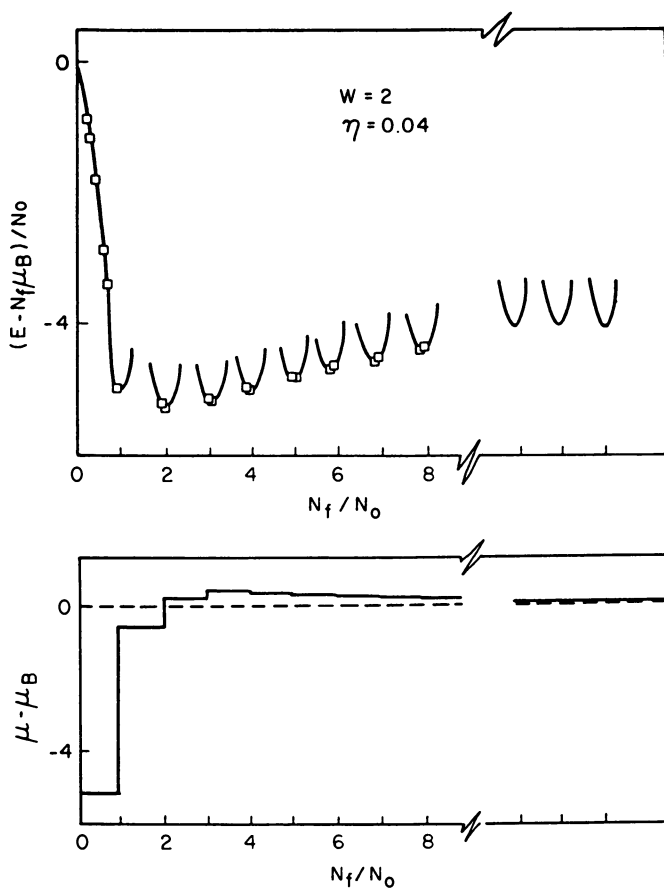


Fig. 8 The energy relative to that of the bulk crystal is plotted in the upper section, versus  $N/N_0$ , where  $N_0$  is the number of substrate atoms per layer;  $\eta=0.04$ . The chemical potential is plotted in the lower section.

represents a film with a single misfit dislocation (two missing (110) layers of atoms out of 120), and the other point depicts the coherent film. Whether either or both of these states can exist as the equilibrium state of the film can be determined by a common tangent construction described below. Here we simply note that misfit dislocations are favored in the thicker films, since the strain energy becomes larger relative to the energy of the misfit dislocations. Thus, as  $N$  increases the lattice constant of the film approaches that of the bulk crystal. For this reason the increase in  $E - N\mu_B$  between adjacent minima decreases with thickness and eventually all minima have the same value.

Each new layer is populated by adding the particles in rows that are uniformly spaced along the  $y$  axis; that is, by changing the density of misfit dislocations. The grouping of atoms into 2D clusters is an important effect that is excluded by this approach. However, the effects of this type of clustering can be inferred from these results. Since the chemical potential of the film material is  $\mu = \partial E / \partial N$ , the tangent to this curve is  $\mu - \mu_B$ . As  $N$  is increased, the equilibrium film will not traverse all of the states represented by the continuous curve, but will instead revert to an inhomogeneous structure consisting of linear combinations of states near the minima on either side, as determined by the common tangent construction, and this describes the expected behavior of the clustered configuration.

For  $N$  below one monolayer the deposit may consist of an inhomogeneous mixture of a bare substrate and clusters approximately one monolayer thick. The state with the lowest chemical potential is represented by a line through the origin and tangent to the  $E(N)$  curve near the first local minimum, at  $N_{1-} \approx N_0$ . The slope of this tangent defines a chemical potential  $\mu^{(0 \leftrightarrow 1)}$ . Thus, as  $N$  is increased from 0 to  $\approx N_0$ , the fraction of the substrate covered by the film increases from 0 to unity. Alternatively, if  $\mu$  is the independent variable, then as the chemical potential is increased from  $-\infty$ , the substrate remains bare until  $\mu$  reaches the value  $\mu^{(0 \leftrightarrow 1)}$ . At this point approximately one monolayer is deposited. The film will not be precluded by clusters or other forms of bulk crystallization, since  $\mu^{(0 \leftrightarrow 1)} < \mu_B$ . The common tangent construction can be represented as

$$\left. \frac{\partial E}{\partial N} \right|_{N=N_{1-}} = \frac{[E(N_{1-}) - E(0)]}{N_{1-}} \quad (7)$$

For larger values of  $\mu$  the density of the film may, for some systems, increase somewhat before the second layer is initiated. That is, there may be a narrow single-phase region which extends from  $N = N_{1-}$  to  $N_{1+}$ , and where  $\mu^{(0 \leftrightarrow 1)} < \mu < \mu^{(1 \leftrightarrow 2)}$ . Because  $\mu$  is larger at  $N = N_{1+}$  than at  $N = N_{1-}$ , the density of a monolayer coexisting with a bilayer may be larger than

that for the monolayer in equilibrium with the substrate; i.e., the number of misfit dislocations may be smaller. At  $N=N_{1+}$  and  $\mu=\mu^{(1\leftrightarrow 2)}$ , the tangent to the  $E(N)$  curve forms a common tangent with the second local minimum at  $N=N_{2-}$ , which corresponds to approximately two monolayers. Thus, the system traverses a two-phase region connecting the monolayer to the bilayer. Again,  $\mu$  of the common tangent construction should be compared with  $\mu_B$  to determine whether bulk precipitation is the preferred state, although the state with the lower chemical potential may not appear in practice if it is inhibited by a nucleation barrier. The chemical potential is plotted in the lower part of Fig. 8, also as a function of  $N$ . This plot shows that the equilibrium structure of the system includes a uniform film for deposits up to two monolayers, but above this value of  $N$  the chemical potential exceeds that of the bulk. This implies that 3D clusters on the two-layer film, the Stranski-Krastanov growth mode, is the preferred state. (The tangent between the second and third local minima has a positive slope, indicating that  $\mu > \mu_B$ .)

A different scenario occurs when the bonding between the substrate and film is relatively weak. For  $W \leq 1$  the first minimum in  $E(N) - N\mu_B$  is positive, and the chemical potential  $\mu^{(0\leftrightarrow 1)}$  is greater than  $\mu_B$ . In that case the equilibrium configuration with  $N$  below a monolayer equivalent consists of a mixture of a bare substrate and large, 3D clusters. The Volmer-Weber growth mode is implied (Fig. 1).

Complete wetting of the substrate is not exhibited in either case. This is only satisfied by a system for which the film thickness diverges continuously as  $\mu \rightarrow \mu_B$ . In the system with  $W=2$ , the thickness reaches a limit of two layers when  $\mu \rightarrow \mu_B$ , since the strain energy in the film inhibits the deposition of material at larger distances from the substrate where the attractive field is not effective (see eq. (4) and note the truncation of the potential). Substrates with full van der Waal's fields may yield relatively thick films at  $\mu = \mu_B$ , but only when the misfit is small. Systems with  $W=1$  can not satisfy the condition for complete wetting for any value of the misfit.

The difficulty in practice of finding systems with uniform thin films is apparent from this discussion. The misfit between the film and the substrate leads to a strain energy that serves as the driving force for cluster generation in almost every case. The only driving force for uniform films is a strong interaction between the film and substrate, which requires that  $W > 1$ . It is only when the film atoms interact directly with the substrate that there will be a driving force for layer-by-layer growth, and even then it is effective only up to a limited film thickness for finite misfit.

Huse has pointed out that strain is to be expected in most thin-film systems, since even in the incommensurate case the intrinsic surface stress will strain the film (18). As a result, we conclude that incomplete wetting is expected for all crystalline films, except in the case where there is an epitaxial relationship between film and substrate and that the film is maintained at its bulk equilibrium lattice spacing.

Therefore, we predict that for a system with any finite misfit, a uniform film with a thickness greater than several monolayers is not the equilibrium state; the system can lower the chemical potential by the formation of clusters. Clusters will form on either the bare substrate (Volmer-Weber mode; any finite misfit with  $W \leq 1$  and large misfits if  $W > 1$ ) or on a few layers of uniform film (Stranski-Krastanov mode; up to moderate misfits with  $W > 1$ ). This will be true for any system without long-range (e.g. electrostatic) forces.

The MD simulations provided the necessary thermodynamic information to obtain the equilibrium configurations of the films. Often the deposition process will produce films which are not in the equilibrium configuration, and then the problem is to determine the stability of these films against changes in morphology. Here simulations can also be helpful, since data on the surface energies and chemical potentials of strained films can be used to calculate the probability of cluster nucleation, using classical nucleation theory.

### Conclusions

We have discussed simulations that were intended to elucidate aspects of crystal growth under diverse conditions. In most cases a direct simulation of growth using realistic conditions is impractical. The growth rate may be many orders of magnitude slower than that required to produce observable crystalline material in the available computer time. We have described several methods to obtain information about the crystallization process in this situation.

First, some of the fundamental aspects of crystal growth have been investigated by use of the kinetic Ising model. The simplicity of the model permits simulations of systems with relatively slow growth rates. Surface roughening was shown to be a genuine phase transition with important consequences for the growth kinetics. Second, we were able to examine the crystal-vapor interface region using molecular dynamics techniques. The rate of mass transport along the surface provides an indication of the ability of the surface region to incorporate atoms impinging by molecular beams or vapor deposition. Under experimental conditions these processes are about ten orders of magnitude too slow for direct simulations using existing computer technology. Third, we have discussed crystallization at a highly

supercooled crystal-melt interface. Here the growth rate is sufficiently large that the direct simulation produces useful results. Finally, in the case of epitaxial growth with misfit, favored low-temperature configurations were obtained by "annealing", and comparing the resulting energies. In this way it is possible to explore the important potential energy minima in configuration space, and to determine whether misfit dislocations or other defects are to be expected.

### Literature Cited

- 1 W. K. Burton, N. Cabrera and F. C. Frank, *Philos. Trans. R. Soc. London* 1951, **A243**, 243.
- 2 K. A. Jackson, in: "Liquid Metals and Solidification", (American Society for Metals, Metals Park, Ohio, 1958), p 174.
- 3 H. van Beijeren, *Phys. Rev. Lett.* 1977, **38**, 993.
- 4 J. D. Weeks and G. H. Gilmer, *Adv. Chem. Phys.* 1979, **40**, 157.
- 5 G. H. Gilmer, *Science* 1980, **208**, 355.
- 6 K. A. Jackson, in: "Crystal Growth", S. Peiser, ed. (Pergamon, New York, 1967), p 17.
- 7 J. C. Tully, G. H. Gilmer and M. Shugard, *J. Chem. Phys.* 1979, **71**, 1630.
- 8 G. H. Rhead, *Surf. Sci.* 1975, **47**, 207.
- 9 H. P. Bonzel, in: "Surface Physics of Materials II", (Academic, New York, 1975), p 279.
- 10 Schneider, Schuler and Rahman, *Materials Research Symposium*, December 1986.
- 11 U. Landman, C. L. Cleveland and C. S. Brown, *Phys. Rev. Lett.* 1980, **45**, 2032.
- 12 C. L. Cleveland, U. Landman and R. N. Barnett, *Phys. Rev. Lett.* 1982, **49**, 790.
- 13 J. Q. Broughton, G. H. Gilmer and K. A. Jackson, *Phys. Rev. Lett.* 1982, **49**, 1496.
- 14 D. Turnbull and B. G. Bagley, in: "Treatise on Solid State Chemistry", N. B. Hannay, ed. (Plenum, New York, 1975), Vol. 5, p 526.
- 15 F. J. A. den Broeder, *Acta. Metall.* 1972, **20**, 319.
- 16 G. A. Colligan and B. J. Bayles, *Acta. Metall.* 1962, **10**, 895.
- 17 M. Bienfait, J. L. Seguin, J. Suzanne, E. Lerner, J. Krim and J. G. Dash, *Phys. Rev.* 1984, **B29**, 983.
- 18 D. A. Huse, *Phys. Rev.* 1984, **B29**, 6985.

RECEIVED June 15, 1987

## Chapter 14

# New Horizons for Computational Chemistry: Global Simulation Approach

E. Clementi and G. C. Lie

Data Systems Division, Department 48B-MS428, IBM Corporation,  
Kingston, NY 12401

In this report we explore the newly evolved concept of a global simulations. This is very similar to the emergence of a new concept which characterized the industrial revolution. There for the first time, complicated products were assembled using many successive single and generally simple steps: the assembly line approach. The global simulation concept is exemplified by carrying out a series of calculations on water. We show how one can investigate the many facets of water as a single molecule, a cluster of molecules, liquid, and solvent, by using only Planck constant, electronic charge, and masses of atomic nuclei as the raw materials. With faster supercomputers, we can even hope to go one step further to observe hydrodynamic phenomena, described classically by the set of hydrodynamic equations, of water by doing simulations at the molecular level.

Mathematical models require computation to secure concrete predictions. Successes in relatively simple cases spurs interest in more complex situations. Somewhat specialized computer hardware and software have emerged in response to these demands. Examples are the high-end processors with vector architecture, such as the Cray series, the CDC Cyber 205, and the recently announced IBM 3090 with vector attachment. When a computation can effectively utilize vector architecture, such machines will out-perform even the most powerful conventional scalar machine by a substantial margin. Such performance has given rise to the term "supercomputer."

An independent but complementary approach has been the development of parallel computing systems, where many processors can be concurrently applied in cooperation on a single calculation. This idea is certainly not new. It has already been the subject of numerous research projects and a very vast

0097-6156/87/0353-0237\$06.00/0  
© 1987 American Chemical Society

literature.<sup>(1-4)</sup> Interest in this type of computing has gained recent impetus as vector-oriented supercomputing matures and its limitations emerge. Increasing the speed of the already very fast cycle times of high-end vector processors requires improvements in basic technology that are difficult to achieve. Parallelism offers another road to faster computation. The two approaches, vector and parallel execution, are found to be in fact complementary; we see this for example where both the current Cray series and the IBM 3090 series offer a combination of vector and parallel architectures.

Our laboratory's interest in parallel computing originated with the computational demands of our work in theoretical chemistry and biophysics. We have already discussed some of our researches in parallel computing elsewhere,<sup>(5,6)</sup> and we expand and update these discussions here.

The computing system we have assembled is intended to respond to the newly emerging viewpoint in science and engineering, the "global simulation" approach, exemplified elsewhere in this paper. In the "global simulation" one attempts to realistically simulate complex problems. In the past, theory and mathematical models have stripped reality of many "details," because of its unbearable complexity. Thus, often, many-body effects, non-linear terms and boundary conditions have been either over-simplified or ignored, or not even identified. But slowly we are coming to the understanding that "reality" is just a collection of interacting "details." Whereas some "details" could be approached via vectors, some will require parallelism and some will request "super-scalar." The space within which the "global simulation" evolves is most definitely at least three-dimensional; namely, scalar, vector, and parallel.

### STRATEGY

Our approach to research in parallel processing has been, and remains, very pragmatic; it reflects our basic priorities, which are to secure a workable parallel processing system as quickly as possible, and begin using it on the large-scale scientific and engineering applications that are central to our research.

Many of the characteristics of our parallel strategy follow from these priorities. These characteristics are: 1) parallelism based on relatively few (less than 20), but quite powerful processors, with 64-bit hardware; 2) architecture as simple as possible, but extendable; 3) system software that varies as little as possible from that normally available for sequential processing; 4) initial applications programming entirely in FORTRAN, since this is the most widely used scientific application language; 5) migration from sequential execution to parallel execution with a minimal amount of recoding; 6) enhance, whenever feasible, each processor with vector features; 7) extend gradually and hierarchically, from loosely to tightly coupled, with a variety of approaches.

Our system is based on tens of processors, rather than hundreds or thousands of processors, in order to avoid questions concerning the binding together of large number of processors into a single system, since this would complicate and delay our attempts to apply parallel processing to our applications. It follows that the individual processors must be quite powerful in order to secure "supercomputer" performance, and hardware supporting 64-bit floating-point precision is essential for almost all of the applications of interest to us.

In line with our priorities, we have avoided the time-consuming effort of developing specialized hardware, preferring instead to acquire products which are



available "off the shelf." Specifically, we have selected the Floating Point Systems FPS-164 (currently with the MAX vector boards) or FPS-264 attached processors (AP) for our parallel processors. This choice was dictated by the fact that the FPS-164 was the only 64-bit attached processor available when we began. In principle, we could just as well substitute something else, such as a group of IBM 3090 computers, for the attached processors in our configuration, but these machines are far more expensive, and we want a configuration that does not cost too much.

We have IBM hosts (IBM 4381, IBM 3081, IBM 3084, and IBM 3090, at present) for our AP's. One advantage of this choice for the host computer is the multiple-channel I/O architecture used for the AP attachments. These channels (3 Mbytes/sec) were originally the only paths for data and synchronization between processors, giving rise to our term "loosely coupled array of processors" (ICAP) for our architecture. There are currently additional data paths, such as shared memories and FPS buses, thus bringing us closer to a "tightly coupled array of processors" type of architecture. Our architecture is currently implemented in two distinct systems, called simply ICAP-1 and ICAP-2. The first of these systems is hosted either by an IBM 4381 or 3081 with ten FPS-164/MAX processors attached. The second more powerful system employs as host an IBM 3084 and has ten FPS-264 processors as slaves. Aside from these hardware differences, they are distinguished by the operating systems on the host machines. A consequence of which is the development of softwares to support parallel processing for both VM/SP and MVS/XA operation systems.<sup>⑦</sup>

There have been many experiments in migrating software applications to parallel processing on our system. Ideally, one would like a completely automatic language processor to handle conversion from code for normal sequential execution to code supporting parallel processing. We are still a long way from this, but we have developed a number of aids to ease the labor of programming parallel processing. Prominent among these is a precompiler that recognizes experimental extensions to FORTRAN that we have introduced, and develops detailed code from this source code for compilation and parallel execution.<sup>⑧</sup>

### GLOBAL SIMULATION

By now it is a rather accepted viewpoint that science can be divided into "laboratory-experimental" and "theoretical-computational." Possibly, however, it is not sufficiently realized that computational science has made "enormous" progress in the last few years because of the availability of very fast, high performance computers, generally referred to as supercomputers. In referring to the "tremendous progress," we do not wish to put our emphasis on the size and the magnitude of the computations, but rather on the *viewpoint*. Indeed, now we can think in terms of "*global simulations*," namely simulations of a full problem, no longer limited to a specific subspecialized field. Let us clarify with an example related to chemistry and physics; when we consider the motions of an ensemble of molecules of water, we can either think in terms of the motions of the atoms within a single molecule or the motion of one molecule of water within the solvation cavity of other molecules of water (namely within the solvation cell), or we can think in terms of the collective motions where molecules act in unison. We can even go one step further and think in terms of very large systems where traditionally one would use fluid dynamics rather than a discrete representation

like quantum or statistical mechanics. In other words, because of supercomputers we are able to analyze an ensemble of molecules of water from quantum to statistical to fluid dynamics. In this paper we shall demonstrate the feasibility of our *global* approach by presenting a detailed discussion on simulations of liquid water. This is likely to be the first application of the *global viewpoint* but surely more and more will follow.

As we have previously pointed out,<sup>(9)</sup> there are a few simple rules which characterize our *global ab initio simulation* approach. The first rule is that the total model for the simulation can be decomposed into an ordered set of submodels, for example, submodels 1, . . . ,i, . . . ,N. The second rule is that the output of submodel (i - 1) contains all that is needed as the input for the submodel i. The third rule—for a global simulation—is that the input to the first submodel should be very simple and minimal. For example, in the particular case of a study of liquid water by global simulation, all we need as input is to know that the hydrogen atom has one electron, that the oxygen atom has eight electrons, and the masses for the nuclei of hydrogen and oxygen. With this knowledge we should be able, in principle and in practice, to characterize a molecule of water, clusters of water, liquid water at different pressure and temperature, and liquid water as a flow medium.

Below we shall start with our problem — namely the prediction of the properties of a molecular liquid — first at the quantum mechanical and then at the statistical level up to hydrodynamic limit. We shall then conclude by showing the feasibility of using molecular dynamics to solve problems of fluid mechanics and the results obtained by using water as a solvent for DNA in the presence of counterions.

**QUANTUM MECHANICS AS THE FIRST SUBMODEL.** From quantum mechanical simulation we can obtain the correct structure of a molecule of water, namely a molecule which has the OH bond length and the HOH bond angle pretty much in agreement with the best experimental data for a single molecule of water.<sup>(10)</sup> Again, from quantum mechanical simulation we can obtain a binding energy, dipole moment, quadrupole moment,<sup>(11)</sup> vibrational frequencies,<sup>(12)</sup> and the excited spectrum in the visible and the ultraviolet; the agreement of those quantities relative to accurate laboratory experiments depends on the choice of the model adopted in the simulation. Broadly speaking, we can talk about two "models": the first model is the *Hartree-Fock model* which represents the electronic structure of a molecule in the form of a determinantal product of molecular orbitals. Despite the enormous number of quantum mechanical calculations in the last 20 years, very seldom does one find molecular computation very near to (namely, within a few hundredths of a kcal) the Hartree-Fock limit. In the case of the molecule of water it is well known<sup>(13)</sup> that in order to reach the near Hartree-Fock limit one needs at least two d functions and one f function located on the oxygen atom; in addition, 2p and, possibly, 3d functions located on the hydrogen atom are also required. The best Hartree-Fock type computation has an energy of -76.06682 a.u. (Corongiu, G., IBM Kingston, personal communication, 1987) and has been obtained with a geometrical basis set<sup>(14)</sup> at the experimental equilibrium geometry.

A number of techniques have been introduced since 1930 to overcome the problem of the neglect of correlation energy in the Hartree-Fock approximation.

In molecular physics among the most popular techniques are the configuration interaction (C.I.), the many body perturbation approaches and, finally, the density functional approximations. The well known drawback of the configuration method is that the linear combination of determinants is very slow converging; indeed, we could even say that it is "not convergent." Despite much work in the past 20 years, a problem as simple as the interaction of two molecules of water represents, even today, a notable challenge for the configuration interaction technique. Perturbation techniques are also well known in the field of quantum chemistry and have become somewhat more popular in the last 10 years; these techniques reach a practical computational limit at around 30 to 40 electrons. Density functional techniques have long been introduced in quantum chemistry and here the names of Wigner,<sup>(15)</sup> Gombas,<sup>(16)</sup> and Bruckner<sup>(17)</sup> are worth mentioning. In the last 15 years, density functional techniques have become somewhat more popular due to the work by Kohn and Sham.<sup>(18)</sup> Whereas in the early days one would attempt to use density functionals as a correction to the Hartree-Fock energy,<sup>(19-22)</sup> more and more today one uses the density functional technique attempting to obtain the total energy. One more approach is now becoming more and more in evident; namely, Monte Carlo sampling of the electronic configurational space; we shall not stress this technique, since it is relatively new, but we wish to stress its potentiality.

The above preliminary comments are presented in order to appreciate problems which one faces in attempting to use quantum mechanics to obtain the interaction energy of two molecules of water or, differently stated, to obtain the two-body interaction potential.

In the early 1970s Popkie, *et al.*<sup>(23)</sup> obtained an interaction potential for two molecules of water by fitting the computed energy of many dimers of water at different orientations and positions. These computations were at a level near the Hartree-Fock limit. The potential was used in Monte Carlo simulations of liquid water: the obtained internal energy and the pair correlation functions were crude, but unmistakably those for water in the condense phase.<sup>(24)</sup> This marked the beginning of *ab initio* potentials in statistical mechanics for systems that were not trivially simple. Shortly thereafter there were a few attempts to introduce as much of the correlation energy correction as possible.<sup>(25)</sup> The simulated oxygen-oxygen pair correlation functions obtained with the improved potentials and Monte Carlo simulations were in reasonable agreement with experimental data. In one work, Matsuoka, Clementi, and Yoshimine<sup>(26)</sup> computed the energy of interaction between two molecules of water using the configuration interaction technique for 66 different geometries of the dimers. The model selected for fitting an analytical potential to the 66 interaction energies was a three-point charge model; two positive charges were placed at the hydrogen position and a balancing negative charge was placed along the  $C_{2v}$  axis. The value of the point charges as well as the position of the negative charge along the bisecting axis were considered fitting parameters. In addition to coulombic terms, other exponential terms were added involving couplings between the hydrogen atoms, the oxygen atoms, and hydrogen with oxygen atoms. Two potentials, CI(1) and CI(2), were derived and the former has subsequently been called MCY potential in the literature. Since the configuration interaction points were relatively few and since the overall shape of the interaction potential was assumed to remain close to the one given by the Hartree-Fock potential, Matsuoka, Clementi and Yoshimine kept the same model as in Ref. 23 and added to it new terms which

are to be considered mainly as corrections. Monte Carlo simulations were computed with the MCY potential<sup>(27)</sup> and yielded most reasonable pair correlation functions, and good agreement with X-ray and neutron beam scattering intensities. Clearly, *ab initio potentials* could be used competitively with empirical potentials. Quantum mechanics is, *de facto*, the submodel which provided the input to statistical mechanics. This potential was later revisited<sup>(28,29)</sup> with additions to the 66 configuration interaction energies previously mentioned.

As is known, if we consider three molecules of water their interaction is not simply the sum of the three pairs of different dimers composing the trimer of water. The three-body correction can in itself be partitioned into a Hartree-Fock contribution and a correlation correction contribution. The Hartree-Fock contribution can be obtained by considering a large number of trimers of molecules of water with different positions and orientations, thus scanning the three-body interaction hypersurface. The correlation correction can be obtained equivalently by performing configuration interaction type computation on the trimers. Clearly, if we have already found so many problems in computing dimers of water, we can expect only to be in a much worse situation when considering trimers. Fortunately one should expect that the correlation energy correction to the three-body forces be very small. Indeed, the major effect in the three-body correction is the induction energy which is a classical electrostatic effect and therefore well represented by the Hartree-Fock model. To verify this point a small number of trimers of water calculations were performed, both at the Hartree-Fock level and at the configuration interaction level. For the configuration analyzed, the correlation energy correction to the three-body effect was found indeed to be essentially zero.<sup>(30)</sup>

Let us now improve our two-body model by allowing the molecule of water to vibrate. A rather straightforward way to achieve the goal is simply to consider the potential energy between the two molecules as a sum of two contributions, one arising from the *intermolecular* and the second from the *intramolecular* motions; an approximate interaction potential has been reported by Lie and Clementi rather recently,<sup>(31)</sup> where the intramolecular potential was simply taken over from the many body perturbation computation by Bartlett, Shavitt, and Purvis.<sup>(32)</sup> The potential will henceforth be referred to as MCYL.

Let us now consider the question concerning the verification of all the above modeling. There is not much experimental data to check the predictions of quantum mechanical modeling, exception made when we consider a single water molecule. All the *ab initio* potentials predict that the most stable dimer configuration is of the open form with near linear hydrogen bond, which is confirmed by molecular beam study.<sup>(32)</sup> The O-O distance predicted by the MCY and the MCYL model is 2.87 Å, whereas experimental value is 2.98 Å.<sup>(32)</sup> The experimental binding energy for water dimer is known only to a rather low accuracy level (no better than within a 5% error, corresponding to about 0.2 kcal/mol) and for higher clusters the structural information is rather meager. (For some computational work on the cluster we refer to an older<sup>(33)</sup> and a more recent analysis.<sup>(34)</sup>)

The experimental second and third virial coefficients for steam are however widely available.<sup>(35)</sup> But these experimental quantities should be used with more care than has been usual in the past. The prevailing notion asserts that a "good" two-body potential should yield the second virial *in full agreement* with the exper-

imental values. This view should be "amended" on at least two accounts. First, the experimental second virials are only available at high temperature (over 100°C, whereas most biologically interesting environments and simulations are at the room temperature. Second, the experimental value of the second virial includes both vibrational and other quantum effects, generally ignored in many potentials, with contributions ranging from 5% to 10%, or even more.<sup>(36)</sup>

In Figure 1 we show the computed<sup>(37)</sup> and the experimental second virial for the two potentials obtained in Ref. 26, for the most widely used semi-empirical ST2 potential,<sup>(38)</sup> and for the Hartree-Fock potential.<sup>(2)</sup> For the third virial coefficient we refer elsewhere.<sup>(39)</sup>

STATISTICAL MECHANICS AS THE SECOND SUBMODEL. The interaction potential obtained via quantum mechanics constitutes the input necessary to obtain a statistical description of many water molecules interacting at a given pressure and temperature.

As is well known, we can consider the ensemble of many molecules of water either at equilibrium conditions or not. To start with, we shall describe our result within the equilibrium constraint, even if we realize that temperature gradients, velocity gradients, density, and concentration gradients are characterizations nearly essential to describe anything which is in the liquid state. The traditional approaches to equilibrium statistics are Monte Carlo<sup>(40)</sup> and molecular dynamics.<sup>(41)</sup> Some of the results are discussed in the following (The details can be found in the references cited).

In Figure 2, we show the x-ray and the neutron scattering intensity obtained from simulations of Monte Carlo type and from experimental data.<sup>(42)</sup> Let us consider the x-ray intensities. The two-body liquid reproduces well the experimental positions of the peaks and the peak-to-peak separation,<sup>(2)</sup> but not the relative intensity, especially for the initial split peak, a characteristic of liquid water. In the three-body liquid<sup>(39)</sup> the intensities show an improvement which is even better in the four-body liquid.<sup>(43)</sup> In the latter, however, the peaks are somewhat out of phase. Contrary to tradition, we do not display the pair correlation functions  $g_{OO}$ ,  $g_{OH}$ , and  $g_{HH}$ , since these are not direct experimental data and presently are not too accurate regarding the relative heights of the peaks.<sup>(44)</sup> All those simulations yield a pressure which is much too large relative to the experimental ones. The high pressure<sup>(2)</sup> can be removed by a small correction in the MCY potential as we found out recently in our laboratory (Dupuis, M., Huang, M. J., and Corongiu, G., IBM Kingston, personal communication, 1987).

With the MCYL model, we could also study the changes in water geometry going from monomer to the liquid state,<sup>(2)</sup> which has recently been inferred from neutron scattering experiments.<sup>(45)</sup> The oxygen-hydrogen separation in the gas phase is 0.9572Å; in the liquid phase, experimentally it is 0.966±0.006Å, to be compared with our simulation of 0.975Å. The average hydrogen-hydrogen separation is 1.514Å in the gas phase, 1.51±0.03Å from experiment in the liquid phase, and 1.53Å from our liquid simulation. Thus the experimental trend is well reproduced from *ab initio* MCYL potential where no empirical data other than fundamental constants have been used.<sup>(2)</sup>

From laboratory experiments, the internal energy of liquid water at room temperature is -8.1 kcal/mol. From our simulations, the two-body liquid yields an internal energy of -6.8 kcal/mol. The three-body liquid improves to -7.7 kcal/mol and the four-body liquid brings it to -8.95 kcal/mol. The *quantum cor-*

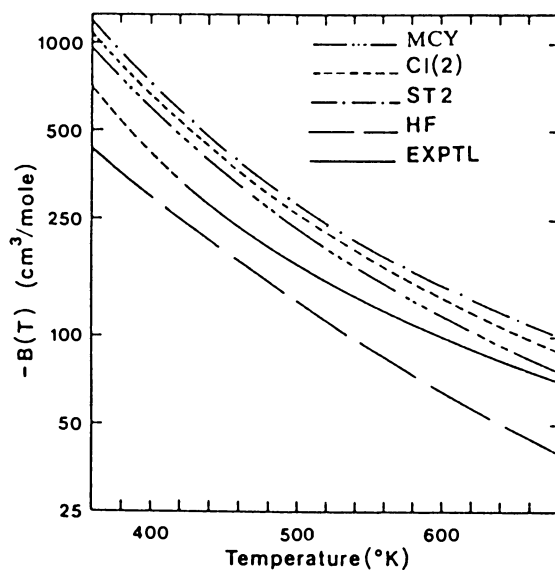


**Figure 1.** Comparison of the second virial coefficients from experiments and computations with empirical ST2 and ab-initio Hartree-Fock, MCY and CI(2) potentials.

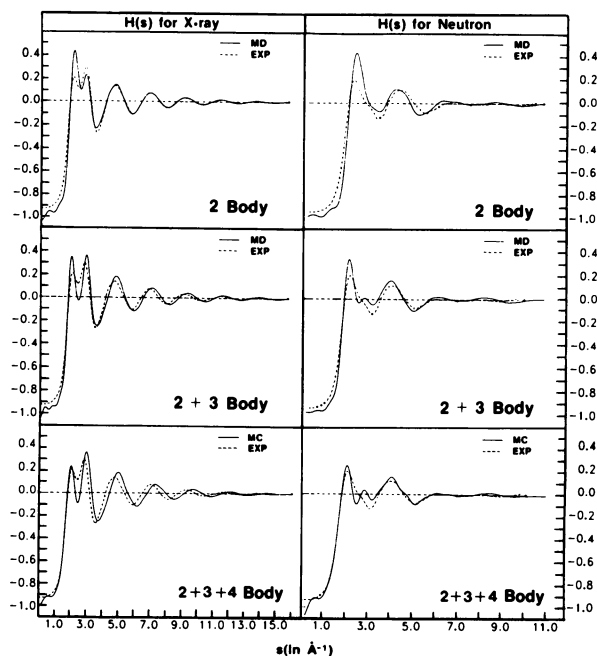


**Figure 2.** X-ray and neutron beam scattering intensities with MCY, with addition of three- and four-body corrections.

reaction decreases the above value by approximately 0.93 kcal/mol,<sup>(1)</sup> thus yielding a total internal energy of -8.02 kcal/mol, nearly in agreement with the experimental one. The heat capacity calculated using MCYL is 17.6 cal/(mol K) after quantum correction,<sup>(2)</sup> to be compared with the experimental value of 17.9 cal/(mol K). MCY and three-body potentials give 14.9 cal/(mol K) and 17.3 cal/(mol K), respectively.

Up to now we have considered non-dynamical equilibrium properties, namely time-independent properties; but the richness of a liquid is related to its flow, gradients, and dynamics. We will briefly consider a few dynamical properties of liquid water here and refer the interested readers to Refs. 31, 46, and 47 for details and others.

The self-diffusion coefficient calculated for the three body potential is  $D = 1.3 \times 10^{-5}$  cm<sup>2</sup>/sec. This is to be compared with the experimental value of  $2.3 \times 10^{-5}$  cm<sup>2</sup>/sec and to the value of  $2.25 \times 10^{-5}$  cm<sup>2</sup>/sec for the two-body liquid. It could be said that the three-body liquid shows more rigidity in some sense than the two-body liquid.

From the autocorrelation functions studied,<sup>(46,47)</sup> we obtain the following overall picture for the dynamics of liquid water: a single molecule of water in a liquid appears to be located within a potential well created by the tetrahedrally oriented neighboring molecules. The single molecule moves about in this well with translational velocity and with angular velocity. The angular process is much faster than the translational process and both are strongly non-isotropic, as can be expected by an overall tetrahedral rather than spherically symmetric arrangement.

**Table I.** Reorientational relaxation times  $\tau_l^r$  (in psec) of the  $C_l^r(t)$  for two-body and three-body liquid water models. The value of  $\tau_{NMR}$  is taken from Jonas, J.; deFries, T.; Wilbur, D. J. *J. Chem. Phys.* 1976, **65**, 582. Note that the experimental value is an average over x, y, and z directions

$\alpha$	$\tau_1^r$		$\tau_2^r$		$\tau_{NMR}$ Expt'l
	2B	2+3B	2B	2+3B	
x	2.7	7.2	1.6	3.8	4.8
y	4.9	11.6	2.3	5.5	
z	3.1	8.5	1.6	3.9	

Reorientational relaxation times,  $\tau_l^r$  can be estimated from the assumed exponential decay of the orientational correlation functions  $c_l^r(t)$ , defined as the average of the  $l^{\text{th}}$  Legendre polynomial of  $\cos \theta_\alpha$ :

$$C_l^r(t) = \langle P_l(\cos \theta_\alpha) \rangle$$

where  $\theta_\alpha$  is the angle between the  $\alpha^{\text{th}}$  principal axis at some time  $t = 0$  and at a later time  $t$ . Those are given in Table I for  $l=1$  and 2. The decay of the

orientational correlation is significantly slowed by the three-body forces, and the relaxation times more than doubled in the three-body liquid. The time integral of  $C_2^2(t)$  gives an estimate of the NMR relaxation time,  $\tau_{NMR}$ , associated with intermolecular dipolar coupling. Those are also given in Table I where it can be seen that the three-body forces significantly improve agreement with the experiment.

Let us now consider the velocity autocorrelation function (VACF) obtained from the MCYL potential, (namely, with the inclusion of vibrations). Figure 3 shows the velocity autocorrelation function for the oxygen and hydrogen atoms calculated for a temperature of about 300 K. The global shape of the VACF for the oxygen is very similar to what was previously determined for the MCY model. Very notable are the fast oscillations for the hydrogens relative to the oxygen.

The Fourier transform of the VACF, namely the spectral density, are also given in Figure 3. As known, those are related to the infrared spectrum of the liquid water. The band centered at about  $1,740\text{ cm}^{-1}$  is the intramolecular bending mode while those at  $3,648\text{ cm}^{-1}$  and  $3,752\text{ cm}^{-1}$  are associated with the intramolecular O-H bond stretches. In going from gas to liquid phase there is an upshift of  $55\text{ cm}^{-1}$  in the bending frequency and downshifts of  $198$  and  $203\text{ cm}^{-1}$  in the stretching frequencies. These shifts are all in good agreement with experimental IR and Raman results of  $50$ ,  $167$ , and  $266\text{ cm}^{-1}$ , respectively.<sup>(48)</sup> They are also better than shifts obtained from other semi-empirical potentials,<sup>(41)</sup> such as ST2. Notice that, since the center of mass of the water molecule is very close to the oxygen atom, the drastic intensity difference between the Fourier transform of hydrogen and oxygen in Figure 3 allows us to identify immediately that the broad band centered about  $500\text{ cm}^{-1}$  is due mainly to the rotational motion of the molecules, whereas the bands centered around  $40$  and  $190\text{ cm}^{-1}$  arise from the hindered translational motions.

#### TOWARDS THE HYDRODYNAMIC LIMIT: STRUCTURE FACTORS AND SOUND DISPERSION.

The collective motions of water molecules give rise to many hydrodynamical phenomena observable in the laboratories. They are most conveniently studied in terms of the spatial Fourier ( $k$ ) components of the density, particle currents, stress, and energy fluxes. The time correlation function of those Fourier components detail the decay of density, current, and fluctuation on the length scale of the  $1/k$ .

Figure 4 (left) shows the spatial Fourier transform of the density correlation function,  $F(k,t)/S(k)$ , for the two- and three-body models of water, for the first few wavevectors  $k = 0.253, 0.358, 0.438, 0.506, 0.566\text{ \AA}^{-1}$  allowed due to the use of the periodic boundary conditions in the simulation. In this range of  $k$  values both systems exhibit an initial rapid decay followed by a slower oscillatory decay. The rapid decay and oscillations are associated with the compressive elasticity of the fluid while the slower decay at longer times is related to the diffusive mixing of the molecules. The most apparent difference between the two- and three-body liquids is the overall slower decay of spatial order in the latter system. The first minima and maxima in  $F(k, t)$  are shifted to somewhat smaller times, indicating that at these wavelengths the three-body liquid is less compressible. The oscillations in  $F(k, t)$  are generally more damped in the three-body liquid. Thus, sound waves will travel faster and will be more strongly damped than in the two-body liquid.



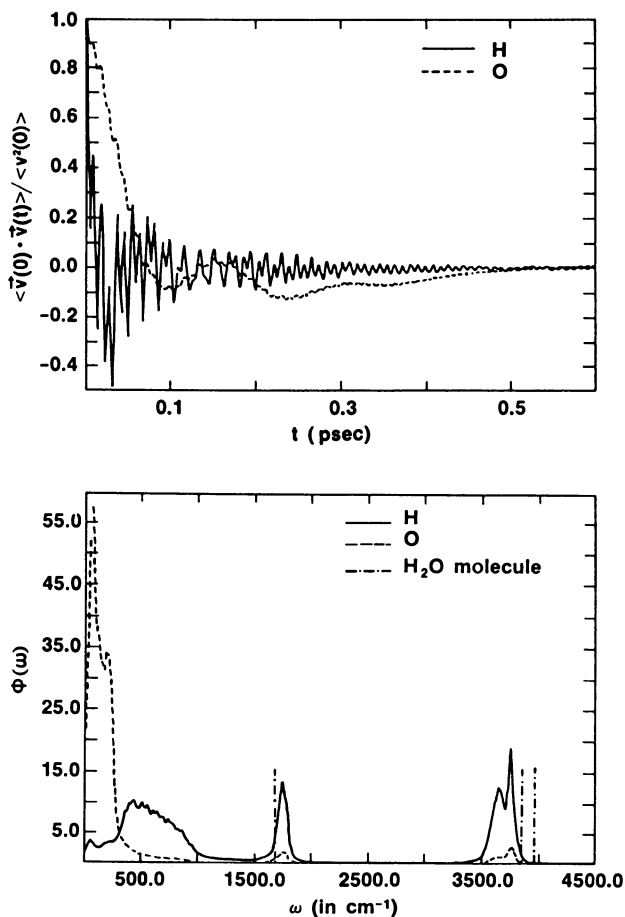


**Figure 3.** Hydrogen and oxygen velocity autocorrelation function from two-body MCY with vibrations allowed (MCYL), and computed infrared spectrum for intramolecular bending modes and bond stretching.

**American Chemical Society**  
**Library**  
 1155 16th St., N.W.  
 Washington, D.C. 20036

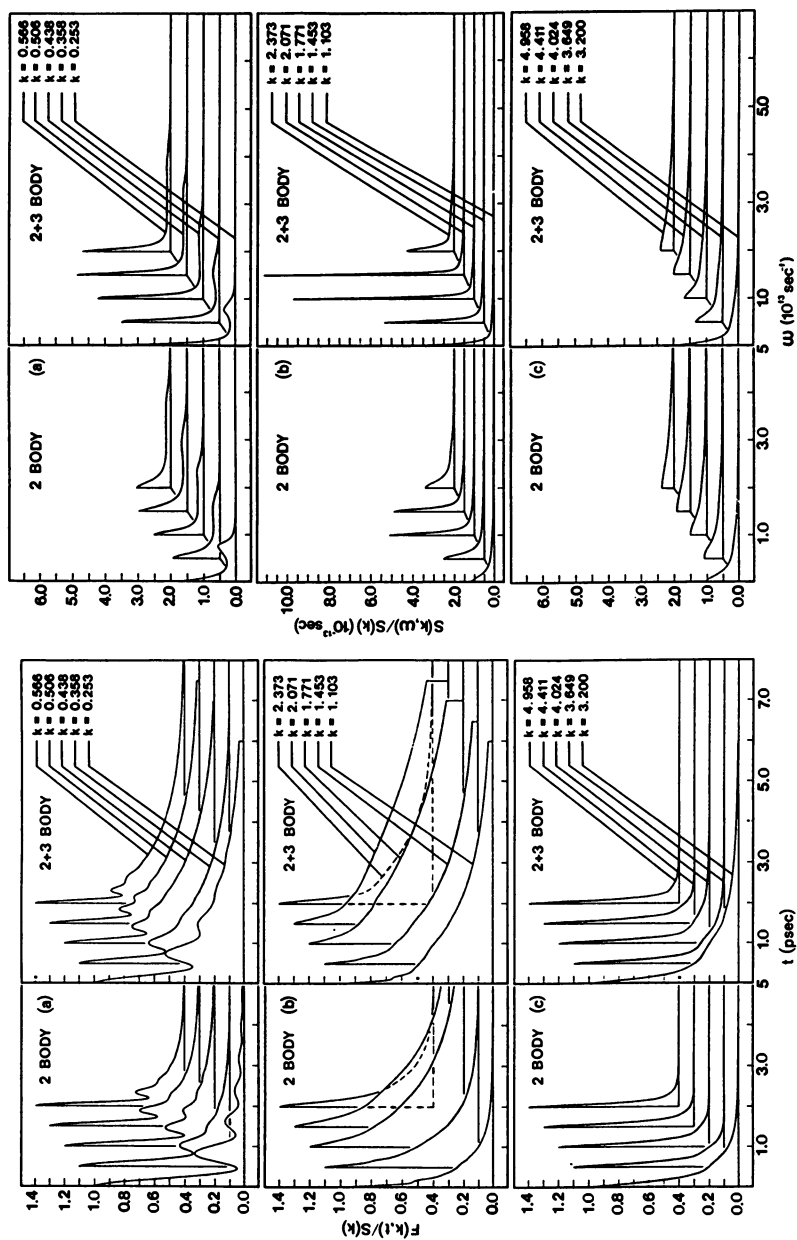


Figure 4. Intermediate scattering function (left),  $F(k,t)$  and dynamic structure factor (right),  $S(k,\omega)$ , computed from MCY with and without three-body correlations.

Figure 4 (right) shows  $F(k, t)$  for values of  $k$  near the first peak in the x-ray and neutron scattering spectra. The rapid and slow decay processes merge into a more gradual decay of quite long duration. This long decay is evidence of the persistence of the first shell of neighbors for the smaller  $k$  shown. The even slower decay at larger  $k$  indicates that, on average, pairs of molecules remain together for quite long times. The slower decay for the three-body liquid is again explained by the stronger intermolecular binding in that system. At still larger  $k$  values the  $F(k, t)$  begin to look the same for the two liquids, as is shown in Figure 4 (left, c). This is as expected because on very small length scales all systems asymptotically exhibit ideal gas behavior, irrespective of the intermolecular potential.

The temporal Fourier transform of the  $F(k, t)$  shows the propagation of normal sound modes at  $k \rightarrow 0$  and  $t \rightarrow 0$ . At higher frequencies and shorter wave lengths the fluid no longer behaves as a continuum and the effects of local structure become important, which could then give rise to the phenomena of sound dispersion. The sound speed calculated from the MCY potential at  $k \sim 0.4 \text{ \AA}^{-1}$ , about 3000 m/sec, was originally thought of as a defect of the potential<sup>(49)</sup> when compared to the experimental value of 1500 m/sec. However, in view of the positive dispersion observed in the two body MCY liquid for  $0.25 < k < 0.6 \text{ \AA}^{-1}$ ,<sup>(46,47)</sup> it seems clear that dispersion is the cause for the discrepancy. In fact, a recent experimental neutron diffraction did find the sound to propagate at 3310 m/sec around  $k \sim 0.5 \text{ \AA}^{-1}$ .<sup>(50)</sup>

**FLUID DYNAMICAL ASPECTS AND MACROSCOPIC THEORY.** The following section shows that one can join statistical mechanics with fluid dynamics; in the spirit of the "global simulations" this link is essential. The conceptual, intellectual and practical importance of this "link" is equally important and we are confident to have opened an important path to further understand physical phenomena.

As is well known, fluid dynamics is the study of motion and transport in liquids and gases. It is primarily concerned with macroscopic phenomena in non-equilibrium fluids and covers such behavior as diffusion in quiescent fluids, convection, laminar flows, and fully developed turbulence.

Since the phenomena studied in fluid dynamics are macroscopic, the fluid is considered to be a continuous medium, and the theory is not based on the behavior of individual molecules in the fluid but, rather, on their averages. Thus, fluid dynamics studies the motion of fluid volume elements which contain a large number of molecules. Such a volume element defines in the continuous medium a point which is small compared to the total system volume, but large when compared to typical intermolecular distances.

We present and discuss results for MD modeling of fluid systems. We restrict our discussion to systems which are in a macroscopically steady state, thus eliminating the added complexity of any temporal behavior. We start with a simple fluid system where the hydrodynamic equations are exactly solvable. We conclude with fluid systems for which the hydrodynamic equations are nonlinear. Solutions for these equations can be obtained only through numerical methods.

All of these experiments were accomplished using Argon atoms interacting through the short range Lennard-Jones or the soft sphere potential. The number of atoms,  $N$ , ranges from  $10^3$  to  $10^5$ , depending on the length scales over which

the desired phenomena will appear.<sup>(51)</sup> The densities and temperatures of the systems are such that the Argon is in liquid state. In the future, we hope to be able to consider molecular liquids, water in particular. However, the results reported below are sufficient to prove that we can overlap molecular dynamics with fluid dynamics, thus providing a valid bridge between macroscopic and microscopic theory. Additional evidence in support of this statement are the work by Ciccotti and co-workers.<sup>(52,53)</sup>

As a first example we consider a system bounded periodically in two coordinates and by thermal walls in the other coordinate.<sup>(54)</sup> The two thermal walls are at rest and maintained at the same temperature,  $T_w$ . The system is subjected to an acceleration field which gives rise to a net flow in the direction of one of the periodic coordinates. For this system, the hydrodynamic equations yield solutions of quadratic form for the velocity and quartic for the temperature.

We have modeled this system using MD with both short range as well as soft sphere Lennard-Jones potentials. For particles colliding with the thermal walls, they are re-injected into the system with new velocities drawn randomly from a Boltzmann distribution characterized by the wall temperature. We found the MD system to exhibit the predicted *quadratic profile* for the velocity response and *quartic profile* for the temperature response, as shown in Figure 5 for the soft sphere potential. In addition, with this system we can check for qualitative agreement with macroscopic theory. Using regression analysis to fit the MD results to the appropriate curves, we can calculate values for the shear viscosity coefficient,  $\eta$ , and the thermal conductivity coefficient,  $\kappa$ . We find the calculated values to be in good agreement with experimental values found for liquid Argon.

In fluid dynamics the behavior in this system is described by the full set of hydrodynamic equations. This behavior can be characterized by the Reynolds number,  $Re$ , which is the ratio of characteristic flow scales to viscosity scales. We recall that the Reynolds number is a measure of the dominating terms in the Navier-Stokes equation and, if the Reynolds number is small, linear terms will dominate; if it is large, nonlinear terms will dominate. In this system, the nonlinear term,  $(\vec{v} \cdot \nabla)\vec{v}$ , serves to convert linear momentum into angular momentum. This phenomena is evidenced by the appearance of two counter-rotating vortices or eddies immediately behind the obstacle. Experiments<sup>(55,56)</sup> and numerical integration of the Navier-Stokes equations predict the formation of these vortices at the length scale of the obstacle. Further, they predict that the distance between the vortex center and the obstacle is proportional to the Reynolds number. All these have been observed in our 2-dimensional flow system obstructed by a thermal *plate* at microscopic scales.<sup>(57)</sup>

Let us now consider in some detail another example of a fluid flow past an obstacle, this time a circle of diameter  $D$ .<sup>(58)</sup> Experimentally, the initial departure from Stokes flow occurs at Reynolds number  $Re \sim 5$ , at which point a pair of counter-rotating eddies (or vortices) begin to develop at the downstream boundary of the cylinder. The eddies grow in size while at  $Re \sim 34$  and an oscillatory wake is seen in the flow downstream of the obstacle. At slightly higher  $Re$ , somewhere in the range 55–70, transverse oscillations begin to occur in the eddy structure accompanied by periodic shedding of rotating fluid regions, and the von Karman vortex street makes its first appearance. Above  $Re \sim 100$  the eddy structure immediately behind the cylinder ceases to be visible. There exists a considerable body of photographic documentation of these effects.<sup>(59,60)</sup> Similar low- $Re$  behavior has also been seen in numerical solution of the equations of

continuum hydrodynamics.<sup>(6)</sup> We describe below the principal features seen in one typical simulation run.

The uniform flow at time  $t = 0$  rapidly changed into Stokes flow around the obstacle. By  $t \sim 100$  psec a pair of counter-rotating eddies had developed adjacent to the downstream edge of the obstacle. The length of the re-circulatory region grew steadily, reaching approximately  $1.4D$  at  $t \sim 260$  psec. The time-averaged flow field at  $t = 230$  psec is shown in Figure 6. The flow separation from the obstacle boundary is clearly visible, as are the flows within the eddies. The backflow velocity amounts to only about 10% of the overall flow speed; the compressible nature of the fluid is manifested most strongly just downstream of the obstacle where a 25% density drop occurs.

The next qualitative change that occurs is the breakdown of the bilateral symmetry of the flow — the counterclockwise (left) eddy begins to grow at the expense of the clockwise (right) eddy, the latter effectively disappearing at  $t \sim 300$  psec. The symmetry is restored by  $t \sim 370$  psec, but at  $t \sim 470$  psec only the clockwise eddy is seen. This in turn separates from the obstacle and the opposite eddy develops. Alternate eddy formation and shedding is repeated several times and an oscillatory wake develops at  $t \sim 600$  psec. Figure 6 shows the central portion of the flow field at  $t \sim 740$  psec; the wake — a remnant of previously shed eddies — is clearly visible, as is a counterclockwise eddy still attached to the obstacle. By  $t \sim 740$  psec the transverse flow component has reversed itself, and the flow pattern is essentially the mirror image of Figure 6. While the wake oscillations continue until (and presumably beyond) the end of the run ( $t = 1100$  psec), the recirculation that characterizes the eddies eventually vanishes and the sinuous wake is found to extend right up to the obstacle.

The results presented here are quite remarkable. The theory underlying derivation of the hydrodynamic equations assumes that all gradients and forces acting on the fluid are small. The MD fluids are under the influence of extremely large gradients and forces. Yet, we find results which are in both qualitative and quantitative agreement with macroscopic predictions. The appearance of spatial structure on such a small scale ( $10^{-6}$  cm) provides strong indications that fluid dynamics can be understood from a microscopic viewpoint.

A great deal of research remains to be done in this area. We are currently extending in the study of spatial correlations in the non-equilibrium fluids to time correlations with the hope of establishing a correspondence between MD and fluctuating hydrodynamic theory.<sup>(62,63)</sup> We are also using these systems to study the roles of viscosity and conductivity in fluid behavior under different external constraints. Finally, we plan to continue our research into the formation of spatial structures in fluids.

**MOLECULAR DYNAMICS STUDY OF DNA SOLUTIONS.** One of the main reasons for studying water is because of its importance in biological environment. A good understanding of the properties of water is thus essential as we move to more complicated systems. We have been involving in the study of aqueous solution of many important biological molecules, such as acetylcholine,<sup>(64)</sup> Gramicidin,<sup>(65)</sup> deoxydinucleoside phosphate and proflavin,<sup>(66)</sup> and DNA,<sup>(67)</sup> etc., first at the Monte Carlo level and slowly moving to the molecular dynamics simulations. We will discuss some of the new results on the molecular structure and the dynamics of B- and Z-DNA in the presence of counterions in the following.

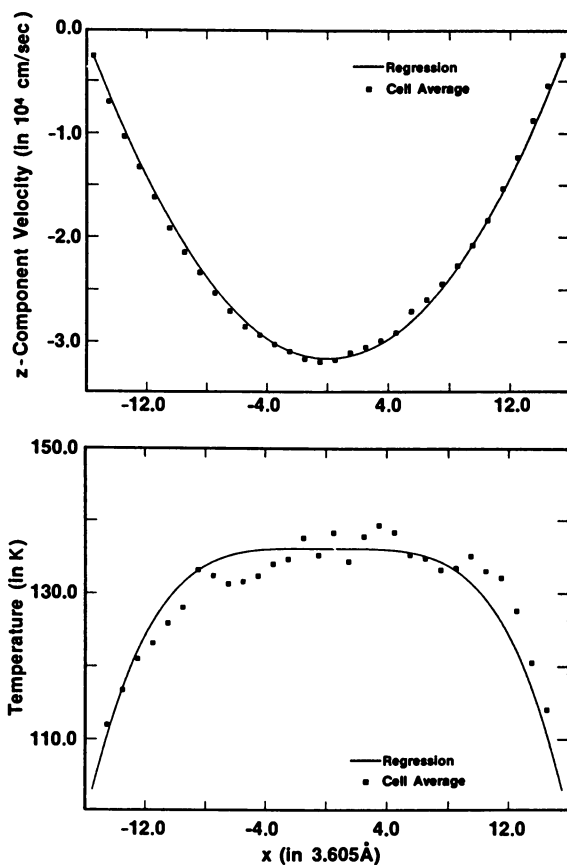


**Figure 5.** Velocity and temperature profiles for the cut-off Lennard-Jones potential. The system consists of 1152 atoms enclosed in a box of side length equal to 32:6:6.

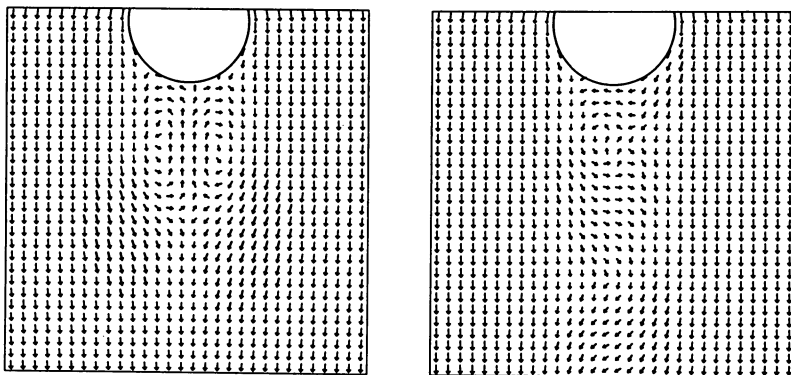


**Figure 6.** Central region showing eddy pair and location of the circular obstacle at  $t = 230$  psec (left) and a single eddy and portion of the oscillatory wake at  $t = 740$  psec (right). The flow is from top to bottom.

It should be noted that in the spirit of the global simulation, all the interaction potentials used are obtained from *ab initio* computations, although at the present time only at the SCF level with minimum basis sets.

The systems reported here are a single turn of B-DNA with G-C, A-T base pair sequence and the left handed Z-DNA with G-C base pair sequence. The B-DNA system is simulated for 4.0 psec and Z-DNA is simulated for 3.5 psec after equilibration. The simulation results are then analyzed for structural and dynamical properties.<sup>(6)</sup>

From a global analysis of the distribution of water molecules within 3.0Å from the DNA segment, it has been found that there are 241 and 292 oxygen atoms of the water molecules surrounding B- and Z-DNA respectively. The phosphate-water radial distribution functions indicated a layer of hydrogen atoms in the region between the counterion and the phosphate group, which shows up clearly as a peak at  $r \sim 2.8$  Å in the radial distribution functions of hydrogen atoms around the phosphorous atom. The analysis of the ion-water radial distribution functions suggest 3.8 and 4.9 for the number of water molecules within the first hydration shell of the ion in B- and Z-DNA respectively. The corresponding number is 7.5 in the case of an ionic solution.

An analysis of the hydration structure of water molecules in the major and minor grooves in B-DNA has shown that there is a filament of water molecules connecting both the inter and the intra phosphate groups of the two strands of B-DNA. However, such a connectivity is absent in the case of Z-DNA confirming earlier MC simulation results. The probability density distributions of the counterions around DNA shows deep penetration of the counterions in Z-DNA compared to B-DNA. Further, these distributions suggest very limited mobility for the counterions and show well defined counter-ion pattern as originally suggested in the MC study.<sup>(6)</sup>

For the analysis of the dynamical properties of the water and ions, the simulation cell is divided into eight subshells of thickness 3.0Å and of height equal to the height of one turn of DNA. The dynamical properties, such as diffusion coefficients and velocity autocorrelation functions, of the water molecules and the ions are computed in various shells. From the study of the dipole orientational correlation function

$$C(t) = \langle \vec{\mu}(t) \cdot \vec{\mu}(0) \rangle / \langle \vec{\mu}(0) \cdot \vec{\mu}(0) \rangle$$

in each subshell for both B- and Z-DNA. We have concluded that the dipole correlation functions decay more slowly for those water molecules close to the helix than those away from the helix. This observation is in agreement with the relaxation experiments of Lindsay on the hydration of Z-DNA (Lindsay, S. M., University of Arizona, personal communication, 1986). The ion probability distributions show a well defined pattern and suggest limited mobility for the ions close to the helix.

## CONCLUSION

In conclusion, as stated in Section III, building up from nuclei and electrons we extend the system to atoms, molecules, molecules in solutions and fluids with eddies and spatial-temporal structures of macroscopic dimensions. We hope to

have stimulated the readers in adopting the *global simulation* approach we have advocated, with the appreciation that super-computer are the necessary tools.

### ACKNOWLEDGMENTS

This review is based on a number of IBM-Tech. Reports prepared for a Chaire Francqui series of lectures delivered by E.C. in the spring of 1986 at the Free University of Bruxelles. We wish to thank all the people in our Department for their contributions, particularly Drs. E. L. Hannon, K. N. Swamy, G. Corongiu, J. Detrich, S. Chin, M. Dupuis, and R. Gomperts.

### LITERATURE CITED

1. Proceedings of the 1985 International Conference on Parallel Processing; Degroot, D. Ed.; Computer Soc. Press: Washington, DC, 1985.
2. Hockney, R. W. in Parallel Computers: Architecture, Programming and Algorithms; Hockney, R. W.; Jesshope, C. R., Eds.; Adam Hilger: Bristol, U. K., 1981.
3. Parallel Processing Systems; Evans, J., Ed.; Cambridge University Press: New York, 1982.
4. Wallach, Y. Alternating Sequential/Parallel Processing; Lecture Note in Computer Science, Vol. 124; Springer-Verlag: Berlin, 1982.
5. Clementi, E.; Corongiu, G.; Detrich, J. H.; Chin, S.; Domingo, L.; Int. J. Quantum Chem. Symp. 1984, **18**, 601.
6. Corongiu, G.; Detrich, J. H. IBM Journal Res. and Dev. 1985, **29**, 422.
7. IBM Program Product: MVS/Extended Architecture Operations; International Business Machines, 1984.
8. Chin, S.; Domingo, L.; Carnevali, A.; Caltabiano, R.; Detrich, J. H. IBM Kingston Technical Report 1985, **KGN-42**.
9. Clementi, E. J. Phys. Chem. 1985, **89**, 4426.
10. Benedict, W. S.; Gailer, N.; Plyler, E. K. J. Phys. Chem. 1956, **24**, 1139.
11. Werner, H. J.; Mayer, W. Mol. Phys. 1976, **31**, 885.
12. Bartlett, R. J.; Shavitt, I.; Purvis, G. D. J. Chem. Phys. 1979, **71**, 281.
13. Clementi, E.; Popkie, H. J. Chem. Phys. 1972, **57**, 1077.
14. Clementi, E.; Corongiu, G. Chem. Phys. Lett. 1983, **90**, 359.
15. Wigner, E. Phys. Rev. 1934, **46**, 1002.
16. Gombas, P. Pseudopotentials; Springer-Verlag: New York, 1967.
17. Brueckner, K. A.; Ma, S. K. Document IRPA 67-150; University of California: La Jolla, 1967.
18. Kohn, W.; Sham, L. J. Phys. Rev. A 1965, **140**, 1133.
19. Clementi, E. IBM J. Res. and Dev. 1965, **9**, 2.
20. Clementi, E. Proc. Nat. Acad. Sci. (USA) 1972, **69**, 2942.
21. Lie, G. C.; Clementi, E. J. Chem. Phys. 1974, **60**, 1275.
22. Lie, G. C.; Clementi, E. J. Chem. Phys. 1974, **60**, 1288.
23. Popkie, H.; Kistenmaker, H.; Clementi, E. J. Chem. Phys. 1973, **59**, 1325.
24. Kistenmaker, H.; Popkie, H.; Clementi, E.; Watts, R. O. J. Chem. Phys. 1974, **60**, 4455.
25. Lie, G. C.; Clementi, E. J. Chem. Phys. 1975, **62**, 2060.
26. Matsuoaka, O.; Clementi, E.; Yoshimine, M. J. Chem. Phys. 1976, **64**, 1351.
27. Lie, G. C.; Clementi, E.; Yoshimine, M. J. Chem. Phys. 1976, **64**, 2314.



28. Habitz, P.; Clementi, E. *J. Phys. Chem.* 1983, **87**, 2815.
29. Carravetta, V.; Clementi, E. *J. Chem. Phys.* 1984, **81**, 2646.
30. Clementi, E.; Corongiu, G. *Int. J. Quantum Chem. Symp.* 1983, **10**, 31.
31. Lie, G. C.; Clementi, E. *Phys. Rev. A* 1986, **33**, 2679.
32. Odutola, J. A.; Dyke, T. R., *J. Chem. Phys.* 1980, **72**, 5062.
33. Kistenmaker, H.; Lie, G. C.; Popkie, H.; Clementi, E. *J. Chem. Phys.* 1974, **61**, 546.
34. Kim, K. S.; Dupuis, M.; Lie, G. C.; Clementi, E. *IBM Technical Report* 1986, KGN-45.
35. Dymond, J. H.; Smith, E. B. *The Virial Coefficients of Pure Gases and Mixtures*; Oxford Press: New York, 1980.
36. Refson, K.; Lie, G. C.; Clementi, E. *IBM Technical Report* 1987, KGN-92.
37. Lie, G. C.; Clementi, E. *J. Chem. Phys.* 1976, **64**, 5308.
38. Stillinger, F. H.; Raman, A. *J. Chem. Phys.* 1974, **60**, 1545.
39. Lie, G. C.; Corongiu, G.; Clementi, E. *J. Phys. Chem.* 1985, **89**, 4131.
40. Metropolis, N.; Rosenbluth, A. W.; Rosenbluth, M. N.; Teller, A. H.; Teller, E. *J. Chem Phys.* 1953, **21**, 1078.
41. Wood, D. W. in *Water-A Comprehensive Treatise*; Franks, F., Ed.; Plenum Press: New York, 1979; Vol. 6, p 279.
42. Narten, A. H.; Levy, A. H. *J. Chem. Phys.* 1971, **55**, 2263.
43. Detrich, J. H.; Corongiu, G.; Clementi, E. *Int. J. Quantum Chem. Symp.* 1984, **18**, 701.
44. Lie, G. C. *J. Chem. Phys.* 1986, **85**, 7495.
45. Thiessen, W. E.; Narten, A. H. *J. Chem. Phys.* 1982, **77**, 2656.
46. Wojcik, M.; Clementi, E. *J. Chem. Phys.* 1986, **85**, 3544.
47. Wojcik, M.; Clementi, E. *J. Chem. Phys.* 1986, **85**, 6085.
48. Eisenberg, D.; Kauzmann, W. *The Structure and Properties of Water*; Oxford University Press: New York, 1969.
49. Impey, R. W.; Madden, P. A.; McDonald, I. R. *Molec. Phys.* 1982, **46**, 513.
50. Chen, S. H.; Toukan, K.; Loon, C. K.; Price, D. L.; Teixeira, J. *Phys. Rev. Lett.* 1985, **54**, 2681.
51. Hannon, L.; Kestemont, E.; Lie, G. C.; Mareschal, M.; Rapaport, D. C.; Chin, S.; Clementi, E. *IBM Technical Report* 1986, Chaire Francqui Lecture Series: Part 7.
52. Tannenbaum, A.; Ciccotti, G.; Gallico, R. *Phys. Rev. A* 1982, **25**, 2278.
53. Trozzi, C.; Ciccotti, G. *Phys. Rev. A* 1984, **29**, 916.
54. Hannon, L.; Lie, G. C.; Clementi, E. *Phys. Lett. A* 1986, **119**, 174.
55. Gerrard, J. H. *Phil. Trans. Roy. Soc. (London)* 1978, **A288**, 351.
56. Penny, A. E.; Chang, M. S.; Lim, T. T. *J. Fluid Mech.* 1982, **116**, 77.
57. Hannon, L.; Lie, G. C.; Clementi, E. *J. Sci. Computing* 1986, **1**, 145.
58. Rapaport, D. C.; Clementi, E. *Phys. Rev. Lett.* 1986, **57**, 695.
59. Batchelor, G. K. *An Introduction to Fluid Dynamics*; Cambridge University Press: Cambridge, U. K., 1967.
60. Van Dyke, M. *An Album of Fluid Motions*; Parabolic Press: Stanford, CA, 1982.
61. Jordan, S. K.; Fromm, J. E. *Phys. Fluids* 1972, **15**, 371.
62. Mansour, M. M.; Garcia, A. L.; Lie, G. C.; Clementi, E. *Phys. Rev. Lett.* 1987, **58**, 874.
63. Mansour, M. M.; Garcia, A. L.; Lie, G. C.; Clementi, E. *J. Stat. Phys.* 1987, **47**, 209.

64. Margheritis, C.; Corongiu, G.; Clementi, E. IBM Kingston Technical Report 1985, KG N-40.
65. Kim, K. S.; Vercauteren, D. P.; Welti, M.; Chin, S.; Clementi, E. J. Biophys. Soc. 1985, 47, 327.
66. Kim, K. S.; Clementi, E. J. Phys. Chem. 1985, 89, 3655.
67. Corongiu, G.; Clementi, E. Biopolymers 1982, 21, 763.
68. Swamy, K. N.; Clementi, E. IBM Kingston Technical Report 1987, KG N-94.
69. Clementi, E.; Corongiu, G. J. Biol. Phys. 1983, 11, 33.

RECEIVED June 15, 1987

## Chapter 15

# Theory and Computer Simulation of Structure, Transport, and Flow of Fluid in Micropores

H. T. Davis, I. Bitsanis, T. K. Vanderlick, and M. V. Tirrell

Chemical Engineering and Materials Science Department, University of Minnesota,  
Minneapolis, MN 55455

An overview is given of recent progress made in our laboratory on this topic. The density profiles of fluid in micropores are found by solving numerically an approximate Yvon-Born-Green equation. A related local average density model (LADM) allows prediction of transport and flow in inhomogeneous fluids from density profiles. A rigorous extension of the Enskog theory of transport is also outlined. Simple results of this general approach for the tracer diffusion and Couette flow between planar micropore walls are presented. Equilibrium and flow (molecular dynamics) simulations are compared with the theoretical predictions. Simulated density profiles of the micropore fluid exhibit substantial fluid layering. The number and sharpness of fluid layers depend sensitively on the pore width. The solvation force and the pore average density and diffusivity are oscillating functions of the pore width. The theoretical predictions for these quantities agree qualitatively with the simulation results. The flow simulations indicate that the flow does not affect the fluid structure and diffusivity even at extremely high shear rates ( $10^{10}\text{s}^{-1}$ ). The fluid structure induces large deviations of the shear stress and the effective viscosity from the bulk fluid values. The flow velocity profiles are correlated with the density profiles and differ from those of a bulk fluid. The LADM and extended Enskog theory predictions for the velocity profiles and the pore average diffusivity agree very well with each other and with the simulation results. The LADM predictions for the shear stress and the effective viscosity agree fairly well with the simulation results.

Examples of fluids confined in pores and spaces of molecular or nanometer dimensions abound in technological and natural products and processes. These include wetting and lubrication, zeolite supported catalysis, silica gel based chromatographic separations, drying of paper

0097-6156/87/0353-0257\$07.25/0  
© 1987 American Chemical Society

products and clay dispersions, aggregation of colloids, permeation of Vico and other sintered glasses, the formation of soap films, foams and emulsions, and water or oil rich zones in lyotropic liquid crystals and vesicular bilayer structures. In such confinement the fluids can be strongly inhomogeneous and so the usual theories of fluid structure and dynamics may not be applicable. Owing to the molecular dimensions involved, experimental characterization of fluid in micropores is also difficult. Thus, computer simulation on model systems becomes an important tool to test ideas and supplement experiments on real systems in trying to understand the behavior of fluids confined on the nanometer scale.

In this paper, we report recent progress made in our laboratory in using molecular theory and computer simulation to understand the structure, flow and transport of fluids confined by planar solid walls separated by a few molecular diameters.

### Molecular Theory of Structure and Transport

Equilibrium Theory of Fluid Structure. In all the theoretical work reported herein, we assume that the particles interact with pair additive forces whose pair potentials can be approximated by

$$u(s) = u_R(s) + u_A(s) \quad (1)$$

where

$$\begin{aligned} u_R(x) &= \infty, \quad s < \sigma \\ &= 0, \quad s > \sigma \end{aligned} \quad (2)$$

and  $u_A(s)$  is the continuous, attractive part of the pair potential. The pore walls confining the fluid will be represented by the conservative potential  $u^e(\mathbf{r})$ . At equilibrium the density  $n(\mathbf{r})$  of the fluid obeys the Yvon-Born-Green (YBG) equation

$$\begin{aligned} k_B T \nabla n + n \nabla u^e - n \int n(\mathbf{r}+\mathbf{s}) g(\mathbf{r}, \mathbf{r}+\mathbf{s}) \frac{\mathbf{s}}{s} u_A'(s) d^3s \\ + n k_B T \int n(\mathbf{r}+\sigma \mathbf{k}) g(\mathbf{r}, \mathbf{r}+\sigma \mathbf{k}) \sigma^2 \mathbf{k} d^2\mathbf{k} = 0 \end{aligned} \quad (3)$$

where  $g(\mathbf{r}, \mathbf{r}')$  is the pair correlation function,  $k_B$  is Boltzmann's constant and  $T$  is the absolute temperature.  $\mathbf{k}$  is a unit vector lying along the line of centers of a pair of molecules in contact.  $d^2\mathbf{k}$  denotes an element of solid angle associated with  $\mathbf{k}$ .

Equation 3 is exact for fluids obeying Equations 1 and 2. However, in order to compute the density  $n(\mathbf{r})$  from the YBG equation one must know the relationship between density distribution and the pair correlation function of inhomogeneous fluid. Such a relationship is not available in general. However, an approximation introduced by Fischer and Methfessel (1) has been shown to give fairly accurate predictions of the density

profiles in liquid-vapor and liquid-solid interfaces. It has also been shown that their approximation gives the exact density distribution for one-dimensional hard rods in an external potential  $u^e$ . The main assumption of Fischer and Methfessel is that the pair correlation function can be approximated as

$$g(\mathbf{r}, \mathbf{r} + \mathbf{s}) = g^o(s; \bar{n}(\mathbf{r} + \frac{1}{2}\mathbf{s})) \quad (4)$$

where  $g^o$  is the correlation function of homogeneous fluid and  $\bar{n}$  is a local average density defined by

$$\bar{n}(\mathbf{r}) = \frac{1}{(\pi\sigma^3/\delta)} \int_{R < \sigma/2} n(\mathbf{r} + \mathbf{R}) d^3R \quad (5)$$

Equation 4 renders the YBG equation solvable. However, as did Fischer and Methfessel we shall further simplify the theory by making the van der Waals' structureless fluid approximation ( $g = 0$ ,  $s < \sigma$ ,  $g = 1$ ,  $s > \sigma$ ) in the integral involving the long-ranged continuous force  $u_A'$ . The YBG equation thus becomes

$$\begin{aligned} \nabla [k_B T \ln n + u^e + \int n(\mathbf{r} + \mathbf{s}) u_A(\mathbf{s}) d^3s] \\ + k_B T \int g^o(\sigma; \bar{n}(\mathbf{r} + \frac{\sigma}{2}\mathbf{k})) \sigma^2 k d^2k = 0 \end{aligned} \quad (6)$$

To finally complete the model a formula for the contact value of the pair correlation function  $g^o$  must be given. We choose the Carnahan formula

$$g^o(\sigma; \bar{n}) = \frac{1 - \frac{\pi}{12} \sigma^3 \bar{n}}{(1 - \frac{\pi}{6} \sigma^3 \bar{n})^3} \quad (7)$$

shown by Carnahan and Starling (2) to be accurate in hard sphere fluids.

In the calculations to be reported in what follows we shall consider planar systems, i.e., flat pore walls so that  $u^e = u^e(x)$  and  $n = n(x)$ , where  $x$  is the distance from a pore wall. In this case Equation 6 can be integrated to give

$$\begin{aligned} \mu^* = \ln n(x) + \frac{1}{k_B T} \int_{-\infty}^{+\infty} n(x') \bar{u}_A(x - x') dx' \\ + 2\pi\sigma^2 \int_0^x dx' \int_{-1}^1 d\zeta \zeta n(x' + \sigma\zeta) g(\bar{n}(x' + \frac{1}{2}\sigma\zeta)) - \frac{u^e(x)}{k_B T} \end{aligned} \quad (8)$$

where

$$\bar{n}(x) = (6/\sigma^3) \int_{-\sigma/2}^{+\sigma/2} (.25\sigma^2 - (x - x')^2)n(x')dx' \quad (9)$$

The constant of integration  $\mu^*$  is a field variable similar to the chemical potential ( $\mu^* = -3.6227$  in our calculations).

The external potential,  $u^e(x)$ , arises from the solid walls at  $x = 0$  and  $x = h$ .

$$u^e(x) = \phi_w(x) + \phi_w(h - x) \quad (10)$$

where each wall exerts a 10-4-3 potential (3):

$$\phi_w = \epsilon_w \left[ \left( \frac{2}{5} \right) \left( \frac{\sigma_w}{x} \right)^{10} - \left( \frac{\sigma_w}{x} \right)^4 - \frac{\sqrt{2}\sigma_w^3}{3(x + \frac{0.61\sigma_w}{\sqrt{2}})^3} \right], \quad x > 0 \quad (11)$$

$\epsilon_w$  and  $\sigma_w$  are characteristic wall-fluid particle energy and separation distance parameters.

The fluid-fluid intermolecular potential,

$$\bar{u}_A(x) = \int_{-\infty}^{+\infty} \int u^A(s)dydz \quad (12)$$

is taken to be

$$\begin{aligned} \bar{u}_A(x) &= -2\pi\epsilon\sigma^2, \quad |k| < \sigma \\ &= -\frac{2\pi\epsilon\sigma^6}{x^4}, \quad |k| > \sigma \end{aligned} \quad (13)$$

This corresponds to the attractive part of a "6 -  $\infty$ " Lennard-Jones potential; namely,

$$\begin{aligned} u^A(s) &= -4\epsilon \left( \frac{\sigma}{s} \right)^6, \quad s > \sigma \\ &= 0, \quad s < \sigma \end{aligned} \quad (14)$$

The normal pressure  $P_N$  in the fluid confined between the walls varies with wall separation and is not, in general, equal to the bulk pressure  $P_B$  of fluid at the same chemical potential. The difference  $P_N - P_B$  is the solvation force per unit area, (4)  $f_s$ , and can be calculated from the equilibrium density profiles by

$$f_s = - \int_0^h n(x) \frac{d\phi_w(x)}{dx} dx + \int_0^\infty n(x) \frac{d\phi_w(x)}{dx} dx \quad (15)$$

The equilibrium density profiles are obtained by solving Equations 8 and 9 for a modified density  $n^*(x)$ , where

$$n^*(x) = n(x) e^{u^*(x)/kT} \quad (16)$$

This modified density is a more slowly varying function of  $x$  than the density. The domain of interest,  $0 < x < h$ , is discretized uniformly and the trapezoidal rule is used to evaluate the integrals in Equations 8 and 9. This results in a system of nonlinear, coupled, algebraic equations for the nodal values of  $n^*$  and  $\bar{n}$ . Newton's method is used to solve for  $n^*$  and  $\bar{n}$  simultaneously. The domain is discretized finely enough so that the solution changes negligibly with further refinement. A mesh size of  $0.05\sigma$  was adopted in our calculations.

Solutions were obtained initially for a wall separation  $h = 40\sigma$ , where at the midpoint the density is equal to the bulk fluid density,  $n_b$ . Then, solutions for decreasing pore width were found using the previous solution at larger  $h$  as a first guess for the next width. Pore width was gradually decreased to  $h = 2.25\sigma$  using small enough steps to ensure that quadratic convergence was observed at each new pore width. Step sizes ranged from a few  $\sigma$ 's to  $0.05\sigma$ .

**Local Average Density Model (LADM) of Transport.** In the spirit of the Fischer-Methfessel local average density model, Equation 4, for the pair correlation function of inhomogeneous fluid, a local average density model (LADM) of transport coefficients has been proposed (5) whereby the local value of the transport coefficient,  $\lambda(\mathbf{r})$ , is approximated by

$$\lambda(\mathbf{r}) = \lambda^0(\bar{n}(\mathbf{r})) \quad (17)$$

$\lambda^0(\bar{n}(\mathbf{r}))$  is the transport coefficient of homogeneous fluid at the local average density  $\bar{n}(\mathbf{r})$ .

According to this model the diffusivity of a molecule at position  $x$  in the planar pore system of interest in this paper is  $D^0(\bar{n}(x))$  and so the pore diffusivity is

$$D_{\text{pore}} = \int_0^h n(x) D^0(\bar{n}(x)) dx / \int_0^h n(x) dx \quad (18)$$

since  $D^0(\bar{n}(x))n(x)dx/N$  is the probable diffusivity of a particle lying between  $x$  and  $x + dx$  in the pore.

The stress tensor  $\tau$  according to LADM is

$$\tau(\mathbf{r}) = \frac{\eta^0(\bar{n}(\mathbf{r}))}{2} [\nabla \bar{\mathbf{v}} + \nabla \bar{\mathbf{v}}^T] + [\eta_b^0(\bar{n}(\mathbf{r})) - \frac{2}{3}\eta^0(\bar{n}(\mathbf{r}))] \nabla \cdot \mathbf{v} \mathbf{I} \quad (19)$$

where  $\bar{\mathbf{v}}$  is the mean flow velocity,  $\nabla \bar{\mathbf{v}}^T$  is the transpose of  $\nabla \bar{\mathbf{v}}$ ,  $\eta^0(\bar{n})$  and  $\eta_b^0(\bar{n})$  the shear and bulk viscosity coefficients of homogeneous fluid at density  $\bar{n}$ .

The attractive feature of LADM is that once the fluid structure is known (e.g., by solution of the YBG equations given in the previous section or by a computer simulation) then theoretical or empirical formulas for the transport coefficients of homogeneous fluids can be used to predict flow and transport in inhomogeneous fluid. For diffusion and Couette flow in planar pores LADM turns out to be a surprisingly good approximation, as will be shown in a later section.

**Enskog Theory of Transport.** Enskog's theory of hard spheres, with introduction of a temperature dependent hard sphere diameter, gives surprisingly accurate estimates of the diffusivity and viscosity of real fluids (6). This is because in simple fluids the short-ranged repulsive forces between molecules dominate in the collisional dissipation leading to transport phenomena. The long-ranged attractive interactions contribute importantly to the energy of the fluid, and thus to phase transitions and interfacial structure, but apparently are less effective in collisional dissipation. With this view of fluid behavior Enskog's theory of transport in bulk fluid has been generalized to strongly inhomogeneous fluids.

Consider a fluid of molecules interacting with pair additive, centrally symmetric forces in the presence of an external field and assume that the collisional contribution to the equation of motion for the singlet distribution function is given by Enskog's theory. In a multicomponent fluid, the distribution function  $f_i(\mathbf{r}, \mathbf{v}_i, t)$  of a particle of type  $i$  at position  $\mathbf{r}$ , with velocity  $\mathbf{v}_i$  at time  $t$  obeys the equation of change (7)

$$\begin{aligned} \frac{\partial f_i}{\partial t} + \mathbf{v}_i \cdot \nabla f_i - \frac{1}{m_i} \nabla u_i^e \cdot \nabla_{\mathbf{v}_i} f_i \\ - \sum_j \frac{1}{m_i} \int \nabla u_{ij}^A(\mathbf{r} - \mathbf{r}') \cdot \nabla_{\mathbf{v}_i} f_i f_j g_{ij}(\mathbf{r}, \mathbf{r}', t) d^3 r' d^3 \mathbf{v}_j \\ = \sum_j \int_{\mathbf{v}_j \cdot \mathbf{k} > 0} [g_{ij}(\mathbf{r}, \mathbf{r} + \sigma_{ij} \mathbf{k}) f_i(\mathbf{r}, \mathbf{v}_i', t) f_j(\mathbf{r} + \sigma_{ij} \mathbf{k}, \mathbf{v}_j', t) \\ - g_{ij}(\mathbf{r}, \mathbf{r} - \sigma_{ij} \mathbf{k}) f_i(\mathbf{r}, \mathbf{v}_i, t) f_j(\mathbf{r} - \sigma_{ij} \mathbf{k}, \mathbf{v}_j, t)] \sigma_{ij}^2 \mathbf{v}_{ji} \cdot \mathbf{k} d^2 \mathbf{k} d^3 \mathbf{v}_j \quad (20) \end{aligned}$$

where  $\nabla$  and  $\nabla_{\mathbf{v}_i}$  are gradient operators with respect to  $\mathbf{r}$  and  $\mathbf{v}_i$ ,  $m_i$  molecular mass,  $u_i^e$  the potential of the external force,  $u_{ij}^A$  the pair potential of attractive forces between particles of types  $i$  and  $j$ ,  $g_{ij}$  the pair correlation function between  $i$  and  $j$ ,  $\sigma_{ij} \equiv (\sigma_{ii} + \sigma_{jj})/2$ ,  $\sigma_{ii}$  the hard sphere diameter of  $i$ ,  $\mathbf{k}$  a unit vector directed from the center of  $i$  to that of  $j$ , and  $\mathbf{v}_i'$  the velocity of  $i$  after a hard-sphere collision with  $j$ . We recall that



$\mathbf{v}'_i = \mathbf{v}_i - \mathbf{v}_{ij} \cdot \mathbf{k} \mathbf{k}$ , where  $\mathbf{v}_{ij} \equiv \mathbf{v}_i - \mathbf{v}_j(\mathbf{Z})$ . The attractive interaction  $u_{ij}^A$  is assumed to be sufficiently slowly varying that it does not contribute to collisional dissipation.

The local density  $n_i$  of species 1 is related to the velocity distribution function by

$$n_i(\mathbf{r}, t) = \int f_i(\mathbf{r}, \mathbf{v}_i, t) d^3 v_i \quad (21)$$

At equilibrium the distribution function is of the form

$$f_i = n_i(\mathbf{r}) \phi_i(\mathbf{v}_i) \quad (22)$$

where  $\phi_i$  is the Maxwell velocity distribution function,

$$\phi_i(\mathbf{v}_i) = \left( \frac{m_i}{2\pi k_B T} \right)^{3/2} \exp(-m_i v_i^2 / 2k_B T) \quad (23)$$

With this distribution function, velocity factors out of Equation 20 yielding the exact YBG equation, Equation 3, for equilibrium fluids whose interaction potential is given by Equation 1.

The Chapman-Enskog method has been used to solve for steady state tracer diffusion ( $\mathbf{g}$ ). According to the method the singlet distribution function for the diffusing species 1, present in a trace amount ( $n_1 \ll n_i, 1 \neq i$ ) in an otherwise equilibrium fluid, is approximated by

$$f_1 = n_1(\mathbf{r}) \phi_1(\mathbf{v}_1) [1 + \mathbf{a}_1(\mathbf{r}) \cdot \mathbf{v}_1] \quad (24)$$

and  $\mathbf{a}_1(\mathbf{r})$  is obtained from the Enskog equation. The result for the linearized diffusion flux  $\mathbf{J}_1$  of species 1:

$$\mathbf{J}_1 = \int f_1 \mathbf{v}_1 d^3 v_1 = -n_1^0 k_B T \zeta_1^{-1} \cdot \nabla \ln(n_1/n_1^0) \quad (25)$$

where  $\zeta_1$  is the friction tensor,

$$\zeta_1(\mathbf{r}) = \sum_{j \neq 1} \frac{m_1}{\pi} \left( \frac{2\pi k_B T}{m_{1j}} \right)^{1/2} \int g_{1j}(\mathbf{r}, \mathbf{r} + \sigma_{1j} \mathbf{k}) n_j^0(\mathbf{r} + \sigma_{1j} \mathbf{k}) \sigma_{1j}^2 \mathbf{k} k d^2 k \quad (26)$$

$m_{1j} \equiv m_1 m_j / (m_1 + m_j)$ ,  $g_{1j}(\mathbf{r}, \mathbf{r} + \sigma_{1j} \mathbf{k})$  the equilibrium pair correlation function,  $n_j^0(\mathbf{r})$  the equilibrium density distribution of species 1, and  $n_1(\mathbf{r})$  the diffusive density distribution.

As expected from continuum theory, the friction and diffusion coefficients are replaced in inhomogeneous fluid by tensors whose symmetry reflects that of the inhomogeneous media.

For the special case of self-diffusion (tracer molecules dynamically

identical to solvent molecules) in the  $y$ -direction in a planar pore, it follows from Equation 25 that the pore average flux obeys (2)

$$J_{\text{pore}} = \frac{1}{h} \int_0^h J_{1y} dx = - D_{\text{pore}} \frac{dn_{\text{pore}}}{dx} \quad (27)$$

where  $n_{\text{pore}} = h^{-1} \int_0^h n_1 dx$  and

$$D_{\text{pore}} = \int_0^h D_T(x) n^0(x) dx / \int_0^h n^0(x) dx \quad (28)$$

$D_T(x)$ , the local diffusivity parallel to the pore walls, is given by

$$D_T(x) = \frac{(k_B T / \pi m)^{1/2}}{4\sigma^2 \int_{-1}^1 g^0(\sigma, \bar{n}^0(x + \frac{\sigma}{2}\xi)) n^0(x + \sigma\xi) (1 - \xi^2) d\xi} \quad (29)$$

a result enabling one to calculate the pore diffusivity from the equilibrium density distribution function.

Equation 28 is similar to the LADM formula for pore diffusivity, except that in LADM  $D_T(x)$  is replaced by

$$D^0(\bar{n}(x)) = \frac{(k_B T / \pi m)^{1/2}}{(8\sigma^2/3) g^0(\sigma, \bar{n}(x)) \bar{n}(x)} \quad (30)$$

The Chapman-Enskog theory of flow in a one-component fluid yields the following approximation to the momentum balance equation (10).

$$n \partial_t \bar{v} + n \bar{v} \cdot \nabla \bar{v} + \frac{n}{m} \nabla u^e - \nabla \cdot \mathbf{P} = - \mathbf{M}_1 : \nabla \bar{v} + \mathbf{M}_2 : \nabla \nabla \bar{v} \quad (31)$$

where  $\mathbf{P}$  is the local pressure tensor and  $\mathbf{M}_1$  and  $\mathbf{M}_2$  are third and fourth rank tensors accounting for viscous dissipation. In isotropic fluid  $\mathbf{P} = P\mathbf{I}$ ,  $\mathbf{I}$  the unit tensor,  $\mathbf{M}_1 = 0$  and  $\mathbf{M}_2$  is a fourth rank isotropic tensor. The symmetries of  $\mathbf{P}$ ,  $\mathbf{M}_1$  and  $\mathbf{M}_2$  depend on the symmetry of the inhomogeneous fluid. The general Chapman-Enskog formulas for  $\mathbf{M}_1$  and  $\mathbf{M}_2$  are very complicated and will not be recorded here. However, if the deviation of the velocity distribution function from its local Maxwellian form ( $\phi = (m/2\pi k_B T)^{3/2} \exp[-m(\mathbf{v} - \bar{\mathbf{v}}(r))^2/k_B T]$ ) is neglected, the following relatively simple formulas are obtained (10)

$$\mathbf{M}_1(\mathbf{r}) = \left( \frac{mk_B T}{\pi} \right)^{1/2} \sigma^3 n(\mathbf{r}) \int n(\mathbf{r} + \sigma \mathbf{k}) g(\mathbf{r}, \mathbf{r} + \sigma \mathbf{k}) \mathbf{k} \mathbf{k} k d^2 \mathbf{k} \quad (32)$$

$$\mathbf{M}_2 = \left( \frac{mk_B T}{\pi} \right)^{1/2} \sigma^4 n(\mathbf{r}) \int n(\mathbf{r} + \sigma \mathbf{k}) g(\mathbf{r}, \mathbf{r} + \sigma \mathbf{k}) \mathbf{k} \mathbf{k} k k d^2 \mathbf{k} \quad (33)$$

These formulas become increasingly better approximations as the density increases (11).

For the steady, planar Couette flow to be examined in a later section, the momentum balance equation yields

$$n \frac{du^e}{dx} + \frac{dP_N}{dx} = 0 \quad (34)$$

and

$$0 = M_1(x) \frac{\partial \bar{v}_y}{\partial x} + M_2(x) \frac{\partial^2 \bar{v}_y}{\partial x^2} \quad (35)$$

where

$$M_1(x) = 2(\pi mk_B T)^{1/2} \sigma^3 n(x) \int_{-1}^1 n(x + \sigma \xi) g(\sigma; x, x + \sigma \xi) (1 - \xi^2) \xi d\xi \quad (36)$$

$$M_2(x) = (\pi mk_B T)^{1/2} \sigma^4 n(x) \int_{-1}^1 n(x + \sigma \xi) g(\sigma; x, x + \sigma \xi) (1 - \xi^2) \xi^2 d\xi \quad (37)$$

It can be shown that Equation 34 is the YBG equation determining the density distribution  $n(x)$  of the fluid. With the Fischer-Methfessel closure, the density distribution is all that is needed to calculate the coefficients  $M_1(x)$  and  $M_2(x)$ . Integrating Equation 35, we find

$$\bar{v}_y(x) = \bar{v}_y(0) + [\bar{v}_y(h) - \bar{v}_y(0)] \frac{\int_0^x dx'' Q(x'')}{\int_0^h dx'' Q(x'')} \quad (38)$$

where

$$Q(x'') = \exp \left[ - \int_0^{x''} dx' M_1(x') / M_2(x') \right] \quad (39)$$

LADM also leads to Equation 35, but with  $M_1 = d\eta^\circ(\bar{n}(x))/dx$  and  $M_2 = \eta^\circ(\bar{n}(x))$ , which yields

$$\bar{v}_y(x) = \bar{v}_y(0) + [\bar{v}(h) - \bar{v}_y(0)] \frac{\int_0^x dx'' [\eta^\circ(\bar{n}(x''))]^{-1}}{\int_0^h dx'' [\eta^\circ(\bar{n}(x''))]^{-1}} \quad (40)$$

The theories of structure and transport outlined above will be compared with molecular dynamics in what follows.

### Molecular Dynamics

**Equilibrium Simulation.** The equilibrium simulations described here were carried out by Magda *et al.* (12). The pore walls modelled are two flat, semi-infinite solids separated by a distance  $h$  in the  $x$ -direction. The wall-fluid potential is the 10-4 or 10-4-3 potential, i.e.,

$$\phi_w(x) = \epsilon_w \left\{ 0.4(\sigma_w/x)^{10} - (\sigma_w/x)^4 + \frac{\sqrt{2}\delta}{3(x/\sigma_w + 0.61/\sqrt{2})^3} \right\} \quad (41)$$

where  $\delta = 1$  in some simulations and  $\delta = 0$  in others. The particle-particle potential energy is chosen to be the truncated 6-12 Lennard-Jones potential

$$\begin{aligned} u(r) &= \phi_{LJ}(r) - \phi_{LJ}(r_e), & r < r_e \\ &= 0, & r > r_e \end{aligned} \quad (42)$$

where

$$\phi_{LJ}(r) = 4\epsilon \left[ \left( \frac{\sigma}{r} \right)^{12} - \left( \frac{\sigma}{r} \right)^6 \right] \quad (43)$$

$\epsilon$  and  $\sigma$  are energy and particle size parameters and  $r_e$  is the truncation distance (typically taken to be 2.5 to 3.5 $\sigma$  in computer simulations).

The temperature, pore width and average pore densities were the same as those used by Snook and van Megen in their Monte Carlo simulations, which were performed for a constant chemical potential (13). Periodic boundary conditions were used in the  $y$  and  $z$  directions. The periodic length was chosen to be twice  $r_e$ . Newton's equations of motion were solved using the predictor-corrector method developed by Beeman (14). The local fluid density was computed from

$$n(x) = \frac{1}{A} \frac{dN}{dx}(0 \rightarrow x) \quad (44)$$

where  $A$  is the area of a pore wall and  $N(0 \rightarrow x)$  is the long time average of the number of molecules found between 0 and  $x$ . The normal pressure exerted by the fluid on the pore wall was computed from

$$\begin{aligned} P_N &= \frac{1}{2A} \left\langle - \sum_{i=1}^N \frac{du^e(x_i)}{dx} \right\rangle \\ &= - \frac{1}{2} \int_0^h n(x) \frac{du^e(x)}{dx} dx \end{aligned} \quad (45)$$

or the Irving-Kirkwood pressure tensor mentioned below (15).  $\langle \dots \rangle$  denotes an ensemble average or a long-time average (used in molecular dynamics).

The self-diffusion coefficient parallel to the pore walls was computed from the mean square particle displacement,

$$D_{\text{pore}} = \lim_{t \rightarrow \infty} \frac{1}{N} \sum_{i=1}^N \frac{1}{4t} \left\langle [y_i(t) - y_i(0)]^2 + [z_i(t) - z_i(0)]^2 \right\rangle \quad (46)$$

and the Green-Kubo formula

$$D_{\text{pore}} = \frac{1}{2} \int_0^{\infty} [\psi_y(t) + \psi_z(t)] dt \quad (47)$$

where the velocity autocorrelation function  $\psi_\nu(t)$  is defined by

$$\psi_\nu(t) \equiv \frac{1}{N} \sum_{i=1}^N \langle v_{i\nu}(t) v_{i\nu}(0) \rangle, \quad \nu = x, y, \text{ or } z \quad (48)$$

**Couette Flow Simulation.** MD typically simulate systems at thermodynamic equilibrium. For the simulation of systems undergoing flow various methods of nonequilibrium MD have been developed (18, 17). In all of these methods the viscosity is calculated directly from the constitutive equation.

The nonequilibrium MD method we employed (5) is the reservoir method (18) which simulates plane Couette flow. The effective viscosity is calculated from the constitutive relation

$$\tau_{xy} = \eta_{\text{eff}} \dot{\gamma}_{\text{imp}} \quad (49)$$

where  $\tau_{xy}$  is the  $xy$  component of the stress tensor,  $\eta_{\text{eff}}$  an effective coefficient of shear viscosity,  $\dot{\gamma}_{\text{imp}}$  is the imposed shear rate.

In this method the liquid of interest is sheared between two semi-infinite reservoirs. The reservoirs contain particles identical with the ones in the main liquid slab and at the same density. The reservoir particles and the particles of the main liquid slab interact by exerting forces on each other but they do not mix because they are separated by impenetrable hard walls extending on the  $yz$  plane. Therefore, the reservoirs are fluid-like and confine the main liquid slab in the  $x$  direction. Despite appearances, the main liquid slab behaves like a bulk fluid because the reservoirs induce no significant structure in the confined liquid. Furthermore, the hard impenetrable reservoir walls are not to be confused with the flat 10-4 LJ pore walls mentioned in the previous subsection.

*The flow is induced in the following way:* External forces are applied on the particles of each reservoir in order to keep the average  $y$  velocities of the reservoirs constant. The imposed motion of the reservoirs shears the liquid slab. The work supplied in order to keep the reservoirs moving eventually is dissipated and heats up the liquid. In order to remove this extra heat from the system the velocities of the reservoir molecules are scaled at each time step so as to keep the average reservoir temperatures constant. The imposed shear rate is obviously

$$\dot{\gamma}_{\text{imp}} = (\bar{v}_{y,u} - \bar{v}_{y,l})/s \quad (50)$$

where,  $\bar{v}_{y,u}$  is the average velocity of the upper reservoir particles,  $\bar{v}_{y,l}$  the average velocity of the lower reservoir particles, and  $s$  the width of the main liquid slab.

Depending on the density in the vicinity of the reservoir walls some slip might be observed. Therefore, the actual shear rate that the liquid slab experiences might be lower than the imposed one. This actual shear rate  $\dot{\gamma}$  is determined empirically from the simulation by calculating the average velocity of the liquid slab particles which are located next to the reservoir walls. The actual shear rate  $\dot{\gamma}$  rather than the imposed shear rate  $\dot{\gamma}_{\text{imp}}$  is to be used in Equation 49 for the calculation of the effective viscosity  $\eta_{\text{eff}}$ .

*The structure is induced by a pore wall potential,* which has the form of the potential used in the equilibrium simulations (Equation 41) with  $\delta = 0$ ,  $\epsilon_w = 4\epsilon$  and  $\sigma_w = \sigma$ , ( $\epsilon$ ,  $\sigma$  are the parameters of the truncated 12-6 LJ potential of the pair interactions of particles in the main liquid slab and the reservoirs.)

The arrangement described above allows one to turn off the flow and/or the wall potential at will and, therefore, to simulate bulk fluid and fluid confined between planar micropore walls both at equilibrium and under flow.

We simulated two systems: (1) bulk fluid (no wall potential) at equilibrium and undergoing Couette flow, and (2) fluid confined between planar micropore walls at equilibrium and undergoing Couette flow.

The location of the pore walls does not coincide with the location of the reservoir walls that confine the particles of the main liquid slab. This was done in order to minimize the slip at the reservoir walls as explained in detail in Reference (5).

In the flow simulations we address the following issues:

- the effect of density structure on the flow properties, such as the flow velocity profile, the shear stress and the viscosity, by comparing the bulk and the structured systems under flow.
- the effect of flow on the density structure and the diffusivity by comparing the density profiles and the diffusivities of both systems at equilibrium and under flow. Furthermore, we compare the two diffusivities on the plane parallel to the reservoir walls, i.e., the diffusivity in the direction of flow and the one normal to the flow, for both systems undergoing flow.
- the effect of structure on the diffusivity by comparing the diffusivities of the structured and the bulk system at equilibrium.

The density profile for the micropore fluid was determined as in the equilibrium simulations. In a similar way the flow velocity profile for both systems was determined by dividing the liquid slab into ten slices and calculating the average velocity of the particles in each slice. The velocity profile for the bulk system must be linear as macroscopic fluid mechanics predict.

The diffusivities parallel to the pore walls at equilibrium were determined from the mean square particle displacements and the Green-Kubo formula as described in the previous subsection. The Green-Kubo Formula cannot be applied, at least in principle, for the calculation of the diffusivity under flow. The diffusivity can be still calculated from the mean square particle displacements provided that the part of the displacement that is due to the macroscopic flow is excluded. The presence of flow in the  $y$  direction destroys the symmetry on the  $yz$  plane. Hence the diffusivities in the  $y$  direction (parallel to the flow) and the  $z$  direction (normal to the flow) can in principle be different. In order to calculate the diffusivities the part of the displacement that is due to the flow must of course be excluded. Therefore,

$$D_{y,\text{pore}} = \lim_{t \rightarrow \infty} \frac{1}{N} \sum_{i=1}^N \frac{1}{2t} \langle [y_i(t) - \bar{v}t - y_i(0)]^2 \rangle \quad (51)$$

where  $\bar{v}$  is the flow velocity at the location of particle  $i$  and

$$D_{z,\text{pore}} = \lim_{t \rightarrow \infty} \frac{1}{N} \sum_{i=1}^N \frac{1}{2t} \langle [z_i(t) - z_i(0)]^2 \rangle \quad (52)$$

since there is no flow in the  $z$  direction.

The shear stress is uniform throughout the main liquid slab for Couette flow (5). Therefore, two independent methods for the calculation of the shear stress are available; it can be calculated either from the  $y$  component of the force exerted by the particles of the liquid slab upon each reservoir or from the volume average of the shear stress developed inside the liquid slab from the Irving-Kirkwood formula (15). For reasons explained in Reference (5) the simpler version of this formula can be used in both our systems although this version does not apply in general to structured systems. The Irving-Kirkwood expression for the  $xy$  component of the stress tensor used in our simulation is

$$\bar{\tau}_{xy} V_{\text{pore}} = \left\langle \sum_{i=1}^{N_l} m v_{x,i} (v_{y,i} - \bar{v}_y(y_i)) \right. \\ \left. + \frac{1}{2} \sum_{j,k=1}^N (x_j - x_k) F_{kj}^{(y)} + \sum_{j=k=1}^{N_r} \sum_{k=1}^{N_l} (x_k - x_{\text{GDS}}) F_{kj}^{(y)} \right\rangle \quad (23)$$

where,  $\bar{\tau}_{xy}$  is the average shear stress over the main liquid slab

$V_{\text{pore}}$  is the volume of the main liquid slab.

$N_l$  is the number of particles in the main liquid slab

$N_r$  is the number of particles in both reservoirs.

$v_{x,i}, v_{y,i}$  are the x and y components of the velocity of particle i

$\bar{v}_y(y_i)$  is the y component of the flow velocity at the current position of particle i

$x_i, y_i$  are the x and y coordinates of particle i

$x_{\text{GDS}}$  is the location of the Gibbs dividing surface between the main liquid slab and the reservoirs.

### Discussion of Results

**Equilibrium Systems.** Magda *et al.* (12) have carried out an equilibrium molecular dynamics (MD) simulation on a 6-12 Lennard-Jones fluid in a slit pore described by Equation 41 with  $\delta = 1$  with fluid particle interactions given by Equation 42. They used the Monte Carlo results of Snook and van Megen to set the mean pore density so that the chemical potential was the same in all the simulations. The parameters and conditions set in this work were  $\epsilon_w = 2\pi\epsilon$ ,  $\sigma_w = \sigma$ ,  $r_e = 3.5\sigma$ ,  $kT/\epsilon = 1.2$ , and  $n_b\sigma^3 = 0.5925$ .  $\epsilon$  and  $\sigma$  are the Lennard-Jones parameters of the fluid and  $n_b$  is the density of a bulk phase in equilibrium with the pore fluid.

To compare molecular theoretical and molecular dynamics results, we have chosen the same wall-particle potential but have used the 6- $\infty$  fluid particle potential, Equation 14, instead of the truncated 6-12 LJ potential. This is done because the molecular theory is developed in terms of attractive particles with hard sphere cores. The parameter  $\mu^*$  in Equation 8 is chosen so that the density of the bulk fluid in equilibrium with the pore fluid is the same,  $n_b\sigma^3 = 0.5925$ , as that in the MD simulations.

Figure 1 typifies the agreement found between the fluid density profiles predicted by Equation 8 and that obtained in the MD simulations. For this example the porewidth equals  $4\sigma$ . The fluid density distribution has three large peaks (the maximum bulk density possible for a Carnahan-Starling fluid is  $n_b\sigma^3 = 6/\pi \approx 1.9$ ) indicating a strong layering effect of the pore walls on the confined fluid.

The number and sharpness of fluid layers depend sensitively on the porewidth as is illustrated by the theoretical results (which agree qualitatively with simulations) plotted in Figure 2. As porewidth is increased from say  $h = \sigma$ , there appear one, two, three, etc. density peaks. A transition from  $N$  to  $N + 1$  peaks occurs as the porewidth varies from a value at which  $N$  layers are favored to a value at which  $N + 1$  are favored. A



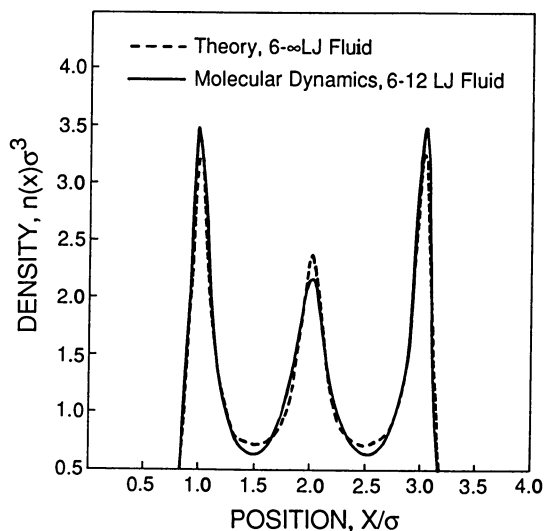


Figure 1. Fluid density versus distance from pore wall.

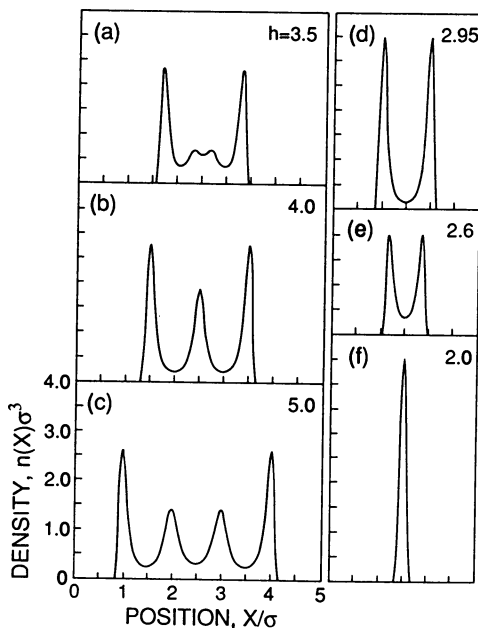


Figure 2. Density profiles illustrating effect of pore width on layering structure. Theory with 6 -  $\infty$  LJ fluid.

quantity which measures this tendency is the so-called restricted pore average density.

$$n_{\text{ave}} = \frac{1}{h - 2\Delta} \int_0^h n(x) dx \quad (54)$$

where  $\Delta$  is the thickness of the region near the pore wall which is empty of particles ( $\Delta = 0.8\sigma$  for the wall potential used here). Predicted and simulated values of  $n_{\text{ave}}$  are plotted in Figure 3.  $n_{\text{ave}}$  has local maxima where a given number  $N$  of layers is favored and local minima where this number is not favored. For example, one layer is favored at  $h = 1.95\sigma$  and two layers are favored at  $h = 2.95\sigma$ , as witnessed by local maxima in  $n_{\text{ave}}$ , whereas the local minimum between 1.95 and 2.95 $\sigma$  indicates a defective layering 1.95 and 2.95 $\sigma$  state in which neither one nor two layers are optimal. This behavior can be seen in Figure 2 in which the two density peaks decrease dramatically as the pore width is decreased from  $h = 2.95\sigma$  to 2.60 $\sigma$ .

In the simulations the maxima and minima of  $n_{\text{ave}}$  are shifted to slightly smaller porewidths compared to predictions of the theory. This trend is consistent with the fact that the 6-12 Lennard-Jones potential is not infinitely repulsive at an interparticle separation of  $\sigma$ , whereas the 6- $\infty$  potential is infinitely repulsive at  $\sigma$ .

It is now well established experimentally that the solvation force,  $f_s$ , of confined fluid is an oscillating function of pore wall separation. In Figure 4 we compare the theoretical and MD results for  $f_s$  as a function of  $h$ . Given that pressure predictions are very demanding of a molecular theory, the observed agreement between our simple theory and the MD simulations must be viewed as quite good. The local maxima and minima in  $f_s$  coincide with those in  $n_{\text{ave}}$  and therefore also reflect porewidths favorable and unfavorable to an integral number of fluid layers.

Similarly, the pore diffusivity  $D_{\text{pore}}$  (Figure 5) has local maxima and minima resulting from the layering structure of the confined fluid. As one might expect the local maxima and minima in  $D_{\text{pore}}$  coincide with the minima and maxima in  $n_{\text{ave}}$ .

In Figure 5, the MD results are compared with predictions of the Vanderhoff-Davis extension of Enskog's theory and with LADM predictions using for  $D^0$  the Enskog formula, Equation 30, and the theoretical density profile. The extended Enskog theory and LADM agree quite well with one another and are in qualitative agreement with the MD results. The maxima and minima of the MD results are shifted to smaller porewidths because of the softer core of the 6-12 LJ potential as compared to the 6- $\infty$  potential. For the same reason, the bulk diffusivities of the theories are lower than that of the simulation. If, as is done in applying the Enskog theory of bulk phase transport coefficients to real fluids, we choose for the 6- $\infty$  model an effective diameter  $\sigma_{\text{eff}}$  the agreement between theory and simulation can be improved. For example, with  $\sigma_{\text{eff}} = 0.972\sigma$  Enskog's diffusivity of bulk fluid agrees with the simulation and improved agreement pore diffusivities result (Figure 6).

Beyond a porewidth of about 12 $\sigma$ , the theory and the MD results

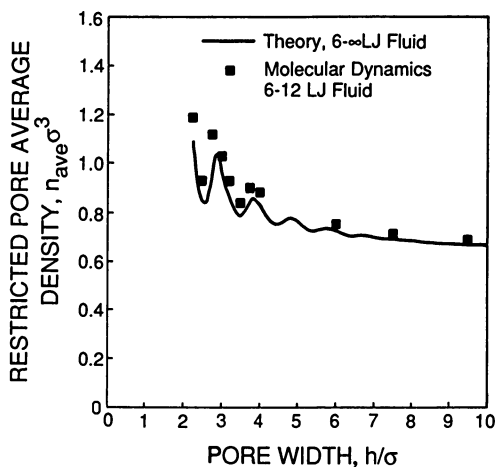


Figure 3. Molecular dynamics results for restricted pore average density versus pore width.

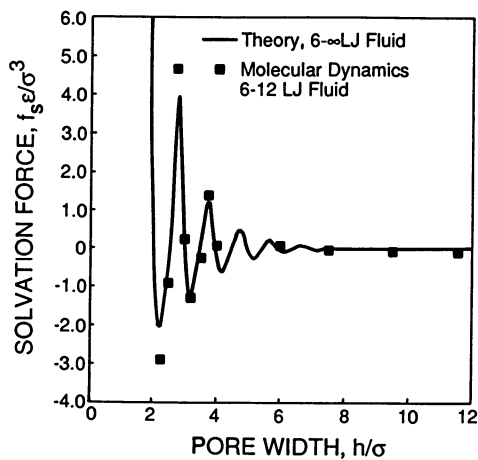


Figure 4. Molecular dynamics results for solvation force versus pore width.

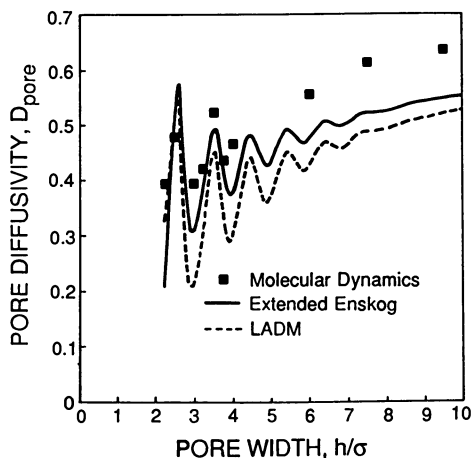


Figure 5. Pore diffusivity versus pore width. Theory is for  $\delta\text{-}\infty$  LJ fluid. Units of diffusivity are  $(3\sigma/8)(k_B T/\pi m)^{1/2}$ .

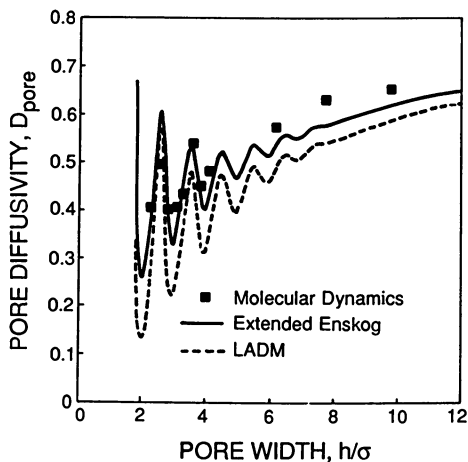


Figure 6. Pore diffusivity versus pore width. Theory is for  $\delta\text{-}\infty$  LJ fluid with an effective hard sphere diameter  $\sigma_{\text{eff}} = 0.972$ . Units of diffusivity are  $(3\sigma/8)(k_B T/\pi m)^{1/2}$ .

agree that the fluid profile is fully developed at each pore wall and further wall separation simply recruits more almost bulk fluid the middle region of pore with very little change in the density profile of the four or five layers near the pore wall.

**Flow systems.** In this subsection we present the results of our Couette flow simulations. Most of these results were first presented in Reference (5).

1) *Density profiles:* The density profiles for the bulk fluid and the micropore fluid are shown in Figures 7 and 8. We first note that the density profile for the bulk fluid is uniform throughout the pore except from a very narrow region next to the reservoir walls. But even there, the density gradients are entirely insignificant compared to the extremely strong density gradients of the micropore fluid caused by the pore wall potential. Therefore, we conclude that the presence of the reservoirs does not induce any significant structure in the fluid.

The density profile for the micropore fluid is highly structured, showing substantial fluid layering. The local average density profile (see Section 1) of this system is also shown in Figure 8. A very important feature of the local average density that results from the smoothing procedure involved in its calculation is that it varies slowly and remains bound to physically possible homogeneous fluid densities. This is essential if one is to employ some theory for the viscosity of homogeneous fluids to predict local viscosities and flow velocity profiles as explained in Section 1. From Figure 8 we see that the local average density of the micropore fluid is everywhere lower than the hard-sphere closest packing density ( $\sqrt{2}/\sigma^3$ ) and the maximum density for the solution of the Percus-Yevick equation ( $6/\pi\sigma^3$ ).

Although only one density profile is shown in each of Figures 7 and 8 the density profiles of the two systems both at equilibrium and in the presence of flow that have been determined. *A conclusion of great importance that is suggested by the Couette flow simulations is that the density profiles of the two systems in the presence of flow coincide with the equilibrium density profiles, even at the extremely high shear rates employed in our simulation.* A detailed statistical analysis that justifies this point was presented in Reference (5).

11) *Diffusivities.* Our results for the diffusivities of both systems are summarized in Table I. The pore average transverse diffusivity for the bulk fluid at equilibrium agrees very well with experimental and simulation values for the diffusivity of Argon at the same density and temperature (18,12,5).

As explained in Section 1 three diffusivities were calculated for each system. These were the equilibrium transverse diffusivity and the two nonequilibrium (flow) diffusivities parallel and normal to the direction of flow. As we can see from Table I, they all agree with each other within the limits of statistical uncertainty. *We conclude, therefore, that the flow has no effect on the diffusivity even at such high shear rates as the ones employed in our simulation.* At even higher shear rates a significant dependence of the diffusivity on the shear rate has been reported (19) but one should consider that our shear rate is already orders of magnitude higher than the ones encountered in realistic flow situations.

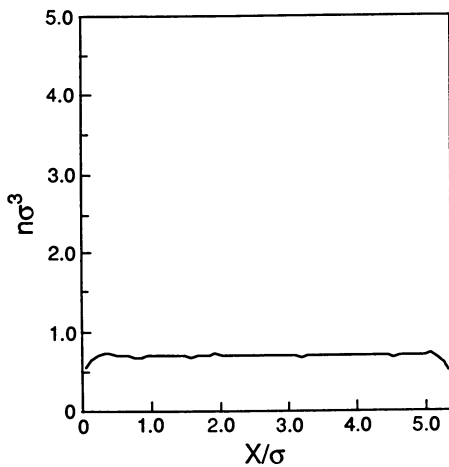


Figure 7. Density profile of the bulk system.

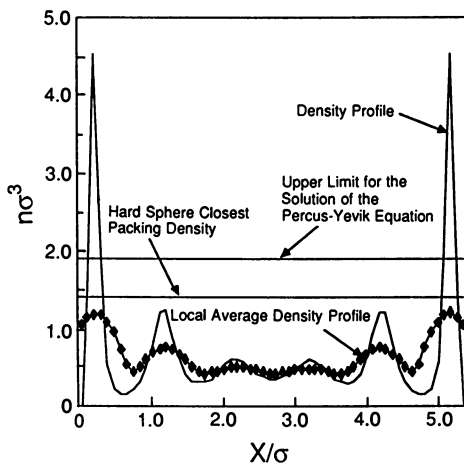


Figure 8. Density and local average density profiles of the micropore fluid

Table I. Diffusivities. Units are  $(\sigma^2\epsilon/m)^{1/2}$ 

	Bulk Fluid	Micropore Fluid
Simulation		
equilibrium	0.109 ± 0.002	0.107 ± 0.002
parallel to the flow	0.109 ± 0.003	0.114 ± 0.004
normal to the flow	0.109 ± 0.002	0.113 ± 0.003
Experiment	0.111	
LADM		
using Enskog theory		0.107
using empirical formula		0.112
Extended Enskog		0.108

As shown in Table I the LADM predictions agree very well with the simulation results. The first of these values employed the Enskog hard-sphere theory for homogeneous fluids for the prediction of the local diffusivities. The second value employed an empirical formula that fits MD results for the diffusivity of liquid Argon (5,18). As we can see much of the disagreement is due to the inaccuracy of the Enskog theory and not to the LADM. The third value is the prediction of the generalization of the Enskog theory for tracer diffusion in strongly inhomogeneous fluids (8,9). This value also agrees very well with the simulation result.

A final point has to do with the relative insensitivity of the pore averaged diffusivity on the density structure. Both the LADM and the generalized tracer diffusion theory provide a rational explanation for this fact. The reasons for the insensitivity may be identified in the double (triple for the tracer diffusion theory) smoothing induced by the volume averaging and by the very nature of the molecular interactions in liquids which makes some type of averaging over the densities in the neighborhood of a certain point necessary.

iii) *Velocity profiles.* The velocity profiles for the bulk fluid and the micropore fluid are shown in Figures 9 and 10. The profile for the bulk system is linear in agreement with the macroscopic prediction of fluid mechanics. This fact shows that the flow properties of our first system are identical with the ones of a bulk fluid, despite the presence of the reservoirs.

The velocity profile for the micropore fluid exhibits large deviations from linearity. An extremely important point which motivated the development of the LADM is the *clear correlation between the velocity and the density profiles of the micropore fluid.* One can easily distinguish two regions of low slope (shear rate) next to the reservoir walls and a center region of high slope. These clearly correspond to the two large density peaks next to each reservoir wall and the low density center region of the density profile. The theoretical velocity profile predicted from the

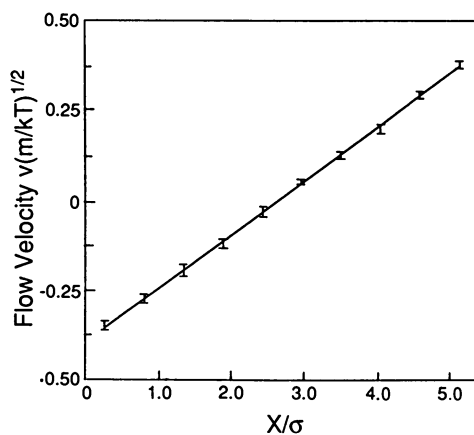


Figure 9. Velocity profile for the bulk system

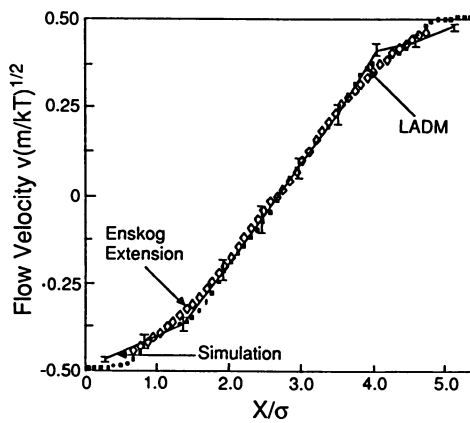


Figure 10. Theoretical and simulation velocity profiles for the micropore fluid.



LADM is also shown in Figure 4. It agrees with the simulation profile almost within the limits of the statistical uncertainty.

In Figure 10, we present flow velocity predictions of the high density approximation, Equations 32 - 33, 38 and 39, of Davis' extension of Enskog's theory to flow in strongly inhomogeneous fluids (10). The velocity profile predicted in this way is also plotted in Figure 10. The predicted profile, the simulated profile, and the profile predicted from the LADM are quite similar.

Finally the knowledge of the velocity profiles allows the determination of the actual shear rate exerted upon the liquid slab. For the bulk system some slip is observed at the reservoir walls. No slip is observed for the micropore fluid as a result of the high density close to the reservoir walls, which facilitates the momentum transfer between the reservoir and the liquid slab particles.

iv) *Shear stress and viscosity.* As explained in Section 1 three independent estimates of the shear stress can be made for this particular type of flow. For both systems they all agree within the limits of statistical uncertainty as shown in Table II. The shear stress in the micropore fluid is significantly lower than the bulk fluid, which shows that *strong density inhomogeneities can induce large changes of the shear stress.*

For the bulk system the constitutive equation

$$\eta = \tau_{xy} / \dot{\gamma} \quad (55)$$

is rigorously valid. The simulation result for the viscosity of the bulk system agrees with the experimental argon viscosity within the limits of the statistical uncertainty.

If one insists on Equation 55 for the micropore fluid an effective viscosity (which is an experimental observable) must be used instead, i.e.,

$$\eta_{\text{eff}} = \tau_{xy} / \dot{\gamma} \quad (56)$$

The simulation value for the effective viscosity is almost half the viscosity of the bulk fluid. According to the LADM the effective viscosity for plane Couette flow can be identified as

$$\eta_{\text{eff}}^{-1} = s^{-1} \int_0^s [\eta^0(\bar{n}(x))]^{-1} dx \quad (57)$$

where  $s$  is the distance between the reservoir walls,  $\bar{n}(x)$  the local average density at  $x$  (defined by Equation 9), and  $\eta^0(\bar{n}(x))$  is the local viscosity at  $x$ , i.e., the homogeneous fluid viscosity at density  $\bar{n}(x)$ .

Two predictions of the LADM for the effective viscosity are shown in Table II. The first was made by using the Enskog hard-sphere theory for the calculation of the local viscosities. It agrees qualitatively with the simulation result in that it predicts a large decrease of the effective viscosity as a result of the density structure. For the second prediction the local

Table II. Shear stress and viscosity

Bulk fluid in planar Couette flow			
	Shear Stress	Shear Rate	Viscosity
Simulation			
force on upper reservoir	0.182		
force on lower reservoir	0.180		
Irving-Kirkwood formula	0.181		
average	$0.181 \pm 0.004$	$0.149 \pm 0.005$	$1.21 \pm 0.04$
Experiment			1.23
Enskog			1.14
Micropore fluid in planar Couette flow			
	Shear Stress	Shear Rate	Viscosity
Simulation			
force on upper reservoir	0.119		
force on lower reservoir	0.122		
Irving-Kirkwood formula	0.122		
average	$0.121 \pm 0.003$	0.186	$0.65 \pm 0.02$
LADM			
using Enskog theory			0.77
using empirical fit			0.70
Units	$\epsilon/\sigma^3$	$(\epsilon/m\sigma^2)^{1/2}$	$(m\epsilon)^{1/2}\sigma^2$

viscosities were calculated from an empirical formula (23) that fits experimental value of the argon shear viscosity over a wide range of densities and temperatures (20,21). The agreement with the simulation result is much better, which suggests that much of the discrepancy is a result of the poor Enskog predictions at high densities and not a deficiency of the LADM.

A final comment has to do with the concept of effective viscosity in strongly inhomogeneous fluids. For these systems the definition of the effective viscosity depends on the type flow, hence different effective viscosities will be measured for different flow situations in the same system with the same density profile. Therefore, the effective viscosity is a concept of limited value and measurements of this quantity do not provide much information about the effects of density structure on the flow behavior.

### Literature Cited

1. Fischer, J.; Methfessel, M. *Phys. Rev A* 1980 **22**, 2836.
2. Carnahan, N. F.; Starling, K. E. *J. Chem. Phys.* 1969 **51**, 635.
3. Steele, W. A., *The Interaction of Gases with Solid Surfaces* Pergamon, New York, 1974; Chap. 2.

4. Horn, R. G.; Israelachvili, J. N. *J. Chem. Phys.* 1981 **75**, 1400
5. Bitsanis, I.; Tirrell, M. V.; Davis, H. T. *J. Chem. Phys.* (accepted).
6. Dymond, J. H.; Woolf, L. A. *J. Chem. Soc. Faraday Trans. 1* 1982 **78**, 991.
7. Chapman, S.; Cowling, T. G. *The Mathematical Theory of Non-Uniform Gases and Liquids*, Cambridge University Press, New York, 1954.
8. Davis, H. T., *J. Chem. Phys.* (accepted).
9. Vanderlick, T. K.; Davis, H. T. *J. Chem. Phys.* (accepted).
10. Davis, H. T., *Chem. Eng. Comm.* (accepted).
11. Luks, K.D.; Miller, M.; Davis, H. T. *AIChE J.* 1966 **12**, 1079.
12. Magda, J. J.; Tirrell, M. V.; Davis, H. T. *J. Chem. Phys.* 1985 **83**, 1888.
13. Snook, I. K.; van Megen, W. *J. Chem. Phys.* 1980 **72**, 2907.
14. Beeman, D. *J. Comput. Phys.* 1976 **20**, 130.
15. Irving, J. H.; Kirkwood, J. G. *J. Chem. Phys.* 1950 **18**, 817.
16. Ashurst, W. T.; Hoover, W. G. *Phys. Rev. A* 1975 **11**, 658.
17. Heyes, D. M.; Montrose, C. J.; Litovitz, T. A. *J. Chem. Soc. Faraday Trans. 2* 1983 **79**, 611.
18. Levesque, D.; Verlet, L. *Phys. Rev. A* 1970 **6**, 2514.
19. Heyes, D. M. *J. Chem. Soc. Faraday Trans. 2* 1985 **82**, 1365.
20. Haynes, W. M. *Physica* 1973 **67**, 440.
21. Michels, A.; Sengers, J. V.; van der Klundert, L. J. M., *Physica* 1963 **29**, 149.

RECEIVED June 15, 1987

## Chapter 16

# Computational Aspects of Complex Dynamics

Ioannis G. Kevrekidis

Department of Chemical Engineering, Princeton University, Princeton, NJ 08544

The partial differential equations used to model the dynamic behavior of physicochemical processes often exhibit complicated, non-recurrent dynamic behavior. Simple simulation is often not capable of correlating and interpreting such results. We present two illustrative cases in which the computation of unstable, saddle-type solutions and their stable and unstable manifolds is critical to the understanding of the system dynamics. Implementation characteristics of algorithms that perform such computations are also discussed.

The partial differential equations (PDEs) used to model physicochemical and chemical engineering processes are usually nonlinear; these nonlinearities give rise to very interesting and complex dynamic phenomena. From steady-state multiplicity and oscillations in lumped reactors to the development of hydrodynamic instabilities and chaotic flows, this is an area of intense research through theory, experiment and computation (see for example (1, 2) and the references therein). This research has been to a large extent triggered by recent advances in the theory of dynamical systems, pointing towards universal characteristics of dynamic transitions in large classes of physical systems and their models.

We are concerned in this paper with the systematic computational study of certain "complex" dynamic phenomena that are frequently encountered in experiments or simulations of process dynamics. We will show that simple simulation and local stability analysis are not capable of tracking and analyzing such phenomena; that the computation of saddle-type unstable solutions (whether steady state or oscillatory) and of their stable and unstable manifolds are necessary ingredients of a systematic, computer-aided study of the so-called global bifurcations and their effect on the system dynamics (3). We will describe two classes of algorithms for this study: a "simulation" formulation and a "fixed point" formulation. In both cases it is essential to track families of trajectories of the dynamical system. These families include the boundaries of the basins of attraction of different attractors in multistable systems. The "fixed point" formulation also involves extensive variational and sensitivity integrations along with the system equations. Often interactive graphics are indispensable in visualizing and interpreting the computational results. We will use two illustrative examples: one comes from a model of thin-film flow and flame-front instabilities, the other from

0097-6156/87/0353-0284\$06.00/0  
© 1987 American Chemical Society

thermally induced convection in a low aspect ratio cell. Although in both cases the systems have infinite degrees of freedom, both exhibit a "spatially coherent" route to temporal complexity. This "low-dimensionality" of their dynamic behavior, which in the case of the first model can be rigorously shown via the Inertial Manifold Theory (4), is essential for our computations.

#### First Example: The Kuramoto-Shivashinsky Equation

We examine some aspects of the dynamic behavior of the Kuramoto-Shivashinsky (K-S) equation

$$u_t + 4u_{xxxx} + \alpha (u_{xx} + (u_x)^2) = 0$$

This equation has been derived as a model amplitude equation in several contexts, from the flow of thin fluid films down an inclined plane to the development of instabilities on flame fronts and pattern formation in reaction-diffusion systems; we will not discuss here the validity of the K-S as a model of the above physicochemical processes (see (5) and references therein). Extensive theoretical and numerical work on several versions of the K-S has been performed by many researchers (5). One of the main reasons is the rich patterns of dynamic behavior and transitions that this model exhibits even in one spatial dimension. This makes it a testing ground for methods and algorithms for the study and analysis of complex dynamics. Another reason is the recent theory of Inertial Manifolds, through which it can be shown that the K-S is strictly equivalent to a low dimensional dynamical system (a set of Ordinary Differential Equations) (6). The dimension of this set of course varies as the parameter  $\alpha$  varies. This implies that the various bifurcations of the solutions of the K-S as well as the chaotic dynamics associated with them can be predicted by low-dimensional sets of ODEs. It is interesting that the Inertial Manifold Theory provides an algorithmic approach for the construction of this set of ODEs.

We discuss some characteristics of the bifurcation diagram of the K-S for low values of the parameter  $\alpha$  (for details see (7)). We will work in one dimension and with periodic boundary conditions. In what follows, we always subtract the mean drift

$$m(t): \frac{dm}{dt} = -\frac{\alpha}{4\pi} \int_0^{2\pi} (u_x)^2 dx$$

We have used two distinct numerical algorithms for the integration of the initial value problem. Both were variable step, variable order backward difference schemes integrating in Fourier space. The first algorithm, due to J. M. Hyman used a high precision pseudospectral (via Fast Fourier Transform) approximation to the spatial derivatives, while the second used a Galerkin pseudospectral discretization for which the appropriate set of ODEs was explicitly constructed in FORTRAN through the symbolic manipulator MACSYMA. Our preliminary simulations yielded the following observations for increasing  $\alpha$ :

(i) For  $\alpha < 4$  every set of initial conditions is attracted to the flat steady-state solution  $u_0 \equiv 0$ . This is in accordance with the linearized stability results.

(ii) Between  $\alpha = 4$  and  $\alpha = 13.005$  transients get attracted to a nontrivial standing wave (a steady state with spatial structure). Because of the periodic boundary conditions, every translation of the steady state is also a steady state. This means that we have a one-parameter family of steady states, each of which is a shift of the others. Indeed, we observe that different transients become attracted to different members of this one-parameter family. For  $\alpha$  near 4 these steady states are both small and qualitatively similar to  $\cos(x)$ , i.e. they go through one spatial oscillation between 0 and  $2\pi$ . We label this family of waves the unimodal steady states.

iii) Between  $\alpha = 13.005$  and  $\alpha = 17.399$ , transients will become attracted to a travelling wave solution, a function  $u(x-ct)$  where  $c$  is the velocity of the wave and depends on the parameter  $\alpha$ . For each value of  $\alpha$  two similar waves exist, one travelling in the positive and one in the negative direction. These waves are limit cycles for the PDE and their projection on the sine and cosine coefficients of any single Fourier mode will produce a circle. We label these rotating wave solutions.

iv) Between  $\alpha \approx 16.8$  and  $\alpha = 22.557$  the observed long term behavior consists of a "pulsating wave" alternating between two "almost" steady states that appear to be  $\pi$ -shifts of each other. A family of such pulsations exist, each of which is a shift of the others. Between  $\alpha \approx 16.8$  and  $\alpha = 17.399$  these pulsating waves coexist as stable attractors with the rotating wave we described above. Between  $\alpha = 17.399$  and  $\alpha = 22.557$  the pulsating waves are the only attractor observed computationally. If we project these pulsations on the  $\cos(2x)$ - $\sin(2x)$  plane, they ultimately appear as straight lines passing through the origin.

(v) For values of  $\alpha$  slightly larger than 22.557 the attractor becomes again a steady state with spatial structure: a standing wave which, however, appears two-humped -- qualitatively similar to  $\cos(2x)$  -- and for that reason we term these the bimodal solutions.

The simulation results that we describe here can be corroborated with numerical bifurcation work (7). If the (nonlinear) steady state equations are solved through an iterative procedure (e.g. through a full Newton Raphson) and their Jacobian is evaluated at the steady state, the eigenvalues of this matrix provide linearized stability information for the located steady state. Of course, the translational invariance for the problem will cause this matrix to be singular, due to the one-parameter family of solutions. It is therefore necessary for the convergence of the Newton-Raphson to single out one out of the one-parameter family of standing wave solutions. The transitions between the modes of dynamic behavior described above can be tracked through the spectrum of the linearization. The presence of symmetry in the problem will of course affect the observed bifurcations (8); for example, the transition from a standing wave to a rotating wave (steady state to limit cycle) occurs when one single eigenvalue of the linearization goes through zero to the right hand plane on the real axis at  $\alpha = 13.005$ . This is then not a usual Hopf bifurcation; indeed, at the critical value of  $\alpha$  there are two eigenvalues at zero: the "permanent" one due to the invariance, and the critical one, in the process of crossing. This double zero eigenvalue has geometric multiplicity one; it can be shown that the bifurcation of the rotating wave occurs in the direction of a generalized eigenvector.

This linearized stability analysis can be extended for the rotating waves. The problem of locating a rotating wave is posed as a two point free boundary value problem -- a typical formulation for finding a limit cycle (9) -- and this is solved through shooting techniques. The construction of the Jacobian of this procedure (i.e. the linearization of a Poincaré map around a fixed point of the map) requires the cocurrent integration of the variational equations along with system equations.

For a large discretization ( $N$  ODEs) the variational equations are  $N^2$ . They typically are integrated through a simple modification of the implicit or semiimplicit integrator of the system equations that takes advantage of their linearity (10, 11). If the eigenvalues of the linearization around the rotating wave (the so-called characteristic or Floquet multipliers (12) are calculated, we observe that a pair of them leave the unit circle in the complex plane at  $\alpha = 17.399$  as complex conjugates at an angle  $\phi \cong 145^\circ$ . We do not however observe any supercritical solution bifurcation from the rotating waves; what is observed instead, is that the solution is attracted to the "pulsating wave" that alternates between two quasi-static states that are  $\pi$ -shifts of each other. This pulsation is "far away" in phase space from the rotating wave that lost stability and, as we mentioned above, coexists with it for values of  $\alpha$  below 17.399. This pulsation is not a "typical" solution since it is neither steady nor periodic, and it does not appear chaotic. The long quasi-stationary intervals in time are telltale signs of the approach to a steady state, but, on the other hand the time it takes to "flip" from one quasi-steady state to its shift does not appear to grow towards infinity, as would happen if we were nearing an infinite period bifurcation.

Understanding the nature of this pulsating solution is assisted by numerical bifurcation theory. It is indeed possible to show (5, 7) that a family of saddle-type two-humped (bimodal) standing waves bifurcate from the flat solution at  $\alpha = 16$ , that their linearization then possesses two positive and one zero eigenvalue (due to the invariance), and that one of the two positive eigenvalues crosses zero and becomes negative at  $\alpha = 16.1399$  as the bimodal and the unimodal branch -both of them saddle-type and unstable- collide. It is also possible to show that the two "quasi-stationary" states encountered during a pulsation are very close to these saddle-type, bimodal standing waves; indeed, the solution approaches a bimodal standing wave along some stable eigendirection, slows down as it approaches, and eventually builds up enough error to escape in the unstable eigendirection. It then approaches the  $\pi$ -shift of the "quasi-stationary" state, where the process repeats itself.

What cannot be obtained through local bifurcation analysis however, is that both sides of the one-dimensional unstable manifold of a saddle-type unstable bimodal standing wave connect with the  $\pi$ -shift of the standing wave & vice versa. This explains the pulsating wave: it winds around a homoclinic loop consisting of the bimodal unstable standing waves and their one-dimensional unstable manifolds that connect them with each other. It is remarkable that this connection is a persistent homoclinic loop i.e. it exists for an entire interval in parameter space (13). It is possible to show that such a loop exists, based on the existence of a number of invariant subspaces in the phase space of the PDE. It is also possible to show that the loop starts existing as soon as the bimodal states bifurcate from the zero solution at  $\alpha = 16$ . In that case we have a persistent heteroclinic loop that involves both bimodal and unimodal states; this heteroclinic loop collapses to a homoclinic loop when the unimodal branch collapses on the bimodal one at  $\alpha = 16.1399$ . It is important to stress, however, that the theoretical work leading to these proofs in (7) was motivated by the computational results. More specifically, the existence of the invariant subspaces, and the saddle-connections were first observed in simulations where the saddle-steady states were found, initial local approximations to their invariant manifolds were constructed numerically and the manifolds subsequently followed forward in time (see Figure 1).

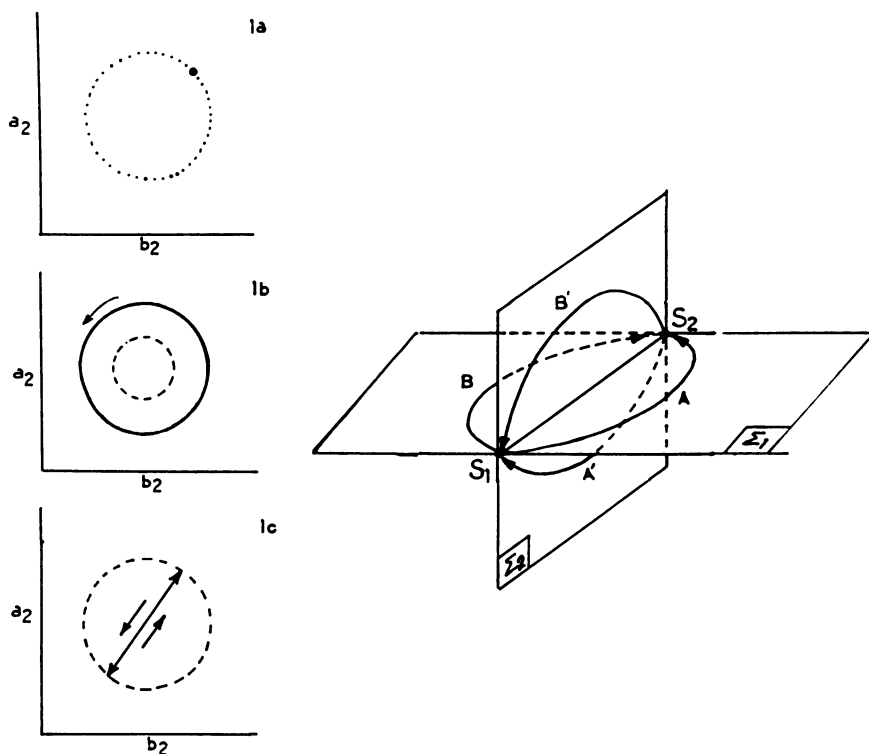


Figure 1. Underlying structure of the "pulsating wave" solution: two saddle-type standing waves  $S_1$  and  $S_2$  that are  $\pi$  shifts of each other are connected by their one-dimensional unstable manifolds in a persistent homoclinic loop. This structure can be explained in terms of the invariant subspaces  $\Sigma_2$  and  $\Sigma_1$  on which the saddle-type standing waves are attractors respectively. The insets show typical projections of the K-S attractors on the plane of the coefficients  $a_2$  and  $b_2$  of the cosine and sine of the second Fourier mode. A standing wave is a point (1a) singled out of a one-parameter family of points, the rotating wave appears as a circle (1b) while the pulsating wave projects on a straight line passing through the origin (1c).



### Second Example: Small Aspect Ratio Rayleigh-Bénard Dynamics

Thermally driven convective instabilities in fluid flow, and, more specifically, Rayleigh-Bénard instabilities are favorite working examples in the area of low-dimensional dynamics of distributed systems (see (14) and references therein). By appropriately choosing the cell dimensions (aspect ratio) we can either drive the system to temporal chaos while keeping it spatially coherent, or, alternatively, produce complex spatial patterns.

In a recent paper (15) we have presented a detailed two-parameter experimental study of the quasiperiodic regime of Rayleigh-Bénard convection in dilute solutions of  $^3\text{He}$  in superfluid  $^4\text{He}$ . In this regime the flow is characterized by two distinct frequencies. Figure 2 shows schematic results of two typical runs: the rotation number  $W = f_2/f_1$ , the ratio of these two frequencies, is plotted as a function of the Rayleigh number  $R$  for two distinct values of the Prandtl number  $\sigma$ . The data have been obtained in the following way: one single variable has been recorded in time, and then this single time series has been used to reconstruct the attractor through two time-delays (16). The restriction of the resulting three-dimensional flow to a transverse plane generates a two dimensional map. The insets in Figure 2 show schematics of the relevant characteristics of the phase plane of this map, consistent with the experimental data.

At point A (inset 2a) the response is characterized by two incommensurate frequencies. The three-dimensional flow winds around a two-torus (a doughnut-shaped surface) whose Poincaré cut is an invariant circle. The phase point hops along the circle and becomes dense on it without ever returning to the exact same location. At point B two rest points appear on the circle (a frequency locking or resonance). The ratio of the two frequencies "locks" on a rational value ( $2/13$  in the experiment) and stays locked for a closed interval in parameter space (the Cantor "step" in the experimental data). At point C (inset 2b) we have a pair of periodic (frequency locked) solutions, a stable node period 2 (N) and a saddle period 2 (S). The invariant circle now consists of the unstable manifolds of the saddle-type solutions and the stable periodic solutions N. In a simulation, the boundaries of frequency locking will be found as turning point bifurcations of periodic solutions. For a large scale system of ODEs, a part of the computational effort in a fixed point formulation of the periodic solution goes to the accurate integration of the variational equations, as we discussed above. No hysteresis is observed as we cycle the values of  $R$  from low to high and back again. It is important to note that the apparently smoothly changing graph of  $W$  vs.  $R$  consists really of an infinite number of "steps" like the strong frequency locking shown, which however are too small to resolve experimentally, and will eventually be too small to resolve in any computational effort.

The lower  $\sigma$  graph is more interesting. While initially the Poincaré phase portrait looks the same as before (point E, inset 2c) an interval of hysteresis is observed. The saddle-node bifurcation of the periodic solutions occurs off the invariant circle, and a region of two distinct attractors ensues: a stable, quasiperiodic one and a stable periodic one (Point F, inset 2d). The boundary of the basins of attraction of these two attractors is the one-dimensional (for the map) stable manifold of the saddle-type periodic solutions, SA and SB. One side of the unstable manifold will get attracted to one attractor (SC to the invariant circle) while the other side will approach the other attractor (SD to the periodic solution).

As we further change the parameter  $R$ , the hysteresis interval ends (the invariant circle stops existing) and the only attractor is the stable periodic frequency locked solution N. Both sides of the unstable manifold of the saddle-type frequency locked solution are attracted to N (Point G, inset 2e).

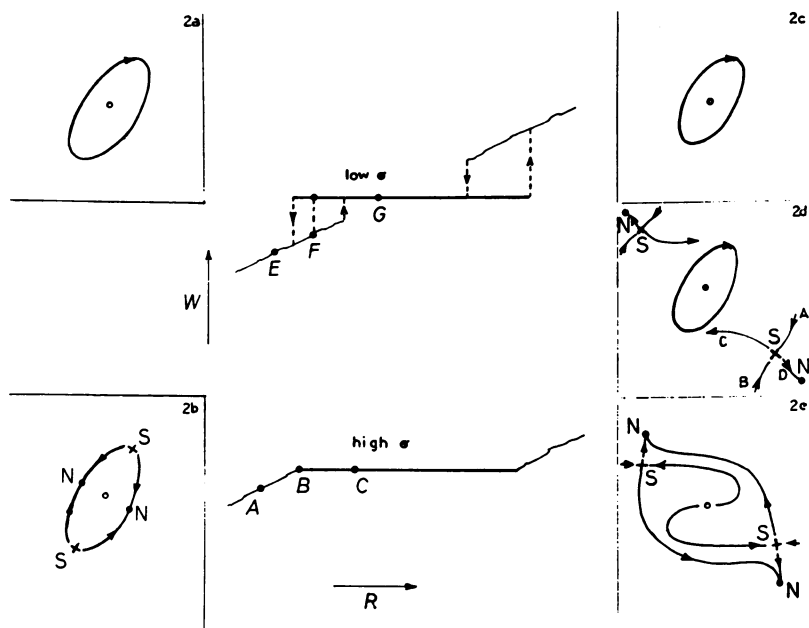


Figure 2. Schematic of typical data and consistent Poincaré sections from the quasiperiodic regime of Rayleigh-Bénard convection. The rotation number  $W$  (in arbitrary units) is plotted versus Rayleigh number  $R$  for two different values of the Prandtl number  $\sigma$ . The hysteretic behavior for low  $\sigma$  implies the existence of homoclinic tangles and global bifurcations giving rise to nontrivial dynamics.

The mechanism of these transitions is nontrivial and has been discussed in detail elsewhere (3, 17); it involves the development of a homoclinic tangency and subsequently of a homoclinic tangle between the stable and unstable manifolds of the saddle-type periodic solution S. This tangle is accompanied by nontrivial dynamics (chaotic transients, large multiplicity of solutions etc.). It is impossible to locate and analyze these phenomena without computing the unstable, saddle-type periodic frequency locked solution as well as its stable and unstable manifolds. It is precisely the interactions of such manifolds that are termed global bifurcations and cause in this case the loss of the quasiperiodic solution.

### Saddle and Invariant Manifold Computation

The above two examples were chosen so as to point out the similarity between a physical experiment and a simple numerical experiment (Initial Value Problem). In both cases, after the initial transients die out, we can only observe attractors (i.e. stable solutions). In both of the above examples however, a simple observation of the attractors does not provide information about the nature of the instabilities involved, or even about the nature of the observed solution. In both of these examples it is necessary to compute unstable solutions and their stable and/or unstable manifolds in order to track and analyze the hidden structure, and its implications for the observable system dynamics.

A fixed point formulation for the location of a non-chaotic solution allows us to locate such saddle-type, unstable structures, be they steady states, limit cycles or tori. The computer provides us the capability of constructing a dynamical system (e.g. the Newton-Raphson of the coupled nonlinear algebraic equations of such a fixed point formulation) whose fixed point is a solution of the parent dynamical system, but with different stability characteristics (the Newton Raphson for a good initial guess will converge on the fixed point). The computation of segments of stable and unstable manifolds for saddle-type solutions follows. It should be stressed that such computations must be combined if possible with interactive graphics; this is often crucial for the understanding of the computational results.

Global bifurcations (as opposed to local ones) leading to complex dynamic behavior and chaos are ubiquitous. The homoclinic tangle of the second example should be expected for large classes of systems with quasiperiodic dynamics, ranging from periodically forced chemical reactors (18) to modulated, self-pulsed semiconductor lasers (19). By locating saddle-type solutions and segments of their invariant manifolds we construct a "skeleton" around which chaotic solutions travel. The advantage is that we can monitor the onset of, or qualitative changes in the chaotic behavior, not by following statistics of chaotic trajectories, but by locating structural changes of this "skeleton" in parameter space.

Two alternatives present themselves in formulating algorithms for the tracking of segments of stable and unstable manifolds. The first involves observing the initial value problem for an appropriately chosen family of initial conditions, henceforth referred to as simulation of invariant manifolds. A second generation of algorithms for the computation of invariant manifolds involves numerical fixed point techniques.

First Generation Algorithms (Simulation of Invariant Manifolds). These algorithms should consist of the following characteristic procedures:

- (1) Location of the saddle-type objects whose stable and/or unstable manifolds we want to compute by established numerical methods.
- (2) Approximate construction of the manifolds in the neighborhood of these objects through local methods -linear and perhaps higher order (20).

(3) "Judicious" distribution of initial conditions on the approximate local manifold. The mesh of initial conditions is chosen so that the trajectories emanating from them are closely and uniformly enough spaced for effective interpolation. This interpolation, performed numerically or even visually in real time graphics provides us with a global approximation of the manifold (see also (21)).

(4) Simultaneous numerical solution of the initial value problem for this entire family of initial conditions, forward (unstable manifolds) or backward (stable ones) in time. This simultaneous integration, can be implemented naively as a parallel computation in a rather trivial sense (several processors, each integrating the same equations with different initial conditions, each computation completely independent from the rest). It is conceivable however, that a few, strategically chosen initial conditions will be integrated with great accuracy, "feeling the ground" for stiffness in the spreading manifold. Integrations emanating from initial conditions in the neighborhood of the above "spinal" ones will then be greatly facilitated by information already gained (time step distribution, order of a backward difference or a Runge-Kutta scheme). This "staged" integration appears to be a new and intriguing software possibility.

There are a number of recurring characteristics of this class of algorithms worth mentioning at this point. One single trajectory is sufficient for a 1-D manifold of a set of ODEs or a discretization of PDEs, while a one-parameter family of trajectories is necessary for a 1-D manifold of a fixed point of a Poincaré map, or a map of the plane. It is evident that detailed calculations can only be done at the present time for low-dimensional invariant manifolds. Another important point is that *stable* manifolds are computed by integration backward in time, or by iteration of the inverse map. Simulation algorithms will thus have serious problems with noninvertible maps, or with the backward integration of discretizations of PDEs, a notoriously difficult problem. These problems can be overcome by computing *stable* manifolds through trajectories forward in time in a fixed point formulation of the problem. Another apparent problem is that since trajectories on a 2-d manifold will "bunch" together severely, one must implement a dynamic redistribution of the initial conditions of the marching cocurrent initial value problems.

General purpose simulation programs interfaced with interactive graphics will prove invaluable in the exploration of global dynamics in general, and of the structure of basin of attraction boundaries in particular. Results from the application of these algorithms will also be used to provide accurate initial guesses for the next set of algorithms.

Second Generation Algorithms (Fixed Point Formulation). A viable, and possibly more theoretically tractable, alternative involves the development of fixed point algorithms that converge iteratively on some discretization of the manifold or of a segment of it. In this case our main effort lies in posing the invariant manifold or submanifold segment as a fixed point problem in the appropriate space, and ascertaining the well-posedness of this problem. The fundamental components of such algorithms are:

(1) Parameterization of the manifold. This is a very sensitive step, since a number of possible parameterizations may apply, each with its own advantages and handicaps. An ad hoc, geometrically motivated parameterization for example may lead to sparse matrix computations but can be inflexible in one-parameter continuations. A more general geometrical parameterization (e.g. through arclength) is more flexible, but leads to full matrix computations. Error equidistribution or other numerical considerations may lead to a host of potential parameterizations, involving variable computational loads (22).

(2) Formulation of the functional equation stating the manifold's invariance under the flow of the dynamical system. This invariance could be under a time  $t$  map, under some specific Poincaré map, or under the stroboscopic map for periodically forced systems. It is evident that one can also consider functional equations describing invariance with respect to any iterate of the above maps. The boundary conditions entering in this formulation vary according to the problem. They are periodic for an invariant circle or a torus. They are fixed at both ends for a saddle connection problem, while they are free at one end for a manifold segment computation. Additional conditions on this free end can be imposed and solved for the parameter value (in a one-parameter continuation) when something significant occurs to the manifold segment (e.g. it becomes tangent to another manifold segment, signalling the onset of a homoclinic tangle).

(3) Discretization of this functional equation through standard numerical techniques to a large set of coupled nonlinear algebraic equations. These equations are solved through iterative techniques. Evaluation of these equations will necessitate one batch of the parallel integrations we described in the first generation algorithms per iteration. The Jacobian of these equations, which involves integration of the variational equations, can be evaluated through an integrator modification concurrently with the system integrations, with minimal computational effort.

This approach gives rise to very interesting interplay between dynamical systems theory and numerical analysis, and is a fertile ground for the applications of modern computational software and hardware including supercomputing. Preliminary promising results on such algorithms are already available, and they point -among other directions- to the development of special purpose hardware for this family of problems. Another potential new application field rising from such work, is the study of the bifurcations of these fixed point problems *per se*, eventually leading to a classification of global bifurcations. Such potentially tractable phenomena include the fractalization of tori as well as the accurate location of the onset of homoclinic tangles in one-parameter diagrams.

### Summary and Conclusions

The computation of stable and unstable manifolds and submanifolds of steady states and limit cycles for ODEs and PDEs is critical to the understanding of nontrivial behavior in physicochemical processes and their models. Due to the very instability of these saddle-type objects it is extremely difficult, if not impossible, to extract information on invariant manifolds and their global interactions from the initial value problem (simple simulation of physical experiment). We have described the characteristics of a class of algorithms tuned to locate and analyze such traits of the phase space of a dynamical system, as well as their effect on the observable system dynamics. We believe that such algorithms will prove invaluable tools in understanding and effectively modelling complicated temporal responses in models of physicochemical processes, especially during the initial transitions to chaotic chemical dynamics or hydrodynamics. Such procedures should be applicable to distributed systems whose behavior is essentially low-dimensional (i.e. they exhibit temporal complexity while retaining some degree of spatial coherence). We believe that the numerical analysis and implementation aspects of this class of algorithms is a fascinating research subject *per se*.

### Acknowledgments

The illustrative examples in this paper are taken from ongoing joint research of the author with J. M. Hyman, B. Nicolaenko and J. C. Scovel (for the Kuramoto-Shivashinsky PDE) and with R. E. Ecke (for the Rayleigh-Bénard experiments). Research on both of these projects is performed under the auspices of the U.S Department of Energy. The author would also like to acknowledge many helpful discussions with D. G. Aronson, R. P. McGehee and M. S. Jolly.

### Literature Cited

1. Hao Bai-Lin. Chaos; World Scientific Publishing Co.: Singapore, 1984.
2. Guckenheimer, J.; Holmes, P. Nonlinear Oscillations, Dynamical Systems and Bifurcation of Vector Fields; Springer, 1983.
3. Kevrekidis, I. G. AIChE J. 1987. Accepted for publication.
4. Foias, C.; Sell, G. R.; Temam, R. Inertial Manifolds for Nonlinear Evolution Equations. IMA Preprint: University of Minnesota, 1985.
5. Chang, H.-C. Chem. Eng. Sci. 1986, **41**, 2477.
6. Nicolaenko, B.; Scheurer, B.; Temam, R. Physica **16D**, 1985, 155.
7. Kevrekidis, I. G.; Nicolaenko, B.; Scovel, J. C. To be submitted.
8. Guckenheimer, J. Contemporary Mathematics 1986, **56**, 175.
9. Doedel, E. J. Cong. Num. 1981, **30**, 265.
10. Petzold, L. Sandia Tech. Rep. **82-8637**, 1982.
11. Caracotsios, M.; Stewart, W. E. Comp. Chem. Eng. 1985, **9**, 359.
12. Ioos, G.; Joseph, D. D. Elementary Stability and Bifurcation Theory; Springer: New York, 1980.
13. Guckenheimer, J.; Holmes, P. Preprint, 1986.
14. Haucke, H.; Ecke, R. E. Physica D, in press, 1987.
15. Ecke, R. E.; Kevrekidis, I. G.; Aronson, D. G.; McGehee, R. P. Phys. Rev. Lett., submitted, 1987.
16. Packard, N. H.; Crutchfield, J. P.; Farmer, J. P.; Shaw, R. S. Phys. Rev. Lett. 1980, **47**, 1448.
17. Aronson, D. G.; Chory, M. A.; Hall, G. R.; McGehee, R. P. Comm. Math. Phys. 1982, **83**, 303.
18. Kevrekidis, I. G.; Schmidt, L. D.; Aris, R. Chem. Eng. Sci. 1986, **41**, 1263.
19. Winful, H. G.; Chen, Y. C.; Liu, J. M. Appl. Phys. Lett. 1986, **48**, 616.
20. Hassard, B. D. In New Approaches to Nonlinear Problems in Dynamics; Holmes, P. J., Ed.; SIAM Publ., p. 7.
21. Rheinboldt, W. C. On the Computation of Multi-Dimensional Solution Manifolds of Parameterized Equations, Tech. Report ICMA-86-102, 1986.
22. Kevrekidis, I. G.; Aris, R.; Schmidt, L. D.; Pelikan, S. Physica **16D**, 1985, 243.

RECEIVED June 15, 1987

## Chapter 17

# Numerical Analysis of Cellular Solidification Microstructures

Robert A. Brown, N. Ramprasad, and Mark J. Bennett

Department of Chemical Engineering and Materials Processing Center,  
Massachusetts Institute of Technology, Cambridge, MA 02139

Large-scale numerical calculations are used to simulate the formation of cellular microstructures during directional solidification of a binary alloy. The analyses are based on finite-element methods developed especially for solving the free- and moving-boundary problems that describe the solute field in the melt and solid and the melt/solid interface shape in the Solutal Model of microscopic solidification. Calculations are reported for individual cells that show the transitions from steady-state solidification of shallow cells near the onset of morphological instability to deep cells separated by narrow grooves as seen in experiments. Simulations with multiple cells show the importance of nonlinear interactions between shapes with resonant spatial structures in determining the time-dependent dynamics of large collections of cells. The results of cellular dynamics calculations for multiple cells show the possibility of long time-scale time-periodic and quasi-periodic interactions.

Solid microstructures have, in the form of cellular and dendritic morphologies in metals and semiconductor alloys solidified from the melt, have long been recognized as playing a crucial role in determining the mechanical and electrical properties of these materials. The length scales associated with the microstructure, such as the size scales for intercellular spacing and the existence and length scale for dendritic sidearms, lead to microscale variation of crystallographic orientation and to microscopic inhomogeneity of solutes. The interest in microstructure formation in this study and many other related efforts hinges on the relationships between the details of the shapes of cells and dendrites and the heat and mass transport and surface physics important during the solidification.

0097-6156/87/0353-0295\$10.75/0  
© 1987 American Chemical Society

Since the pioneering experiments of Jackson and Hunt (1), thin film solidification experiments have become a popular configuration for studying pattern formation in directional solidification; a schematic of a typical configuration is shown as Fig. 1. The system consists of a thin sample of a binary alloy sandwiched between two solid plates. This cell is translated at a constant rate  $V_g$  through a temperature gradient established by a furnace consisting of hot and cold regions separated by a nearly adiabatic zone. An exponential concentration profile is established in the melt ahead of the solidifying interface for a long sample without convective mixing. This concentration gradient is responsible for the constitutional supercooling instability described below. Solidification occurs along a thin strip which is approximately perpendicular to the solid surfaces. The conditions for two-dimensional solidification are discussed in Section 2. The analysis here assumes that the sample can be treated as two-dimensional.

By proposing the 'constitutional supercooling' mechanism for the formation of interfacial microstructure Tiller, Rutter and Chalmers (2) were the first to begin to quantify the relationship between material processing parameters and solid-state structure for controlled solidification in a uniaxially aligned temperature field. The basic idea of constitutional supercooling is that segregation of purposely added solutes or overlooked impurities leads to higher concentrations of these components just ahead of the melt/crystal interface. Then freezing point depression caused by the dependence of the melting temperature on concentration may, depending on the magnitude of the local temperature gradient, lead to melt there that is below its freezing point and so rapidly solidifies. This simple picture, which is available in most popular texts (3,4), gives the simple scaling relationship that for stability of a planar interface

$$\frac{\tilde{G}}{V_g} \geq -\frac{\tilde{m}c_0(1-k)}{kD} \quad (1)$$

where  $\tilde{G}$  is the applied temperature gradient,  $\tilde{m}$  is the slope of the liquidus curve from the phase diagram,  $k$  is the equilibrium segregation coefficient for the solute,  $D$  is the diffusion coefficient for solute in the melt, and  $c_0$  is the solute concentration far from the interface. This relationship approximately predicts the onset of cellular solidification from an initially planar melt/solid interface and the dependence of this limit on processing parameters, as has been proven by many experimental studies; see the examples in Flemings (3) and in Coriell et al. (5). The mechanism for constitutional supercooling leads to morphological instability when either the growth rate or solute concentration is increased above a critical value, or the temperature gradient is lowered appropriately.



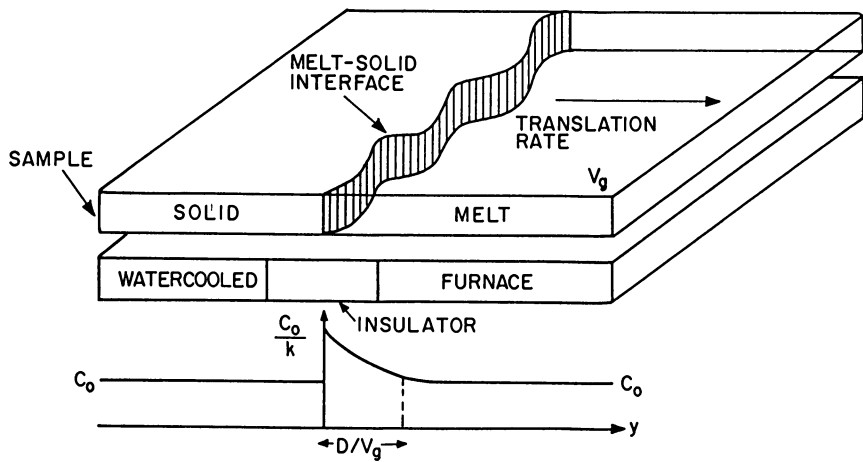


Figure 1. Schematic of thin-film solidification system.

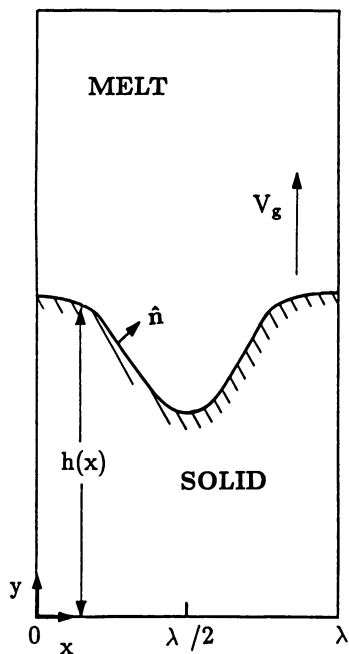
The details of cellular and dendritic solidification are not well understood. Figure 2 shows three photographs taken by Somboonsuk and Trivedi (6) during various stages of cellular and dendritic solidification of an organic alloy in a thin film experiment. The photographs correspond to increasing growth rates, so increasing instability according to the constitutional supercooling criterion. The evolution from shallow, to deep cells and finally to dendritic sidebranching is obvious, as is the changing wavelength of the microstructure.

The length scales for solidification microstructures are governed by interactions of heat and mass transport near the melt/solid interface, thermodynamics of the multi-phase system and by the interfacial physics and chemistry associated with the solidification front. The goal of modelling of solidification microstructures is theoretical understanding and, eventually, quantitative prediction, of the relationship between the microstructure, macroscopic processing conditions and the details of the interfacial physics of the alloys. Particularly interesting issues involve the details of the development of deep cellular interface structures, including the cell shape and prediction of the apparent wavelength for the cellular front and the prediction of dendritic sidebranching and the effect of the sidebranches on the intercellular wavelength of the microstructure.

Underlying these questions is the central issue of whether or not the patterns seen in experiments are deterministic or stochastic. If they are deterministic, a discrete set of stable, steady-state or time-periodic forms must exist for a given set of macroscopic operating conditions and the experiment then selects between these forms depending on its history. If the dynamics of the system is chaotic, pictures like Fig. 1 only constitute an instantaneous image of the microstructure and meaningful analysis must be statistical, averaged over the longest time scale for the variations.

The problem of determining the mechanism for pattern selection in solidification has received intense interest in the last several years. Most of the research has focussed on modelling the solidification problem of a crystal growing at constant velocity into an undercooled bath of pure material. The crystal is assumed to have a needle-like shape that extends arbitrarily far back from the tip and the shape there is assumed to be independent of the surface energy. As is described by Langer (7) and Glicksman (8), the interest in this problem comes from the fact that a family of parabolic-shaped crystals exists in the absence of surface energy at the solidification interface. These solutions do not uniquely specify the product of the tip radius and the growth rate, but careful experiments (8) suggest that a unique relationship exists between these parameters when a real dendrite with sidebranching is studied. Much analysis has been aimed at predicting this relationship.

Considerable mathematical pathology seems to be associated with this problem when the surface energy of the solid/melt interface is vanishingly small. Langer

**MELT**

$$\nabla^2 c + P \frac{\partial c}{\partial y} = \frac{\partial c}{\partial t}$$

**INTERFACE**

$$[\hat{n} \cdot \nabla c] + R_m [\hat{n} \cdot \nabla c_m] = [\hat{n} \cdot \hat{e}_y] (P + V_e) c (k - 1)$$

$$c_s = kc$$

$$T = 1 + mc + \Gamma (2\lambda) = T_r + Gy$$

**SOLID**

$$R_m \nabla^2 c_s + P \frac{\partial c_s}{\partial y} = \frac{\partial c_s}{\partial t}$$

$$R_m = D_s/D$$

$$P = \lambda^* V_g / D$$

$$\lambda = \tilde{\lambda} / \lambda^*$$

$$G = \tilde{G} \lambda^* / T_m^0$$

$$\Gamma = \tilde{\Gamma} / \lambda^*$$

Figure 2. Photographs of cellular and dendritic structures in a thin-film solidification experiment of an organic alloy (succinonitrile-acetone) reported by Ref. 6.

(9,10) have shown for simplified model problems that the parabolic form is singular in the sense that a Taylor series expansion in powers of the surface energy about this solution is incorrect because of exponentially small terms that are missing from the series. The solvability condition associated with these terms is not satisfied when the surface energy is isotropic and no steady-state, needle-shaped crystals exist close to the parabola. This loss-of-existence of the solution is caused by an eigensolution to the linearized free-boundary problem that has high frequency spatial oscillations near the tip, but decay away from it. These conclusions also have been reached by Caroli et al. (11) for realistic solidification models in the limit of high growth rate.

Meiron (12) and Kessler et al. (13) have shown that numerical studies for small surface energy give indications of the loss-of-existence of the steady-state solutions. In these analyses numerical approximations to boundary integral forms of the free-boundary problem that are spliced to the parabolic shape far from the tip don't satisfy the symmetry condition at the cell tip when small values of the surface energy are introduced. The computed shapes near the tip show oscillations reminiscent of the eigensolution seen in the asymptotic analyses. Karma (14) has extended this analysis to a model for directional solidification in the absence of a temperature gradient.

The presentation in this paper concentrates on the use of large-scale numerical simulation in unraveling these questions for models of two-dimensional directional solidification in an imposed temperature gradient. The simplest models for transport and interfacial physics in these processes are presented in Section 2 along with a summary of the analytical results for the onset of the cellular instability. The finite-element analyses used in the numerical calculations are described in Section 3. Steady-state and time-dependent results for shallow cell near the onset of the instability are presented in Section 4. The issue of the presence of a fundamental mechanism for wavelength selection for deep cells is discussed in Section 5 in the context of calculations with varying spatial wavelength.

The approach used in these studies follows ideas from bifurcation theory. We consider the structure of solution families with a single evolving parameter with all others held fixed. The lateral size of the element of the melt/crystal interface appears as one of these parameters and, in this context, the evolution of interfacial patterns are addressed for specific sizes of this element. Our approach is to examine families of cell shapes with increasing growth rate with respect to the form of the cells and to nonlinear interactions between adjacent shape families which may affect pattern formation.

The issues of selection of the spatial wavelength and the deterministic character of the fine scale features of the microstructure are closely related to similar questions in nonlinear transitions in a host of other physical systems, such as macroscopic models of immiscible displacement in porous media - - the Hele Shaw Problem (15) - and flow transitions in fluid mechanical systems (16).

**MODELS FOR SOLIDIFICATION MICROSTRUCTURE IN DIRECTIONAL SOLIDIFICATION**

The analyses discussed here and all the theoretical efforts to date are predicated on the assumption that microstructure formation in solidification can be predicted by models which include diffusion of heat and solute in both phases, freezing point depression caused by the solute, and the dependence of the melting temperature of the surface energy through the curvature of the solidification front. Such models are *continuum descriptions* because the melt and solid are modelled as bulk phases and surface effects are included only as boundary conditions which treat the melt/solid interface as a Gibbs dividing surface. The relevance of this type of description hinges on the length scales for morphological instability, which are considerably above the limits where local density variations in the melt and crystal must be considered.

The mathematical statement of the *Solutal Model* (SM) is given in Fig. 3. The equations are presented in a coordinate frame fixed in space in which melt is convected to the interface and solid is pull away, both at the growth rate  $V_g$ . The variables there are given in dimensionless form where the concentration is scaled with  $c_0$ , the temperature with the melting temperature of the pure material at a planar interface  $T_m^0$ , the spatial coordinates with a characteristic wavelength  $\lambda^*$  for the cellular instability, and time with the characteristic diffusion time  $\lambda^{*2}/D$ . Important dimensionless groups are shown in the figure and are listed in Table 1. These include the ratio of solute diffusivities in the solid and melt  $R_m$ , the solutal Peclet number  $P \equiv \lambda^*V_g/D$ , and the dimensionless temperature gradient  $G \equiv \tilde{G}\lambda^*/T_m^0$ . The Peclet number scales the importance of diffusive transport to the uniaxial convection caused by melt and solid moving through the solidification zone.

In this description the temperature field has been taken to be linear in the coordinate  $y$  and to be independent of the shape of the melt/crystal interface. This is a good assumption for systems with equal thermal conductivities in melt and crystal and negligible convective heat transport and latent heat release. Extensions of the model that include determination of the temperature field are discussed in the original analysis of Mullins and Sekerka (17) and in other papers (18,19).

The melting temperature of the solid is modelled by the Gibbs-Thomson condition written in dimensionless form as

$$T_i(y) = T_r + Gy = T_m^0 + mc + \Gamma(2H) \quad (2)$$

where  $T_i$  is the temperature of the melt/solid interface,  $T_r$  is a reference temperature,  $H$  is its local mean curvature of the interface, and  $\Gamma \equiv (\gamma/\Delta H_f\lambda^*)$  is the dimensionless

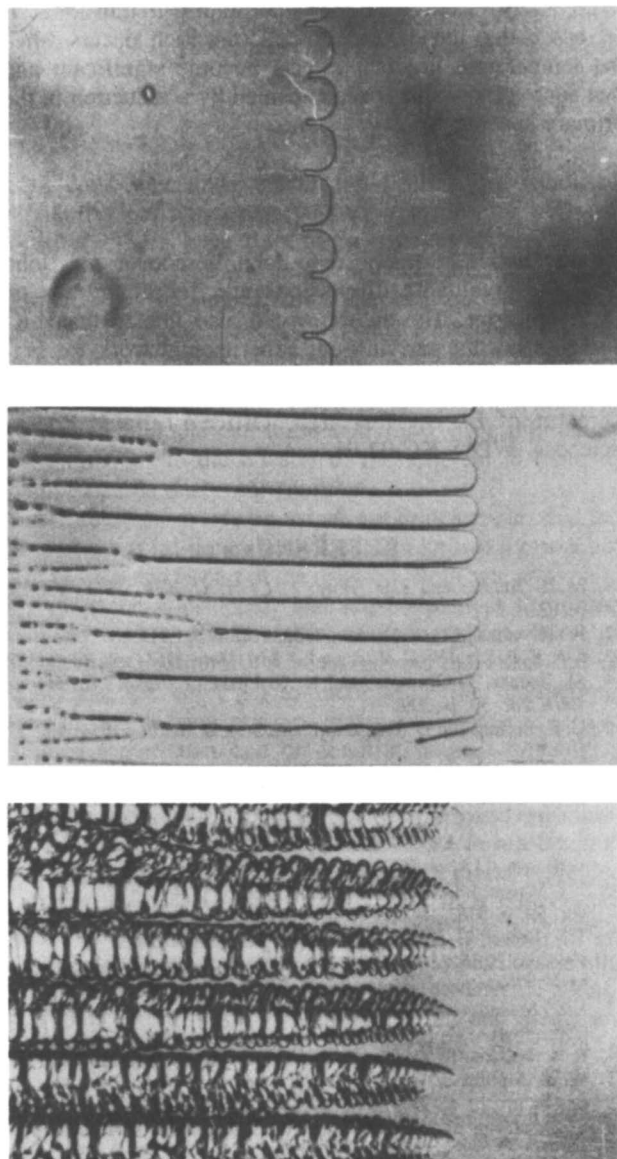


**Figure 3. Mathematical statement of Solutal Model (SM) for microscopic solidification.**

capillary constant ( $\gamma$  is the surface energy and  $\Delta H_f$  is the latent heat of fusion). The Gibbs-Thomson equation expresses the dependence of the melting temperature on the phase diagram (m-c) and the surface energy ( $\Gamma \cdot 2H$ ). Our analyses consider only with solidification at low enough rates that the assumptions of local thermal equilibrium given by (2) and of solutal equilibrium given by the segregation coefficient from the phase diagram,

$$c_{solid} = kc_{melt}, \quad (3)$$

are valid. Coriell and Sekerka (20; also see ref. 21) have examined the effect on cell formation of the kinetics of solute incorporation for rapid solidification conditions.

Equation (2) is identified as a second-order, nonlinear differential equation once, the curvature is expressed in terms of a shape function of the melt/crystal interface. The mean curvature for the Monge' representation  $y = h(x,t)$  is

$$2H = \frac{\partial}{\partial x} \frac{\partial h / \partial x}{[1 + (\partial h / \partial x)^2]^{1/2}} \quad (4)$$

Reflective symmetry boundary conditions are specified at the sides of the sample as

$$\partial h / \partial x = 0, \quad \text{at } x = 0 \text{ and } x = \lambda, \quad (5)$$

where  $\lambda \equiv \tilde{\lambda} / \lambda^*$  is the dimensionless size of the sample.

It is important to recognize the differences in scales for the temperature field, solute gradient and the importance of surface energy. Values of the dimensionless groups are listed in Table 1 for the simulations presented in Sections 4 and 5. The important feature of these scales is that the length scale for the action of the surface energy is orders-magnitude smaller than the scales associated with the solute distribution  $P^{-1}$  and the temperature field  $G$ . Since the surface energy scale is the primary one associated with the lateral dimension (perpendicular to the direction of growth), small length scales are expected in the microstructure and the mechanism for wavelength selection in this dimension can be expected to be weak.

Mullins and Sekerka (17) were the first to construct continuum descriptions like the Solutal Model introduced above and to analyze the stability of a planar interface to small amplitude perturbations of the form

$$h(x,t) = h_0 + \epsilon \sin(\omega_n x) \exp(\sigma_n t), \quad (6)$$

where  $\omega_n$  is the spatial frequency of the disturbance and  $\sigma_n$  is the exponential growth factor. Instabilities begin at the value of the control parameter (either  $G$  or  $Vg$ ) where  $\sigma_n = 0$  for a particular value of the wavelength  $\lambda_n \equiv 2\pi / \omega_n$ . In this discussion the growth velocity or dimensionless Peclet number is treated as the parameter for

Table 1. Dimensionless values of parameters in the Solutal Model for two cases studied here. The systems I and II are representative of the thermophysical properties of the succinonitrile-acetone systems with differing values of the diffusivity ratio  $R_m$ , temperature gradient  $G$  and capillary parameter  $\Gamma$ . System III corresponds to parameters for a Pb-Sb alloy with equal diffusivities in melt and crystal

Dimensionless Group	System I	System II	System III
Segregation Coefficient: $k$	0.1 - 0.865	0.1	0.4
Diffusivity Ratio: $R_m \equiv D/D_s$	0.0	1.0	1.0
Dimensionless Temperature Gradient: $G \equiv \tilde{G}\lambda^*/T_0$	$1.7 \times 10^{-4}$	$2.1 \times 10^{-4}$	$4.5 \times 10^{-5}$
Dimensionless Liquidus Slope: $m \equiv \tilde{m}c_0/T_m^0$	$-6.7 \times 10^{-4}$	$-6.7 \times 10^{-4}$	$-1.67 \times 10^{-4}$
Dimensionless Capillary Length: $\Gamma \equiv \tilde{\Gamma}T_m^0/\lambda^*$	$2.2 \times 10^{-6}$	$2.2 \times 10^{-6}$	$8.2 \times 10^{-7}$
Reference length Scale $\lambda^*$	8.41 $\mu\text{m}$	117 $\mu\text{m}$	100 $\mu\text{m}$



controlling the instability, as is most conveniently done experimentally. Then the condition for neutral stability defines the dispersion equation for predicting the curves of either  $V_g = V_c(\lambda)$  in dimensional or  $P = P_c(\lambda)$  in dimensionless form.

Figure 4 shows sample neutral stability curves for two of the systems listed in Table 1. Long wavelengths ( $\tilde{\lambda} \gg 1$ ) are stabilized by diffusion of solute and short wavelengths are stabilized by surface energy. The region of unstable wavelengths for  $V_g$  much above  $V_c(\lambda_c)$  is large because of the small value of  $\Gamma$ . The most generic feature of these curves is the *flatness* of the region near the most dangerous wavelength  $\lambda_c$ , i.e. the one corresponding to the lowest value of the growth rate. This flatness is a manifestation of the weakness of the surface energy and means that a range of wavelengths are almost equally unstable. Then interactions between these wavelengths can be expected for a small increase in the growth velocity above the critical value  $V_c(\lambda_c)$ .

The neutral stability curves are closed for constant  $\tilde{G}$ , so that at high growth rates the interface is restabilized. In this limit the solute diffusion layer shrinks to the extent that perturbations are stabilized by diffusion. Increasing the segregation coefficient toward unity, as shown in Fig. 4a, decreases the range of unstable wavelengths. The region for the morphological instability shrinks in the limit  $k \rightarrow 1$ , as expected from [1], because the concentration layer adjacent to the interface disappears.

Bifurcation analysis gives a useful framework for discussing the evolution of the cell shape and wavelength with increasing  $P$ . Cells with fixed wavelength, say  $\lambda_c$ , evolve toward either increasing (super-critical) or decreasing (sub-critical) Peclet number. Standard weakly nonlinear analyses of finite amplitude cellular growth at fixed wavelength was first reported by Wollkind and Segel (22) and was duplicated by Ungar and Brown (23) for the solutal model. Multiple length scale asymptotic analyses have been used (24) to calculate the stability of these low amplitude states to long wavelength perturbations.

In both asymptotic approaches, it is assumed that resonant harmonics of the fundamental spatial wavelength do not interact at leading order. In fact, for any value of Peclet number except the minimum, two values of  $\lambda$  simultaneously lead to bifurcation. If these modes are integer multiples of each other, e.g.  $\lambda$  and  $\lambda/2$ , this value of  $P$  corresponds to a codimension-two bifurcation (25) and direct interaction of the two modes is expected for values of  $P$  and  $\lambda$  close to this point. The flatness of the curve  $P_c(\lambda)$  puts bounds on the magnitude of  $|P - P_c(\lambda)|$  before these nonlinear interactions occur. This constraint is so stringent that any theory which neglects resonant interactions is limited to an almost useless range of growth rates. Ungar and Brown (23) realized the existence of these codimension two bifurcations and

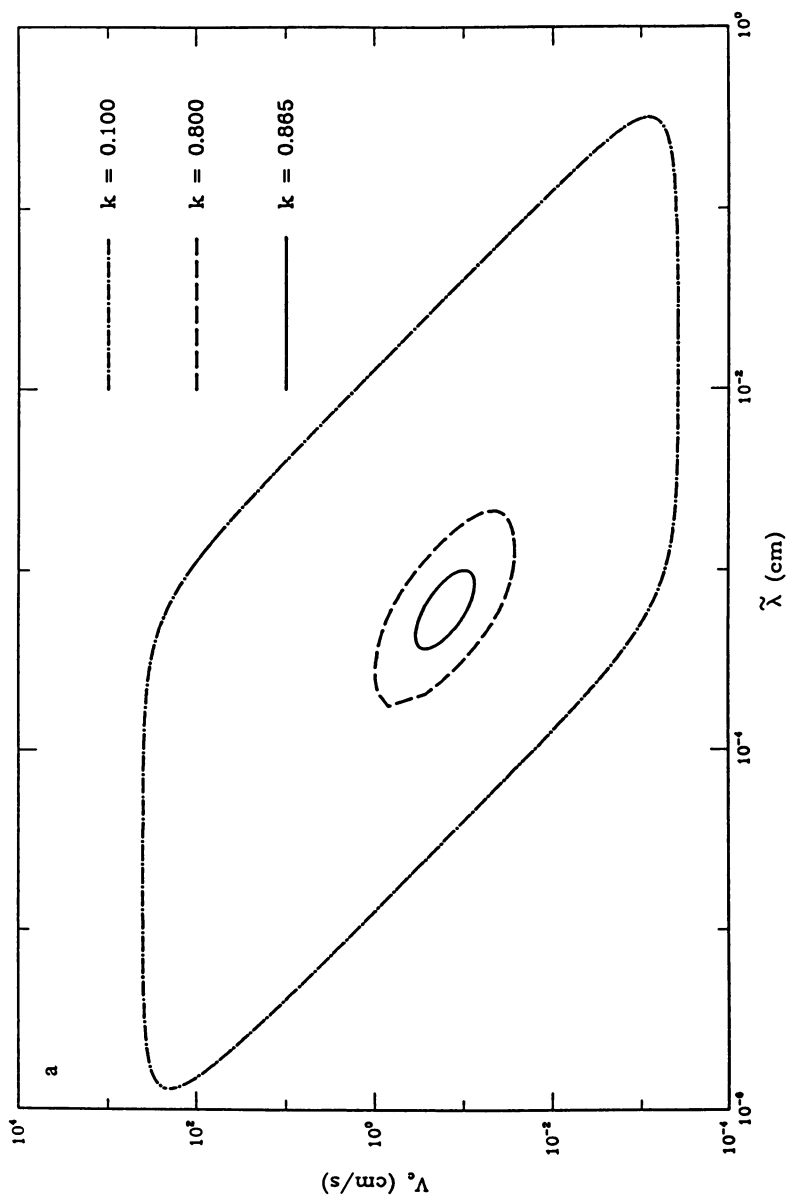


Figure 4. Neutral stability diagrams from linear analysis for values of the thermophysical properties considered in this paper. (a) Diagram for properties given as Case I in Table I as a function of the segregation coefficient  $k$ . *Continued on next page.*

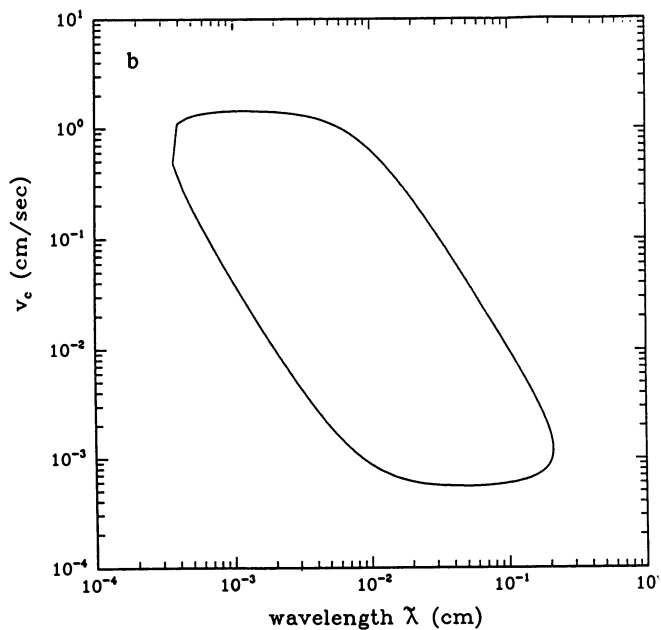


Figure 4. *Continued.* Neutral stability diagrams from linear analysis for values of the thermophysical properties considered in this paper. (b) Diagram for properties given as Case III in Table I.

computed the bifurcation diagram about one for sample thermophysical parameters. Haug (26) used normal form analysis to describe the shapes of the possible bifurcation diagrams resulting from interactions of a variety of different modes. The relevance of these asymptotic calculations to understanding microstructure formation is discussed in Section 4.

### NUMERICAL ANALYSIS

Full numerical solution of the free- and moving- boundary value problems defined by continuum solidification models is the only effective means of determining the structure of the evolution from a planar interface to deep cells and dendrites. Numerical algorithms have been developed for this purpose by several research groups. The techniques used range from boundary integral methods (12,14) to finite-difference (19) and finite element methods (23,27). These methods differ in the methodology used to represent the melt/solid interface, in the type of approximation used to satisfy the field equations for energy and solute transport, and in the iteration schemes for solution of the resulting nonlinear algebraic equations. Except for the algorithm presented by Ungar (28), the other calculations determine only steady-state cell shapes.

We have developed finite-element/Newton methods which allow for simultaneous calculation of steadily solidifying cellular forms and for computer-implemented perturbation analysis of the stability of these shapes and secondary bifurcations with other families (23,29). The finite-element/Newton methods were first described by Ettouney and Brown (27) and are based on employing non-orthogonal transformations to map the shape of the melt/solid interface and the regions of bulk phases to a fixed domain where the interface is a coordinate surface. The mapping used by Ungar and Brown (23) describes the surface by a Monge' representation  $y = h(x,t)$  that can follow the evolution of the interface from a plane to a cell which is not reentrant, so that no melting of the solid can be modelled. The non-orthogonal transformation to the new coordinate system  $(\epsilon, \eta)$  is represented diagrammatically in Fig. 5a and is written as

$$\epsilon = x, \quad \eta = y/h(x,t) . \quad (7)$$

The mapping (7) introduces the unknown interface shape explicitly into the equation set and fixes the boundary shapes. The shape function  $h(x,t)$  is viewed as an auxiliary function determined by an added condition at the melt/crystal interface. The Gibbs-Thomson condition is distinguished as this condition. This approach is similar to methods used for liquid/fluid interface problems that include interfacial tension (30) and preserves the inherent accuracy of the finite element approximation to the field equation (27)

The transformed field equations, boundary conditions and the Gibbs-Thomson

condition are discretized by a finite-element Galerkin method. Lagrangian bi-quadratic polynomials are used to approximate the solute field in both phases and one-dimensional quadratic polynomials are used for the shape function  $h(x,t)$ .

The Galerkin formulation results in a large set of differential/algebraic equations that are most easily expressed in the form

$$M \frac{du}{dt} \equiv \begin{bmatrix} M_1(\beta) & M_2(\alpha, \beta) \\ 0 & 0 \end{bmatrix} \frac{d}{dt} \begin{bmatrix} \alpha \\ \beta \end{bmatrix} = R(\alpha, \beta) \equiv \begin{bmatrix} R_1(\alpha, \beta) \\ R_2(\alpha, \beta) \end{bmatrix} \quad (8)$$

where the coefficients  $\alpha_i$  interpolate the temperature field and the  $\beta_i$  interpolate the interface shape. The mass matrix  $M$  is singular because no time derivatives appear in the residual equations formed from the Gibbs-Thomson equation. This singularity prevents the use of explicit integration schemes. The nonzero components of  $M$  involve the interface shape because of the mapping eq. (7).

Steady-state solutions are found by iterative solution of the nonlinear residual equations  $R(\alpha, \beta) = 0$  using Newton's methods, as described elsewhere (28). Contributions to the Jacobian matrix are formed explicitly in terms of the finite element coefficients for the interface shape and the field variables. Special matrix software (31) is used for Gaussian elimination of the linear equation sets which result at each Newton iteration. This software accounts for the special "arrow structure" of the Jacobian matrix and computes an LU-decomposition of the matrix so that quasi-Newton iteration schemes can be used for additional savings.

Besides being an extremely robust algorithm for the calculation of steady state solutions, the Newton iteration is the basis for computer-implemented perturbation methods for tracking particular families of solutions, for determining the stability of each solution and for following solutions through bifurcation and limit points. These techniques are described in several publications (32,33) and are directly applicable to the solidification problem. Heavy use of these tracking schemes is made to produce the results discussed below.

Time dependent integration of the evolution equations (8) with an initial condition given by

$$u(0) = u_0 \quad (9)$$

demands a numerical method that can effectively approximate the dynamics caused by the mixture of transport processes and equilibrium interface physics incorporated into the continuum models. We have developed a fully implicit time-integration scheme based on a second-order accurate Adams-Bashforth approximation for predicting the solution at the next time step and a fully-implicit Adams-Moulton approximation for correcting this approximation. The nonlinear equations at each time step are solved by quasi-Newton iterations using the matrix software developed for the steady-state

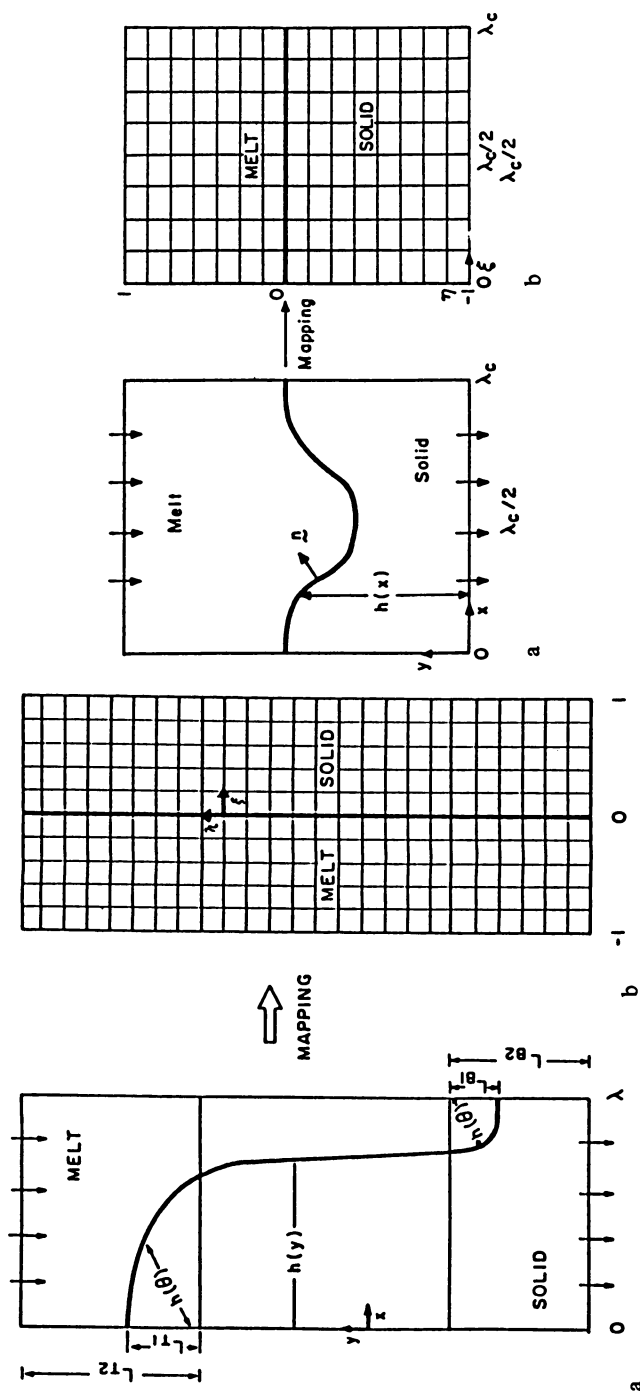


Figure 5. Schematic of nonorthogonal transformations used in finite-element/Newton algorithms for calculating cellular interfaces. (a) Monge cartesian representation for almost planar interfaces. (b) Mixed cylindrical/cartesian mapping for representing deep cells.

problem. The implicit time integration algorithm is coupled with an algorithm for adaptive prediction of the time step so that large step sizes can be used for long time scale integrations; sample results are discussed in the next Section.

As can be seen in Fig. 2a, the grooves that separate deep cells may be reentrant in that material solidifies along the tip, is translated with the solid, melts in the groove and finally resolidifies near the bottom of the groove. To account for this sequence, Ungar and Brown (29) developed a 'deep cell mapping' composed of cylindrical polar and rectangular coordinate pieces, as shown in Fig. 5b. The implementation of the finite-element/Newton algorithm for this transformation is identical to the one for the Monge' representation and is described by Ungar (28). A system of differential/algebraic equations (8) also results, so that the techniques for computer-implemented bifurcation analysis and the time integration procedures are also applicable to this transformation.

### INTERACTION OF SHALLOW CELLS: CELLULAR DYNAMICS

#### Evolution of Shallow Cells: The Role of Codimension Two Bifurcations.

The importance of nonlinear interactions between spatially resonant structures is demonstrated by calculations with thermophysical properties for System I with  $k = 0.865$ . Sample sizes of  $\lambda = \lambda_c/2$  and  $\lambda = 2\lambda_c$  are considered. An expanded view of the neutral stability diagram near the critical value is shown as Fig. 6. The critical values of  $P$  for disturbances which meet the symmetry conditions (5) for the  $2\lambda_c$  sample size are marked on this figure and denote bifurcation points for new shape families from the planar state. The nomenclature for these families gives the number of cells in the sample at the onset  $P = P_c(\lambda)$ ; for example, the  $(4\lambda/7)$ -family has 3.5 cells and the  $(\lambda_c/2)$ - family has 4 cells in a  $2\lambda_c$  sample. Only the  $(1\lambda_c)$ - and  $(\lambda_c/2)$ -families exist in the  $\lambda_c/2$  sample.

The families of steadily solidifying cellular forms for the  $\lambda_c/2$  sample are represented on Fig. 7 by the dimensionless arc-length  $S$  along the interface (normalized by the sample size) plotted as a function of Peclet number. The bifurcation points for the  $(1\lambda_c)$ - and  $(\lambda_c/2)$ -families are denoted by dots. The first family evolves supercritically and the second sub-critically in  $P$ . The most generic feature of this plot is the secondary bifurcation point between these families at finite amplitude; shapes with a single cell in a  $1\lambda_c$  sample size only exist for a limited range of Peclet number before they split and evolve into two cells within the same spacing. Sample interface shapes are shown in Fig. 8 for the values of  $P$  marked by the letters on Fig. 7 and show the "birth" of the second cell by splitting of the original form in the  $(1\lambda_c)$ - family. The appearance of the secondary bifurcation point is a consequence of the codimension two bifurcation that exists between these two shape families for a slightly different value of the sample size (wavelength)  $\lambda$ . Changing the sample size to be closer to the

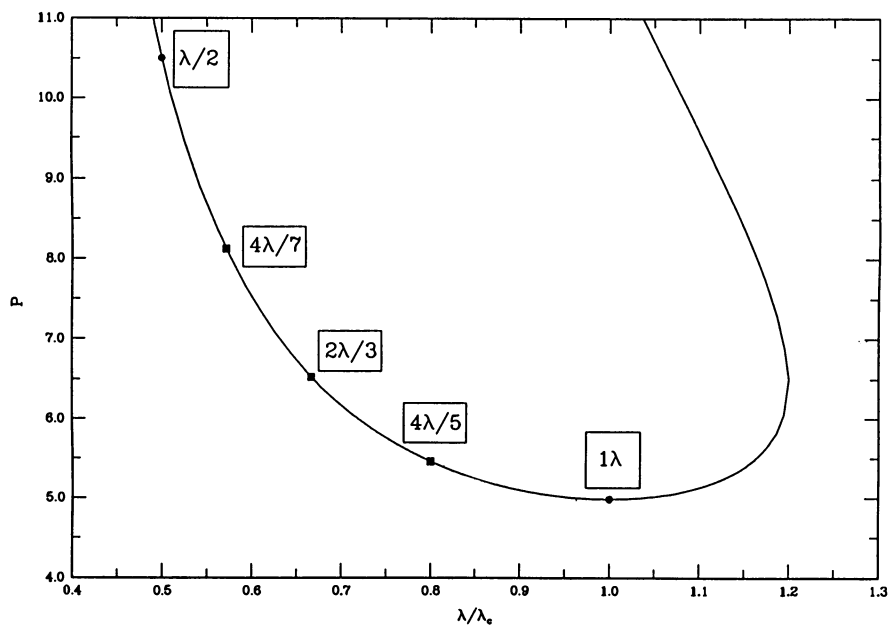


Figure 6. Expanded view of neutral stability diagram for System I with  $k = 0.865$ . Critical values for bifurcation of families of cells in a  $2\lambda_c$  sample size are marked.



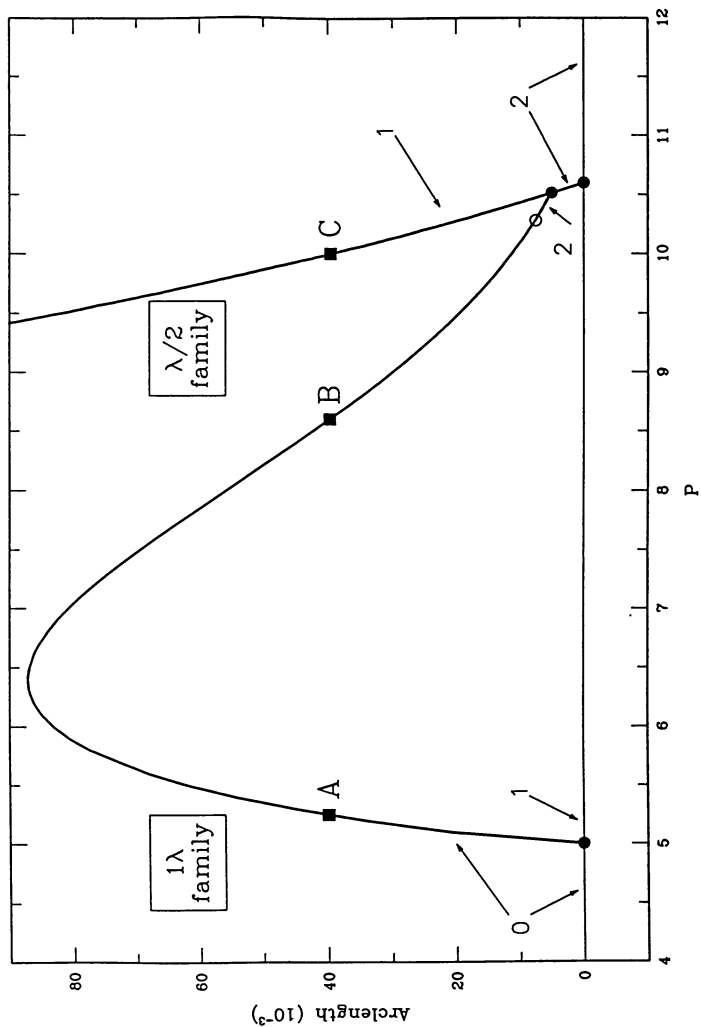


Figure 7. Families of cellular interfaces computed for System I with  $k = 0.865$  as a function of increasing  $P$  in a  $\lambda/2$  sample size. The cells are represented by the dimensionless arc length. The letters refer to sample interface shapes shown in Figure 8.

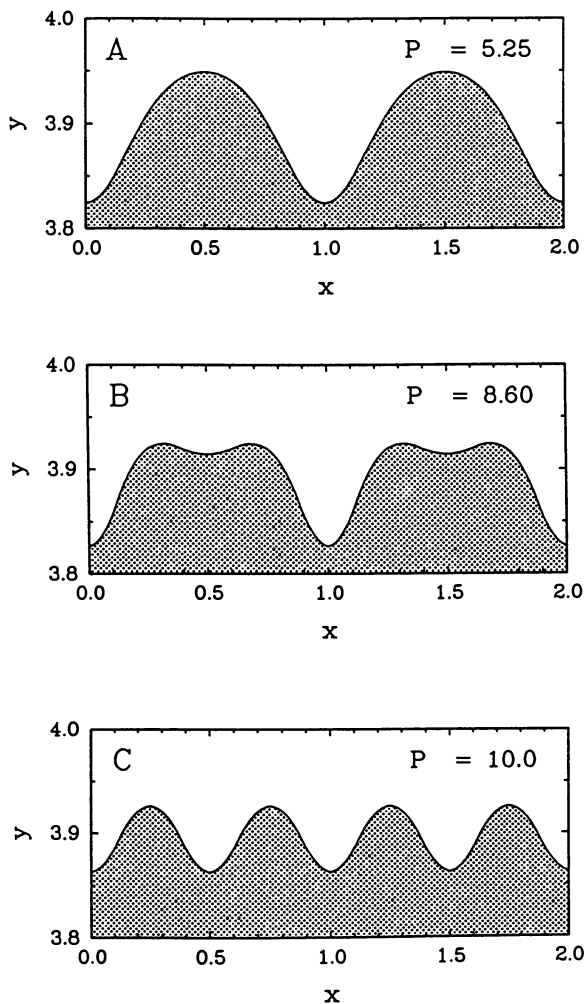


Figure 8. Sample interface shapes for System I with  $k = 0.865$  for the parameter values marked on Figure 7.

critical value where both modes become unstable simultaneously reduces the region of  $P$  before the secondary bifurcation occurs.

The numbers on Fig. 7 refer to the number of unstable modes (corresponding to eigenvalues of the linearized form of (8) with positive real part) for shapes along segments of the families. Only the planar shape up the bifurcation point with the  $(1\lambda_c)$ -family and a portion of the  $(1\lambda_c)$ -family are stable to disturbances with the symmetry imposed by this sample size.

The stability of the  $(1\lambda_c)$ -family is lost at a Hopf bifurcation point denoted by the open circle (o) on Fig. 7, where the real parts of a complex conjugate pair of eigenvalues change sign. No stable time-periodic solutions were found near this point, indicating that the time-periodic states evolve sub-critically in  $P$  and are unstable. Haug (1986) predicted Hopf bifurcations for codimension two bifurcations of the form shown in Fig. 7. but did not compute the stability of the time-periodic states.

Time dependent simulations starting with given steady-state solutions have confirmed the stability results of the linear theory. Figure 9a represents the time evolution of the melt/solid interface shape for a calculation initiated at an almost planar interface for a value of Peclet number greater than  $Pc(4/\lambda_c)$ . Sample shapes are shown in Fig. 10 at varying times to demonstrate the evolution to a shape in the  $(1\lambda_c)$ -family is evident. Figures 9b and 9c show the response of steadily solidifying interfaces in the  $(1\lambda_c)$ -family or either side of the Hopf bifurcation point at  $P = Ph$ . For  $P < Ph$  (Fig. 9b), the shape evolves to the form in the  $(1\lambda_c)$ -family by a decayed oscillation caused by the almost unstable complex-conjugate pair of linear eigenvalues. For  $P > Ph$ , the shape evolves away from the shape in the  $(1\lambda_c)$ -family in a growing oscillation until the trajectory is attracted into the member of the  $(\lambda_c/2)$ -family at the same value of  $P$ ; this evolution is shown in Fig. 9c.

Expanding the sample size to  $2\lambda_c$  admits the other shape families shown on Fig. 6 into the analysis and leads to additional codimension-two interactions between the shapes in the  $(1\lambda_c)$ - family and shapes with other numbers of cells in the sample. The bifurcation diagram computed for this sample size with System I and  $k = 0.865$  is shown as Fig. 11. The  $(1\lambda_c)$ - and  $(\lambda_c/2)$ -families are exactly as computed in the smaller sample size, but the stability of the cell shapes is altered by perturbations that are admissible in the larger sample. The secondary bifurcation between the  $(1\lambda_c)$ - and  $(2\lambda_c/3)$ -families is also a result of a codimension two interaction of these families at a slightly different wavelength. Two other secondary bifurcation points are located along the  $(1\lambda_c)$ -family and may be intersections with the  $(4\lambda_c)$  and  $(4\lambda_c/7)$  families, as is expected because of the nearly multiple eigenvalues for these families.

The exchange-of-stabilities associated with each of the secondary bifurcations

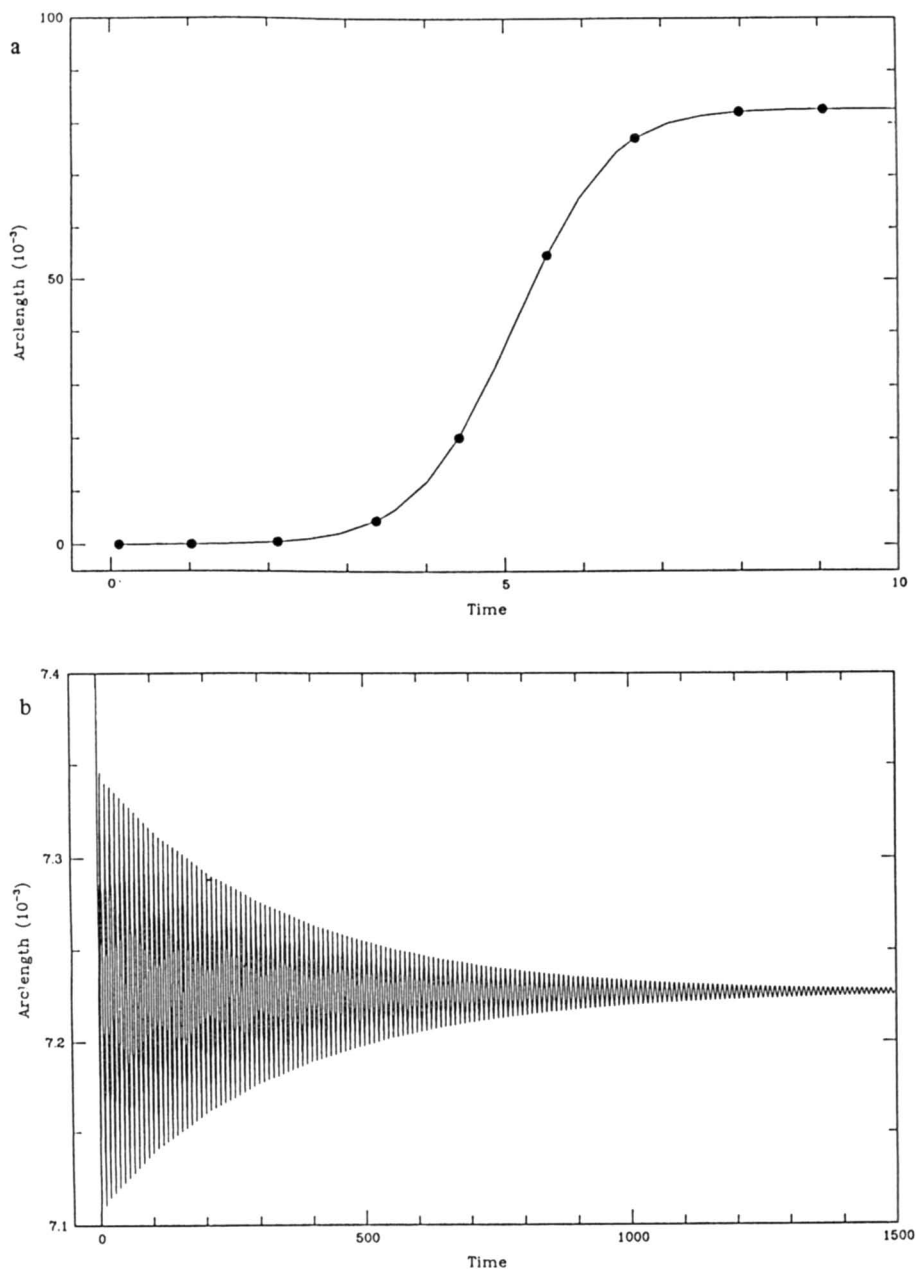


**Figure 9.** Arc length as a function of time for three time transient calculations. (a) Evolution of interface from an unstable planar interface to a shape in the  $(1\lambda_c)$ -family. (b) Evolution of perturbation to a shape in the  $(1\lambda_c)$ -family for  $P < P_h$ . *Continued on next page.*

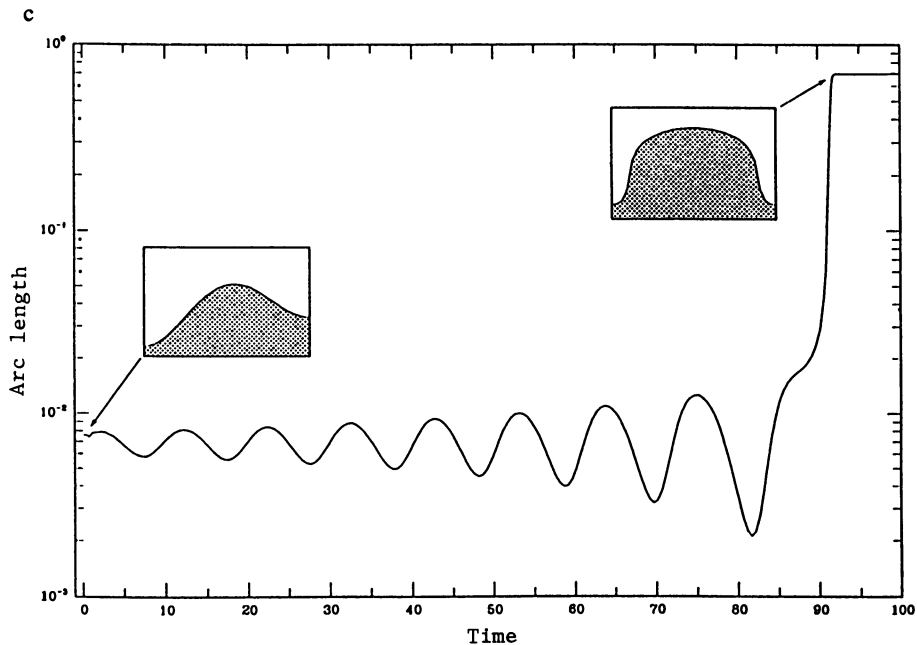


Figure 9. *Continued.* Arc length as a function of time for three time transient calculations. (c) Evolution of perturbation to a shape in  $(1\lambda_c)$ -family to a stable shape in  $(\lambda_c/2)$ -family for  $P > P_k$ .

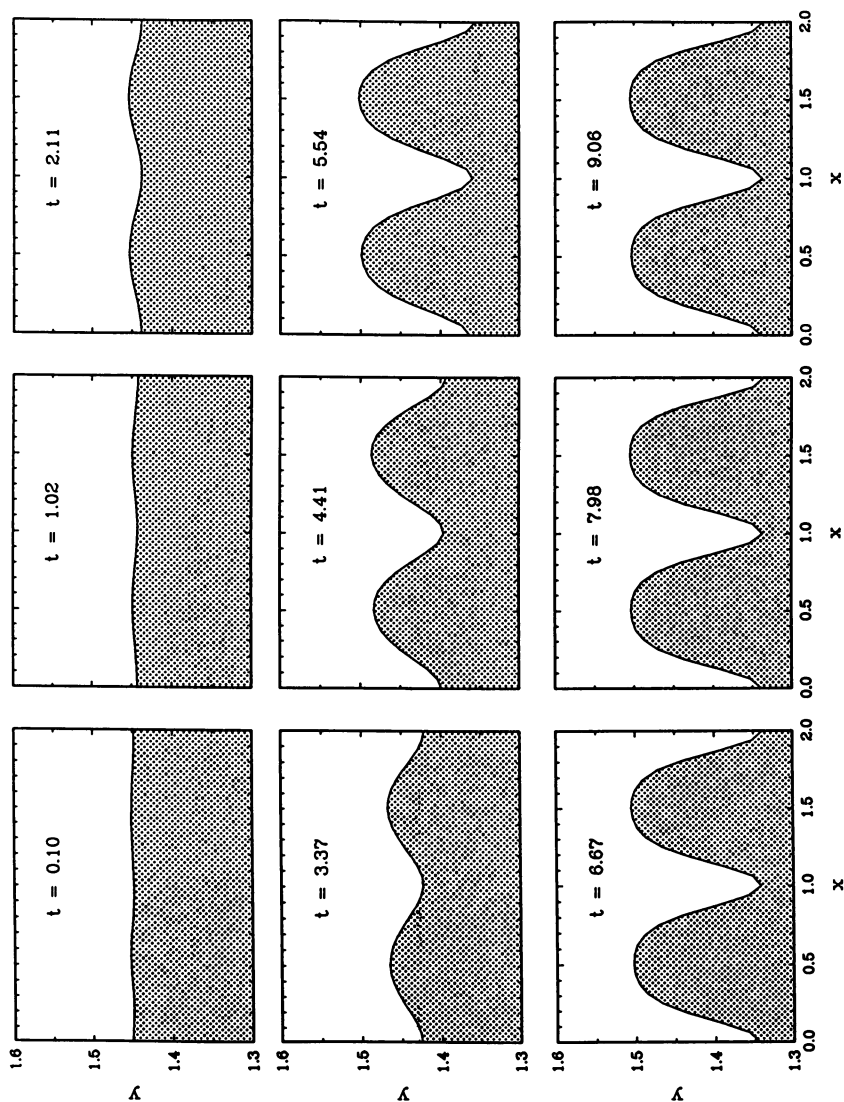


Figure 10. Interface shapes for calculation represented in Fig. 9a.

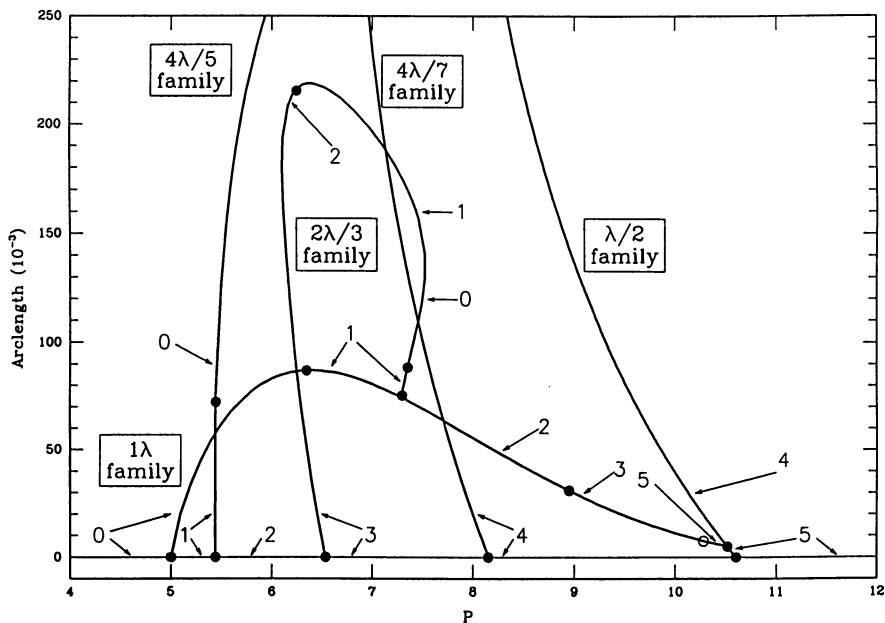


Figure 11. Families of cellular interfaces computed for System I with  $k = 0.865$  as a function of increasing  $P$  in a  $2\lambda_c$  sample size. The cells are represented by the dimensionless arc-length.

causes the shapes in the  $(1\lambda_c)$ -family to become progressively more unstable. Only the first portion of the planar interface and portions of the  $1\lambda_c$ ,  $2\lambda_c/3$  and  $4\lambda_c/5$  families are stable to perturbations that fit into the  $2\lambda_c$  sample size for the range of Peclet numbers shown.

#### Long Time Scale Dynamics Associated with Increased Sample Size.

Changing the thermophysical properties of the system changes the ordering of the primary bifurcation points along the planar state and the secondary ones along the  $(1\lambda_c)$ -family and can lead to differences in the dynamics of the interface. Several families computed for System II are represented in Fig. 12. The important feature of these calculations is the presence of a Hopf bifurcation along the  $(1\lambda_c)$ -family with time-periodic states that evolve to larger values of  $P$ . Sample interface shapes in each of these families are shown in Fig. 13. The shapes in the tusk family show the interactions of modes involving different spatial structure. We believe that these shapes will evolve to the  $(2\lambda_c/3)$ - family, however, the cells that exist at higher values of  $P$  become too deep for accurate approximation in the Monge' representation for this conjecture to be verified.

A sample oscillatory solution is shown in Fig. 14 by a plot of the interfacial arc-length as a function of time. The interface shapes through a half period of the oscillation are plotted in Fig. 15. During a half cycle one of the two cells widens at the expense of the other until the large one begins to divide by a splitting mechanism similar to the one associated with the secondary bifurcations between steady-state families. One these new cells "rolls" into the groove separating the new pair from the remaining large cell and disappears as the largest cell grows. The cycle of cell splitting and the death of a small cell is repeated. The entire cycle is represented by two periods of the curve on Fig. 14, because the value of the arc-length is invariant to a reflection of the interface shape about the center of the cell.

It is interesting to note that the period of these oscillations is extremely long, nearly 1000 diffusion time units in the case shown in Fig. 13, unlike the short time-scale oscillations depicted in Figs. 9b and 9c and attributed to the codimension-two interaction. Therefore the long time scale interaction must be caused to another mechanism, which probably involves the lateral freedom of the cells caused expressly by increasing the size of the sample. Increasing the growth rate  $P$  leads to aperiodic dynamics between the three cells within the sample. Kerszberg (34-36) has seen similar dynamical interactions between cells in calculations based on an asymptotic truncation of a solidification model. Experiments that have attempted to observe the onset of cellular solidification (37) also have observed aperiodic dynamics for shallow cells, and thus support the qualitative observations of our calculations.



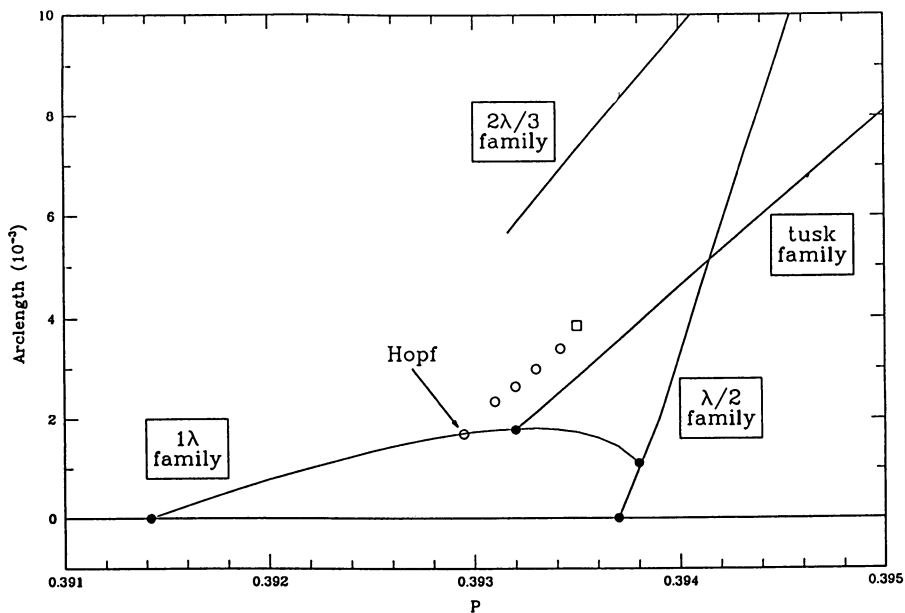


Figure 12. Families of steady and time-dependent cellular interfaces for system II as a function of increasing growth rate  $P$ , as computed in a  $2\lambda_c$  sample size.

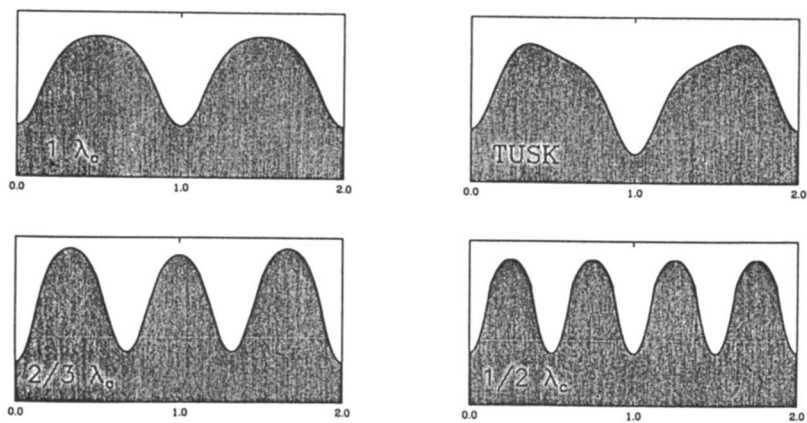


Figure 13. Sample interface shapes from each of the families shown in Fig. 12.

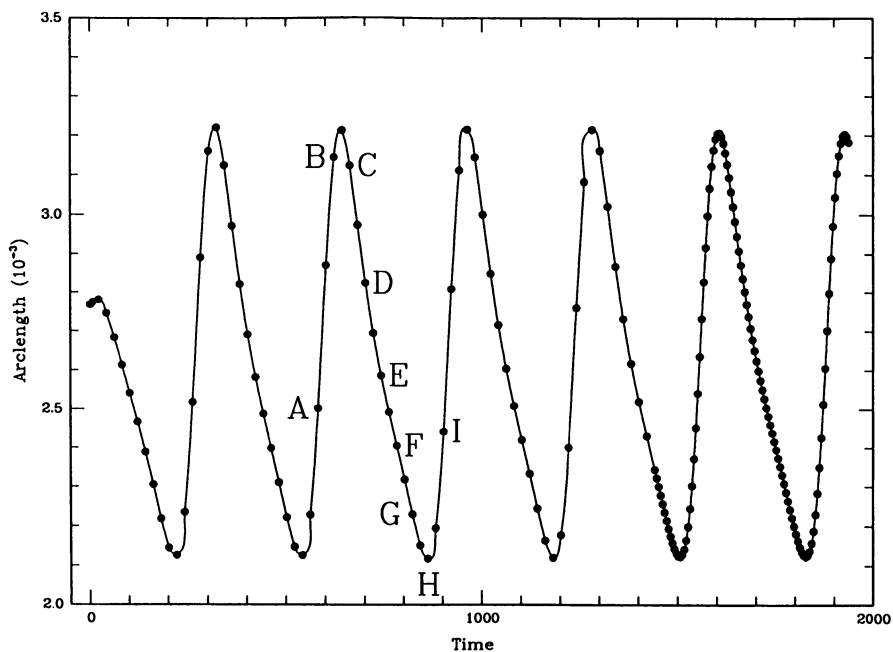


Figure 14. Interfacial arc-length as a function of time for time-periodic cellular interactions denoted on Fig. 12;  $P = 0.3930$ .

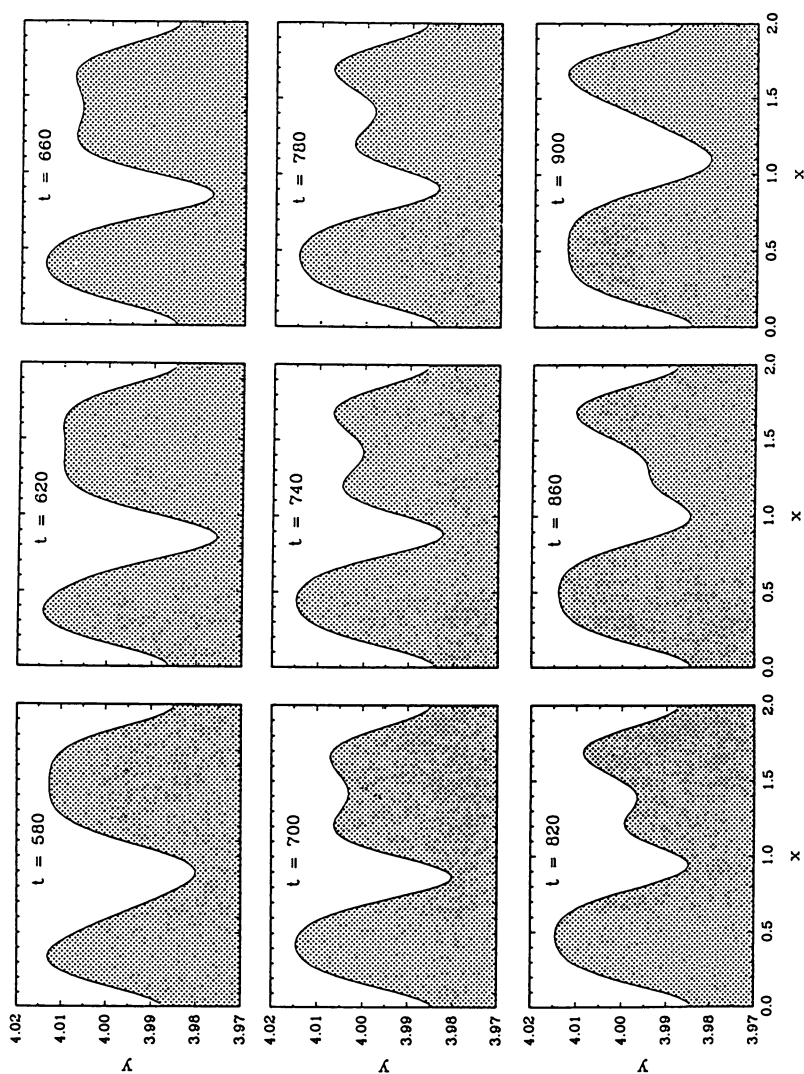


Figure 15. Interface shapes at selected times during time-periodic interaction cycle;  $P = 0.3930$ .

**TRANSITION TO DEEP CELLULAR SHAPES; THE ROLE OF WAVELENGTH**

The cellular structures discussed above were all shallow in the sense that the maximum depth of the interface, measured as the dimensionless height between the tips and grooves was less than 0.5 of the sample size. Increasing Peclet number to higher values leads to deep cells. Calculations of deep cells are reported in this Section for the thermophysical properties of System III; see the neutral stability diagram, Fig. 4b. Nonlinear cellular shapes evolve from the critical value  $Pc(\lambda_c)$  just as in the cases discussed previously. Figure 16 summarizes the interface shapes computed in a  $(\lambda_c/2)$ -size sample for increasing  $P$ , where  $\lambda_c \simeq 4.5$ . Two secondary bifurcation points are detected for  $P < 2Pc(\lambda_c)$  which reduce the wavelength of the computed cell shape to  $\lambda_c/4$ . The amplitude of the cells is represented by the dimensionless cell depth defined as

$$\Delta \equiv \tilde{\Delta}/\tilde{\lambda} \quad , \quad (10)$$

where  $\tilde{\Delta}$  is the dimensional value and  $\tilde{\lambda}$  is the dimensional cell wavelength. Representative cell shapes are shown on Fig. 16 to demonstrate the steepening of the cell shape with increasing Peclet number. Calculations with the Monge' interface representation were stopped because of the possibility that the interface would become reentrant, signifying that the solid melts and then resolidifies in the groove; this is not representable using the the Monge' transformation and so the analysis must be continued by switching to the mixed cylindrical/cartesian transformation shown as Fig. 5b.

Figure 17 shows interface shapes computed using this representation with fixed wavelength  $\lambda = 1$  and increasing  $P$ . The long cells have a distinct three-region structure with a rounded tip, a long sidewall and a small bottom. Increasing the Peclet number lengthens the sidewall disproportionately to the other regions, and suggests an asymptotic structure.

To test for the existence of a mechanism for wavelength selection calculations for relatively deep cells were extended to ranges of wavelength  $\lambda$  for the sample size of an individual cell. Figure 18 shows these calculations. The growth velocity is constant along each curve and is reported as a multiple of the critical value for the most dangerous wavelength  $V_c(\lambda_c)$ . Along each curve  $G$  and  $P$  decrease and  $\Gamma$  increases as  $\lambda$  is lowered.

An important feature is that for each growth rate there is a deepest cell and this cell occurs for a decreasing value of the wavelength with increasing growth rate. For growth rates as low as  $(1.9) V_c(\lambda_c)$  this maximum occurs at wavelengths less than  $\lambda = 1$ , compared to  $\lambda_c = 4.5$ . This is not unexpected, because the wavelength splitting mechanisms demonstrated in Fig. 16, indicate rapid transitions to shorter

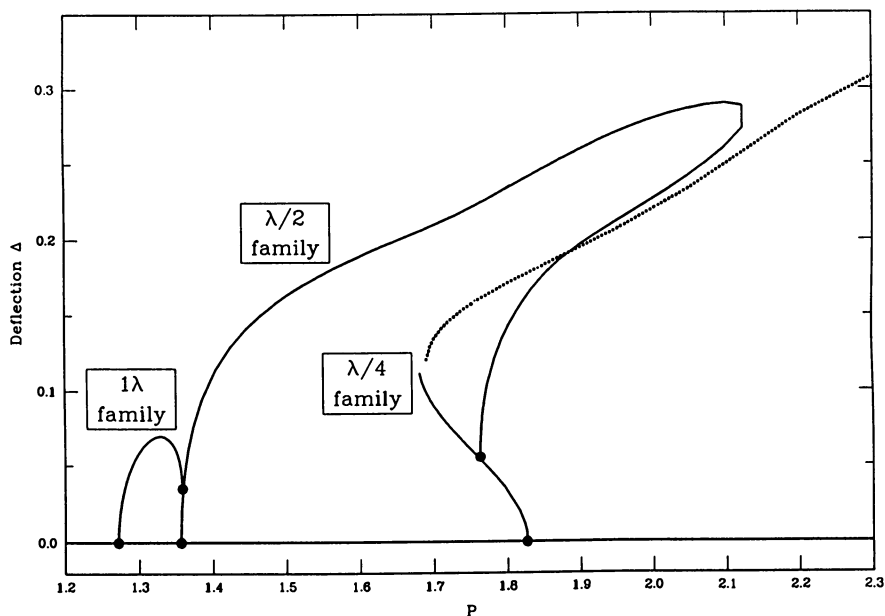


**Figure 16.** Families of steady-state shapes for System III as a function of increasing growth rate  $P$ , as computed in a  $\lambda_c/2$  sample size, including the transition to deep cells. The amplitude of the cellular shapes is denoted by  $\Delta$ , as defined by (10). Continuation of  $(\lambda/4)$ -family computed with the mixed cylindrical/cartesian representation is shown as a dotted (...) curve.

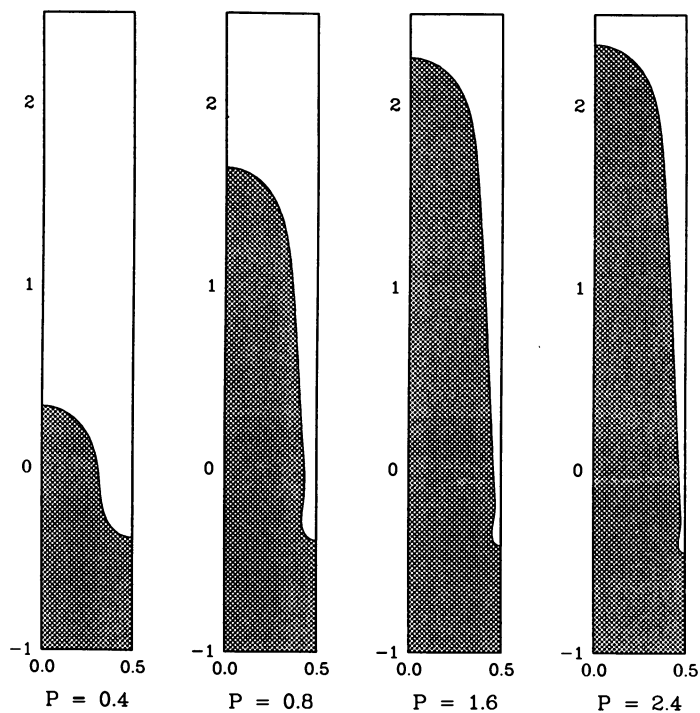


Figure 17. Sample interface shapes for System III for increasing  $P$  and  $\lambda = 1.0$  as computed using the mixed cylindrical/cartesian representation.

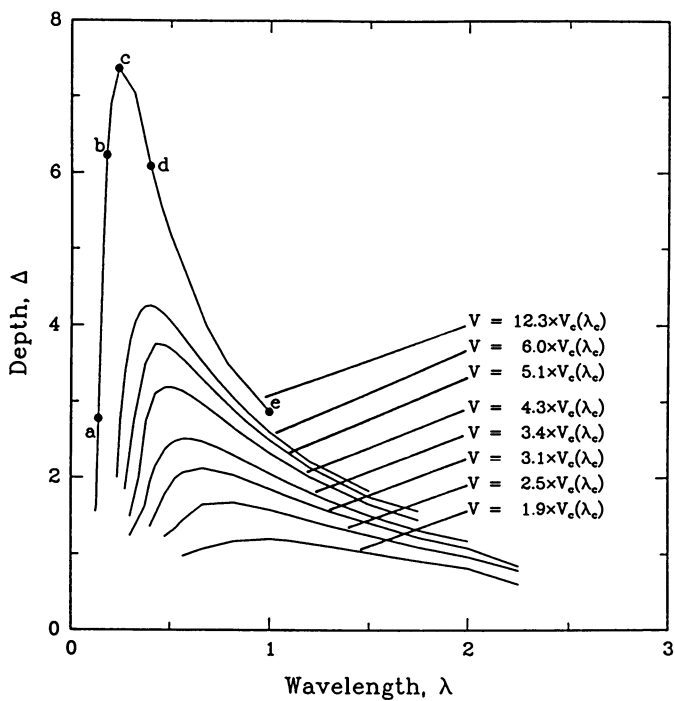


Figure 18. Dependence of cell depth on wavelength for specific values of growth rate  $P$  and other parameter values for System III.



wavelengths. Deep cells ( $\Delta \geq 2$ ) are computed within an increasingly narrower band of spatial wavelengths as the growth rate increases. This is an important observation because it gives evidence that some wavelength selection toward smaller values of  $\lambda$  does occur when the transitions from shallow cells to ones separated by deep grooves is considered; this point is discussed further in another publication (Ramprasad, N.; Bennett, M.J.; Brown, R.A., preprint 1987).

Sample cell shapes for varying wavelengths along the curves with the highest growth rate are shown in Fig. 19 rescaled so the lateral dimension of each cell varies between zero and one. The top and bottom of the cell shape for the shortest wavelength (Fig. 19a) are extremely rounded, showing the dominant influence of surface energy in these regions. Calculations cannot be continued to lower values of  $\lambda$  using the mixed cylindrical/cartesian representation. As the cell lengthens with increasing  $\lambda$ , a long sidewall or groove forms that separates the tip from the bottom. The interface shape and the axial variation of the concentration field are linear along the sidewall, showing that the contributions from the temperature field and the liquidus curve dominate the Gibbs/Thomson equation and that surface energy contributions are unimportant in this region. The cell bottoms are self-similar with increasing  $\lambda$ , but decrease in size relative to  $\lambda$ , because the capillary constant decreases proportional to  $\lambda$ .

### SUMMARY

The calculations discussed here only begin to demonstrate the mathematical complexity associated with microstructure formation in directional solidification. The most generic feature is the importance of nonlinear resonant interactions of cells with different spatial wavelengths. These nonlinear interactions control the evolution of spatial pattern and lead, especially for shallow cells, to the possibility of stochastic dynamics. The number and complexity of these interactions becomes increasingly complex as larger sample sizes are considered. The flatness of the neutral stability curve caused by the small effect of the surface energy leads to the interactions of many codimension-two bifurcations. In some sense, the system can be viewed as being extremely close to a higher-order codimension point and the dynamics for shallow cells can be expected to be indicative of such a singularity. There is some hope of further analytical understanding of the dynamics of wavelength selection based on this approach.

Large-scale numerical simulation for samples that are many times as large as the critical wavelength is perhaps the only way to develop a quantitative understanding of the dynamics of solidification systems. Even for shallow cells, such calculations will be costly, because of the fine discretizations needed to be sure the dynamics associated with the small capillary length scales are adequately approximated. Such calculations may be feasible with the next generation of supercomputers.

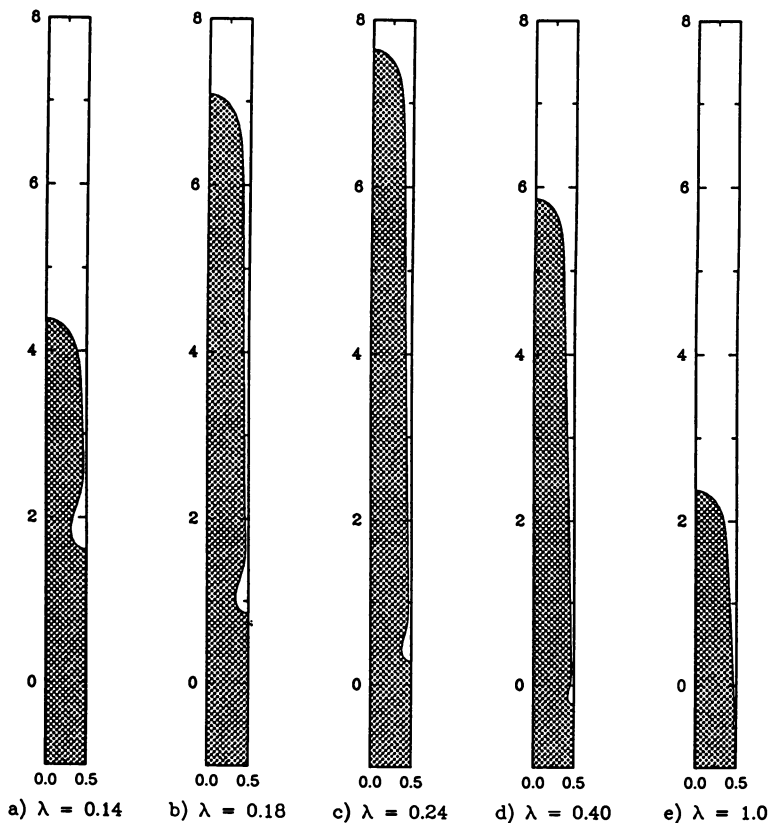


Figure 19. Cell shapes for representative calculations from Fig. 18 and the highest growth rate. The letters correspond to the points shown there. The wavelengths have been normalized so that the aspect ratio of the cells, measured as  $\Delta$ , can be compared directly.

The calculations for a single deep cell, but with a bottom suggests that adequate modelling of the dynamics of real cells probably must account for more detail of the cellular structure than is currently being considered in studies of idealized problems. Because of the finite length of these structures, the small surface energy seems to be controlling the length of the cell and selection of the wavelength through interactions that involve the matching of regions of the shape, like the tip and the sidewall where it is relatively unimportant with the highly curved cell bottom. There is some hope that this structure can be captured by asymptotic analysis for simple solidification models; large-scale calculations are playing an important role in developing such a theory. A similar relationship may exist between the shapes of the tip and the sidebranching along a freely growing dendrite.

#### ACKNOWLEDGMENTS

The preparation of this manuscript and the research described herein was supported by grants from the Microgravity Sciences Program of the National Aeronautics and Space Administration, by the Mobil Foundation and by a Teacher-Scholar Award from the Camille and Henry Dreyfus Foundation to RAB.

#### LITERATURE CITED

1. Jackson, K.A.; Hunt, J.D., *Acta Metall.* 1965, **13**, 1212–1215.
2. Tiller, W.A.; Rutter, J.W.; Jackson, K.A.; Chalmers, B. *Acta Metall.* 1953, **1**, 428–437.
3. Flemings, M.C., *Solidification Processing*; McGraw-Hill, New York, 1974.
4. Woodruff, D.P., *The Solid-Liquid Interface*. Cambridge Press, Cambridge, 1973.
5. Coriell, S.R.; McFadden, G.B.; Sekerka, R.F., *Ann. Rev. Mat. Sci.* 1985, **15**, 119–145.
6. Trivedi, R.; Somboonsuk, K., in *Proc. Flat-Plate Solar Array Research Forum on the High Speed Growth and Characterization of Crystals for Solar Cells*; K. Dumas Ed., JPL-Publication 84-23, 1984.
7. Langer, J.S., *Rev. Mod. Phys.* 1980, **52**, 1–28.
8. Glicksman, M.E., in *Crystal Growth of Electronic Materials*; E. Kaldis Ed., Elsevier, New York, 1985.
9. Langer, J.S., *Phys. Rev. A* 1986, **33**, 435–441. (1986).
10. Langer, J.S.; D.C. Hong, *Phys. Rev. A* 1986, **34**, 1462–1471.

11. Caroli, B.; Caroli, C.; Roulet, B., *Phys. Rev. A* 1986, **33**, 442–452.
12. Meiron, D.I., *Phys. Rev. A* 1986, **33**, 2704–2715.
13. Kessler, D.A.; Koplik, J.; Levine, H., *Phys. Rev. A* 1986, **33**, 3352–3357.
14. Karma, A. *Phys. Rev. A* 1986, **34** 4353–4362.
15. Swinney, H.L.; Gollub, J.P., *Hydrodynamic Instabilities and the Transition to Turbulence*, Springer-Verlag, New York, 1981.
16. Homsy, G.M., *Ann. Rev. Fluid Mech.* 1987, **19**, 271–311.
17. Mullins, W.W.; Sekerka, R.F., *J. Appl. Phys.* 1964, **35**, 444–451.
18. Ungar, L.H.; Bennett, M.B.; Brown, R.A., *Phys. Rev. B* 1985a, **31**, 5923–5930.
19. McFadden, G.B.; Coriell, S.R., *Physica* 1984, **12D**, 253–261.
20. Coriell, S.R.; Sekerka, R.F., *J. Crystal Growth* 1983, **61**, 499–508.
21. Kelly, F.X.; Ungar, L.H., *Phys. Rev. B* 1986, **34**, 1746–1753.
22. Wollkind, D.J.; Segel, L.A., *Philos. Trans. Roy. Soc. Lond.* 1970, **268A**, 351–380.
23. Ungar, L.H.; Brown, R.A. *Phys. Rev. B* 1984, **29**, 1367–1380.
24. Dee, G.; Mathur, R., *Phys. Rev. B* 1984, **27**, 7073–7092.
25. Guckenheimer, J.; Holmes, P. *Nonlinear Oscillations, Dynamical Systems, and Bifurcations of Vector Fields*; Springer-Verlag, New York, 1983.
26. Haug, P., in *Proc. 1986 Inter. Symp. on the Physics of Structure Formation*, Springer-Verlag, New York, 1987.
27. Ettouney, H.M.; Brown, R.A., *J. Comput. Phys.* 1983, **49**, 118–150.
28. Ungar, L.H., Ph.D. Thesis, Massachusetts Institute of Technology, Cambridge, 1984.
29. Ungar, L.H.; Brown, R.A. *Phys. Rev. B* 1985b, **31**, 5831–5940.
30. Brown, R.A., *J. Computat. Physics* 1978, **33**, 217–235.
31. Thomas, P.D.; Brown, R.A., *Inter. J. Numer. Meths. Engng.* 1987, **xx**, xxx–xxx.
32. Ungar, L.H.; Brown, R.A., *Philos. Trans. Roy. Soc. Lond.* 1982, **306A**, 457–480.

33. Yamaguchi, Y.; Chang, C.J.; Brown, R.A., *Philos. Trans. Roy. Soc. Lond.* 1984, **312A**, 519-552.
34. Kerszberg, M., *Phys. Rev. B* 1983a, **27**, 3909-3912.
35. Kerszberg, M., *Phys. Rev. B* 1983b, **28**, 247-254.
36. Kerszberg, M., *Physica* 1984, **12D**, 262-269.
37. Venugopalan, D.; Kirkaldy, J.S., *Acta Metall.* 1984, **32**, 893-906.

RECEIVED June 15, 1987

## Chapter 18

# Application of Supercomputers To Model Fluid Transport and Chemical Kinetics in Chemical Vapor Deposition Reactors

Robert J. Kee<sup>1</sup>, Greg H. Evans<sup>1</sup>, and Michael E. Coltrin<sup>2</sup>

<sup>1</sup>Computational Mechanics Division, Sandia National Laboratories,  
Livermore, CA 94550

<sup>2</sup>Laser and Atomic Physics Division, Sandia National Laboratories,  
Albuquerque, NM 87185

Using a rotating-disk chemical vapor deposition (CVD) reactor as an example, we discuss the application of supercomputing to simulation of gas-phase chemical kinetics and fluid transport. Because a simulation that simultaneously incorporates multidimensional fluid transport and complex chemical kinetics is impractical, we break the simulation into pieces that are appropriate for today's supercomputers. The analysis takes advantage of similarity transformations that, in certain operating regimes, reduce the governing equations to a one-dimensional boundary value problem. The regions in which these transformations are valid are determined through extensive two-dimensional fluid mechanical simulations of the carrier gas alone. For the boundary value problem, a full elementary gas-phase chemical reaction mechanism can be included in the analysis. In addition to discussing the rotating-disk CVD analysis, we discuss our approach to software implementation, which makes simulating large chemical systems practical.

Supercomputers together with software to use them effectively, provide capabilities to solve important problems that combine both scientific complexity and engineering practicality. The supercomputing environment allows a level of sophistication in physical models that is not possible analytically and is prohibitively expensive without supercomputing speed and storage capabilities.

Our purpose in this paper is to illustrate our approach to applying supercomputers in solving complex technological problems. The approach we take is to discuss in some detail the fluid mechanical and chemical kinetics aspects of a rotating-disk chemical vapor deposition (CVD) reactor. The paper goes into both the problem formulation and solution methods. And, even though they are not our main focus, we discuss some CVD results, with the idea that they provide concrete examples of supercomputer applications. Access to supercomputing hardware is of course essential, but we view the implementation of high-level applications software as equally important. In this paper, we discuss the philosophy of our software implementations, and show why this is an important issue in the supercomputing environment, especially as new machine architectures evolve.

0097-6156/87/0353-0334\$06.75/0  
© 1987 American Chemical Society

The rotating-disk CVD reactor (Fig. 1) can be used to deposit thin films in the fabrication of microelectronic components. The susceptor on which the deposition occurs is heated (typically around 1000K) and rotated (speeds around 1000 rpm). A boundary layer is formed as the gas is drawn in a swirling motion across the spinning, heated susceptor. In spite of its three-dimensional nature, a peculiar property of this flow is that, in the absence of buoyant forces and geometrical constraints, the species and temperature gradients normal to the disk are the same everywhere on the disk. Consequently, the deposition is highly uniform – an especially desirable property when the deposition is on a microelectronic substrate.

The importance of fluid flow in CVD processes is now widely recognized.<sup>1,2</sup> Understanding the flow and chemistry in CVD reactors, and using this understanding to design and predict the performance of reactors requires an ability to model the complex interplay of chemical kinetics and molecular transport in flowing systems. This is a task that is only practical in a supercomputing environment. However, modeling the full three-dimensional problem with complex chemistry and transport models is beyond the practical limits of current supercomputing facilities. Therefore, we use analysis to divide the problem into computable pieces. Application of supercomputing power to each piece provides a picture that is sufficiently complete to design and operate confidently such a reactor over a range of operating conditions.

The analysis of the rotating-disk reactor takes advantage of a similarity transformation that, in certain operating regimes, reduces the governing equations to a one-dimensional boundary value problem. We determine the regions in which these transformations are valid through extensive two-dimensional simulations of the carrier gas alone. Once these regions have been identified, a full elementary gas-phase chemical reaction mechanism can be included in the analysis. Quantum chemistry computations are used to predict the thermodynamic properties of species and to help estimate rate expressions for some of the elementary reaction steps.

Software implementations are especially important, especially in a rapidly changing supercomputing environment. In our work a major objective is to understand elementary chemical kinetics processes, and consequently modeling large systems of chemical reactions is required. For this class of problems we discuss two software issues. On one hand, high-level software is required simply to generate the large systems of equations that result from considering large reaction mechanisms. On the other hand, mathematical software is required to solve these systems effectively on supercomputing machines.

### The Fluid Mechanical Problem

The gas motion near a disk spinning in an unconfined space in the absence of buoyancy, can be described in terms of a similar solution.<sup>3,4</sup> Of course, the disk in a real reactor is confined, and since the disk is heated buoyancy can play a large role. However, it is possible to operate the reactor in ways that minimize the effects of buoyancy and confinement. In these regimes the species and temperature gradients normal to the surface are the same everywhere on the disk. From a physical point of view, this property leads to uniform deposition – an important objective in CVD reactors. From a mathematical point of view, this property leads to the similarity transformation that reduces a complex three-dimensional swirling flow to a relatively simple two-point boundary value problem. Once in boundary-value problem form, the computational models can readily incorporate complex chemical kinetics and molecular transport models.

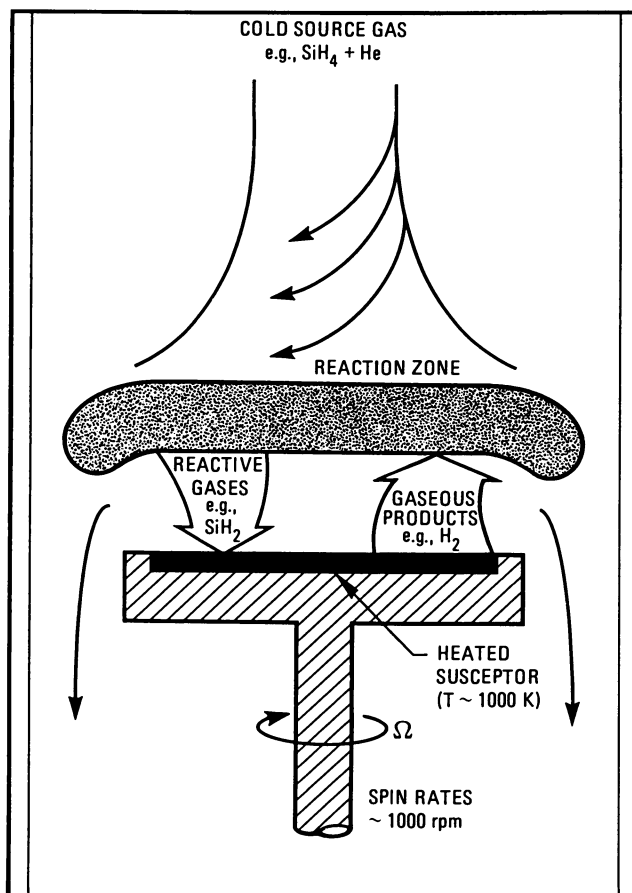


Figure 1. Schematic of the rotating-disk chemical vapor deposition reactor.



Thus our first objective is to discover the operating conditions that lead to both a uniform deposition and a mathematical simplification.

We use computational solution of the steady Navier-Stokes equations in cylindrical coordinates to determine the optimal operating conditions.<sup>5-7</sup> Fortunately in most CVD processes the active gases that lead to deposition are present in only trace amounts in a carrier gas. Since the active gases are present in such small amounts, their presence has a negligible effect on the flow of the carrier. Thus, for the purposes of determining the effects of buoyancy and confinement, the simulations can model the carrier gas alone (or with simplified chemical reaction models) - an enormous reduction in the problem size. This approach to CVD modeling has been used extensively by Jensen and his coworkers (cf. Houtman, et al.)<sup>6</sup>

When the Navier-Stokes equations are written in dimensionless form, certain dimensionless groups appear as parameters in the equations and boundary conditions. By solving the equations over ranges of these parameters one can produce families of solutions that are applicable to a large variety of specific reactor situations. The power of this approach is that one can analyze a particular reactor operating condition by interpolating between the nondimensional solutions. The nondimensionalization can be done in a variety of ways; here we choose parameters that are characteristic of the spinning disk configuration. The dimensionless, circumferentially invariant, equations that we actually solve are stated as

Conservation of mass:

$$\frac{1}{r} \frac{\partial}{\partial r}(\rho r v) + \frac{\partial}{\partial x}(\rho u) = 0 \quad (1)$$

Conservation of axial momentum:

$$\begin{aligned} \frac{1}{r} \frac{\partial}{\partial r}(r \rho v u) + \frac{\partial}{\partial x}(\rho u u) = & -\frac{\partial p_m}{\partial x} + \frac{Gr}{Re^{3/2}} \frac{\rho_w(1-\rho)}{(1-\rho_w)} + \frac{1}{r} \frac{\partial}{\partial r} \left[ r \mu \left( \frac{1}{Re} \frac{\partial u}{\partial r} + \frac{\partial v}{\partial x} \right) \right] \\ & + \frac{\partial}{\partial x} \left\{ 2\mu \frac{\partial u}{\partial x} - \frac{2}{3}\mu \left[ \frac{1}{r} \frac{\partial}{\partial r}(r v) + \frac{\partial u}{\partial x} \right] \right\} \end{aligned} \quad (2)$$

Conservation of radial momentum:

$$\begin{aligned} \frac{1}{r} \frac{\partial}{\partial r}(r \rho v v) + \frac{\partial}{\partial x}(\rho v u) - \frac{\rho w^2}{r} = & -\frac{1}{Re} \frac{\partial p_m}{\partial r} + \\ & \frac{1}{Re} \frac{1}{r} \frac{\partial}{\partial r} \left\{ r \mu \left[ 2 \frac{\partial v}{\partial r} - \frac{2}{3} \left( \frac{1}{r} \frac{\partial}{\partial r}(r v) + \frac{\partial u}{\partial x} \right) \right] \right\} - \\ & \frac{1}{Re} \frac{\mu}{r} \left\{ 2 \frac{v}{r} - \frac{2}{3} \left[ \frac{1}{r} \frac{\partial}{\partial r}(r v) + \frac{\partial u}{\partial x} \right] \right\} + \frac{\partial}{\partial x} \left[ \mu \left( \frac{1}{Re} \frac{\partial u}{\partial r} + \frac{\partial v}{\partial x} \right) \right] \end{aligned} \quad (3)$$

Conservation of circumferential momentum:

$$\frac{1}{r} \frac{\partial}{\partial r}(r \rho v w) + \frac{\partial}{\partial x}(\rho u w) = -\frac{\rho v w}{r} + \frac{1}{Re} \frac{1}{r^2} \frac{\partial}{\partial r} \left[ r^3 \mu \frac{\partial}{\partial r} \left( \frac{w}{r} \right) \right] + \frac{\partial}{\partial x} \left( \mu \frac{\partial w}{\partial x} \right) \quad (4)$$

Conservation of energy:

$$\frac{1}{r} \frac{\partial}{\partial r}(r \rho v \Theta) + \frac{\partial}{\partial x}(\rho u \Theta) = \frac{1}{Re} \frac{1}{Pr_{\infty}} \frac{1}{r} \frac{\partial}{\partial r} \left( r \lambda \frac{\partial \Theta}{\partial r} \right) + \frac{1}{Pr_{\infty}} \frac{\partial}{\partial x} \left( \lambda \frac{\partial \Theta}{\partial x} \right) \quad (5)$$

The independent variables in these equations are the dimensionless spatial coordinates,  $x$  and  $r$ . The dependent variables are the dimensionless velocity components ( $u$  the axial velocity,  $v$  the radial velocity, and  $w$  circumferential velocity), temperature  $\Theta$ , and pressure  $p_m$ . The viscosity and thermal conductivity are given by  $\mu$  and  $\lambda$ , and the mass density by  $\rho$ . Density is determined from the temperature and pressure via an ideal-gas equation of state. The dimensionless variables are defined by  $r = \bar{r}/\bar{r}_d$ ,  $x = \bar{x}\sqrt{\bar{\Omega}/\bar{\nu}_\infty}$ ,  $u = \bar{u}/\sqrt{\bar{\Omega}\bar{\nu}_\infty}$ ,  $v = \bar{v}/(\bar{r}_d\bar{\Omega})$ ,  $w = \bar{w}/(\bar{r}_d\bar{\Omega})$ ,  $p_m = \bar{p}_m/(\bar{\mu}_\infty\bar{\Omega})$ ,  $\Theta = (\bar{T} - \bar{T}_\infty)/(\bar{T}_s - \bar{T}_\infty)$ ,  $\rho = \bar{\rho}/\bar{\rho}_\infty$ ,  $\mu = \bar{\mu}/\bar{\mu}_\infty$ ,  $\lambda = \bar{\lambda}/\bar{\lambda}_\infty$ , where the "bar" indicates dimensional quantities and the subscript  $\infty$  indicates properties evaluated at the inlet conditions. The disk spinning rate is given by  $\bar{\Omega}$ , the kinematic viscosity by  $\bar{\nu}$ , and the disk radius by  $\bar{r}_d$ .

At the solid walls, the boundary conditions state that the velocity is zero (i.e. no slip). Also at the walls, the temperature is either fixed or a zero-gradient condition is applied. At the surface of the spinning disk the gas moves with the disk velocity and it has the disk temperature, which is constant. The inlet flow is considered a plug flow of fixed temperature, and the outlet is modeled by a zero gradient condition on all dependent variables, except pressure, which is determined from the solution.

Several dimensionless groups characterize these equations. The Reynolds number  $Re = \bar{r}_d^2\bar{\Omega}/\bar{\nu}_\infty$  indicates the ratio of centrifugal forces to viscous forces. The ratio of the Grashof number and the Reynolds number to the 3/2 power,  $Gr/\sqrt{Re^3} = g(\bar{T}_s - \bar{T}_\infty)/(\bar{T}_\infty\sqrt{\bar{\Omega}^3\bar{\nu}_\infty})$ , indicates the ratio of buoyant forces to centrifugal forces. When the ratio of the substrate to inlet temperature  $\bar{T}_s/\bar{T}_\infty$  is high, variable properties are important. Two parameters describe the reactor geometry; they are the ratio of the reactor radius to the disk radius,  $\bar{r}_0/\bar{r}_d$ , and the ratio of the reactor height to the disk radius,  $\bar{L}/\bar{r}_d$ . Boundary conditions represent additional parameters. These include the inlet velocity distribution and the thermal boundary conditions on the reactor walls.

These equations form a nonlinear system of elliptic partial differential equations. The solution method is a semi-implicit finite-difference method based on the techniques implemented in the TEACH code by Gosman and Pun.<sup>8</sup> Our computations typically use a nonuniformly spaced cylindrical coordinate grid consisting of 50 radial points and 80 axial points. The axial points are concentrated in the area just above the disk because of the steep gradients expected there. A single simulation requires one to three hours on the Cray 1-S, and we have simulated roughly 100 different combinations of parameters to form a reasonably complete picture of possible reactor operating conditions. Figure 2 shows the radial-axial velocity vectors and isotherm contours for a typical computational result. This figure shows a situation in which the buoyant forces are sufficiently large that a recirculation vortex has been established. As a result, it is evident from the isotherms that the temperature gradients above the disk surface are beginning to deviate from their desired uniformity.

Figure 3 shows a composite result from several simulations and considers the relationship between disk temperature and spin rate for a helium carrier in a fixed reactor geometry ( $\bar{r}_0/\bar{r}_d = 1.28$ ,  $\bar{L}/\bar{r}_d = 2.16$ ) with adiabatic walls. The figure shows a dividing line below which the surface temperature gradients are within 10 percent of the one-dimensional solution over the central 90 percent of the disk ( $r < 0.9$ ). As the disk temperature is increased, the spin rate must also increase so that the buoyant forces do not cause the solution to deviate from its one-dimensionality for this reactor geometry. A plot such as this has

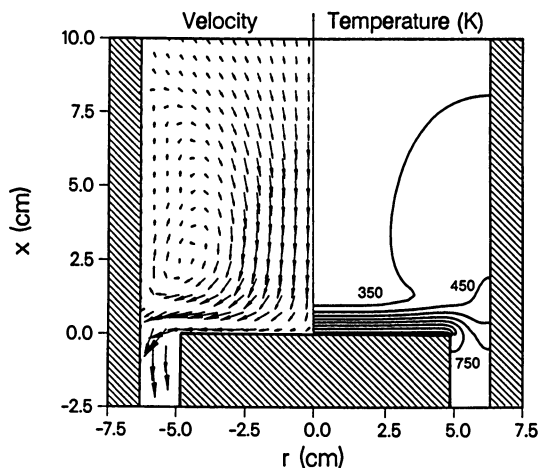


Figure 2. Radial-axial velocity field and temperature contours for a rotating-disk reactor at an operating condition where a buoyancy-driven recirculation vortex has developed. The disk temperature is 1100K, the Reynolds number is 1000,  $Gr/Re^{3/2} = 6.2$ ,  $\bar{r}_0/\bar{r}_d = 1.28$ , and  $\bar{L}/\bar{r}_d = 2.16$ . The disk radius is 4.9 cm, the spin rate is 495 rpm. The maximum axial velocity is 55.3 cm/sec. The gas is helium.

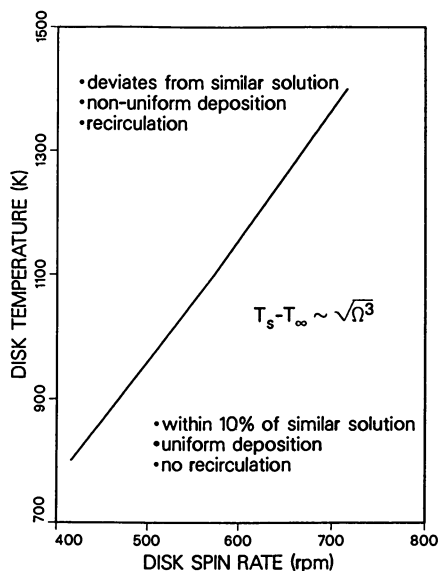


Figure 3. Relationship of susceptor temperature to spin rate that is required to operate a particular reactor geometry in the "one-dimensional" regime.

great practical utility in deciding how to operate a reactor when the processing temperature is changed.

Reactor wall thermal boundary conditions can have a strong effect on the gas flow and thus the deposition. Here, for example, we indicate how cooling the reactor walls can enhance deposition uniformity. We consider the results of three simulations comparing the effects of two different wall boundary conditions. Figure 4 shows how the ratio of the computed susceptor heat flux to the "one-dimensional" heat flux varies with the disk radius for the different conditions (the Nusselt number  $Nu$  is a dimensionless surface heat flux). In two cases the reactor walls are held at 300 K ( $\Theta = 0$ ), and in one case the walls are insulated ( $\partial\Theta/\partial r = 0$ ). Consider first the cases where the mixed-convection parameter,  $Gr/\sqrt{Re^3}$ , equals 6.4. When the reactor walls are insulated, the susceptor heat flux is clearly not uniform, especially over the outer half of the disk. However, when the walls are cooled (all other conditions being the same) the heat flux is highly uniform and agrees with the one-dimensional result. Furthermore, with the cool walls, the mixed-convection parameter can even be increased (shown here  $Gr/\sqrt{Re^3} = 9.6$ ) without causing recirculation, and thus nonuniform surface flux. Since the disk temperature is fixed in this simulation, a smaller value of the mixed-convection parameter corresponds to a larger value of the disk spin rate.

### The One-Dimensional Problem With Chemistry

Once the "one-dimensional" operating regime is established, we can proceed to take advantage of that simplification to construct models that consider the chemical kinetics and molecular transport in considerable detail. The von Karman similarity transformation for the non-reacting, unconfined, non-buoyant situation is a classic application similarity solution methods to the Navier-Stokes equations. Derivation of the similar equations appears in several fluid mechanics texts (e.g. Schlichting<sup>3</sup>). Figure 5 shows a sketch of the rotating disk configuration, and indicates the boundary layer profiles. Notice, especially, that the axial velocity is independent of radius - the same is true for the temperature and species profiles.

Pollard and Newman<sup>4</sup> have also studied CVD near an infinite rotating disk, and the equations we solve are essentially the ones stated in their paper. Since predicting details of the chemical kinetic behavior is a main objective here, the system now includes a species conservation equation for each species that occurs in the gas phase. These equations account for convective and diffusive transport of species as well as their production and consumption by chemical reaction. The equations stated below are given in dimensional form since there is little generalization that can be achieved once large chemical reaction mechanisms are incorporated.

Mixture continuity:

$$\frac{\partial u}{\partial x} + 2V - \frac{\rho}{\rho_\infty T_\infty} u \frac{\partial T}{\partial x} = 0 \quad (6)$$

Radial momentum:

$$\frac{\partial}{\partial x} \left( \mu \frac{\partial V}{\partial x} \right) - \rho u \frac{\partial V}{\partial x} - \rho(V^2 - W^2) = 0 \quad (7)$$

Circumferential momentum:

$$\frac{\partial}{\partial x} \left( \mu \frac{\partial W}{\partial x} \right) - \rho u \frac{\partial W}{\partial x} - 2\rho VW = 0 \quad (8)$$

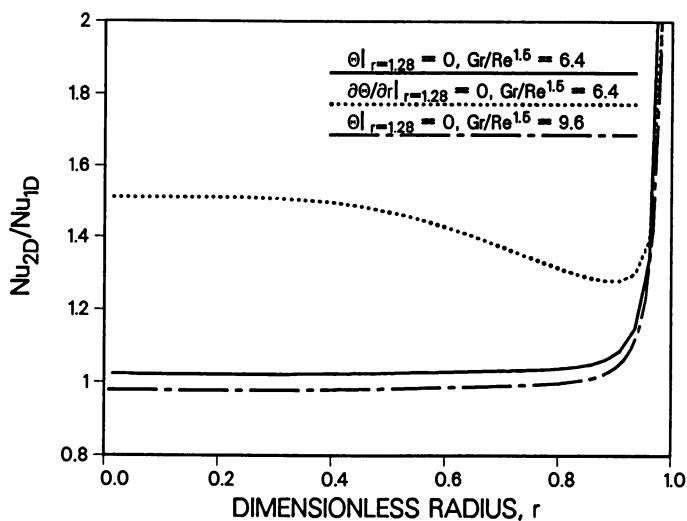


Figure 4. The effect of wall cooling on susceptor heat flux uniformity.

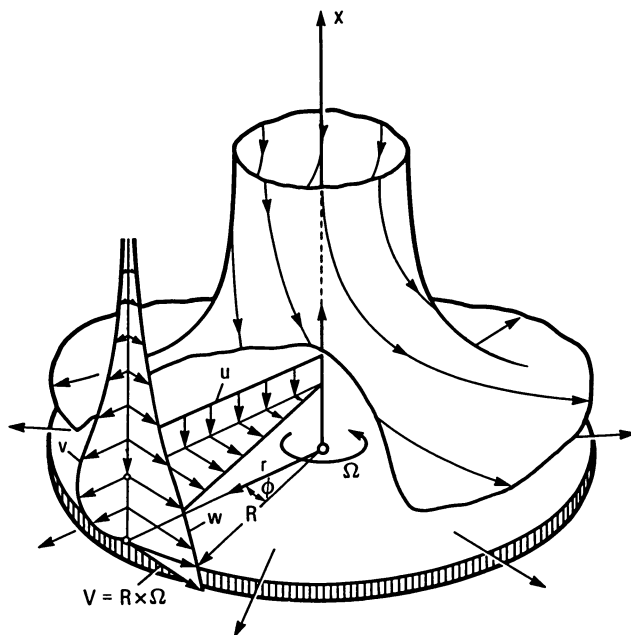


Figure 5. Sketch of the similar solution to the rotating disk problem. (Reproduced with permission from Ref. 3. Copyright 1979 McGraw-Hill.)

Thermal energy:

$$\frac{\partial}{\partial x} \left( \lambda \frac{\partial T}{\partial x} \right) - \rho c_p u \frac{\partial T}{\partial x} - \sum_{k=1}^K \left( c_{pk} \rho Y_k V_k \frac{\partial T}{\partial x} + \dot{\omega}_k h_k \right) = 0 \quad (9)$$

Species continuity:

$$\frac{\partial \rho Y_k V_k}{\partial x} + \rho u \frac{\partial Y_k}{\partial x} - W_k \dot{\omega}_k = 0 \quad (k = 1, K_g - 1) \quad (10)$$

In these equations the independent variable  $x$  is the distance normal to the disk surface. The dependent variables are the velocities, the temperature  $T$ , and the species mass fractions  $Y_k$ . The axial velocity is  $u$ , and the radial and circumferential velocities are scaled by the radius as  $V = v/r$  and  $W = w/r$ . The viscosity and thermal conductivity are given by  $\mu$  and  $\lambda$ . The chemical production rate  $\dot{\omega}_k$  is presumed to result from a system of elementary chemical reactions that proceed according to the law of mass action, and  $K_g$  is the number of gas-phase species. Equation (10) is not solved for the carrier gas mass fraction,  $Y_{K_g}$ , which is determined by ensuring that the mass fractions sum to one. An Arrhenius rate expression is presumed for each of the elementary reaction steps.

The diffusion velocities,

$$V_k = \frac{1}{X_k \bar{W}} \sum_{j=1}^{K_g} W_j D_{kj} \nabla X_j - \frac{D_k^T}{\rho Y_k} \frac{\nabla T}{T} \quad (11)$$

have both an ordinary multicomponent diffusion component and a thermal diffusion (Soret effect) component. In CVD problems, the thermal diffusion often plays an important role, causing high molecular-weight gases in a low molecular-weight carrier to diffuse rapidly in the presence of strong temperature gradients near the susceptor.

The ordinary multicomponent diffusion coefficients  $D_{kj}$  and the viscosity and thermal conductivity are computed from appropriate kinetic theory expressions. First, pure species properties are computed from the standard kinetic theory expressions. For example, the binary diffusion coefficients are given in terms of pressure and temperature<sup>9</sup> as

$$D_{jk} = \frac{3}{16} \frac{\sqrt{2\pi k_B^3 T^3 / m_{jk}}}{P \pi \sigma_{jk}^2 \Omega^{(1,1)*}} \quad (12)$$

where  $m_{jk}$  is the reduced molecular mass for the  $(j, k)$  species pair and  $\sigma_{jk}$  is the reduced collision diameter. The collision integral  $\Omega^{(1,1)*}$  (based on Stockmayer potentials) depends on the reduced temperature,  $T_{jk}^*$ , which in turn may depend on the species dipole moments  $\mu_k$ , and polarizabilities  $\alpha_k$ . The multicomponent mixture properties are computed from the pure species properties using the averaging procedures given by Dixon-Lewis.<sup>10</sup>

In the presence of surface deposition, the disk boundary condition becomes relatively complex. It states that the gas-phase mass flux of each species to the surface is balanced by the creation or depletion rate of that species by surface

reaction,  $j_k = \dot{s}_k$ . The rate of consumption or creation of each gas-phase species by irreversible surface reaction (e.g.  $\text{SiH}_4 \rightarrow \text{Si}(\text{solid}) + 2\text{H}_2$ ), is given by the following expressions

$$\dot{s}_k = W_k \sum_{i=1}^{I_s} \nu_{ki} q_i \quad (13)$$

$$q_i = \gamma_i \prod_{k=1}^{K_g} \left( \sqrt{\frac{k_B T}{2\pi W_k}} [X_k] \right)^{\nu_{ki}} \quad (14)$$

where,  $q_i$  is the rate of progress and  $\gamma_i$  is a reaction probability for each of the  $I_s$  surface reactions,  $k_B$  is the Boltzmann constant,  $W_k$  are the species molecular weights,  $\nu_{ki}$  are the stoichiometric coefficients for the surface reactions.

The gas-phase mass flux of species  $k$  at the surface is a combination of diffusive and convective processes,

$$j_k = \rho Y_k u + \rho Y_k V_k \quad (15)$$

where  $u$  is the bulk normal fluid velocity at the surface and  $V_k$  is the diffusion velocity of the  $k$ th species. The bulk normal fluid velocity at the surface is stated in terms of the surface reaction rates summed over all the gas-phase species  $K_g$

$$u = \sum_{k=1}^{K_g} \frac{\dot{s}_k}{\rho} \quad (16)$$

Even though the susceptor surface is solid, there is a bulk fluid velocity into the surface that accounts for the mass of solids that are deposited.

The other boundary conditions are relatively simple. The temperature and species composition far from the disk (the reactor inlet) are specified. The radial and circumferential velocities are zero far from the disk; a boundary condition is not required for the axial velocity at large  $x$ . The radial velocity on the disk is zero, the circumferential velocity is determined from the spinning rate  $W = \Omega$ , and the disk temperature is specified.

The system of equations is a boundary value problem, and we solve it by a method that we have developed to compute the structure of premixed flames.<sup>11,12</sup> The numerical solution procedure begins by making finite difference approximations to reduce the boundary value problem to a system of algebraic equations. The problem is normally started on a very coarse mesh, often containing as few as five or six points. After obtaining a solution on the coarse mesh, new mesh points are added in regions where the solution or its gradients change rapidly. Interpolating the coarse mesh solution provides the initial iterate for the solution on the finer mesh. This procedure continues until no new mesh points are needed to resolve the solution to sufficient accuracy. We attempt to solve the system of algebraic equations by the damped modified Newton algorithm. However, if the Newton algorithm fails to converge, the solution estimate is conditioned by a period of time integration. This provides a new starting point for the Newton algorithm that is closer to the solution, and thus more likely to be in the domain of convergence for Newton's method. As the mesh becomes finer the estimate interpolated from the previous mesh is more likely to be within the domain of convergence of Newton's method.

To illustrate some typical results, consider the deposition of silicon from silane. The gas-phase reaction mechanism consists of 27 elementary reaction

steps involving 17 chemical species.<sup>13</sup> We choose a reactor in which the disk is heated to 1000 K and spins at 1000 rpm. The inlet flow is 0.1 percent silane in a carrier of 99.9 percent helium. Figure 6 shows the computed species mole fractions as a function of the height above the susceptor. Analysis of such simulations leads to understanding about the relative effects of fluid transport and chemical reaction, and can isolate the important reaction pathways. For example, we can determine which gas-phase species are most responsible for the surface deposition. For this set of reactor conditions 57 percent of the deposition comes from the flux of  $\text{SiH}_2$  to the surface, 24 percent from the flux of  $\text{H}_2\text{SiSiH}_2$ , and 13 percent from  $\text{SiH}_4$ . Furthermore, by doing these computations with and without thermal diffusion, we can see that thermal diffusion decreases the silicon-containing species fluxes at the surface by about 20 percent.

Figure 7 summarizes the results of several simulations. It shows that the net silicon deposition rate depends strongly on the susceptor temperature and the carrier gas. At low temperature, the deposition is mainly reaction limited, and thus the deposition follows an Arrhenius dependence on temperature (i.e., the logarithm of the deposition rate is linear in reciprocal temperature). However, as the temperature increases, the reactions become faster, allowing transport processes to become rate limiting. In other words, the gases most responsible for the deposition cannot be transported to the susceptor as fast as they are produced chemically. This behavior is indicated by the curvature in the plots at high temperature. The fact that the deposition rates are higher in a helium carrier is also a chemical effect. Hydrogen is one of the reaction products as the silane decomposes to form surface-reactive species. Thus, when hydrogen is the carrier, it works to inhibit the progress of these reactions, and consequently impede deposition.

A typical computation such as the ones described here used about 100 adaptively placed mesh points and required about 5 minutes on a Cray 1-S. Of course, larger reaction mechanisms take more time. Also, simpler transport models can be used to reduce computation time. Since the solution methods are iterative, the computer time for a certain simulation can be reduced by starting it from the solution of a related problem. For example, it may be efficient to determine the solution to a problem with a susceptor temperature of 900 K starting from a converged solution for a reactor with a susceptor temperature of 1000 K. In fact, it is typical to compute families of solutions by this type of continuation procedure.

### Chemical Reaction Mechanisms

Solving for rates of production of chemical species requires as input an elementary reaction mechanism, rate constants for each elementary reaction (usually in Arrhenius form), and information about the thermochemistry ( $\Delta H_f$ ,  $S$ , and  $C_p$  as a function of temperature) for each chemical species in the mechanism.

The needed thermochemistry for many thousands of molecules is available from standard sources such as the JANAF tables.<sup>14</sup> Polynomial fits of this data in the form required by our kinetics software are also available. However, experimental thermochemical data is often lacking for many of the intermediate species that should be included in a detailed kinetics mechanism. Standard methods have been developed for estimating these properties, discussed in detail by Benson.<sup>15</sup>

Calculation of thermochemical data using high-quality *ab initio* electronic structure calculations has been a long-standing goal. However, the availability of supercomputers and new theoretical techniques now allow the calculation of thermochemical properties with chemical accuracy, i.e.,  $\Delta H_f$  to within



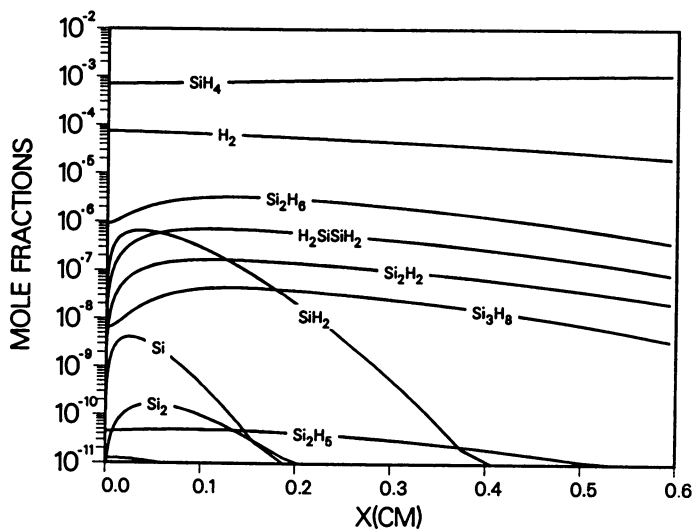


Figure 6. Species profiles in a rotating disk CVD reactor. Inlet gas is 0.1 percent silane in a carrier of 99.9 percent helium. The disk temperature is 1000 K and the spin rate is 1000 rpm.

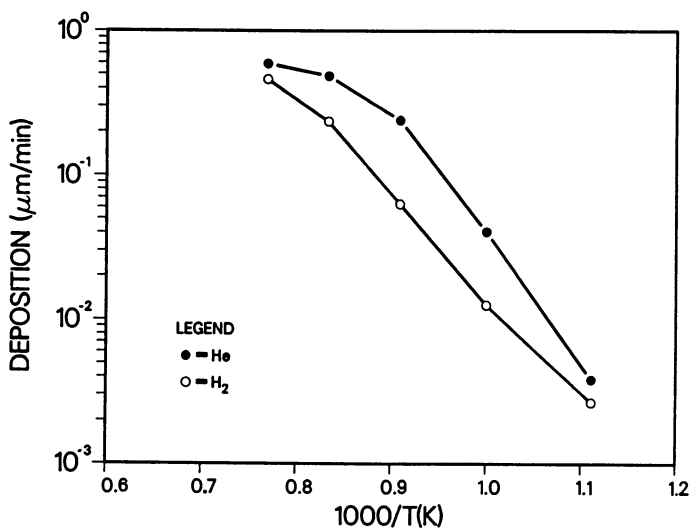


Figure 7. Net silicon deposition rates as a function of susceptor temperature for both hydrogen and helium as the carrier gas. Rotation rate is 1000 rpm.

$\pm 3$  kcal/mole. A technique that has been applied to over 900 combustion-related chemical species and to our study of silicon-containing species is denoted the BAC-MP4 method.<sup>16-20</sup> It combines electronic structure calculations using fourth-order Møller-Plesset perturbation theory<sup>21-23</sup> (MP4) with empirically-derived bond additivity correction (BAC) factors to account for systematic error in the *ab initio* calculations due to truncated wave functions and incomplete basis sets. Details on the application of this technique to the thermochemistry of species containing silicon, chlorine, and hydrogen are given by Ho, et al.<sup>19,20</sup>

Obtaining a realistic, complete, and detailed reaction mechanism for a chemical system is a formidable task. Some chemical systems, e.g., combustion systems, have been extensively studied for many years by dozens of kineticists. The reaction mechanism for a methane/air oxidation can involve well over 100 elementary reactions. No automated or easy method exists for obtaining a reaction mechanism when considering a new chemical system. A new mechanism is generally derived through a combination of experimental kinetics studies, analogy with similar systems, and chemical intuition. In our studies of silane decomposition kinetics<sup>13,24</sup> we began with an initial reaction mechanism of over 120 reactions. Through a combination of sensitivity studies and computer experiments we were able to distill the reaction mechanism down to 27 elementary reactions that describe the silane kinetics over a wide range of temperatures and reaction conditions.

The reaction rate constant for each elementary reaction in the mechanism must be specified, usually in Arrhenius form. Experimental rate constants are available for many of the elementary reactions, and clearly these are the most desirable. However, often such experimental rate constants will be lacking for the majority of the reactions. Standard techniques have been developed for estimating these rate constants.<sup>15</sup> A fundamental input for these estimation techniques is information on the thermochemistry and geometry of reactant, product, and transition-state species. Such thermochemical information is often obtainable from electronic structure calculations, such as those discussed above.

### Chemical Kinetics and Transport Software

Supercomputing capabilities open the possibility of incorporating highly complex chemical and transport models in the simulations. However, without appropriate software, it is often impractical even to prepare such problems for solution. At the very minimum one needs a way to handle the "book keeping" associated with large reaction mechanisms. Moreover, the software should be sufficiently general so that it can be applied to large classes of problems without modification. Because we work regularly with such systems, we have developed a rather extensive system of general-purpose software.<sup>25</sup>

Figure 8 depicts our view of an "ideal" structure for an applications program. The boxes with the heavy borders represent those functions that are problem specific, while the light-border boxes represent those functions that can be relegated to problem-independent software. This structure is well-suited to problems that are mathematically either systems of nonlinear algebraic equations, ordinary differential equation initial or boundary value problems, or parabolic partial differential equations. In these cases the problem-independent mathematical software is usually written in the form of a subroutine that in turn calls a user-supplied subroutine to define the system of equations. Of course, the user must write the subroutine that defines his particular system of equations. However, that subroutine should be able to make calls to problem-independent software to return many of the components that are needed to assemble the governing equations. Specifically, such software could be called to return in-

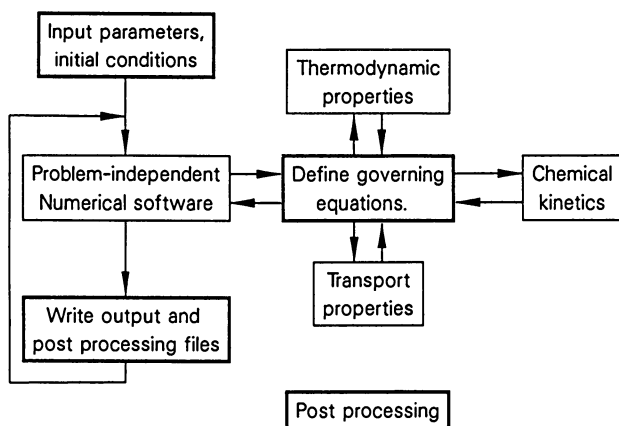


Figure 8. Schematic representation of an "ideal" applications program. The boxes with the heavy borders represent those functions that are problem specific, while the light-border boxes represent those functions that can be relegated to problem-independent software.

**American Chemical Society  
Library  
1155 16th St., N.W.  
Washington, D.C. 20036**

formation about chemical production rates, equation of state, thermodynamic properties, or transport properties.

Consider Equations (6-10) that represent the CVD reactor problem. This is a boundary value problem in which the dependent variables are velocities ( $u, V, W$ ), temperature  $T$ , and mass fractions  $Y_k$ . The mathematical software is a stand-alone boundary value solver whose first application was to compute the structure of premixed flames.<sup>11,12</sup> Subsequently, we have applied it to the simulation of well stirred reactors,<sup>26,27</sup> and now chemical vapor deposition reactors. The user interface to the mathematical software requires that, given an estimate of the dependent variable vector, the user can return the residuals of the governing equations. That is, for arbitrary values of velocity, temperature, and mass fraction, by how much do the left hand sides of Equations (6-10) differ from zero?

The supercomputing environment is one that is changing very rapidly, especially with the introduction of parallel, multitasking machines. The efficient use of parallel machines depends strongly on the development of new algorithms that take advantage of a machine's particular architecture. The architecture between parallel machines can vary significantly, and may call for quite different mathematical algorithms to use them effectively. Of course, the user of such machines hopes not to have to rewrite all his applications codes to map them onto a specific machine architecture. Nevertheless, some code certainly has to change. Hopefully, those changes can be concentrated in the mathematical software in such a way that the user interfaces to the application-specific code does not change. The code structure as illustrated in Fig. 8 provides the modularity between the "problem definition" and the "solution procedure" that is required to facilitate applications on various machine architectures.

The task of the problem-independent chemistry software is to make evaluating the terms in Equations (6-10) as straightforward as possible. In this case subroutine calls to the Chemkin<sup>28</sup> software are made to return values of  $\rho$ ,  $c_p$ , and the  $\omega_k$  and  $h_k$  vectors. Also, subroutine calls are made to a Transport package<sup>29</sup> to return the ordinary multicomponent diffusion matrices  $D_{kj}$ , the mixture viscosities  $\mu$ , the thermal conductivities  $\lambda$ , and the thermal diffusion coefficients  $D_k^T$ . Once this is done, finite difference representations of the equations are evaluated, and the residuals returned to the boundary value solver.

The other "problem-dependent boxes" in Fig. 8 relate to reading input and writing output - tasks that are clearly application-specific. We view writing post processing files to be part of the output function. It is usually inefficient to force the code that computes the solution to perform simultaneously all the interpretive functions. Moreover, if the solution itself is saved, then any number of post-processing functions can be exercised without requiring the problem to be solved again.

Due to its modularity, the software comes in many parts (shown in Fig. 9). The Chemkin<sup>28</sup> package is composed of four important pieces: the Interpreter, the Thermodynamic Data Base, the Linking File, and the Gas-Phase Subroutine Library. The Interpreter is a program that first reads the user's symbolic description of the reaction mechanism. It then extracts thermodynamic information for the species involved from the Thermodynamic Data Base. The user may add to or modify the information in the data base by input to the Interpreter. In addition to printed output, the Interpreter writes a Linking File, which contains all the pertinent information on the elements, species, and reactions in the mechanism.

Once the Interpreter has been executed and the Linking File created, the user is ready to use the Gas-Phase Subroutine Library. These subroutines are called

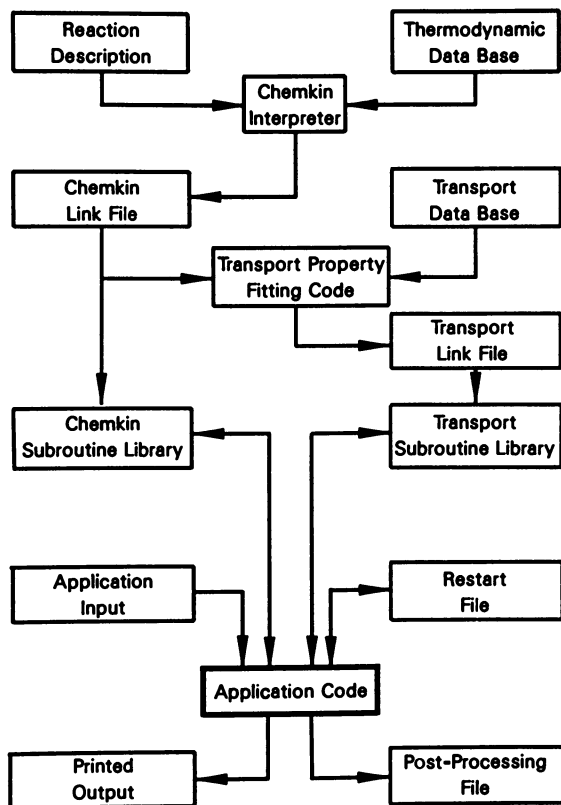


Figure 9. Schematic representation of the relationship of the Chemkin and Transport software packages with an application code.

from the user's FORTRAN code. The Chemkin gas-phase subroutines, of which there are over 100, are called as needed to return information on the elements, species, reactions, equations of state, thermodynamic properties, chemical production rates, sensitivity parameters, derivatives of chemical production rates, and derivatives of thermodynamic properties. Generally the inputs to these routines are the state variables of the gas - pressure or density, temperature, and the species composition. The Chemkin documentation is designed to facilitate selection of the particular Chemkin subroutines that are needed for a given problem.

The Chemkin package deals with problems that can be stated in terms of equation of state, thermodynamic properties, and chemical kinetics, but it does not consider the effects of fluid transport. Once fluid transport is introduced it is usually necessary to model diffusive fluxes of mass, momentum, and energy, which requires knowledge of transport coefficients such as viscosity, thermal conductivity, species diffusion coefficients, and thermal diffusion coefficients. Therefore, in a software package analogous to Chemkin, we provide the capabilities for evaluating these coefficients.<sup>29</sup>

Looking again at Fig. 9, it is seen that, like Chemkin, the Transport Package also has four distinct parts. The first part is a Transport Data Base that contains information such as Lennard-Jones parameters, dipole moments, and polarizabilities for individual species. The second part is a preprocessor that computes polynomial fits to the temperature-dependent parts of the pure-species viscosities, conductivities, and binary diffusion coefficients. The coefficients of these fits are passed to a library of subroutines via a Linking File. Then, any subroutine from the Transport Library may be called to return either pure-species properties or multicomponent gas mixture properties. The fitting code uses the Chemkin package, and the Transport Subroutines are designed to be used in conjunction with the Chemkin Subroutine Library. The transport package considers only those species that were identified by input to the Chemkin Interpreter.

### Summary

We have used supercomputing capabilities to simulate the fluid mechanical and the chemical kinetic aspects of chemical vapor deposition reactors. The example results shown here indicate the power of such modeling to provide an in-depth understanding of CVD processes. The results are useful both from a basic research standpoint and as a practical design tool. Because of the complexity of the full problem, it was necessary to divide it into manageable pieces that isolated either the fluid mechanical or the chemical kinetic behavior. Then supercomputers are used to perform the many simulations that are required to provide extensive parameter studies for research or design application. We also indicated that high-level software is an important ingredient in preparing and solving the complex problems that are possible in the supercomputing environment.

### Acknowledgment

We appreciate the continuing contributions of our colleagues W. G. Breiland, P. Ho, R. Greif, J. F. Grcar, J. S. Binkley, C. F. Melius, and J. A. Miller to our CVD modeling. This work was performed at Sandia National Laboratories, supported by the U.S. Department of Energy, Office of Basic Energy Sciences.

References

1. K. F. Jensen, in "Chemical Vapor Deposition," McD. Robinson, C. H. J. van den Brekel, G. W. Cullen, J. M. Blocher, and P. Rai-Choudhury, Eds., p. 3, The Electrochemical Society, Softbound Proceedings Series, Pennington, NJ (1984).
2. B. J. Curtis, *Physico Chemical Hydrodynamics* **2** no. 4, 357 (1981).
3. H. Schlichting, 7th ed., McGraw-Hill, New York, (1979).
4. R. Pollard, and J. Newman, *J. Electrochem. Soc.* **127** 744 (1980).
5. G. H. Evans and R. Greif, Sandia National Laboratories Report SAND86-8843, (1986).
6. C. Houtman, D. B. Graves, and K. F. Jensen, *J. Electrochem. Soc.* **133** no. 5 961 (1986).
7. G. Wahl, in "Chemical Vapor Deposition," McD. Robinson, C. H. J. van den Brekel, G. W. Cullen, J. M. Blocher, and P. Rai-Choudhury, Eds., p. 60, The Electrochemical Society, Softbound Proceedings Series, Pennington, NJ (1984).
8. A. D. Gosman and W. M. Pun, Lecture Notes, Imperial College of Science and Technology, London, England (1973).
9. Hirschfelder, J. O., Curtiss, C. F., and Bird, R. B., John Wiley and Sons, Inc., New York, (1954).
10. Dixon-Lewis, G., *Proc. Royal Soc. A.* **307**, 111-135, (1968).
11. Kee, R. J., Grcar, J. F., Smooke, M. D., and Miller, J. A., Sandia National Laboratories Report SAND85-8240, (1985).
12. Grcar, J. F., Kee, R. J., Smooke, M. D., Miller, J. A., *Twenty First Symposium (International) on Combustion*, The Combustion Institute, Pittsburgh, PA, (1986).
13. M. E. Coltrin, R. J. Kee, and J. A. Miller, *J. Electrochem. Soc.* **133**, 1206 (1986).
14. JANAF Thermochemical Tables, Natl. Stand. Ref. Data Ser. NSRDS-NBS 37, (1971); also Dow Chemical Company, distributed by Clearinghouse for Federal Scientific and Technical Information, PB168370 (1965) and subsequent updates.
15. S. W. Benson, 2nd ed., John Wiley and Sons, New York (1976).
16. C. F. Melius and J. S. Binkley, Paper WSS/CI 83-61, 1983 Fall Meeting of the Western States Section of the Combustion Institute, University of California, Los Angeles, CA. October 17-18, 1983.
17. C. F. Melius and J. S. Binkley, *20th Symp. (International.) on Comb., Comb. Inst.* 575, 1984.
18. C. F. Melius and J. S. Binkley, *ACS Symposium Series* **249**, 103 (1984).
19. P. Ho, M. E. Coltrin, J. S. Binkley and C. F. Melius, *J. Phys. Chem.*, **89** 4647 (1985).
20. P. Ho, M. E. Coltrin, J. S. Binkley and C. F. Melius, *J. Phys. Chem.*, **90** 3399 (1986).
21. J. A. Pople, J. S. Binkley and R. Seeger, *Int. J. Quant. Chem.* **S10**, 1 (1976).
22. R. Krishnan and J. A. Pople, *Int. J. Quant. Chem.* **14**, 91 (1978).
23. R. Krishnan, M. J. Frisch and J. A. Pople, *J. Chem. Phys.* **72**, 4244 (1980).
24. M. E. Coltrin, R. J. Kee, and J. A. Miller, *J. Electrochem. Soc.* **131**, 425 (1984).
25. Kee, R. J. and Miller, J. A. Sandia National Laboratories Report SAND86-8841, to appear *Springer Series in Chemical Physics* (1986).
26. Glarborg, P., Kee, R. J., Grcar, J. F., and Miller, J. A., Sandia National Laboratories Report SAND86-8209, (1986).

27. Glarborg, P., Miller, J. A., and Kee, R. J., *Combust. and Flame* **65** no. 2, (1986).
28. Kee, R. J., Miller, J. A. and Jefferson, T. H., Sandia National Laboratories Report, SAND80-8003, (1980).
29. Kee, R. J., Dixon-Lewis, G., Warnatz, J., Coltrin, M. E., Miller, J. A., Sandia National Laboratories Report SAND86-8246 (1986).

RECEIVED June 15, 1987



## Chapter 19

# Growth of Compound Semiconductors and Superlattices by Organometallic Chemical Vapor Deposition Transport Phenomena

Klavs F. Jensen, Dimitrios I. Fotiadis, Donald R. McKenna, and Harry K. Moffat

Minnesota Supercomputer Institute and Department of Chemical Engineering and  
Materials Science, University of Minnesota, Minneapolis, MN 55455

Large scale computations are used to simulate the growth of GaAs and AlGaAs thin films by organometallic chemical vapor deposition (MOCVD) in horizontal and vertical reactors. The computations provide new insights into flow, heat and mass transfer effects on film thickness uniformity and interface abruptness in superlattice growth. For the horizontal reactor, the simulations demonstrate the existence of longitudinal buoyancy driven flow rolls that adversely affect film thickness uniformity. For the vertical reactor, the film thickness uniformity is shown to be influenced by susceptor edge, susceptor rotation, reactor wall and buoyancy effects. It is demonstrated that nonlinear interactions between the transport processes lead to the existence of multiple steady flows in certain operating regions. Concentration transients in the growth of AlAs/GaAs interfaces are simulated and it is shown that the presence of flow recirculation cells widens the interface.

Processing of electronic materials is essentially the fabrication of artificially microstructured materials with unique electronic and optical properties. This is accomplished through successive film deposition, patterning, etching and doping operations. Depending on the complexity of the final integrated circuit, the manufacture of the final microstructure may take up to several hundred process steps each of which involves complex physical transport processes and chemical reactions in three-dimensional domains. As the level of circuit integration increases, the minimum device feature size shrinks, and material constraints escalate, it is becoming increasingly costly and difficult to modify processes by design rules and one-parameter-at-a-time-experiments. For example, the fabrication of state-of-the-art multiple quantum well devices for ultrafast electronic and optical components requires the growth of a 5 nm thin film of a

0097-6156/87/0353-0353\$06.75/0  
© 1987 American Chemical Society

compound semiconductor uniformly over a 50 mm substrate. Thus, there is a strong incentive to use detailed mathematical models to predict process performance.

In order for these models to be useful in process design, operation and control, they must give an accurate picture of the underlying time dependent hydrodynamics, energy transfer, mass transport and chemical reactions within the processing systems. This means moving away from oversimplified analytical models towards detailed models in the form of multiple nonlinear, coupled partial differential equations in time and three spatial dimensions. This necessarily entails large scale computations similar to those encountered in combustion and atmospheric chemistry modeling. In this paper we present supercomputer simulations of transport phenomena in the growth of compound semiconductors, in particular GaAs and AlGaAs by organometallic chemical vapor deposition (MOCVD). This technique has received considerable attention because of its potential for large scale production of optical and digital device structures (1-3). As the name MOCVD indicates, the process entails the gas phase transport of organometallic precursors of at least one of the film constituents to a heated substrate where the film is formed. Common overall reactions in MOCVD are:

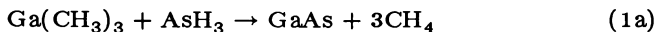


Figure 1 illustrates two general MOCVD reactor configurations, the horizontal reactor and the axisymmetric vertical reactor. The reactant gas ( $\text{AsH}_3$ ,  $\text{Ga}(\text{CH}_3)_3$  and  $\text{Al}(\text{CH}_3)_3$ ) enters cold and heats up as it flows toward the substrate where a solid film of AlGaAs is being deposited. The chemical transformations involved in the deposition process may occur both in the gas phase and on the surface of the growing film.

The usefulness of a particular film or heterostructure (i.e. an assembly of films of different compositions) depends on several factors including: (i) the level and spatial distribution of dopants (intentionally as well as unintentionally added), (ii) film thickness uniformity over the substrate, and (iii) the interface abruptness between layers of different compositions (3). These performance criteria are strongly affected by the flow profiles within the reactor enclosure. Entrance effects and buoyancy driven flows, caused by large thermal differences between wall and susceptor temperatures, are known to produce complex mass transfer patterns leading to severe growth rate and film composition nonuniformities (4,5). Consequently, there has been considerable interest in experimental observations of flow structures in MOCVD reactors. Flow visualizations with  $\text{TiO}_2$  smoke have revealed the existence of longitudinal rolls and a particle free region adjacent to the surface in horizontal reactors (6-9). This region resulting from thermophoretic transport of  $\text{TiO}_2$  particles away from the hot substrate has often been misinterpreted as a stagnant layer (10).  $\text{TiO}_2$  smoke experiments have also demonstrated the existence of recirculation

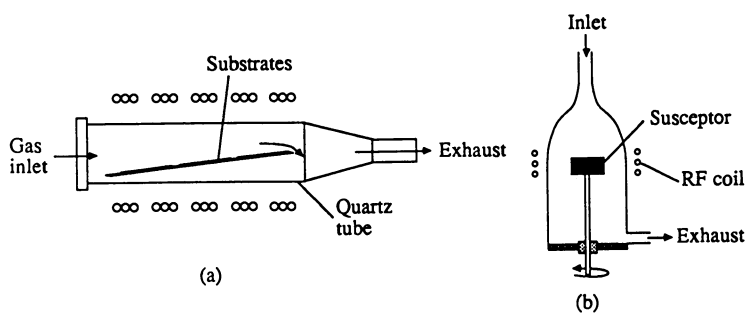


Figure 1. Two typical MOCVD reactor configurations; (a) horizontal reactor (b) vertical reactor.

cells in vertical reactors (11,12). Laser holography of axially averaged density gradients in horizontal reactors and radially average density gradients in vertical reactors have further demonstrated that the MOCVD reactor flows may be strongly perturbed by entrance and buoyancy effects (4,13).

The experiments have led to considerable insights into MOCVD reactor flows, but a complete understanding of the detailed flow structure is still missing and it is not likely to be achieved through experiments alone. Smoke testing suffers from artifacts introduced by thermophoretic transport of the seed particles while interference holography gives spatially averaged density gradients. Thus, transport phenomena modelling is a necessary component in understanding and designing MOCVD reactors capable of producing large area uniformity and sharp interfaces. In the following sections we summarize recent large scale finite element computations of detailed two- and three-dimensional models for the two classical MOCVD reactor configurations illustrated in Figure 1.

### Modelling Equations

MOCVD reactor models consist of momentum, energy and species balances with corresponding boundary conditions. The general form of these balance equations are given in standard transport phenomena texts (14). Since the reactants in MOCVD are used dilute in  $H_2$  or some inert carrier gas (e.g. He), volume expansion due to the change in number of moles between reactants and products is negligible. In addition, energy contributions caused by the heat of reaction are insignificant. Therefore, it is reasonable to separate the flow and heat transfer problem from the reaction-convection-diffusion problem which leads to reduced storage and CPU time requirements. It also has the added advantage that different chemical mechanisms and kinetics can be considered for the same flow simulation. Even if the problems were weakly coupled, a Picard type iteration might be computationally more efficient than solving the fully coupled equations together. Expansion effects due to density changes in the gas phase play a major role in the flow behavior and have to be included in the computations. However, because of the low Mach numbers of MOCVD flows, it is reasonable to neglect compressibility effects which otherwise would unnecessarily complicate the computations. Since the film growth rate in chemical vapor deposition is slow compared to the gas phase dynamics, the flow dynamics may be assumed to be in pseudo-steady state, i.e. the time derivatives in the momentum and energy balance may be set to zero. The flow description then takes the form:

$$\rho(\mathbf{v} \cdot \nabla \mathbf{v}) = \nabla \cdot \boldsymbol{\tau} + \rho \mathbf{g}, \quad \boldsymbol{\tau} = \mu \left[ \nabla \mathbf{v} + (\nabla \mathbf{v})^T \right] - \left[ \frac{2}{3} \mu \nabla \cdot \mathbf{v} + P \right] \mathbf{I} \quad (2)$$

where  $P$ ,  $\rho$ , and  $\mu$  are the pressure, density and viscosity, respectively.  $\mathbf{g}$  represents the acceleration due to gravity and  $\mathbf{v}$  is a vector of the velocity

components. The momentum balance must be combined with the overall continuity balance:

$$\nabla \cdot \rho \mathbf{v} = 0 \quad (3)$$

and the ideal gas law as an equation of state:

$$\rho = P_0 M_w / RT \quad (4)$$

Since variations in the pressure induced by fluid dynamic effects are negligible for MOCVD reactor flows, the inlet pressure,  $P_0$ , is used. In formulating the energy balance, the contributions from pressure changes, viscous dissipation and Dufour effects may be neglected for MOCVD conditions (14,15) so the equation becomes:

$$\rho C_p \mathbf{v} \cdot \nabla T = \nabla \cdot (k \nabla T) + \sum_{i=1}^S \bar{H}_i \left[ \nabla \cdot \mathbf{J}_i - \sum_{j=1}^{n^g} \nu_{ji}^g R_j^g \right] \quad (5)$$

where  $C_p$ ,  $k$ , and  $T$  are the heat capacity, thermal conductivity and temperature, respectively. The second term on the right-hand-side represents the contribution from gas phase reactions. This can be neglected since MOCVD is usually performed with a large excess of carrier gas and the enthalpies of reactions,  $\bar{H}_i$ , are small compared to combustion reactions. In addition, simple Fickian diffusion rather than multicomponent diffusion may be used to formulate balances over the dilute reactants:

$$\frac{\partial c_i}{\partial t} + c \mathbf{v} \cdot \nabla x_i = \nabla \cdot c D_{im} \left[ \nabla x_i + k_T \nabla \ln T \right] + \sum_{j=1}^{n^g} \nu_{ji}^g R_j^g \quad (6)$$

where  $j=1, \dots, n^g$  is the number of gas phase reactions and  $i=1, \dots, S-1$  number species. Since the mole fractions must sum to unity, only  $S-1$  equations need to be solved.  $c$  is the total concentration and  $x_i$  is the mole fraction of component  $i$ . The sum on the right-hand-side represents the production of species  $i$  in  $n^g$  gas phase reactions.  $D_{im}$  and  $k_T$  are the Fickian diffusion coefficient and the thermal diffusion ratio, respectively. Because of the often large thermal gradients in CVD, the Soret effect (thermal diffusion) may contribute to the overall growth behavior (16,17), but it will not be considered further in this summary paper.

No slip is used as the velocity boundary conditions at all walls. Actually there is a finite normal velocity at the deposition surface, but it is insignificant in the case of dilute reactants. The inlet flow is assumed to be Poiseuille flow while zero stresses are specified at the reactor exit. The boundary conditions for the temperature play a central role in CVD reactor behavior. Here we employ idealized boundary conditions in the absence of detailed heat transfer modelling of an actual reactor. Two wall conditions will be considered: (1) adiabatic side walls, i.e.  $dT/dn = 0$ , and (2) fixed side wall temperatures corresponding to cooled reactor walls. For the reactive species, no net normal flux is specified on nonreacting surfaces. At substrate surface, the flux of the  $i$ 'th species equals the rate of reaction of  $i$  in  $n^s$  surface reactions, i.e.

$$-cD_{im} \left[ \nabla x_i + k_T \nabla \ln T \right] \cdot \mathbf{n} = - \sum_{j=1}^{n^s} \nu_{ji}^s R_j^s \quad (7)$$

To complete the modelling equations, kinetic rate expressions and transport coefficients must be specified. However, the elementary kinetics of the MOCVD reactions [1a and 1b] are largely unknown. Nevertheless, since experimental observations have shown that MOCVD of GaAs at atmospheric conditions is controlled by mass transfer of the group III containing species (18), it is possible to describe the growth rate by a group III species ( $\text{Ga}(\text{CH}_3)_3$  and/or  $\text{Al}(\text{CH}_3)_3$ ) diffusion model with fast surface reaction. The observations leading to this conclusion include the independence of growth rate on the partial pressure of  $\text{AsH}_3$ , the first order dependence on the partial pressure of  $\text{Ga}(\text{CH}_3)_3$ , and the small dependence of growth rate on substrate temperature (3,18).

### Numerical Solution

The combined fluid flow, heat transfer, mass transfer and reaction problem, described by Equations 2-7, lead to three-dimensional, nonlinear, time dependent partial differential equations. The general numerical solution of these goes beyond the memory and speed capabilities of the current generation of supercomputers. Therefore, we consider appropriate physical assumptions to reduce the computations.

For typical flow rates in the horizontal reactor (Figure 1a) it is reasonable to assume that the longitudinal diffusion of momentum is small in comparison with the advection. This implies that the steady state flow and temperature profiles can be computed by marching a two-dimensional (2D) finite element discretization of the transverse reactor section along the length of the reactor. Thus, the original steady state three-dimensional (3D) problem has been transformed into a form that is equivalent to a 2D time dependent transport problem. The Galerkin Finite element method (19) was employed to discretize the equations in the transverse direction. In the flow problem, Equations 2-5, mixed order interpolation was used (16,20). The resulting set of nonlinear ordinary differential equations and algebraic constraints were integrated along the length of the reactor by the differential-algebraic equation solver, DASSL (21). In the reaction-advection-diffusion problem bilinear elements were used. A different mesh and integration steps than the flow problem were employed to improve the efficiency of the solution. The transverse velocities and temperatures needed in the mass transfer code were computed by interpolation in the finite element solution while interpolation in the axial direction of the velocity and temperature field between flow program integration steps was done with the same polynomial used by DASSL to approximate the flow solution. The flow and mass transfer problems each typically involved 3000 unknowns and took 5-10 minutes of Cray-2 CPU time.

The vertical reactor (Figure 1b) is assumed to be axisymmetric which

leads to a 2D formulation. The problem remains 2D when susceptor rotation is included, but three momentum balances corresponding to the radial, azimuthal and axial directions have to be solved (22-24). The Galerkin finite element method was used to discretize the equations in the same manner as done for the transverse plane in the horizontal reactor (16,22,24). In order to simulate more realistic reactor shapes than a simple rectangular domain, the weak constraint method of Ryskin and Leal (25) was used to generate orthogonal grids for the reaction domains. Figure 2 shows examples of grids used for reactor shapes that will be considered in the results section.

The Galerkin finite element discretization leads to a set of nonlinear algebraic equations of the general form:

$$\mathbf{G}(\mathbf{u}, \mathbf{p}) = 0 \quad (8)$$

where  $\mathbf{u}$  is the vector of the values of the dependent variables at the node points and  $\mathbf{p}$  is the vector of parameters. This set of equations can be solved by Newton-Raphson iteration, i.e.

$$\mathbf{G}_u(\mathbf{u}^{(n)}, \mathbf{p}) \left[ \mathbf{u}^{(n+1)} - \mathbf{u}^{(n)} \right] = - \mathbf{G}(\mathbf{u}^{(n)}, \mathbf{p}) \quad (9)$$

where

$$\left[ \mathbf{G}_u \right]_{ij} = \frac{\partial G_i}{\partial u_j}$$

However, because of the strong nonlinearities in the reactor flow problem, continuation procedures must be used to obtain a good initial guess for the Newton iteration. A simple first order continuation scheme fails at flow transition points (bifurcations) where the Jacobian,  $\mathbf{G}_u$ , becomes singular. To circumvent this problem an arclength continuation scheme discussed by Keller (26,27) and Chan (28) is used which leads to the inflated system:

$$\begin{bmatrix} \mathbf{G}_u^{(n)} & \mathbf{G}_\lambda^{(n)} \\ \mathbf{N}_u^{(n)} & \mathbf{N}_\lambda^{(n)} \end{bmatrix} \begin{bmatrix} \mathbf{u}^{(n+1)} - \mathbf{u}^{(n)} \\ \lambda^{(n+1)} - \lambda^{(n)} \end{bmatrix} = - \begin{bmatrix} \mathbf{G}^{(n)} \\ \mathbf{N}^{(n)} \end{bmatrix} \quad (10)$$

where  $\lambda$  is the continuation parameter,  $s$  is the arclength parameter and  $\mathbf{N}$  is a linearization of the arclength condition, i.e.

$$\begin{aligned} \mathbf{N}(\dot{\mathbf{u}}(s), \dot{\lambda}(s), \dot{s}) &= \dot{\mathbf{u}}^T(s_0) (\mathbf{u}(s) - \mathbf{u}(s_0)) \\ &+ \dot{\lambda}(s_0) (\lambda(s) - \lambda(s_0)) - (s - s_0) = 0 \end{aligned} \quad (11)$$

The inflated system (10) is nonsingular even when the Jacobian of the finite element formulation (8) becomes singular (26) at simple turning points.

Since the solution changes stability at the turning points, these are important to the understanding of the overall reactor behavior. In principle, the inflated system may be used to determine the bifurcation points and switch solution branches by increasing the arclength parameter,  $s$ , and

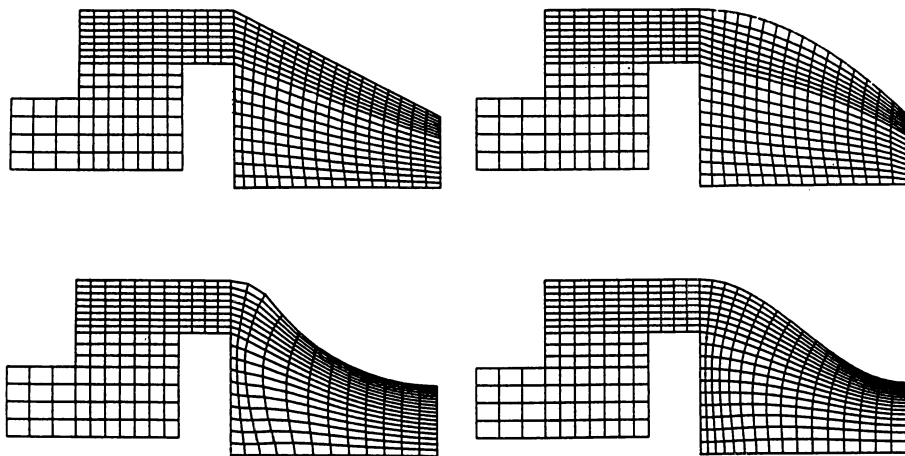


Figure 2. Computed grids for four different shapes of a vertical, axisymmetric MOCVD reactor.



refining the step size when the Jacobian,  $G_u$ , becomes singular (i.e.  $\det G_u = 0$ ). However, this often leads to excessively many computations. Therefore, we use a quadratically convergent method based on applying Newton's method to the characterization,  $d\lambda(s)/ds = 0$  (28). This procedure works well for locating simple turning points present in the mixed convection flow governing vertical reactors. The following equation gives an approximation to the second derivative w.r.t. arclength of the bifurcation parameter near the turning point:

$$\begin{bmatrix} G_u(s_0) & G_\lambda(s_0) \\ N_u(s_0) & N_\lambda(s_0) \end{bmatrix} \begin{bmatrix} \ddot{u}(s_0) \\ \ddot{\lambda}(s_0) \end{bmatrix} = - \begin{bmatrix} G_{uu}(s_0)\dot{u}(s_0)\dot{u}(s_0) \\ N_{uu}(s_0)\dot{u}(s_0)\dot{u}(s_0) \\ + 2G_{u\lambda}(s_0)\dot{u}(s_0)\dot{\lambda}(s_0) + G_{\lambda\lambda}(s_0)\dot{\lambda}(s_0)^2 \\ + 2N_{u\lambda}(s_0)\dot{u}(s_0)\dot{\lambda}(s_0) + N_{\lambda\lambda}(s_0)\dot{\lambda}(s_0)^2 + N_{ss}(s_0) \end{bmatrix} \quad (12)$$

Following Chan (28) a difference approximation is used to compute the second derivatives of  $G$ . A Newton iteration is then applied to the equation

$$0 = \dot{\lambda}(s_0) = \dot{\lambda}(s^n) + \ddot{\lambda}(s^n)(s^{n+1} - s^n) \quad (13)$$

to determine the turning point, i.e. where  $\dot{\lambda}(s_0) = 0$ .

The vertical reactor simulations reported in this paper typically involved 14,000 unknowns and took 25 CPU seconds per Newton iteration on a Cray-2. The tracing of a complete family of solutions for one parameter (e.g. susceptor temperature) cost approximately 25 CPU minutes. The latter number underscores the advantage of using supercomputers to understand the structure of the solution space for physical problems which often involve many parameters.

In the following sections we describe simulation results providing new insights into general MOCVD reactor behavior as well as the two major practical considerations, film uniformity and interface width.

### MOCVD in Horizontal Reactors

Boundary layer similarity solution treatments have been used extensively to develop analytical models for CVD processes (29). These have been useful in correlating experimental observations (e.g. 5). However, because of the oversimplified flow description they cannot be used to extrapolate to new process conditions or for reactor design. Moreover, they cannot predict transverse variations in film thickness which may occur even in the absence of secondary flows because of the presence of side walls. Two-dimensional fully parabolized transport equations have been used to predict velocity, concentration and temperature profiles along the length of horizontal reactors for Si CVD (17,30-32). Although these models are detailed, they can neither capture the effect of buoyancy driven secondary flows or transverse thickness variations caused by the side walls. Thus, large scale simulation of 3D models are needed to obtain a realistic picture of horizontal reactor performance.

By using the 3D fully parabolic approximation of the general transport equations described in the previous section, we have simulated entrance effects and the development of longitudinal roll patterns in horizontal reactors for growth of GaAs (33) and Si (16). Here we review the results for two case studies based on: H<sub>2</sub> as carrier gas, 1000K susceptor, 300 K top reactor wall temperature, 30 mm reactor height, 60 mm reactor width, and an inlet velocity of 58 mm/s. Two idealized side wall thermal boundary conditions, (i) no cooling (adiabatic) and (ii) infinite cooling, will be used to illustrate that they strongly affect the flow pattern and thus the deposition uniformity.

The case where the side walls are adiabatic approximates the behavior of an air cooled reactor. The entrance flow is dominated by the expansion of gas contacting the hot susceptor. Convection rolls, schematically illustrated in Figure 3(i), form in the corners and expand along the reactor length. This secondary flow is driven by the density gradient between the slower moving fluid at the corners and the faster and therefore less heated fluid in the midplane. Consequently the rolls rotate towards the midplane increasing the mass transfer and thus the deposition rate of GaAs in the middle of the reactor as shown in Figure 3(i). Depending on the value of the average Rayleigh number the rolls will persist when the flow becomes fully developed. However, even if the rolls are not present the side walls affect the transverse film uniformity because the fluid velocity decreases to zero at the walls (16).

In the second case the side walls are cooled to the top wall temperature. Again the gas expansion dominates the entrance flow and the rolls emanate from the corners. Because of the cold side walls the fluid becomes more dense at the walls than that in the center of the flow region. This produces a roll rotating up from the midsection and down along the walls as illustrated in Figure 3(ii). The result is reduced mass transfer in the midregion and increased mass transfer near the walls. This is reflected in the growth rate shown in Figure 3(ii) and it is opposite to the situation where the side walls are not cooled. Thus, these two examples demonstrate the key role played by the reactor thermal boundary conditions in obtaining film thickness uniformity. These effects have been shown to be in agreement with published experimental growth rate data (33) and recent, detailed laser Doppler anemometry investigations support the development of longitudinal convection rolls (34).

### Transport Phenomena in Vertical MOCVD Reactors

A vertical CVD reactor (cf. Figure 1b) consists of an axisymmetric enclosure with the deposition surface perpendicular to the incoming gas stream. The reactant gases are typically introduced at the top and flow down towards the heated susceptor. Thus, the least dense gas is closest to the growth interface which destabilizes the flow. The result is recirculation cells which introduce not only film thickness and composition variations but also broaden junctions between layers. This is particularly of

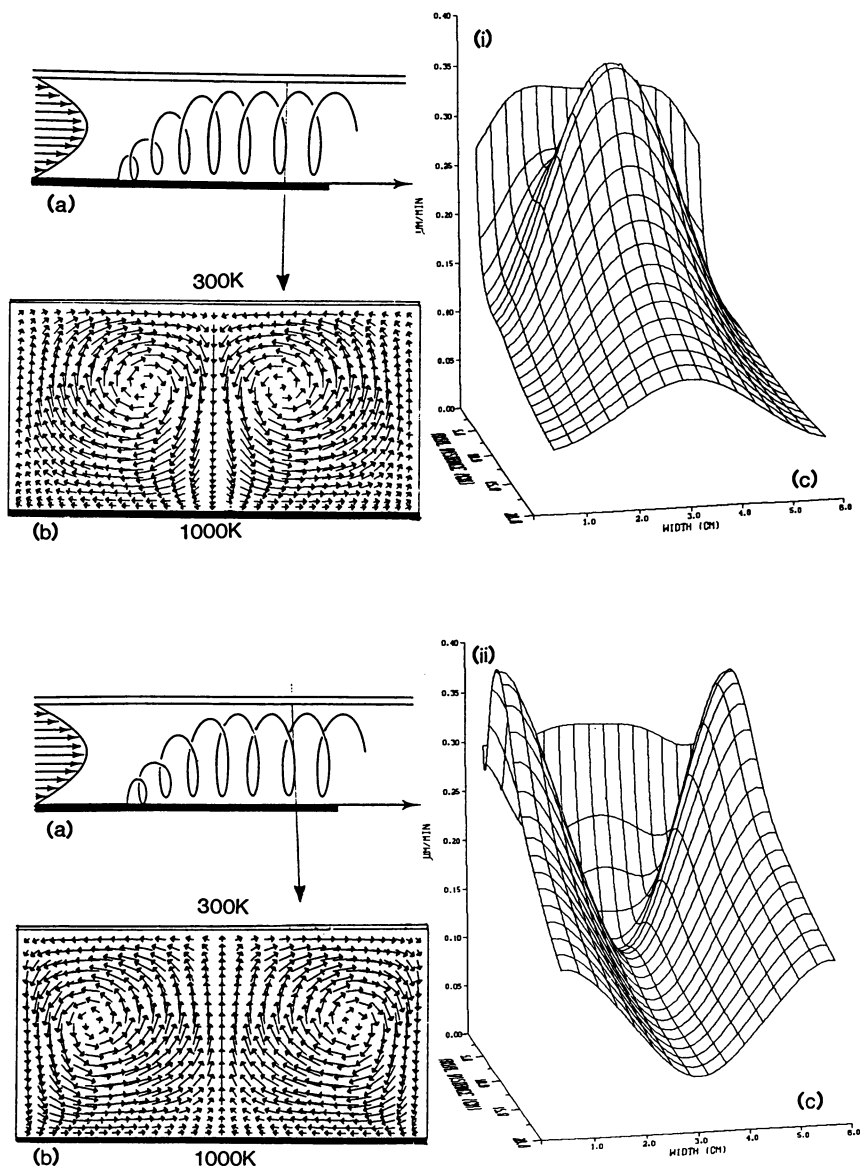


Figure 3. Flow profiles and corresponding growth rate of GaAs from  $\text{Ga}(\text{CH}_3)_3$  and  $\text{AsH}_3$  in a horizontal MOCVD reactor with (i) no cooling of the side walls and (ii) cold (300 K) side walls; (a) schematic representation of the longitudinal roll, (b) transverse velocities 50 mm into the reactor, and (c) growth rate of GaAs (after ref. 33).

concern in growing multiple quantum-well structures for lasers and novel optoelectronic devices where one desires abrupt composition changes over a few monolayers.

Because of the nonuniformity problems caused by recirculations and inlet flow maldistributions, there has been an interest in realizing ideal rotating disk, impinging jet or stagnation point flows which have a uniform mass transfer layer in a region around the flow stagnation point (35). Since the classical analysis of these flow configurations assumes infinite substrates and is one-dimensional, it cannot account for wall effects, finite susceptor size, and buoyancy driven recirculations. Thus, it is critical to go beyond the classical treatment by using the large scale finite element analysis described above in the modelling and numerical solution sections. The following simulation examples are based on the system parameters: mass transfer controlled growth of GaAs, H<sub>2</sub> carrier gas, 100 Torr total pressure, 300 K inlet temperature, 900 K susceptor, 200 mm inner diameter at the susceptor, 140 mm susceptor diameter and 120 mm between susceptor and inlet.

Figure 4 illustrates the effect of varying the inlet flow rate on flow streamlines and the corresponding radial variation in the growth rate relative to the growth rate at the center of the susceptor. At the low inlet flow rate (70 cc/sec (standard conditions)) the flow is dominated by a buoyancy driven recirculation cell above the susceptor, which reduces the film thickness in the center region as shown by curve (a). As the inlet flow rate is increased, the buoyancy driven recirculation cell is eliminated and the flow becomes forced convection dominated and resembles an impinging jet. In that case the film thickness decreases away from the center of the susceptor, except for a narrow edge region. Thus, it should be possible to adjust the inlet flow velocity to give uniform film thickness. Because of flow separation along the reactor wall, recirculations can occur even in forced convection situations. These recirculations have a minor effect on film thickness uniformity, but they could adversely affect the interface sharpness in heterojunction growth.

To this date, most reactor studies have dealt with fixed, regular reactor shapes. For example, the vertical reactor enclosures have been modelled as tubes. However, in practice one often tries to modify the shape of the enclosure to avoid flow separations and improve uniformity. This procedure is done by costly trial and error, where a quartz tube is made into a particular shape, cleaned and mounted in the reactor system. Several films typically have to be grown before it is possible to judge whether or not the chosen shape is appropriate. Thus, there is a considerable practical advantage in being able to predict *a priori* the optimum reactor shape. This problem also raises interesting computational challenges. Figure 5 shows four different shapes corresponding to the grids illustrated in Figure 2. The "champagne bottle" (Figure 5e) gives the best flow pattern but not the optimal uniformity. Thus, one has to balance uniformity considerations against recirculations that primarily affect the sharpness of the interface in heterojunction growth.

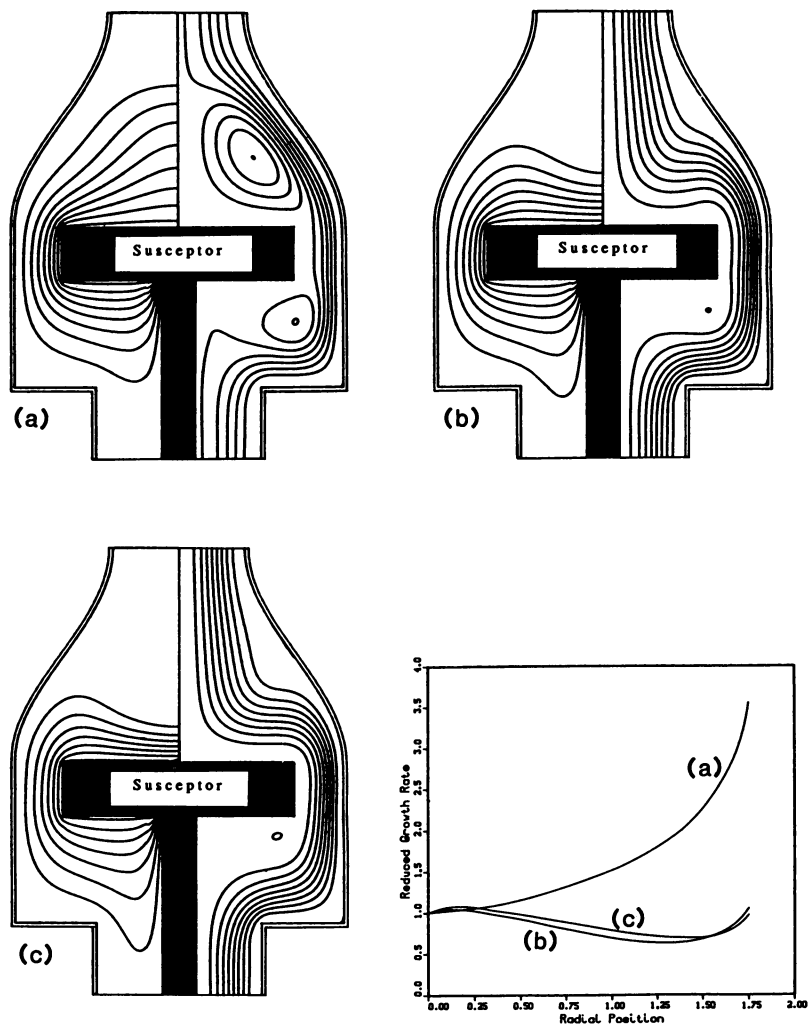


Figure 4. Effect of inlet flow rates on isotherms, flow streamlines and relative deposition rates of GaAs; (a) 70 cc/sec (standard conditions) (b) 140 cc/sec (c) 210 cc/sec. The absolute growth rates scale as 1 (a): 2.6 (b): 3.1 (c).

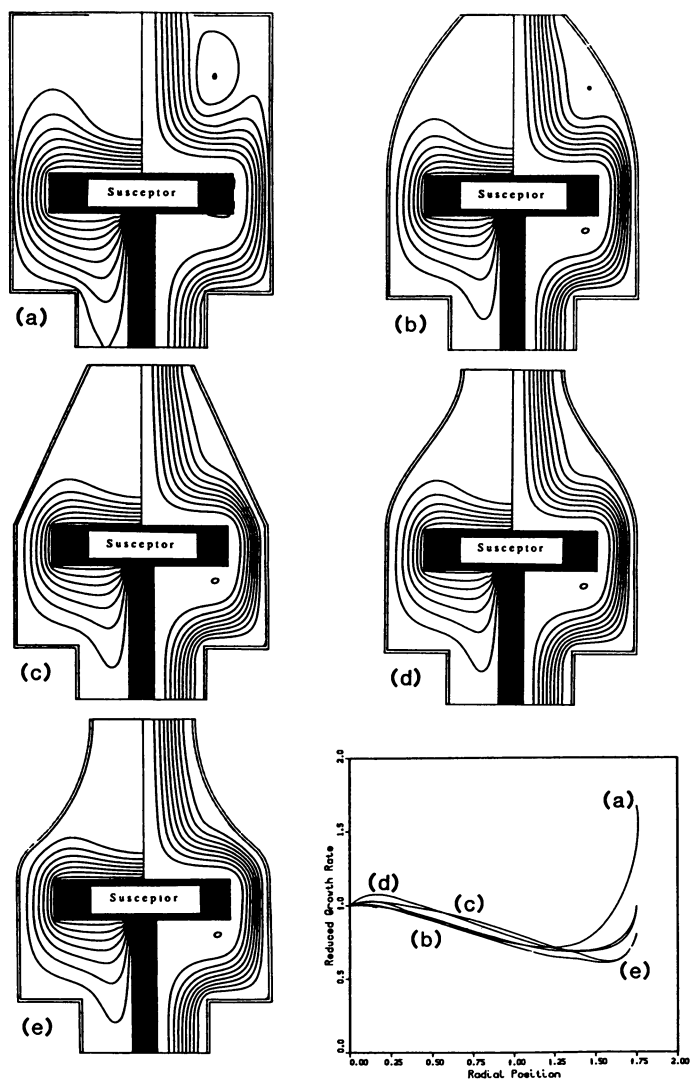


Figure 5. Effect of reactor shapes on isotherms, flow streamlines and relative deposition rates of GaAs. The absolute growth rates scale as 0.88 (a): 0.91 (b): 0.94 (c): 1.0 (d): 1.08 (e).

Figure 6 illustrates the effect of rotation speed on flow streamlines and the film thickness relative to that at the center of the susceptor. For a stationary susceptor (a) the flow is equivalent to the buoyancy dominated case in Figure 4(a). As the rotation speed is increased, the pump action of the susceptor eliminates the buoyancy cell creating a forced convection flow without the disadvantages of increasing the flow as was done in Figure 4. The rotation speed also has the advantage of increasing the deposition rate. However, the rotation speed can also be too rapid in which case (cf. Figure 6(c)) flow separation occurs along the reactor wall which will lead to broadening of interfaces in the growth of heterojunctions.

Because of nonlinear interactions between buoyancy, viscous and inertia terms multiple stable flow fields may exist for the same parameter values as also predicted by Kusumoto *et al.* (36). The bifurcations underlying this phenomenon may be computed by the techniques described in the numerical analysis section. The solution structure is illustrated in Figure 7 in terms of the Nusselt number (Nu, a measure of the growth rate) for varying inlet flow rate and susceptor temperature. Here the Nusselt number is defined as:

$$\text{Nu} = \frac{L(dc/dn)|_{\text{susceptor}}}{c_{\text{inlet}} - c_{\text{susceptor}}} \quad (14)$$

For inlet flow rates and susceptor temperatures within the cross-hatched area of Figure 7, two stable flow fields exist corresponding to buoyancy dominated low mass transfer and forced convection dominated high mass transfer rates. Between these stable flow fields there is an unstable state on the underside of the fold, where both buoyancy and inertia effects are present. If the susceptor rotation speed is chosen as a parameter instead of the temperature, a similar nonlinear dependence of Nu on flow rate and rotation speed is observed as illustrated in Figure 8. As the rotation speed is increased the multiplicity region shifts towards lower inlet flow rates and eventually vanishes. This nonlinear behavior means that reactor operation could be dependent on its start-up history and implicitly on the operator. For example, if the operating conditions fall within the multiplicity region, a recirculation dominated flow and correspondingly low Nu is reached by starting the flow once the susceptor is hot while a forced convection dominated flow and correspondingly high Nu is achieved by establishing the flow before heating the susceptor. In addition, if operation conditions for heterojunction growth were chosen near one of the edges in the fold, drastic uniformity and growth rate variations could result. Thus, these examples demonstrate the advantages of using supercomputing to delineate the variation in system performance with parameters.

### Simulation of Superlattice Growth

The growth of superlattices is one of the key issues in MOCVD reactor analysis and design. In addition to growing highly uniform, pure films one must be able to form sharp or accurately graded interfaces between

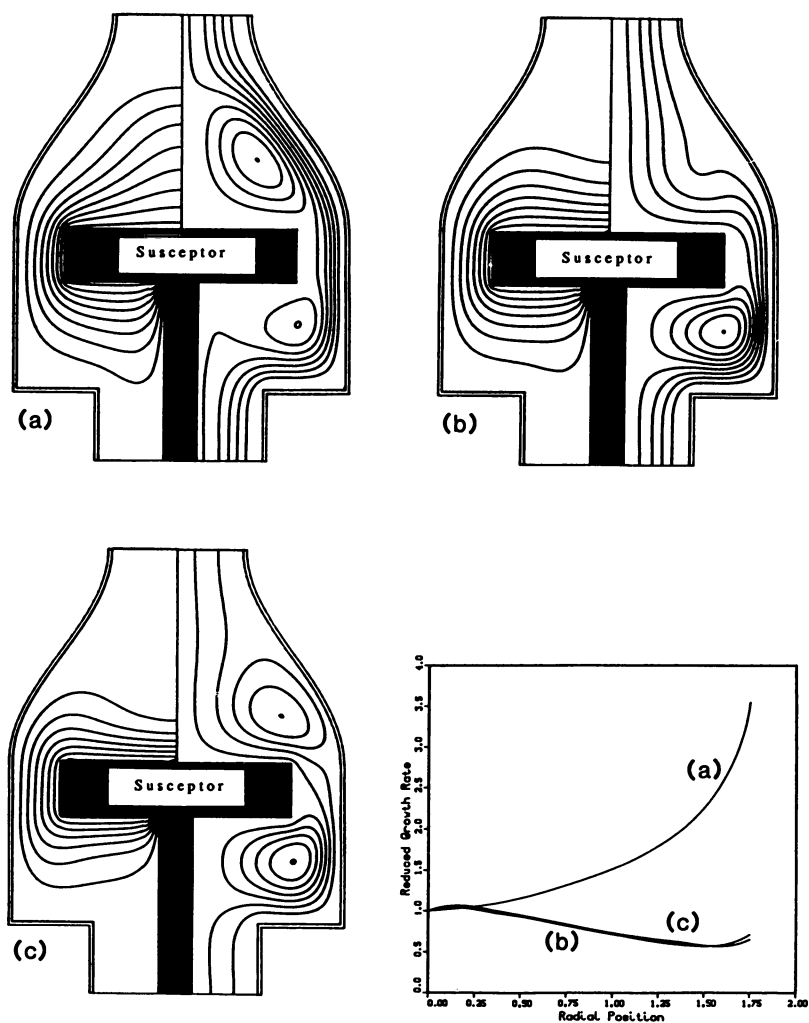


Figure 6. Effect of susceptor rotation speeds on isotherms, flow streamlines and relative deposition rates of GaAs; (a) zero rpm, (b) 1200 rpm, (c) 2400 rpm. The absolute growth rates vary as 1.0 (a): 4.0 (b): 4.7 (c).



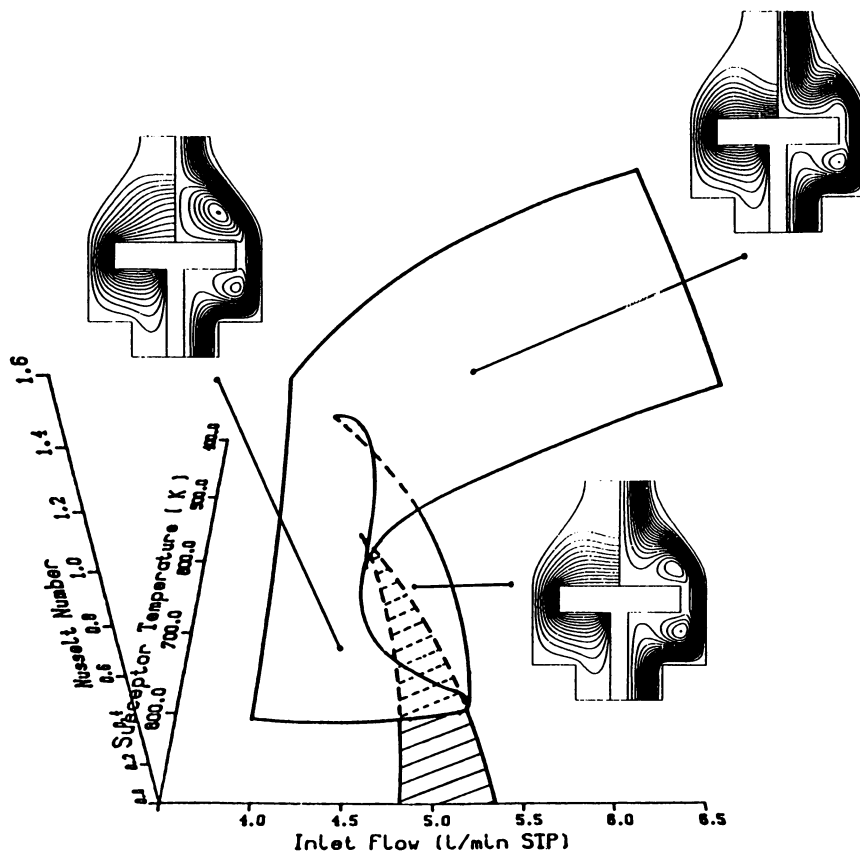


Figure 7. Reduced Nusselt number for mass transfer to the substrate in a vertical reactor for varying inlet flow rate and susceptor temperature.

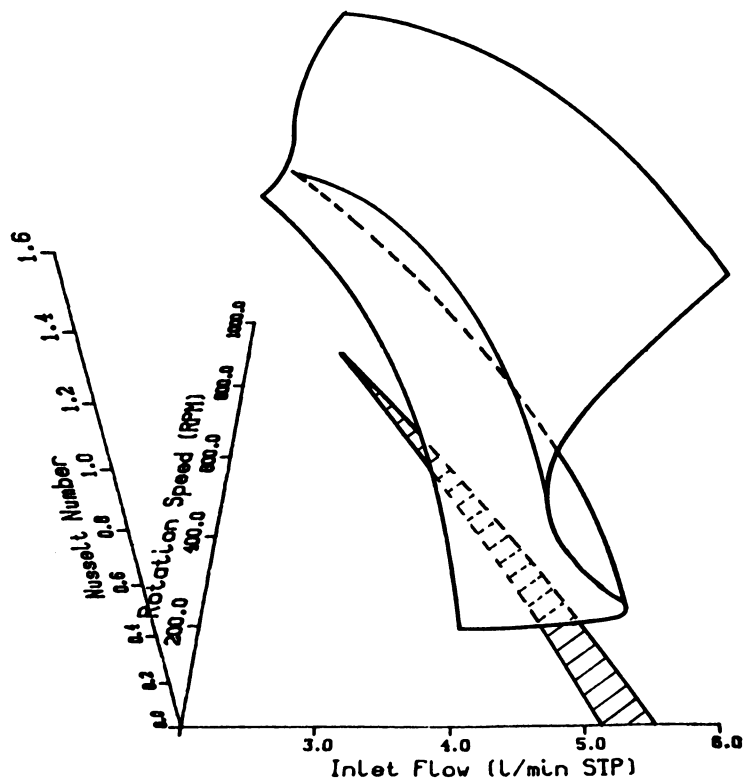


Figure 8. Reduced Nusselt number for mass transfer to the substrate in a vertical reactor for varying inlet flow rate and susceptor rotation speed.

subsequent layers to realize advanced digital and optical device designs. To illustrate the effect transport phenomena on the sharpness of the interface between two successive layers, the growth of AlAs on GaAs will be used as a model. This is a convenient example since the transport rates of Al and Ga species are similar (37). To further simplify the analysis it is assumed that the switching system is perfectly balanced so that the flow is unperturbed by the switching between organometallic source compounds. Thus, the steady state flow and temperature field may be used as input to the time dependent mass transfer code. The set of ordinary differential equations resulting from the finite element discretization of the spatial derivatives in Equation 7 was integrated by a modified version of EPISODE (38) and mass lumping (19) was used. Up to 2500 unknowns were used corresponding to 15 minutes of Cray 2 CPU time.

Figures 9 and 10 show the steady state streamlines and simulated concentration transition between growth of GaAs and AlAs for two cases, one strongly affected by buoyancy driven secondary flow (Figure 9) and the other dominated by forced convection (Figure 10). At time zero the alkyl source is switched from  $\text{Ga}(\text{CH}_3)_3$  to  $\text{Al}(\text{CH}_3)_3$ . The color scale gives the relative fraction of the Al-species, i.e. red corresponds to pure Al-alkyl while violet corresponds to no Al-alkyl (pure Ga-alkyl). When the flow is dominated by buoyancy effects it takes more than 10 seconds before the Ga-species has been flushed out of the reactor. The result is an interface wider than  $100\text{\AA}$ , which is unacceptable for most advanced devices. On the other hand, when the flow is forced convection dominated (Figure 10), the Al-species rapidly reaches the deposition surface, giving a reasonably sharp interface approximately  $6\text{\AA}$  wide. However, the recirculations caused by the expansion of the flow cross-section at the inlet retain the Ga-species for several seconds which could cause background doping. Fortunately, these recirculations can easily be removed by appropriately reshaping the walls as discussed above and illustrated in Figure 5. A comparison between the cases shown in Figures 9 and 10 clearly demonstrates the detrimental effect of recirculations on interface abruptness.

Although the above predictions have focused on immediate switching between organometallic source compounds, they are also relevant to stop growth procedures, where the flow of group III species (e.g.  $\text{Ga}(\text{CH}_3)_3$ ) is stopped, the overall flow is balanced, and the species is flushed out before the new species (e.g.  $\text{Al}(\text{CH}_3)_3$ ) is introduced. For this procedure it is critical that the reactor residence time is known. The present analysis readily predicts the time needed to flush out a particular reactant. Thus, supercomputer simulation could play a role in developing strategies for manufacturing superlattice based electronic and photonic device structures.

### Conclusions

The large scale reactor simulations represent a step towards realistic

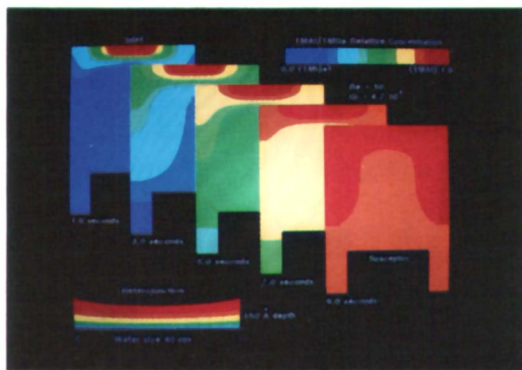
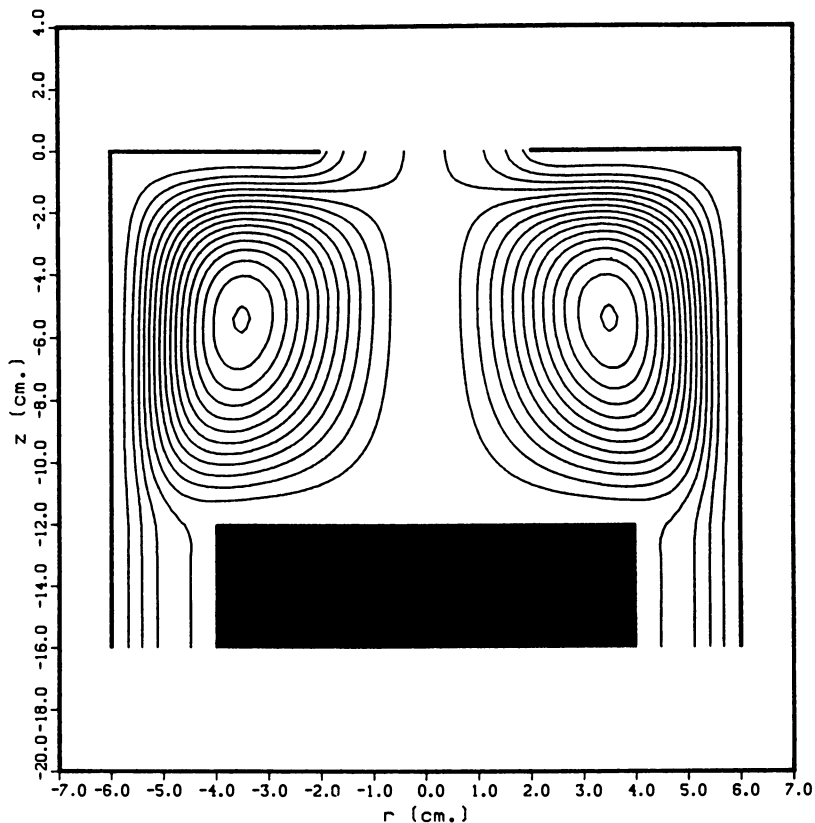


**Figure 9.** Streamlines (top) and relative gas phase composition of Al species (bottom) in a vertical axisymmetric reactor at five different times during growth of an AlAs/GaAs superlattice. Red corresponds to all Al species, violet to no Al species. The corner insert portrays the variation in solid fraction of Al across the interface. Buoyancy dominated flow.

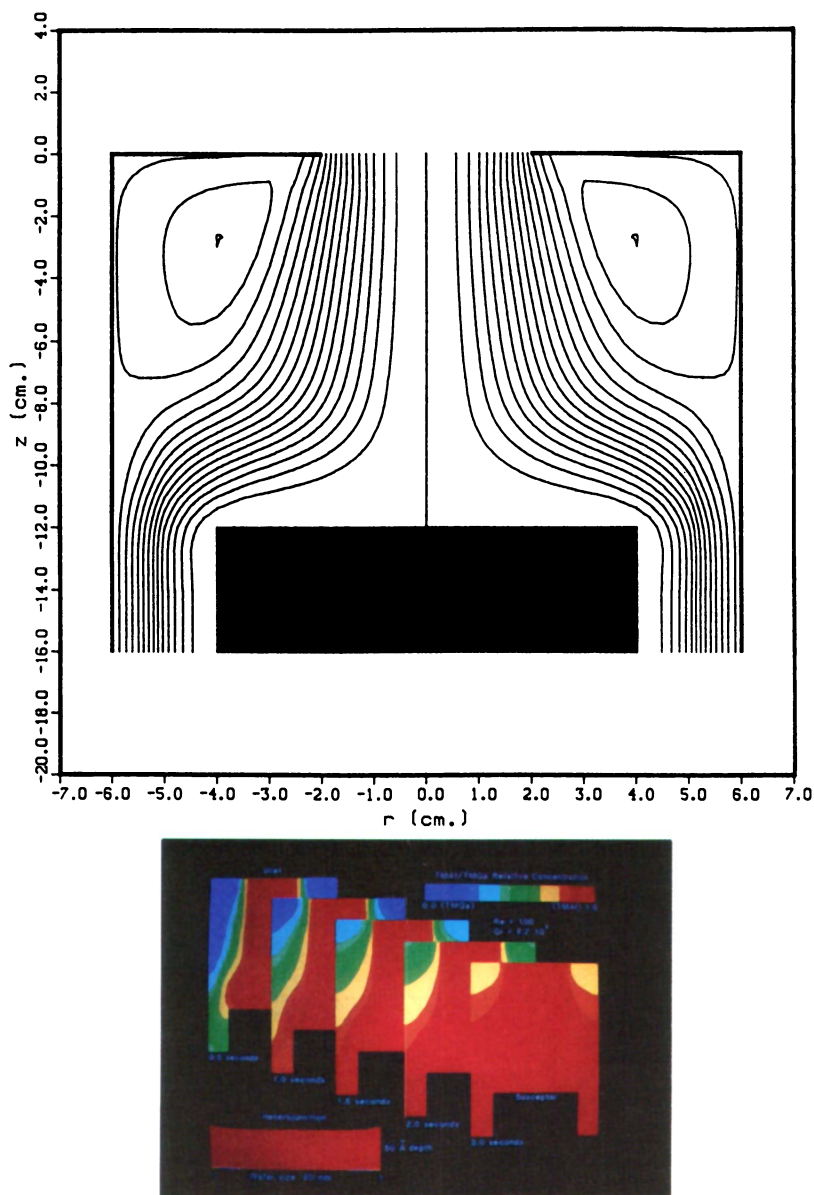


Figure 10. Streamlines (top) and relative gas phase composition of Al species (bottom) in a vertical axisymmetric reactor at five different times during growth of an AlAs/GaAs superlattice. Red corresponds to all Al species, violet to no Al species. The corner insert portrays the variation in solid fraction of Al across the interface. Forced convection dominated flow.

CVD reactor descriptions and away from oversimplified boundary layer and film theory models. The model predictions of flow, temperature, and concentration fields in horizontal reactors demonstrate that three-dimensional effects may be important even in the absence of buoyancy effects. Furthermore, the presence of buoyancy driven rolls greatly enhance growth rate variations. The vertical reactor analyses show that the film thickness uniformity is strongly influenced by susceptor edge, reactor wall, and buoyancy effects. Furthermore, nonlinear interactions between transport processes may lead to abrupt flow transitions with detrimental effects on growth performance. The simulation of superlattice growth illustrates that realization of sharp heterojunction interfaces require that flow recirculations and eddies be avoided. However, additional modelling efforts are needed to relax assumptions and further develop realistic models. The nature of the three-dimensional flow field needs to be understood. The treatment of surface reactions in current models is limited, in particular with respect to the initial nucleation and growth of the solid film. Further development of supercomputers and numerical methods in conjunction with experimental investigation are needed to formulate accurate models linking process conditions (flow, concentration, temperature) to microscopic material properties such as film crystal structure and defect concentrations.

#### Acknowledgments

The research forming the basis for this paper was supported by the National Science Foundation, by the Minnesota Supercomputer Institute, by the University of Minnesota Microelectronics and Information Sciences Center, and by a Teacher-Scholar Award from the Camille and Henry Dreyfus Foundation to KFJ.

#### Literature Cited

1. Ludowise, M. J. *J. Appl. Phys.* 1985, **58**, R31.
2. Dupuis, R. D. *Science* 1984, **226**, 623.
3. Kuech, T. F.; Veuhoff, E.; Kuan, T. S.; Deline, V.; Potemski, R. *J. Crystal Growth* 1986, **77**, 257.
4. Gilling, L. J. *J. Electrochem. Soc.* 1982, **129**, 634.
5. Van de Ven, J.; Rutten, G. M. J.; Raaijmakers, M. J.; Gilling, L. J. *J. Crystal Growth* 1986, **76**, 352.
6. Ban, V. S. *J. Electrochem. Soc.* 1978, **125**, 317.
7. Everstijn, F. C.; Peek, H. L. *Phillips Res. Rep.* 1972, **25**, 472.
8. Takahashi, R.; Koza Y.; Sugawara, K. *J. Electrochem. Soc.* 1972, **119**, 1406.
9. Stock, L.; Richter, W. *J. Crystal Growth* 1986, **77**, 128.
10. Talbot, L.; Cheng, R. K.; Scheffer, R. W.; Willits, *J. Fluid Mech.* 1980, **101**, 737.

11. Wang, C. A.; Groves, S. H.; Palmteer, S. C.; Weyburne, D. W.; Brown, R. A. *J. Crystal Growth* 1986, **77**, 136.
12. Wahl, G. *Thin Solid Films* 1977, **40**, 13.
13. Williams, J. E.; Peterson, R. W. *J. Crystal Growth* 1986, **77**, 128.
14. Bird, R. B.; Stewart, W. E.; Lightfoot, E. N. *Transport Phenomena*, Wiley: New York, 1960.
15. Jenklinsen, J. P.; Pollard, R. *J. Electrochem. Soc.* 1984, **131**, 425.
16. Moffat, H.; Jensen, K. F. *J. Electrochem. Soc.* (submitted).
17. Coltrin, M. E.; Kee, R. J.; Miller, J. A. *J. Electrochem. Soc.* 1986, **133**, 1206.
18. Reep, D. H.; Ghandl, S. K. *J. Electrochem. Soc.* 1983, **130**, 675.
19. Zienkiewicz, O. C. *The Finite Element Method*, Third Edition, McGraw-Hill (UK): London, 1983.
20. Huyakom, P.; Taylor, C.; Lee, R.; Gresho, P. *Computers and Fluids* 1978, **6**, 25.
21. Petzold, L. R. Sandia National Laboratories Report, SAND82-8637, Sept. 1982.
22. Houtman, C.; Graves, D. B.; Jensen, K. *J. Electrochem. Soc.* 1986, **133**, 961.
23. Kleda, S.; Fotladis, D. I.; Jensen, K. F. *J. Crystal Growth* (in preparation).
24. Fotladis, D. I.; Jensen, K. F. *Int. J. Num. Meth. Fluids* (in preparation).
25. Ryskin, G.; Leal, L. G. *J. Comp. Phys.* 1983, **50**, 71.
26. Keller, H. B. "Numerical Solution of Bifurcation and Nonlinear Eigenvalue Problems," in *Applications of Bifurcation Theory*, Rabinowitz, P., Ed.; Academic Press: New York, 1977.
27. Keller, H. B. *SIAM J. Sci. and Stat. Comp.* 1983, **4** 573.
28. Chan, T. F. *SIAM J. Sci. and Stat. Comp.* 1984, **5**, 135.
29. Hess, D. W.; Jensen, K. F.; Anderson, T. J. *Reviews in Chem. Engn.* 1985, **3**, 97.
30. Juza, J.; Cermak, J. *J. Electrochem. Soc.* 1982, **129**, 1627.
31. Coltrin, M. E.; Kee, R. J.; Miller, J. A. *J. Electrochem. Soc.* 1984, **131**, 425.
32. Brelland, W. G.; Coltrin, M. E.; Ho, P. *J. Appl. Phys.* 1986, **59**, 3267.
33. Moffat, H.; Jensen, K. F. *J. Crystal Growth* 1986, **77**, 108.
34. Chlu, K. C.; Rosenberg, F. *Int. J. Heat and Mass Transfer* (in press).
35. Schlichting, H. *Boundary Layer Theory*, McGraw-Hill: New York, 1979.
36. Kusumoto, Y.; Hayashi, T.; Komlya, S. *Japan J. Appl. Phys.* 1985, **24**, 620.
37. Suzuki, M.; Sato, M. *J. Electrochem. Soc.* 1985, **132**, 1684.
38. Byrne, G.; Hindmarsh, A. *ACM Transactions on Mathematical Software* 1975, **1**, 71.

RECEIVED June 15, 1987

## Chapter 20

# Numerical Resolution of Front Phenomena by Regridding Techniques

J. Degreve<sup>1</sup>, P. Dimitriou<sup>1</sup>, J. Puszynski<sup>1</sup>, V. Hlavacek<sup>1</sup>, S. Valone<sup>2</sup>, and R. Behrens<sup>2</sup>

<sup>1</sup>Department of Chemical Engineering, State University of New York,  
Buffalo, NY 14260

<sup>2</sup>Department MST-3, Los Alamos National Laboratory, Los Alamos, NM 87545

Solutions to models with different length scales may contain regions such as shocks, steep fronts and other near discontinuities. Adaptive meshing strategies, in which a spatial mesh network is adjusted dynamically so as to capture the local behavior accurately, will be described. The algorithm will be tested on an example of filtration combustion.

For many physical problems, described by partial differential equations, the solution in some parts of the region is accompanied by steep gradients. If rapid variations in the solution are confined to thin isolated regions, the total number of grid points used in a numerical simulation on an equispaced mesh may be very high to get a good resolution of these boundary layers. Frequently mathematical models of real physical processes are characterized by the simultaneous presence of significantly different time and length scales. The solution to these models will have regions of strongly localized behavior such as shocks, steep fronts and other near discontinuities.

Fluid flow and reaction engineering problems represent a rich spectrum of examples of multiple and disparate scales. In chemical kinetics such problems involve high values of Thiele modulus (diffusion-reaction problems), Damköhler and Peclet numbers (diffusion-convection-reaction problems). For fluid flow problems a large value of the Mach number, which represents the ratio of flow velocity to the speed of sound, indicates the possibility of shock waves; a large value of the Reynolds number causes boundary layers to be formed near solid walls and a large value of the Prandtl number gives rise to thermal boundary layers. Evidently, the inherently disparate scales for fluid flow, heat transfer and chemical reaction are responsible for the presence of thin regions or "fronts" in the solution.

Another particularly important topic in the modeling of strongly nonlinear phenomena is the occurrence of multiple fronts. For instance, in a supersonic reactive flow problem the position and speed of propagation of the shock wave and reaction front are different.

0097-6156/87/0353-0376\$08.00/0  
© 1987 American Chemical Society



A similar situation occurs in the case of free convection and exothermic chemical reaction phenomena where the hydrodynamic boundary layer is separated from the reaction front.

Spontaneous pattern formation in biological, hydrodynamic or combustion problems is another possible example of complex front phenomena. For a diffusion-autocatalytic reaction problem a great variety of patterns such as rotating and spiral waves can be triggered by bifurcation. These dissipative structures may exhibit large spatial gradients and stiffness. Recent numerical simulation reveals that in many combustion problems the reaction front may become unstable to two-dimensional or three-dimensional perturbations and a family of spinning and fingering waves results.

A very common approach in solving these problems is "flooding" the computational domain with mesh points regardless of the cost. Frequently, the run time increases as the square or cube of the number of grid points present. As a result, this brutal approach of flooding the region with grid points is feasible on current computers only for certain problems (one-dimensional problems are the prime candidate). For a typical 2D problem  $10^3$ - $10^4$  equidistant grid points are necessary, but a 3D-problem may require as many as  $10^4$ - $10^6$  equidistant grid points. This precludes a systematic numerical simulation of 2D and 3D problems featuring singular behavior. There are two major routes to overcome this dilemma: a) adaptive regridding techniques, b) use of routines amenable to vectorization and the use of vector processors.

#### METHODS OF GRID GENERATION

For realistic simulation problems it is rarely feasible to implement a numerical solution method that is reliable and accurate at a reasonable cost and yet that does not utilize some form of adaptivity. Most 2D and virtually all 3D problems are undercomputed without an efficient regridding algorithm. The gist of the regridding approach is to distribute the computational effort nonuniformly in a way such that the points are concentrated in the most singular part of the solution. The goal of a regridding algorithm is to choose a mesh of grid points that is located optimally with respect to the solution in space and time.

Several different methods may be used to generate and adaptive mesh. Saltzman (1) categorized them as follows: i) fixed meshes, ii) selectively refined meshes, and iii) moving meshes.

A fixed mesh is a structure of grid points which is fixed during the entire calculational process. The construction of the grid is based on a priori knowledge of the qualitative behavior of the solution and the location of the mesh points is primarily determined by the expected position of the boundary layer. This type of adaptive mesh is very good for steady state, boundary value problems (2). As an example, we cite the calculation of a burner stabilized flame where we can expect a thin region with high reaction rate close to the burner. Another example is the existence of a viscous layer near the solid wall in fluid flow problems. For transient problems we will use the fixed mesh algorithm if steep gradients are expected for standing wave phenomena. As an example here we can consider a model of ignition of solid propellants or

explosives by a heat flux (3). Analytically determined coordinate transformations belong to this category. Typically, all these methods will use a coarse mesh for the flat part of the solution and compress the points in the boundary layer.

For propagating fronts which travel with a constant (or almost constant) speed the algorithm can be modified. The fine mesh region should be large enough to provide sufficient room for a traveling front (4), i.e. the front will stay in the fine mesh domain for say fifty time steps. After the front has moved to the edge of the fine mesh domain interpolation is performed and the strip of fine mesh is moved in the direction of the front propagation. This method represents a transition between fixed and selectively refined meshes.

A selectively refined mesh algorithm adds or subtracts computation points in response to the evolution of the solution. This strategy was used by one of the authors (3) towards the simulation of a spherical flame two decades ago. At each time an estimate of the error of the solution is made. This error can be easily estimated from the truncation error of the finite-difference approximation. Based on this error estimate, points are added to reduce the local error, or removed if the local error of approximation is low enough. Gropp (5) and Lam and Simpson (6) have performed selectively refined mesh calculations in two dimensions. For flame calculations this algorithm was advocated by Smooke et al. both for 1D (7) and 2D (8) cases. For a 1D problem the algorithm is very efficient, and can safely be used for problems with multiple singular regions. The algorithm also performs very well for 2D problems which show only a low degree of front corrugation, i.e. quasi 1D problems. For strongly corrugated fronts this strategy of adaptive meshing generates too many lines and is computationally not effective.

The last class of adaptive meshes consists of the moving meshes (1). The idea behind moving meshes is the enhancement of the resolution by clustering a fixed number of points at the appropriate places, i.e. in regions of high gradients or large curvature. Brackbill and Saltzman (9) and Yanenko et al. (10) introduced a moving mesh method that decouples the generation of the mesh from the solution of the equations being approximated. It is this method which will be used in this paper and it will be discussed in the next paragraph.

#### ADAPTIVE MESH GENERATION - VARIATIONAL APPROACH

It will be convenient to define a time and solution dependent transformation which proportions grid points on the derivative. We will require that the grid will be uniform in this so called "computational space". In order to normalize, allow for optimization, and remove singularities we can write for the transformed coordinate  $\xi(x,t)$  (11):

$$\xi(x,t) = \frac{\int_0^x (1+b \left| \frac{\partial T}{\partial x} \right|) dx}{\int_0^{x_{\max}} (1+b \left| \frac{\partial T}{\partial x} \right|) dx} \quad (1)$$

Here  $b$  is an adjustable constant. This criterion can be written in a more general form, which will also include effects of regions with high curvature:

$$\xi(x,t) = \frac{\int_0^x (1+b \left| \frac{\partial T}{\partial x} \right| + C \left| \frac{\partial^2 T}{\partial x^2} \right|) dx}{\int_0^{x_{\max}} (1+b \left| \frac{\partial T}{\partial x} \right| + C \left| \frac{\partial^2 T}{\partial x^2} \right|) dx} \quad (2)$$

Here the constant  $C$  takes care of the relative importance of the second derivative influence. Instead of solving a front problem in the coordinates  $(x,t)$  (physical space) we perform the calculations in the computational space  $(\xi,t)$ . For one dimensional problems this adaptive grid transformation proved to be very successful. We can perform a transformation in a similar spirit for a two dimensional domain  $(x,y,t) \rightarrow (\xi,\eta,t)$ . A general sketch of this transformation is presented in Figure 1. The weak point of this strategy is the fact that we have no effective way to control the grid shape in the adaptive calculation. As a result, for a two dimensional problem this transformation can produce an unacceptable mesh for particular regions. Rapid variations in cell size and lack of orthogonality can have a deleterious effect on the accuracy of the calculations by introducing substantial errors in the finite difference approximations of the governing equations. Therefore the need to measure and control the properties of smoothness and orthogonality is imperative. Smoothness or roughness of the grid is measured by the integral

$$I_s = \int_D [(\nabla\xi)^2 + (\nabla\eta)^2] dx dy \quad (3)$$

and orthogonality by

$$I_o = \int_D (\nabla\xi\nabla\eta)^2 J^3 dx dy \quad (4)$$

The Jacobian  $J$  of the mapping  $(x,y) \leftrightarrow (\xi,\eta)$  is a measure of the cell size. Many of the methods that have been used to construct adaptive meshes for one-dimensional problems are based on the idea of equidistribution of a positive weight function. This idea can be extended to two or more dimensions and we can measure the adaptive property by the integral

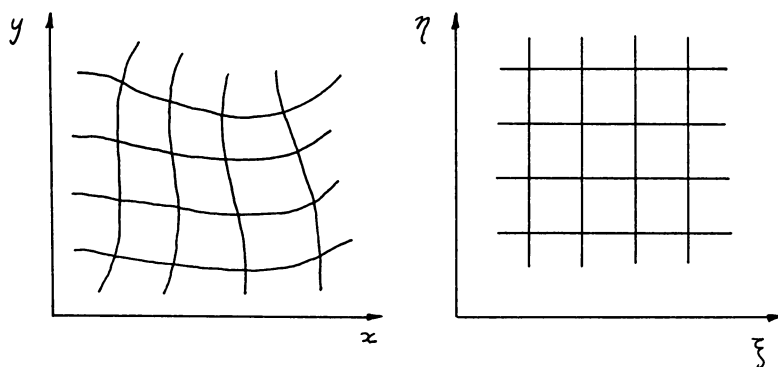


Figure 1. Schematic of physical and computational spaces.

$$I_v = \int_D w(x,y)J \, dx dy \quad (5)$$

Evidently a formulation of an adaptive grid with properties of being smooth and orthogonal is a problem of optimization of a vector performance index. The simplest way of optimizing this problem is an amalgamation of different criteria in one scalar function by assigning appropriate values (weights) to each criterion. Following Saltzman (1), a weighted sum of the integrals is minimized:

$$I = I_s + \lambda_o I_o + \lambda_v I_v, \quad \lambda_o \geq 0, \quad \lambda_v \geq 0 \quad (6)$$

Since the computational mesh is always uniform and since we are interested in determining optimal positions of grid points in the physical space  $(x,y)$ , it is more appropriate to minimize the integral  $I$  over the region in  $(\xi,\eta)$ -space. The expression (6) is a functional and Euler variational calculus must be used towards optimization of  $I$ . After expressing the separate integrals in this transformed region by making use of the relationships

$$\xi_x = y_\eta/J, \quad \xi_y = -x_\eta/J, \quad \eta_x = -y_\xi/J, \quad \eta_y = x_\xi/J \quad (7)$$

the Euler equations for this variational problem can be derived. They are represented by a set of nonlinear elliptic partial differential equations of the form

$$b_1 x_{\xi\xi} + b_2 x_{\xi\eta} + b_3 x_{\eta\eta} + a_1 y_{\xi\xi} + a_2 y_{\xi\eta} + a_3 y_{\eta\eta} = - \frac{J^2}{2w} \cdot \frac{\partial w}{\partial x} \quad (8)$$

$$a_1 x_{\xi\xi} + a_2 x_{\xi\eta} + a_3 x_{\eta\eta} + c_1 y_{\xi\xi} + c_2 y_{\xi\eta} + c_3 y_{\eta\eta} = - \frac{J^2}{2w} \cdot \frac{\partial w}{\partial y} \quad (9)$$

where the coefficients are functions of the metrics  $x_\eta$ ,  $x_\xi$ ,  $y_\xi$  and  $y_\eta$  (9). For the generation of an adaptive mesh in one spatial dimension, the above equations simplify, giving rise to the following boundary value problem:

$$\frac{x_{\xi\xi}}{x_\xi} + \lambda_v (2w x_{\xi\xi} + x_{\xi w}^2) = 0, \quad x(\xi_1) = x_1, \quad x(\xi_2) = x_2 \quad (10)$$

The user can control the properties of the mesh to be generated by choosing the factors  $\lambda_o$  and  $\lambda_v$ . Although some experimentation is required, a dimensional analysis of the problem at hand can be helpful in selecting suitable values for  $\lambda_o$  and  $\lambda_v$  (1).

#### NUMERICAL SOLUTION

After formulating the problem in the physical  $(x,y)$ -space, the governing equations are transformed to the uniform computational space  $(\xi,\eta)$ , using relationships such as

$$\frac{\partial}{\partial x} = \frac{y_{\eta}}{J} \cdot \frac{\partial}{\partial \xi} - \frac{y_{\xi}}{J} \cdot \frac{\partial}{\partial \eta} \quad (11)$$

$$\frac{\partial}{\partial y} = -\frac{x_{\eta}}{J} \cdot \frac{\partial}{\partial \xi} + \frac{x_{\xi}}{J} \cdot \frac{\partial}{\partial \eta} \quad (12)$$

Similar expressions can be derived for second spatial derivatives. The final form of the equations that result after a generalized coordinate transformation depends on the degree of differentiation by using the chain rule, i.e. on the treatment of the metrics  $x_{\xi}$ ,  $x_{\eta}$ ,  $y_{\xi}$  and  $y_{\eta}$ . For more details we refer to the work by Hindman (12). In our computational work we have used the Chain Rule Conservation Law Form (CRCLF).

Since the computational mesh in  $(\xi, \eta)$ -space is always orthogonal and uniform, the finite difference approximations can be expressed quite easily. (Central finite differences were used to discretize the governing equations. Although the formal accuracy of this approximation might appear to be  $O(\Delta\xi^2, \Delta\eta^2)$  this is not true since the mesh spacings  $\Delta\xi$  and  $\Delta\eta$  will cancel out when the discretization is made. More on this can be found in (13).

Equations 8 and 9 and the equations governing the physical problem should be solved simultaneously at every time step to make the grid truly dynamically adaptive. However, this approach is computationally expensive since the adaptive mesh at the new time level depends implicitly (through the weight function which measures properties of the solution that have to be resolved by the mesh) on the solution at this new time level. Therefore, the coupling between the solution of the governing equations and the adaptive mesh was done in the following way. Consider we have obtained a solution at time level  $t$  by (implicit) time integration of the governing equations. Using this solution, new values of the weight function  $w(x,y)$  can be calculated. After substitution of  $w(x,y)$  into Equations 8 and 9 one can then solve for new positions of the grid points. The solution is then transferred from the old grid to the new grid by interpolation and the governing equations will now be integrated on this new grid for one time step. In this way, the adaptive grid lags the solution by one time step. We found that it is not necessary to adjust the positions of the grid points every time step if we smooth the weight function  $w(x,y)$  by letting the diffusion equation act for a few dimensionless time steps:

$$w_{i,j}^{k+1} = w_{i,j}^k + v(w_{i-1,j}^k + w_{i+1,j}^k - 4w_{i,j}^k + w_{i,j+1}^k + w_{i,j-1}^k) \quad (13)$$

This smoothing of the weight function will enlarge clustered regions of the grid so that the high activity parts of the solution are prevented from moving out in just a few time steps. Lower frequency of grid adjustment (e.g. every five timesteps) also has the added positive effect of reducing interpolation. Very frequent interpolation results in artificial diffusion being imposed on the solution, thereby decreasing the accuracy of the calculations.

EXAMPLE

The algorithm described above was successfully used for simulation of the filtration combustion process for the synthesis of nitrogen ceramics.

Direct reaction of transition metals (Ti, Ta, Nb, Zr) or Al or Si results in adiabatic combustion temperatures of 2500-4500°C. These nitridation reactions are also characterized by very high values of activation energy. As a result, the nitridation front represents a strongly nonlinear combustion wave which may be extremely thin and corrugated.

After local initiation of the reaction by an ignition source, a reaction front starts to propagate throughout the system. The gaseous reactant is delivered to the reaction zone by means of filtration through the porous layer containing unreacted solid material so that melting or sintering phenomena cannot disable the process. The reader is referred to Aldushin et al. (14-15) for additional information on the filtration combustion process.

In terms of suitably chosen nondimensional variables, the governing equations for a two-dimensional description of the physical system may be written as follows:  
mass balance on the gas phase

$$\alpha \frac{\partial \rho}{\partial t} = - \frac{\partial u \rho}{\partial x} - \frac{\partial v \rho}{\partial y} - R \quad (14)$$

heat balance on the gas-solid system

$$\frac{\partial (\alpha \delta \rho + 1 + \delta \eta) \theta}{\partial t} = \frac{\partial^2 \theta}{\partial x^2} + \frac{\partial^2 \theta}{\partial y^2} - \delta \frac{\partial u \rho \theta}{\partial x} - \delta \frac{\partial v \rho \theta}{\partial y} + \frac{1}{\gamma} R \quad (15)$$

Darcy's law

$$u = -\alpha \omega \frac{\partial \pi}{\partial x} \quad (16)$$

$$v = -\alpha \omega \frac{\partial \pi}{\partial y} \quad (17)$$

equation of state

$$\pi = \rho \frac{(1 + \beta \theta)}{(1 + \beta \theta_0)} \quad (18)$$

reaction rate expression

$$\frac{\partial \eta}{\partial t} = R = \frac{1}{\gamma} (1 - \eta) \pi \exp\left(\frac{\theta}{1 + \beta \theta}\right) \quad (19)$$

$\theta$  is the nondimensional temperature and  $\eta$  is the conversion of solid reactant. The nondimensional gas density and pressure are denoted by  $\rho$  and  $\pi$ , respectively.  $u$  and  $v$  represent the dimensionless gasflow velocities in the  $x$  and  $y$  direction.

The system of governing equations contains several parameters.  $\beta$  is a nondimensional activation energy and  $\gamma$  is a nondimensional

heat of reaction.  $\alpha$  is related to the initial amount of gaseous reactant,  $\delta$  is the ratio of gas heat capacity to solid heat capacity, and  $\omega$  is a measure of the permeability of the porous medium to gas flow.

We will first discuss some results obtained for a one-dimensional formulation of the filtration combustion process. The initial conditions are given by

$$\rho = 1, \pi = 1, \eta = 0, u = 0, \theta = \theta_0 \text{ for } 0 \leq x \leq L_x, t = 0 \quad (20)$$

and the boundary conditions by

$$\theta = \theta_1, u = 0 \text{ at } x = L_x \text{ for } t > 0 \quad (21)$$

$$\frac{\partial \theta}{\partial x} = \delta \omega \rho (\theta - \theta_0), \pi = 1 \text{ at } x = 0 \text{ for } t > 0. \quad (22)$$

Figures 2a and 2b show the calculated temperature and conversion profiles for the problem with  $\alpha = 0.50$ ,  $\beta = 0.1026786$ ,  $\gamma = 0.0625$ ,  $\delta = 1.0$ ,  $\omega = 50.0$ ,  $L_x = 50.0$  and  $\theta_0 = -8.0$ . The calculations were performed using the adaptive mesh with 50 points. The use of an equidistant mesh for this particular problem would require at least 300 points in order to obtain a comparable resolution of the high gradient region. Results obtained on an equidistant mesh with 1000 points showed graphically no difference with those obtained on a 55 point adaptive mesh. It was noted that a lack of resolution in the high gradient region results in artificial numerical oscillations, rendering the calculations useless. Figure 2c shows the relationship between the physical coordinate  $x$  and the computational coordinate  $\xi$  as a function of time. This figure reveals that the adaptive mesh generator keeps grid points clustered in the high gradient regions. The weight function was based on a combination of first and second spatial derivatives calculated from the temperature, conversion and pressure profiles.

Whereas the previous case revealed temperature and conversion profiles propagating with almost constant velocity ("constant-pattern profiles"), the next case shows oscillatory behavior of the filtration combustion process for parameters  $\alpha = 1.0$ ,  $\beta = 0.08$ ,  $\gamma = 0.05$ ,  $\delta = 1.0$ ,  $\omega = 100.0$ ,  $L_x = 50.0$  and  $\theta_0 = -10.0$ . Figure 3a displays the calculated temperature profiles. The temperature in the reaction zone oscillates wildly. As a result, a spatially inhomogeneous product is obtained since some of the material is formed at high temperatures, and some of it at lower temperatures. Figure 3b gives the conversion profiles and Figure 3c shows the adaptive mesh. Clearly, the adaptive mesh responds very well to the accelerations and decelerations of the propagating reaction front. It is obvious that a strong coupling between the solution of the governing equations and the generation of the adaptive mesh is of prime importance for a case like this one, since a priori knowledge on how the solution will evolve is not available.

One-dimensional simulations provide useful information about the filtration combustion system such as values for propagation velocity under various conditions and an indication of the mode of



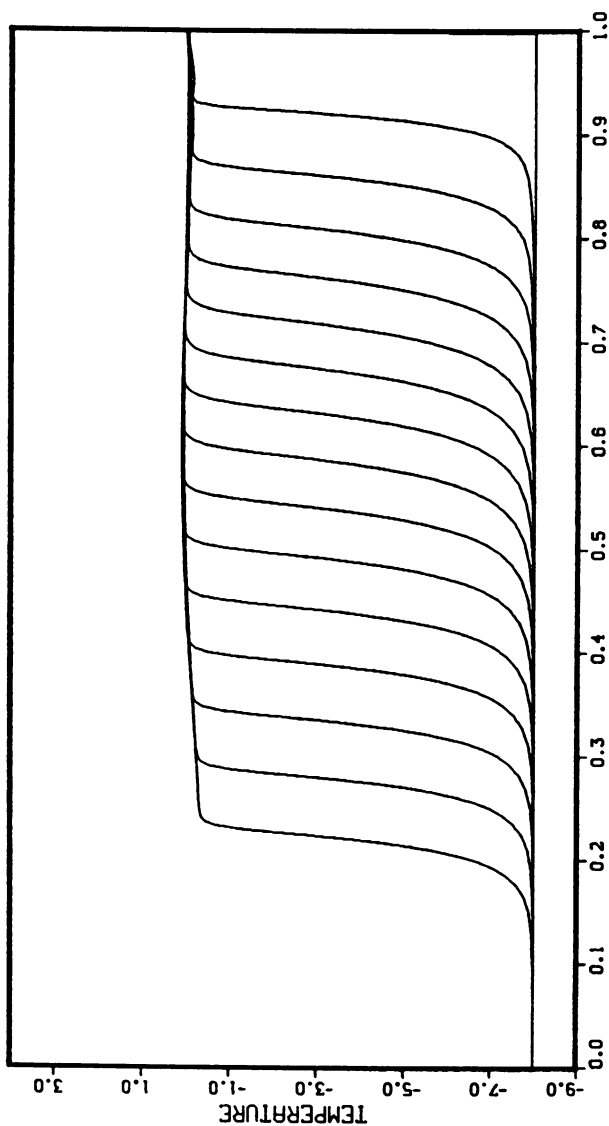


Figure 2a. Temperature profiles.

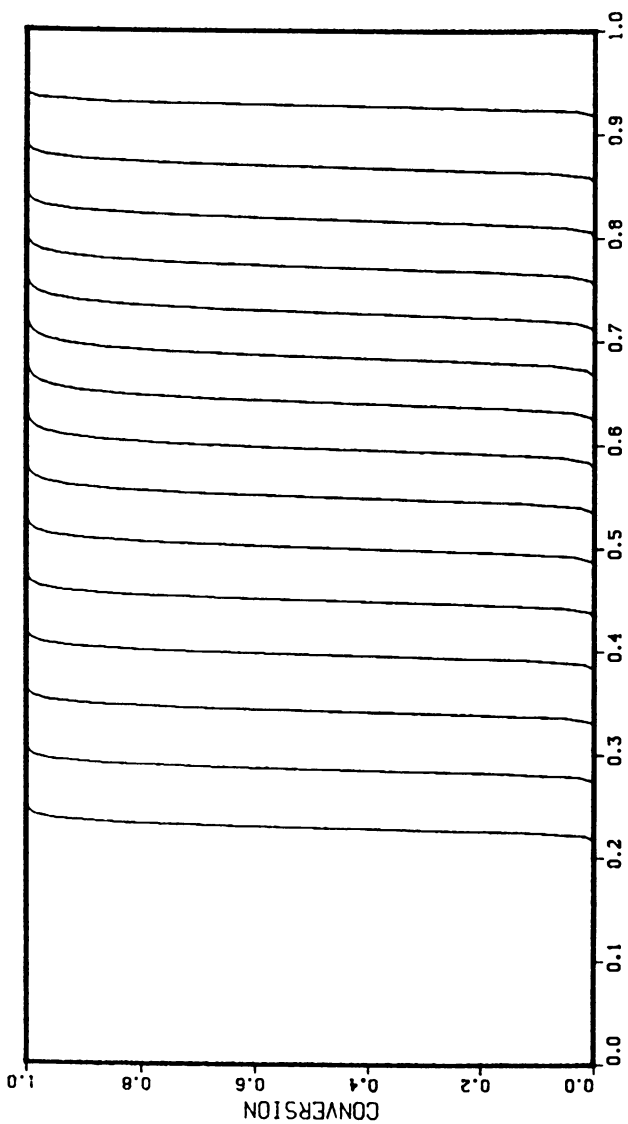


Figure 2b. Conversion profiles.

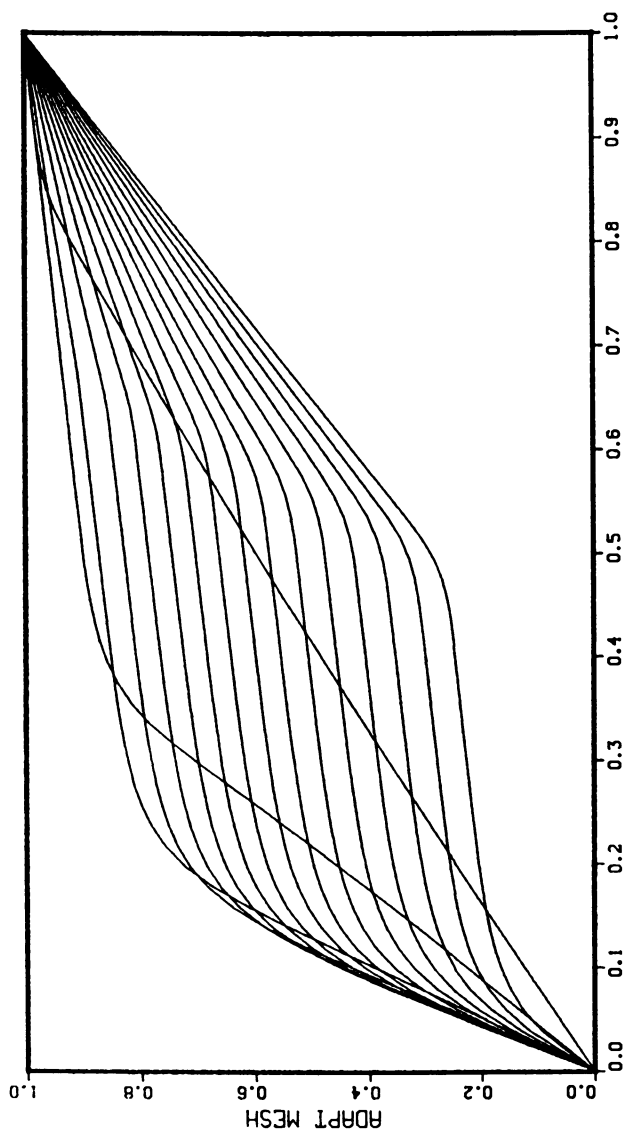


Figure 2c. Adaptive mesh. (Time interval between consecutive profiles,  $\Delta t = 0.1$ .)

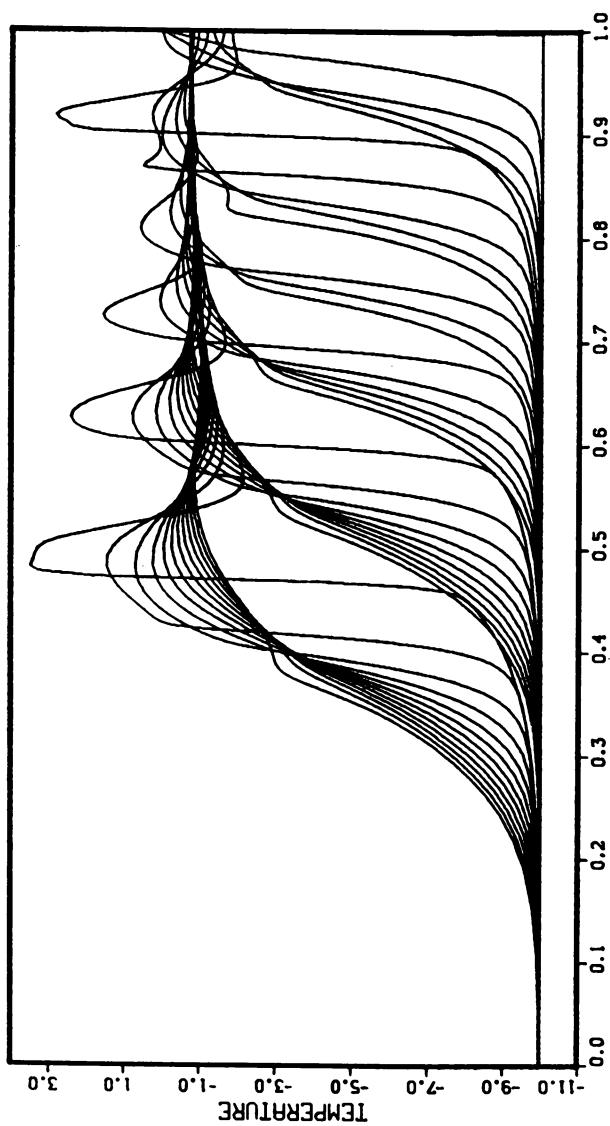


Figure 3a. Temperature profiles.

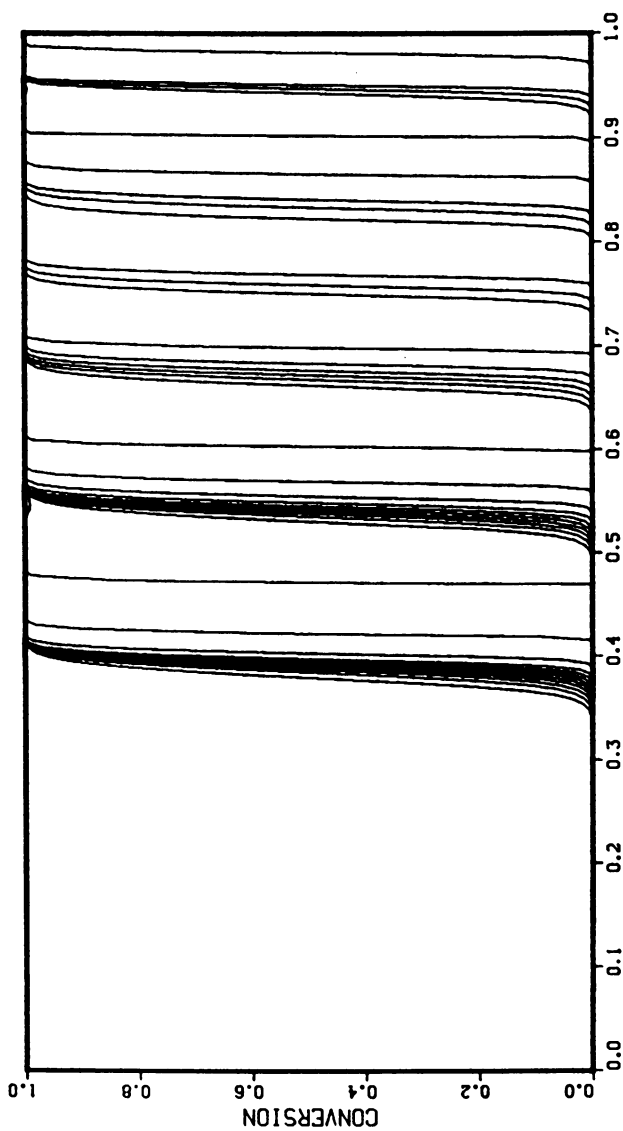


Figure 3b. Conversion profiles.

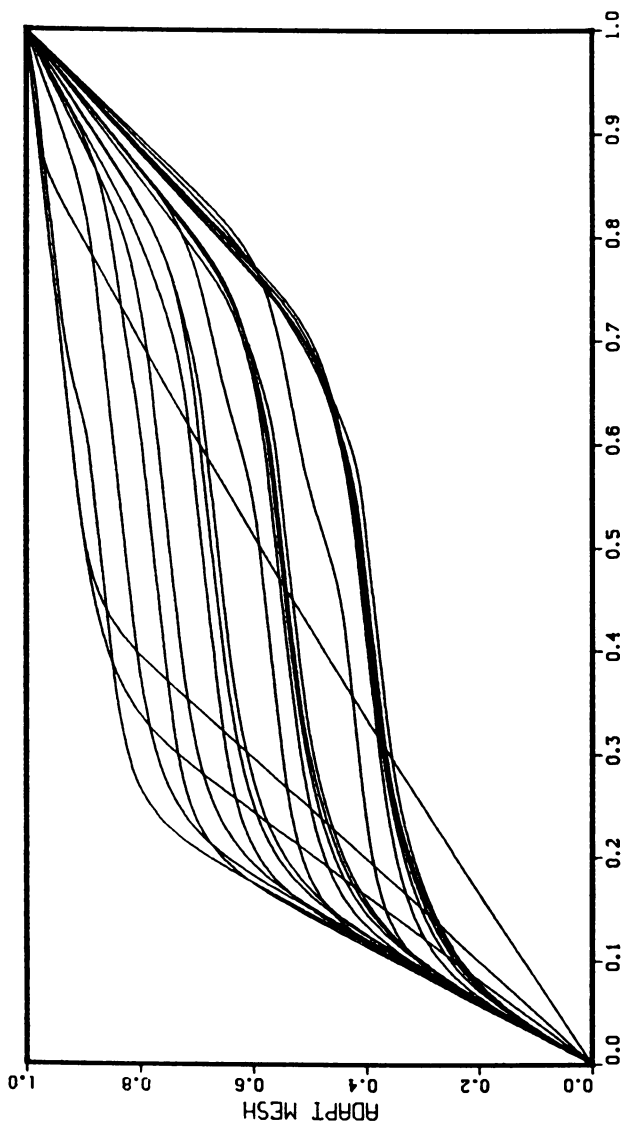


Figure 3c. Adaptive mesh. (Time interval between consecutive profiles,  $\Delta t = 0.1$ .)

propagation (quasi-steady or oscillatory) of a planar combustion front. However, planar combustion fronts can be unstable with respect to spatial disturbances. The flame front becomes corrugated and a one-dimensional calculation does not suffice. Since a full three-dimensional simulation was beyond our computational capabilities, we restricted ourselves to a two dimensional simulation. The system we chose to study is depicted in Figure 4. The initial conditions on the entire spatial domain ( $0 \leq x \leq L_x$ ,  $0 \leq y \leq L_y$ ) are the same as for the one-dimensional case, as are the boundary conditions for the sides  $x = 0$ ,  $0 \leq y \leq L_y$  and  $x = L_x$ ,  $0 \leq y \leq L_y$ . The lateral sides of the system ( $y = 0$  and  $y = L_y$ ,  $0 \leq x \leq L_x$ ) were assumed to be thermally insulated and impermeable. We solved the problem for  $\alpha = 1.0$ ,  $\beta = 0.1026786$ ,  $\gamma = 0.0625$ ,  $\delta = 1.0$ ,  $\omega = 50.0$ ,  $L_x = 50.0$ ,  $L_y = 10.0$  and  $\theta_o = -8.0$ . In a one-dimensional simulation of this problem, we found that the system exhibited mild temperature oscillations, see Figure 5. The two-dimensional calculation, however, not only revealed temporal oscillations in temperature but also a breakup of the planar combustion front, Figure 6. Hot spots appear along the front, disappear, reappear again, etc, but in positions different than before. A qualitatively similar phenomenon was observed in our experiments. Small luminous regions moved around in a seemingly erratic way along the reaction front. The two-dimensional calculations also showed another important feature of the process. The temperature in a hot spot (maximum value observed:  $\theta_{\max} \approx 2.54$ ) can exceed by far the value predicted from a one-dimensional calculation (maximum value observed:  $\theta_{\max} \approx 0.80$ )! The discrepancy between these observations can easily be explained.

A corrugated front has parts protruding into the oncoming gas flow, Figure 7. These parts of the front can access not only the gaseous reactant straight ahead but also some of the gas from the left and right. This makes the protrusions even more pronounced and creates spots of very high temperature at the expense of neighboring parts which remain cold since they are deprived of gaseous reactant. The hot spot penetrates too deeply into the cold unreacted material and will eventually die. In the case of a planar reaction front (an assumption implicitly made in a one-dimensional formulation of the problem) such competition for gaseous reactant between the different parts of the reaction front does not exist. Figure 8, representing contour plots of pressure, shows hot spots surrounded by "pockets" indicating that gaseous reactant is supplied to them from the whole surrounding area. Plots of the adaptive mesh at different times are given in Figure 9.

The computations were performed on a 50 x 10 interior grid. A lot of grid points are clustered in the region of sharp temperature, conversion and pressure variation and as can be seen, this very fine grid moves along with the propagating flame. To prevent entanglement of the mesh lines, the movement of each grid point was limited in such a way as to maintain a given minimum distance between it and all of its neighbors. Unfortunately, our implementation of this constraint was too conservative, as can be

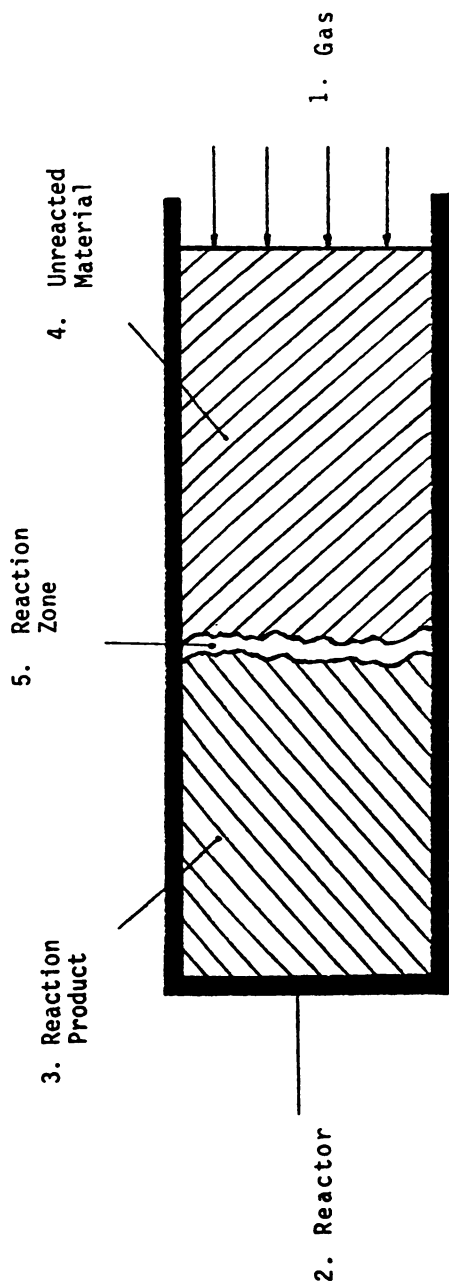


Figure 4. Sketch of filtration combustion principle.



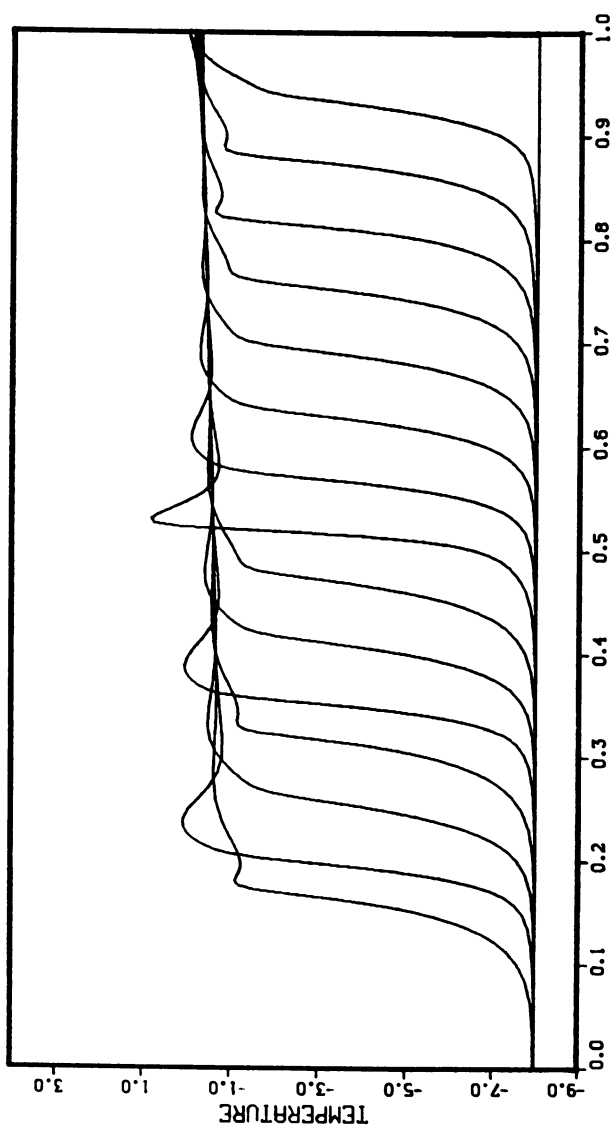


Figure 5. Temperature profiles. (Time interval between consecutive profiles,  $\Delta t = 0.1$ .)

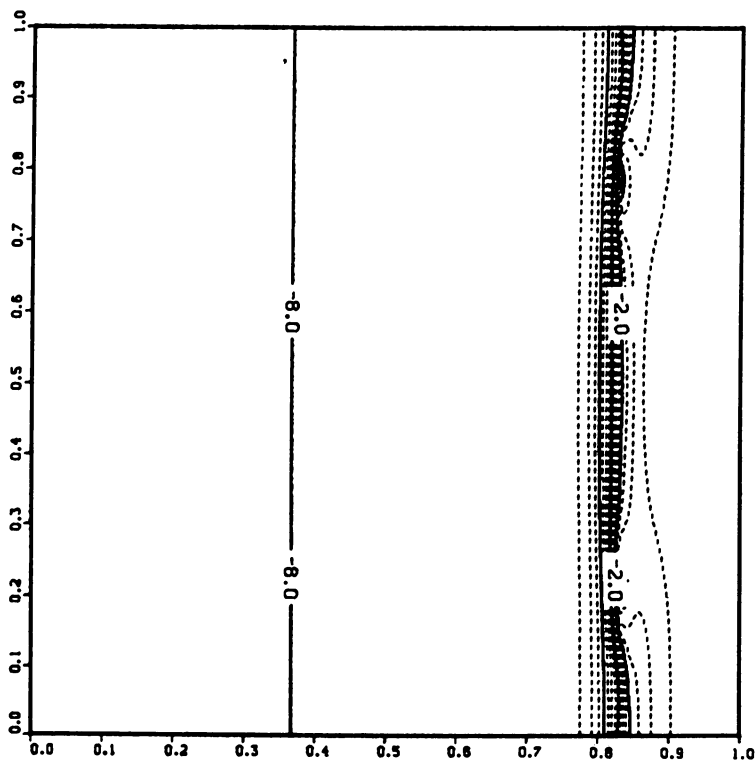


Figure 6. Temperature contours. (a)  $t = 0.3$ . *Continued on next page.*

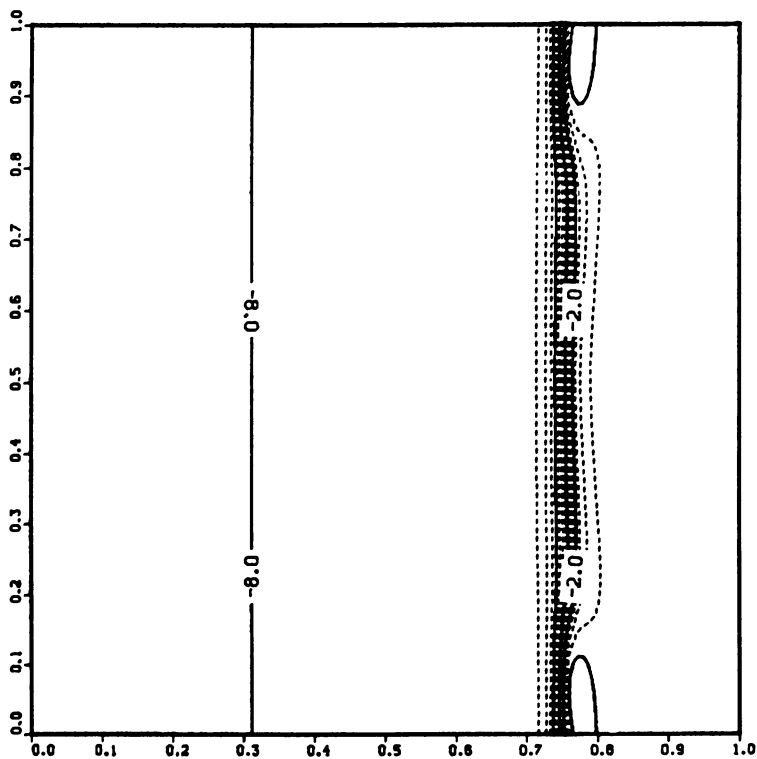


Figure 6. *Continued.* (b)  $t = 0.4$ . *Continued on next page.*

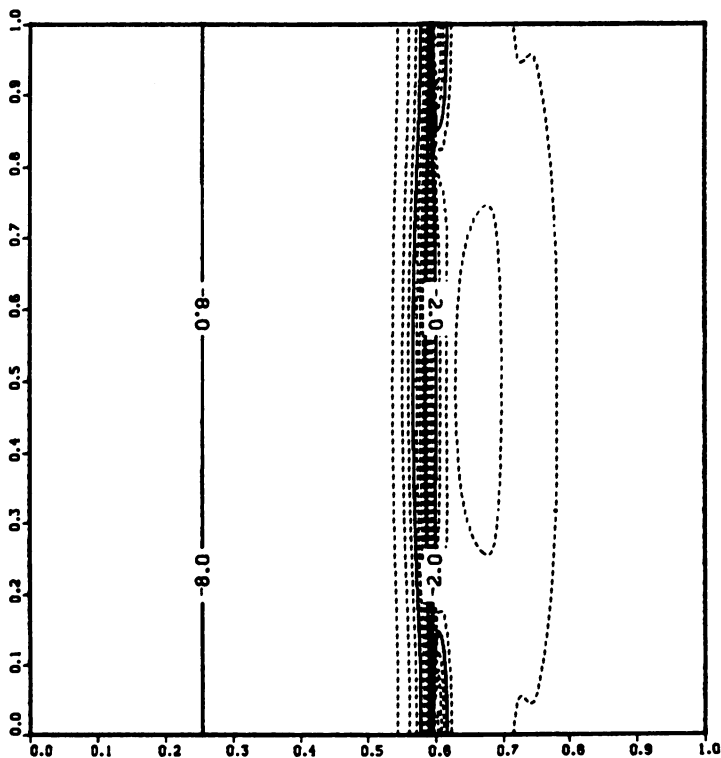
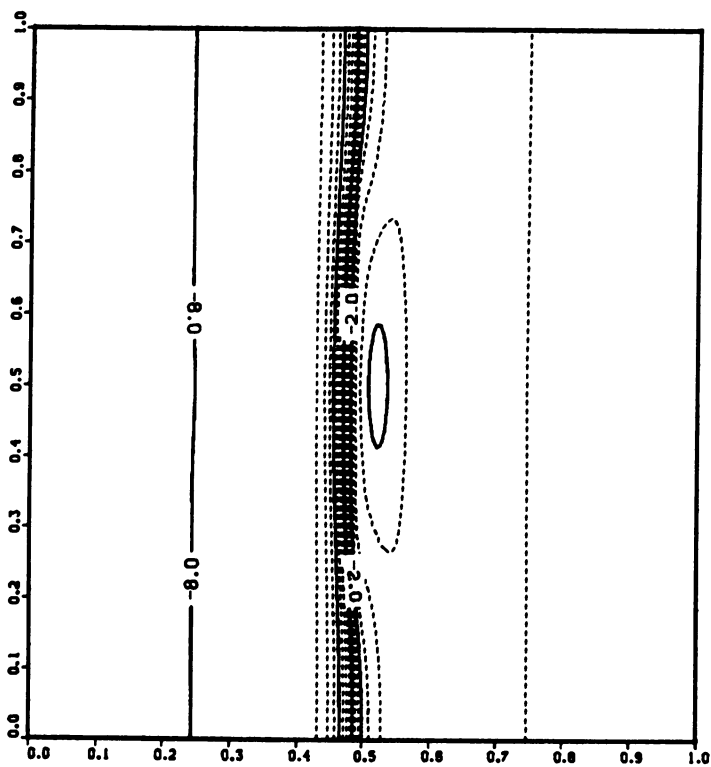


Figure 6. Continued. (c)  $t = 0.7$ . Continued on next page.

Figure 6. *Continued.* (d)  $t = 0.9$ .

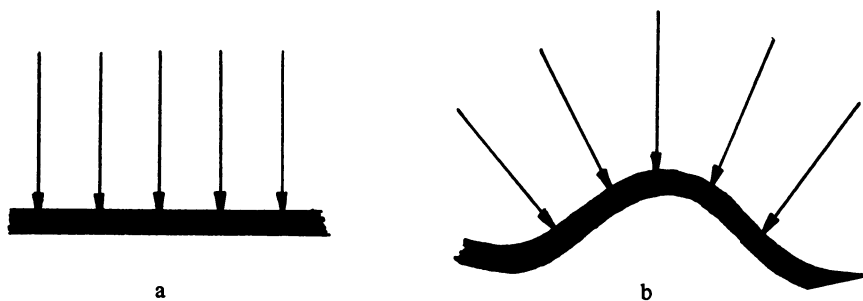


Figure 7. (a) Planar front. (b) Corrugated front.

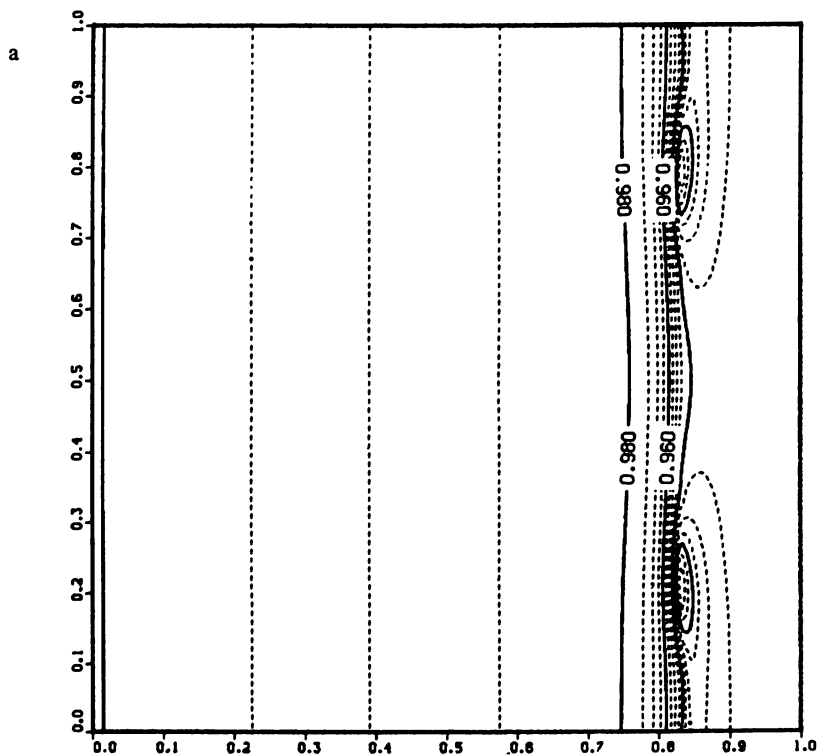


Figure 8. Pressure contours. (a)  $t = 0.3$ . Continued on next page.

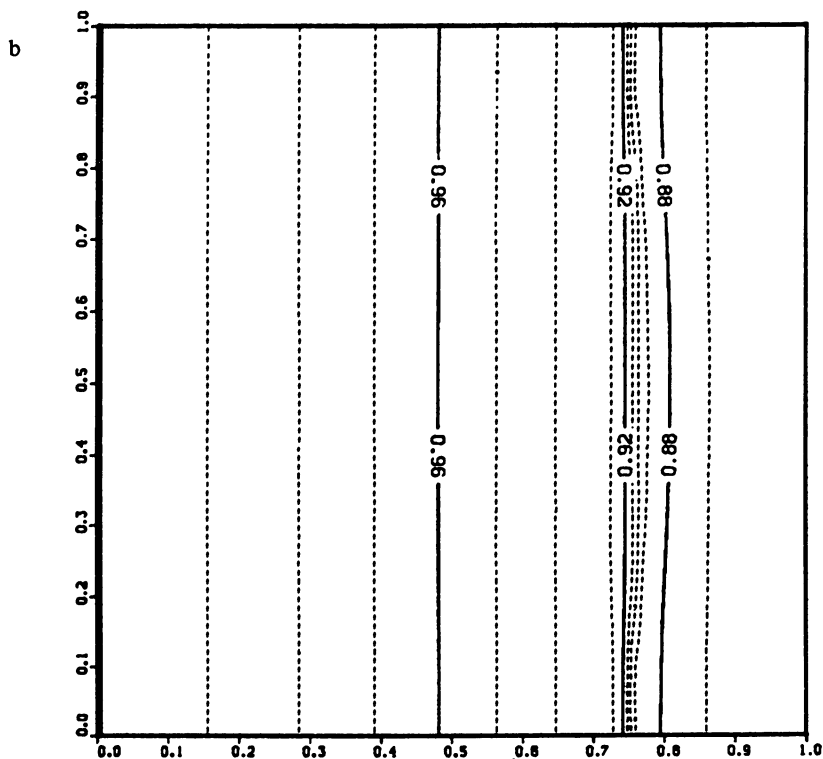


Figure 8. *Continued.* (b)  $t = 0.4$ . *Continued on next page.*

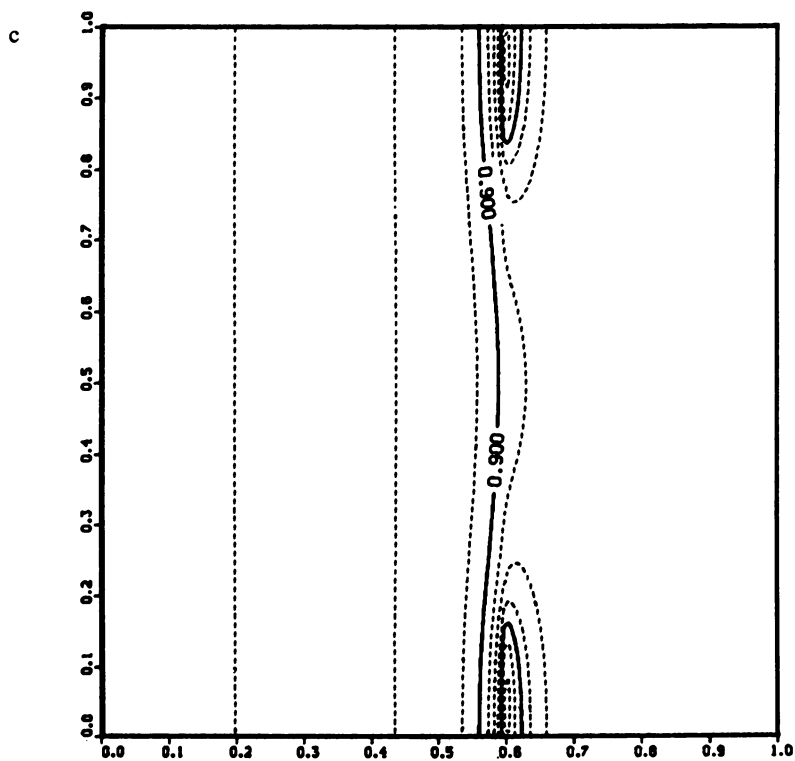


Figure 8. *Continued.* (c)  $t = 0.7$ . *Continued on next page.*



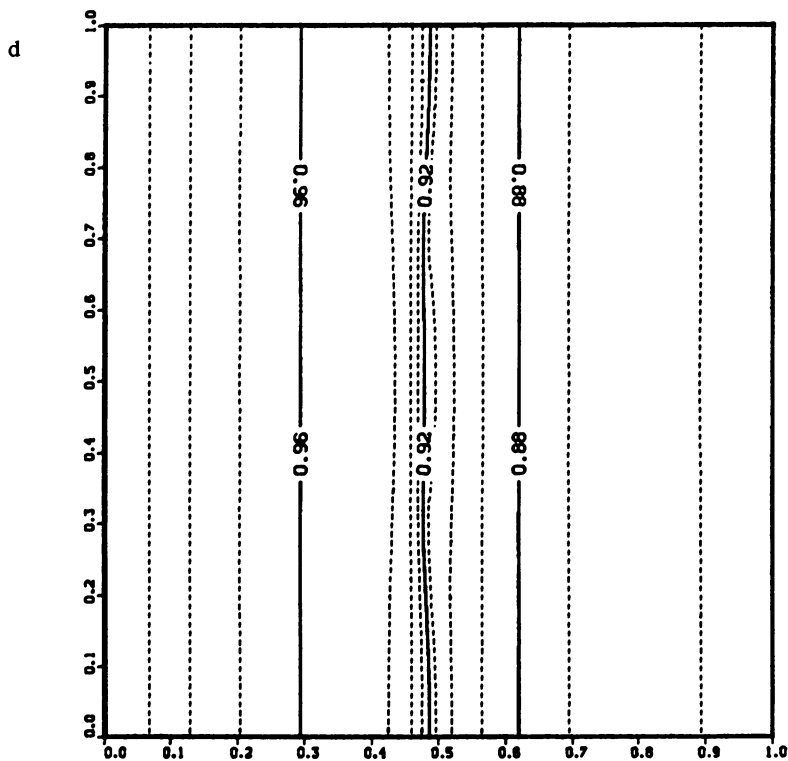


Figure 8. *Continued.* (d)  $t = 0.9$ . *Continued on next page.*

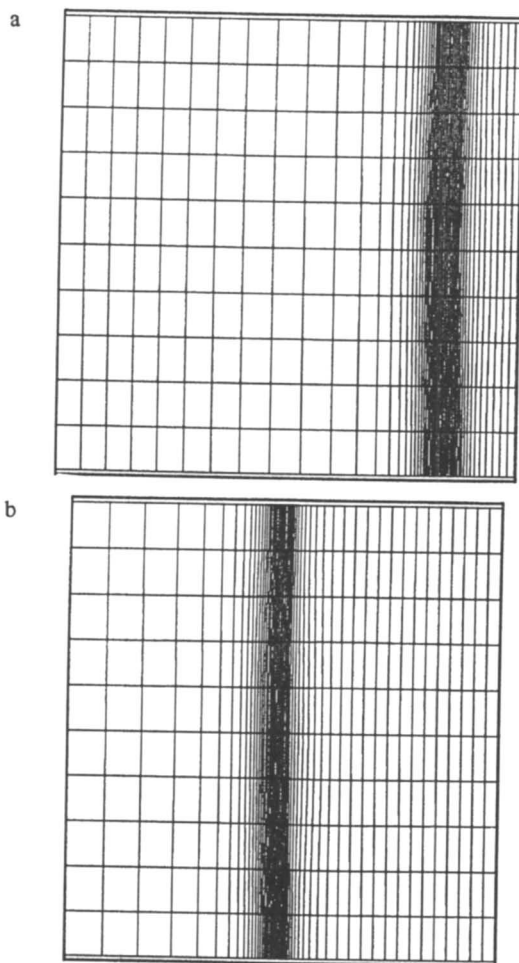


Figure 9. Adaptive mesh plot. (a)  $t = 0.3$ . (b)  $t = 0.9$ .

seen in Figure 9. The grid points move very close to one another in one coordinate direction, but virtually no adaption takes place in the other direction, as should have, observing the pockets in the pressure contours in Figure 8. We hope to improve on our implementation of this in the future.

We did not attempt to perform two-dimensional calculations on an equispaced grid. According to our estimates, it would have taken approximately 3 hours of CPU time to integrate the governing equations from time  $t = 0.0$  till  $t = 1.0$  on a Cray-1 computer as compared to 25 minutes of CPU time using the adaptive mesh.

CONCLUSIONS AND DISCUSSION

It was shown that adaptive regridding techniques can provide us with a very powerful tool for the solution of problems involving front phenomena. The adaptive mesh with built in properties of smoothness and orthogonality reduces the error in the solution by accurately resolving the high gradient regions. For a 2D problem the time of calculation can be reduced by an order of magnitude. The adaptive technique proved that difficult 2D and 3D problems can be solved on the current generation of supercomputers and that simulation of problems is possible which without regridding were considered to be computationally infeasible.

LITERATURE CITED

1. Saltzman, J. A Variational Method for Generating Multidimensional Adaptive Grids; Courant Mathematics and Computing Laboratory, New York University, 1982.
2. Kubicek, M.; Hlavacek, V. In Numerical Solution of Nonlinear Boundary Value Problems with Applications; Prentice Hall: Englewoods-Cliffs, N.Y., 1983.
3. Hlavacek, V.; Marek, M. 4th European Symp. Chem. React. Eng., Pergamon Press: Oxford, 1971.
4. Chong, T. H. SIAM J. Num. Anal. 1978, 15, 835.
5. Gropp, W. SIAM J. Sci. Stat. Comp. 1980, 1, 191.
6. Lam, D.; Simpson, R. In Advances in Computer Methods for Partial Differential Equations II; Vichnevetsky, R., Ed.; IMACS (AICA), 1977.
7. Smooke, M. D.; Koszykowski, M. L. Fully Adaptive Solutions of One-Dimensional Mixed Initial-Boundary Value Problems with Applications to Unstable Problems in Combustion; Sandia Report 83-8219.
8. Smooke, M. D.; Koszykowski, M. L. Two Dimensional Fully Adaptive Solutions of Solid-Solid Alloying Reactions; Sandia Report 83-8909.
9. Brackbill, J.; Saltzman, J. J. Comp. Physics 1982, 46, 342.
10. Yanenko, N. N.; Lisseiken, V. D.; Kovenia, V. M. Lecture Notes in Physics 1979, 90, 565.
11. Dwyer, H. A.; Kee, R. J.; Sanders, B. R. AIAA J. 1980, 18, 1205.
12. Hindman, R. G. AIAA J. 1982, 20, 1359.
13. Thompson, J. F. AIAA 21st Aerospace Sciences Meeting, 1983, paper 83-0447.
14. Aldushin, A. P.; Merzhanov, A. G.; Seplyarskii, B. S. Fizika Goreniya i Vzryva 1976, 12, 323.
15. Aldushin, A. P.; Seplyarskii, B. S.; Shkadinskii, K. G. Fizika Goreniya i Vzryva 1980, 16, 36.

RECEIVED June 15, 1987

## Chapter 21

# Extinction of Counterflow Premixed Laminar Flames

M. D. Smooke<sup>1</sup> and V. Giovangigli<sup>2</sup>

<sup>1</sup>Department of Mechanical Engineering, Yale University, New Haven, CT 06520

<sup>2</sup>Laboratoire de Mécanique Théorique, Université Paris VI, 4 Place Jussieu, 75230 Paris Cedex 05, France and Laboratoire d'Energétique, Ecole Centrale des Arts et Manufactures, 92290 Chatenay-Malabry, France

Problems in combustion and heat and mass transfer often depend upon one or more physical/chemical parameters. In many cases the combustion scientist is interested in knowing how the solution will behave if one or more of these parameters is varied. For some parameter regimes the governing equations can produce multiple solutions and the branches of the solution curve are linked via singular points. It is at these singular points, however, that the system exhibits special behavior. To be able to predict the solution structure in the neighborhood of these points, we employ a phase-space, pseudo arclength, continuation method that utilizes Newton-like iterations and adaptive gridding techniques. We apply the method in the solution of counterflow premixed laminar flames.

The modeling of steady-state problems in combustion and heat and mass transfer can often be reduced to the solution of a system of ordinary or partial differential equations. In many of these systems the governing equations are highly nonlinear and one must employ numerical methods to obtain approximate solutions. The solutions of these problems can also depend upon one or more physical/chemical parameters. For example, the parameters may include the strain rate or the equivalence ratio in a counterflow premixed laminar flame (1-2). In some cases the combustion scientist is interested in knowing how the system *will* behave if one or more of these parameters is varied. This information can be obtained by applying a first-order sensitivity analysis to the physical system (3). In other cases, the researcher may want to know how the system *actually* behaves as the parameters are adjusted. As an example, in the counterflow premixed laminar flame problem, a solution could be obtained for a specified value of the strain

0097-6156/87/0353-0404\$06.00/0  
© 1987 American Chemical Society

rate; this solution could then be used as a starting estimate for a predictor-corrector continuation process in the same parameter. In many applications this procedure works well. However, when there are multiple solutions and the solution curve, when plotted versus the parameter that is varied, turns back on itself by passing through a singular point, this procedure encounters difficulty. It is at these singular points, however, that the system often experiences special behavior. For example, in the solution of counterflow premixed laminar flames, as the strain rate is increased past a critical value, the flame will extinguish. Similarly, for a given strain rate, as the equivalence ratio is either increased or decreased past a critical value, the flame will also extinguish. Hence, accurate knowledge of these points provides information about the flame's flammability limits.

To solve problems of physical interest numerically one often discretizes the spatial operators of the governing ordinary or partial differential equations with the result that the solution of the original continuous problem is reduced to finding an approximation to this solution at each point of a discrete mesh. The discrete nonlinear equations can be solved by Newton's method, or a variant thereof. In addition, if the solution contains regions of high spatial activity, then it is essential for reasons of both efficiency and accuracy that adaptive spatial grids be employed. However, in the neighborhood of singular points, i.e., turning points, where the derivative of the solution curve with respect to the parameter possesses a vertical tangent, Newton's method encounters difficulties. To be able to follow the solution in the neighborhood of turning points, we modify the basic solution algorithm and employ a path tracing continuation method in which points on the arc of solutions are computed. In this paper we apply a powerful combination of continuation techniques, Newton-like iterations and adaptive gridding in the study of the extinction of strained premixed laminar flames. In particular, we investigate the extinction of hydrogen-air flames by a combination of strain rate and equivalence ratio variation. The governing conservation equations are modeled with complex transport and detailed chemical kinetics.

### **Problem Formulation**

Strained premixed laminar flames have played an important role in recent theories of turbulent premixed combustion. The reacting surface in such models can be viewed as being composed of a number of laminar flamelets (see e.g., Libby and Bray, (4), Libby and Williams, (5) and Bray, Libby and Moss, (6)). The flamelets are often modeled by considering counterflowing streams of reactants or counterflowing streams of reactants and products. From an experimental viewpoint, these flames can be produced when a single reactant stream impinges on an adiabatic wall or when two counterflowing reactant streams (or a reactant stream and a product stream) emerge from two counterflowing coaxial jets. In the neighborhood of the stagnation point produced by these flows, a chemically reacting boundary layer is established. The governing conservation

equations can be reduced to a set of nonlinear two-point boundary value problems along the stagnation point streamline. When there is a single reactant jet, only one reaction zone is produced. However, if there are two reactant streams and each has the same exit velocity and equivalence ratio, then a double flame is produced with a plane of symmetry through the stagnation point and parallel to the two jets (see Figure 1).

In this paper we consider doubly premixed laminar flames produced by two counterflowing coaxial jets. By applying appropriate boundary conditions at the plane of symmetry, the model we consider is, in principle, equivalent to that of a single reactant stream impinging on an adiabatic wall with slip. Our model for counterflowing premixed laminar flames assumes a laminar, stagnation point flow. We model the system by employing a boundary layer approximation. The governing equations for mass, momentum, chemical species and energy in rectangular coordinates can be written in the form (2)

$$\frac{\partial(\rho u)}{\partial x} + \frac{\partial(\rho v)}{\partial y} = 0 \quad (2.1)$$

$$\rho u \frac{\partial u}{\partial x} + \rho v \frac{\partial u}{\partial y} + \frac{\partial p}{\partial x} - \frac{\partial}{\partial y} \left( \mu \frac{\partial u}{\partial y} \right) = 0 \quad (2.2)$$

$$\rho u \frac{\partial Y_k}{\partial x} + \rho v \frac{\partial Y_k}{\partial y} + \frac{\partial}{\partial y} (\rho Y_k V_{ky}) - \dot{w}_k W_k = 0, \quad k = 1, 2, \dots, K \quad (2.3)$$

$$\rho u c_p \frac{\partial T}{\partial x} + \rho v c_p \frac{\partial T}{\partial y} - \frac{\partial}{\partial y} \left( \lambda \frac{\partial T}{\partial y} \right) + \sum_{k=1}^K \rho Y_k V_{ky} c_{pk} \frac{\partial T}{\partial y} + \sum_{k=1}^K \dot{w}_k W_k h_k = 0 \quad (2.4)$$

The system is closed with the ideal gas law,

$$\rho = \frac{p \bar{W}}{RT} \quad (2.5)$$

In these equations  $x$  and  $y$  denote independent spatial coordinates;  $T$ , the temperature;  $Y_k$ , the mass fraction of the  $k^{\text{th}}$  species;  $p$ , the pressure;  $u$  and  $v$  the tangential and the transverse components of the velocity, respectively;  $\rho$ , the mass density;  $W_k$ , the molecular weight of the  $k^{\text{th}}$  species;  $\bar{W}$ , the mean molecular weight of the mixture;  $R$ , the universal gas constant;  $\lambda$ , the thermal conductivity of the mixture;  $c_p$ , the constant pressure heat capacity of the mixture;  $c_{pk}$ , the constant pressure heat capacity of the  $k^{\text{th}}$  species;  $\dot{w}_k$ , the molar rate of production of the  $k^{\text{th}}$  species per unit volume;  $h_k$ , the specific enthalpy of the  $k^{\text{th}}$  species;  $\mu$  the viscosity of the mixture and  $V_{ky}$ , the diffusion velocity of the  $k^{\text{th}}$  species in the  $y$  direction. The free stream tangential and transverse velocities at the edge of the boundary layer are given by  $u_e = ax$  and  $v_e = -ay$ , respectively, where  $a$  is the strain rate. The strain rate is a measure of the "stretch" in the flame due to the imposed flow. The form of the chemical production rates and the diffusion velocities can be found in (7-8).

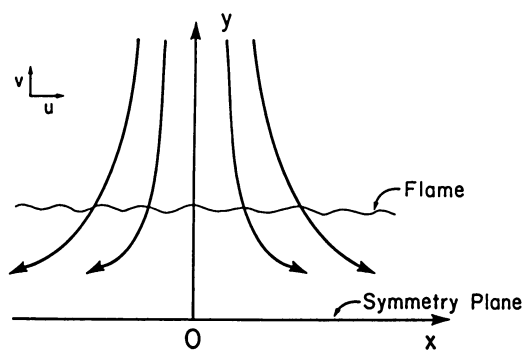


Figure 1. Schematic of the stagnation point flow configuration.

Upon introducing the notation

$$f' = \frac{u}{ax} \quad (2.6)$$

$$V = \rho v \quad (2.7)$$

where  $f'$  is related to the derivative of a modified stream function (see e.g., Dixon-Lewis et al., (9)), the boundary layer equations can be transformed into a system of ordinary differential equations valid along the stagnation-point streamline  $x = 0$ . For a system in rectangular coordinates, we have

$$\frac{dV}{dy} + a\rho f' = 0 \quad (2.8)$$

$$\frac{d}{dy} \left( \mu \frac{df'}{dy} \right) - V \frac{df'}{dy} + a(\rho_e(\phi) - \rho(f')^2) = 0 \quad (2.9)$$

$$-\frac{d}{dy}(\rho Y_k V_{k_y}) - V \frac{dY_k}{dy} + \dot{w}_k W_k = 0, \quad k = 1, 2, \dots, K \quad (2.10)$$

$$\frac{d}{dy} \left( \lambda \frac{dT}{dy} \right) - c_p V \frac{dT}{dy} - \sum_{k=1}^K \rho Y_k V_{k_y} c_{pk} \frac{dT}{dy} - \sum_{k=1}^K \dot{w}_k W_k h_k = 0 \quad (2.11)$$

where  $\rho_e$  refers to the density at the edge of the boundary layer. The system is again closed with the ideal gas law.

Complete specification of the problem requires that boundary conditions be imposed at each end of the computational domain. At  $y = 0$  we have

$$V = 0 \quad (2.12)$$

$$\frac{df'}{dy} = 0 \quad (2.13)$$

$$\frac{dY_k}{dy} = 0, \quad k = 1, 2, \dots, K \quad (2.14)$$

$$\frac{dT}{dy} = 0 \quad (2.15)$$

and as  $y \rightarrow \infty$

$$f' = 1 \quad (2.16)$$

$$Y_k = Y_{k_e}(\phi), \quad k = 1, 2, \dots, K \quad (2.17)$$

$$T = T_e \quad (2.18)$$

where the temperature  $T_e$  and mass fractions  $Y_{k_e}(\phi)$ ,  $k = 1, 2, \dots, K$  at the edge of the boundary layer are specified.

We observe that, in addition to the strain rate  $a$ , the computational model depends on the equivalence ratio  $\phi$  which is a measure of the relative proportion



of fuel to air in the reactant stream. If the strain rate is increased past a critical value the flame will extinguish. Similarly, if the equivalence ratio is either increased or decreased past a critical point, the flame will extinguish. Hence, accurate knowledge of the behavior of counterflow premixed flames as these quantities are varied can provide information about the flame's flammability limits. Our goal is to predict accurately and efficiently these extinction limits. This information can then be used in theories of turbulent premixed combustion.

### Method of Solution

Solution of the equations in (2.8-2.18) proceeds with an adaptive nonlinear boundary value method. The solution procedure has been discussed in detail elsewhere (10) and we outline only the essential features here. Our goal is to obtain a discrete solution of the governing equations on the mesh  $\mathcal{M}$

$$\mathcal{M} = \{0 = y_0 < y_1 < \dots < y_m = L\} \quad (3.1)$$

where  $h_j = y_j - y_{j-1}$ ,  $j = 1, 2, \dots, m$ , and where the value of  $L$  is related to the jet separation distance.

With the continuous differential operators replaced by difference expressions, we convert the problem of finding an analytic solution of the governing equations to one of finding an approximation to this solution at each point of the mesh  $\mathcal{M}$ . We seek the solution  $U^*$  of the nonlinear system of difference equations

$$F(U) = 0 \quad (3.2)$$

For an initial solution estimate  $U^0$  that is sufficiently "close" to  $U^*$ , the system of equations in (3.2) can be solved by Newton's method. We write

$$J(U^k)(U^{k+1} - U^k) = -\lambda_k F(U^k), \quad k = 0, 1, \dots \quad (3.3)$$

where  $U^k$  denotes the  $k^{\text{th}}$  solution iterate,  $\lambda_k$  the  $k^{\text{th}}$  damping parameter ( $0 < \lambda \leq 1$ ) which should be chosen to ensure a reduction in the size of the Newton corrections at each iteration (see, e.g., Deuffhard, (11)) and  $J(U^k) = \partial F(U^k)/\partial U$  the Jacobian matrix. A system of linear block tridiagonal equations must be solved at each iteration for corrections to the previous solution vector. In practice, a modified Newton method is employed in which the Jacobian is re-evaluated periodically (12).

Once a solution is obtained on an initial mesh, we adapt the grid in regions where the dependent solution components exhibit high spatial activity. We determine the mesh by subequidistributing the difference in the components of the discrete solution and its gradient between adjacent mesh points (10). Upon denoting the vector of  $N$  dependent solution components by  $\tilde{U} = [\tilde{U}_1, \tilde{U}_2, \dots, \tilde{U}_N]^T$ , we seek a mesh  $\mathcal{M}$  such that

$$\int_{y_j}^{y_{j+1}} \left| \frac{d\tilde{U}_i}{dy} \right| dy \leq \delta \left| \max_{0 \leq v \leq L} \tilde{U}_i - \min_{0 \leq v \leq L} \tilde{U}_i \right| \quad \begin{matrix} j = 0, 1, \dots, m-1 \\ i = 1, 2, \dots, N \end{matrix} \quad (3.4)$$

and

$$\int_{y_j}^{y_{j+1}} \left| \frac{d^2 \tilde{U}_i}{dy^2} \right| dy \leq \gamma \left| \max_{0 \leq y \leq L} \frac{d\tilde{U}_i}{dy} - \min_{0 \leq y \leq L} \frac{d\tilde{U}_i}{dy} \right| \quad \begin{matrix} j = 1, 2, \dots, m-1 \\ i = 1, 2, \dots, N \end{matrix} \quad (3.5)$$

where  $\delta$  and  $\gamma$  are small numbers less than one and the maximum and minimum values of  $\tilde{U}_i$  and  $d\tilde{U}_i/dy$  are obtained from a converged numerical solution on a previously determined mesh. We also impose the added constraint that the mesh produced by employing (3.4) and (3.5) be locally bounded. This smooths out rapid changes in the size of the mesh intervals. The advantage of this gridding procedure is that most of the expensive Jacobian evaluations are performed on relatively coarse grids and once the grid is sufficiently refined, Newton's method usually converges with only one or two iterations. The method also takes into account every component of the solution in forming a new mesh.

### Arclength Continuation

Procedures enabling the calculation of bifurcation and limit points for systems of nonlinear equations have been discussed, for example, by Keller (13) Heinemann et al. (14-15) and Chan (16). In particular, in the work of Heineman et al., a version of Keller's pseudo-arclength continuation method was used to calculate the multiple steady-states of a model one-step, nonadiabatic, premixed laminar flame (Heinemann et al., (14)) and a premixed, nonadiabatic, hydrogen-air system (Heinemann et al., (15)).

In our computational model the strain rate and the equivalence ratio are the natural bifurcation parameters. If we denote either of these parameters by  $\alpha$ , then the system of equations in (3.2) can be written in the form

$$F(U, \alpha) = 0 \quad (4.1)$$

where specific reference to the parametric dependence of  $F$  on  $\alpha$  has been made. As the flame nears extinction (either from an increase in the strain rate or from a change in the equivalence ratio), the maximum value of the temperature decreases. At the extinction point the Jacobian of the system is singular. To alleviate the computational difficulties, a modified form of the governing equations is solved (13). We introduce the parameter  $\alpha$  as a new dependent variable. The vector of dependent variables  $(U, \alpha)^T$  can now be considered functions of a new independent parameter  $s$ . If we define

$$Z(s) = (U(s), \alpha(s))^T \quad (4.2)$$

then the new problem we want to solve is given by

$$G(Z, s) = 0 \quad (4.3)$$

where

$$G(Z, s) = \begin{bmatrix} F(U(s), \alpha(s)) \\ N(U(s), \alpha(s), s) \end{bmatrix} = \begin{bmatrix} F(Z(s)) \\ N(Z(s), s) \end{bmatrix} \quad (4.4)$$

and where  $N$  is an arbitrary normalization. The normalization is chosen such that  $s$  approximates the arclength of the solution branch in the space  $(U, \alpha)$ .

The Jacobian of the new system can be written in the form

$$J(Z, s) = G_Z(Z, s) = \begin{bmatrix} F_U(U(s), \alpha(s)) & F_\alpha(U(s), \alpha(s)) \\ N_U(U(s), \alpha(s), s) & N_\alpha(U(s), \alpha(s), s) \end{bmatrix} \quad (4.5)$$

where  $F_U, F_\alpha, N_U$  and  $N_\alpha$  denote the appropriate partial derivatives. It can be shown that at a simple turning point, even though  $F_U$  is singular  $J$  is not. We point out that the Jacobian of the system in (3.2) is block tridiagonal. However, after introduction of  $\alpha$  as a dependent variable along with the extra normalization condition, the block tridiagonal structure of the Jacobian is destroyed. For the normalizations considered by Heinemann et al. (14-15) (see also Keller, (13)) this is the case. Although solution of the system of linear equations corresponding to (4.3) can proceed by methods discussed in (16), we would like to maintain the basic block tridiagonal structure of the Jacobian. In this way we can utilize the solution method used in solving adiabatic, premixed, laminar flames (17), burner-stabilized, premixed, laminar flames (10), counterflow, laminar, diffusion flames (18), and the extinction problems we consider here (2).

For each value of the parameter  $s$ , we want to obtain the corresponding value of  $\alpha$  and the remaining dependent solution components. We point out that, for each value of the pseudo-arclength,  $\alpha$  is constant. It satisfies the trivial differential equation

$$\frac{d}{dy}(\alpha) = 0 \quad (4.6)$$

Hence, we can maintain the block tridiagonal structure of the Jacobian in (4.5) if we introduce the parameter  $\alpha$  as a dependent variable at  $m$  of the  $m + 1$  grid points and if we specify a normalization condition at the remaining grid point that does not introduce nonzero Jacobian entries outside of the three block diagonals. The success of this procedure depends upon the choice of the normalization condition.

In flame extinction studies the maximum temperature is used often as the ordinate in bifurcation curves. In the counterflowing premixed flames we consider here, the maximum temperature is attained at the symmetry plane  $y = 0$ . Hence, it is natural to introduce the temperature at the first grid point along with the reciprocal of the strain rate or the equivalence ratio as the dependent variables in the normalization condition. In this way the block tridiagonal structure of the Jacobian can be maintained. The final form of the governing equations we solve is given by (2.8)-(2.18), (4.6) and the normalization condition

$$N = \frac{dT(0, s_0)}{ds}(T(0, s) - T(0, s_0)) + \frac{d}{ds}(\alpha(0, s_0))(\alpha(0, s) - \alpha(0, s_0)) - (s - s_0) = 0 \quad (4.7)$$

where  $\alpha$  represents either  $1/a$  or  $\phi$ . This normalization is such that  $s$  approximates the arclength of the solution branch in the space  $(T(0), \alpha)$ .

## Numerical Results

In this section we apply the adaptive boundary value solution procedure and the pseudo-arclength continuation method to a set of strained premixed hydrogen-air flames. Our goal is to predict accurately and efficiently the extinction behavior of these flames as a function of the strain rate and the equivalence ratio. Detailed transport and complex chemical kinetics are included in all of the calculations. The reaction mechanism for the hydrogen-air system is listed in Table I (17).

**Strain Rate Extinction.** We performed a sequence of strain rate calculations for an 8.4% and a 9.3% (mole fraction) hydrogen-air flame. The equivalence ratios of these flames are  $\phi = 0.219$  and  $\phi = 0.245$ , respectively. In both cases the Lewis number of the deficient reactant (hydrogen) was significantly less than one. In particular, at the input jet, the Lewis numbers were equal to 0.29 for both the 8.4% flame and the 9.3% flame. We also found that these values did not change by more than 15% through the flame.

A number of theoretical (5), (19-23), experimental (24-28) and computational (2), (23), (29-32), studies of premixed flames in a stagnation point flow have appeared recently in the literature. In many of these papers it was found that the Lewis number of the deficient reactant played an important role in the behavior of the flames near extinction. In particular, in the absence of downstream heat loss, it was shown that extinction of strained premixed laminar flames can be accomplished via one of the following two mechanisms. If the Lewis number (the ratio of the thermal diffusivity to the mass diffusivity) of the deficient reactant is greater than a critical value,  $Le_c > 1$ , then extinction can be achieved by flame stretch alone. In such flames (e.g., rich methane-air and lean propane-air flames) extinction occurs at a finite distance from the plane of symmetry. However, if the Lewis number of the deficient reactant is less than this value (e.g., lean hydrogen-air and lean methane-air flames), then extinction occurs from a combination of flame stretch and incomplete chemical reaction. Based upon these results we anticipate that the Lewis number of hydrogen will play an important role in the extinction process.

For an initial value of the strain rate, the adaptive boundary value method was used to obtain a solution on a computational domain of one cm. In Figures 2 and 3 we plot the temperature and the normal velocity component as a function of the distance from the symmetry plane for the 9.3% (mole fraction) flame with a strain rate of  $a = 200 \text{ sec}^{-1}$ . In Figures 4 and 5 we illustrate the major and minor species profiles. As we found in the solution of freely propagating premixed hydrogen-air flames, the  $HO_2$  and  $H_2O_2$  profiles peak before the flame zone. The remaining radical species peak in the region of maximum temperature. Once the initial strain rate calculation was completed, the modified arclength continuation procedure was implemented to obtain profiles of the maximum temperature versus the inverse of the strain rate. For each hydrogen-air mixture, the equidistribution procedure discussed in (3.4)-(3.5) was used to determine the mesh for the continuation steps. Each solution contained between

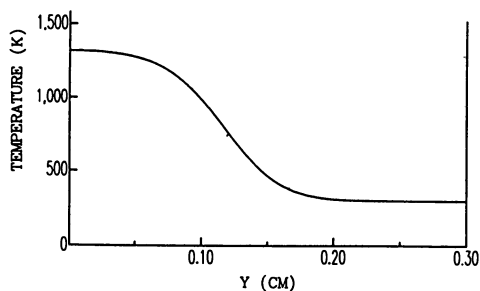


Figure 2. Temperature profile in K for the 9.3% (mole fraction) hydrogen-air flame with a strain rate of  $a = 200 \text{ sec}^{-1}$ .

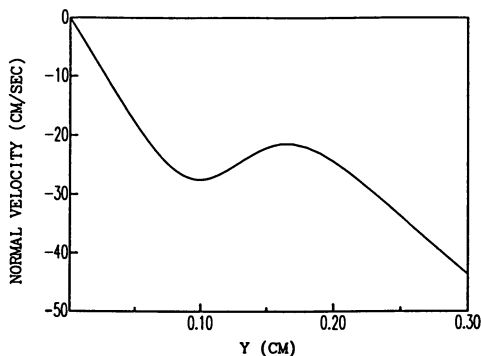


Figure 3. Normal velocity profile in cm/sec for the 9.3% (mole fraction) hydrogen air flame with a strain rate of  $a = 200 \text{ sec}^{-1}$ .

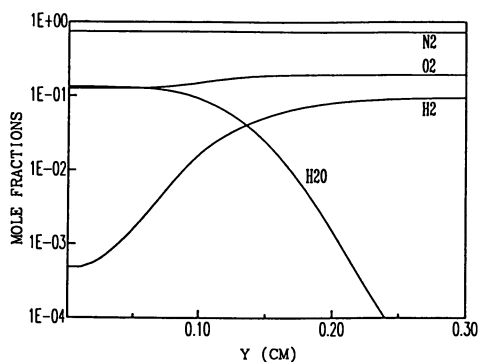


Figure 4. Major species profiles for the 9.3% (mole fraction) hydrogen-air flame with a strain rate of  $a = 200 \text{ sec}^{-1}$ .

TABLE I

Hydrogen-Air Reaction Mechanism  
 Rate Coefficients In The Form  $k_f = AT^\beta \exp(-E_0/RT)$ .  
 Units are moles, cubic centimeters, seconds, Kelvins and calories/mole

REACTION	A	$\beta$	E
1. $H_2 + O_2 \rightleftharpoons 2OH$	1.70E+13	0.000	47780.
2. $OH + H_2 \rightleftharpoons H_2O + H$	1.17E+09	1.300	3626.
3. $H + O_2 \rightleftharpoons OH + O$	5.13E+16	-0.816	16507.
4. $O + H_2 \rightleftharpoons OH + H$	1.80E+10	1.000	8826.
5. $H + O_2 + M \rightleftharpoons HO_2 + M^a$	2.10E+18	-1.000	0.
6. $H + O_2 + O_2 \rightleftharpoons HO_2 + O_2$	6.70E+19	-1.420	0.
7. $H + O_2 + N_2 \rightleftharpoons HO_2 + N_2$	6.70E+19	-1.420	0.
8. $OH + HO_2 \rightleftharpoons H_2O + O_2$	5.00E+13	0.000	1000.
9. $H + HO_2 \rightleftharpoons 2OH$	2.50E+14	0.000	1900.
10. $O + HO_2 \rightleftharpoons O_2 + OH$	4.80E+13	0.000	1000.
11. $2OH \rightleftharpoons O + H_2O$	6.00E+08	1.300	0.
12. $H_2 + M \rightleftharpoons H + H + M^b$	2.23E+12	0.500	92600.
13. $O_2 + M \rightleftharpoons O + O + M$	1.85E+11	0.500	95560.
14. $H + OH + M \rightleftharpoons H_2O + M^c$	7.50E+23	-2.600	0.
15. $H + HO_2 \rightleftharpoons H_2 + O_2$	2.50E+13	0.000	700.
16. $HO_2 + HO_2 \rightleftharpoons H_2O_2 + O_2$	2.00E+12	0.000	0.
17. $H_2O_2 + M \rightleftharpoons OH + OH + M$	1.30E+17	0.000	45500.
18. $H_2O_2 + H \rightleftharpoons HO_2 + H_2$	1.60E+12	0.000	3800.
19. $H_2O_2 + OH \rightleftharpoons H_2O + HO_2$	1.00E+13	0.000	1800.

<sup>a</sup> Third body efficiencies:  $k_5(H_2O) = 21k_5(Ar)$ ,  $k_5(H_2) = 3.3k_5(Ar)$ ,  $k_5(N_2) = k_5(O_2) = 0$ .

<sup>b</sup> Third body efficiencies:  $k_{12}(H_2O) = 6k_{12}(Ar)$ ,  $k_{12}(H) = 2k_{12}(Ar)$ ,  $k_{12}(H_2) = 3k_{12}(Ar)$ .

<sup>c</sup> Third body efficiency:  $k_{14}(H_2O) = 20k_{14}(Ar)$ .

50-70 adaptively chosen grid points. In addition, the Euler-Newton continuation procedure was used to help obtain solutions (physical and unphysical) for both increasing and decreasing values of the strain rate.

In Figure 6 we plot the maximum temperature versus the inverse of the strain rate for the 8.4% and 9.3% (mole fraction) hydrogen-air flames. Each C-shaped extinction curve was the result of 84-93 continuation steps. If we consider the 9.3% curve, we see that as we move along the upper branch in the direction of increasing strain rate, the peak temperature first increases and then decreases. Ultimately, as the value of  $dT_{max}/d(1/a) \rightarrow \infty$ , the flames extinguish ( $a_{ext} = 1443 \text{ sec}^{-1}$  for the 9.3 % flame and  $a_{ext} = 760 \text{ sec}^{-1}$  for the 8.3 % flame). We can, however, continue past the extinction point with the arclength procedure. We find that, as the strain rate begins to decrease, the peak temperature continues to fall. In the absence of Hopf bifurcation, the upper branch represents physical solutions and the lower branch unphysical solutions. The increase in the temperature can be attributed to the additional heat release

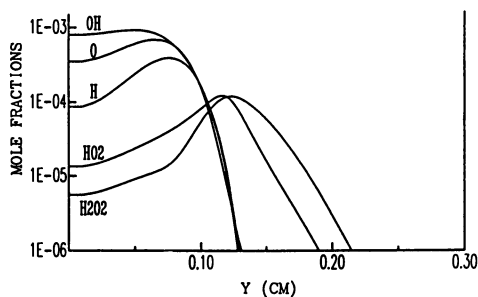


Figure 5. Minor species profiles for the 9.3% (mole fraction) hydrogen-air flame with a strain rate of  $a = 200 \text{ sec}^{-1}$ .

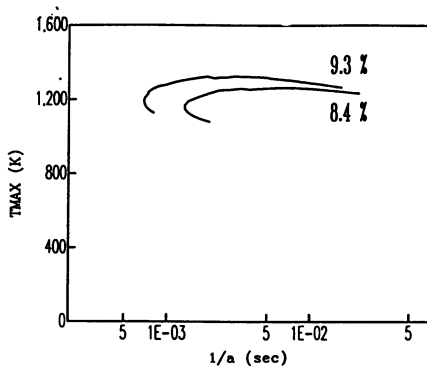


Figure 6. C-shaped extinction curves illustrating the maximum temperature versus the inverse of the strain rate for the 8.4% and 9.3% (mole fraction) hydrogen-air flames.

that results from the diffusion of hydrogen (the deficient reactant) from the unburnt mixture into the reaction zone. This excess heat release is larger than the conductive heat flow from the reaction zone to the unburnt mixture. As the strain rate continues to increase, however, the peak temperature finally decreases. Eventually, as the reaction zone is pressed against the stagnation surface, incomplete combustion occurs due to the decreased residence time and the flame extinguishes.

It is interesting to note that the adiabatic flame temperature of a freely propagating (unstrained) 9.3% (mole fraction) hydrogen-air flame is 1046 K while the peak temperature in Figure 6 is approximately 1324 K. Similarly, the adiabatic flame temperature of a freely propagating 8.4% (mole fraction) hydrogen-air flame is 977 K while the peak temperature in Figure 6 is 1264 K. Hence, we have Lewis number temperature increases of 278 K and 287 K, respectively. These peak temperatures as well as the extinction behavior illustrated in Figure 6 are in excellent qualitative agreement with the asymptotic results of Libby and Williams (22). Good quantitative agreement, however, is, in general, not feasible (Giovangigli and Candel, (23)).

If we continue the arclength process such that the strain rate decreases even further, we will continue to move along the unphysical branch and eventually reach another turning point—an ignition point. After the ignition point is passed, we will move on to the extinguished solution branch. We have not calculated the ignition points since they occur at strain rates so low that the corresponding flames are physically uninteresting and it is impossible to stabilize such a flame in the laboratory (see also Smith et al., (29)).

**Lean and Rich Extinction.** Extinction of strained premixed laminar flames can also be obtained (for a given strain rate) by adjusting the equivalence ratio. In particular, experimental results show that as the equivalence ratio is either increased or decreased past a critical point, the flame extinguishes. Starting with a hydrogen-air flame having an equivalence ratio  $\phi = 0.245$  (9.3 % mole fraction) and a strain rate of  $a = 1000 \text{ sec}^{-1}$  which was obtained during the strain rate extinction calculations, the Euler-Newton adaptive continuation procedure was used to obtain solutions (physical and unphysical) for all values of the equivalence ratio. Each solution contained between 80-120 adaptively chosen grid points.

Starting from stoichiometric conditions ( $\phi = 1$ ) and then proceeding in the lean direction ( $\phi < 1$ ), we anticipate that the peak flame temperature will be reduced gradually. In addition, as the maximum temperature is lowered and the corresponding adiabatic flame speed of an unstrained ( $a = 0$ ) flame is reduced, we anticipate that the flame will move closer to the plane of symmetry. Ultimately, as the fuel to air ratio is lowered below a critical value, radical production in the flame will be severely restricted and the flame will extinguish (lean extinction). The arclength continuation procedure will then generate unphysical solutions for additional continuation steps until a maximum value of the



equivalence ratio is reached. At this point (rich extinction) physical solutions will again be generated and the maximum flame temperature will begin to rise and the distance of the flame from the plane of symmetry will increase as well.

The adaptive continuation method was able to generate closed response curves illustrating these phenomena. In particular, in Figure 7 we illustrate the maximum temperature versus the equivalence ratio for a hydrogen-air system with  $a = 1000 \text{ sec}^{-1}$ . We observe a 1500 K temperature variation among all the flames computed. The lean extinction occurred at  $\phi = 0.227$  with  $T = 1177 \text{ K}$  and the rich extinction at  $\phi = 4.6$  with  $T = 1256 \text{ K}$ . Variations in the peak temperature occur over a much smaller range of equivalence ratios for lean systems than under rich conditions. In Figure 8 we illustrate the distance of the flame from the plane of symmetry. The flame can shift its position by almost 0.9 cm from lean to slightly rich conditions and then back again to very rich conditions. In particular, the position of the flame from the symmetry plane was equal to 0.03556 cm at the lean extinction limit, 0.8639 cm at its furthest point and 0.1073 cm at the rich extinction limit. A total of 2500 continuation steps were used in generating the closed curves in Figures 7 and 8. In all cases the adaptive mesh was able to maintain resolution in the flame zone as the flame's position adjusted accordingly.

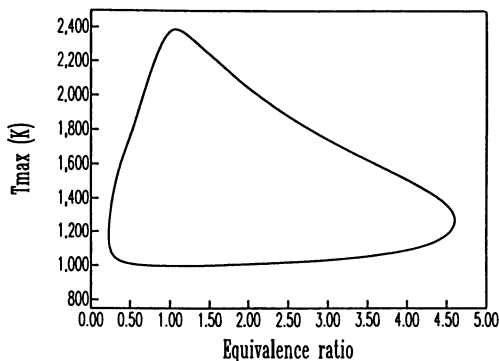


Figure 7. Extinction curve illustrating the maximum temperature versus the equivalence ratio for hydrogen-air flames with a strain rate of  $a = 1000 \text{ sec}^{-1}$ .

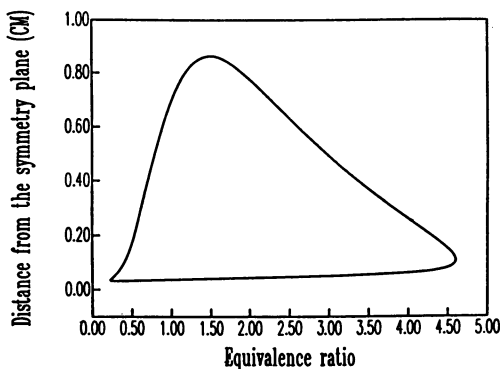


Figure 8. Distance of the flame from the symmetry plane versus the equivalence ratio for hydrogen-air flames with a strain rate of  $a = 1000 \text{ sec}^{-1}$ .

### Acknowledgment

The research was supported in part by Direction des Recherches et Etudes Techniques and the Office of Naval Research. We would like to thank the Scientific Council of the Centre de Calcul Vectoriel pour la Recherche for providing access to a CRAY-1 computer and the Centre Inter Regional de Calcul Electronique for providing computational resources. In addition, we would like to thank Professors S. Candel and G. Duvaut for their support and helpful discussions.

### References

1. Giovangigli, V. and Smooke, M. D. (1987). *J. Comp. Phys.* **68**, p. 327.
2. Giovangigli, V. and Smooke, M. D. (1987). *Comb. Sci. and Tech.* **53**, p. 23.
3. Smooke, M. D., Reuven, Y., Rabitz, H. and Dryer, F. L., to be published in *Comb. Sci. and Tech.*, (1987).
4. Libby, P. A. and Bray, K. N. C (1980). *Comb. and Flame* **39**, p. 33.
5. Libby, P. A. and Williams, F. A. (1982). *Comb. and Flame* **44**, p. 287.
6. Bray, K. N. C., Libby, P. A. and Moss, J. B. (1984). *Comb. Sci. and Tech.* **41**, p. 143.
7. Kee, R. J., Miller, J. A. and Jefferson, T. H. (1980). Sandia National Laboratories Report, SAND80-8003.
8. Kee, R. J., Warnatz, J., and Miller, J. A. (1983). Sandia National Laboratories Report, SAND83-8209.
9. Dixon-Lewis, G., David, T., Haskell, P. H., Fukutani, S., Jinno, H., Miller, J. A., Kee, R. J., Smooke, M. D., Peters, N., Effelsberg, E., Warnatz, J. and Behrendt, F. (1982). Twentieth Symposium (International) on Combustion, Reinhold, New York, p. 1893.
10. Smooke, M. D. (1982). *J. Comp. Phys.* **48**, p. 72.
11. Deufhard, P. (1974). *Numer. Math.* **22**, p. 289.

12. Smooke, M. D. (1983). *J. Opt. Theory and Appl.* **39**, p. 489.
13. Keller, H. B. (1977). in *Applications of Bifurcation Theory*, P. Rabinowitz, Ed., Academic Press, New York.
14. Heinemann, R. F., Overholser, K. A. and Reddien, G. W. (1979). *Chem Eng. Sci.* **34**, p. 833.
15. Heinemann, R. F., Overholser, K. A. and Reddien, G. W. (1980). *AIChE Journal* **26**, p. 725.
16. Chan, T. (1984). in *Numerical Methods for Bifurcation Problems*, T. Kupper, H. Mittelmann and H. Weber, Eds., Birkhauser Verlag, Basel.
17. Smooke, M. D., Miller, J. A. and Kee, R. J. (1983). *Comb. Sci. and Tech.* **34**, p. 79.
18. Smooke, M. D., Miller, J. A. and Kee, R. J. (1985). in *Numerical Boundary Value ODEs*, U. M. Ascher and R. D. Russell, Eds., Birkhauser, Basel.
19. Sivashinsky, G. I. (1976). *ACTA Astronautica* **3**, p. 889.
20. Buckmaster, J. (1982). *Seventeenth Symposium (International) on Combustion*, Reinhold, New York, p. 835.
21. Libby, P. A., Liñan, A. and Williams, F. A. (1983). *Comb. Sci. and Tech.* **34**, p. 257.
22. Libby, P. A. and Williams, F. A. (1984). *Comb. Sci. and Tech.* **37**, p. 221.
23. Giovangigli, V. and Candel, S. (1986). *Comb. Sci. and Tech.*, in press.
24. Fang, M., Schmitz, R. A. and Ladd, R. G. (1971). *Comb. Sci. and Tech.* **4**, p. 143.
25. Law, C. K., Ishizuka, S. and Mizomoto, M. (1981). *Eighteenth Symposium (International) on Combustion*, Reinhold, New York, p. 1791.
26. Ishizuka, S. and Law C. K. (1982). *Nineteenth Symposium (International) on Combustion*, Reinhold, New York, p. 327.
27. Sato, J. (1982). *Nineteenth Symposium (International) on Combustion*, Reinhold, New York, p. 1541.
28. Tsuji, H. and Yamaoka, I. (1982). *Nineteenth Symposium (International) on Combustion*, Reinhold, New York, p. 1533.
29. Smith, H. W., Schmitz, R. A. and Ladd, R. G. (1971). *Comb. Sci. and Tech.* **4**, p. 131.
30. Sato, J. and Tsuji, H. (1978). in *Proceedings of the Sixteenth Japanese Symposium on Combustion*, p. 13.
31. Sato, J. and Tsuji, H. (1983). *Comb. Sci. and Tech.* **33**, p. 193
32. Darabiha, N., Candel, S. and Marble, F. E. (1985). *Comb. and Flame* **64**, p. 203.

RECEIVED June 15, 1987

## Author Index

- Almlöf, Jan, 35  
 Bauschlicher, Charles W., Jr., 16  
 Behrens, R., 376  
 Bennett, Mark J., 295  
 Berendsen, H. J. C., 106  
 Bitsanis, I., 257  
 Blake, James F., 200  
 Brooks, Bernard R., 123  
 Brown, Robert A., 295  
 Cao, P.-L., 49  
 Catlow, C. R. A., 69  
 Chou, S.-H., 49  
 Clementi, E., 69,146,237  
 Coltrin, Michael E., 334  
 Davidson, Marc G., 162  
 Davis, H. T., 257  
 Degreve, J., 376  
 Delley, B., 49  
 de Vlieg, J., 106  
 Dimitriou, P., 376  
 Dupuis, M., 69,146  
 Egberts, E., 106  
 Evans, Greg H., 334  
 Fotiadis, Dimitrios I., 353  
 Freeman, A. J., 49  
 Fu, C.-L., 49  
 Gilmer, George H., 218  
 Giovangigli, V., 404  
 Grabow, Marcia H., 218  
 Halicioğlu, Timur, 16  
 Hirata, Fumio, 82  
 Hlavacek, V., 376  
 Jensen, Klavs F., 1,353  
 Jorgensen, William L., 200  
 Kee, Robert J., 334  
 Kevrekidis, Ioannis G., 284  
 Kim, Kwang, 82  
 Langhoff, Stephen R., 16  
 Levy, Ronald M., 82  
 Lie, G. C., 237  
 Lüthi, Hans Peter, 35  
 Ludovice, Peter J., 162  
 Madura, Jeffrey D., 200  
 McKenna, Donald R., 533  
 Moffat, Harry K., 353  
 Partridge, Harry, 16  
 Puszynski, J., 376  
 Ramprasad, N., 295  
 Schwenke, David W., 176  
 Sim, F., 69  
 Smooke, M. D., 404  
 Suter, Ulrich W., 162  
 Taylor, Peter R., 16  
 Tirrell, M. V., 257  
 Truhlar, Donald G., 1,176  
 Valone, S., 376  
 van Gunsteren, W. F., 106  
 Vanderlick, T. K., 257  
 Villar, H. O., 146  
 Watts, J. D., 69  
 Wierschke, Scott D., 200  
 Wimmer, E., 49  
 Zhang, Peisen, 82

## Affiliation Index

- AT&T Bell Laboratories, 218  
 Cray Research, Inc., 49  
 ELORET Institute, 16  
 Ecole Centrale des Arts  
 et Manufactures, 404  
 IBM Corporation, 69,146,237  
 Los Alamos National Laboratory, 376  
 Massachusetts Institute  
 of Technology, 162,295  
 National Aeronautics and Space  
 Administration, 16  
 National Institutes of Health, 123  
 Northwestern University, 49  
 Princeton University, 284  
 Purdue University, 200  
 RCA Laboratories, 49  
 Rutgers University, 82  
 Sandia National Laboratories, 334

Stanford University, 16  
 State University of New York, 376  
 Université Paris VI, 404  
 University College of London, 69

University of Groningen, 106  
 University of Houston, 200  
 University of Keele, 69  
 University of Minnesota, 1,35,176,257,353  
 Yale University, 404

## Subject Index

### A

Ab initio calculations  
 addition of hydroxide ion to formaldehyde, 212  
 energy surfaces, 201–211  
 Adaptive continuation method, hydrogen–air flame, 417  
 Adaptive mesh  
 generation, variational approach, 378–381  
 model of filtration combustion process, 384  
 one spatial dimension, 381  
 plots, 391,402f  
 resolution in the hydrogen–air flame zone, 417  
 Adaptive nonlinear boundary value method, 409–410  
 Adatoms, density versus temperature, 222  
 Adsorbates, metal clusters, 28–29  
 Al clusters, 25–27,29  
 Al<sub>2</sub>  
 ground state, 29  
 theoretical spectroscopic constants, 20–22  
 Al<sub>3</sub>, degenerate states, 22  
 AlAs, growth, 371  
 AlGaAs, growth by MOCVD, 353–374  
 Algorithms  
 first generation, 291–292  
 models of physicochemical processes, 293  
 Alliant FX/1, performance on minimization problem, 168f  
 Alliant FX/8, performance on minimization problem, 168f  
 AMBER, 125  
 Amides, alkaline hydrolysis, 215  
 Anharmonic systems, direct evaluation of quantum time-correlation functions, 93  
 Apollo DSP–160, CHARMM performance, 129f  
 Arc-length continuation, steady states of a model premixed laminar flame, 410  
 Architecture, between parallel machines, 348  
 Arithmetic control processor, ST–100, 125  
 Arithmetic floating point operations, ST–100, 127  
 Arrhenius factor, equation, 226  
 Atmospheric chemistry, modeling, 12

Atomic natural orbitals, use, 18  
 Attached processors  
 FPS–164, 238–239  
 IBM hosts, 239  
 Aufbau principle, 51–52  
 Axial momentum, conservation of, CVD reactor, 337  
 Axilrod–Teller form, three-body interaction, 26

### B

BAC–MP4 method, description, 344–346  
 Band theory, crystal orbital method, 149  
 Be clusters, structures, 24–25  
 Bifurcation  
 fixed-point problems, 293  
 MOCVD reactor, 367  
 Bifurcation analysis, evolution of the cell shape in solidification, 305  
 Bifurcation diagram  
 cellular solidification microstructures, 315  
 thermophysical parameters, 305–308  
 Bifurcation parameters, computational model of premixed laminar flames, 410  
 Bifurcation theory, 300  
 Bilayer membranes, simulations, 115–117  
 Binary diffusion coefficients, CVD processes, 342  
 Binding energy, Al clusters, 26–27  
 Biochemical simulations, supercomputer use, 8  
 Biopolymers  
 interpretation of vibrational spectra, 92–100  
 restrained X-ray refinement, 86  
 simulations, solvent effects, 83  
 structure and dynamics, 82–103  
 Bond angles  
 ethylene, 59f  
 LDF theory, 63–65  
 Bond distances  
 diamondlike carbon clusters, 42f  
 doped polyacetylene, 154f  
 Bond indices, doped polyacetylene, 154f

Stanford University, 16  
 State University of New York, 376  
 Université Paris VI, 404  
 University College of London, 69

University of Groningen, 106  
 University of Houston, 200  
 University of Keele, 69  
 University of Minnesota, 1,35,176,257,353  
 Yale University, 404

## Subject Index

### A

Ab initio calculations  
 addition of hydroxide ion to formaldehyde, 212  
 energy surfaces, 201–211  
 Adaptive continuation method, hydrogen–air flame, 417  
 Adaptive mesh  
 generation, variational approach, 378–381  
 model of filtration combustion process, 384  
 one spatial dimension, 381  
 plots, 391,402f  
 resolution in the hydrogen–air flame zone, 417  
 Adaptive nonlinear boundary value method, 409–410  
 Adatoms, density versus temperature, 222  
 Adsorbates, metal clusters, 28–29  
 Al clusters, 25–27,29  
 Al<sub>2</sub>  
 ground state, 29  
 theoretical spectroscopic constants, 20–22  
 Al<sub>3</sub>, degenerate states, 22  
 AlAs, growth, 371  
 AlGaAs, growth by MOCVD, 353–374  
 Algorithms  
 first generation, 291–292  
 models of physicochemical processes, 293  
 Alliant FX/1, performance on minimization problem, 168f  
 Alliant FX/8, performance on minimization problem, 168f  
 AMBER, 125  
 Amides, alkaline hydrolysis, 215  
 Anharmonic systems, direct evaluation of quantum time-correlation functions, 93  
 Apollo DSP–160, CHARMM performance, 129f  
 Arc-length continuation, steady states of a model premixed laminar flame, 410  
 Architecture, between parallel machines, 348  
 Arithmetic control processor, ST–100, 125  
 Arithmetic floating point operations, ST–100, 127  
 Arrhenius factor, equation, 226  
 Atmospheric chemistry, modeling, 12

Atomic natural orbitals, use, 18  
 Attached processors  
 FPS–164, 238–239  
 IBM hosts, 239  
 Aufbau principle, 51–52  
 Axial momentum, conservation of, CVD reactor, 337  
 Axilrod–Teller form, three-body interaction, 26

### B

BAC–MP4 method, description, 344–346  
 Band theory, crystal orbital method, 149  
 Be clusters, structures, 24–25  
 Bifurcation  
 fixed-point problems, 293  
 MOCVD reactor, 367  
 Bifurcation analysis, evolution of the cell shape in solidification, 305  
 Bifurcation diagram  
 cellular solidification microstructures, 315  
 thermophysical parameters, 305–308  
 Bifurcation parameters, computational model of premixed laminar flames, 410  
 Bifurcation theory, 300  
 Bilayer membranes, simulations, 115–117  
 Binary diffusion coefficients, CVD processes, 342  
 Binding energy, Al clusters, 26–27  
 Biochemical simulations, supercomputer use, 8  
 Biopolymers  
 interpretation of vibrational spectra, 92–100  
 restrained X-ray refinement, 86  
 simulations, solvent effects, 83  
 structure and dynamics, 82–103  
 Bond angles  
 ethylene, 59f  
 LDF theory, 63–65  
 Bond distances  
 diamondlike carbon clusters, 42f  
 doped polyacetylene, 154f  
 Bond indices, doped polyacetylene, 154f

- Bond lengths**  
buckminsterfullerene, 44  
ethylene, 59*t*  
fluorine, 59*t*  
metal clusters, 25*t*, 28–29
- Bonding**  
metal clusters, 17  
transition-metal compounds, 20
- Born–Oppenheimer approximation**, 107, 177–178
- Boundary conditions**  
CVD reactor, 338, 342–343, 357–358  
model for strained premixed laminar flames, 408  
one-dimensional formulation of filtration combustion process, 384
- Boundary value problem**  
adaptive mesh generation in one direction, 381  
CVD processes, 343  
CVD reactor, 348
- Buckminsterfullerene**  
bond lengths, 44  
cohesive energy, 44  
stability, 46  
structure, 43–46
- Bulk fluid**  
couette flow, 280*t*  
*See also* Fluids, Micropore fluid
- Bulk graphite**, cohesive energy per carbon atom, 46
- Bulk normal fluid velocity**, CVD reactor, 343
- Butane**, quasiharmonic frequencies, 93, 94*t*
- C**
- Carbon clusters**  
carbon chains, 43  
clustering mechanisms, 35  
diamondlike clusters, 42–43  
electronic structure calculations, 35–46  
energy per carbon atom, 37, 40  
five-membered rings, 43–46  
graphite fragments, 37–38  
investigations, 35  
production, 35–26  
saturated peripheral bonds, 38–42  
*See also* Clusters
- Carbonyl compounds**  
addition of anionic nucleophiles, 200  
nucleophilic reactions, 200–215
- Carboxy-myoglobin**, molecular dynamics simulation, 133
- Carnahan formula**, hard space sphere fluids, 259
- Catalysts**, electronic structure calculations, 4
- Celerity 1260**, performance on minimization problem, 168*t*
- Cell interfaces**  
families, 313*f*  
nonorthogonal transformations, 310*f*
- Cellular dynamics**, interaction of shallow cells, 311–323
- Cellular interfaces**, families, 319*f*
- Cellular solidification**  
aperiodic dynamics for shallow cells, 320  
constitutional supercooling, 296  
details, 298  
microstructures, numerical analysis, 295–330  
onset from an initially planar melt–solid interface, 296  
*See also* Solidification  
microstructure
- Central processing unit (CPU) time**  
potential energy function calculation, 191  
solutions to vertical reactor simulations, 361
- Chain Rule Conservation Law Form**, 382
- Chapman–Enskog theory**, flow in a one-component fluid, 264
- Charge density**, DPPH molecule, 62*f*
- CHARMM**, 125, 127, 129*t*
- Chemical kinetics**, modeling in CVD reactors, 334–350
- Chemical plant design**, supercomputer use, 13
- Chemical reaction mechanisms**, CVD reactor, 344–346
- Chemical vapor deposition (CVD)**  
growth of thin films, 11  
importance of fluid flow, 335
- Chemical vapor deposition (CVD) reactor**  
chemical kinetics and transport, 346–350  
chemical reaction mechanisms, 344–346  
effect of wall cooling on susceptor heat flux uniformity, 341*f*  
ideal applications program, 347*f*  
radial-axial velocity field and temperature contours, 336*f*  
reactor wall thermal boundary conditions, 340  
relationship between disk temperature and spin rate, 338–340  
relationship of susceptor temperature to spin rate, 339*f*  
rotating disk, 336*f*  
silicon deposition rates as a function of susceptor temperature, 345*f*  
species profiles, 345*f*  
supercomputer applications to modeling, 334–350  
uniform deposition, 336–340
- Chemisorption**, atoms on Be<sub>13</sub> and Al<sub>13</sub> clusters, 28–29
- Chemkin**, relationship to transport software packages, 349*f*
- Chemkin 28**, software, 248

- Chloride ion, reaction with formyl and acetyl chloride, 206–209
- Chromophore line shapes, 100
- Circumferential momentum conservation of, CVD reactor, 337
- CVD near an infinite rotating disk, 340
- Close coupling formalism, description, 184–191
- Clusters  
convergence behavior, 149  
film–substrate material combinations, 231  
generation, 219  
polyacetylene, 150  
thin films, 235  
*See also* Carbon clusters, Metal clusters
- Codimension-two bifurcations, role in evolution of shallow cells, 311–320
- Cohesive energy  
buckminsterfullerene, 44  
carbon clusters, 37  
definition, 167–168  
monolayer graphite, 40
- Combustion, fuels, 12
- Complete active self-consistent field, calculation, 18
- Composite materials, modeling, 3
- Computational chemistry, global simulation approach, 237–254
- Computational investigations, nucleophilic reactions of carbonyl compounds, 200–215
- Computational science, progress, 239
- Computer simulations, biopolymers, 82–103
- Concentration fields, model predictions in MOCVD reactors, 374
- Configuration interaction method, energy of interaction between two molecules of water, 241–242
- Configuration space  
diffusive systems, 110  
nondiffusive systems, 110–111
- Conformational analysis, molecular dynamics, 140
- Consistent force field type potentials, use, 92
- Constitutional supercooling, 296
- Continuum solidification models  
numerical analysis, 308–311  
time integration scheme, 309–311
- Control processor, ST–100, 125
- Copper, reactions on silicon surfaces, 60–63
- Corannulene molecule, 45*f*
- Correlation energy, neglected in the Hartree–Fock approximation, 240–241
- Corrugated front, 391,398*f*
- Couette flow  
bulk fluid, 280*t*  
induction, 268  
micropore fluid, 280*t*  
momentum balance equation, 265
- Couette flow—*Continued*  
simulations  
density profiles, 275  
diffusivities, 275–277  
molecular dynamics, 267–270  
shear stress, 279–280  
velocity profiles, 277–279  
viscosity, 279–280  
structure induced by pore wall potential, 268
- Counterflow premixed laminar flames  
boundary layer approximation, 406  
extinction, 404–417  
flammability limits, 409  
*See also* Strained premixed laminar flames
- Coupled-air functional approach, 18–19
- Cray 1, 108,112,184
- Cray 1-S, 129*t*,344
- Cray 2, 36–37,358,371
- Cray X–MP, 168
- Cray X–MP/48  
CHARMM performance, 129*t*  
performance on minimization problem, 168*t*
- Crystal, energy relative to that of the bulk, 232*f*
- Crystal faces, cluster model, 17–18
- Crystal growth  
direct molecular dynamic simulations, 8  
entropy of fusion, 226  
high temperatures, 219  
kinetic Ising model, 235  
kinetics, 225  
modeling the solidification problem, 298  
molecular dynamics studies, 218–236  
sensitivity to the binding energy of atoms, 218  
supercomputer use, 10–11
- Crystal orbital method, systems with translational periodicity, 149
- Crystal surface  
close-packed orientation, 218  
schematic representation, 220*f*
- Crystalline films, incomplete wetting, 235
- Crystallization  
crystal–melt interface, 236  
low temperatures, 226  
simple melts, 228
- Crystallization rates, temperatures below the melting point, 225–226
- Crystallographic refinement, description, 87
- Crystallography  
observed structure factor amplitude, 88  
*See also* X-ray crystallography
- Crystals  
deposition from the vapor, 230  
morphology, 221
- Cu<sub>2</sub>, theoretical spectroscopic constants, 20
- Cu<sub>3</sub>, ab initio study, 22
- Cumulenes, 43



- Cu Be  
  *ab initio* study, 22–24  
  spectroscopic constants, 23*t*  
Cyber 205, 108,112,168,170,201
- D**
- Darcy's law, 383  
Debye–Waller factor, 88,92  
Defects, polyacetylene, 149–159  
Dendrites, microstructure formation, 295  
Dendritic solidification, details, 298  
Density distributions, bilayer membrane components, 117  
Density profiles  
  couette flow simulations, 275  
  micropore fluid, 269  
Deposition, silicon from silane in CVD reactor, 343–344  
Dielectric constants, biopolymers, 100  
Differential algebraic equation solver, 358  
Differential equations, boundary layer equations for strained premixed laminar flames, 408  
Diffuse functions, use, 202  
Diffusive systems  
  configuration space, 110  
  description, 110  
Diffusivities, couette flow simulations, 275–277  
Dihydrofolate reductase (DHFR), binding properties of an inhibitor, 112  
 $\alpha$ ,  $\alpha'$ -Diphenyl- $\beta$ -picryl-hydrazyl (DPPH) radical, 60  
Diphenyl- $\beta$ -picryl-hydrazyl (DPPH) molecule  
  charge density, 62*f*  
  spin density, 62*f*  
Directional solidification—*See* Cellular solidification, Solidification microstructure
- DNA**  
  conformation, salt effects, 103  
  counterion motions, aqueous salt solutions, 6  
  hydration structure of water molecules, 253  
  solutions, molecular dynamics study, 251–253  
  structural transitions, ionic effects, 103
- Doped polyacetylene  
  IR active modes, 154  
  mutual exclusion of IR and Raman lines, 150
- Drugs, computer-aided design, 5  
Dynamics, computational aspects, 284–293
- E**
- ECEPP, program, 140,141*f*,142*f*
- Effective viscosity  
  couette flow, 267–268  
  inhomogeneous fluids, 280
- Electron correlation, ingredient for accurate molecular calculations, 148
- Electron density, density functional theory, 50
- Electronic components, process modeling, 353–354
- Electronic materials, processing, 353
- Electronic structure  
  calculations on very large systems, 35–46  
  DPPH radical, 60  
  supercomputer research, 3–5  
  Energy, conservation of, CVD reactor, 337
- Energy distribution, molecular dynamics simulation of a peptide, 143*f*
- Energy gradients, calculation, 148
- Energy surfaces  
  *ab initio* calculations, 201–211  
  reaction of chloride with acetyl and formyl chloride, 206–207
- Energy time series, molecular dynamics simulations, 137
- Energy transfer, simplest models, 177
- Enskog theory, transport, 262–266
- Entropy of fusion, crystal growth, 226
- EPISODE, 371
- Equilibrium properties  
  derivation from molecular dynamics, 109  
  supercomputer research, 5–7
- Equilibrium theory, fluid structure, 258–261
- Ethylene  
  bond angles, 59*t*  
  bond lengths, 58,59*t*  
  rotational barrier, 57–58
- Euler variational calculus, 381
- Extinction  
  counterflow premixed laminar flames, 404–417  
  lean and rich, 416–417
- Extinction curve, hydrogen–air flames, 414
- F**
- FASTRUN, interface with GEMM, 130
- FASTRUN project, 124
- Fermi level, W(001) surfaces, 55
- Fickian diffusion, MOCVD, 357
- Film–substrate potential, relative strength, 230
- Filtration combustion process  
  one-dimensional formulation, 384,385*f*  
  oscillatory behavior, 384  
  planar combustion fronts, 384–391  
  synthesis of nitrogen ceramics, 383–402
- Finite range problem, atomic modeling of polymers, 164
- Fixed mesh, definition, 377–378

Fixed-point formulation  
 description, 284–285  
 location of a nonchaotic solution, 291  
 Flame fronts, resolution, 12  
 Flow  
 dilute solutions of  $^3\text{He}$  in superfluid  $^4\text{He}$ , 289  
 MOCVD reactors, 356,364,374  
 Flow systems, couette flow  
 simulations, 275–280  
 Fluid density, molecular dynamics  
 simulations, 270  
 Fluid dynamics, description, 249  
 Fluid flow  
 mach number, 376  
 past an obstacle, 250  
 supercomputer use, 8–9  
 Fluid–fluid intermolecular potential,  
 equilibrium theory of fluid  
 structure, 260  
 Fluid mechanical problem, CVD  
 reactor, 335–340  
 Fluid structure, equilibrium theory, 258–261  
 Fluid transport  
 Chemkin package, 350  
 modeling in CVD reactors, 334–350  
 Fluids  
 confined in micropores, 257–258  
 Enskog theory of transport, 262–266  
 estimates of the diffusivity and  
 viscosity, 262  
 structure, transport, and flow in  
 micropores, 257–258  
*See also* Bulk fluid, Micropore fluid  
 Fluorine molecule  
 bond lengths, 59f  
 Hartree–Fock theory, 58  
 LDF approach, 58–59  
 vibrational frequencies, 59f  
 Formaldehyde, reaction with  
 hydroxide, 211–215  
 Formyl fluoride, reaction with fluoride  
 ion, 209–211  
 FORTRAN, 160,239,348–350  
 FORTRAN 77, 162,168  
 Fourier transform, velocity autocorrelation  
 function, 246  
 FPS–164, processors, 238–239  
 FPS–264, processors, 239  
 FPS–X64, processors, 159  
 Free energy, determination, 110–112  
 Front phenomena, numerical  
 resolution, 376–403  
 Front problem, adaptive grid  
 transformation, 379  
 Fuels, combustion, 12  
 Full-potential linearized augmented plane  
 wave (FLAPW) method, 52–53

## G

GaAs  
 effect of inlet flow rates, 365f  
 effect of reactor shapes, 366f  
 effect of susceptor rotation speeds, 368f  
 growth by MOCVD, 353–374  
 Galerkin finite element method, 358,359  
 Galerkin formulation, 309  
 Gas-phase displacement reactions,  
 nucleophiles with acyl halides, 206–209  
 Gas-phase subroutine library, Chemkin  
 software, 348–350  
 Gaussian/82 program, 202  
 GEMM  
 features, 128  
 future directions, 130  
 goals, 127  
 performance, 129  
 system description, 124  
 timings for each section of code, 129f  
 Gibbs–Thompson condition, 301–303,308  
 Global bifurcations  
 classifications, 293  
 complex dynamic behavior, 291  
 definition, 291  
 Global simulation, definition, 239  
 Global simulation approach  
 computational chemistry, 237–254  
 description, 238  
 rules, 240  
 Gould 32/8750, 201  
 Graphite, fragments of  $D_{6h}$  symmetry, 39f  
 Graphite clusters, energy per carbon  
 atom, 40  
 Graphite fragments, carbon clusters, 37–38  
 Grashof number, 338  
 Green–Kubo formula, diffusivity under  
 flow, 269  
 Grid generation, methods, 377–378  
 Growth rate, vertical MOCVD reactors, 364

## H

Hamiltonian, 95  
 Hartree–Fock contribution, three-body  
 correction, 242  
 Hartree–Fock description, transition-metal  
 diatomics, 19  
 Hartree–Fock theory  
 advantage, 36  
 description, 19,148,240  
 fluorine molecule, 58  
 limitations, 49–50  
 quantum chemical approaches, 49  
 Slater determinant, 50  
 solutions to equations, 4  
*See also* Restricted Hartree–Fock method

Heat balance, gas–solid system, 383  
Heisenberg equation of motion, 98  
Helmholtz free energy, diffusive systems, 110  
HF, collisions, 177–178  
HF–HF collisions, two-dimensional cuts through the potential energy surface, 185–189f  
Hildebrand solubility parameter, 168  
HOMO orbital energies, 40–42,45f  
Homoclinic tangency, 291  
HONDO, 160  
Hopf bifurcation, 315,320  
Hydrodynamic limit, water, 246–249  
Hydrogen–air flame  
  adiabatic flame temperature, 416  
  distance of flame from symmetry plane versus the equivalence ratio, 418f  
  extinction curves, 415f  
  species profiles, 415f  
  temperature profile, 413f,414  
  velocity profile, 413f  
Hydrogen–air reaction mechanism, 414t  
Hydroxide  
  reaction with formaldehyde, 211–215  
  reaction with methyl formate, 201–206

## I

IBM 308X processor, 159  
IBM 3090, 129t,237  
IBM 4381, 239  
Ignition point, hydrogen–air flames, 416  
Inelastic transition probabilities, potentials as functions of relative transitional energy, 192t  
Inertial manifolds, Kuramoto–Shivashinsky equation, 285  
Inhomogeneous fluid  
  effective viscosity, 280  
  relationship between density distribution and pair correlation function, 258–259  
Initial value problem  
  algorithms for integration, 285  
  description, 291  
  invariant manifolds, 292  
Input–output subsystem, ST–100, 125,127  
Interaction energy functions, poly(vinyl chloride), 167  
Interaction potential, space-fixed coordinate system, 183  
Interface shapes  
  families, 321f  
  microstructure solidification, 314f,318f  
  time-periodic interaction cycle, 323f  
Interface velocity  
  liquid atoms, 228  
  nickel dendrites, 228–229

Interfaces  
  adatom density versus temperature, 222  
  competition between different sites for liquid atoms, 229  
  influence of surface roughening, 222–225  
  molecular dynamics studies, 221–225  
  interfacial phenomena, field for supercomputation, 7  
  Internal degrees of freedom, macromolecular systems, 162  
  Invariant imbedding procedure, description, 191  
  Invariant manifold computation, 291–293  
  Ionization potential, buckminsterfullerene, 44  
  IR intensities  
    analysis of polyacetylene, 152  
    C<sub>5</sub>H<sub>7</sub> to C<sub>11</sub>H<sub>13</sub><sup>+</sup>, 157t  
    isolated polyacetylene, 149–159  
  IR vibrational line shapes, calculation of moments, 96–98  
  Irving–Kirkwood formula, 269–270  
  Ising model, complex surface structures, 221  
  Ising model simulations  
    growth rate as function of driving force, 223f  
    surfaces observed, 219  
  Ising model surfaces, produced by computer simulations, 220f

## J

Jacobian, arc-length continuation method, 411

## K

Kuramoto–Shivashinsky equation, dynamic behavior, 285–288

## L

Lac repressor  
  manual reorientation of a backbone loop, 114f  
  restrained dynamics, 113  
  structure in solution, 116f  
Langevin dynamics, 130  
Lateral diffusion coefficients, bilayer membrane components, 117  
Lattice defects, Lennard–Jones crystal, 229  
Lennard–Jones liquid, low temperature, 226–228  
Lennard–Jones potential  
  attraction part, 260  
  two-body term, 26

- Leucine residues, order parameters, 84–86
- Lewis number, role in behavior of the flames near extinction, 412
- Liquids, molecular mechanics potentials, 82–83
- Local average density model (LADM) correlation between the velocity and density profiles of micropore liquid, 277
- effective viscosity for plane couette flow, 279
- transport, 261–262
- Local density approximation, 51
- Local density functional (LDF) Hamiltonian, matrix elements, 53
- Local density functional (LDF) theory application range, 65
- Cu and Ag on Si(111) surfaces, 60–63
- description of the C–C bond, 57
- disadvantage, 65–66
- effective potential, 51
- fluorine molecule, 58–59
- metallic tungsten, 54
- molecular systems, 53–54
- prediction of surface geometries, 57
- single slab geometry, 52
- surfaces and molecules, 49–66
- Local fluid density, calculation, 266–267
- Loosely coupled array of attached processors (LCAP), 159–160, 239
- Low-energy electron diffraction (LEED) pattern, W(001) surface, 54
- LUMO orbital energies, 40–42, 44f, 45f
- M**
- Macromolecular simulations, difficulty, 83
- Macromolecular systems, simulations, 162–173
- Macromolecule, determining the partition coefficient, 169
- Macros, nonbond energy evaluation, 128–129
- Mass, conservation of, CVD reactor, 337
- Mass flux, gas-phase, CVD reactor, 343
- Mass spectrometry, carbon cluster, 35–36
- Mass transport, rate, 222–225
- Materials processing modeling goals, 11–12
- supercomputer simulations, 8
- Materials research forefront of science, 146–147
- supercomputer use, 3–5
- Maxwell velocity distribution function, 263
- Membrane bilayer density distribution, 119f
- equilibrated simulation, 118f
- Memory LCAP supercomputer, 159–160
- size, 2
- ST-100, 125, 127
- Mesh determination in strained premixed laminar flame model, 409–410
- generation methods, 377–378
- Metal adsorbate bond lengths, Be and Al clusters, 31f
- Metal chemistry, theoretical approaches, 16–32
- Metal clusters adsorbates, 28–29
- Be and Cu, 27–28
- chemistry, 3–4
- methodological advances, 18–19
- size, 24
- small, 17
- See also* Clusters
- Metals, cellular and dendritic morphologies, 295
- Methyl formate, reaction with hydroxide ion, 201–206
- Micropore fluid correlation between velocity and density profiles, 277–279
- couette flow, 280f
- density profile, 269, 275
- flow, 257–258
- local average density profile, 275
- shear rate, 279
- shear stress, 279–280
- See also* Bulk fluid, Fluids
- Microscopic dynamics, supercomputer research, 7–9
- Microstructure, formation in directional solidification, 328
- Microstructure solidification cell shapes, 329f
- deep cell mapping, 311
- role in microstructure solidification, 324–328
- time scale dynamics associated with increased sample size, 320–323
- Minimum image problem, atomic modeling, 163–168
- Mixture continuity, CVD near an infinite rotating disk, 340
- Molecular dynamics biologically important processes, 82
- calculations complex surface structures, 221
- solidification at a crystal–melt interface, 225
- velocity of crystal–melt interface versus temperature, 227f
- compound with molecular theoretical results, 270–275
- computational aspects, 108–109
- conformational analysis, 140
- couette flow simulation, 267–270
- crystal–vapor interface region, 235–236

Molecular dynamics— *Continued*

derivation of relevant properties, 109–110  
description, 108  
equilibrium simulation, 266–267  
interpretation of NMR data, 112–115  
limits of applicability, 117  
modeling, fluid systems, 249–253  
neighbor tables, 163  
overlap with fluid dynamics, 249–251  
proteins and peptides, 123–144  
simulations  
  6–12 Lennard–Jones fluid in a slit pore, 270  
  biopolymers, 82  
  carboxy-myoglobin, 133  
  complex molecular systems, 106–120  
  configurations of thin films, 235  
  energy time series, 137  
  long-range truncation of proteins, 131–133  
  RMS deviation, 133–137  
  ST-100, 125  
  time behavior for conformational analysis, 142  
  solvation force of confined fluid, 272  
  studies  
    crystal growth and thin films, 218–236  
    DNA solutions, 251–253  
    interfaces, 221–225  
    supercomputer simulation time, 108–109  
    supercomputer use, 6, 123–124  
  *See also* Small molecule gas-phase dynamics  
Molecular self-consistent field methods, use, 147  
Molecular systems, description, 106  
Molecular theory, structure and transport, 258–266  
Molecules, LDF theory, 49–66  
Moller–Plesset perturbation theory use, 346  
  *See also* Perturbation theory  
Monte Carlo method  
  description, 6  
  determining the partition coefficient, 169–170  
  evaluation of chain partitioning, 172*f*  
  free energy profile for reaction path, 211–212  
  freely jointed chains, 169–173  
  solvation effects, 212  
  vibrational spectra calculations, 92–93  
Moving meshes, 378  
Multiple processors, use, 1  
Multireference singles plus doubles configuration interaction, 18  
Myoglobin, multiple conformational states, 86

## N

Navier–Stokes equations, 337  
Neighbor tables, molecular dynamics, 163  
Networking, advances, 2  
Neutral stability curves, microstructure solidification, 305  
Neutral stability  
  diagrams, 306–307*f*, 311, 312*f*  
Neutron scattering, simulation, 8  
Newton algorithm, damped modified, 343  
Newton iteration, use, 309  
Newton's method, 405, 409  
Newton–Raphson iteration, Galerkin finite element discretization, 359  
Nickel dendrites, interface velocities, 228–229  
NiH, ground state, 19  
Nitrogen ceramics, filtration combustion process, 383  
NMR  
  angular correlation function, decay, 86  
  molecular dynamics applications, 112–115  
  order parameters, convergence characteristics, 84–86  
NMR relaxation  
  contribution of internal protein motions, 84  
  proteins, 83–86  
Nonbond energy  
  evaluation, macros, 128–129  
  GEMM generation, 128  
Nonbond list, GEMM generation, 128  
Nonlinear models, computational demands, 10  
Nonlinear optical properties  
  polydiacetylenes, 147  
  supercomputer use, 4  
Nonlinear phenomena, 276–377  
Nuclear Overhauser effect, 112–113  
Nucleation, two-dimensional, 219  
Nucleophilic reactions, carbonyl compounds, 200–215  
Numerical analysis  
  cellular solidification microstructures, 295–330  
  continuum solidification models, 308–311  
Numerical resolution, front phenomena by regridding techniques, 376, 381–382  
Numerical results, strained premixed laminar flames, 412–417  
Nusselt number, 367, 369*f*–370*f*

O

Octapeptide simulations, structure, 141*f*  
Oligonucleotides, restrained dynamics, 113  
Organic reaction mechanisms, modern theoretical methods, 201

- Organometallic chemical vapor deposition (MOCVD)  
 common reactions, 354  
 numerical solution of models, 358–361  
 transport phenomena, 353–374
- Organometallic chemical vapor deposition (MOCVD) reactors  
 configurations, 354,355f  
 flow structures, 354–356  
 horizontal, 361–362  
 modeling equations, 356–358  
 shapes, 364  
 usefulness of a particular film, 354–356  
 vertical, 360f,362–367
- Ornstein–Zernike-type integral equation, solvent structure of polar liquids, 100–101
- P**
- Pair-additive potentials, application, 107
- Pair correlation function, approximation, 259
- Pair interactions, poly(vinyl chloride), 167
- Pancreatic trypsin inhibitor, molecular dynamics simulation, 84
- Parallel computing systems, 236–237
- Parallel processing, practical characteristics, 238
- PARAM19, 133
- Partial differential equations  
 modeling of steady-state problems, 404  
 nonlinear, 284  
 supercomputer solutions, 9–10
- Partition coefficient, freely jointed chains, 171f
- Peclet number, 303–305,324,376
- Peptides  
 conformational exploration, 137–144  
 lymphocyte response, 140  
 molecular dynamics, 123–144  
 potential energy as a function of time, 141f  
 potential energy of minimized structures, 142f
- Perturbation theory  
 basis for RB and RBST potentials, 179  
 computation of correlation energies, 207  
*See also* Moller–Plesset perturbation theory
- Phosphates, temperature factors, 89
- Physical processes, mathematical models, 376
- Planar combustion fronts, filtration  
 combustion process, 384–391
- Poincare sections, Rayleigh–Benard convection, 289–291
- Pollutants, environmental modeling, 12
- Poly(vinyl chloride)  
 atomic modeling, 166–168  
 microstructure, 171f  
 minimized microstructure, 167  
 unit cells, 166
- Polyacetylene  
 bipolaron description of defects, 157  
 bipolaron models, 149  
 clusters, IR active frequencies and relative intensities, 152f  
 convergence of  $\pi$  orbital energies with cluster size, 150  
 description, 147  
 doped, models, 152–159  
 experimental frequencies, 150f  
 isolated model, 150–152
- Polydiacetylene, description, 147
- Polymers  
 detailed atomistic modeling, 163–168  
 molecular electronics and photonics, 146–160  
 quantum mechanical simulations, 146–160
- Pore average flux, self-diffusion, 263–264
- Pore diffusivity  
 calculated from the equilibrium density distribution function, 264  
 LADM, 261
- Pore radius, effect on partition coefficient calculation, 170
- Potential  
 Alexander–DePristo (AD)  
 definition, 192  
 difference from other potentials, 193  
 rigid-rotator transition probabilities, 192f
- Brojjer–Murrell (BM), rigid-rotator transition probabilities, 192f
- modified AD  
 calculations, 197  
 vibrational force on the repulsive wall, 184
- RBST  
 definition, 192  
 difference from RB potential, 183–184  
 rigid-rotator transition probabilities, 192f  
 vibrational force on the repulsive wall, 184
- Redmon–Binkley (RB)  
 calculations, 197  
 difference from MAD potential results, 198  
 dilute solutions of  $^3\text{He}$  in superfluid  $^4\text{He}$ , 289  
 rigid-rotator transition probabilities, 192f  
 small aspect ratio, 289–291

- Potential energy contours, two-dimensional cuts through potential energy surfaces, 184
- Potential energy function, HF-HF collisions, 178
- Potential energy surfaces  
collision of two molecules, 176-198  
HF-HF collisions, 178-184  
Redmon-Binkley (RB), quantum mechanical values, 194  
vibrating rotator case, 184
- Potential field, reliable description, 107
- Prandtl number, 376
- Premixed flames, stagnation point flow, 412
- Premixed hydrogen-air flames, extinction behavior, 412-417
- Proteins  
dynamics, effects of long-range cutoffs, 131-137  
molecular dynamics, 123-144  
restrained dynamics, 113  
timings per iteration for ST-100, 130f
- Proton-transfer process, reaction of hydroxide with methyl formate, 206
- Pulsating wave solution, structure, 288f
- Pulsating waves, Kuramoto-Shivashinsky equation, 286,287
- Q**
- Quantum effects, vibrational spectrum, 98
- Quantum mechanics  
collision of two molecules, 176-198  
prediction of properties of a molecular liquid, 240-243
- Quartic oscillator, results for quantum moments, 97,99f
- Quasiharmonic frequencies, butane, 93
- Quasiharmonic oscillator model, vibrational analysis, 93
- R**
- Radial momentum  
conservation of, CVD reactor, 337  
CVD near an infinite rotating disk, 340
- Reacting surface, strained premixed laminar flames, 405
- Reaction profile, reaction of hydroxide with methyl formate, 202
- Regriding techniques  
basic idea, 377  
front phenomena, 376-403
- Reorientational relaxation times, calculation, 245
- Reservoir simulation, supercomputer use, 12-13
- Restrained dynamics, lac repressor, 113
- Restrained X-ray refinement  
DNA molecular dynamics trajectories, 89-92  
simulation from molecular dynamics trajectories, 87
- Restricted Hartree-Fock method  
advantages, 36  
*See also* Hartree-Fock theory
- Restricted pair interaction, computer performance, 124
- Restricted pore average density, 271-272
- Reynolds number, 250,338,376
- RIDGE 3200, performance on minimization problem, 168f
- Rigid-rotator calculations, HF, 191-194
- Rigid-rotator dynamics, calculations, 179
- Rigid-rotator HF-HF collisions, body frame expansion coefficients, 180-182f
- Rigid-rotator interaction potential, expanded, 179
- Rigid-rotator transition probabilities, 192f,194f
- RISM integral equation, solute-solvent interactions, 101
- Riveros complex, 206
- Riveros reaction, single-well energy surface, 206
- Root mean squared (RMS) deviation  
molecular dynamics simulation, 133-137  
switching function, 137
- Rotating-disk CVD reactor, use, 335
- Rotating waves  
Kuramoto-Shivashinsky equation, 286  
linearized stability analysis, 286
- Rotational anisotropy, simplified, 193
- Rotational energy, collision of two molecules, 176-198
- Rotational excitation probability, 195,196f
- S**
- Saddle computation, 291-293
- Scaled-particle theory, cavity free energy, 111
- Scattering theory, goal, 177
- Schrödinger equation  
one particle, 51  
solutions, 8
- Science, computational vs. experimental, 5
- Screening algorithm, efficiency, 166
- Second generation algorithms, fixed-point formulation, 292-293
- Second virial coefficients,
- Selectivity refined mesh algorithm, 378
- Self-consistent field (SCF) calculations  
 $Al_{13}$ , 26  
basis for AD and BM potentials, 179
- Self-consistent field (SCF) level chemisorption on an  $Al_{13}$  cluster, 29
- interaction of  $Be_4$  with the  $Cu_{18}$  cluster, 28

- Self-consistent field (SCF) method, description, 147
- Self-diffusion coefficient, calculated for the three-body potential for liquid water, 245
- Semiconductors  
 alloys, cellular and dendritic morphologies, 295  
 direct simulation of molecular beam epitaxy, 8  
 growth of compound semiconductors and superlattices, 353-374  
 thin-film growth, 11
- Shallow cells, role of codimension-two bifurcations, 311-320
- Shear rate  
 couette flow, 268  
 flow effect on diffusivity, 275
- Shear stress  
 calculation for couette flow, 269-270  
 couette flow simulations, 279-280
- Shifted potential, truncation method, 132
- Si(111) surface, Cu and Ag, 60-63
- Silicon  
 deposition from silane, 343-344  
 maximum crystal growth rate, 228
- Silver  
 adsorption geometry on Si(111) surface, 63  
 reactions on silicon surfaces, 60-63
- Simple point charge model, water, 115
- Simulation algorithms, problems with noninvertible maps, 292
- Simulations, macromolecular systems, 162-173
- Singlet-triplet splitting, computation, 4-5
- Site-site potentials, liquid water, 107
- Slater determinant, 50,148
- Small molecule gas-phase dynamics  
 role of the supercomputer, 7-8  
*See also* Molecular dynamics
- Small molecules, calculations, 20-24
- SN<sub>2</sub> reaction, hydroxide ion with methyl formate, 206
- Software, chemical kinetics and transport, 346-350
- Solidification  
 mechanism for pattern selection, 298  
 relationship between material processing parameters and solid-state structure, 296
- Solidification microstructure  
 goal of modeling, 298  
 length scales, 298  
 model, 301-308  
 numerical analysis, 295-330  
*See also* Cellular solidification
- Solidification systems, understanding the dynamics, 328-330
- Solutal equilibrium, solutal model, 303
- Solutal model  
 dimensionless values of parameters, 304f  
 mathematical statement, 302f  
 solidification microstructure, 301  
 solutal equilibrium, 303  
 stability of a planar interface to small perturbations, 303  
 surface energy, 303
- Solution space, structure, 10
- Solutions, kinetics of simple reactions, 7
- Solvation  
 biopolymers, 100-103  
 confined fluid, 272  
 effect on the gas-phase energy surfaces, 201  
 importance on reaction surfaces, 211-215  
 micropore fluid, 260-261
- Solvent, influence on entropy, 111
- Solvent effects  
 biopolymer simulations, 83  
 reaction of hydroxide with formaldehyde, 215
- Species continuity, CVD near an infinite rotating disk, 342
- Spin density  
 DPPH molecule, 61f  
 DPPH radical, 60
- Spin density populations, 38,39,41f
- ST-100  
 advantage, 131  
 arithmetic floating point operations, 127  
 CHARMM performance, 129f  
 description, 124-131  
 typical application, 126f
- Standing wave, transition to a rotating wave, 286
- Statistical mechanics  
 complex molecular systems, 107  
 prediction of properties of a molecular liquid, 243-246
- Stillinger-Weber potential, silicon, 225
- Stochastic dynamics, 117,328
- Storage move processor (SMP), ST-100, 125
- Strain, thin-film systems, 235
- Strain rate  
 extinction, premixed hydrogen-air flames, 412-416  
 flame, 406
- Strained premixed laminar flames  
 model solutions, 409-410  
 reacting surfaces, 405  
 role in theories of turbulent premixed combustion, 405-406  
 stagnation point flow configuration, 407f  
*See also* Counterflow premixed laminar flames
- Stranski-Krastanov growth mode, 231,234
- Stress tensor, LADM, 261-262



- Structure factors, DNA molecular dynamics trajectories, 88
- Substrates, formation of thick films, 234
- SUN 3/160M, performance on minimization problem, 168f
- Superbox algorithm  
modified, 164–166  
two-dimensional implementation, 165f
- Supercomputers  
calculation of thermochemical properties, 344–345  
equilibrium chain partitioning, 173  
humanitarian applications, 5  
materials with nonlinear optical properties, 4  
modeling fluid transport and chemical kinetics, 334–350  
parallel machines, 348  
performance, 168,237  
price–performance ratio, 108  
processors, 1,238  
research, 1–13  
scalar problem, 173  
simulation time, 108
- Superlattice growth  
compound semiconductors and superlattices, 353–374  
heterojunction interfaces, 374  
simulation, 367–371
- Surface, extension to include vibration processes, 179–183
- Surface energy  
cell length in microstructure solidification, 330  
numerical studies, 300  
solutal model, 303
- Surfaces  
diffusion coefficient, 224f  
LDF theory, 49–66
- Switching function  
potential energy of the cutoff potentials, 138–139f  
RMS deviation, 137  
truncation method, 132
- T**
- Temperature  
effect on clusters, 219  
effect on DNA molecular dynamics trajectories, 92  
effect on surface transport, 221–222  
flame extinction studies, 411  
model predictions in MOCVD reactors, 374
- Temperature factors  
phosphates, 89  
X-ray refinement, 89
- Temperature field, solutal model, 301
- Temperature profiles, filtration combustion process, 384,385f
- Thermal diffusion, CVD problems, 342
- Thermal factor, X-ray refinement, 89–92
- Thiele modulus, 376
- Thin films  
density, 233–234  
epitaxial growth, 230  
equilibrium or metastable configurations, 230  
misfit dislocations, 231–233  
molecular dynamics studies, 218–236  
transient behavior in growth, 11  
two-dimensional condensation, 7–8  
uniform, 234  
weak bonding between substrate and film, 234
- Thin-film solidification, 297f,299f
- Time, molecular dynamics simulations, 108
- Time integration scheme, continuum solidification models, 309–311
- TIPS water model, 101
- Tracer diffusion, Chapman–Enskog method, 263–264
- Transition-metal atoms, molecular systems, 17
- Transition-metal molecules, methodological advances, 18–19
- Transition state, reaction of chloride with acetyl and formyl chloride, 206–207
- Transition-state theory, 120
- Transport coefficient, LADM, 261
- Transport phenomena  
growth of compound semiconductors and superlattices, 353–374  
modeling necessity, 356  
supercomputer research, 9–13  
vertical MOCVD reactors, 362–367
- Triatomic systems, modeling of larger clusters, 22
- Trimethoprim, binding constant to DHFR, 112
- Truncation  
electrostatic potential energy, 134f  
long-range forces in molecular simulations, 131–133  
potential energy of the cutoff potentials, 138–139f
- Tungsten—See W(001) surface
- Twinning, 229
- U**
- Unimodal steady states,  
Kuramoto–Shivashinsky equation, 286
- Unit cells, poly(vinyl chloride), 166
- V**
- Vaccine, supercomputer use, 5
- Vapor growth, molecular dynamics simulations, 225

- Variable quadratic reference system (VQRS)  
 Hamiltonian, 95  
 results on model potentials, 96–100  
 VAX 11/780, CHARMM performance, 129*t*  
 Vectorization  
 partition coefficient calculation, 170–173  
 performance improvement, 173*t*  
 Velocity autocorrelation function,  
 water, 246  
 Velocity profiles, couette flow  
 simulations, 277–279  
 Vibrating rotator calculations, 194–198  
 Vibrational analysis, quasiharmonic  
 oscillator model, 93  
 Vibrational energy, collision of two  
 molecules, 176–198  
 Vibrational frequencies  
 $C_2H_6$  to  $C_{12}H_{24}^{2+}$  clusters, 158*t*  
 $C_4H_6^+$  to  $C_{12}H_{14}^+$ , 157*t*  
 $C_5H_7^+$  and  $C_{12}H_{14}^{2+}$ , 159*t*  
 $C_{11}H_{13}$  and  $C_{12}H_{14}$ , 159*t*  
 fluorine molecule, 59*t*  
 SCF level of theory, 148  
 Vibrational line shapes, path integral  
 approaches, 100  
 Vibrational modes  
 $C_{11}H_{13}^+$ , 155*f*  
 $C_{12}H_{14}^+$ , 153*f*  
 $C_{12}H_{14}^{2+}$ , 156*f*  
 IR and Raman intensities, 148  
 Vibrational spectroscopy, molecular  
 mechanics studies of proteins, 92–100  
 Vibrational spectrum  
 quantum effects, 98  
 quartic oscillator, 99*t*  
 Vibrational-state populations, molecules of  
 a gas, 176  
 Virial coefficients, use, 242–243  
 Viscosity, couette flow simulations, 279–280  
 Volmer–Weber growth mode, 231  
 von Karman similarity transformation, 340
- W**
- W(001) surface  
 computational approaches, 54–57  
 density of states, 56*f*
- W(001) surface—*Continued*  
 single particle density, 56*f*  
 total energy per unit cell, 55*f*
- Water  
 dynamical properties, 245–246  
 Fourier transform of the density  
 correlation function, 246  
 geometry going from monomer to the liquid  
 state, 243  
 interaction of three molecules, 242  
 internal energy, 243–244  
 IR spectra, 246  
 modeling, fluid dynamic aspects and  
 macroscopic theory, 249–251  
 models, reorientational relaxation  
 times, 245*t*  
 simple point charge model, 115  
 stable dimer, 242
- Wave functions, single-particle, variational  
 expansion, 51–54
- Wavelength  
 dependence of cell depth, 327*f*  
 role in microstructure  
 solidification, 324–328
- Wetting, substrate in thin-film growth, 234
- Wigner–Seitz cell, 164
- X**
- X-ray crystallography  
 structure factor, 87–88  
*See also* Crystallography  
 X-ray intensities, liquid water, 243  
 X-ray refinement  
 biopolymers, 86–87  
 temperature factor, 89  
 thermal factor, 89–92
- Y**
- Yvon–Born–Green equation, 258,265